AD A079923

DDC FILE COPY

A

DYNAMICS RESEARCH CORPORATION

Report No. NADC-76097-30— V

R-2540 1273—Vol II

APPLICATION OF THE ESTIMATION-BEFORE-MODELING (EBM) SYSTEM IDENTIFICATION METHOD TO THE HIGH ANGLE OF ATTACK/SIDESLIP FLIGHT OF THE T-2C JET TRAINER AIRCRAFT.

VOLUME II. SIMULATION STUDY USING T-2C WIND TUNNEL MODEL DATA.

23 June 1978

H. [illegible] Holland

E. Kammer

Performed for:

Naval Air Development Center
Warminster, Pennsylvania 18974

Contract No. N62269-76-C-0342

Performed by:

Dynamics Research Corporation
60 Concord Street
Wilmington, Massachusetts 01887

Approved for Public Release: Distribution Unlimited

Unclassified

SECURITY CLASSIFICATION OF THIS PAGE (When Data Entered)

REPORT DOCUMENTATION PAGE		READ INSTRUCTIONS BEFORE COMPLETING FORM
1. REPORT NUMBER NADC-76097-30	2. GOVT ACCESSION NO.	3. RECIPIENT'S CATALOG NUMBER
4. TITLE (and Subtitle) Application of the Estimation-Before-Modeling (EBM) System Identification Method to High Angle-of-Attack/Sideslip Flight of the T-2C Jet Trainer Aircraft. Vol. II Simulation Study Using T-2C Wind Tunnel Model Data		5. TYPE OF REPORT & PERIOD COVERED Final Report 6. PERFORMING ORG. REPORT NUMBER 1273
7. AUTHOR(s) Authors: H.L. Stalford & S. Ramachandran		8. CONTRACT OR GRANT NUMBER(s) N62269-76-C-0342
9. PERFORMING ORGANIZATION NAME AND ADDRESS Dynamics Research Corporation 60 Concord Street, Wilmington, MA 01887		10. PROGRAM ELEMENT, PROJECT, TASK AREA & WORK UNIT NUMBERS
11. CONTROLLING OFFICE NAME AND ADDRESS Naval Air Development Center (Code 6053) Warminster, Pennsylvania 18974		12. REPORT DATE June 23, 1978 13. NUMBER OF PAGES 274
14. MONITORING AGENCY NAME & ADDRESS(if different from Controlling Office)		15. SECURITY CLASS. (of this report) Unclassified 15a. DECLASSIFICATION/DOWNGRADING SCHEDULE

16. DISTRIBUTION STATEMENT (of this Report)

Approved for Public Release; Distribution Unlimited

17. DISTRIBUTION STATEMENT (of the abstract entered in Block 20, if different from Report)

18. SUPPLEMENTARY NOTES

19. KEY WORDS (Continue on reverse side if necessary and identify by block number)

System Identification	Aircraft	EBM
Aerodynamic Derivatives	High Alpha	
Estimation	High Beta	
Modeling	Synthetic Data	

20. ABSTRACT (Continue on reverse side if necessary and identify by block number)

This report presents the results of a feasibility study of the Estimation-Before-Modeling (EBM) method for aerodynamic parameter identification in the stall/post stall flight regimes. The feasibility study is conducted by processing synthetic flight data generated by exciting a wind tunnel model of the Navy's T-2C, a light jet trainer aircraft. It is carried out under realistic conditions by using the controls and the initial conditions of sixteen actual T-2C flight → next page

DD FORM 1 JAN 73 1473 EDITION OF 1 NOV 65 IS OBSOLETE

Unclassified

SECURITY CLASSIFICATION OF THIS PAGE (When Data Entered)

test data records to generate the sixteen synthetic maneuvers used in the study. The synthetic data are corrupted by realistic measurement noise levels representative of the actual. The EBM method is a two stage process. In the first stage, the corrupted data are processed one maneuver at a time using an extended Kalman-Bucy filter/Bryson-Frazier smoother to obtain estimated values of the states and of the forces and moments acting on the aircraft. In the second stage, subspace modeling together with a step-wise multiple linear regression technique is used to process the estimated values from all sixteen maneuvers together in parallel to identify a global state/control dependent model of the three force coefficients and the three moment coefficients. The identified global model compares well with the true values of the T-2C wind tunnel model. The EBM method is demonstrated to accurately identify the high nonlinearities of the T-2C wind tunnel model. The prediction accuracy of the identified global model is shown to be excellent by a comparison of the responses for a new maneuver and for the original sixteen maneuvers.

FOREWORD

The work described in this report was sponsored by the Flight Dynamics Branch of the Air Vehicle Technology Department of the Naval Air Development Center. Mr. Robert L. Fortenbaugh, Mr. A. Piranian, Mr. Ronald L. Nave and Mr. John Clark served as the Navy Technical Monitors for the Naval Air Development Center. Mr. Carmen J. Mazza was NADC Program Manager.

The project was managed by Dr. Harold L. Stalford. The authors thank Professor James Rome, Lowell Univeristy, Lowell, Massachusetts who provided analytical support. Thanks are also extended to Mr. David Welsh, Mr. Joseph D. Mason, Ms. Christine Durand and Ms. Hedgie Brown who provided computational support.

TABLE OF CONTENTS

TABLE OF CONTENTS (Continued)

APPENDICES

LIST OF FIGURES

LIST OF FIGURES (Cont'd)

LIST OF FIGURES (Cont'd)

LIST OF TABLES

LIST OF TABLES (continued)

LIST OF SYMBOLS

Variable	Description	Units
$a_{x_{m_i}}$	Longitudinal acceleration measured along aircraft x-body axis at i, i = nose	(m/sec^2)
$a_{y_{m_i}}$	Lateral acceleration measured along aircraft y-body axis at i, i = cg, nose, tail	(m/sec^2)
$a_{z_{m_i}}$	Vertical acceleration measured along aircraft z-body axis at i, i = cg, nose, tail, R, L	(m/sec^2)
b	Reference wingspan	(m)
C_D	Drag Coefficient	
C_L	Lift Coefficient	
C_ℓ	Roll moment coefficient about x-body axis	
C_m	Pitch moment coefficient about y-body axis	
C_n	Yaw moment coefficient about z-body axis	
C_x	Axial force coefficient along x-body axis	
C_y	Side force coefficient along y-body axis	
C_{y_β}	$\delta C_y / \delta\beta$; Other combinations occur where y is changed to x, z, ℓ, m, n and β is changed to another state, to a control, or to $\dot{\alpha}$ or $\dot{\beta}$.	
$C_{y_{p\alpha}}$	$\delta^2 C_y / \delta p \delta\alpha$; Other combinations occur where y is changed to ℓ or n and p is changed to q or r.	
C_z	Normal force coefficient along z-body axis	
$\bar{c}$	Mean aerodynamic chord	(m)
g	Acceleration due to gravity = 9.806 m/sec^2	(m/sec^2)
h_{e_x}	Engine angular momentum about x-body axis	(Newton-m-sec)

Variable	Description	Units
I_x	Moment of inertia about x body axis	(kg m^2)
I_y	Moment of inertia about y body axis	(kg m^2)
I_z	Moment of inertia about z body axis	(kg m^2)
I_{xz}	Cross product of inertial about x, z body axes	(kg m^2)
L	Roll moment about x body axis	(Newton-m)
ℓ_x	Distance along x-axis between aerodynamic center and center of gravity (positive for AC forward of CG)	(m)
ℓ_z	Distance along z-axis between aerodynamic center and center of gravity (positive for AC below CG)	(m)
ℓ_{z_e}	Distance along z-axis between thrust axis and center of gravity (positive for T axis below CG)	(m)
M	Pitch moment about y body axis	(Newton-m)
m	Aircraft mass	(kg)
N	Yaw moment about z body axis	(Newton-m)
p	Aircraft x-body axis roll rate	(rad/sec)
q	Aircraft y-body axis pitch rate	(rad/sec)
r	Aircraft z-body axis yaw rate	(rad/sec)
S	Reference wing area	(m^2)
T	Total Thrust	(Newtons)
T_x	Thrust component along x body axis direction	(Newtons)
T_z	Thrust component along z body axis direction	(Newtons)
u	Speed along aircraft x-body axis with respect to a nonmoving free stream air mass	(m/sec)
V	Aircraft total air speed	(m/sec)
v	Speed along aircraft y-body axis with respect to a nonmoving free stream air mass	(m/sec)

Variable	Description	Units
w	Speed along aircraft z-body axis with respect to a nonmoving free stream air mass	(m/sec)
X	Longitudinal force along x-body axis	(Newtons)
x	Aircraft c.g. position along the longitudinal axis of earth fixed axes oriented with respect to aircraft body axes by Euler angles. Positive when c.g. is forward of axis system origin.	(m)
$\bar{x}_i$	Distance between c.g. and sensor i measured along x-body axis, i=α,β, V. Positive for sensor forward of c.g.	(m)
$\bar{x}_{x_i}$	Distance between c.g. and longitudinal accelerometer at i measured along x-body axis, i = NOSE. Positive for accelerometer forward of c.g.	(m)
$\bar{x}_{y_i}$	Distance between c.g. and lateral accelerometer at i measured along x-body axis, i = c.g., nose, tail. Positive for accelerometer forward of c.g.	(m)
$\bar{x}_{z_i}$	Distance between c.g. and vertical accelerometer at i measured along x-body axis, i = c.g. nose tail. Positive for accelerometer forward of c.g.	(m)
Y	Lateral force along y-body axis	(Newtons)
y	Aircraft c.g. position along the lateral axis of earth fixed axes oriented with respect to aircraft body axes oriented with respect to aircraft body axes by Euler angles. Positive when c.g. is right of axis system origin.	(m)
$\bar{y}_i$	Distance between c.g. and sensor i. Positive for sensor right of c.g.	(m)
$\bar{y}_{x_i}$	Distance between c.g. and longitudinal accelerometer at i measured along y-body axis, i = NOSE. Positive for accelerometer right of c.g.	(m)

Variable	Description	Units
$\bar{y}_{y_i}$	Distance between c.g. and lateral accelerometer at i measured along y-body axis, i = c.g., NOSE, TAIL. Positive for accelerometer right of c.g.	(m)
$\bar{y}_{z_i}$	Distance between c.g. and vertical accelerometer at i measured along y-body axis, i = CG, NOSE, TAIL, R.L. Positive for accelerometer right of c.g.	(m)
Z	Vertical force along z-body axis	(Newtons)
z	Aircraft c.g. position along the vertical axis of earth fixed axes oriented with respect to aircraft body axes by Euler angles. Positive when c.g. is below axis system origin.	(m)
$\bar{z}_i$	Distance between c.g. and sensor i measured along z-body axis, i = α, β, V. Positive for sensor below c.g.	(m)
$\bar{z}_{x_i}$	Distance between c.g. and longitudinal accelerometer at i measured along z-body axis, i = NOSE. Positive for accelerometer below c.g.	(m)
$\bar{z}_{y_i}$	Distance between c.g. and lateral accelerometer at i measured along z-body axis, i = CG, NOSE, TAIL. Positive for accelerometer below c.g.	(m)
$\bar{z}_{z_i}$	Distance between c.g. and vertical accelerometer at i measured along z-body axis, i = c.g., NOSE, TAIL, R,L. Positive for accelerometer below c.g.	(m)

α	Angle of attack	(rad)
$\dot{\alpha}$	Time derivative of α	(rad/sec)
β	Sideslip angle	(rad)
$\dot{\beta}$	Time derivative of β	(rad/sec)
δ_a	Aileron deflection (+ δ_a → left wing down roll)	(rad)
δ_e	Elevator deflection (+ δ_e → nose down pitch)	(rad)
δ_r	Rudder deflection (+ δ_r → nose left yaw)	(rad)
δ_a^+, δ_a^-, δ_r^+, δ_r^-	See Equations 4.5.5 and 4.5.6 for definition	
θ	Euler pitch angle	(rad)
ρ	Air density	(kg/m^3)
ϕ	Euler bank angle	(rad)
Ψ	Euler yaw angle	(rad)

LIST OF SUPERSCRIPTS

*	Denotes intermediate quantity

LIST OF SUBSCRIPTS

o	Denotes reference value
c.g.	Center of gravity
L	Left wingtip
m	Designates a measured quantity when used as a subscript
R	Right wingtip
s	Stability axes
NOSE	Nose
TAIL	Tail

1. INTRODUCTION

1.1 BACKGROUND

The inability of empirical and theoretical techniques to accurately predict the nonlinear aerodynamics of the high angle of attack/sideslip domain for aircraft has spurred interest in extracting these effects from actual flight data. Success in this endeavor will allow predicted effects to be correlated with the actual effects to determine the scaling, trending, reformulation, etc. that must be applied to the predictions to match the actual. Performing this correlation for several existing aircraft will build confidence in the designer's ability to predict the performance and stability and control characteristics of proposed aircraft.

The T-2C is a light jet trainer aircraft which has been instrumented and operated by the Naval Air Development Center (NADC) for the express purpose of producing high angle of attack flight data. The data along with a wind tunnel model of the T-2C has been supplied to Dynamics Research Corporation (DRC) for processing with an advanced system identification method called the Estimation-Before-Modeling (EBM) technique. The desired results of applying an extraction method such as the EBM technique to flight data are (1) optimal, smoothed, time history estimates of the vehicle state parameters and (2) state-dependent models for the coefficients of the forces and moments acting on the vehicle. The bottom line of such an application is whether the coefficient models can accurately predict vehicle motion for inputs different from those analyzed to develop the models.

The first phase of the processing of the T-2C data and wind tunnel model is a simulation study to check out the accuracy of the EBM technique using synthetic T-2C data. Such synthetic data are generated by exciting the T-2C wind tunnel model with the controls and initial states contained in the actual T-2C flight data records. In the second phase, the actual T-2C flight data are processed. This volume details the results of the first phase.

1.2 SCOPE OF SIMULATION STUDY

This study consists of the following four parts:

- Simulation
- Estimation
- Modeling
- Prediction

In the simulation part, sixteen maneuvers of synthetic T-2C flight data are generated by exciting NADC's T-2C wind tunnel model with the control time histories and the initial states of sixteen actual T-2C flight data records. The data are corrupted by the addition of white, zero-mean gaussian noise having realistic standard deviations. In the estimation part the corrupted data of the sixteen maneuvers are processed by a filter/smoother algorithm to provide estimates of the states and of the forces' and moments' time histories. In the modeling part, these estimates are processed by a stepwise multiple linear regression technique over a network of α, β subspaces to identify global state-dependent models for the coefficients of the forces and moments. The identified models are compared with their counterparts in the wind tunnel model. In the prediction part a new maneuver as well as the original sixteen maneuvers are used to test the accuracy of the identified model.

1.3 ESTIMATION-BEFORE-MODELING (EBM) APPROACH

The Estimation-Before-Modeling (EBM) technique is a two-step approach to system identification. The first step is the estimation of states and aerodynamic forces' and moments' time histories using a nonlinear estimator. In the second step, the state and control input space is divided into many small subspaces. Estimated states from all maneuvers that fall within a chosen subspace are used in modeling the force and moment coefficients over that subspace. For each subspace the state and control dependent model is obtained using Stepwise Multiple

Linear Regression (SMLR). The EBM approach provides the following benefits:

a. Estimation in the time domain provides better data for the modeling phase.

b. No a priori state-dependent model need to be selected to perform state estimation and the identification of aerodynamic derivatives.

c. Multiple maneuvers can be processed in parallel to identify aerodynamic derivatives with greater accuracy.

d. The global state-dependent modeling region can be subdivided into smaller regions, and the identification of aerodynamic derivatives can be performed within each region separately.

1.3.1 Estimation

The equations that describe the motion of an aircraft can be expressed as (i.e., see Appendix A):

$$\dot{x} = f(x) + B(t)$$

where x represents the 9-dimensional state vector $(u, v, w, p, q, r, \theta, \phi, z)$, $f(x)$ denotes the kinematic terms and $B(t) = (B_1(t), B_2(t), \ldots, B_6(t), 0, 0, 0)$ with $B_i(t)$ = acceleration in the x_i-direction due to forces and moments acting on the aircraft. The accelerations $B_i(t)$, $i = 1, 2, \ldots, 6$, are linear functions of the undimensionalized aerodynamic coefficients $C_x(t)$, $C_y(t)$, $C_z(t)$, $C_\ell(t)$, $C_m(t)$, and $C_n(t)$. These aerodynamic coefficients are unknown functions of the states α, β, p, q, r, $\dot{\alpha}$, $\dot{\beta}$, etc. and the controls δ_e, δ_a, δ_r. Since the models of $C_x, \ldots, C_n$ are unavailable, the accelerations $B(t)$, $i = 1, 2, \ldots, 6$, are necessarily unmodeled accelerations. The estimation problem of the first step is that of estimating the state of a nonlinear dynamical system in the presence of unmodeled accelerations.

One method of attack on the problem is the spline estimation method as outlined in Ramachandran, et. al. [1] and detailed in Schneider, et. al. [2].

The approach taken herein is to approximate the unmodeled accelerations $B_i(t)$, $i = 1, 2, \ldots, 6$, by Gauss-Markov processes and to apply an extended Kalman filter/Bryson-Frazier smoother. This method of approach is described in Appendix B.

1.3.2 MODELING

The estimated values of C_x, C_y, C_z, etc., along with the states and control inputs from the estimation phase, are further processed to remove the thrust and c.g. offset effects and converted to suitable form for the purpose of identification.

The steps involved in the model identification are outlined below. A few passes through all these steps are usually necessary to obtain a satisfactory global model.

Construction of Subspaces

The advantage of using subspaces for modeling is that we can determine the highly complex aircraft characteristics accurately, using only simple models. The first step in the model identification stage is the choice of subspaces. The force and moment coefficients are generally functions of several aerodynamic variables. Hence, it is first necessary to determine which independent variables will significantly affect the force or moment coefficient whose model we want to obtain. Here it is important to bear in mind that the objective is not just to arrive at a mathematical formula that will best fit the data at all points but to determine the aerodynamic characteristics of the airplane as accurately as possible. The selection of significant independent variables and the nature of their influence on the dependent variable will determine the choice of subregions. For example, from previous experience, available data on the airplane and engineering judgement it is known that for the given airplane C_m is influenced very strongly by α and δ_e, less strongly by β, by q in a linear fashion and very weakly by lateral controls. In this case the subspaces will be bound by α, δ_e and β, with small widths for α and δ_e and larger widths for β. Having settled upon the important variables and the choice of variables to define the boundaries for modeling subspaces, the boundaries for these regions can be chosen by the nature of the phenomenon being studied and known aircraft characteristics. For instance, if we are analyzing the aircraft behavior in the post stall regime, we may like to use very narrow regions for α right after stall and larger regions farther away from stall angle.

Also it is very important that the width of the subregion in each independent variable should be much greater than the standard deviations of the estimation error and measurement noise for that independent variable.

Having roughly determined the subspaces, the next step is to judge the adequacy of the data and the data density distribution in each region. This is done by simply determining the total number of data points that fall within each subspace using the data from all maneuvers. Only the maneuvers that give consistent and high quality results in the estimation stage are used in all stages of identification. A comparison of the total number of points in each subspace and the number of independent variables to be used in the model will give us an idea as to the sufficiency or scarcity of data for obtaining a model in each region. This will also help us to ascertain whether the subspaces and the type of model will have to be redefined. A high density may make it possible to use still narrower regions to obtain more accurate models with lower order models. Further refinements, where necessary, could be made based upon the quality of the identified model and the statistics of the independent variables in each subspace.

Selection of Independent Variables

The estimated state and control variable time histories obtained by the stochastic estimation method are used to compute the independent variables for the regression. It is possible to choose any desired number of independent variables as candidates for the model. Each independent variable is formed by combining one or more of the following terms or higher powers of them:

$$(\alpha - \alpha_o),\ (\beta - \beta_o),\ (\delta_e - \delta_{e_o}),\ (\delta_a - \delta_{a_o}),\ (\delta_r - \delta_{r_o}),\ \frac{pb}{2V},\ \frac{q\bar{c}}{2V},$$

$$\frac{rb}{2V},\ \frac{\dot{\alpha}\bar{c}}{2V},\ \text{and}\ \frac{\dot{\beta}b}{2V}.$$

Engineering judgment, known aerodynamic properties of the aircraft and the nature of the problem under investigation can be used to eliminate superflous terms.

Model Determination

To model a given coefficient its value along with the appropriate states and control inputs are chosen from all maneuvers if the corresponding α, β and control surface deflections fall within the chosen subspace. By using information from all maneuvers it can be ensured that maximum information is available for modeling.

The SMLR technique is employed in each subspace for several values of F-critical ratio and a model is determined for each F-critical ratio. The adequacy of a model is determined by: a) the mean and standard deviation of the dependent and independent variables in the subspace, b) the noise in the measurements, c) the statistics on the estimates of the states and forces from the stochastic filter, d) the F-ratio and standard deviation of each term of the determined model, e) the Residual Sum of Squares (RSS) and multiple correlation coefficient R^2, and f) engineering judgment.

The best model for a given region is obtained by applying the preceding considerations and analyzing the models obtained at each step of the regression for each F-critical value.

The aerodynamic parameters determined from all subspaces are assembled to provide the global model.

SECTION 2

T-2C WIND TUNNEL MODEL AND SYNTHETIC T-2C DATA

For the purpose of checking out the two step approach, synthetic data are generated from the wind tunnel model. The wind tunnel model was supplied by NADC [7]. Details of the wind tunnel model and the computation of the total aerodynamic force and moment coefficients along the aircraft body axes are given in Appendices A and D. The normal, axial and side forces are given by

$$X = \frac{1}{2}\rho V^2 S C_x + T\cos\xi_e \tag{2.1}$$

$$Y = \frac{1}{2}\rho V^2 S C_y \tag{2.2}$$

$$Z = \frac{1}{2}\rho V^2 S C_z - T\sin\xi_e \tag{2.3}$$

The angle ξ_e between the X force body axis and the thrust axis was supplied as zero. The roll, pitch and yaw moments are given by:

$$L = \frac{\rho V^2 S b}{2} C \tag{2.4}$$

$$M = \frac{\rho V^2 S \bar{c}}{2} C_m + \ell_z (X - T\cos\xi_e) - \ell_x (Z + T\sin\xi_e) + T\cos\xi_e \ell_{z_e} \tag{2.5}$$

$$N = \frac{\rho V^2 S b}{2} C_n \tag{2.6}$$

In order to help make the simulation be more like the real flight data, the mass, control inputs, trim velocity and trim altitude are taken to be the same as those used in the actual flight test of the airplane. The geometry of the aircraft, mass and inertia characteristics were furnished by NADC and are given in Appendix A. All the aircraft constants are the same for all maneuvers except the mass which is given for each individual maneuver. No thrust history was available nor the value of the distance between the aerodynamic center and the center of gravity. In view of possible discrepancies between the wind tunnel model and the actual aircraft it was necessary to calculate the trim angle of attack for the simulation. For each maneuver the trim angle of attack α_{trim}, trim thrust T_{trim}, and the distance between the center of gravity and aerodynamic center ℓ_x were calculated to satisfy the trim equations:

$$\dot{u} = \dot{v} = \dot{w} = \beta = p = q = r = \dot{p} = \dot{q} = \dot{r} = \phi = \delta_a = \delta_r = 0 \qquad (2.7)$$

$$\theta_{trim} = \alpha_{trim} \qquad (2.8)$$

Assumption of perfect trim and lateral symmetry of the given model were used to write the above equations.

The trim angle-of-attack to balance the forces in the vertical direction can be calculated by solving

$$\dot{w} = qu - pv + g \cos\theta \cos\phi + \frac{Z}{m} = 0 \qquad (2.9)$$

and equation (2.8) in an iterative fashion.

Having computed α_{trim}, the equation for $\dot{u}$, given below, is solved to compute T_{trim}.

$$\dot{u} = rv - qw - g\sin\theta + X/m = 0 \qquad (2.10)$$

With α_{trim} and T_{trim}, ℓ_x is computed by solving for

$$\dot{q} = \frac{1}{I_y}[M + pr(I_z - I_x) + (r^2 - p^2)I_{xz}] = 0 \qquad (2.11)$$

An inspection of the flight data revealed that for several maneuvers the aileron and rudder deflections were not zero but of small magnitude at trim. These values were treated as biases and subtracted from the flight time histories to give control inputs for the simulation.

As pointed out above the simulation checkout was to resemble as much as possible the system identification of an actual aircraft. For this reason the three controls δ_a, δ_e and δ_r together with the initial conditions of the states α, β, V, p, q, r, θ, ϕ and z were copied from actual flight data records and used in the generation of the synthetic data. Sixteen maneuvers of available T-2C actual flight test data were used for this purpose. These are summarized in Table 2-1. The first letter S of SF1M1 denotes synthetic, the F denotes flight number and the M denotes the maneuver number of that flight. The designation SF1M1 denotes that the controls and the initial conditions used to generate this synthetic maneuver were copied from maneuver 1 of flight 1 of the actual flight test data provided by NADC. The type of controls is described in the fourth column for each maneuver. Plots of the controls for all maneuvers are given in Appendix D.

Table 2-1 MANEUVERS USED IN THE STUDY

Maneuver No.	NADC* Flight No.	Approximate Duration of Maneuver (secs)	Type of Input	Comments
1	SF1M1	16	Aft stick, full rudder pedal	$\alpha_{max} = 35^{o}$, $\beta_{max} = 8^{o}$. High roll angular rates, roll departure
2	SF2M1	34	Random fore and aft stick	$\alpha_{max} = 30^{o}$, $\beta_{max} = 7^{o}$
3	SF2M2	35	Random side to side lateral stick	Low α, low β
4	SF2M3	45	Sequential doublets δ_e, δ_a, δ_r	$\alpha_{max} = 30^{o}$, $\beta_{max} = 14^{o}$ High angular rates
5	SF3M1	35	Longitudinal doublet	$\alpha_{max} = 25^{o}$. Insignificant lateral excitation
6	SF3M2	26	Random side to side rudder	Low α and β and small excitation of states
7	SF3M3	29	Sequential Random δ_e, δ_a, and δ_r	$\alpha_{max} = 20^{o}$, low β
8	SF4M1	21	Longitudinal stick ramp and sine waves	$\alpha_{max} = 30^{o}$, low β
9	SF4M2	74	Sequential random δ_e, δ_a, δ_r	$\alpha_{max} = 25^{o}$, $\beta_{max} = 20^{o}$ High angular rates. Roll departure

Table 2-1 MANEUVERS USED IN THE STUDY

Maneuver No.	NADC* Flight No.	Approximate Duration of Maneuver (secs)	Type of Input	Comments
10	SF4M3	49	Sequential random $\delta_e, \delta_a, \delta_r$	$\alpha_{max} = 25^o$, $\beta_{max} = 20^o$ Extremely high roll rate
11	SF4M5	60	Longitudinal limit cycle	$\alpha_{max} = 25^o$, $\beta_{max} = 15^o$
12	SF4M6	38	Shallow bank to stall	$\alpha_{max} = 30^o$, low β
13	SF4M7	45	Steep bank to stall	$\alpha_{max} = 34^o$, $\beta_{max} = 13^o$
14	SF4M8	41	Pull up from dive	$\alpha_{max} = 29^o$, low β
15	SF4M9	28	Coordinated control spin entry	$\alpha_{max} = 40^o$, $\beta_{max} = 20^o$ Large angular rates
16	SF4M10	27	Coordinated control spin entry	$\alpha_{max} = 46^o$, $\beta_{max} = 30^o$ Very high roll rate

* The number after SF indicates NADC flight number and the number after M indicates NADC maneuver number.

With the given aerodynamic model and the initial conditions calculated by the above mentioned procedure, the equations of motion were integrated while exciting the airplane with control inputs from flight test data for the chosen maneuver. When this was done, it was found that a few maneuvers diverged after a few seconds, and the responses for most maneuvers were totally different from actual flight data. The wind tunnel model exhibited frequencies and amplitudes that were very much higher than flight data. The plots within Figure 2.1 give a comparison between the response of the wind tunnel model and the aircraft for maneuver 15. It may be noticed that the aircraft motion did not go beyond an angle of attack of 25 degrees, exhibited small oscillations about the maximum and returned to trim value when the elevator was returned to trim setting, whereas the angle of attack for the wind tunnel model first reached a peak of 22 degrees and continued to grow with the amplitude reaching nearly 45 degrees. Even after the return of elevator angle the growth continued with the angle of attack going up to 60 degrees. An inspection of the lateral states reveals much larger magnitudes and a much greater degree of instability for the wind tunnel model.

Subsequently by a trial and error approach the aerodynamic tables were modified slightly to provide more reasonable responses. The modifications consisted of very small adjustments in the tables in the stall and the post stall regions and fixing the value of C_{n_p} at -0.06. The constant value of -.06 for C_{n_p} was found to give stability to the simulated data and to provide data which agreed better with the actual flight data. For example note the improvement in the response of the modified wind tunnel model of maneuver 15 as shown in Figure 2.2. For the modified case the state α and β return to trim values when the control inputs return to trim values. The rates p, q and r become small at trim control for the modified case whereas they continue to grow with large amplitudes for the original model. The maximum values of α, β, p, q, r, θ and ϕ are 40°, 20°, 120 deg/sec. 50 deg/sec, 30 deg/sec, 80° and 700°, respectively whereas for the original model they are 60°, 50°, 320 deg/sec, 80 deg/sec, 100 deg/sec, 160° and 1300°, respectively. The modified T-2C aerodynamic model was used as the basis for the simulation study

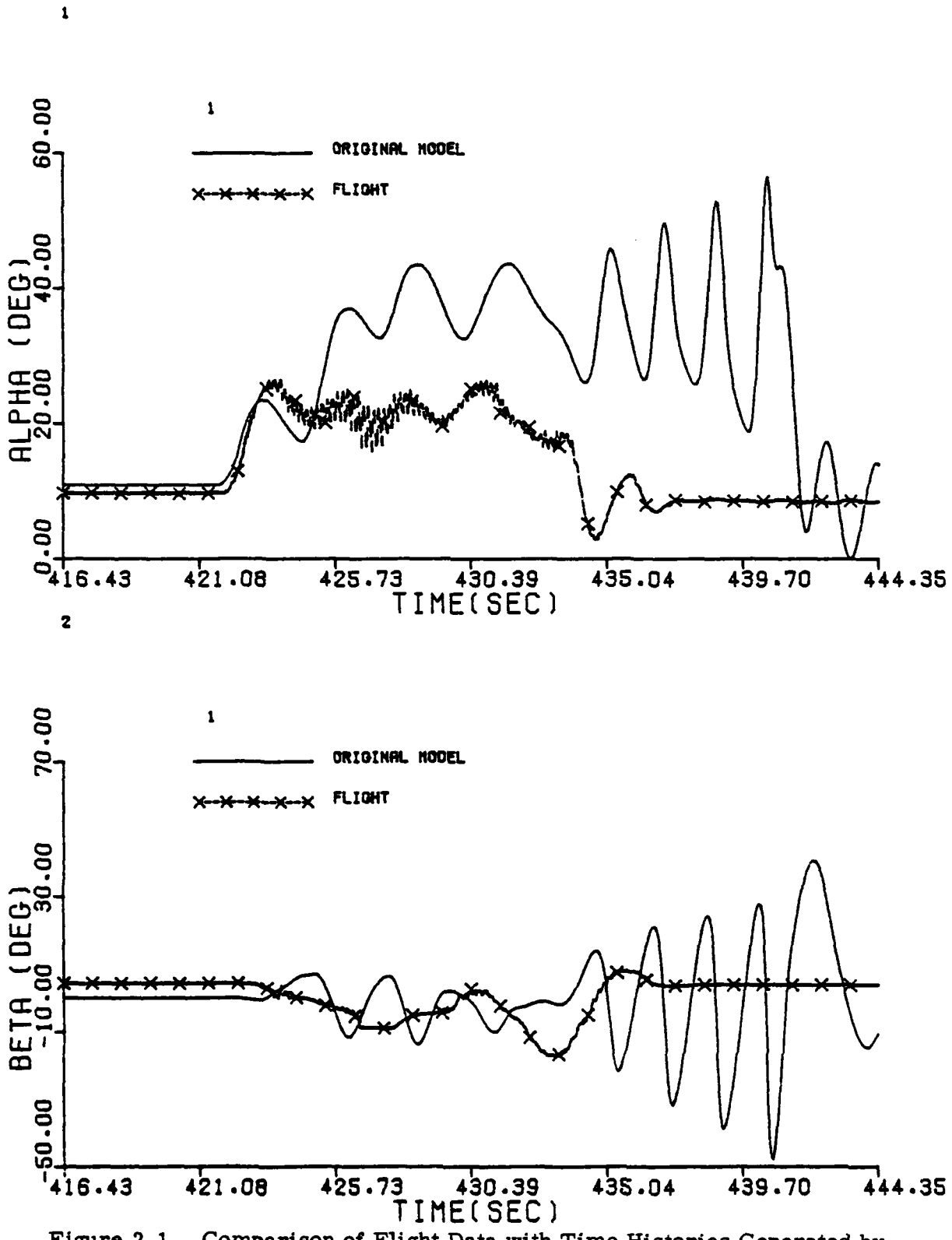

Figure 2.1 Comparison of Flight Data with Time Histories Generated by the Wind Tunnel Model

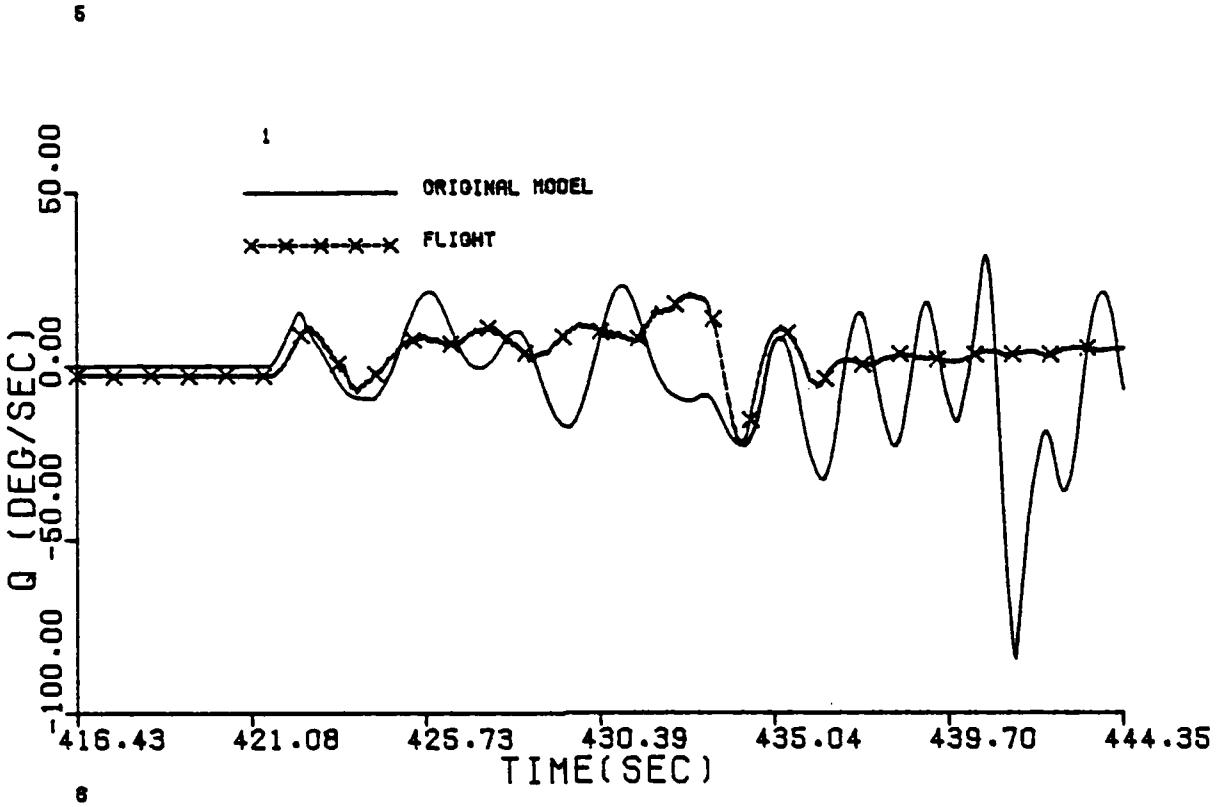

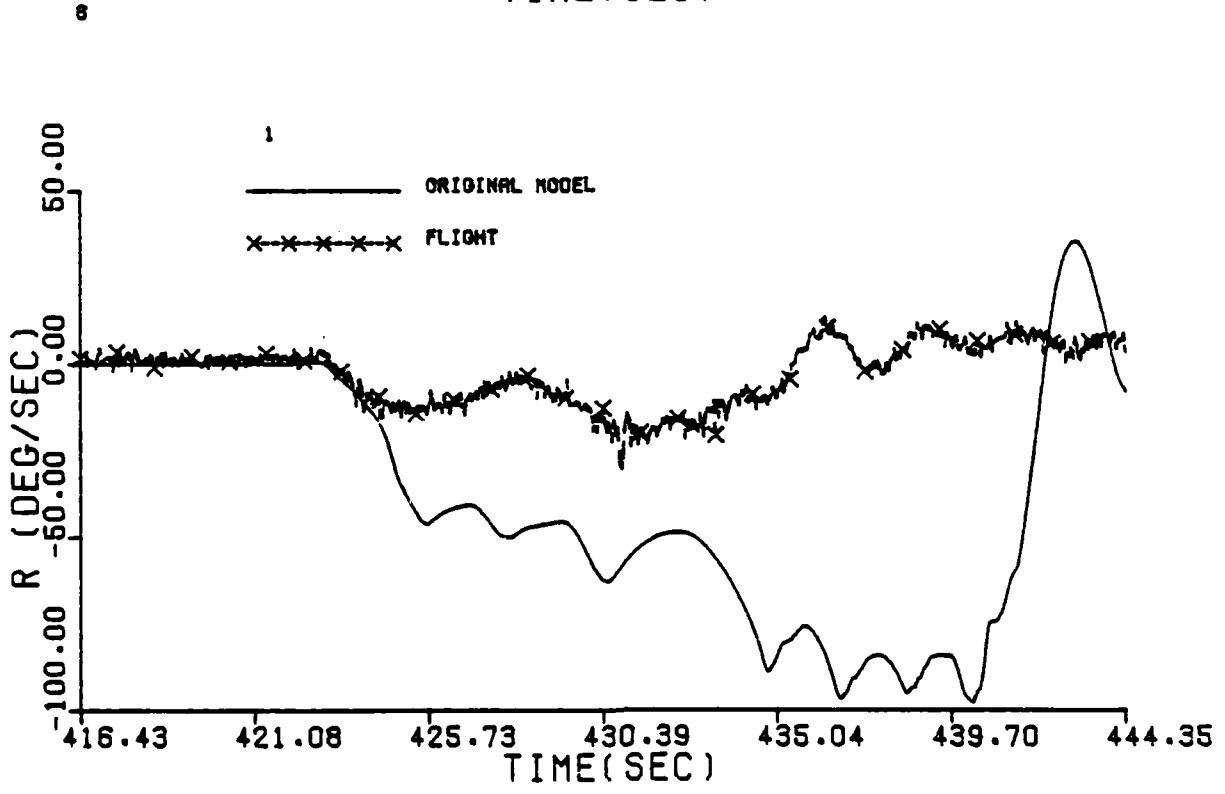

Figure 2.1 (Continued)

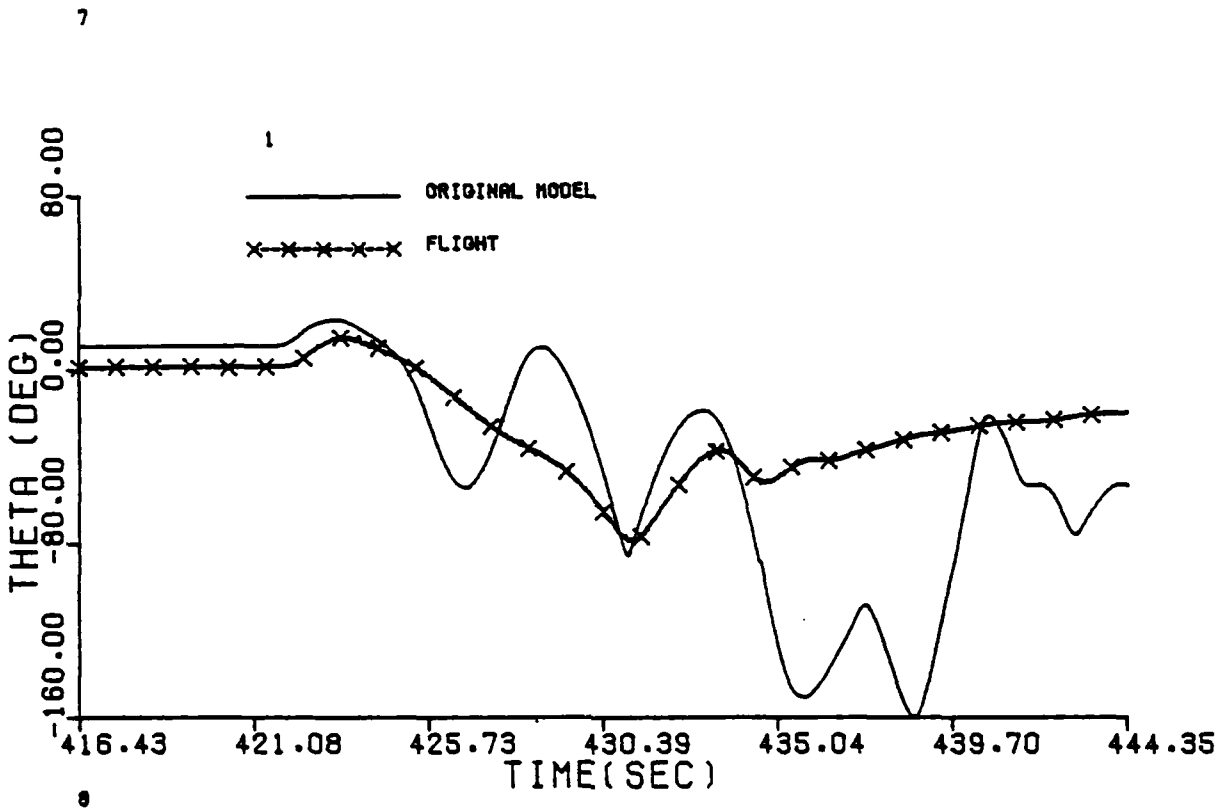

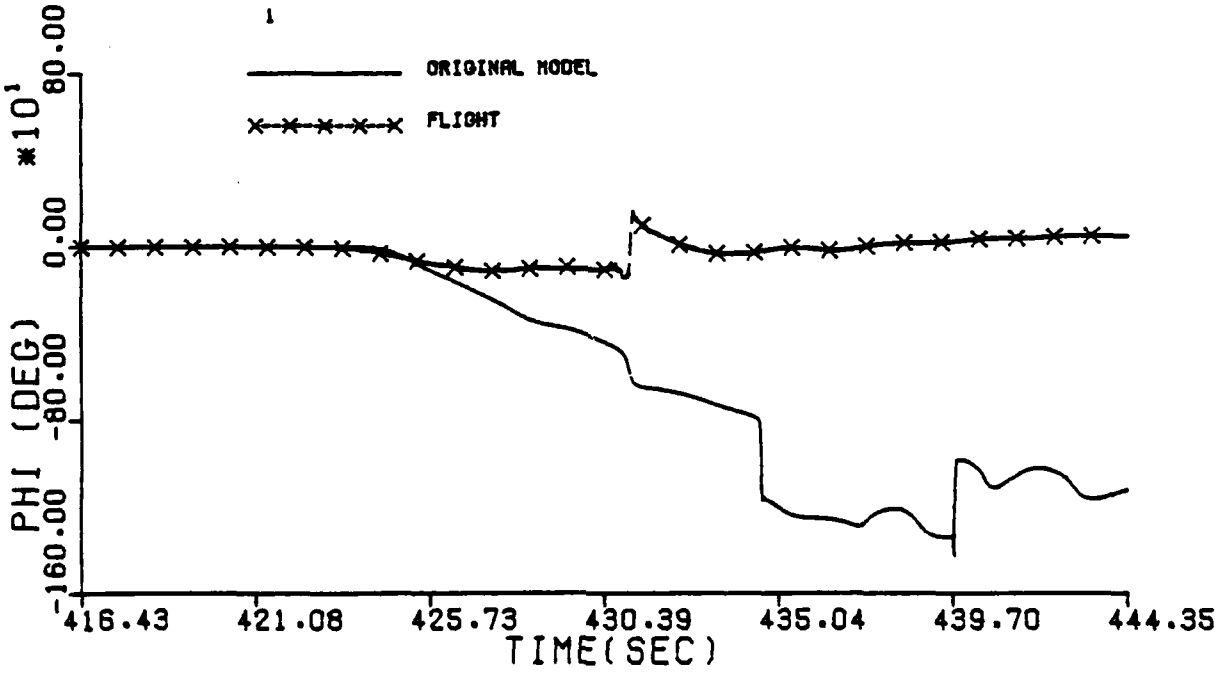

Figure 2.1 (Continued)

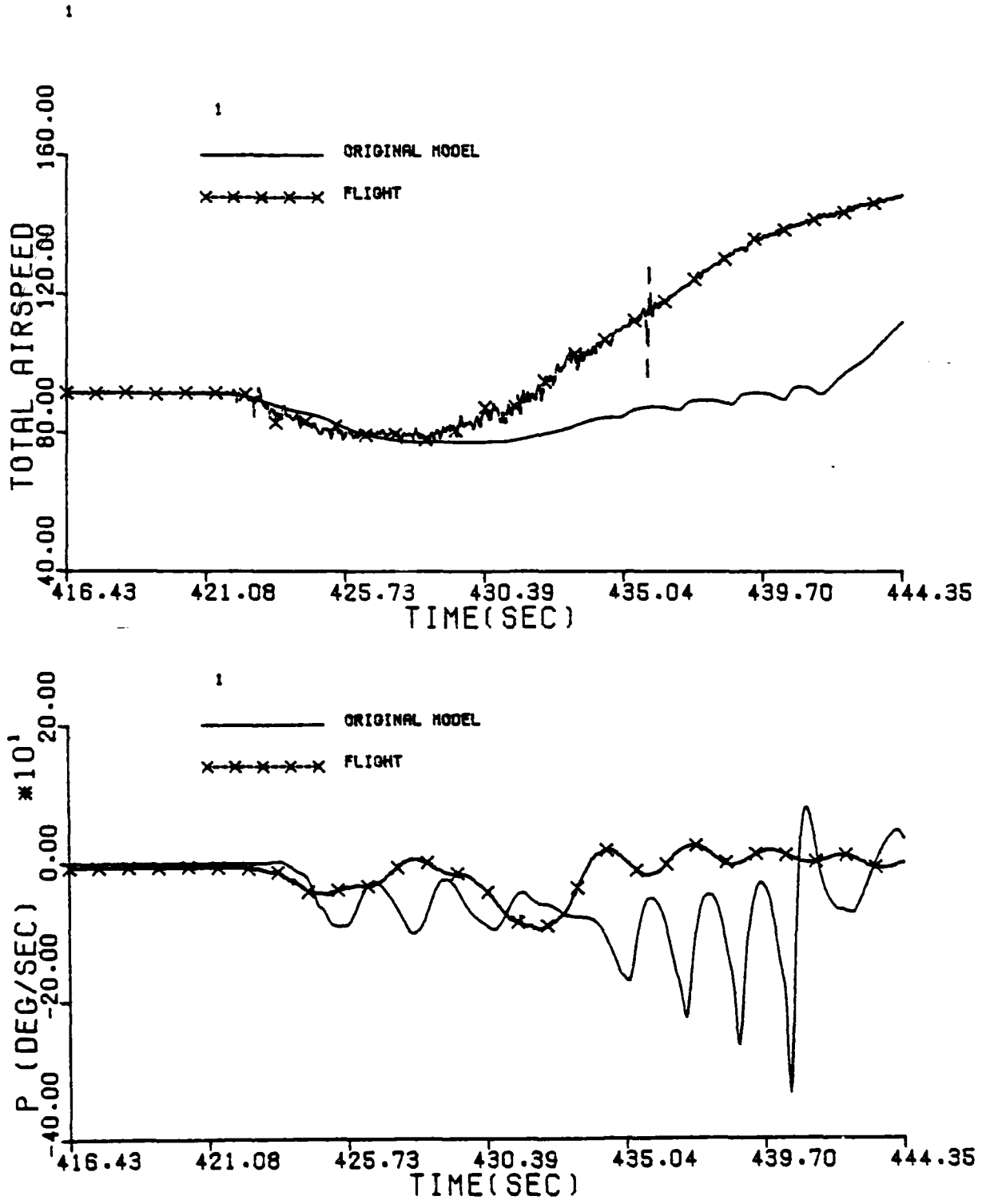

Figure 2.1 (Continued)

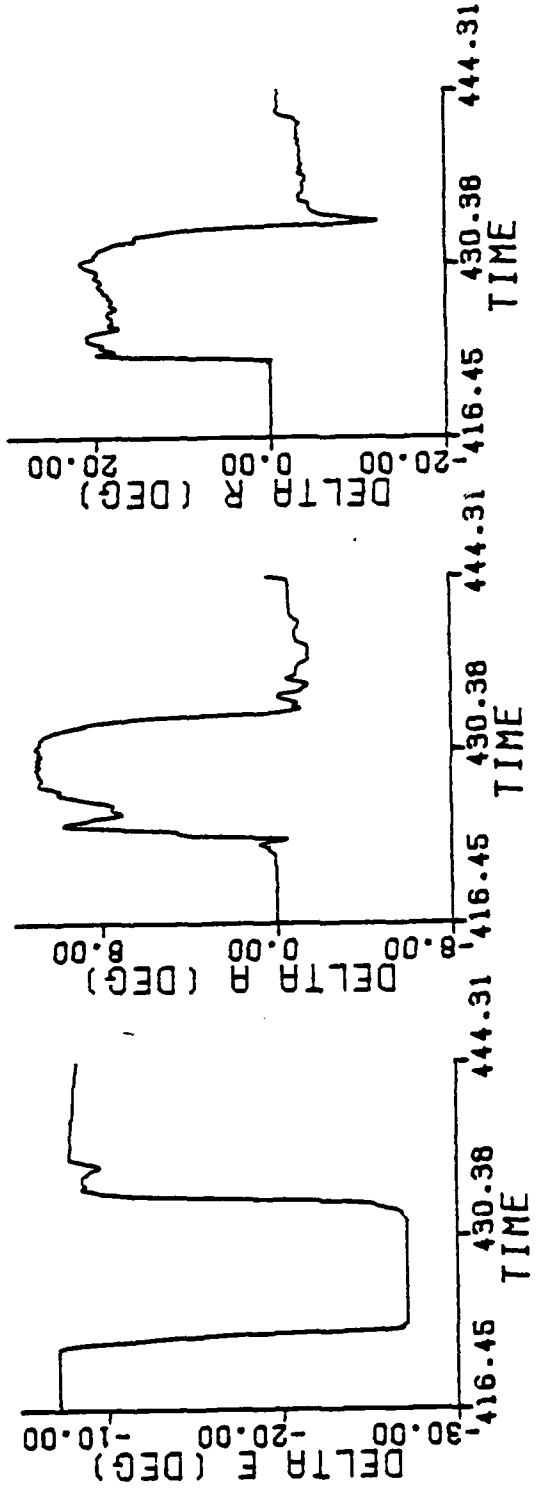

Figure 2.1 (Concluded)

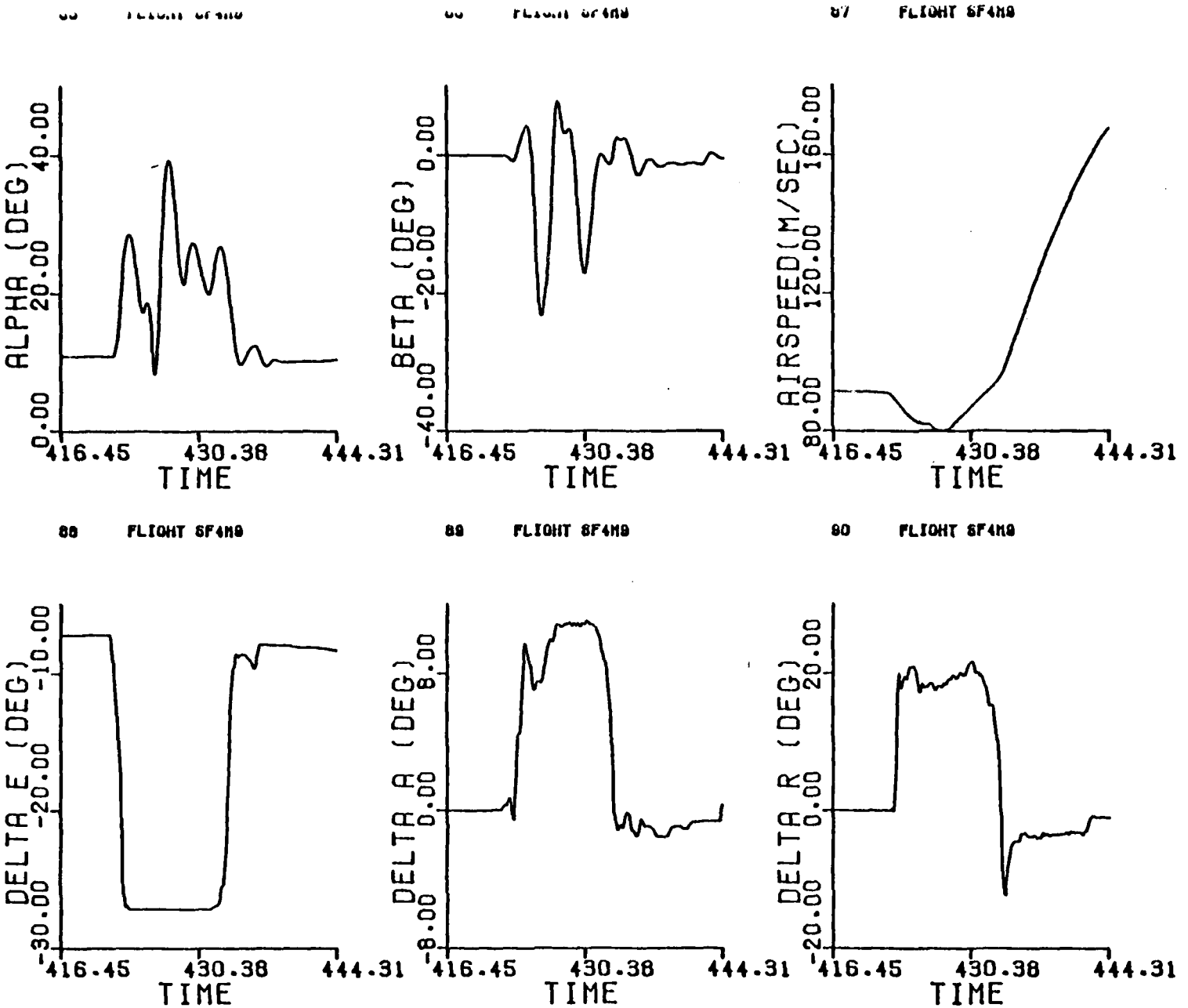

Figure 2.2 Response of Modified Model for Maneuver 15

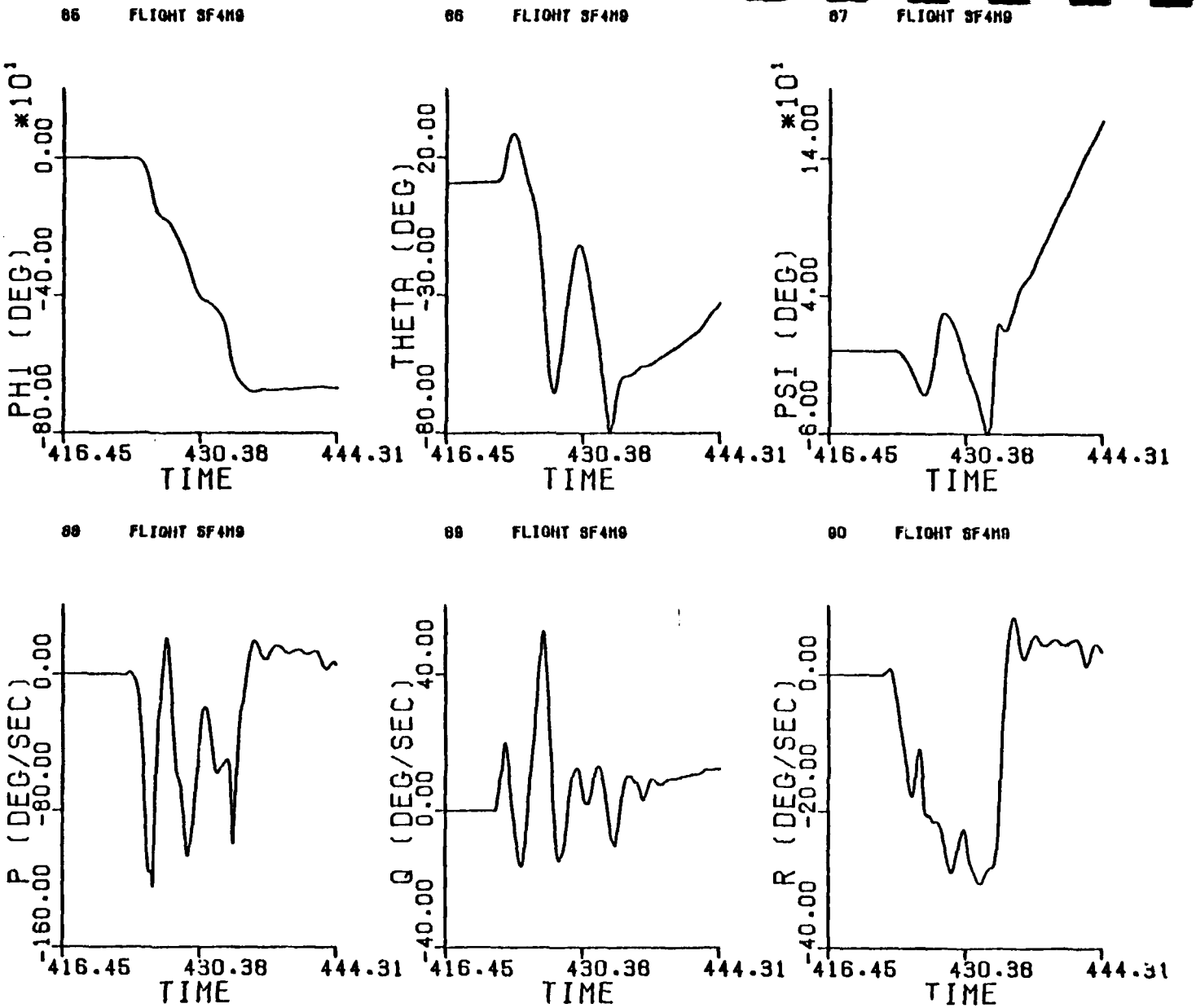

Figure 2.2 (Concluded)

and is referred to as the T-2C wind tunnel model throughout the report.

The nonlinearity exhibited in the original C_{n_p} is similar to the nonlinearities contained in the other dynamic derivatives (e.g., C_{ℓ_p}, C_{ℓ_r} and C_{n_r}). Plots of C_{ℓ_p} and C_{ℓ_r} are given in Figures 4.11 and 4.12. A plot of C_{n_r} is given in Figure 4.18. Note that the modified wind tunnel value of C_{n_p} is plotted as the constant -.06 in Figure 4.17. Consequently, fixing the value of C_{n_p} was no loss to checking out the EBM system identification technique since there was a gain in stability and since the other dynamic derivatives provided similar nonlinearities for testing the goodness of the EBM technique.

3. FILTER/SMOOTHER ESTIMATION RESULTS

For each of the sixteen simulation maneuvers discussed in Section 2 the time history of the states were fed into the measurement equations of Appendix A to produce noise-free measurements. These measurements were corrupted with white, zero-mean gaussian noise having the standard deviations as supplied by NADC. These standard deviations, which are shown in Table 3-1 in the column under the heading "Measurement Noise Level", were derived from analysis of actual T-2C flight data. The corrupted measurements were processed using the filter/smoother algorithm described in Appendix B.

Table 3-1 also contains a column for the RMS values of the estimation errors. These RMS values are obtained by taking the difference between the noise-free measurements and the measurements obtained through substituting the estimated states into the measurement equations. The RMS values in Table 3-1 are for Maneuver 4; the results for the other maneuvers are given in Tables E-1 through E-3 of Appendix E.

The RMS values of the estimated errors of the accelerations B_i (t), i = 1, 2, . . . , 6, are presented in Table 3-2 for Maneuver 4 and in the Tables E-4 and E-5 of Appendix E for the other maneuvers. Time histories of true versus estimated states and acceleration are plotted in Figure 3-1 through 3-7. The true values are plotted with a solid line while the estimates are plotted with a dashed line containing one cross symbol per second.

Table 3-1 Comparison Between Measurement Noise and Estimation Error Levels for Maneuver No. 4

Measured Quantity	Descriptive Name	Units	Measurement Noise Level (1σ)	RMS Value of Estimation Error
Z_1	A X NOSE	m/sec^2	.24	.12
Z_2	A Z C G	m/sec^2	1.05	.24
Z_3	A Z NOSE	m/sec^2	1.05	.27
Z_4	A Z TAIL	m/sec^2	1.05	.26
Z_5	A Z R	m/sec^2	1.05	.34
Z_6	A Z L	m/sec^2	1.05	.35
Z_7	A Y C G	m/sec^2	.24	.08
Z_8	A Y NOSE	m/sec^2	.24	.09
Z_9	A Y TAIL	m/sec^2	.24	.09
Z_{10}	THETA	rad	.00087	.00026
Z_{11}	PHI	rad	.00087	.00031
Z_{12}	Roll Rate	rad/sec	.0017	.0013
Z_{13}	Pitch Rate	rad/sec	.0017	.0011
Z_{14}	Yaw Rate	rad/sec	.0017	.0008
Z_{15}	Altitude	m	10.	1.0
Z_{16}	Air Speed	m/sec	.43	.06
Z_{17}	ALPHA	rad	.0028	.0005
Z_{18}	BETA	rad	.0028	.0004

Table 3-2 RMS of the Estimation Error of B_i (t), i = 1, 2, . . . , 6, for Maneuver No. 4

Estimated Quantity	Units	RMS Value of Estimation Error
B_1	m/sec^2	.12
B_2	m/sec^2	.07
B_3	m/sec^2	.24
B_4	rad/sec^2	.05
B_5	rad/sec^2	.03
B_6	rad/sec^2	.01

Using Table 3-1 we make the following observations of the estimation errors of Maneuver 4. The filter/smoother algorithm has reduced the error level from .24 to .12 for the acceleration measurement A X NOSE. The errors on the acceleration measurements in the z-direction (i.e., AZCG, . . . , AZL) have been reduced by a factor of 3 or 4. The errors on the acceleration measurement in the y-direction have been reduced by a factor of 3. The errors on θ and ϕ have been reduced by a factor of 3. The errors on the roll, pitch and yaw rates have been reduced by less than a factor of 2. The errors on air speed are less by a factor of 7. The errors on α and β have been cut down by a factor of 5 or 6. These observations hold for all maneuvers with the exception of Maneuvers 1 and 7. The RMS value of the estimation error on the roll rate is slightly higher than the noise level for these two maneuvers in Tables E-1 and E-2.

Making use of Table 3-2 and Figures 3-5 through 3-7, we observe that the errors in the estimates of $B_i(t)$, $i = 1, 2, \ldots, 6$, are about one-thirtieth of the peak values of $B_i(t)$. Moreover, the estimate of $B_i(t)$ followed accurately the time history of $B_i(t)$.

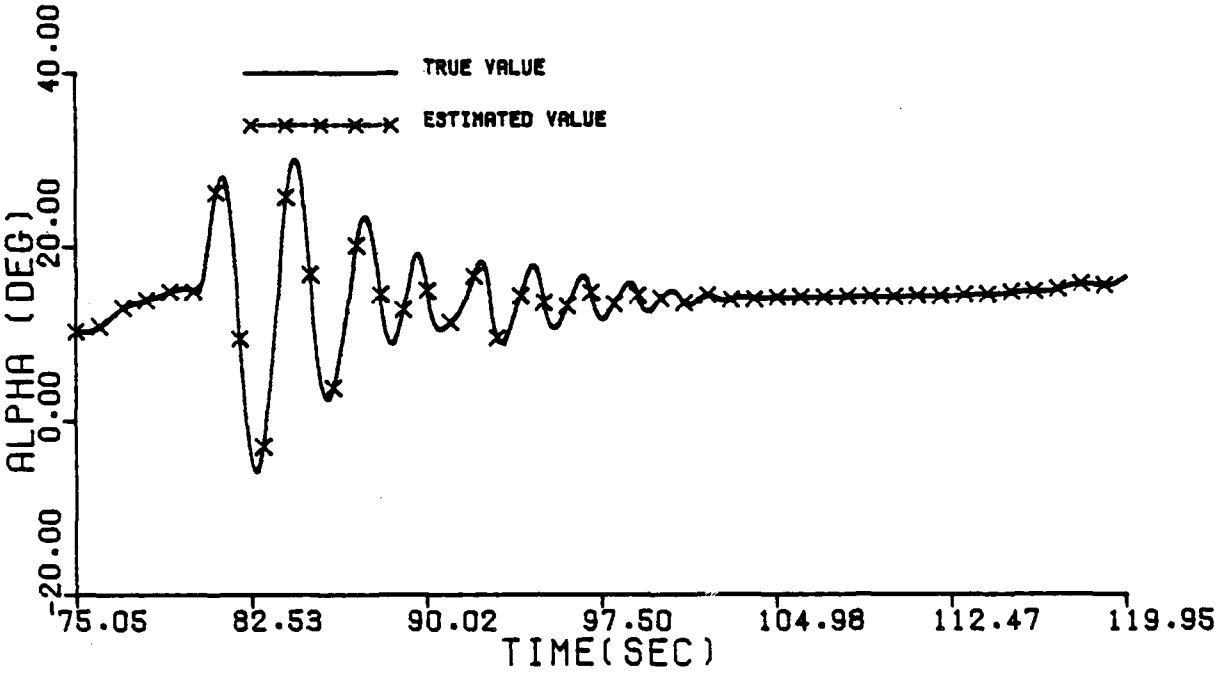

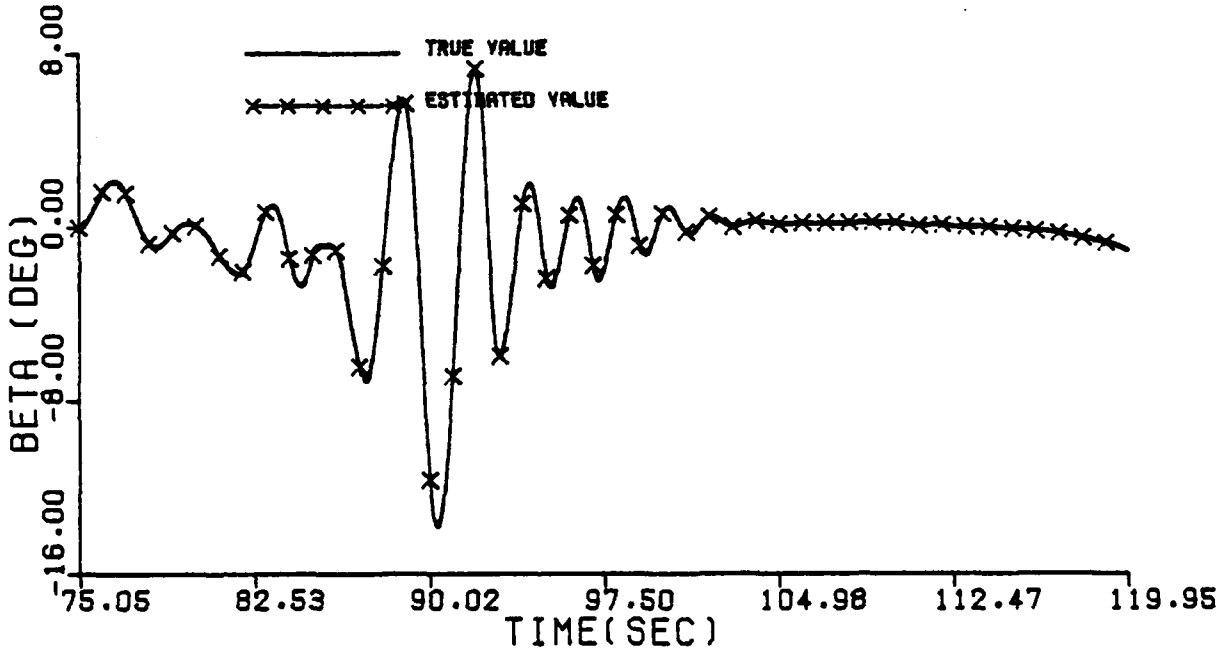

Figure 3-1. Comparison Between the True and Estimated Values of α and β of Maneuver 4

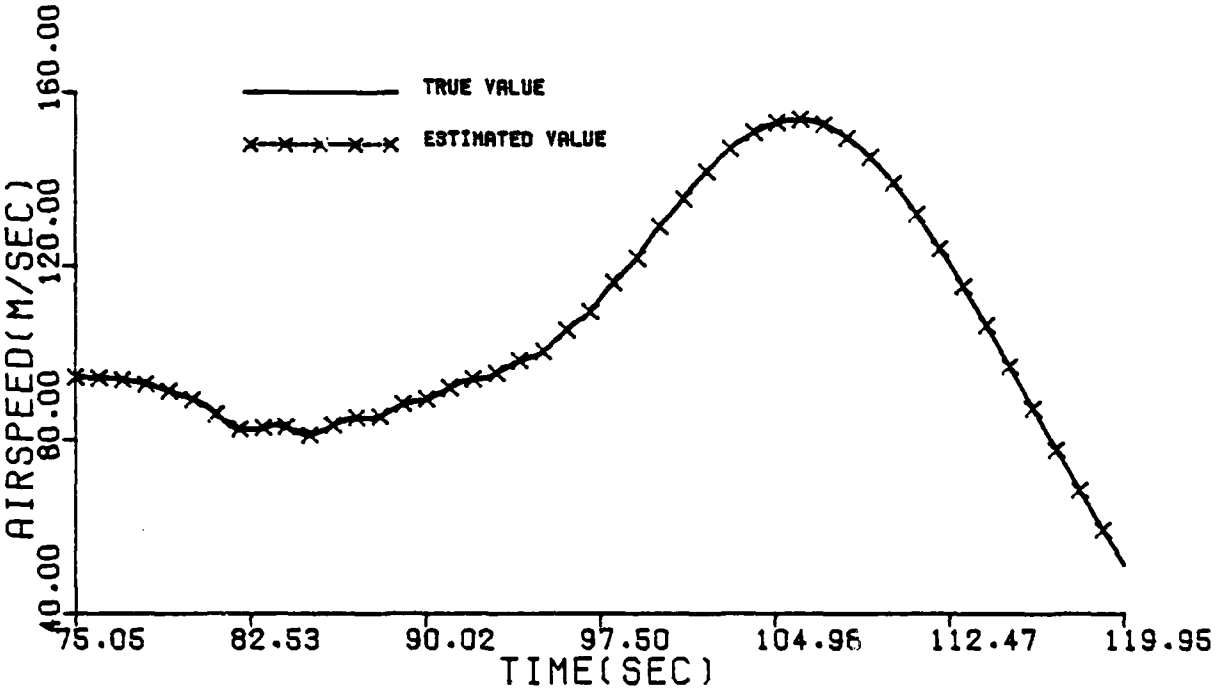

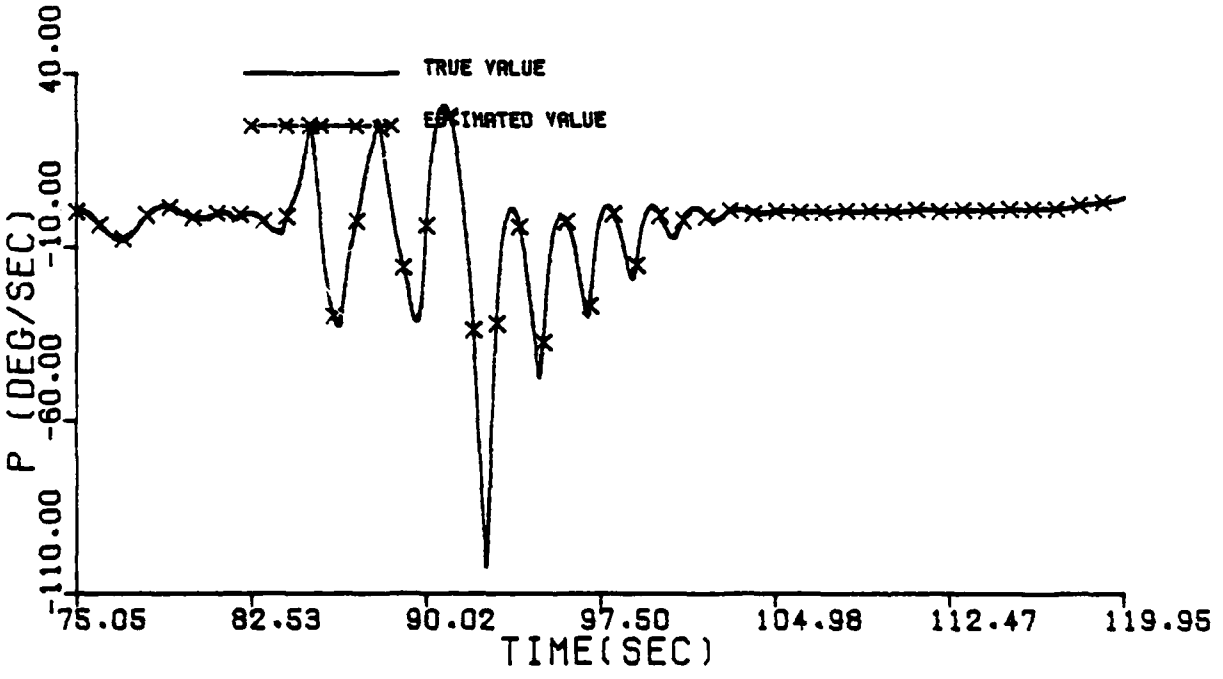

Figure 3-2. Comparison Between the True and Estimated Values of V and P of Maneuver 4

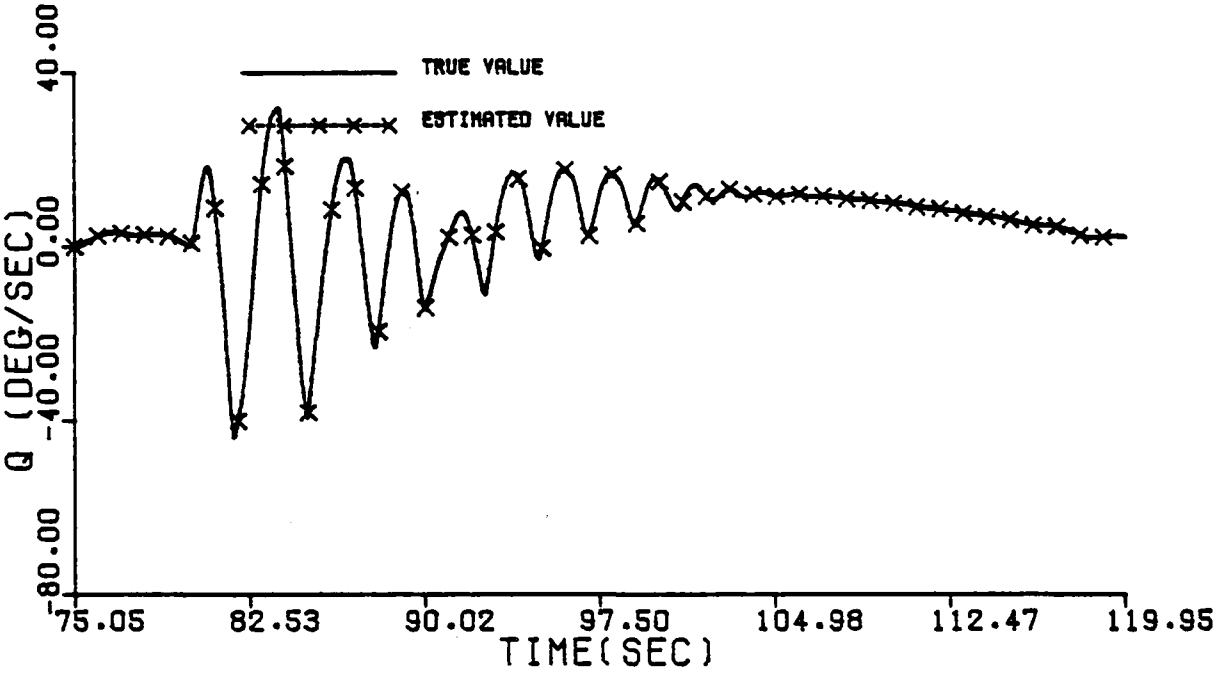

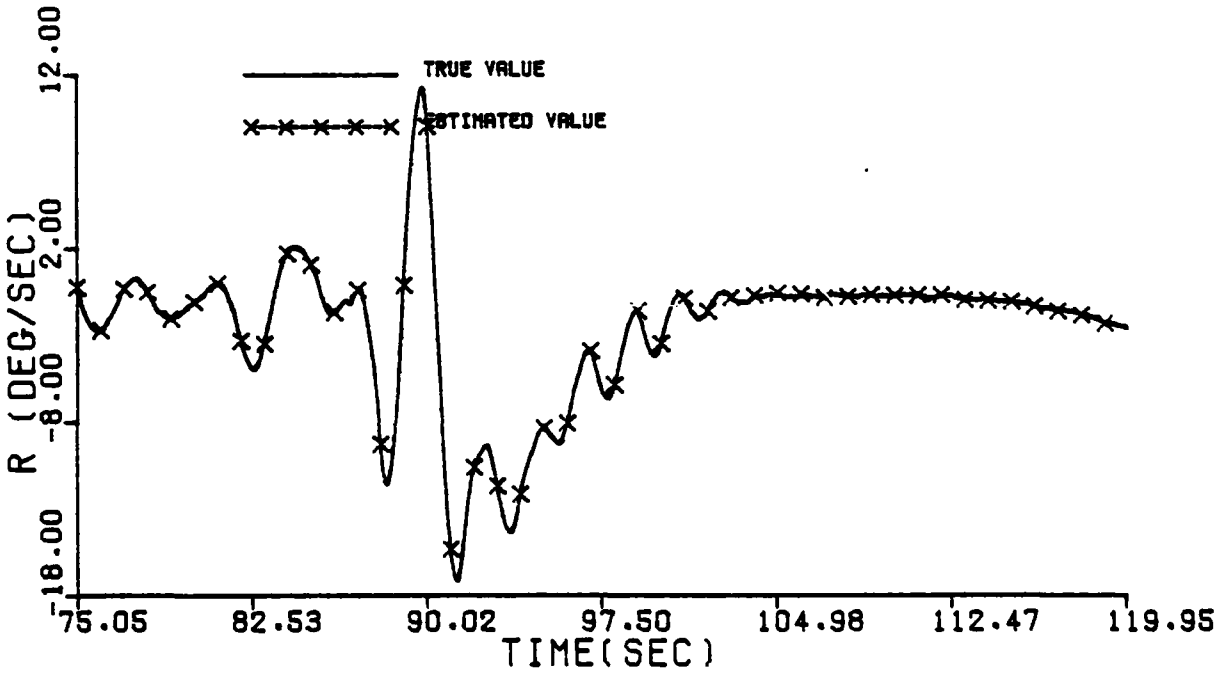

Figure 3-3. Comparison Between the True and Estimated Values of Q and R of Maneuver 4

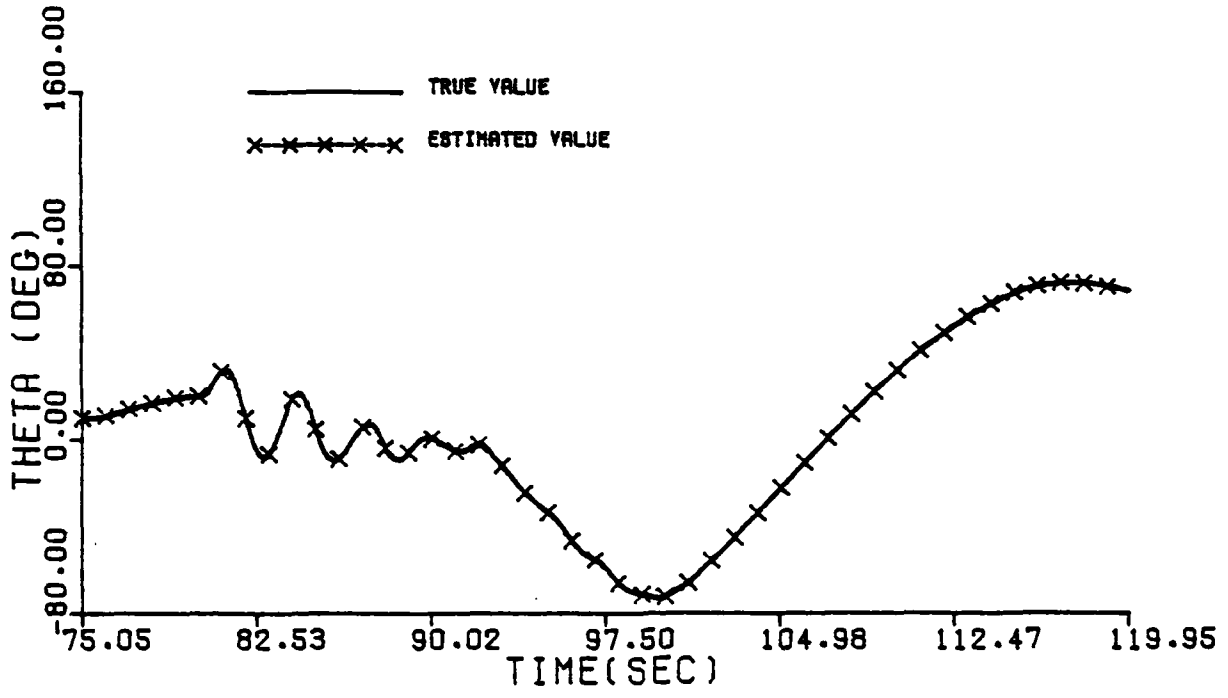

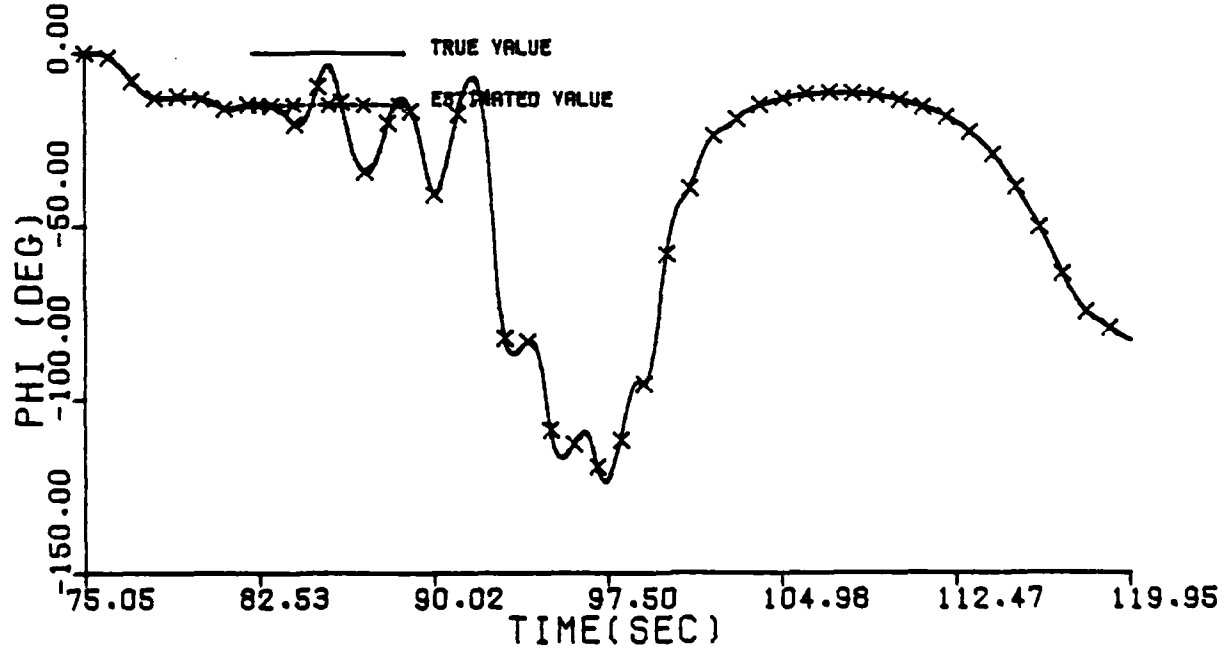

Figure 3-4. Comparison Between the True and Estimated Values of θ and ϕ of Maneuver 4

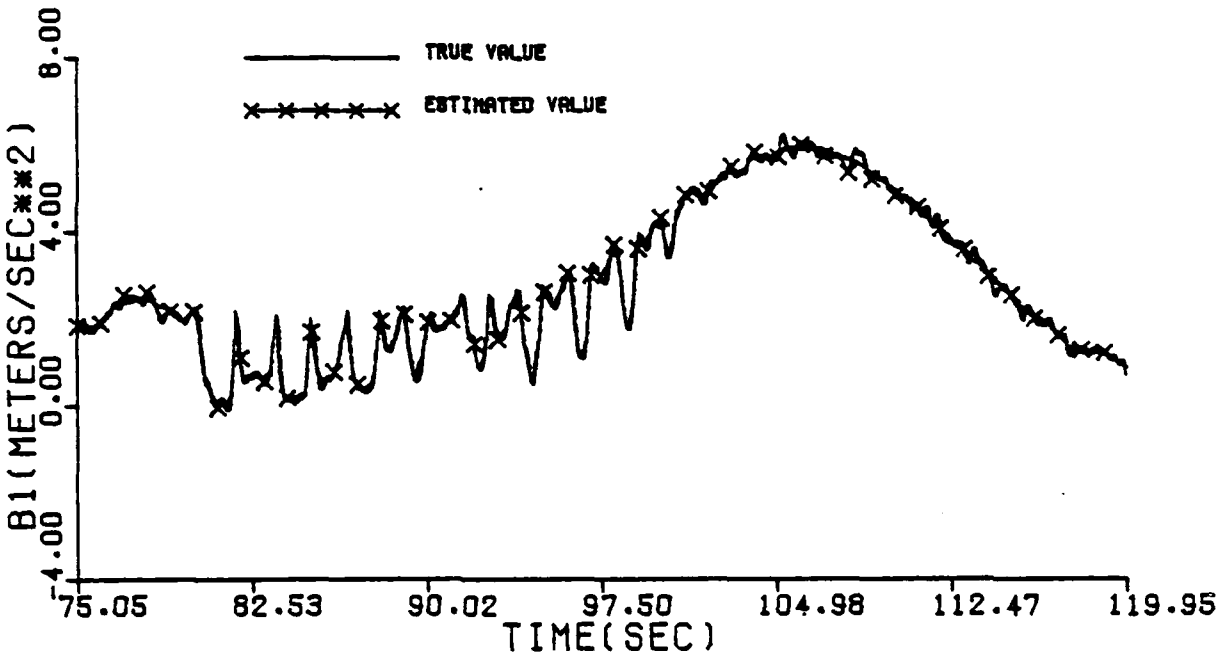

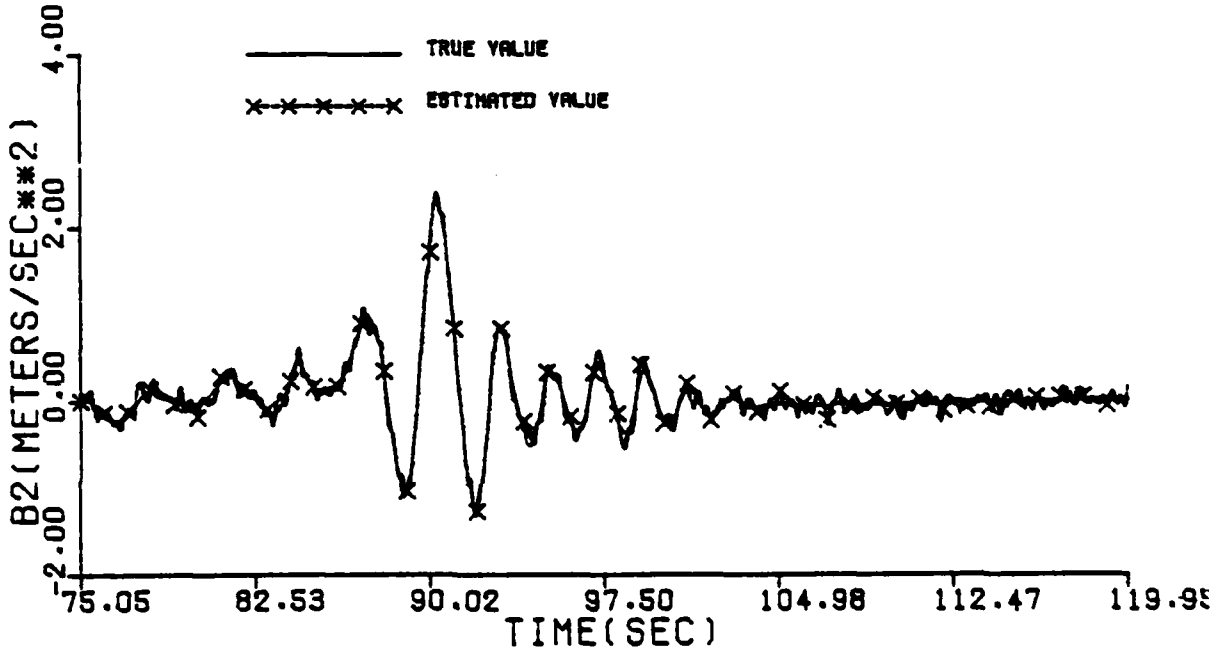

Figure 3-5. Comparison Between the True and the Estimated Values of $B_1(t)$ and $B_2(t)$ of Maneuver 4.

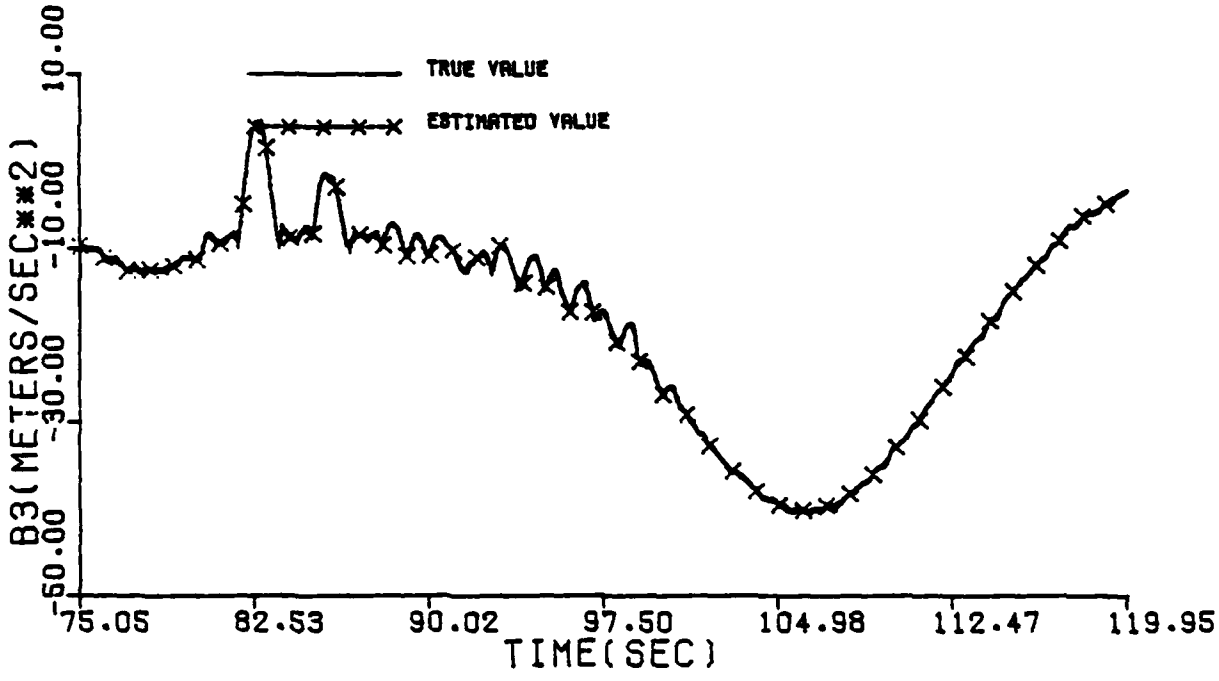

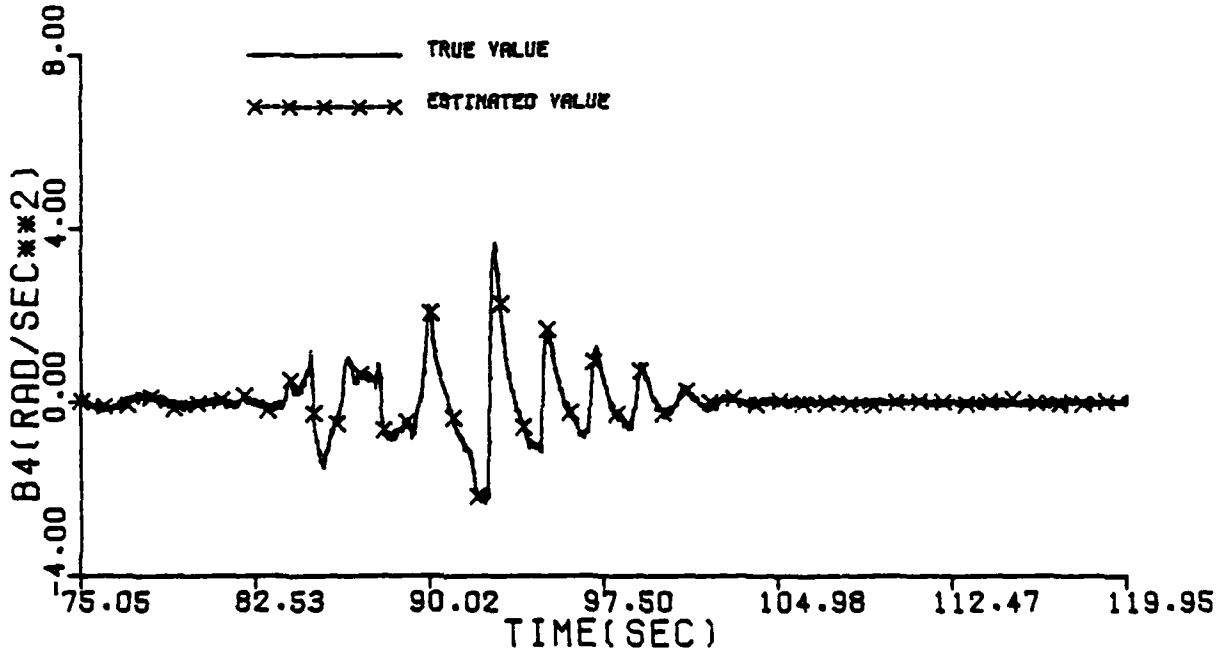

Figure 3-6. Comparison Between the True and the Estimated Values of $B_3(t)$ and $B_4(t)$ of Maneuver 4.

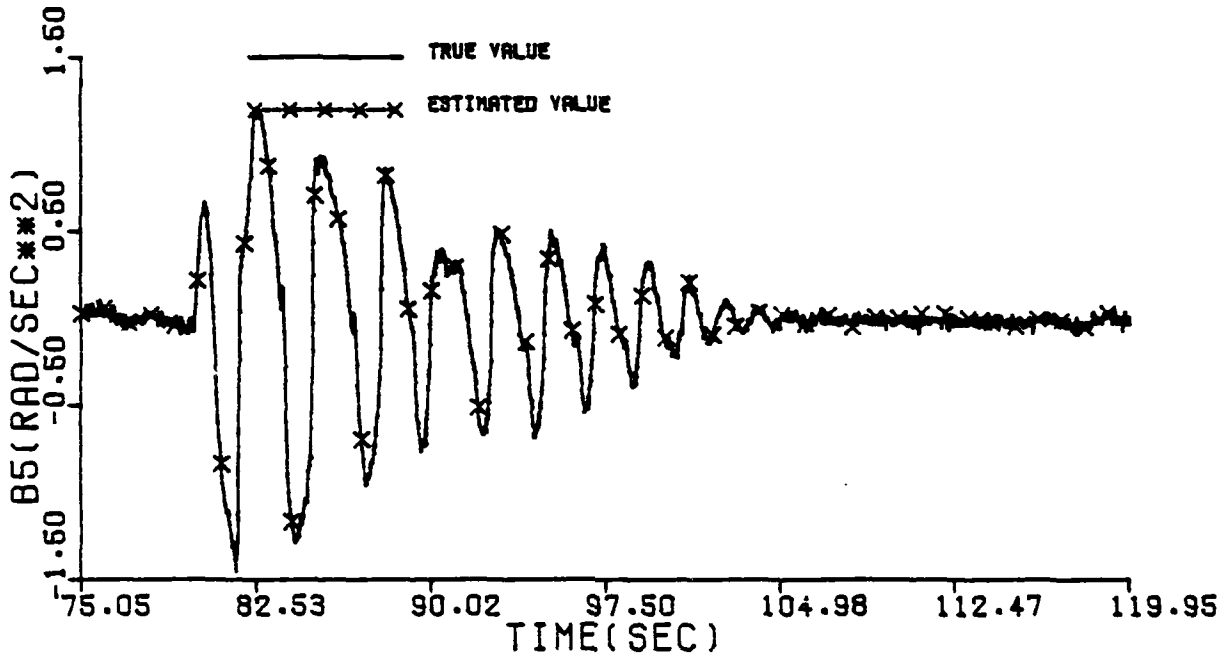

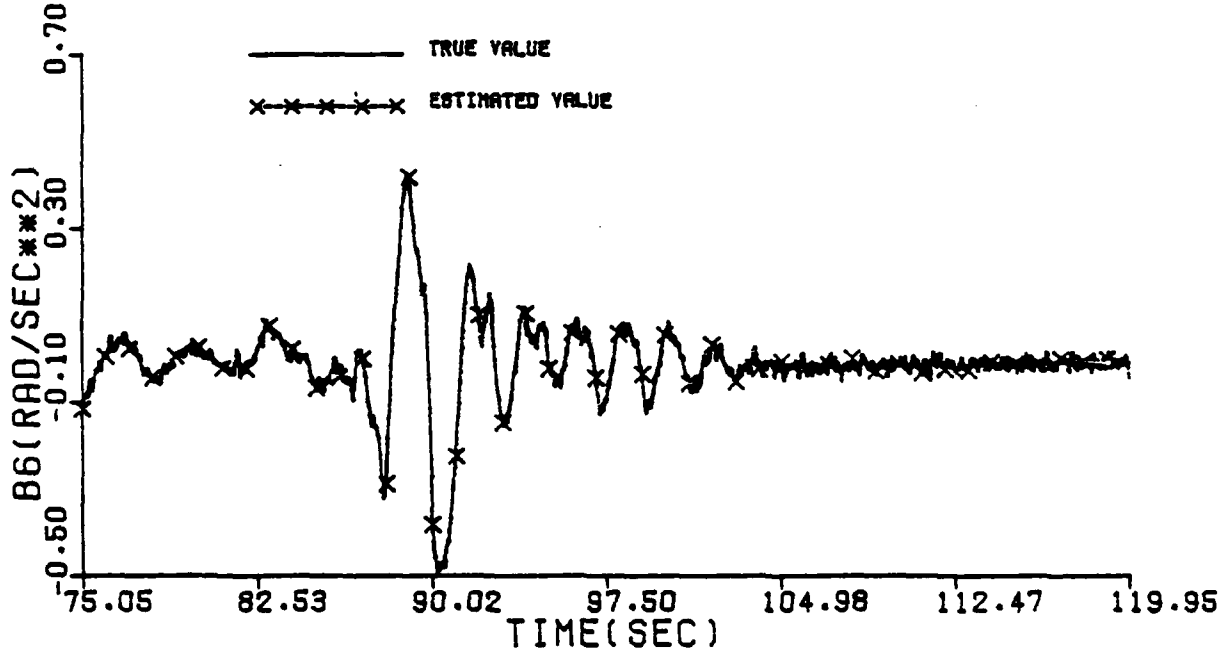

Figure 3-7. Comparison Between the True and the Estimated Values of $B_5(t)$ and $B_6(t)$ of Maneuver 4.

SECTION 4

MODEL IDENTIFICATION AND COMPARISON OF RESULTS

Model comparisons of force and moment coefficients can be done in either equation form or in the look up tables form. Both these methods are equivalent and equally good. To illustrate both the approaches, the tabular form was chosen for longitudinal models and the equation form for lateral models.

4.1 CONSTRUCTION OF SUBSPACES FOR LONGITUDINAL IDENTIFICATION

The method and factors governing the choice of subspaces were discussed in Section 1.3. The stall angle of attack for the aircraft was around 14°. Since C_x, C_z and C_m are strongly dependent upon α, $|\beta|$ and δ_e the subspaces were defined by the following subdivisions:

δ_e: -25°, -15°, -10°, 0°, 10° and 15°

$|\beta|$: 0°, 2°, 5°, 10°, 15°, 20° and 25°

α : -8°, -4°, 0°, 4°, 8°, 12°, 14°, 15°, 16°, 18°, 20°, 25°, 30°, 35°, 40° and 45°

The symmetry of longitudinal coefficients with respect to sideslip angle was taken advantage of in using the same model for both positive and negative sideslip angles. For convenience and ease of comparison against the wind tunnel model, the subdivision values of α, $|\beta|$ and δ_e were chosen to be the points where the values of C_L, C_D and C_m were specified for the wind tunnel model. For real flight data a few trials may be necessary before settling upon the best choice based on the identified models in these trials. Also the assumption of symmetry of C_x, C_z and C_m with respect to β is only a convenience to reduce the number of subspaces and increase the data for modeling in each subspace. When asymmetry is suspected the procedure can be used in exactly the same way by modeling in the positive and negative sideslip angle regions separately.

Using all the maneuvers, data points for all subspaces were calculated. Table 4-1a shows the data distribution in the region contained by $\alpha = -4^{\circ}, 35^{\circ}$, $|\beta| = 0^{\circ}, 30^{\circ}$ and $\delta_e = -15^{\circ}, -10^{\circ}$. Such a table immediately shows us how the data points are distributed and in what regions additional data must be generated for complete modeling. Similar tables were generated for all other subdivisions of δ_e and the results have been summarized in Table 4-1b. Table 4-1b lists modeling regions containing subspaces with at least 15 points. The number of subspaces for each region is also given. Each row of the table shows the maximum and minimum on δ_e, $|\beta|$ and α within which all the points were located and the resultant number of subspaces. For example, the seventh row of the table shows that for $-15^{\circ} < \delta_e \leq -10^{\circ}$ and $0^{\circ} \leq |\beta| < 2^{\circ}$ the data points were located for angles of attack between 0° and 30°. As we can see from Table 4-1a this resulted in ten subspaces since we have ten subdivisios of angle of attack for α between 0° and 30°. It was noticed that there was only a scattering of points outside the regions given in Table 4-1b. In general, it was found that towards the edge of the regions the data points were low and for $5^{\circ} \leq |\beta| \leq 10^{\circ}$ the data were concentrated below $|\beta| = 8^{\circ}$.

From the Table 4-1b we see that the subspaces containing enough data for modeling may not form a covering of the entire space and there may be holes (e.g. third, fourth and fifth rows of the table). We also see that the controls used were inadequate to generate data in several regions, especially at high β and also for the combination of low α and high δ_e. We also do not have enough data points for angle-of-attack beyond 35 degrees.

Table 4-1a Density of Modeling Data for the Subspaces Contained in the Region Defined by $|\beta| = 0°$, $30°$ and $\alpha = -4°$, $35°$ and by δ_e min = $-15°$ and δ_e max = $-10°$

End points of subspaces for α	End points of subspaces for $\|\beta\|$							
	0°	2°	5°	10°	15°	20°	25°	30°
-4°	2	2	0	0	0	0	0	
0°	15	4	1	0	0	0	0	
4°	31	2	1	4	0	0	0	
8°	82	27	6	4	0	0	0	
12°	101	54	6	0	0	0	0	
14°	64	23	22	0	0	1	0	
15°	54	19	32	1	1	2	0	
16°	144	43	35	13	2	0	0	
18°	109	32	33	11	3	0	0	
20°	99	66	53	28	12	0	0	
25°	16	21	17	6	0	0	0	
30°	0	0	1	0	0	0	0	
35°								

Table 4-1b DATA DISTRIBUTION FOR LONGITUDINAL MODELING

$\delta_{e_{min}}$ (deg)	$\delta_{e_{max}}$ (deg)	β min (deg)	β max (deg)	α min (deg)	α max (deg)	No. of Subspaces
-10	0	0	2	-4	25	10
		2	5	0	25	9
		5	10	4	14	3
		5	10	16	18	1
		5	10	20	25	1
		10	15	8	12	1
-15	-10	0	2	0	30	10
		2	5	8	30	8
		5	10	14	30	6
-17	-13	10	15	20	25	1
-25	-15	0	2	8	35	9
		2	5	12	35	8
		5	10	12	14	1
		5	10	16	30	4
-25	-30	0	2	14	35	7
		2	5	16	35	5
		5	10	18	35	4

4.2 LONGITUDINAL MODELING

From Table 4-1b we see that we obtain a total of 88 subspaces for modeling. Instead of trying to match the entire data with one equation containing a very large number of terms, we have divided the data into 88 groups such that we can fit a simple curve for each region and combine these 88 simple local models to determine the global model.

As described in Section 1.3, the SMLR method chooses the best model to fit the data based on the supplied value of F - Critical Ratio. The computer program of Reference [4] was suitably modified for aircraft parameter identification. Since the longitudinal coefficients depend mainly on α, β, q, δ_e and $\dot{\alpha}$, as a first try it was decided to use linear models in α, β, δ_e, q and $\dot{\alpha}$ in all regions and try more complex models if necessary.

In each subspace the reference point is fixed at the subspace corner corresponding to α_{min}, $|\beta|_{min}$ and $\delta_{e_{max}}$ and $q = \dot{\alpha} = 0$. The coefficients C_x, C_z and C_m are then expressed as a first order Taylor series expansion about the reference point. The equation for C_x can be expressed as

$$C_x = C_{x_o} + C_{x_\alpha}(\alpha - \alpha_o) + C_{x_\beta}(|\beta| - |\beta_o|) + C_{x_{\delta_e}}(\delta_e - \delta_{e_o})$$

$$+ C_{x_q}\frac{q\bar{c}}{2V} + C_{x_{\dot{\alpha}}}\frac{\dot{\alpha}c}{2V} \qquad (4.2.1)$$

where α_o, $|\beta_o|$ and δ_{e_o} are values of α, $|\beta|$ and δ_e at the reference point and C_{x_o} is the value of C_x at the reference point. Similar equations can be written for C_z and C_m.

Identification was performed in all subspaces and the models were analyzed. Generally except for C_x, the linear equations were adequate to follow the variation of force and moment coefficients with high multiple correlation coefficients. An inspection of the individual terms showed that

for most regions the standard deviations of the parameters of the model were low. However in the regions near the boundaries where there were less points the uncertainties in the estimates of the parameters were somewhat high and in some cases the multiple correlation coefficient was also low. It was noticed that the identified model contained terms of C_{m_q} or $C_{m_{\dot{\alpha}}}$, but their values were nearly the same. When both C_{m_q} and $C_{m_{\dot{\alpha}}}$ were forced into the model (corresponds to F-critical values being zero) the estimated value of C_{m_q} and $C_{m_{\dot{\alpha}}}$ were far different from their values obtained for other F-ratios but their sum was equal to the value of $C_{m_q} + C_{m_{\dot{\alpha}}}$. This indicated that C_{m_q} and $C_{m_{\dot{\alpha}}}$ cannot be obtained independently and only their sum can be estimated. The same was observed for C_{z_q} and $C_{z_{\dot{\alpha}}}$ also. Comparison of individual terms of the models for all regions showed rapid changes in C_{z_q} and C_{m_q} after stall. For C_z and C_m the nonlinear term $q\alpha$ was included and $\dot{\alpha}$ was dropped. It was also found that because of larger noise on C_x unrealistic values were obtained for C_{x_q}. Consequently only α, β and δ_e were used for modeling C_x.

Identification was repeated in all regions. Models were obtained with high multiple correlation coefficients and low residuals, except for C_x. The value of R^2 was low for C_x even though the RSS was within the noise level of stochastic filter estimates. The multiple correlation coefficients for C_z were above 0.9 for most cases and between 0.96 and 0.99 for C_m. Further addition of higher orders terms in α and β and cross product of δ_e and α made no further improvement indicating the adequacy of the model. In a few cases when the number of data points was large, the multiple correlation coefficient was increased by reducing the δ_e width and splitting the individual subspace into two supspaces. The correlation coefficients for the C_x model were in the interval of 0.7 - 0.8 or sometimes even lower. It was found that the standard deviation of the error on the estimate of C_x from the estimation process was nearly of the same order as the standard deviation of C_x itself in those

regions. (This is due to a higher noise-to-signal ratio in the measurement of C_x). Using higher order terms in the models did not change the model at all indicating that the low correlation was more due to noise than the structure of the model itself. As we will see later in Section 4.3, the excellent agreement between the estimates and wind tunnel values for all these coefficients in almost all the regions also pointed to this. To test the sensitivity of the identified model to spurious terms, the lateral states, p, r, δ_a and δ_r were included as additional candidates. Identification was again performed for C_x, C_z and C_m in many regions. It was found that the regression algorithm successfully rejected the extraneous terms in almost all the cases. However, when the multiple correlation coefficient for C_x was very low, one or more of the lateral states were also included in the C_x model.

Table 4-2 gives an example of the coefficients of C_m model for δ_e between -15° and -10° and $|\beta|$ between 5° and 10°. As pointed out earlier the data points fell within angles of attack of 14 and 30 degrees. Hence no models exist for α greater than 30° or α less than 14°. We see that not only the values of the coefficient C_m but also its derivatives agree with the wind tunnel model. We have essentially chosen the regions to be small enough such that the nonlinear behavior of the force and moment coefficients can be adequately and accurately represented by simpler linear models. As such, the derivatives C_{m_α}, $C_{m_{\delta_e}}$, C_{m_β} etc. represent the best average values of these derivatives over the given subspace. Hence there may be slight discontinuities in the values of C_x, C_z and C_m on the subspace boundaries (each subspace has six boundary surfaces). Similar tables were obtained for all coefficients in all regions and these tables were used to build a global model.

4.3 LONGITUDINAL GLOBAL MODEL

Having constructed models for individual regions our next task was to assemble these to form a global model which can be used for comparison against the wind tunnel model and to predict the response of the estimated model.

Table 4-2 Example of Estimated Coefficients for C_m

Model Equation

$(-15^o < \delta_e \leq -10^o, \quad 5^o \leq |\beta| \leq 10^o)$

α (deg)	C_{m_o}		C_{m_α}		$C_{m_{\delta_e}}$	
	Estimated	Wind Tunnel	Estimated	Wind Tunnel	Estimated	Wind Tunnel
14-15	-0.0397	-0.0311	-1.0000	-1.0439	-1.7660	-1.7107
15-16	-0.0463	-0.0451	-1.3369	-1.6492	-1.5775	-1.6808
16-18	-0.0749	-0.0710	-1.5224	-1.6519	-1.6204	-1.6403
18-20	-0.1246	-0.1210	-1.531	-1.3464	-1.4352	-1.4609
20-25	-0.1460	-0.1690	-1.758	-1.5864	-0.9715	-1.0477
25-30	-0.2829	-0.2872	-0.7236	-0.5999	-0.7444	-0.7829

α (deg)	C_{m_β}		C_{m_q}		$C_{m_{q\alpha}}$	
	Estimated	Wind Tunnel	Estimated	Wind Tunnel	Estimated	Wind Tunnel
14-15	-0.0880	-0.1287	-14.98	-13.20	315.15	431.22
15-16	-0.1658	-0.1552	-8.59	-7.70	624.57	676.26
16-18	-0.1566	-0.1956	1.82	3.20	22.92	132.31
18-20	-0.0502	-0.1433	3.60	2.41	-1.26	-15.09
20-25	-0.0320	-0.0456	1.66	2.3	-47.39	-42.184
25-30	0.0	-0.0089	-2.92	-1.835	-27.85	-70.88

It may be recalled that in general even though data points lay between 0° and 35° of angle of attack, the concentration of these points depended on angle of sideslip and elevator deflection. For instance for δ_e between -15° and -10° and β between 5° and 10° we could obtain models only, α between 14 and 35 degrees. Table 4-1b gave the regions for which data points were available for modeling.

Models from more than one adjacent subspace can be used to fill the hole in the table. Hence, engineering judgment and the quality and behavior of the model in each subspace was taken into consideration in projecting the values of force and moment coefficients into regions where no models were available for lack of sufficient data. With this approach C_x, C_z and C_m values were extrapolated at various points to complete the tables for $0^{\circ} \leq \alpha \leq 35^{\circ}$, $0^{\circ} \leq |\beta| \leq 10^{\circ}$ and $-25^{\circ} \leq \delta_e \leq 0^{\circ}$. It should however be remembered that caution must be exercised in using the extrapolated values. The reason is that such an extrapolation may not be accurate if the variation of the force or moment coefficient is highly nonlinear and the models vary drastically from one subspace to the next.

4.4 DISCUSSION OF LONGITUDINAL MODELING RESULTS

The longitudinal modeling results are discussed in this section. Identified values of C_x, C_z and C_m are compared against wind tunnel values in Figure 4.1, 4.2 and 4.3 respectively. The values of C_x, C_z and C_m are plotted as functions of angle of attack for elevator settings of 0^o, -10^o, -15^o and -25^o at $\beta = 0^o$, 2^o, 5^o and 10^o. The dynamic derivatives $C_{z_q} + C_{z_{\dot{\alpha}}}$ and $C_{m_q} + C_{m_{\dot{\alpha}}}$ are compared against wind tunnel values in Figures 4.4 and 4.5 respectively. Excellent results were obtained by the identification technique. As previously mentioned, Appendix D presents a brief description of the wind tunnel model.

Figure 4.1 shows a comparison of estimated C_x for various values of β and δ_e for the identified model and the wind tunnel model. At $\beta = 0^o$ the C_x increases as the angle of attack increases reaching a maximum at about 14-15 degrees. Then there is a very sharp decline in the value due to stall. This is followed by a gradual increase or decrease depending on the elevator angle and angle of attack. We see that the identification technique has been successful in matching these variations extremely well. We see similar trends for C_x at other β also. We also observe very close agreement between the estimates and wind tunnel values for $\beta = 2^o$ and $\beta = 5^o$ for all α and δ_e. For $\beta = 10^o$ also we get excellent fit on C_x except at $\alpha = 15^o$. This was due to lack of data points around $\beta = 10^o$, $\alpha = 15^o$ and extrapolation from neighboring subspaces.

Figure 4.2 gives a comparison of C_z for the identified model and the wind tunnel model for various α, β and δ_e. In general, with an increase in angle-of-attack the normal force coefficient increases (negatively) in a near linear fashion up to $\alpha = 12^o$. It continues to increase(negatively) up to stall where it drops and continues to decrease up to 18 or 20 degrees. Then it starts increasing (negatively) again though with a much lower slope than in the pre-stall region. The actual values and slopes vary depending on β and δ_e. We find excellent agreement between the identified model and the wind tunnel model for all α, β and δ_e.

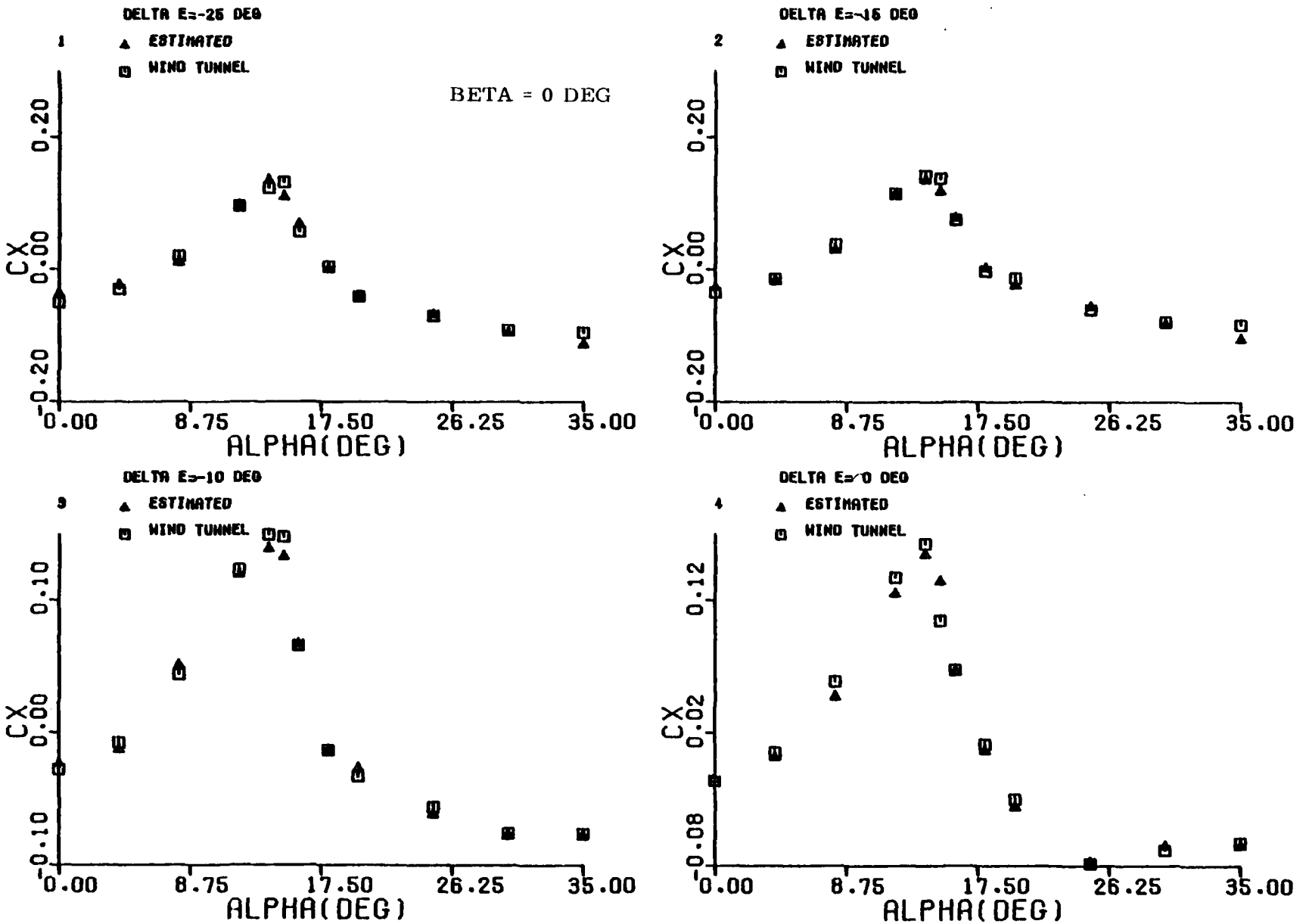

Figure 4.1.a Comparison of the Identified Model With Wind Tunnel Values for C_X (β = 0°)

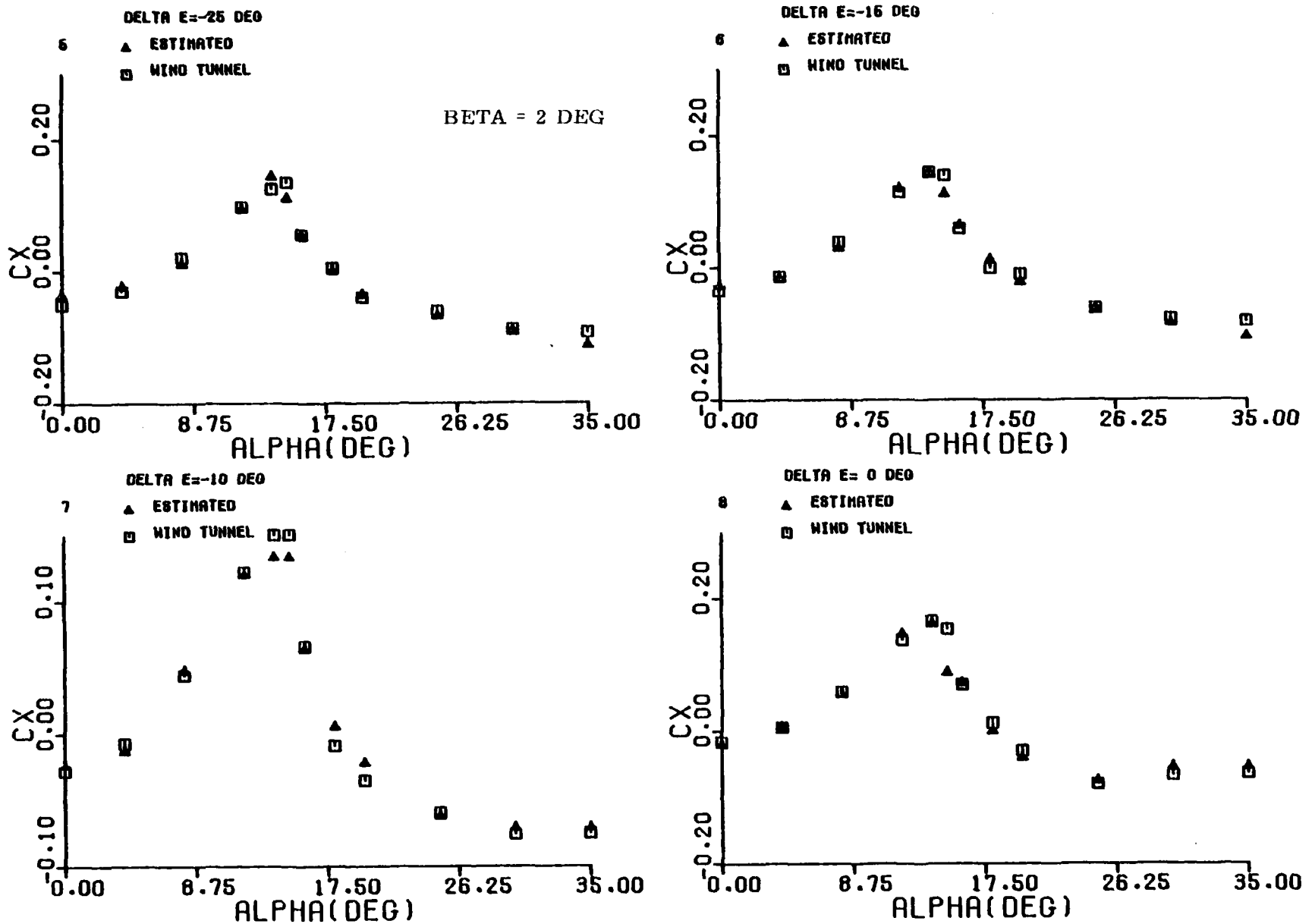

Figure 4.1.b Comparison of the Identified Model with Wind Tunnel Values for C_X (β = 2°)

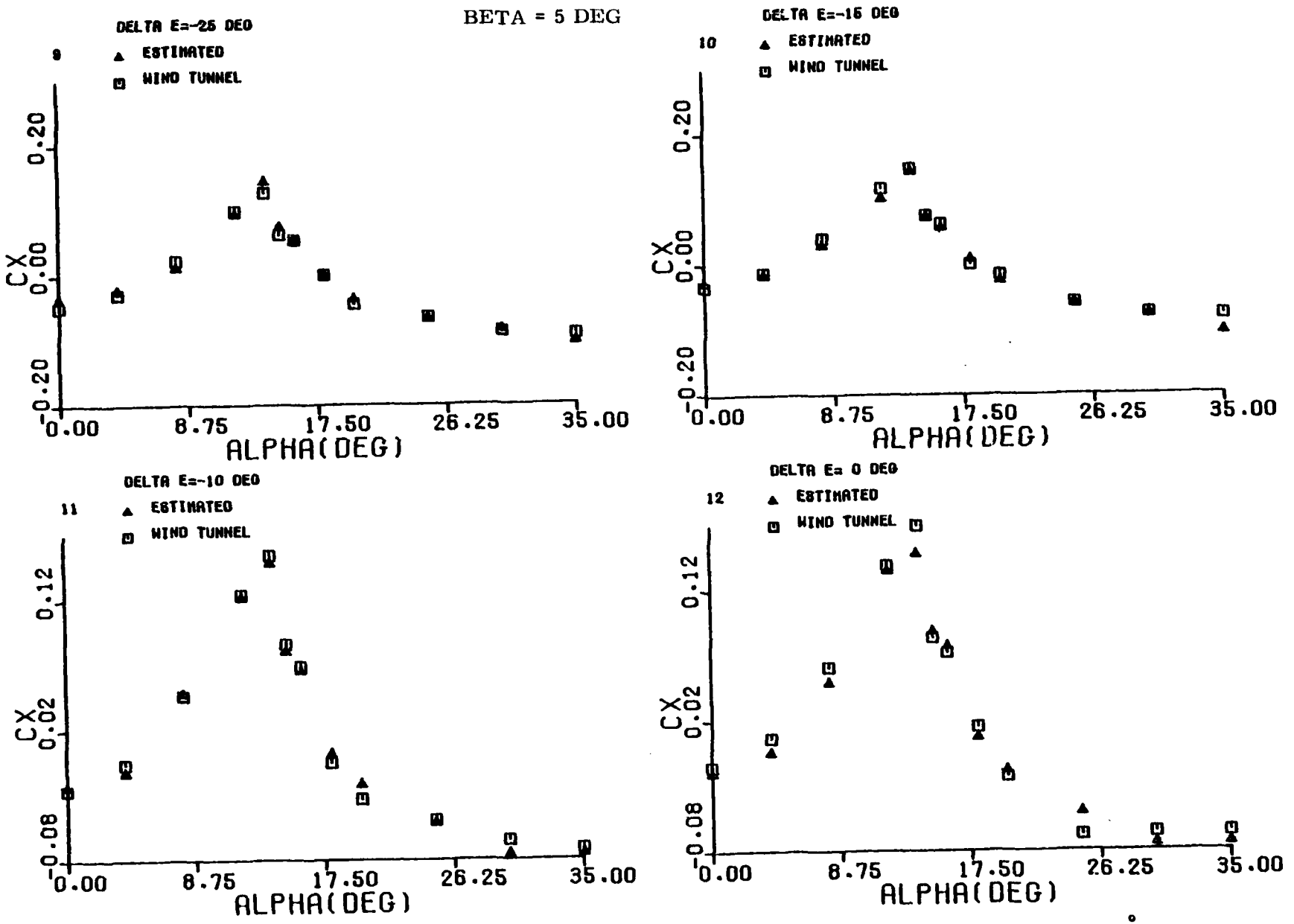

Figure 4.1.c. Comparison of the Identified Model with Wind Tunnel Values for C_X ($\beta = 5^\circ$)

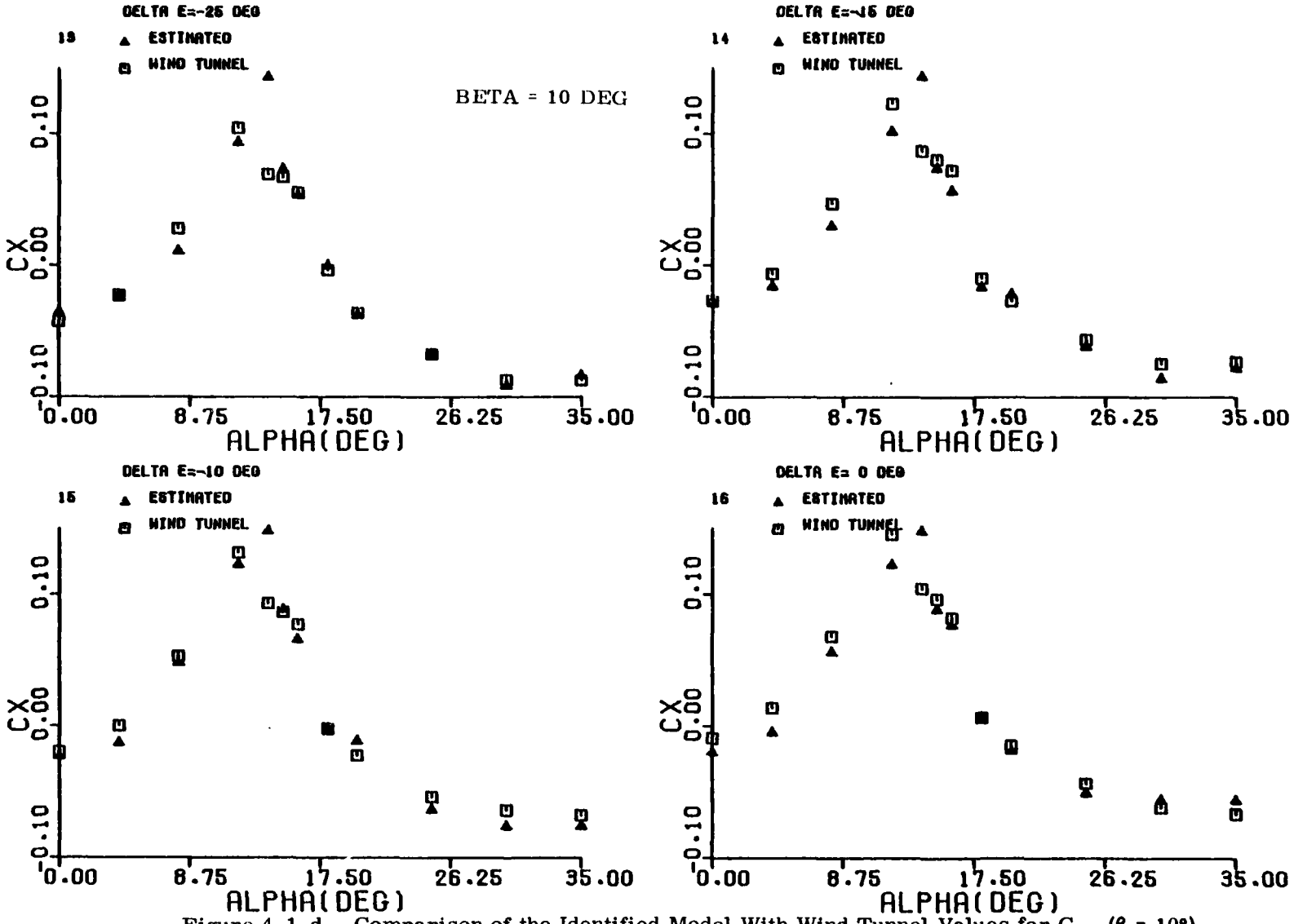

Figure 4.1.d Comparison of the Identified Model With Wind Tunnel Values for C_X (β = 10°)

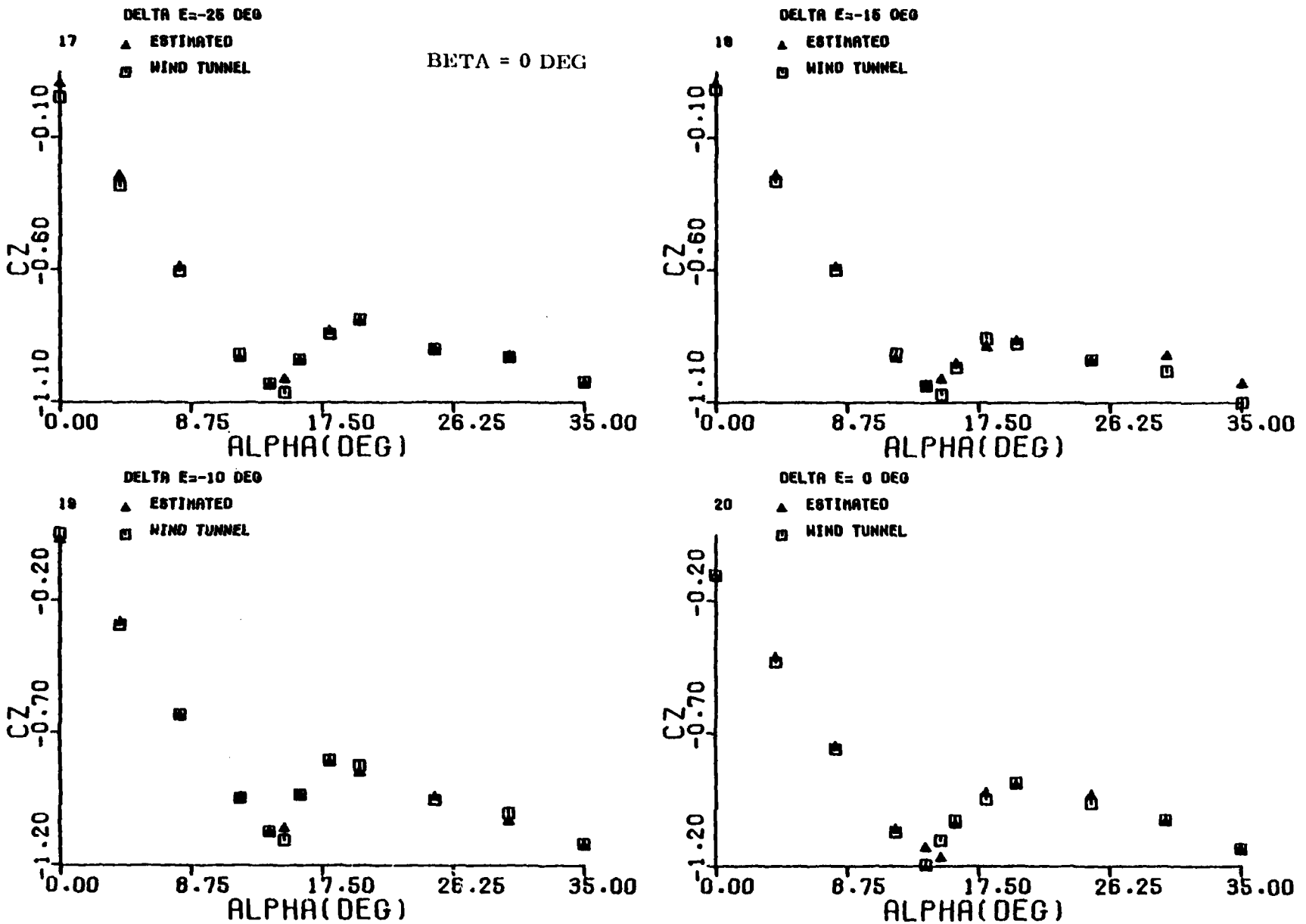

Figure 4.2.a Comparison of the Identified Model with Wind Tunnel Values for C_z ($\beta = 0°$)

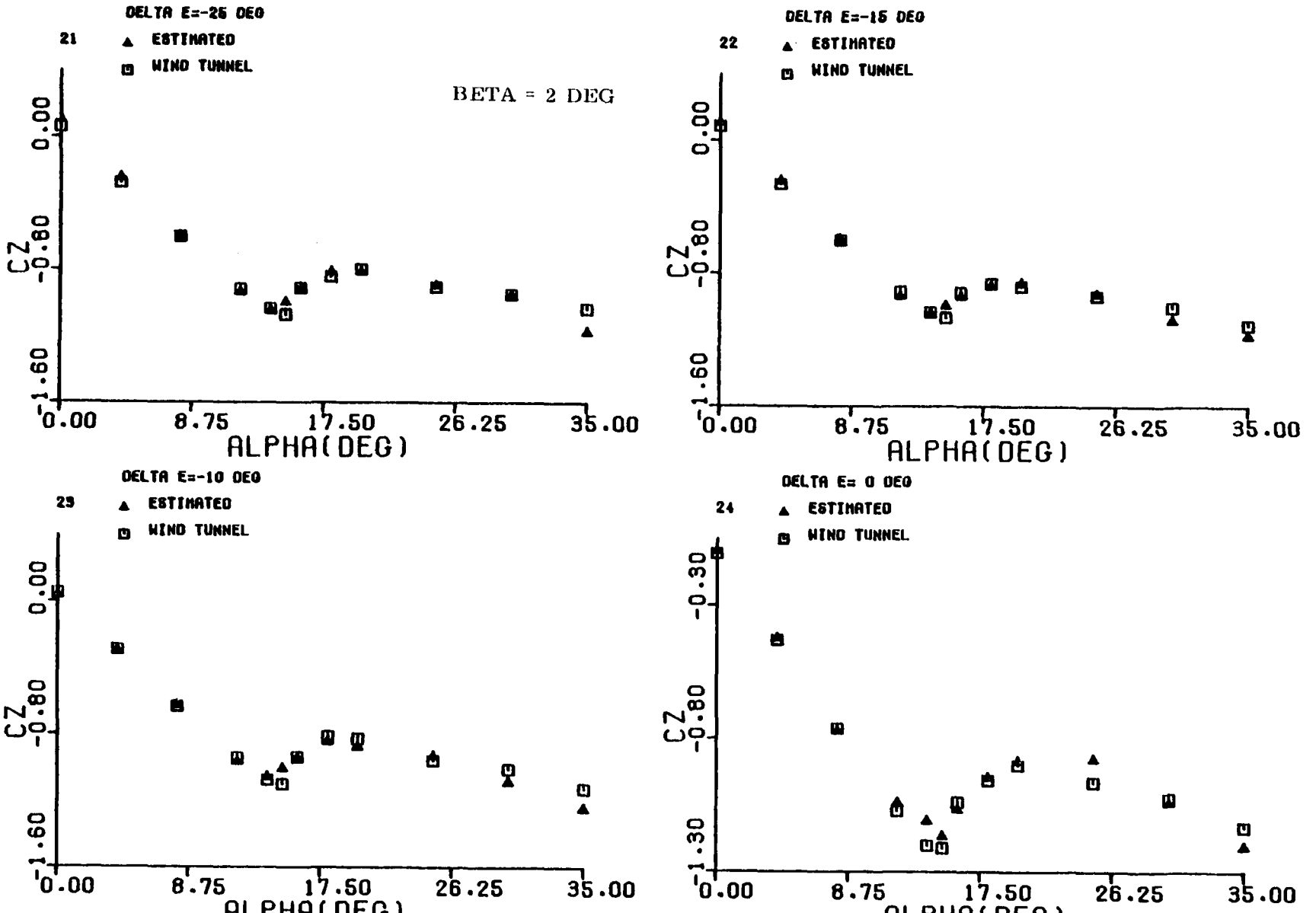

Figure 4.2.b Comparison of the Identified Model With Wind Tunnel Values for C_z (β = 2°)

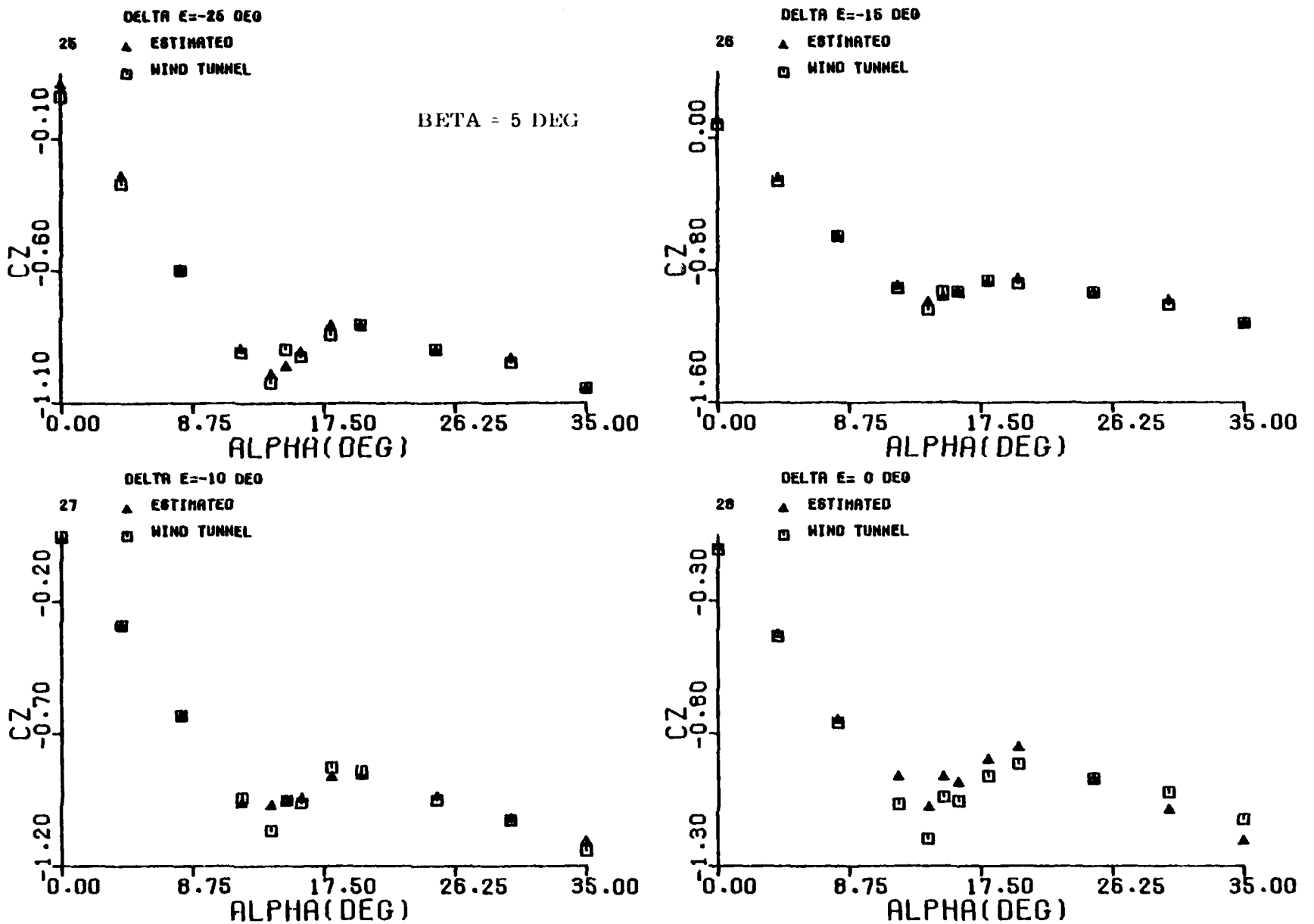

Figure 4.2.c Comparison of the Identified Model With Wind Tunnel Values for C_z (β = 5°)

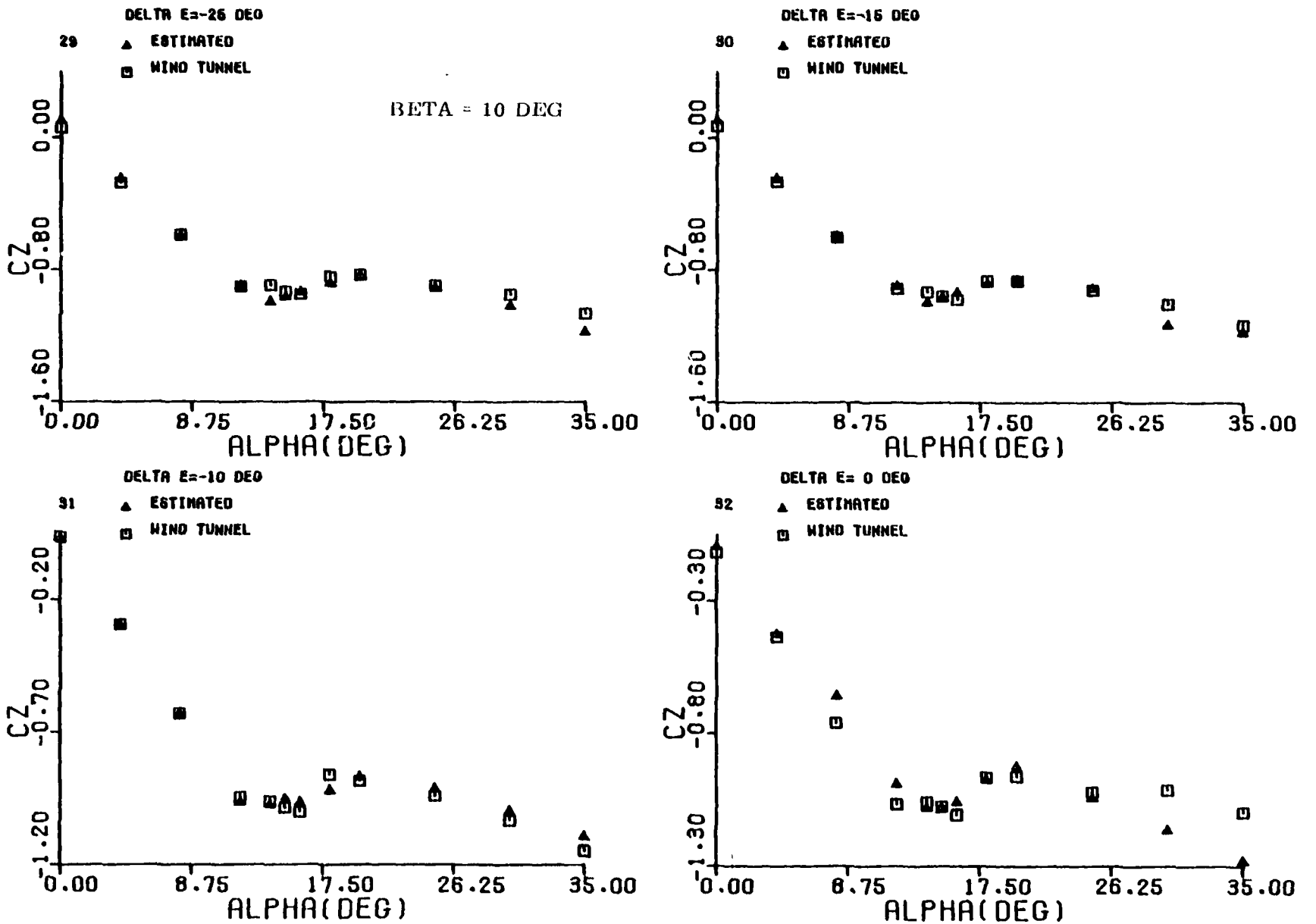

Figure 4.2.d Comparison of the Identified Model With Wind Tunnel Values for C_z (β = 10°)

The pitching moment coefficient C_m provides a much stronger test for the identification method in view of its greater sensitivity to δ_e. Figure 4.3 compares C_m for identified and wind tunnel models at various α, β and δ_e. An inspection of these figures show that not only C_m but also the control effectiveness $C_{m_{\delta_e}}$ and the pitch moment slope C_{m_α} depend on α, β and δ_e.

In general C_m varies linearly up to an angle of attack of 12 degrees after which it decreases more rapidly up to 25° degrees. Beyond 25° there is very little change in C_m with change in α. The pitch moment slope is nearly zero between 25 and 30 degrees for several cases. The control effectiveness shows a great degree of nonlinearity. At low angles of attack, the control effectiveness becomes more negative. The control effectiveness between -10° and -15° is only a fraction of that between 0° and -10°. Beyond -15° there is no control effectiveness at all. With increase in angle of attack the control effectiveness between $\delta_e = 0^\circ$ and $\delta_e = 10^\circ$ and also between $\delta_e = -10^\circ$ and $\delta_e = -15^\circ$ decreases. However, for elevator angle below -15°, the control effectiveness is negligible at low angle of attack. The actual values vary depending on α, β and δ_e.

The dynamic derivatives $C_{z_q} + C_{z_{\dot\alpha}}$ and $C_{m_q} + C_{m_{\dot\alpha}}$ did not vary significantly with β and δ_e for the identified models. Also the given wind tunnel models assumed no variation of these derivatives with respect to β and δ_e. Hence for each α the average values of $C_{z_q} + C_{z_{\dot\alpha}}$ and $C_{m_q} + C_{m_{\dot\alpha}}$ were computed using the estimated values from all subspaces. Figure 4.4 presents a comparison of estimated $C_{z_q} + C_{z_{\dot\alpha}}$ for the identified and wind tunnel models. The value of $C_{z_q} + C_{z_{\dot\alpha}}$ stays nearly constant at -6.0 up to angle of attack of 14°. At stall the derivative jumps to a positive value of 1.55 between $\alpha = 14^\circ$ and $\alpha = 16^\circ$. Beyond $\alpha = 16^\circ$ it gradually decreases to -2. Even though influence of C_{z_q} on C_z was minimal, the identified model followed the wind tunnel values quite well except at $\alpha = 14^\circ$.

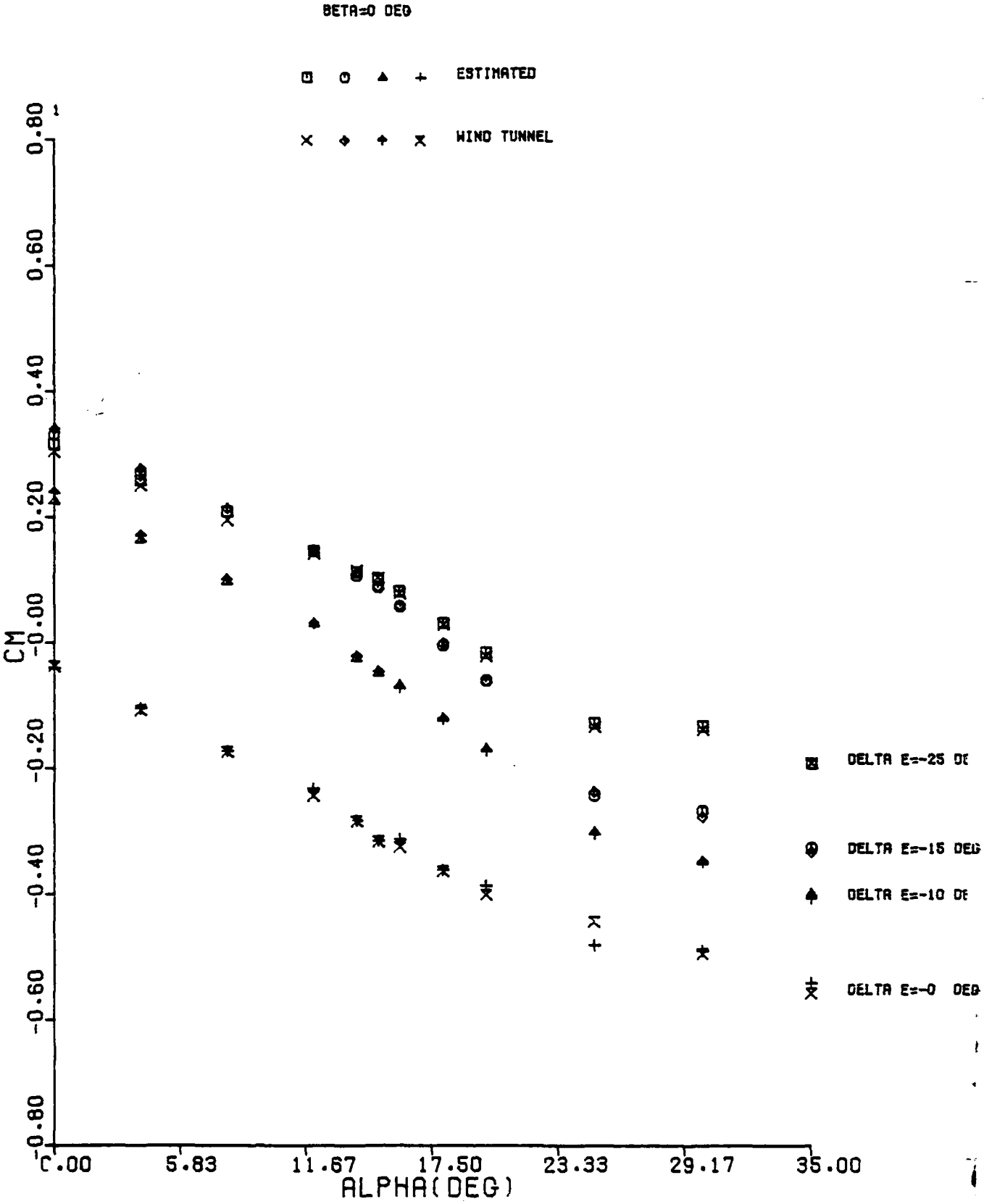

Figure 4.3.a Comparison of the Identified Model with Wind Tunnel Values for C_m ($\beta = 0°$)

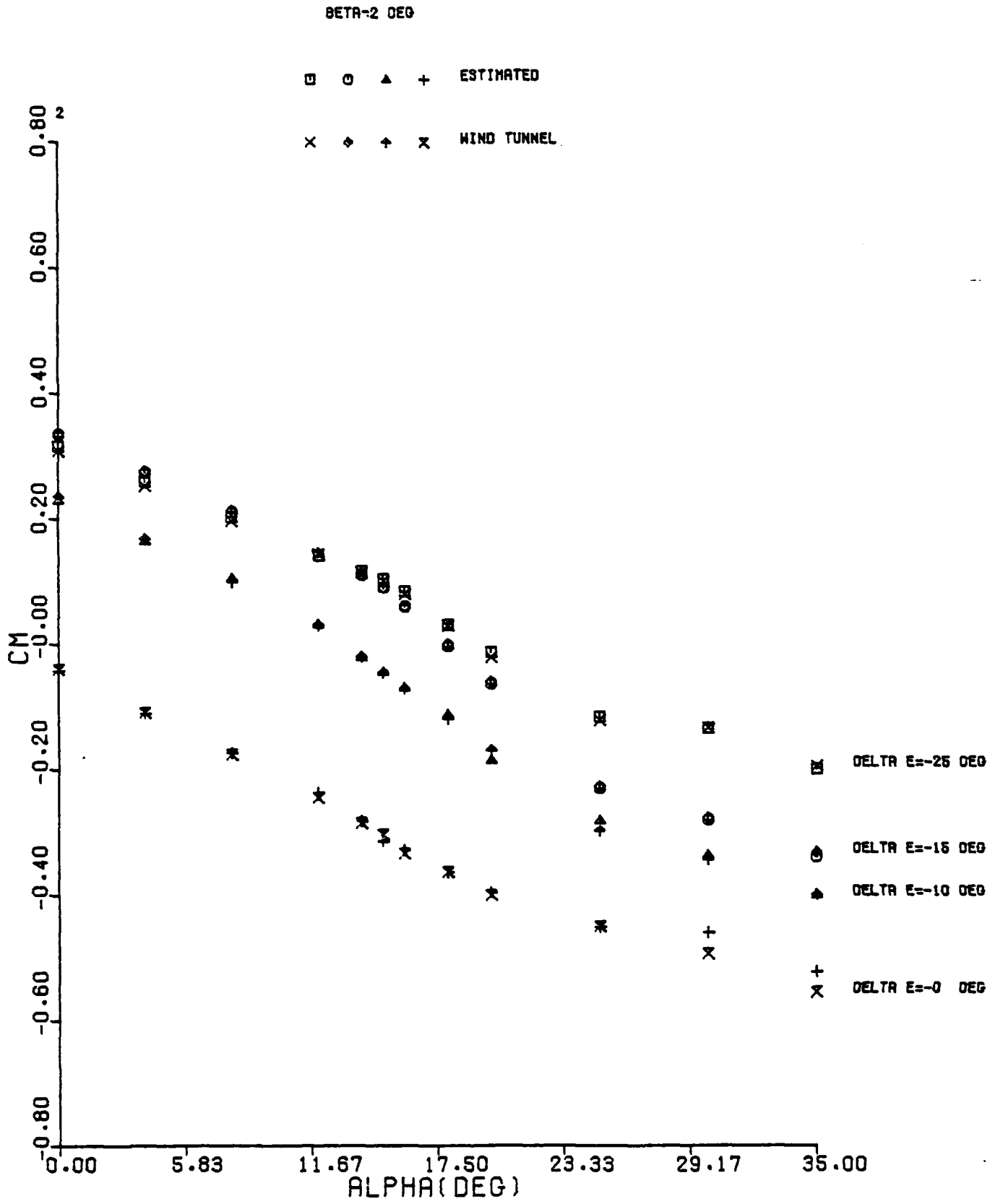

Figure 4.3.b Comparison of the Identified Model With Wind Tunnel Values for C_m (β = 2°)

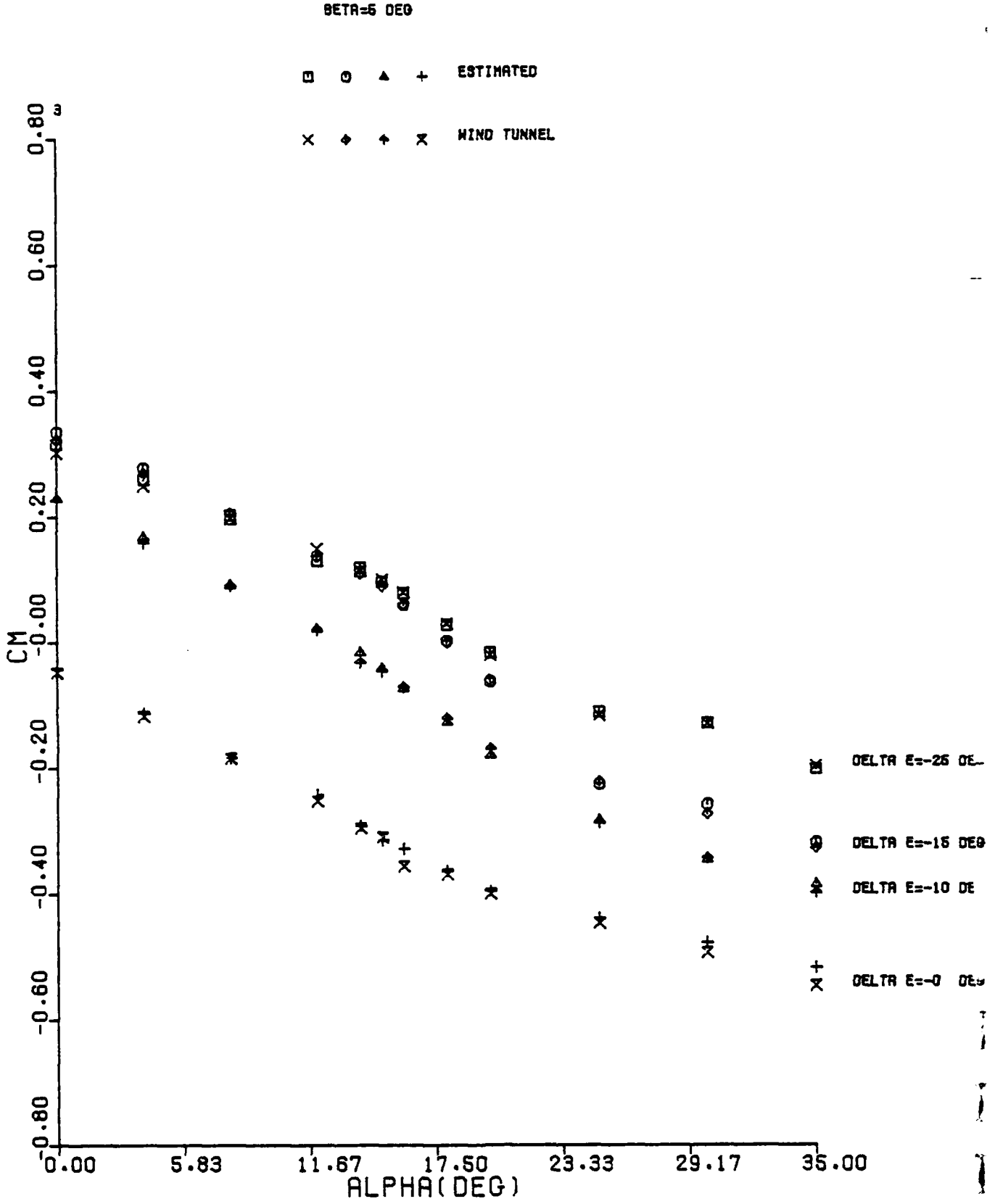

Figure 4.3.c Comparison of the Identified With Wind Tunnels for C_m

(β = 5°)

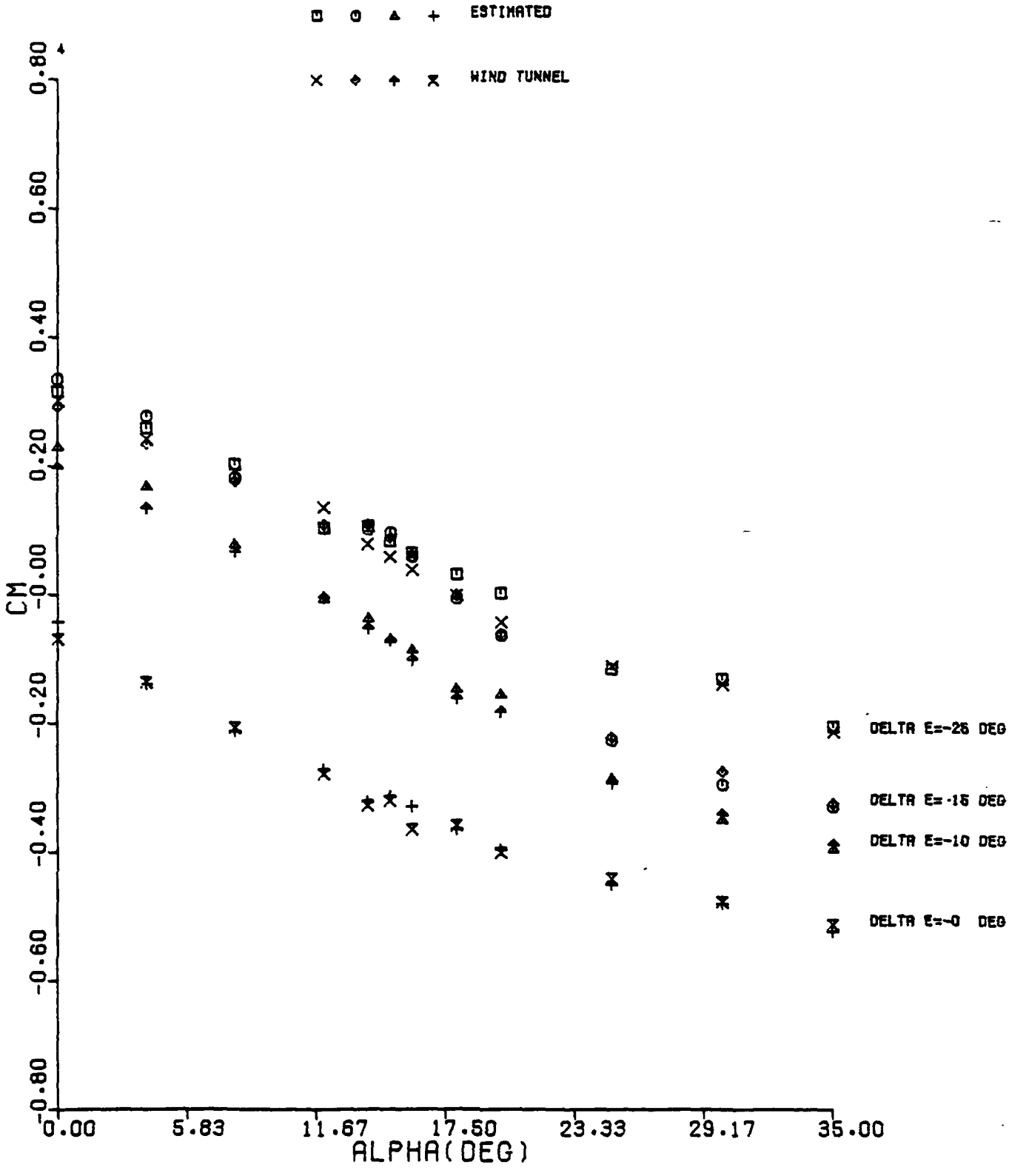

Figure 4.3.d Comparison of the Identified Model With Wind Tunnel Values for C_m ($\beta = 10°$)

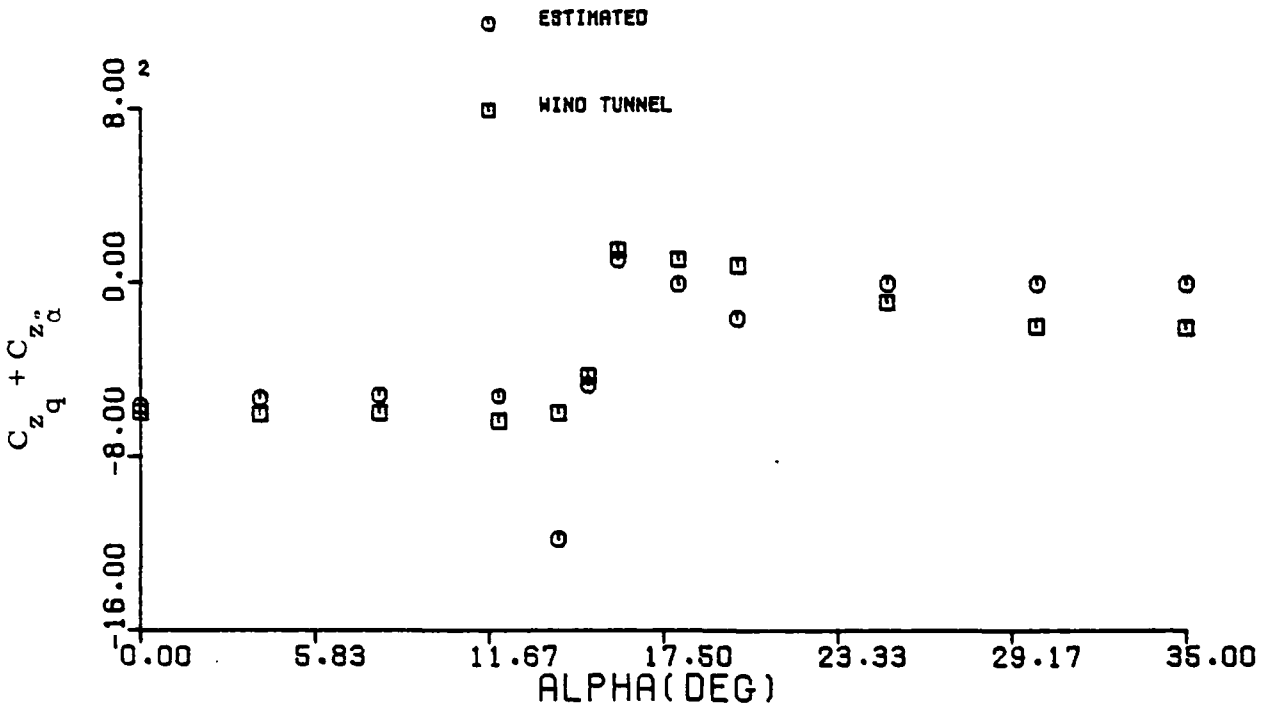

Figure 4.4 Comparison of the Identified Model with Wind Tunnel Values for $C_{z_q} + C_{z_{\dot{\alpha}}}$

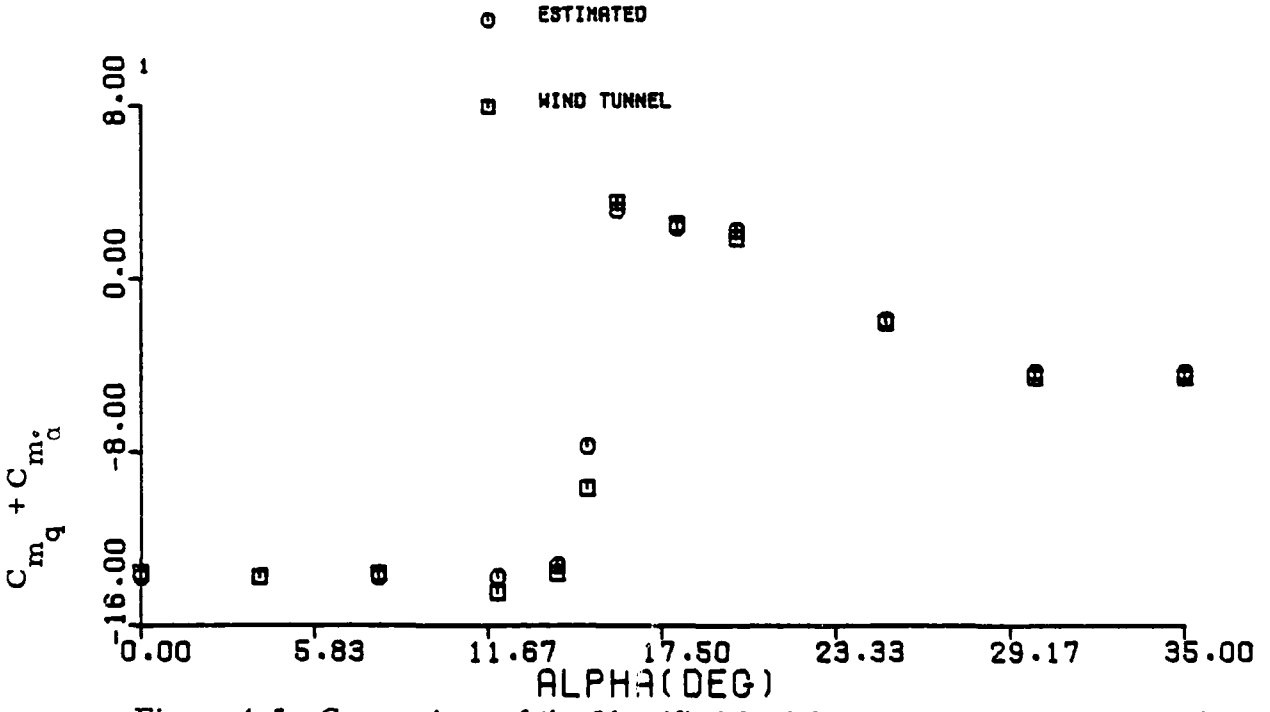

Figure 4.5 Comparison of the Identified Model with Wind Tunnel Values for $C_{m_q} + C_{m_{\dot{\alpha}}}$

Figure 4.5 compares the estimated values of $C_{m_q} + C_{m_{\dot{\alpha}}}$ against wind tunnel values. The pitch damping derivative remains nearly constant at -13.7 up to the stall angle of 14°. Immediately after stall there is a sudden loss of pitch damping and the damping coefficient jumps to a positive value of 3.55. This unstable damping is maintained up to an angle of attack of 22.5° and the damping gradually drops to a value of -4.5 at $\alpha = 30^{\circ}$ and stays constant up to $\alpha = 35^{\circ}$. We have once again excellent agreement between the estimates and the wind tunnel models. Table F- 1 gives the equations for models in the isolated regions not covered by the Figures 4.1 through 4.5.

4.5 PRELIMINARIES FOR LATERAL MODELING

In Section 1.3 the considerations for choosing subregions for modeling were discussed. For the lateral case the coefficients are influenced by both aileron and rudder deflections. It may be advantageous to divide the deflection of these surfaces into several subdivisions. But this can lead to an extremely large number of subspaces for modeling, since the total number of subspaces will be given by $N_\alpha \times N_\beta \times N_{\delta_a} \times N_{\delta_r}$ where N_α, N_β, N_{δ_a} and N_{δ_r} are the numbers of α, β, δ_a and δ_r divisions respectively. To take advantage of the antisymmetric nature of lateral forces and increase the data density in subspaces divisions of control inputs were done indirectly by defining a new set of control variables. Hence it was necessary to use only α and β for defining regions for modeling. To simplify the modeling procedure it was also decided to assume no interference between the effects of aileron, rudder and elevator and that the effects of aileron and rudder can be directly added.

For a given angle of attack, because of the symmetric configuration of the aircraft, we can assume the lateral force coefficients to be antisymmetric with respect to the sideslip angle when the control deflections are zero. Stated formally,

$$C_y(-\beta) = -C_y(\beta) \tag{4.5.1}$$

$$C_\ell(-\beta) = -C_\ell(\beta) \tag{4.5.2}$$

$$C_n(-\beta) = -C_n(\beta) \tag{4.5.3}$$

The static force coefficient at any α, β, δ_a and δ_r can be viewed to be generated by first placing the aircraft in the corresponding angles of attack and sideslip with respect to the wind and then deflecting the controls to their respective values; that is,

$$C_y = C_y(\alpha, \beta) + \Delta C_y(\delta_a) + \Delta C_y(\delta_r) \tag{4.5.4}$$

Similar equations can be written for C_ℓ and C_n.

At a given angle of attack, if we use rudder deflection alone the following four configurations are possible:

(i) β positive and δ_r positive

(ii) β positive and δ_r negative

(iii) β negative and δ_r positive

(iv) β negative and δ_r negative

Now let us consider the changes produced in the lateral forces using the values at $\beta = 0°$, $\delta_a = 0°$ and $\delta_r = 0°$ as the reference values. Because of the anti-symmetric nature of lateral forces, the changes in the force coefficient due to configuration (i) will be equal in magnitude and opposite in sign to the changes produced by (iv). Similarly the change due to configuration (ii) will be equal in magnitude and opposite in sign to that of (iii). We notice that the magnitude of contribution is the same if the sign of the product $\beta\,\delta_r$ is the same irrespective of the individual signs of β and δ_r. This is true for the effect of aileron also.

With the above considerations in mind let us define new control variables

$$\left.\begin{aligned} \delta_r^+ &= \delta_r \;, \quad \beta\,\delta_r \geq 0 \\ \delta_r^- &= 0 \;, \quad \beta\,\delta_r \geq 0 \\ \delta_r^+ &= 0 \;, \quad \beta\,\delta_r < 0 \\ \delta_r^- &= \delta_r \;, \quad \beta\,\delta_r < 0 \end{aligned}\right\} \qquad (4.5.5)$$

Similarly,

$$\left.\begin{aligned} \delta_a^+ &= \delta_a \ , \quad \beta\,\delta_a \geq 0 \\ \delta_a^- &= 0 \ , \quad \beta\,\delta_a \geq 0 \\ \delta_a^+ &= 0 \ , \quad \beta\,\delta_a < 0 \\ \delta_a^- &= \delta_a \ , \quad \beta\,\delta_a < 0 \end{aligned}\right\} \qquad (4.5.6)$$

We see that δ_r^+ corresponds to positive δ_r when β is positive and to negative δ_r when β is negative and that one configuration is the mirror image of the other. This is true for the configurations corresponding to δ_r^-, δ_a^+ and δ_a^- also.

Using Equations (4.5.1) through (4.5.6) we can write C_y as

$$C_y = C_y(\alpha, |\beta|) + \Delta C_y(\delta_r^+) + \Delta C_y(\delta_r^-) + \Delta C_y(\delta_a^+) + \Delta C_y(\delta_a^-) + \Delta C_y(\text{Dynamic}) \ , \ \beta \geq 0 \qquad (4.5.7)$$

when ΔC_y (Dynamic) is the contribution of dynamic derivatives.

Let us assume that δ_r^+, δ_r^-, δ_a^+, δ_a^- remain the same and β just reverses the sign. Recalling the definitions of δ_r^+, δ_r^-, δ_a^+ and δ_a^- and the anti-symmetric nature of the lateral forces we can write

$$C_y = -C_y(\alpha, |\beta|) - \Delta C_y(\delta_r^+) - \Delta C_y(\delta_r^-) - \Delta C_y(\delta_a^+) - \Delta C_y(\delta_a^-) + \Delta C_y(\text{dynamic}) \qquad (4.5.8)$$

Or,

$$-C_y = C_y(\alpha, |\beta|) + \Delta C_y(\delta_r^+) + \Delta C_y(\delta_r^-) + \Delta C_y(\delta_a^+) + \Delta C_y(\delta_a^-) - \Delta C_y(\text{dynamic}), \ \beta < 0 \qquad (4.5.9)$$

Similar equations can be written for C_ℓ and C_n. From the above equations we see that whenever β is negative if we reverse the signs of C_y, C_ℓ and C_n and the corresponding contributions from dynamic derivatives we can map these in the positive β domain and increase the data density for modeling.

It is important to note that the assumption of antisymmetry was made only to facilitate modeling by increasing the data density in a subspace. Such an assumption can be discarded when necessary and modeling can be done separately in the positive and negative β domains. In such a case there is no need to define δ_r^+, etc.

4.6 IDENTIFICATION OF LATERAL MODELS

As noted in the preceding section, the subregions for lateral modeling were created by using α and β. Since no control variable was used directly to define the subspaces, higher data density was obtained than for the longitudinal case. This made it possible to use narrower widths in α. The subspaces were created by partitioning α at 0°, 4°, 6°, 8°, 10°, 12°, 13°, 14°, 15°, 16°, 17°, 18°, 19°, 20°, 22.5°, 25°, 27.5°, 30° and 35°. Since few points were found when the magnitude of sideslip angle exceeded ten degrees the divisions for $|\beta|$ were at 0°, 2°, 5° and 10°. There were also data points in the regions given by: (a) $-4° \le \alpha < 0°$ and $0° \le |\beta| < 2°$; (b) $8° \le \alpha \le 12°$ and $10° \le |\beta| \le 15°$ and (c) $20° \le \alpha \le 25°$ and $10° \le |\beta| \le 15°$. As mentioned in Section 4.1, the data points were fewer at higher angles of attack and also most of the points in the regions given by $5° \le |\beta| \le 10°$ fell below $|\beta| = 8°$. There were not enough data points between $\alpha = 0°$ and $\alpha = 6°$ for $|\beta| > 5°$. The total number of subregions used to obtain lateral model were 55. Instead of trying to find one very complex model for the lateral forces, we have reduced it to finding 55 simpler models in various regions and compiling them to give us a global model.

As a first try linear models in α, β, δ_a^+, δ_a^-, δ_r^+, δ_r^-, p, r and $\dot{\beta}$ were considered. From Eqs. (4.5.7) and (4.5.9) we see that the data points in the negative β region can be considered along with the data points in the positive β region if we

reverse the sign of C_y and the dynamic terms. Then the regression equation can be written as

$$C_y = C_{y_{stat}} + C_{y_{dyn}} \quad , \quad \beta \geq 0 \tag{4.6.1}$$

$$-C_y = C_{y_{stat}} - C_{y_{dyn}} \quad , \quad \beta < 0 \tag{4.6.2}$$

where $C_{y_{stat}}$ and $C_{y_{dyn}}$ are given by

$$C_{y_{stat}} = C_{y_o} + C_{y_\alpha}(\alpha - \alpha_o) + C_{y_\beta}(|\beta| - |\beta_o|) + C_{y_{\delta_a^+}} \delta_a^+ + C_{y_{\delta_a^-}} \delta_a^- + C_{y_{\delta_r^+}} \delta_r^+ + C_{y_{\delta_r^-}} \delta_r^- \tag{4.6.3}$$

$$C_{y_{dyn}} = (C_{y_p} p + C_{y_r} r - C_{y_{\dot\beta}} \dot\beta) \frac{b}{2V} \tag{4.6.4}$$

The reference values α_o & $|\beta_o|$ are the values of α and $|\beta|$ at the lowest corner of the modeling subregion. The regression equations for C_ℓ and C_n are similar. The SMLR method chooses the best values of the coefficients in the regression equations to match C_y, etc. in each region. There may be small discontinuities in C_y etc. at the region boundaries since continuity is not imposed at the boundary. However the differences will be negligible if small region widths are used, the noise on the stochastic estimates of the forces is small and the model matches the data very closely.

Identification was performed to obtain models in all regions. The procedure was the same as that used for the longitudinal model determination. The models seemed adequate and matched the forces with very high correlations for C_ℓ and C_n, but not for C_y. It was also found that the dynamic derivatives changed rapidly after stall. Thus the nonlinear terms $p\alpha$ and $r\alpha$ were chosen to be additional states for modeling.

The new expression for Equation (4.6.4) then becomes

$$C_{y_{dyn}} = (C_{y_p} p + C_{y_r} r + C_{y_{p\alpha}} p(\alpha-\alpha_o)+C_{y_{r\alpha}} r(\alpha-\alpha_o) - C_{y_{\dot\beta}} \dot\beta)\frac{b}{2V} \quad (4.6.5)$$

Equations for $C_{\ell_{dyn}}$ and $C_{n_{dyn}}$ are similar. Using the new model structure models were once again obtained for C_y, C_ℓ and C_n in all regions. Models were obtained with high R^2, low RSS and low standard deviations for parameter values. However in the outer regions where there were less points the uncertainties in the estimates of the parameters were somewhat high and in some cases the multiple correlation coefficient was also low.

For C_y (even though the RSS was within the error level of the stochastic estimate of C_y), the R^2 value was lower. In general, for C_ℓ the R^2 values were close to one. For C_n the R^2 values varied from 0.96 to 0.99. The R^2 values on C_y however varied from 0.7 to 0.9. As was in the case of C_x the reason once again was that the error on C_y estimates was comparable to the variation of C_y in the region. (This is due to higher noise-to-signal ratio in the measurement of a_y.) Using higher order terms did not change the model at all indicating that the low correlation was more due to noise than the structure of the model itself. Comparisons against the wind tunnel value verified this. As in the case of longitudinal models, extraneous terms such as q and δ_e were correctly discarded when introduced as additional variables for lateral modeling.

4.7 GLOBAL MODEL AND DISCUSSION OF LATERAL RESULTS

A short discussion of the lateral modeling results is given below. In view of the assumed antisymmetry of lateral forces, the results are presented for positive or absolute values of sideslip angle only.

Identified values of C_y, C_ℓ, C_{ℓ_β}, $C_{\ell_{\delta_a^+}}$, $C_{\ell_{\delta_a^-}}$, C_{ℓ_p}, C_{ℓ_r}, C_n, C_{n_β}, $C_{n_{\delta_r^+}}$, $C_{n_{\delta_r^-}}$, C_{n_p} and C_{n_r} are plotted as functions of α for $\beta = 0°$, $2°$, $5°$ and $10°$ and compared against wind tunnel values in Figures 4-6 through 4-18. Identified values of C_{y_β}, $C_{y_{\delta_r^+}}$, $C_{y_{\delta_r^-}}$, $C_{y_{\delta_a^+}}$, $C_{y_{\delta_a^-}}$, C_{y_r}, $C_{\ell_{\delta_r^+}}$, $C_{\ell_{\delta_r^-}}$, C_{ℓ_α}, $C_{\ell_{p\alpha}}$, $C_{\ell_{r\alpha}}$, $C_{n_{\delta_a^+}}$, $C_{n_{\delta_a^-}}$, C_{n_α} and $C_{n_{r\alpha}}$ are compared against wind tunnel values for various α and β in Tables F-2 through F-16. Very accurate lateral models were obtained using the two-step approach.

Figure 4.6 shows a comparison between the estimated and wind tunnel values of C_y. The values at $\beta = 10°$ were computed using the model for the region $5° \leq |\beta| \leq 10°$. With increasing β we see a higher degree of nonlinearity in the stall region. The identified model follows the wind tunnel values very well throughout. In this and all the following curves for lateral coefficients, due to lack of data for modeling, the values at $\alpha = 0°$ and $\alpha = 4°$ were extrapolated from neighboring regions when $5° \leq |\beta| \leq 10°$. It was found that for the C_y model the most influential derivative was C_{y_β} whose values are presented and compared against the wind tunnel values in Table F-2. The general trend is that C_{y_β} becomes less negative as angle of attack increases, reaches a maximum value around stall angle and then becomes more negative. The value of C_{y_β} depends on both α and β. Good estimates were obtained for C_{y_β}. It was found that the rudder deflection had a weak effect on C_y. In several regions the contribution from δ_r was not strong enough for lack of excitation of

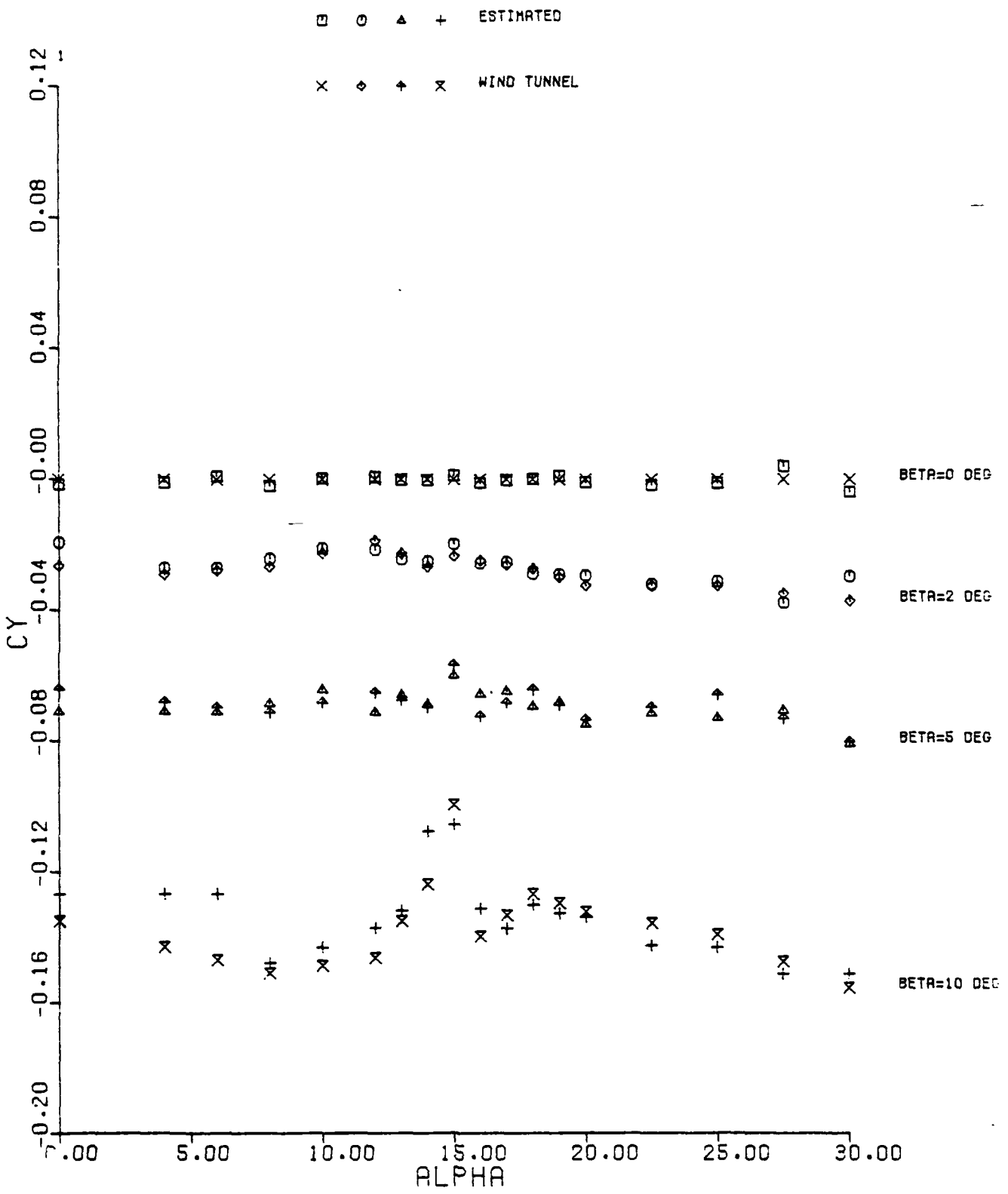

Figure 4.6 Comparison of the Identified Model with Wind Tunnel Values for C_y

δ_r^+ and δ_r^- or the effect was not stronger than the noise level on C_y. The $C_{y_{\delta_r^+}}$ and $C_{y_{\delta_r^-}}$ derivatives and their wind tunnel values are given in Tables F-3 and F-4. In all tables a value of zero is given for a parameter when its contribution was considered insignificant by the SMLR algorithm. The derivatives $C_{y_{\delta_a^+}}$, $C_{y_{\delta_a^-}}$ and C_{y_r} had much weaker influence on C_y and values for these could be extracted only in certain regions. These are given in Tables F-5, F-6 and F-7.

In Figure 4.7 we find that the estimated values of C_ℓ follow the wind tunnel values very well. In general with the increase in angle of attack C_ℓ increases in magnitude reaching a maximum in the stall region. With further increase in angle of attack it decreases in magnitude. The shape of the C_ℓ curve varies with β. Figure 4.8 gives a comparison between estimates of C_{ℓ_β} and wind tunnel values. The parameter C_{ℓ_β} varies in a very complex fashion with α and β.

Decreasing aileron effectiveness in roll is noticed with increasing angle of attack in Figures 4.9 and 4.10. Since the values are constant in a modeling region they have been plotted at the mid point of the regions. Much of the loss in control effectiveness occurs in the stall region. At higher angles of attack the control is still effective though the values are very small compared to those at low angles of attack. Excellent estimates have been obtained for both $C_{\ell_{\delta_a^+}}$ and $C_{\ell_{\delta_a^-}}$. It was also found that $C_{\ell_{\delta_a^+}}$ and $C_{\ell_{\delta_a^-}}$ were not equal at higher values of α and β. From Tables F-8 and F-9 we see that compared to the aileron, the rudder has an almost insignificant influence on C_ℓ. In some regions the effect of rudder was negligible compared to other terms in the model ... estimates were obtained for $C_{\ell_{\delta_r^+}}$ and $C_{\ell_{\delta_r^-}}$. In general the estimates of ... derivatives were quite satisfactory considering their weak effect.

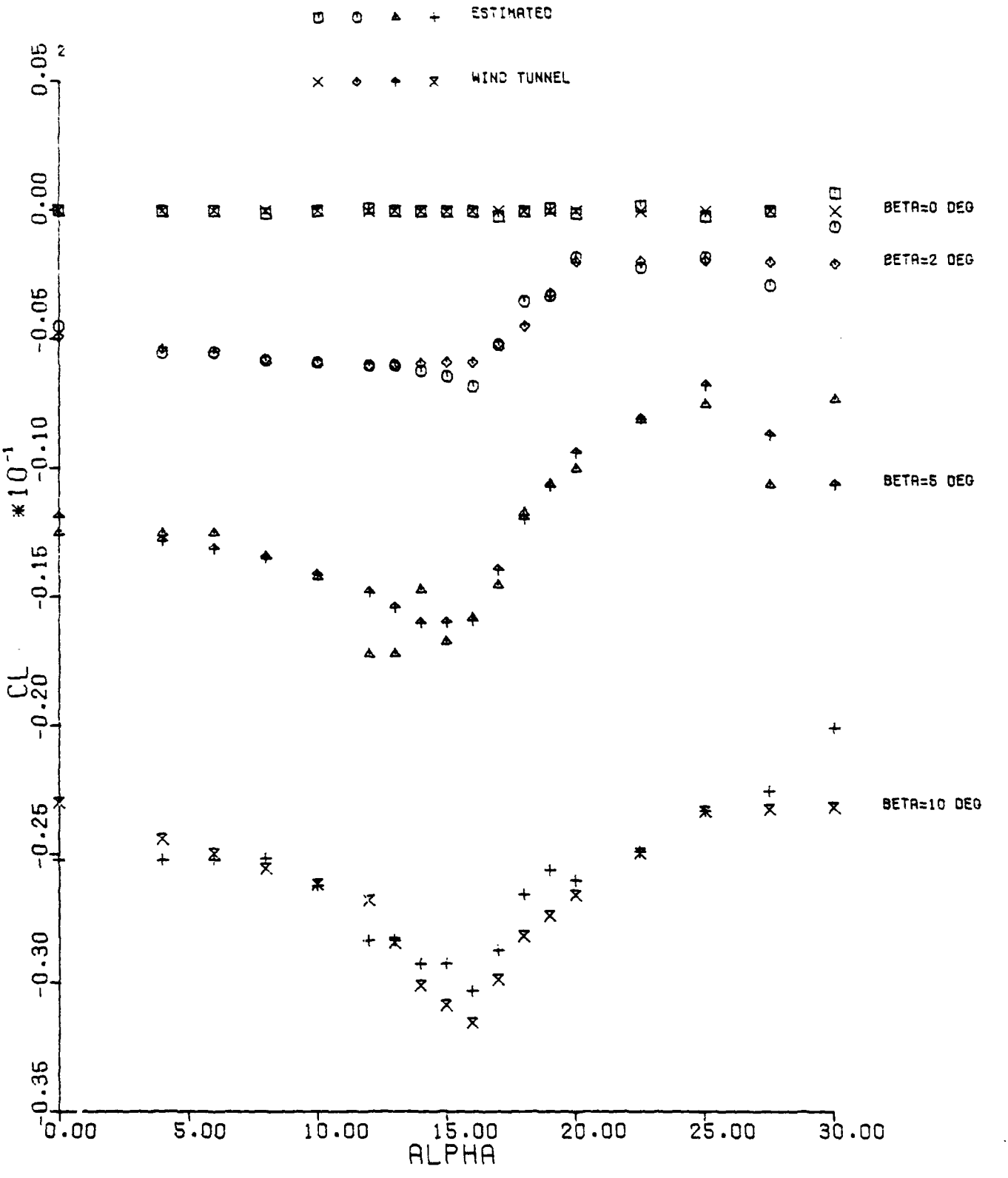

Figure 4.7 Comparison of the Identified Model with Wind Tunnel Values for C_ℓ

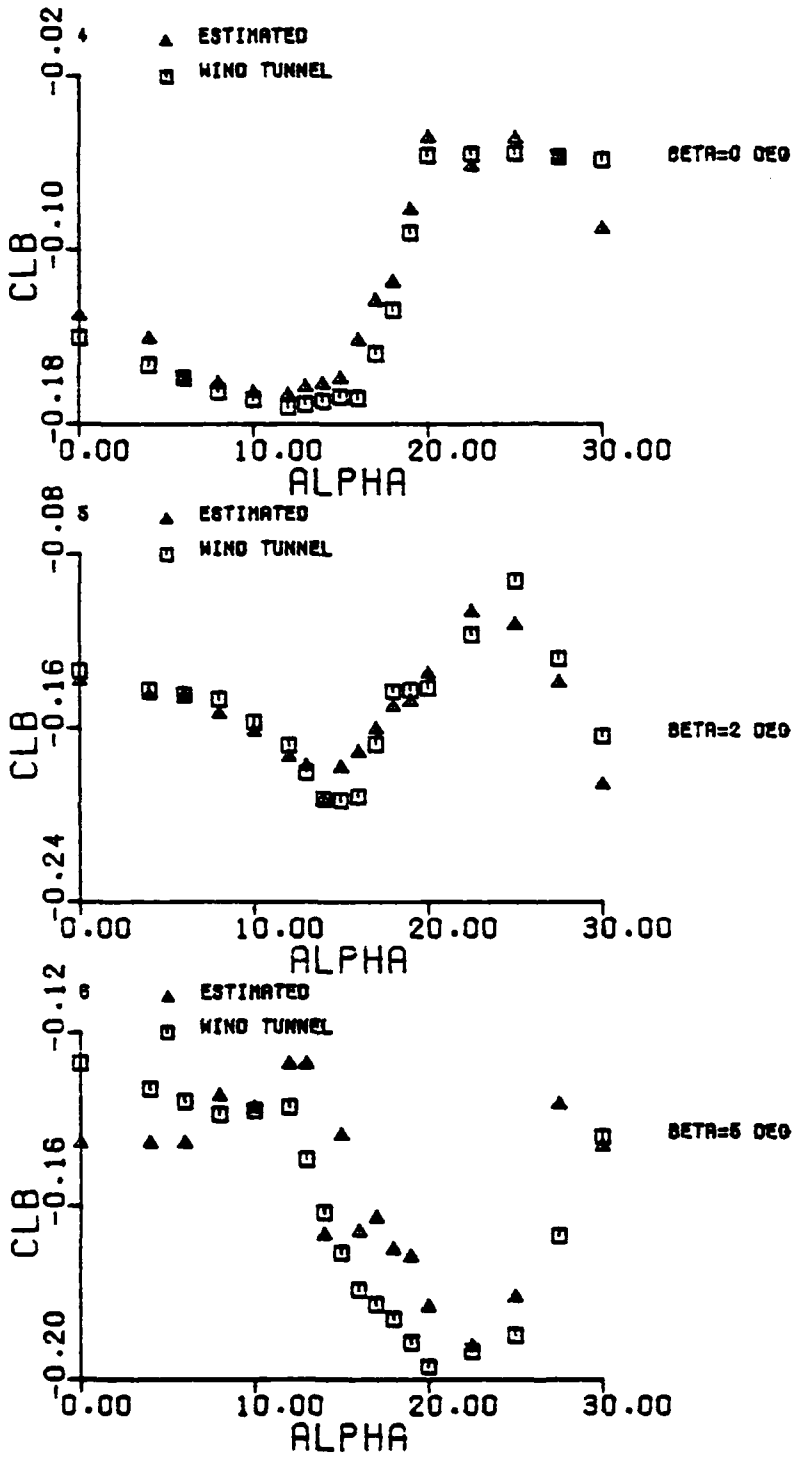

Figure 4.8 Comparison of the Identified Model with Wind Tunnel Values for C_{ℓ_β}

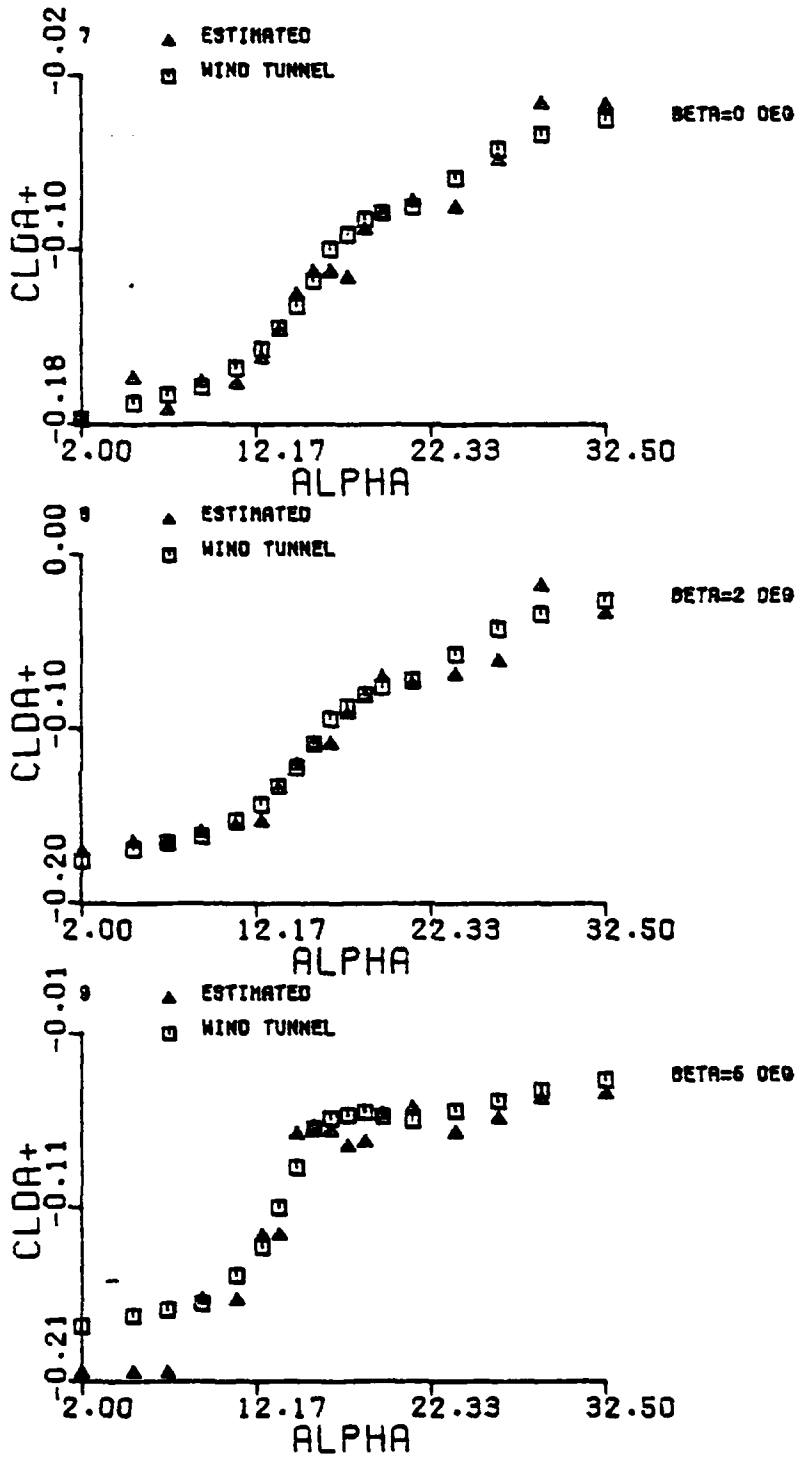

Figure 4.9 Comparison of the Identified Model with Wind Tunnel Values for $C_{\ell_{\delta_a}+}$

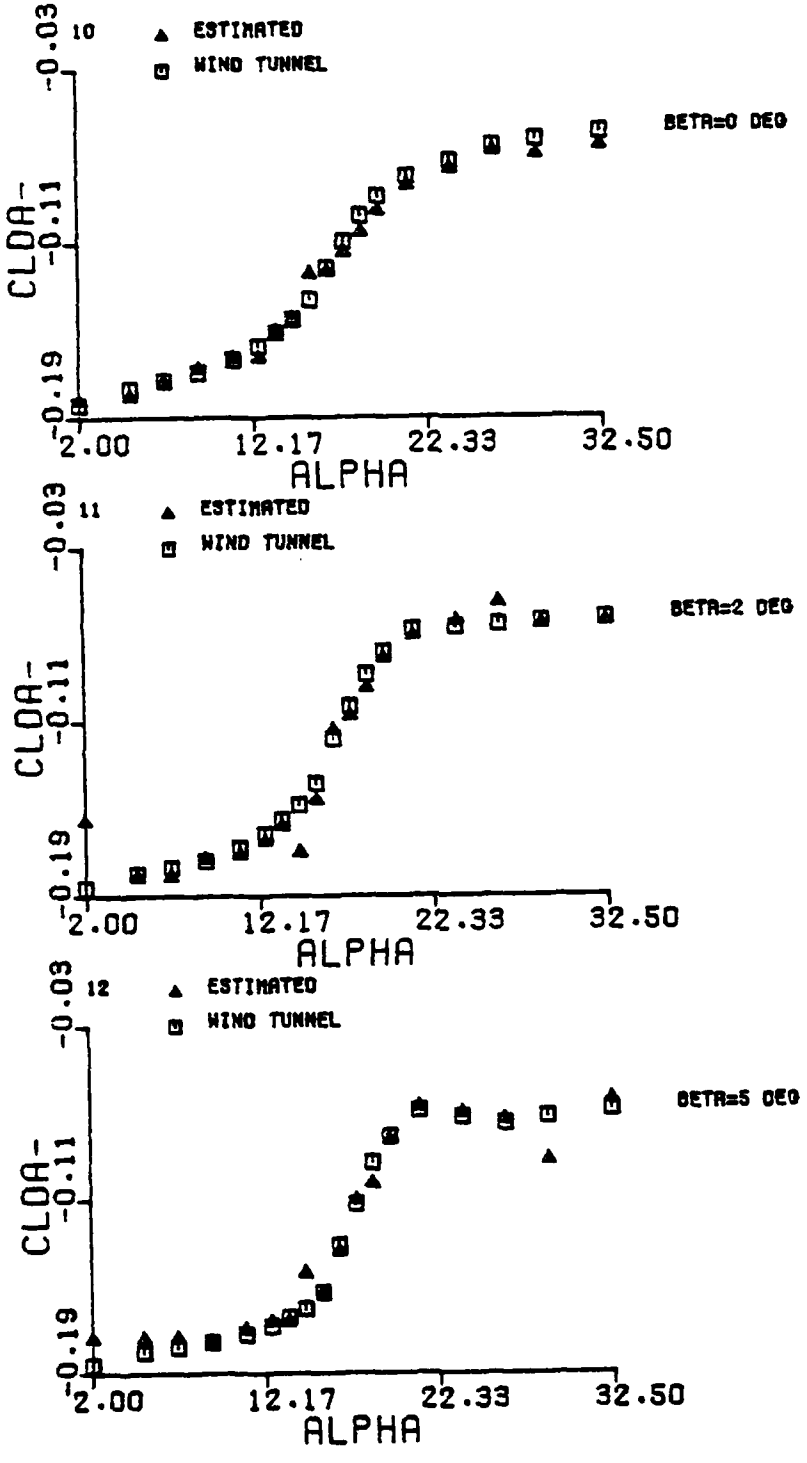

Figure 4.10 Comparison of the Identified Model with Wind Tunnel Values for $C_{\ell_{\delta_a}}$

The roll damping derivative C_{ℓ_p} stays constant up to an angle of attack of ten degrees and starts decreasing after that (Fig. 4.11). Immediately after stall it jumps to an unstable value of 0.3 and stays positive up to an α of 20°. Beyond that the roll damping is very small. The identified model follows this highly nonlinear variation extremely well. As the value of C_{ℓ_p} did not vary significantly with β, the plot gives an average value.

The variation of C_{ℓ_r} is also very nonlinear with α with most of the changes occurring between angles of attack of 14° and 22.5° (Fig. 4.12). Once again we have an excellent estimate of the coefficient. The plot gives an average value of C_{ℓ_p} as there was no significant change in C_{ℓ_r} with β. Even though $\dot{\beta}$ was used as an additional variable, the SMLR correctly excluded the $\dot{\beta}$ term from the identified models. The wind tunnel value for $C_{\ell_{\dot{\beta}}}$ was zero. For the given model the identification technique was successful in separating the parameters C_{ℓ_r} and $C_{\ell_{\dot{\beta}}}$. The estimated values of C_{ℓ_α}, $C_{\ell_{p\alpha}}$ and $C_{\ell_{r\alpha}}$ are given in Tables F-10, F-11 and F-12.

Figure 4.13 compares estimated and wind tunnel values of C_n. For $\beta = 2°$ and $\beta = 5°$, C_n initially decreases in magnitude with α, increases near stall angle, decreases rapidly after stall becoming nearly zero at $\alpha = 20°$ and then remains very small in magnitude. For $\beta = 10°$, C_n decreases in magnitude with α, falls sharply in the stall region and reaches a negative value at $\alpha = 18°$. With further increase in α, the value of C_n increases slightly. Very good agreement is noticed between the estimates and the wind tunnel values. From Figure 4.14 we see that the modeling technique obtained good estimates of C_{n_β} despite its complex variation. The parameter C_{n_β} is positive at low angles, declines in value rapidly through stall and becomes extremely small or negative in the post stall region.

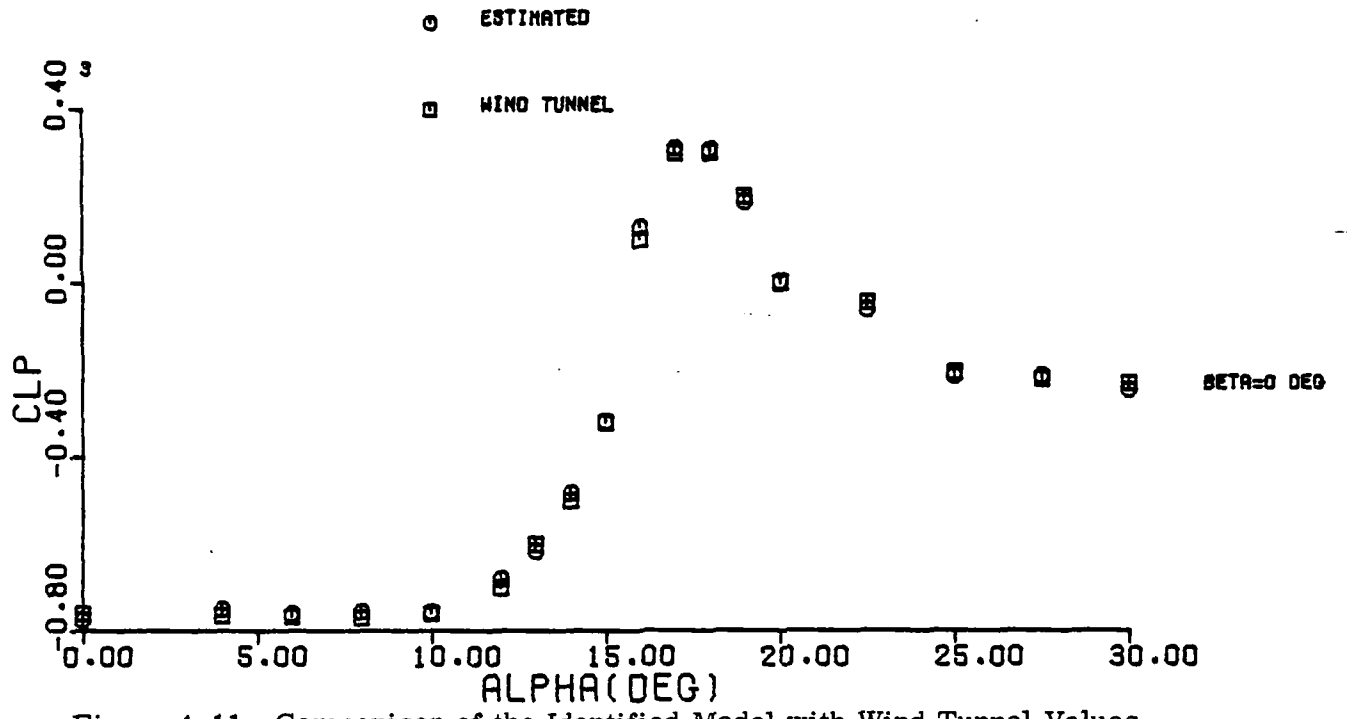

Figure 4.11 Comparison of the Identified Model with Wind Tunnel Values for C_{ℓ_p}

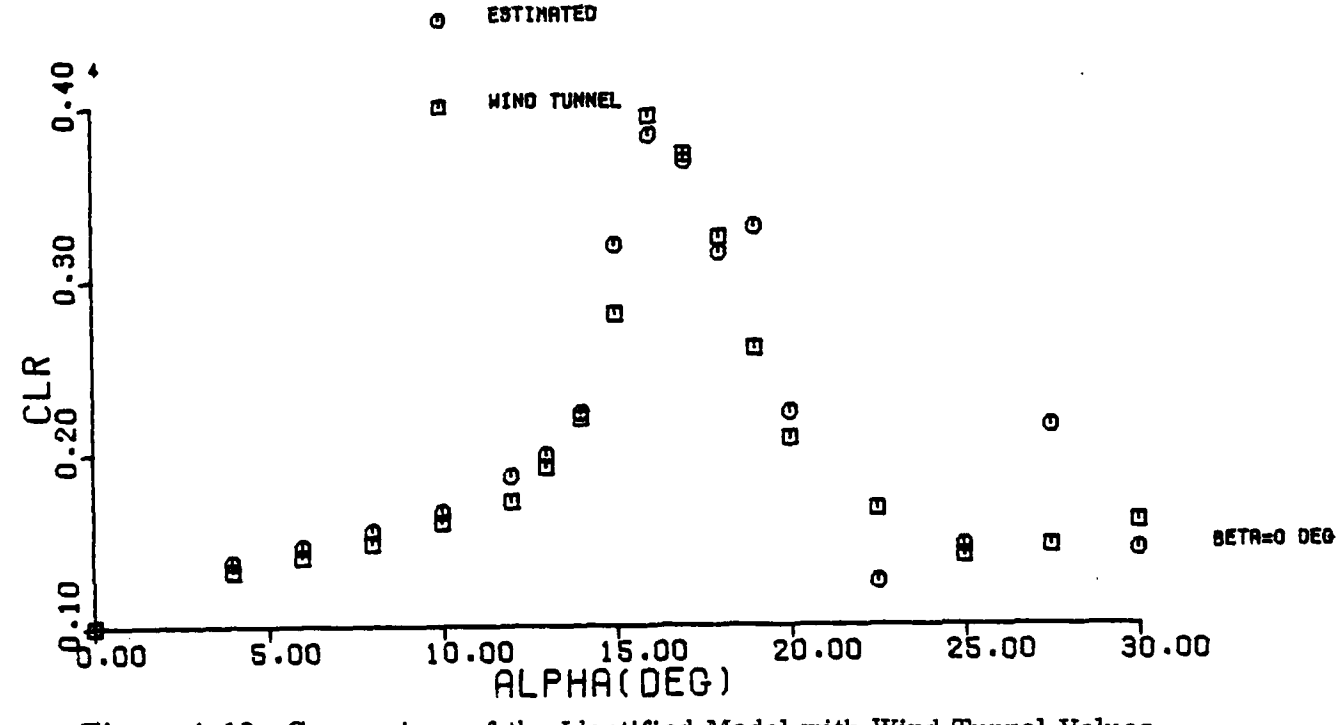

Figure 4.12 Comparison of the Identified Model with Wind Tunnel Values for C_{ℓ_r}

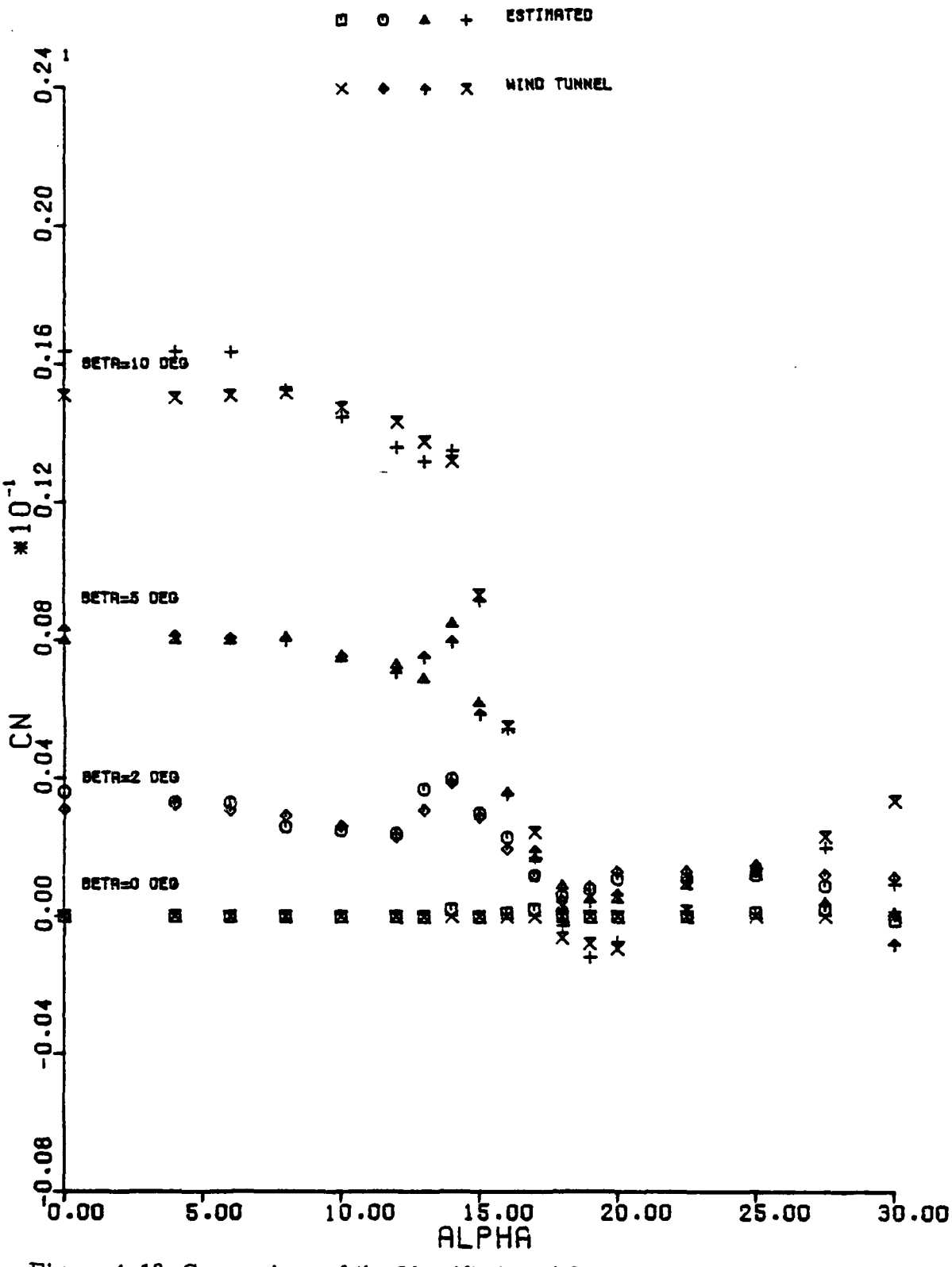

Figure 4.13 Comparison of the Identified Model with Wind Tunnel Values for C_n

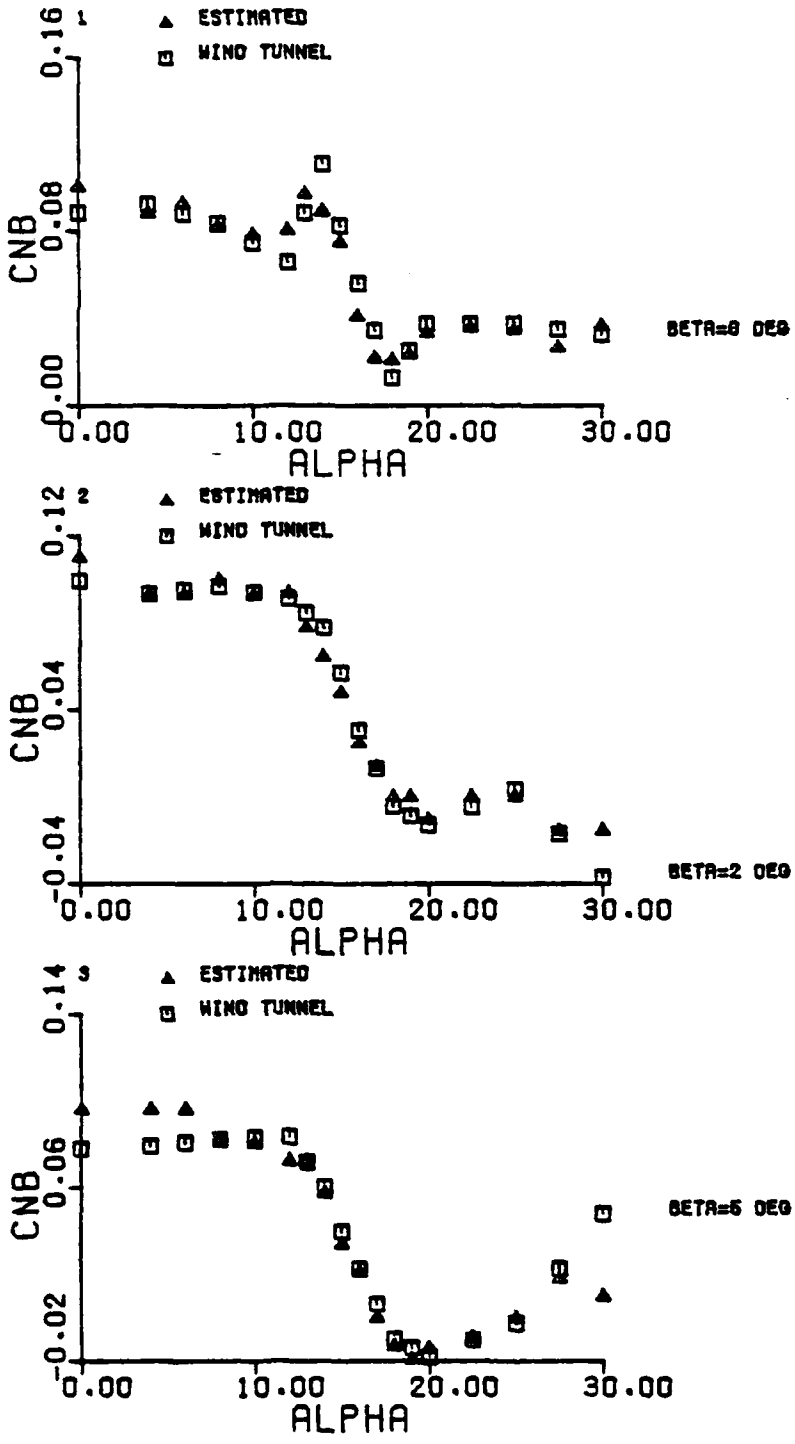

Figure 4.14 Comparison of the Identified Model with Wind Tunnel Values for C_{n_β}

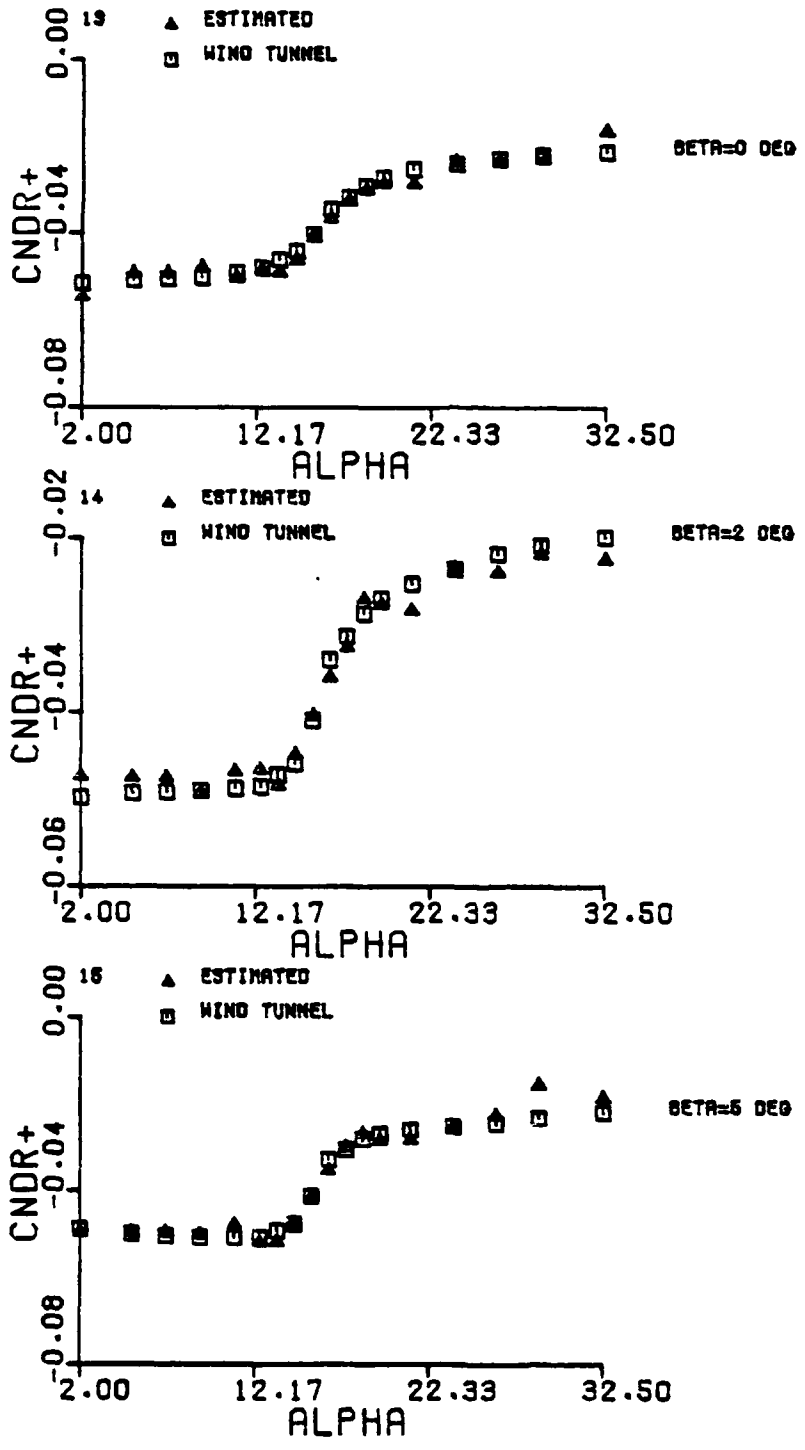

Figure 4.15 Comparison of the Identified Model with Wind Tunnel Values for $C_{n_{\delta_r}+}$

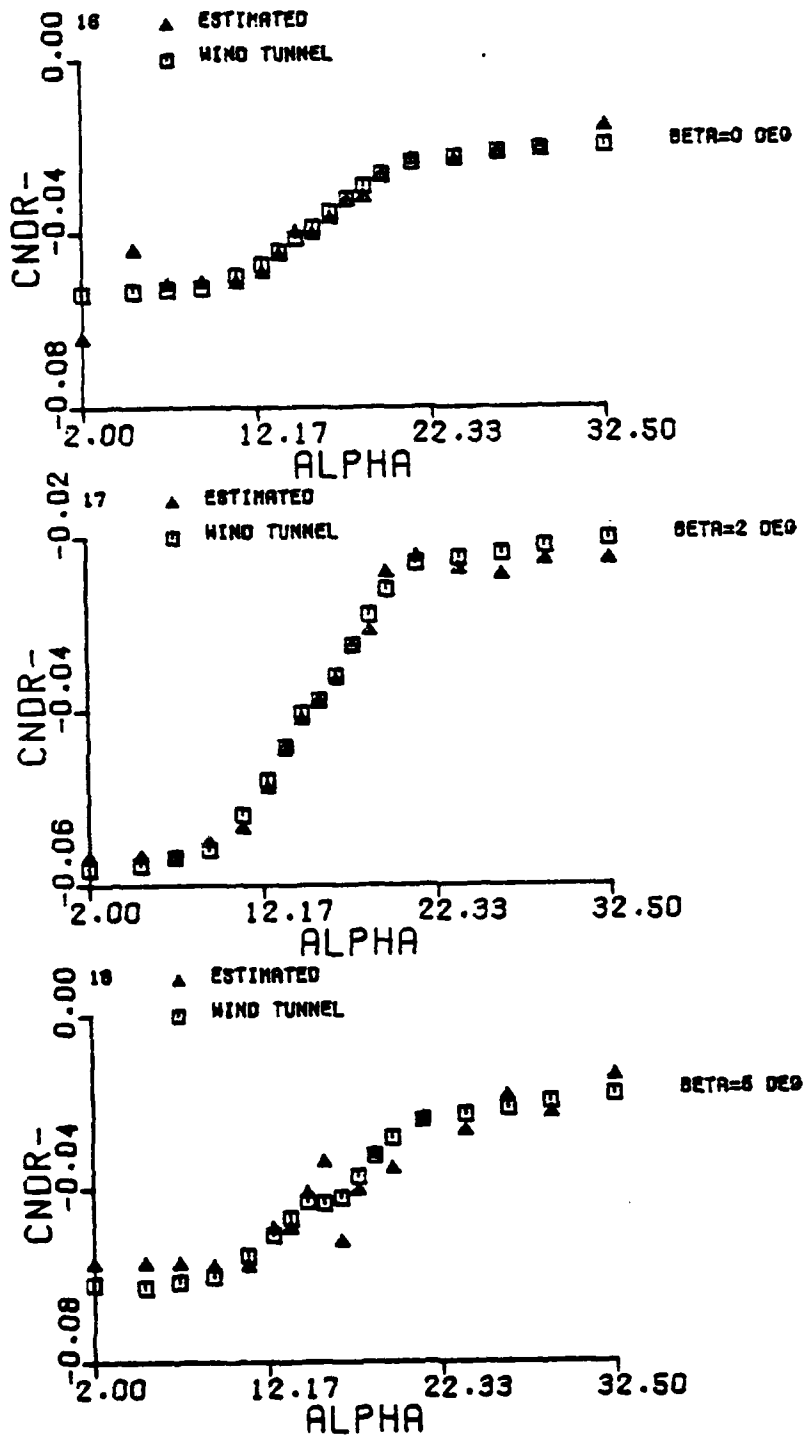

Figure 4.16 Comparison of the Identified Model with Wind Tunnel Values for $C_{n_{\delta_r}}$

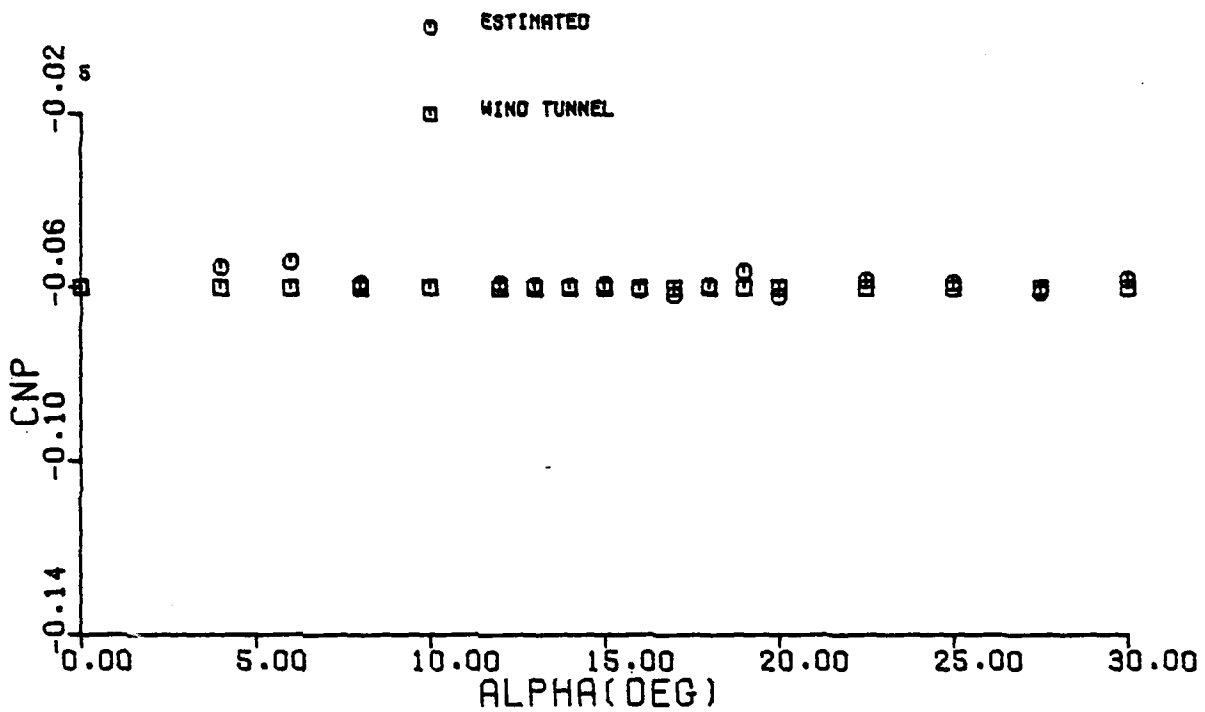

Figure 4.17 Comparison of the Identified Model with Wind Tunnel Values for C_{n_p}

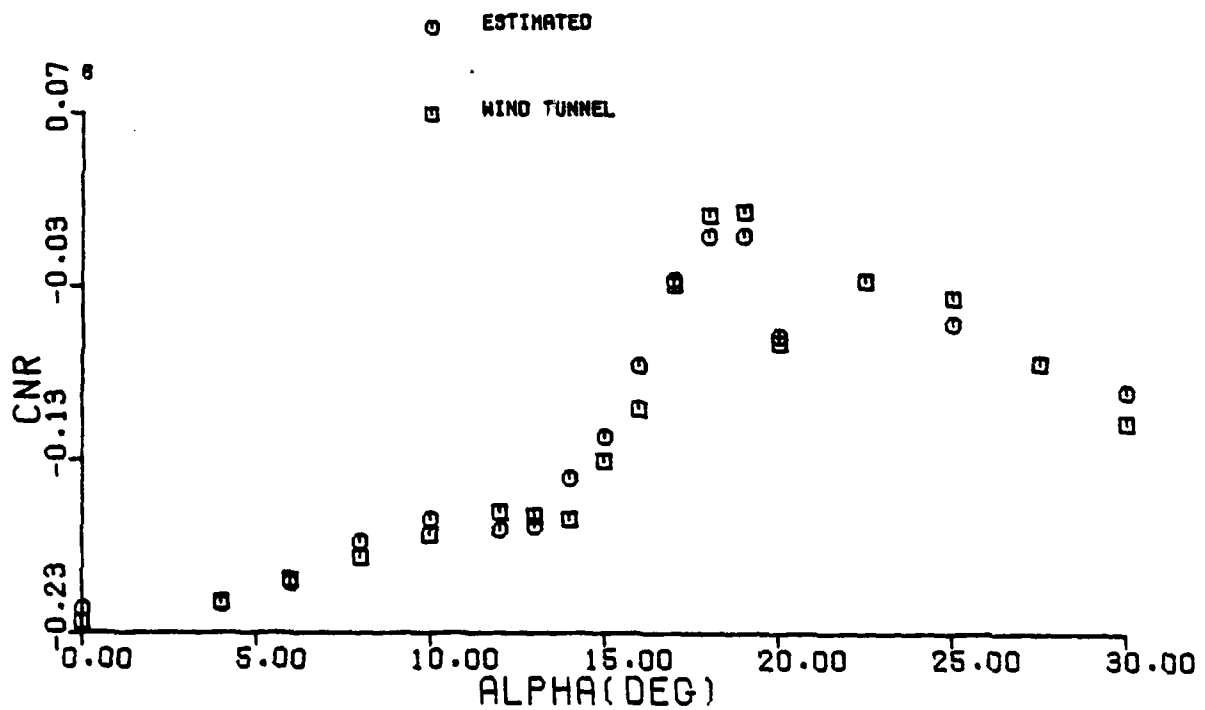

Figure 4.18 Comparison of the Identified Model with Wind Tunnel Values for C_{n_r}

Figures 4.15 and 4.16 show rudder effectiveness as a function of angle of attack at various sideslip angles. In general there is a decrease in rudder effectiveness with increasing angle of attack. Much of the loss in control effectiveness occurs in the stall regions. Very good estimates have been obtained for both $C_{n_{\delta_r^+}}$ and $C_{n_{\delta_r^-}}$. The influence of aileron was very small compared to that of rudder. Because of this, only in a few regions the parameters $C_{n_{\delta_a^+}}$ and $C_{n_{\delta_a^-}}$ were significant enough to be estimated (Tables F-13 and F-14).

From Figures 4.17 and 4.18 we see that the estimated values of the dynamic derivatives C_{n_p} and C_{n_r} are very close to the wind tunnel values. As there was little variation of C_{n_p} and C_{n_r} with β the plots show average values of these two parameters. The parameter C_{n_r} decreases with increasing angle of attack, experiences sudden loss after stall and becomes positive. With further increase in α, the parameter becomes negative again though the value is much smaller than at low angles of attack. Just as in the case of $C_{\ell_{\dot{\beta}}}$ the identification technique was successful in separating C_{n_r} and $C_{n_{\dot{\beta}}}$ and correctly determined the parameter $C_{n_{\dot{\beta}}}$ to be insignificant. The wind tunnel value for $C_{n_{\dot{\beta}}}$ was given as zero. Values of C_{n_α} and $C_{n_{r\alpha}}$ are given in Tables F-15 and F-16. The parameter $C_{n_{p\alpha}}$ was estimated to be zero or negligible in all regions. Models for the regions not covered by Figures 4.6 through 4.18 and Tables F-2 through F-16 are given in Table F-17.

5. PREDICTION OF RESPONSES FOR PROCESSED MANEUVERS

Having obtained the global model, our next objective is to assess how well the identified model predicts the maneuvers used in modeling. The 6 DOF equations of motion (Appendix A) are integrated using the control inputs from each maneuver. The longitudinal coefficients C_x, C_z and C_m are calculated by interpolation from Figures 4.1 through 4.3 and adding the contribution of damping derivatives given in Figures 4.4 and 4.5. Equations (4.5.5), (4.5.6), (4.6.1), (4.6.2), (4.6.3) and (4.6.5) are used to calculate C_y, C_ℓ and C_n. The parameters for these equations are obtained from Figures 4.6 through 4.18 and Tables F-2 through F-17. All other parameters ($C_{y_{\dot{\beta}}}$, etc.) were negligible. All the equations of motion are integrated simultaneously to calculate the response. When a trajectory goes into a region where the model is unknown, estimated values of states are substituted until the trajectory returns to the region where the models are available.

Excellent agreement between true response and the response predicted by the identified model is obtained for most of the maneuvers. Figure 5.1 shows the fit obtained for Maneuver 4. Comparison of responses for all other maneuvers are given in Appendix G.

A comparison of predicted responses against true responses for Maneuvers 1 through 3, 5 through 10, first half of Maneuver 11 and Maneuvers 12 through 16 are given in the plots of Appendix G. The few discontinuities in the states in some of the figures are caused by the switch to the estimated values of the states in regions where no models are available.

The time histories of forces for the predicted response also followed those of true responses very well. Figure 5.2 shows a representative plot. The plot is from Maneuver 4.

For several maneuvers the trajectory went into regions where no models are available. Extrapolating the identified model into these regions led to a response that is entirely different from the true response. Hence estimated values of states are used in these regions.

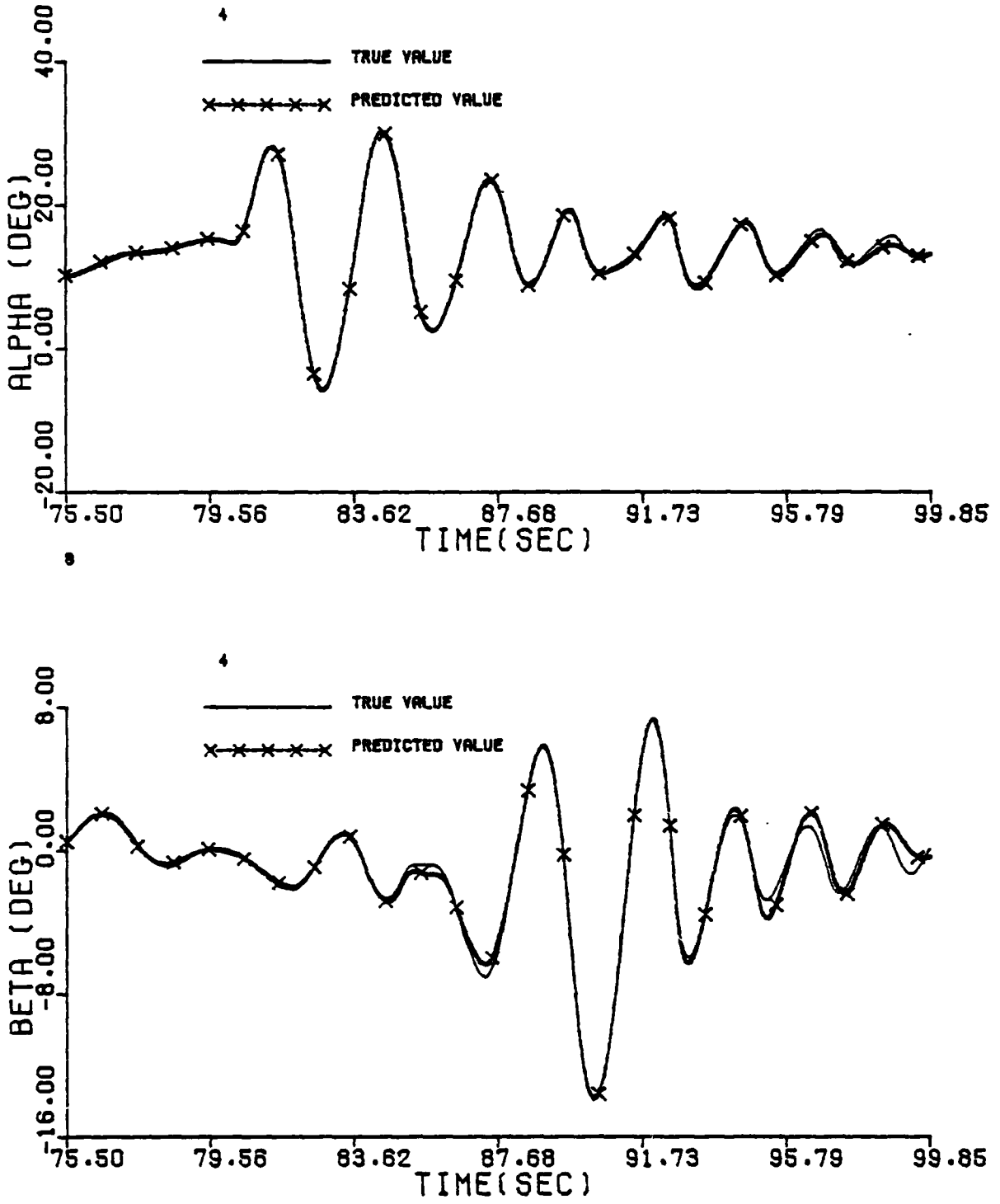

Figure 5.1 Comparison of Predicted and True Time Histories for Maneuver 4

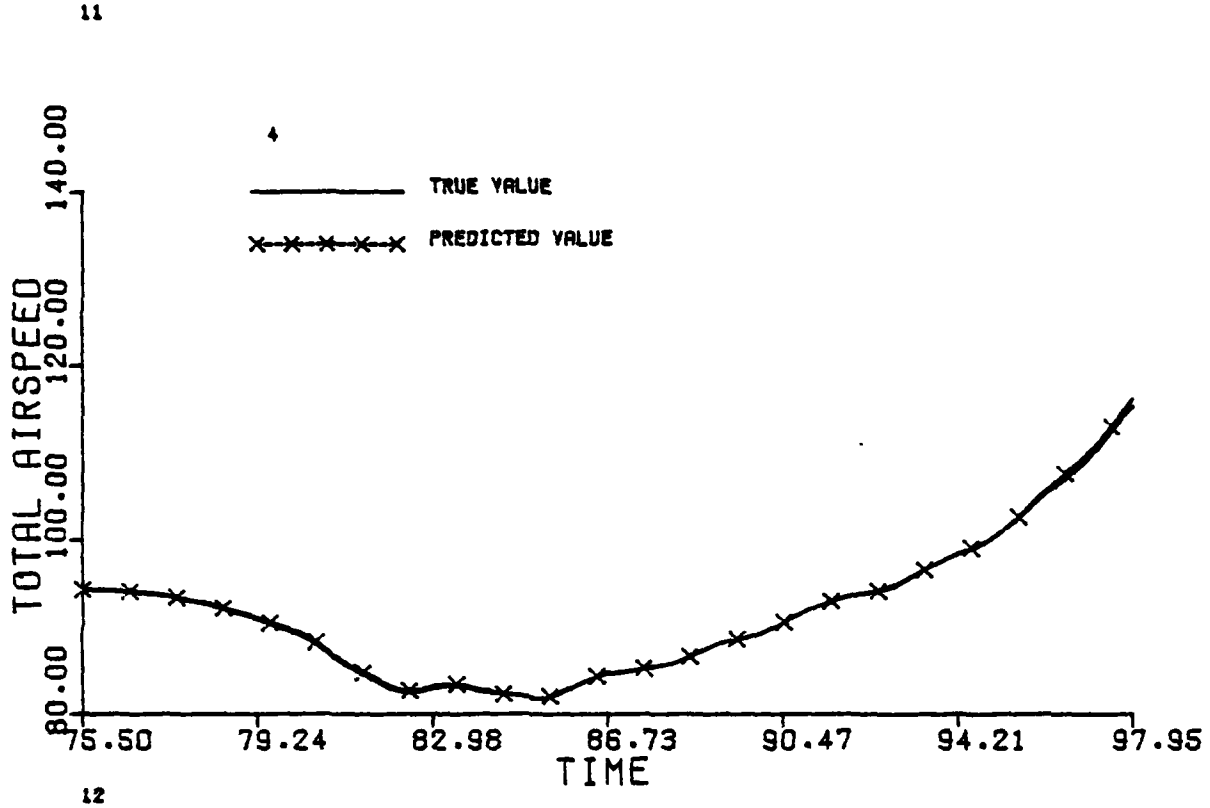

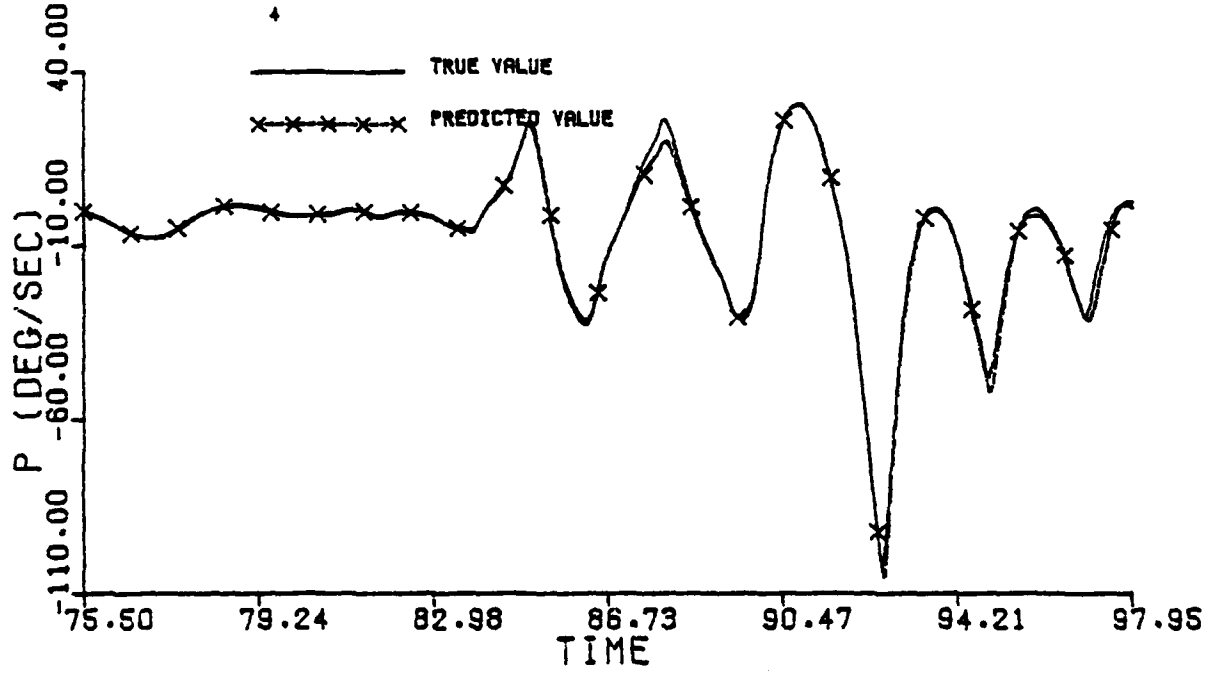

Figure 5.1 Continued (Maneuver 4)

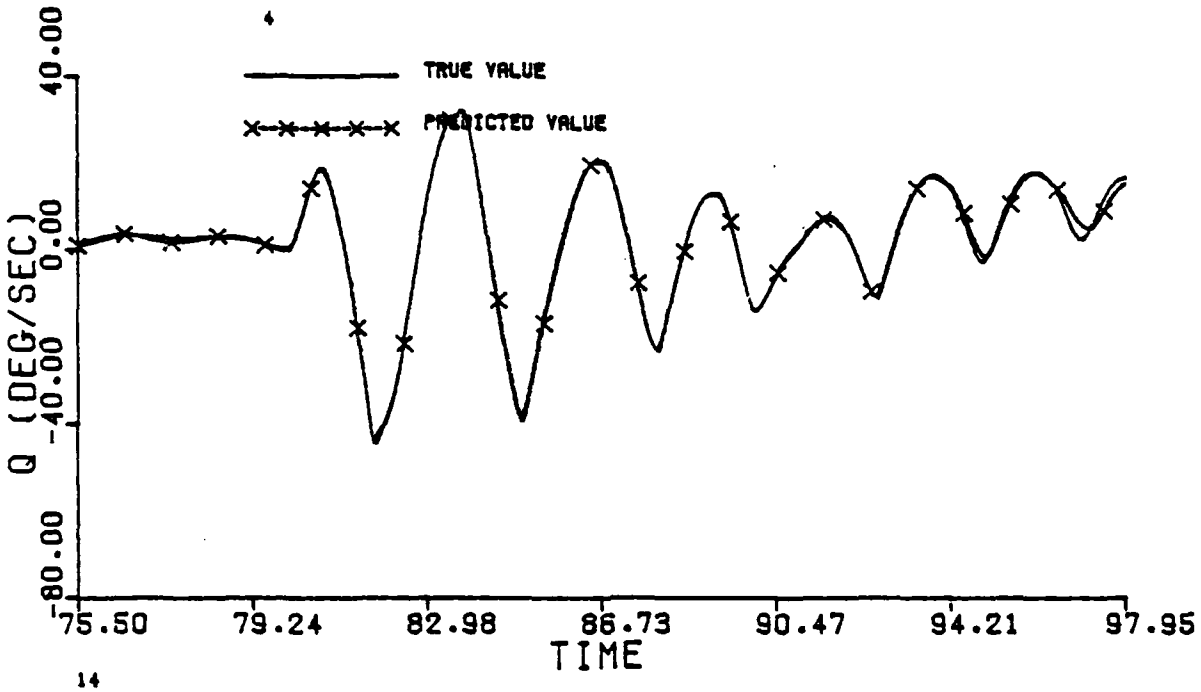

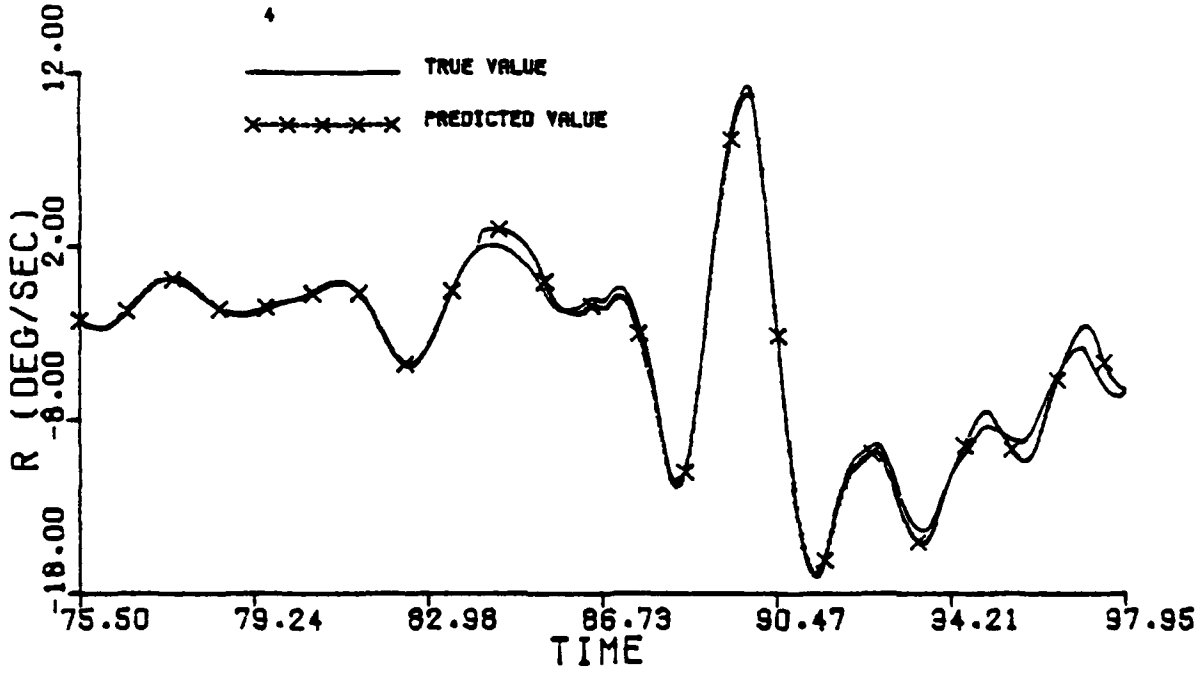

Figure 5.1 Continued (Maneuver 4)

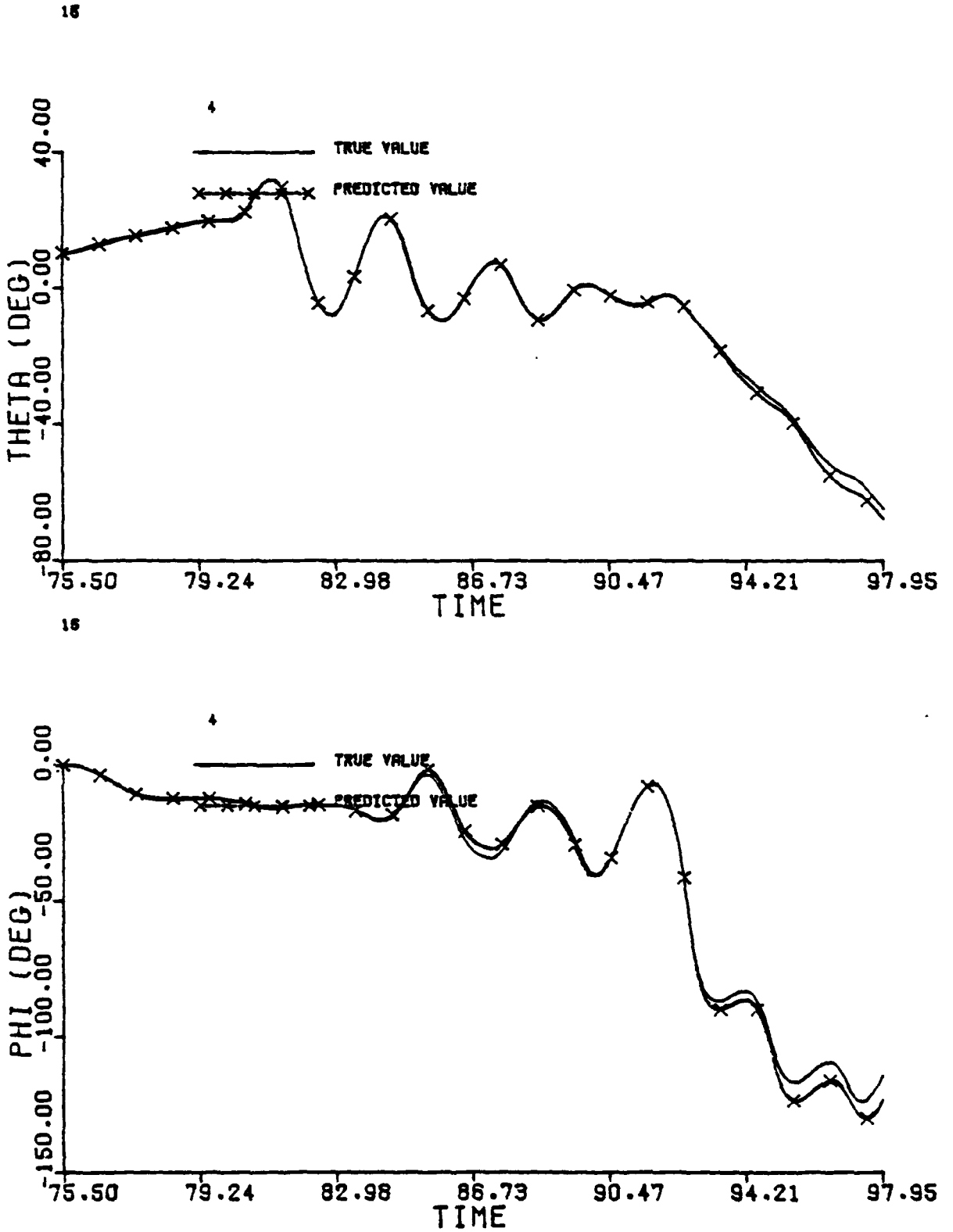

Figure 5.1 (Maneuver 4 Concluded)

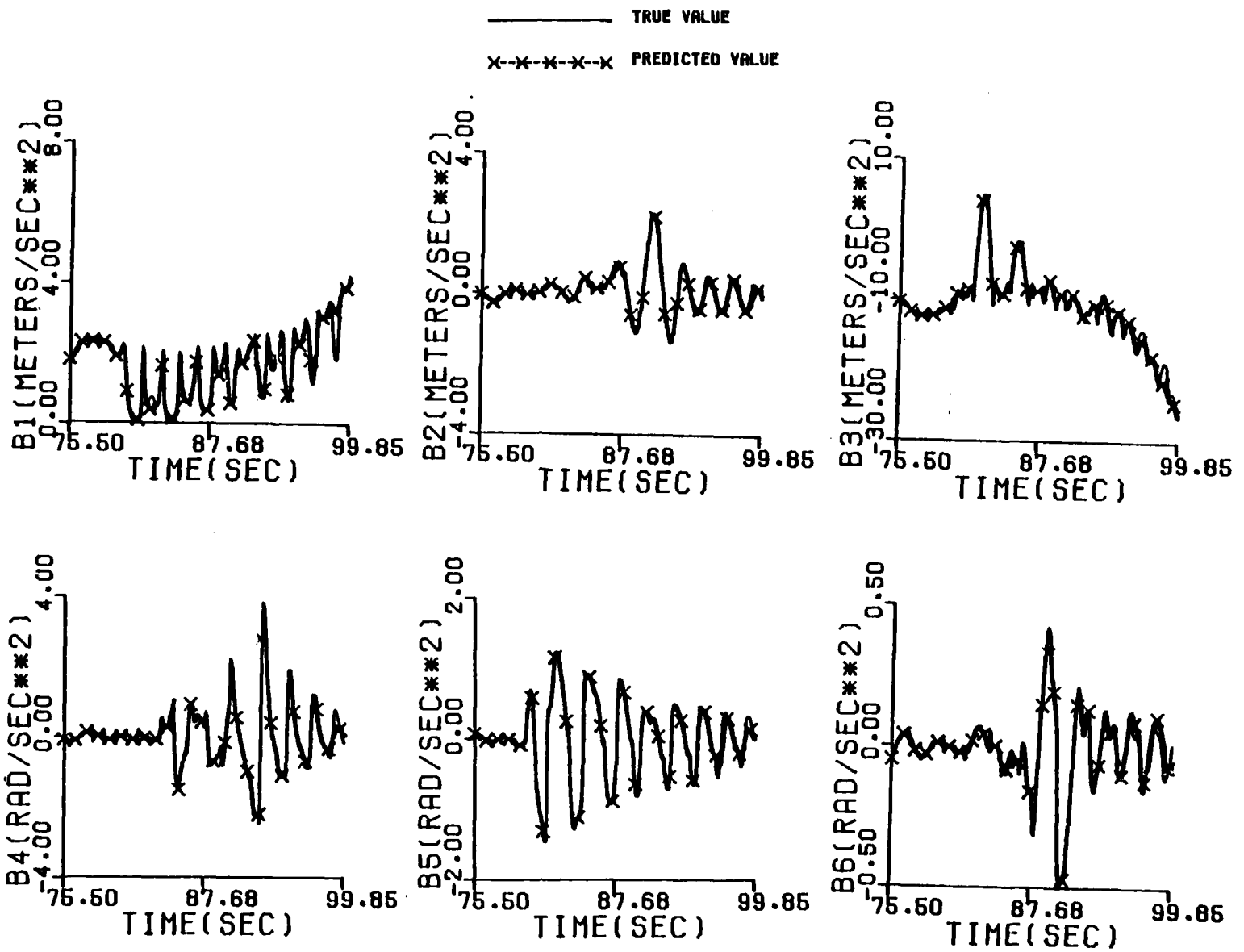

Figure 5.2 Comparison of True and Predicted Force Time Histories for Maneuver 4

Because of the unstable nature of the model in the post stall region the responses are very sensitive to small deviations in the states. An example of this sensitivity is shown in Appendix G, Fig. G.1 for the second half of Maneuver 11. Figure G.2(a) shows the case when all four longitudinal equations were integrated using estimated values of the lateral states. In Figure G.2(b) the longitudinal values are kept at the estimated values while the lateral equations are integrated. In both cases we see excellent agreement between the predicted and true response. Figure G.2(c) shows the case when all eight equations are integrated together. The degeneration in response was dramatic for all the states. Another example of this sensitivity is shown in Figure G.2(d). This time the response for the same maneuver is calculated using the wind tunnel model itself. When integrating the equations of motion, the integrated values of α and β are perturbed by a very small deviation of 0.003 radians at 254 and 256 seconds. The error introduced was nearly the same as the RMS of the measurement error on α and β. As can be seen from Figure G.2(d), this very small perturbation produced extremely large errors in all states. The error is as large as 5° for α, 10° for β, 100 deg/sec for p, 120° for ϕ and 50° for θ.

Output error methods determine model parameters such that even if the models are inaccurate in some regions they are compensated by models in other regions to match the response for the given maneuver. From the above examples we see that even the models obtained by these methods can fail in predicting the response for a maneuver like the one discussed above if it was not used in determining the model since even a very small error in the computation of α and β can lead to a completely different response.

6. PREDICTION OF RESPONSES FOR A NEW MANEUVER

To test how well the model predicts an unknown maneuver, control inputs (Figure 6.1) were chosen to excite both the identified model and the wind tunnel model. Sinusoidal inputs were used. The amplitudes of the controls were chosen large such that they created a trajectory that did not stray too far into unmodeled regions. From Figure 6.1 we notice that the response predicted by the identified model and the actual response are in good agreement.

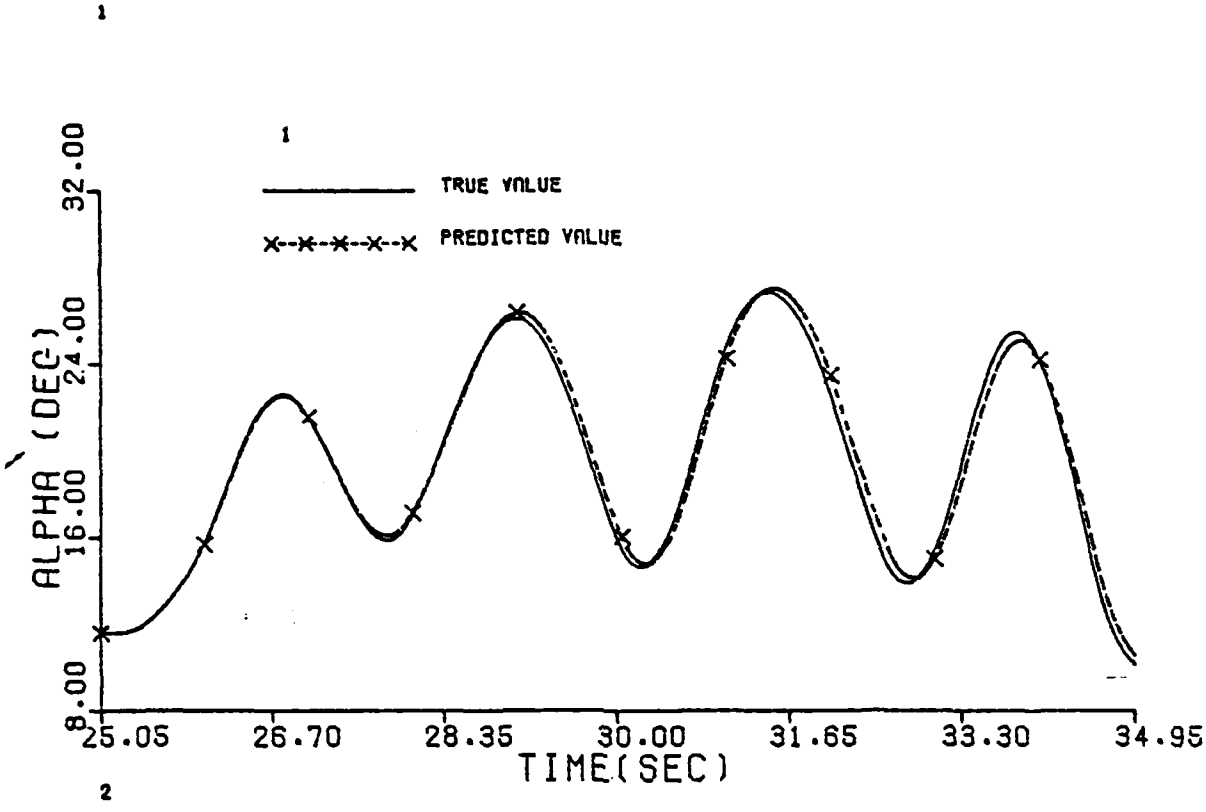

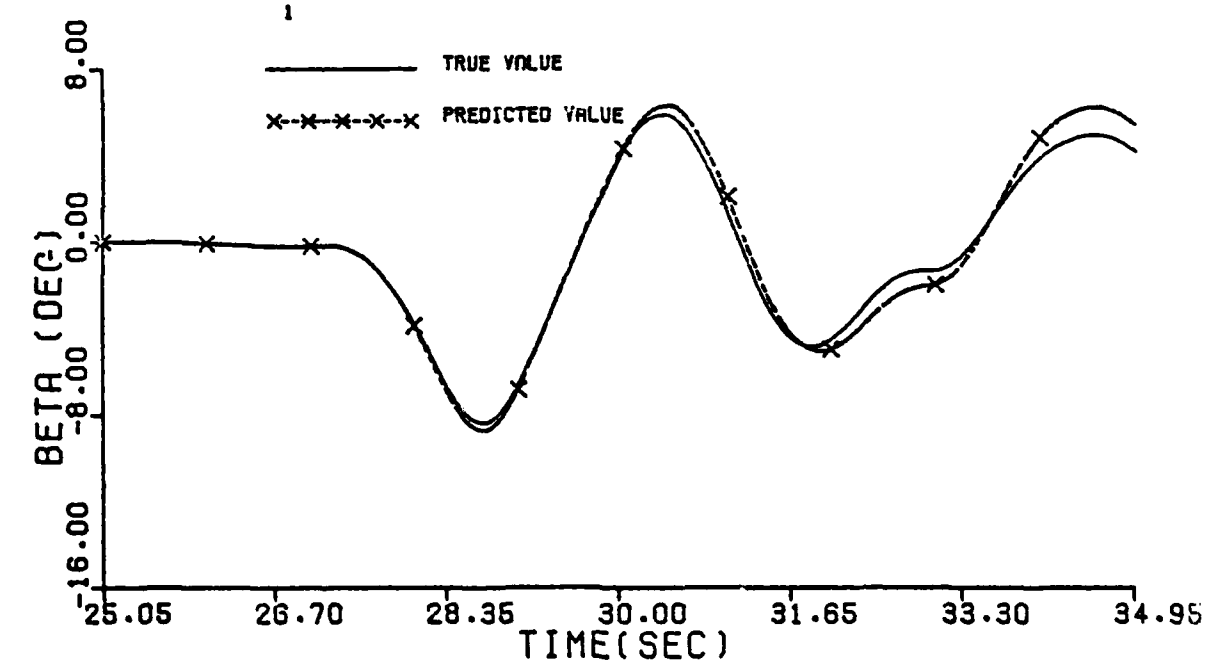

Figure 6.1 Predicted Response for a New Maneuver

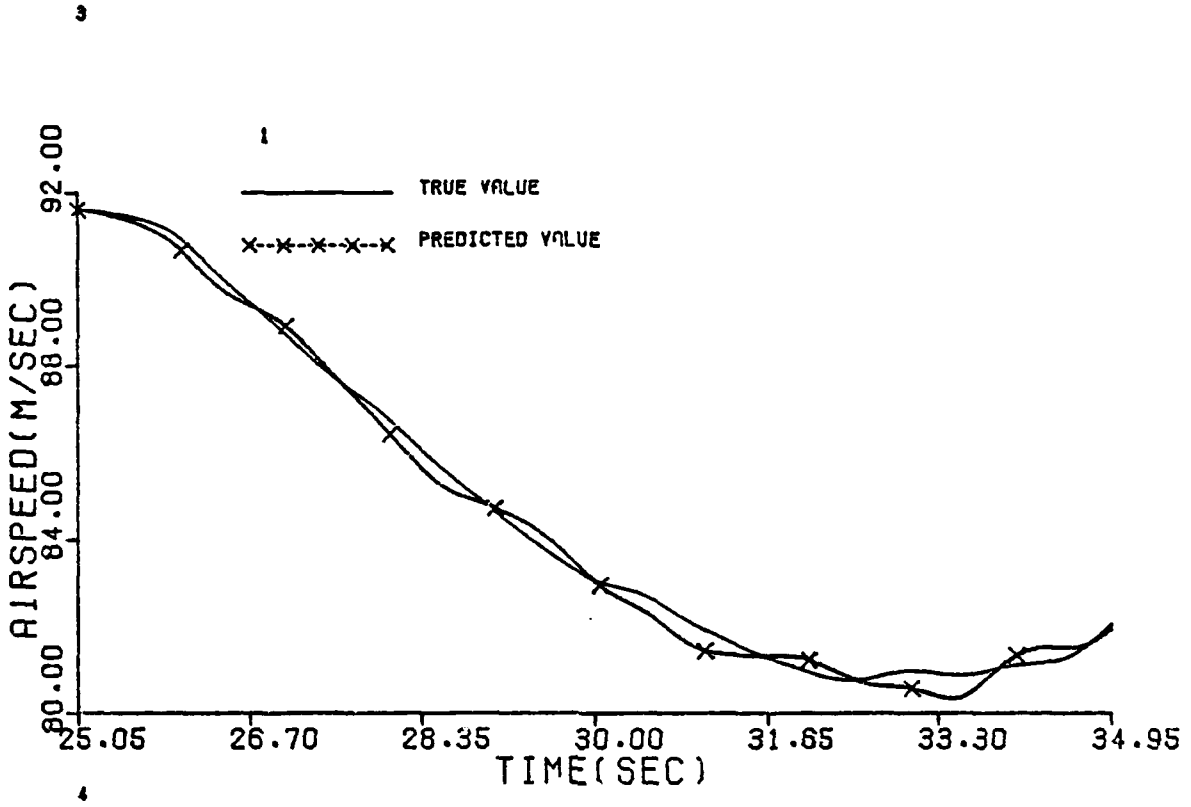

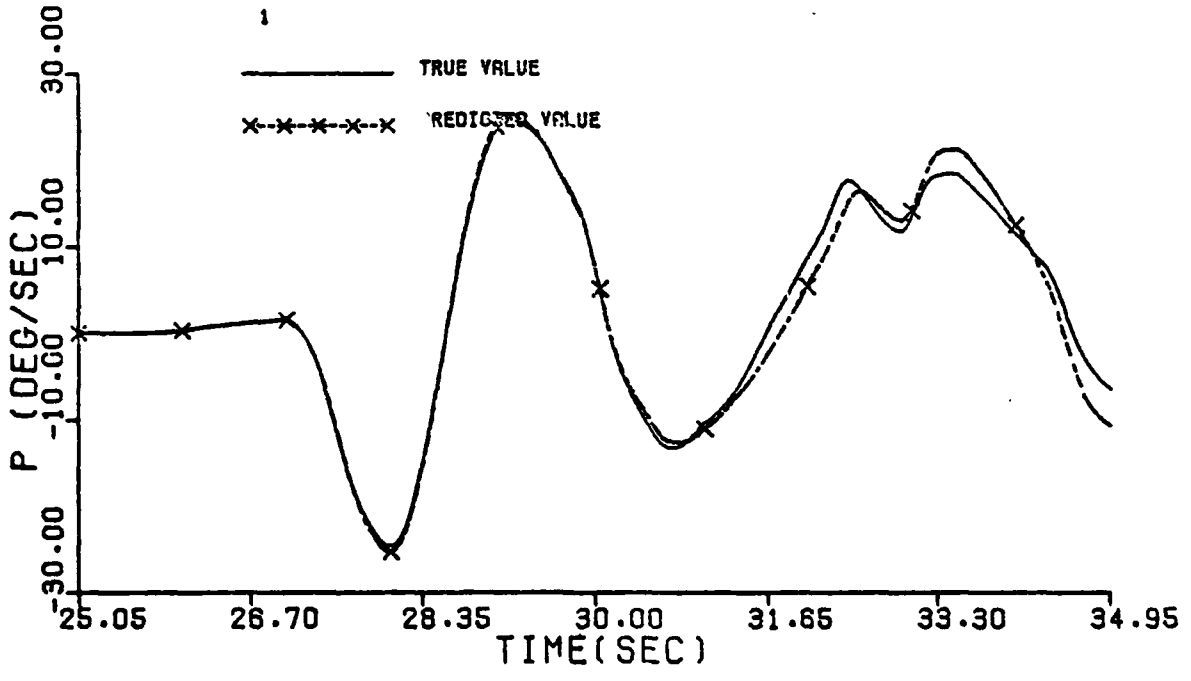

Figure 6.1 Continued

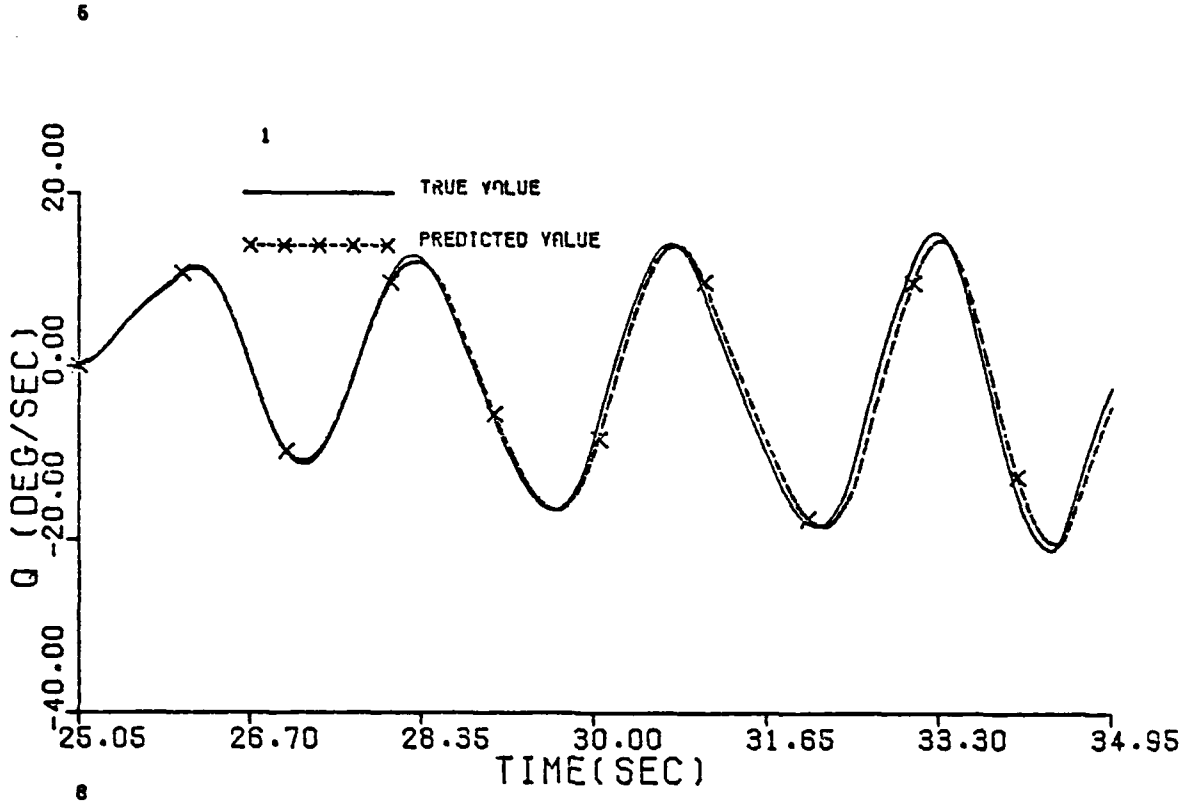

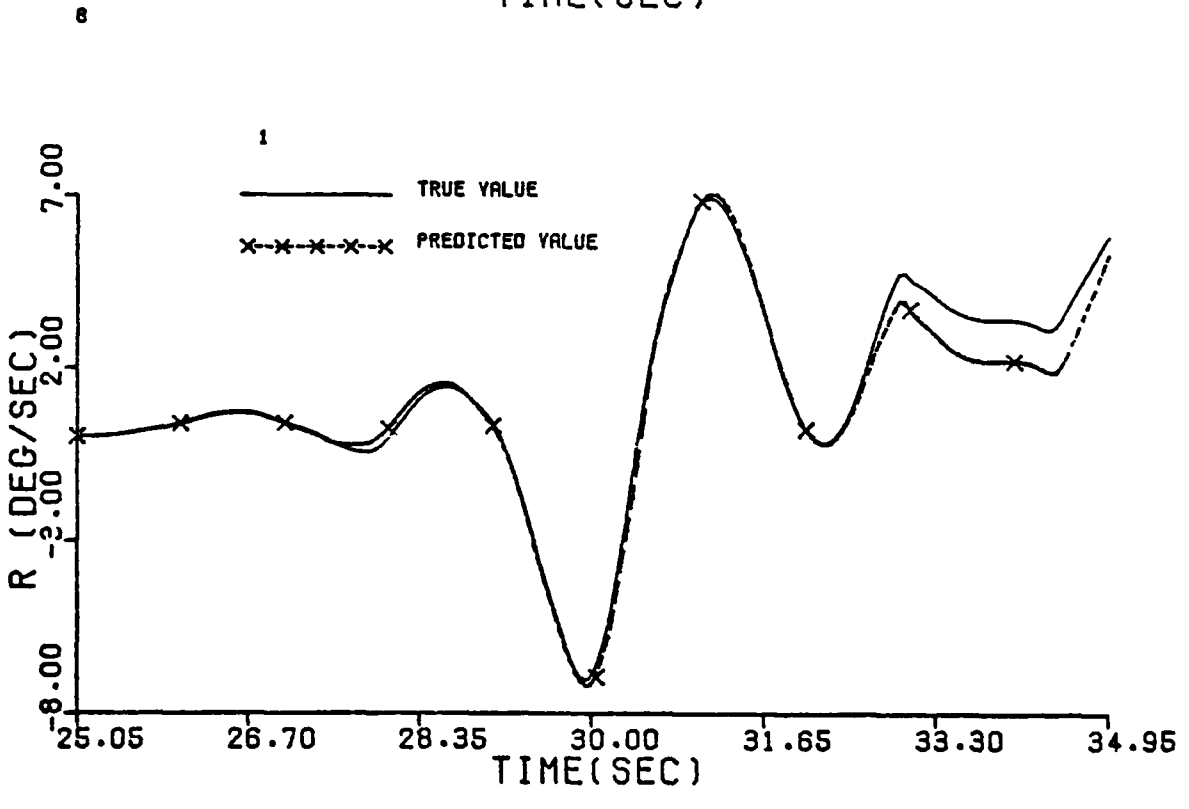

Figure 6.1 Continued

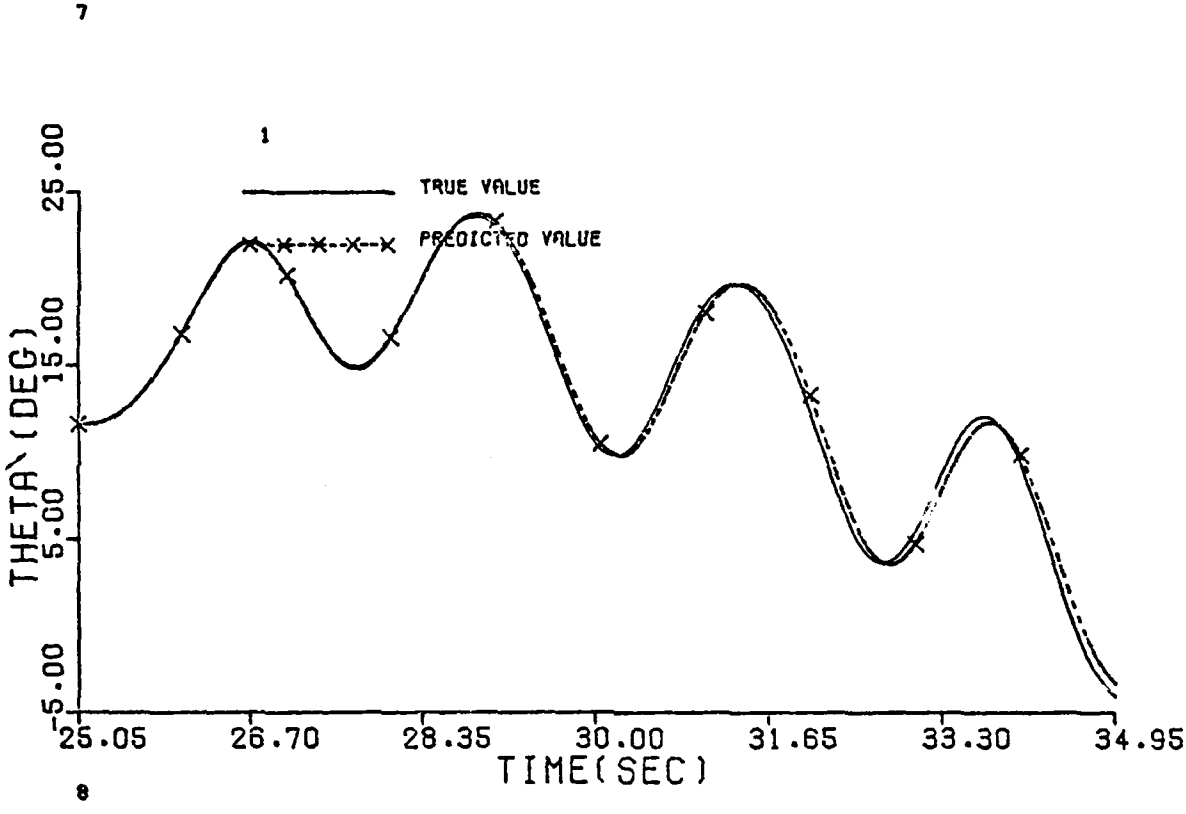

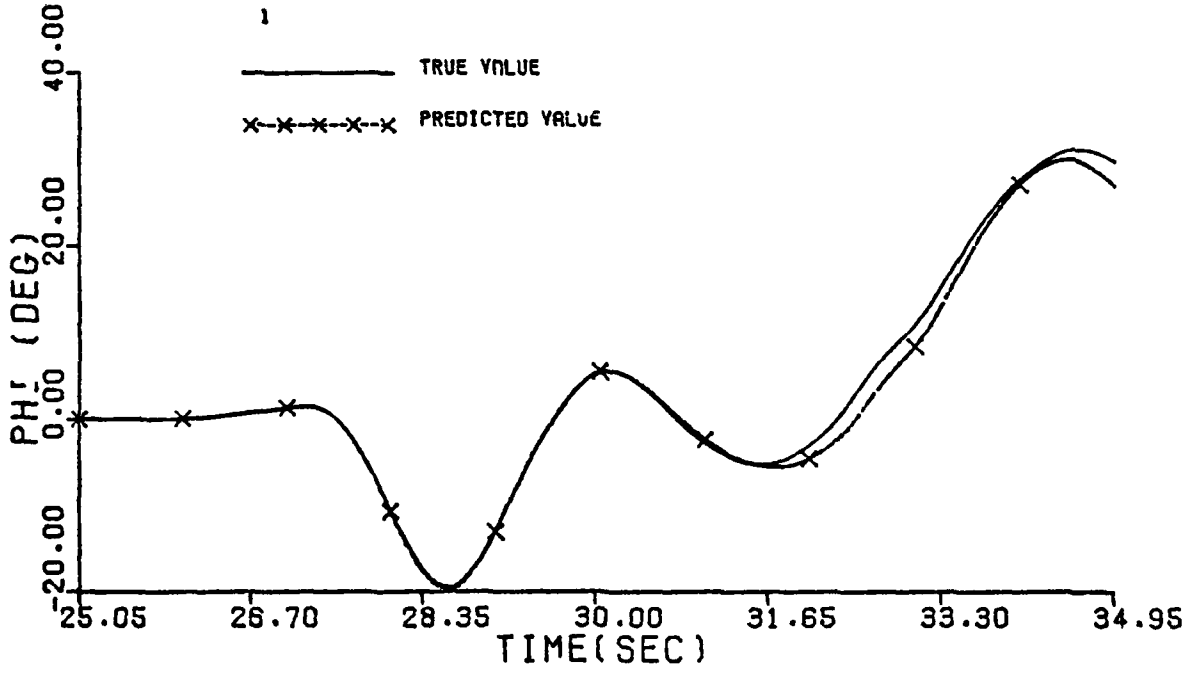

Figure 6.1 Continued

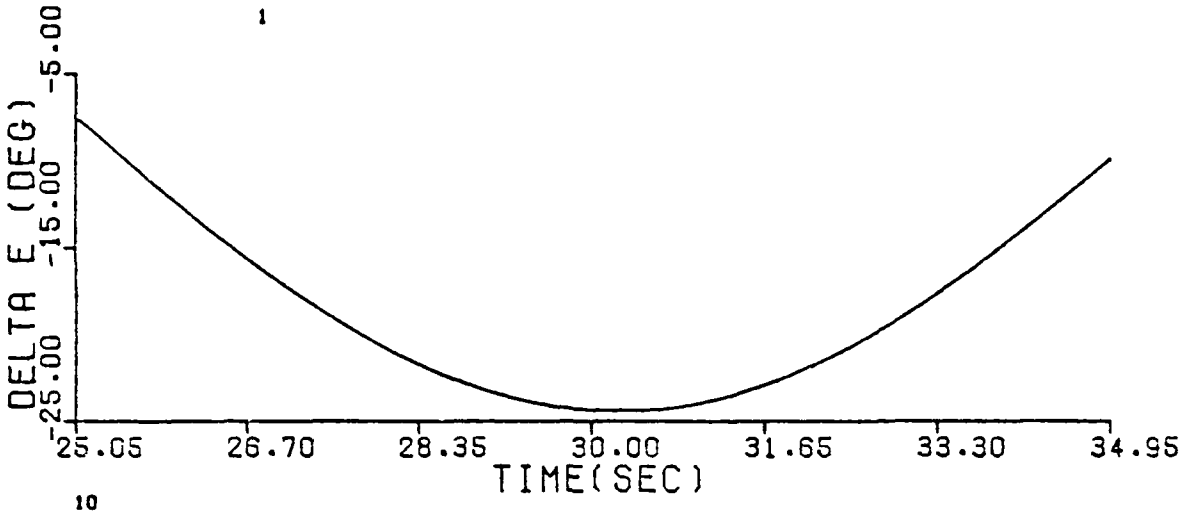

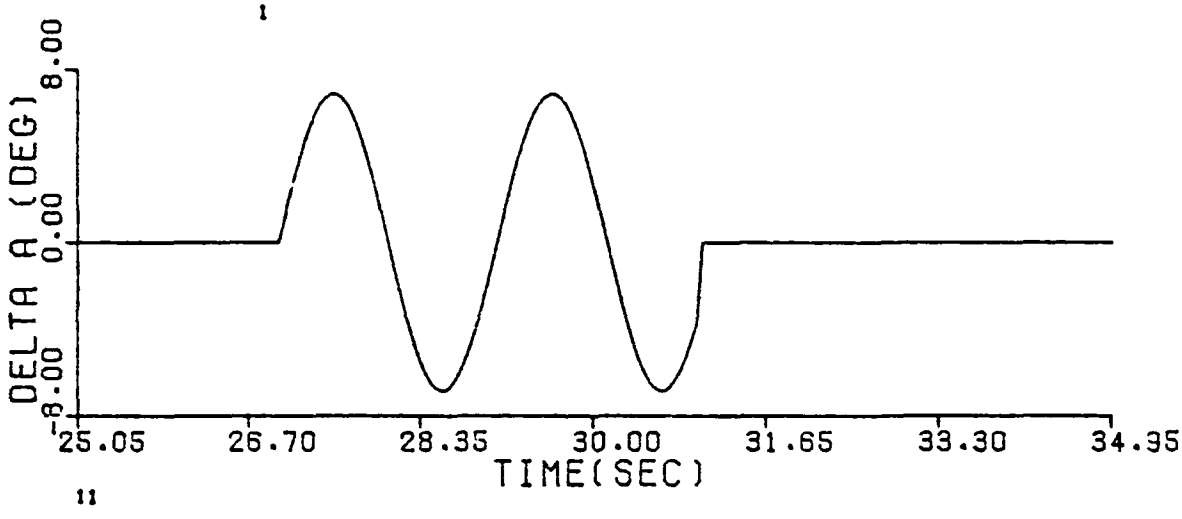

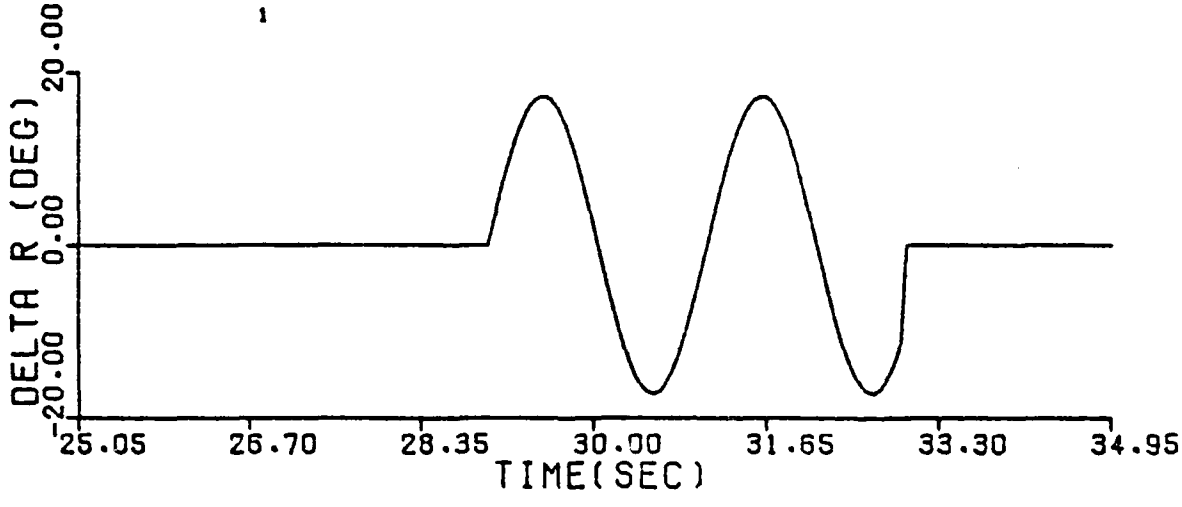

Figure 6.1 Concluded

7. CONCLUSIONS

The EBM methodology has been validated under controlled but realistic simulated conditions. The T-2C wind tunnel model was used to generate synthetic data. The controls, initial conditions, masses and thrusts of sixteen actual T-2C flight test data records were used to excite the T-2C wind tunnel model to generate the sixteen synthetic maneuvers. The synthetic data were corrupted with realistic measurement noise levels and then processed with an extended Kalman-Bucy/ Bryson-Frazier smoother to produce excellent estimated values of the states and of the forces and moments. Subspace modeling together with a step-wise multiple linear regression technique were used to identify a global state/control dependent model of the force and moment coefficients. The identified model agrees well with the T-2C wind tunnel model. The high nonlinearities were accurately identified. The identified global model gave excellent predicted responses for a new maneuver not used in the identification process.

REFERENCES

1. Ramachandran, S., Schneider, H., Mason, J. and Stalford, H., "Identification of Aircraft Aerodynamic Characteristics at High Angles of Attack and Sideslip Using the Estimation before Modeling (EBM) Technique" Proceeding of AIAA Atmospheric Flight Mechanics Conference, Hollywood, Florida, August 8-10, 1977, pp. 374-385.

2. Schneider, H., Ramachandran, S., "Spline Method for Nonlinear Parameters and State Estimation in the Presence of Model Uncertainties" Presented at the AAS/AIAA Astrodynamics Conference, Jackson Hole, Wyoming, Sept. 7-9, 1977.

3. Fortenbaugh, R. L., written communication, 24 August 1976.

4. Anon. Time-Sharing Applications Library Guide, Vol. II - Statistics, Honeywell Information Systems Inc., June 1971.

5. Fortenbaugh, R., "Application of a New Method of Nonlinear State and Parameter Estimation to High Angle of Attack Flight of CTOL and Low Speed/Hover Flight of V/STOL Aircraft" Vol. I, NADC, Warminster, Pa., Internal Report, July 1976.

6. Bierman, G. J., "Fixed Interval Smoothing with Discrete Measurements" Int. J. Control, 1975, Vol. 13, No. 1, pp. 65-75.

7. Fortenbaugh, R. L., "A High Angle of Attack/Sideslip Force and Moment Model of the T-2C Airplane" NADC, Warminster, Pa., Internal Report, July 28, 1976.

APPENDIX A

EQUATIONS OF MOTION & MEASUREMENT EQUATIONS

A.1 AIRCRAFT KINEMATICS

The following kinematical relations for a rigid aircraft are given with reference to body axes at the center of gravity:

$$\dot{u} = rv - qw - g \sin\theta + B_1 \tag{A-1}$$

$$\dot{v} = pw - ru + g \cos\theta \sin\phi + B_2 \tag{A-2}$$

$$\dot{w} = qu - pv + g \cos\theta \cos\phi + B_3 \tag{A-3}$$

$$\dot{p} = pq\, C_{41} + qr\, C_{42} + q\, C_{43} + B_4 + C_{44}\, B_6 \tag{A-4}$$

$$\dot{q} = pr\, C_{51} + (r^2 - p^2)\, C_{52} - r\, C_{53} + B_5 \tag{A-5}$$

$$\dot{r} = pq\, C_{61} + qr\, C_{62} + q\, C_{63} + B_6 + C_{64}\, B_4 \tag{A-6}$$

$$\dot{\theta} = q \cos\phi - r \sin\phi \tag{A-7}$$

$$\dot{\phi} = p + q \tan\theta \sin\phi + r \tan\theta \cos\phi \tag{A-8}$$

$$\dot{z} = -u \sin\theta + v \cos\theta \sin\phi + w \cos\theta \cos\phi \tag{A-9}$$

The acceleration terms B_1, B_2, ..., B_6 which are functions of the aerodynamic coefficients are given by the expressions:

$$B_1 = \frac{T_x}{m} + \frac{\rho V^2}{2m} S\, C_x \tag{A-10a}$$

$$B_2 = \frac{\rho V^2}{2m} S\, C_y \tag{A-10b}$$

$$B_3 = \frac{\rho V^2}{2m} S\, C_z + \frac{T_z}{m} \tag{A-10c}$$

$$B_4 = \frac{\rho V^2}{2} \frac{Sb}{I_x} C_\ell \left(\frac{I_x I_z}{I_x I_z - I_{xz}^2}\right) \quad \text{(A-10d)}$$

$$B_5 = \frac{\rho V^2 S\bar{c}}{2 I_y} C_m + \frac{1}{I_y} \left\{ \ell_{z_e} T_x - \ell_x m \left(B_3 - \frac{T_z}{m}\right) + \ell_z m \left(B_1 - \frac{T_x}{m}\right) \right\} \quad \text{(A-10e)}$$

$$B_6 = \frac{\rho V^2}{2} \frac{Sb}{I_z} C_n \left(\frac{I_x I_z}{I_x I_z - I_{xz}^2}\right) \quad \text{(A-10f)}$$

The constant coefficients C_{41} through C_{64} are given by:

$$C_{41} = \frac{I_{xz} (I_z + I_x - I_y)}{I_x I_z - I_{xz}^2} \quad \text{(A-11)}$$

$$C_{42} = \frac{I_z (I_y - I_z) - I_{xz}^2}{I_x I_z - I_{xz}^2} \quad \text{(A-12)}$$

$$C_{43} = \frac{I_{xz} h_{ex}}{I_x I_z - I_{xz}^2} \quad \text{(A-13)}$$

$$C_{44} = \frac{I_{xz}}{I_x} \quad \text{(A-14)}$$

$$C_{51} = \frac{I_z - I_x}{I_y} \quad \text{(A-15)}$$

$$C_{52} = \frac{I_{xz}}{I_y} \quad \text{(A-16)}$$

$$C_{53} = \frac{h_{ex}}{I_y} \quad \text{(A-17)}$$

$$C_{61} = \frac{I_x (I_x - I_y) + I_{xz}^2}{I_x I_z - I_{xz}^2} \quad \text{(A-18)}$$

$$C_{62} = \frac{I_{xz} (I_y - I_z - I_x)}{I_x I_z - I_{xz}^2} \quad \text{(A-19)}$$

$$C_{63} = \frac{I_x h_{ex}}{I_x I_z - I_{xz}^2} \quad \text{(A-20)} \qquad C_{64} = \frac{I_{xz}}{I_z} \quad \text{(A-21)}$$

A.2 AIRCRAFT CONSTANTS FOR THE T-2C

$S = 23.7\ m^2$ $\quad I_x = 12212\ kg\ m^2$

$\bar{c} = 2.26\ m$ $\quad I_y = 19811\ kg\ m^2$

$b = 11.62$ $\quad I_z = 25781\ kg\ m^2$

$\ell_z = 0\ m$ $\quad I_{xz} = 0$

$\ell_{z_e} = .49\ m$ $\quad h_{ex} = 2448$ Newtons-m-sec

The values for the mass m, the thrust T_x and the moment arm ℓ_x are given in the following table.

Table A-1 Values of the Aircraft Constants that Vary from Maneuver to Maneuver

Maneuver Number	Mass (kg)	Thrust (Newtons)	ℓ_x (Meters)
1	5275.3	4981	-.006
2	5329.7	4182	.031
3	5198.2	3874	.046
4	5039.4	3683	.234
5	5384.1	4666	.018
6	5039.4	4240	.010
7	4944.2	4211	.039
8	5420.4	3800	.047
9	5370.5	3507	.056
10	5325.2	3739	.011
11	5216.3	3658	.059
12	5170.9	3458	.063
13	5125.6	2406	.212
14	5080.2	2426	.189
15	5034.9	3707	.028
16	4989.5	3347	.052

A.3 MEASUREMENT EQUATIONS FOR THE T-2C

Table A-2 lists the 24 variables that are sensed by the T-2C instrumentation package and provides measurement range and location with respect to the normal flight test for each sensor.

The measurement equations relating the sensed variables to aircraft states and controls are as follows:

$$\alpha_m = \tan^{-1}\left(\frac{w - q\bar{x}_\alpha + p\bar{y}_\alpha}{u + q\bar{z}_\alpha - r\bar{y}_\alpha}\right) \tag{A-22}$$

$$\beta_m = \tan^{-1}\left(\frac{v - p\bar{z}_\beta + r\bar{x}_\beta}{u + q\bar{z}_\beta - r\bar{y}_\beta}\right) \tag{A-23}$$

$$V_m = \left[(u + q\bar{z}_v - r\bar{y}_v)^2 + (v + r\bar{x}_v - p\bar{z}_v)^2 + (w + p\bar{y}_v - q\bar{x}_v)^2 \right]^{\frac{1}{2}} \tag{A-24}$$

$$p_m = p \tag{A-25}$$

$$q_m = q \tag{A-26}$$

$$r_m = r \tag{A-27}$$

$$\theta_m = \theta \tag{A-28}$$

$$\phi_m = \phi \tag{A-29}$$

$$h_m = -z \tag{A-30}$$

$$\dot{p}_m = \dot{p} \tag{A-31}$$

$$\dot{q}_m = \dot{q} \tag{A-32}$$

$$\dot{r}_m = \dot{r} \tag{A-33}$$

$$(a_{x_m})_{NOSE} = B_1 - (r^2 + q^2)\,\bar{x}_{x_i} + (pq - \dot{r})\,\bar{y}_{x_i} + (pr + \dot{q})\bar{z}_x \tag{A-34}$$

where i = NOSE.

Three measurement equations result with k corresponding to c.g., NOSE and TAIL in the following expression:

$$(a_{y_m})_k = B_2 + (pq + \dot{r})\,\bar{x}_{y_k} - (p^2 + r^2)\,\bar{y}_{y_k} + (qr - \dot{p})\bar{z}_{y_k} \tag{A-35}$$

Five measurement equations result with k corresponding to c.g., NOSE, TAIL, R and L in the following expression:

$$(a_{z_m})_k = B_3 + (pr - \dot{q})\,\bar{x}_{z_k} + (qr + \dot{p})\,\bar{y}_{z_k} - (p^2 + q^2)\,\bar{z}_{z_k} \tag{A-36}$$

$$\delta_{a_m} = \delta_a \tag{A-37}$$

$$\delta_{e_m} = \delta_e \tag{A-38}$$

$$\delta_{r_m} = \delta_r \tag{A-39}$$

In Table A-2, note that $\bar{x}_{x_{NOSE}} = 4.62$, $\bar{y}_{x_{NOSE}} = -.13$, and $\bar{z}_{x_{NOSE}} = 0.18$. Similarly, $\bar{x}_{y_{c.g.}} = 0.12$, $\bar{y}_{y_{c.g.}} = -.02$, and $\bar{z}_{y_{c.g.}} = 0.58$.

Table A-2. Location Values of Instruments in the T-2C Instrumentation Package; Positive $\bar{x}$ means Instrument is Foward of c.g., Positive $\bar{y}$ - right of c.g., Positive $\bar{z}$ - below c.g.

No.	Measured Quantity	Location in Meters			Measurement Range
		$\bar{x}$	$\bar{y}$	$\bar{z}$	
1.	Angle of Attack (α_m)	7.04	0	0	
2.	Sideslip Angle (β_m)	7.13	0	0	
3.	Airspeed (V_m)	4.62	0.13	0.18	
4.	Roll Rate (p_m)	4.04	0.13	0.05	$\pm$ 150 deg/sec
5.	Pitch Rate (q_m)	0.12	0	0.58	$\pm$ 45 deg/sec
6.	Yaw Rate (r_m)	4.04	-.13	0.05	$\pm$ 150 deg/sec.
7.	Pitch Angle (θ_m)	4.04	0.13	0.05	$\pm$ 90 deg.
8.	Roll Angle (ϕ_m)	4.04	0.13	0.05	$\pm$ 180 deg.
9.	Altitude (h_m)	4.04	0.13	0.05	0 - 10670 m
10.	Roll acceleration ($\dot{p}_m$)	0.12	0	0.58	$\pm$ 275 deg/sec.^{2}
11.	Pitch acceleration ($\dot{q}_m$)	0.12	0	0.58	$\pm$ 450 deg/sec.^{2}
12.	Yaw acceleration ($\dot{r}_m$)	4.62	0	0	$\pm$ 275 deg/sec.^{2}
13.	Fore-Aft Accleration (a_{x_m}) NOSE	4.62	-0.13	0.18	$\pm$ 1.0 g
14.	Lateral Acceleration at c.g. (a_{y_m}) c.g.	0.12	-0.02	0.58	$\pm$ 1.0 g
15.	Lateral Acceleration at NOSE (a_{y_m}) NOSE	4.62	-0.13	0.18	$\pm$ 1.0g
16.	Lateral Acceleration at Tail (a_{y_m}) TAIL	-3.89	0.71	-0.08	$\pm$ 1.0g
17.	Normal Acceleration at c.g. (a_{z_m}) c.g.	0.12	0.02	0.58	$\pm$ 3.5g
18.	Normal Acceleration at Nose (a_{z_m}) NOSE	4.04	-0.13	0.05	$\pm$ 5.0g
19.	Normal Acceleration at TAIL (a_{z_m}) TAIL	-3.89	0.71	-0.08	$\pm$ 3.5g
20.	Normal Acceleration at Right Wing Tip (a_{z_m}) R	-0.89	5.08	0.05	$\pm$ 3.5g

Table A-2. (Continued)

No.	Measured Quantity	Location in Meters $\bar{x}$	$\bar{y}$	$\bar{z}$	Measurement Range
21	Normal Acceleration at Left Wing Tip ($a_{z_{m_L}}$)	-0.89	-5.08	0.05	$\pm$ 3.5 g
22	Aileron (δ_{a_m})	-0.97	4.06	0.05	$\pm$ 13 deg
23	Elevator (δ_{e_m})	-5.01	0.05	-1.19	-27.5 to 15 deg.
24	Rudder (δ_{r_m})	-5.01	0.05	-0.72	$\pm$ 24 deg.

APPENDIX B

DESCRIPTION OF FILTER/SMOOTHER ESTIMATOR

B.1 DESCRIPTION OF THE STATES

The kinematical relations (A-1) through (A-9) consist of 15 states. These are redefined as follows:

$x_1 = u$ $\quad x_4 = p$ $\quad x_7 = \theta$

$x_2 = v$ $\quad x_5 = q$ $\quad x_8 = \phi$

$x_3 = w$ $\quad x_6 = r$ $\quad x_9 = z$

$x_{10} = B_1$ $\quad x_{16} = B_3$ $\quad x_{22} = B_5$

$x_{13} = B_2$ $\quad x_{19} = B_4$ $\quad x_{25} = B_6$

The acceleration $B_i(t)$, $i \in \{1, 2, \ldots, 6\}$, is not a quadratic function usually, but it can be modeled by such a function whose derivatives are allowed to vary with time. In particular, it can be modeled by a quadratic function whose derivatives are driven by white, zero-mean gaussian noise. This type of modeling is adopted herein. The resulting six quadratic stochastic models lead to the following eighteen differential equations:

$\dot{x}_{10} = x_{11} + \eta_{10}$ $\quad \dot{x}_{13} = x_{14} + \eta_{13}$ $\quad \dot{x}_{16} = x_{17} + \eta_{16}$

$\dot{x}_{11} = x_{12} + \eta_{11}$ $\quad \dot{x}_{14} = x_{15} + \eta_{14}$ $\quad \dot{x}_{17} = x_{18} + \eta_{17}$

$\dot{x}_{12} = 0 + \eta_{12}$ $\quad \dot{x}_{15} = 0 + \eta_{15}$ $\quad \dot{x}_{18} = 0 + \eta_{18}$

$$\dot{x}_{19} = x_{20} + \eta_{19} \qquad \dot{x}_{22} = x_{23} + \eta_{22} \qquad \dot{x}_{25} = x_{26} + \eta_{25}$$
$$\dot{x}_{20} = x_{21} + \eta_{20} \qquad \dot{x}_{23} = x_{24} + \eta_{23} \qquad \dot{x}_{26} = x_{27} + \eta_{26}$$
$$\dot{x}_{21} = 0 + \eta_{21} \qquad \dot{x}_{24} = 0 + \eta_{24} \qquad \dot{x}_{27} = 0 + \eta_{27}$$

where η_{10} through η_{27} are white, zero-mean gaussian noise.

The above eighteen differential equations together with (A-1) through (A-9) comprise the 27-state dynamic system for which the filter and smoother are defined.

Let x denote the state vector $(x_1, x_2, \ldots, x_{27})$ and let $f(x)$ be the non-stochastic part of the right-hand sides of the 27 differential equations. The vector $(f(x)$ is a column vector with components $f_1(x), f_2(x), \ldots, f_{27}(x)$. The stochastic dynamic system can be written as:

$$\dot{x} = f(x) + \eta \quad ; \quad x(t_o) = x_o \qquad \text{(B-1)}$$

where

t_o = initial time

η = white, zero-mean gaussian process noise with

$$E[\eta(t_1)\,\eta^T(t_2)] = Q\,\delta(t_2 - t_1)$$

Q = positive semi-definite diagonal matrix - contains the values of the magnitude of the white noises

x_o = gaussian initial condition vector with covariance P_o ; P_o is a positive semi-definite matrix

The vector η is a column vector with components $\eta_1, \eta_2, \ldots, \eta_{27}$. The values of Q_{nn}, $n = 1, 2, \ldots, 9$, are determined by the computational accuracy of the computer. Section B.6 describes how the values Q_{nn}, $n = 10, 11, \ldots, 27$, are set.

B.2 DESCRIPTION OF THE OBSERVATION EQUATIONS

The measurement equations (A-22) through (A-30) and (A-34) through (A-36) consist of eighteen measured quantities. The measured quantities in (A-31) through (A-33) are not considered herein. The eighteen-dimensional observation vector $z = (z_1, z_2, \ldots, z_{18})$ is defined as follows:

Acceleration Group

$z_1 = (a_{x_m})_{\text{NOSE}}$ $\quad z_4 = (a_{z_m})_{\text{TAIL}}$ $\quad z_7 = (a_{y_m})_{\text{C.G.}}$

$z_2 = (a_{z_m})_{\text{C.G.}}$ $\quad z_5 = (a_{z_m})_{\text{R}}$ $\quad z_8 = (a_{y_m})_{\text{NOSE}}$

$z_3 = (a_{z_m})_{\text{NOSE}}$ $\quad z_6 = (a_{z_m})_{\text{L}}$ $\quad z_9 = (a_{y_m})_{\text{TAIL}}$

Velocity and Position Group

$z_{10} = \theta_m$ $\quad z_{12} = p_m$ $\quad z_{16} = V_m$

$z_{11} = \phi_m$ $\quad z_{13} = q_m$ $\quad z_{17} = \alpha_m$

$z_{15} = h_m$ $\quad z_{14} = r_m$ $\quad z_{18} = \beta_m$

Note that Equations (A-34) through (A-36) contain the derivatives $\dot{p}$, $\dot{q}$ and $\dot{r}$. These derivatives are given in terms of the state x by Equations (A-4), (A-5) and (A-6). With these substitutions into Equations (A-34) through (A-36), the resulting equations have right-hand sides that are functions only of the state x. Consequently, we can make the following definitions:

$h_1(x)$ = RHS of Equation (A-34)

$h_2(x), h_3(x), \ldots, h_6(x)$ = RHS of Equation (A-36) as k varies from C.G. to L.

$h_7(x), h_8(x), h_9(x)$ = RHS of Equation (A-35) as k varies from C.G. to TAIL

The functions $h_{10}(x)$, $h_{11}(x)$, . . . , $h_{18}(x)$ are defined as follows:

(a) $h_{10}(x)$ and $h_{11}(x)$ are the RHS's of Equations (A-28) and (A-29), respectively.

(b) $h_{12}(x)$, $h_{13}(x)$ and $h_{14}(x)$ are the RHS's of Equations (A-25) to (A-27), respectively.

(c) $h_{15}(x)$ is the RHS of Equation (A-30)

(d) $h_{17}(x)$, $h_{18}(x)$ and $h_{16}(x)$ are the RHS's of Equations (A-22) to (A-24), respectively.

The observation vector z is measured at discrete times,

$$t_o < t_1 < \ldots < t_N$$

where

$$t_i - t_{i-1} = \Delta t \text{ for all } i = 1, 2, \ldots, N$$

Δt = inverse of the data rate

The observation equation can now be written as

$$z_i = z(t_i) = h(x(t_i)) + \nu_i \qquad \text{(B-2)}$$

where

ν = gaussian, zero-mean, white noise sequence with

$$E(\nu_i \nu_j^T) = R_i \delta_{i,j}$$

R_i = positive - definite matrix - covariance of the measurement noise

B.3 SOME ASSUMPTIONS AND DEFINITIONS

We assume that $r(t)$, ν_i and x_o are uncorrelated, i.e., for all t and i,

$$E(r(t)\,\nu_i^T) = 0$$

$$E(r(t)\,x_o^T) = 0$$

$$E(x_o\,\nu_i^T) = 0$$

We make the following definitions:

$$x_i = \lim_{\epsilon \to 0} x(t_i - \epsilon)$$

$$H_i = \frac{\partial h}{\partial x}(x_i)$$

P_i = covariance of x_i

$$F(x) = \frac{\partial f}{\partial x}(x) \quad \text{for all } x$$

$$V_i = P_i H_i^T$$

$$D_i = H_i P_i H_i^T + R_i \quad \text{(Predicted measurement residual covariance)}$$

$$G_i = P_i H_i^T D_i^{-1} \quad \text{(Kalman gain)}$$

For brevity of notation, we set

$\hat{x}_i$ = filtered estimate of x at time t_i

$\hat{P}_i$ = filtered covariance of x at time t_i

x_i^* = smooth estimate of x at time t_i

B.4 THE FILTERING ALGORITHM

The initialization at time t_o is

$$x(t_o) = x_o$$

$$P(t_o) = P_o$$

The updates of the state and of the covariance at time t_i is given by the Kalman-Bucy filtering algorithm:

$$\Delta z_i = z_i - h(x_i) \quad \text{(predicted residual)}$$

$$\hat{x}_i = x_i + G_i \Delta z_i \quad \text{(state vector update)}$$

$$\hat{P}_i = P_i - G_i V_i^T \quad \text{(optimal Kalman update)}$$

The propagation of the state and the covariance from t_i to t_{i+1} is given by integrating the following equations:

$$\dot{\tilde{x}} = f(\tilde{x}) \quad , \quad \tilde{x}(t_i) = \hat{x}_i$$

$$\dot{\tilde{p}} = \frac{\partial f}{\partial x}(\tilde{x})\,\tilde{p} + \left(\frac{\partial f}{\partial x}(\tilde{x})\,\tilde{p}\right)^T + Q$$

where

$$\tilde{p}(t_i) = \hat{p}_i$$

The integrated values at time t_{i+1} are recognized as x_{i+1} and p_{i+1}; that is,

$$x_{i+1} = \tilde{x}(t_{i+1})$$

$$p_{i+1} = \tilde{p}(t_{i+1})$$

B.5 THE SMOOTHING ALGORITHM

This algorithm uses the recursive form of the discrete Bryson-Frasier smoother, Bierman [6].

Let λ denote the adjoint filter variable generated from a reverse time Kalman-like filter. Define

$$\lambda_i^- = \lim_{\epsilon \to 0} \lambda\,(t_i - \epsilon)$$

$$\lambda_i^+ = \lim_{\epsilon \to 0} \lambda\,(t_i + \epsilon)$$

The initialization of the adjoint variable λ at time t_N is given by

$$\lambda_N^- = -\,H_N^T\, D_N^{-1}\, \underline{\Delta}\, z_N$$

The propagation of λ from t_{i+1} to t_i is carried out by integrating the following adjoint equation backwards:

$$\dot{\lambda} = -\frac{\partial f}{\partial x}\,(\tilde{x}(t))\,\lambda \quad , \quad \lambda\,(t_{i+1}) = \lambda_{i+1}^-$$

The integrated value of λ at time t_i is recognized as λ_i^+; that is,

$$\lambda_i^+ = \lambda\,(t_i)$$

The smooth estimate x_i^* is obtained from the equation

$$x_i^* = \hat{x}_i - \hat{p}_i\, \lambda_i^+$$

The update of λ at time t_i is given by

$$\lambda_i^- = \lambda_i^+ - H_i^T\, D_i^{-1}\, \Delta\, z_i - H_i^T\, G_i^T\, \lambda_i^+$$

B.6 INPUT QUANTITIES FOR THE FILTER/SMOOTHER ALGORITHM

The filter/smoother algorithm outlined above is a suboptimal process. It provides excellent results only if the errors in the estimates are small enough so that the predicted state at the next observation time is contained within the linear region of the true state. The critical factor in maintaining sufficiently small errors is the setting of Q_{nn}, $n = 10, 11, \ldots, 27$. The values of Q_{nn}, $nn = 10, 11, \ldots, 27$ are set after analyzing the peak rates of change of $B_i(t)$, $i = 1, 2, \ldots, 6$. These peaks drive the quadratic model process. The following ad hoc method is used to set the Q_{nn}'s: Let $i \in \{1, 2, \ldots, 6\}$. Recall $\Delta t = 1.0$ divided by the data rate. Define

ΔB_i = peak change in $B_i(t)$ over Δt seconds not due to $\dot{B}_i(t)$

$\Delta \dot{B}_i$ = peak change in $\dot{B}_i(t)$ over $2\ \Delta t$ seconds not due to $\ddot{B}_i(t)$

$\Delta \dddot{B}_i$ = peak change in $\ddot{B}_i(t)$ over $3\ \Delta t$ seconds.

Let $n = 10 + 3(i-1)$. We set

$$Q_{nn}(\Delta t) = (\Delta B_i)^2$$

$$Q_{(n+1)(n+1)}(2\Delta t) = (\Delta \dot{B}_i)^2$$

$$Q_{(n+2)(n+2)}(3\Delta t) = (\Delta \dddot{B}_i)^2$$

The computed values of the Q_{nn}'s that were used in the filtering process are given in Table B-1. The values of Q_{kk}, $k = 1, 2, \ldots, 9$, were set at .000001.

Table B-1. Computed Values of the Q_{nn}'s of the Models of the Accelerations B_i (t), i = 1, 2, . . . 6; herein, n = 10 + 3 (i-1).

Quantity	Magnitude of Process Noise					
	i = 1	i = 2	i = 3	i = 4	i = 5	i = 6
Q_{nn}	.01	.001	.05	10	.5	.1
$Q_{(n+1)\ (n+1)}$	32	10	125	5,000	1,000	100
$Q_{(n+2)\ (n+2)}$	50,000	50,000	50,000	50,000	50,000	3,500

The values of P_o (i.e., the initial values of the covariance matrix) are given in Tables B-2 and B-3.

Table B-2. Covariance Values of the Initial States $x_1, x_2, \ldots, x_9$; herein, k = 1 + 3 (i-1).

Quantity	Values of the Covariance P_o		
	i = 1	i = 2	i = 3
$P_{o\ (k)\ (k)}$	1.04	.01	.004
$P_{o\ (k+1)\ (k+1)}$	.39	.0225	.008
$P_{o\ (k+2)\ (k+2)}$	1.53	.0025	1000.

Table B-3. Covariance Values of the Initial States $x_{10}, x_{11}, \ldots, x_{27}$ herein, $n = 10 + 3(i-1)$

Quantity	Values of the Covariance P_o					
	i = 1	i = 2	i = 3	i = 4	i = 5	i = 6
$P_{o\,(n)\,(n)}$	10.	.01	200.	.01	4.0	1.0
$P_{o\,(n+1)\,(n+1)}$	128.	4.2	500.	2.0	55.	2.0
$P_{o\,(n+2)\,(n+2)}$	22,500.	64.	10,000.	784.	1200.	700.

The values of R (i.e., the covariance of the noise) are given in Table B-4.

Table B-4. Covariance Values of the Noise for the Measured Quantities $z_1, z_2, \ldots, z_{18}$; herein, $n = 1 + 3(i-1)$

Quantity	Covariance Values of the Noise					
	i = 1	i = 2	i = 3	i = 4	i = 5	i = 6
R_{nn}	.0576	1.1025	.0576	$.756 \times 10^{-6}$	2.8×10^{-6}	.1849
$R_{(n+1)\,(n+1)}$	1.1025	1.1025	.0576	$.756 \times 10^{-6}$	2.8×10^{-6}	7.84×10^{-6}
$R_{(n+2)\,(n+2)}$	1.1025	1.1025	.0576	2.8×10^{-6}	100	7.84×10^{-6}

The best initial values of the states x_o are obtained by averaging over the trim portion of the maneuver.

APPENDIX C

STEPWISE MULTIPLE LINEAR REGRESSION (SMLR)

SMLR [4] is used to obtain state and control dependent mode for C_x, C_y, etc. The SMLR algorithm is presented briefly in this Appendix and details can be found in [4]. SMLR determines in stages, the best value in the least squares sense for the coefficients of an equation of the form given below:

$$y = a_o + a_1x_1 + a_2x_2 + \text{---}a_nx_n$$

where y is the dependent variable

x_1, x_2 --- x_n are the dependent variables

a_o, a_1, --- a_n are the coefficients to be determined. For aircraft identification y represents the force or moment coefficient.

The independent variables are formed by combining one or more of the aircraft states and controls. An example is α, β, δ_e, $\frac{qc}{2V}$, $\frac{\dot{\alpha}c}{2V}$, $\alpha\beta$ and α^2.

The algorithm proceeds with the independent variables being added one at a time leading to the following intermediate equations:

$$y = a_o + a_1x_1$$

$$y = a_o' + a_1'x_1 + a_2'x_2$$

$$y = a_o'' + a_1''x_1 + a_2''x_2 + a_3''x_3$$

and so on. Thus at each stage we can obtain valuable statistical information. At each step, the independent variables not used in the regression are inspected and the variable that gives the largest reduction in the variation of y is chosen. This variable is then checked for statistical significance by calculating the F-Ratio of the variable and comparing against the chosen F-Critical value. If it meets this requirement it is included in the solution.

After each new variable has been added those already in the solution are checked to assess if any of them is no longer significant. Any variable with a new F-ratio less than the critical value is deleted. This is repeated until no more variables can be added or deleted, and the final solution contains only statistically significant variables. The algorithm has the option of forcing any variable into the solution even if it is not statistically significant.

APPENDIX D

WIND TUNNEL MODEL

This section describes the wind tunnel model used in generating the synthetic data. Wind tunnel measurements of static and dynamic coefficients for the aircraft were provided by NADC [5]. The longitudinal and lateral models will be dicussed below.

LONGITUDINAL MODEL

The lift coefficient C_L, drag coefficient C_D and the pitching moment coefficient C_{m_s}† were given as functions of angle of attack, sideslip angle and elevator setting. These were made available in the form of look-up tables. For the elevator settings of -25^o, -15^o, -10^o, 0^o, 10^o and 15^o the tables provided values of C_L, C_D and C_{m_s} at angles of attack: -8, -4, 0, 4, 8, 12, 14, 15, 16, 18, 20, 25, 30, 35, 40, 45, 50, 55, 62, 67, 72, 77 and 83 degrees while the sideslip angle assumed values of 0, 2, 5, 10, 15, 20, 25 and 30 degrees at every given angle of attack. The given model assumed symmetry with respect to angle of sideslip. For angles of sideslip greater than 30 degrees the values at $\beta = 30^o$ were used. The dynamic derivatives C_{z_q}, $C_{z_{\dot{\alpha}}}$, C_{m_q} and $C_{m_{\dot{\alpha}}}$ were given as functions of only angle of attack. The dependence of these derivatives on the angle of attack was furnished as curves. The given model assumed negligible effect of sideslip angle on the dynamic derivatives, and lateral controls on the longitudinal coefficients. At any angles of attack, sideslip and elevator deflection, the values of C_L, C_D and C_{m_s} were computed from the tables using a multi-dimensional interpolation scheme. When the values of α or δ_e were outside the given tables the scheme simply extrapolated the values from the tables.

The axial force coefficient C_x, the normal force coefficient C_z and pitching moment coefficient C_m were obtained along the body axes using the following equations:

† - Subscript s denotes static value along stability axes.

$$C_x^*(\alpha, \beta, \delta_e) = -C_D(\alpha, \beta, \delta_e)\cos\alpha + C_L(\alpha, \beta, \delta_e)\sin\alpha \quad (D.1)$$

$$C_z^*(\alpha, \beta, \delta_e) = -C_L(\alpha, \beta, \delta_e)\cos\alpha - C_D(\alpha, \beta, \delta_e)\sin\alpha \quad (D.2)$$

$$C_m^*(\alpha, \beta, \delta_e) = C_{m_s}(\alpha, \beta, \delta_e) \quad (D.3)$$

where C_{m_s} is the static pitching moment coefficient.

$$C_x = C_x^* \quad (D.4)$$

$$C_z = C_z^* + C_{z_q}\frac{q\bar{c}}{2V} + C_{z_{\dot{\alpha}}}\frac{\dot{\alpha}\bar{c}}{2V} \quad (D.5)$$

$$C_m = C_m^* + C_{m_q}\frac{q\bar{c}}{2V} + C_{m_{\dot{\alpha}}}\frac{\dot{\alpha}\bar{c}}{2V} \quad (D.6)$$

LATERAL MODEL

The lateral force coefficient C_{y_s} and the rolling and yawing moment coefficients along stability axes, C_{ℓ_s} and C_{n_s}, were given in tabular form at various α and β for the following combinations of aileron and rudder deflections: 1) $\delta_a = \delta_r = 0^\circ$, (2) $\delta_a = -12^\circ$, $\delta_r = 0^\circ$, (3) $\delta_a = +12^\circ$, $\delta_r = 0^\circ$, (4) $\delta_a = 0^\circ$, $\delta_r = -25^\circ$, (5) $\delta_a = 0^\circ$, $\delta_r = +25^\circ$.

The variations of α and β for each of the above combination were the same as the longitudinal model. The dynamic derivatives C_{y_p}, C_{y_r}, C_{ℓ_p}, C_{ℓ_r}, C_{n_p} and C_{n_r} were given in curve forms as functions of angle of attack only. The derivatives $C_{y_{\dot{\beta}}}$, $C_{\ell_{\dot{\beta}}}$ and $C_{n_{\dot{\beta}}}$ were assumed to be zero as these were not given. Further, the model did not provide any information on the cross effects of δ_a, δ_e and δ_r. The given model also assumed anti-symmetry of the coefficients C_y, C_ℓ and C_r with respect to sideslip angle.

The lateral force and moment coefficients are first computed along stability axes by directly adding the contributions due to aileron and rudder deflections. These are then transformed into body axes. The following equations outline the procedure used for this.

$$C_{y_s}(\alpha, \beta, \delta_a, \delta_r) = C^*_{y_s} + \Delta C_y(\delta_a) + \Delta C_y(\delta_r) \tag{D.7}$$

$$C^*_{y_s} = \text{sgn}(1, \beta)\, C_{y_s}(\alpha, |\beta|, \delta_a = 0, \delta_r = 0) \tag{D.8}$$

$$\Delta C_y(\delta_a) = |\delta_a| \,(C_y(\delta_a) - C^*_{y_s})/12 \tag{D.9}$$

$$C_y(\delta_a) = \begin{cases} C_{y_s}(\alpha, \beta, \delta_a = 12, \delta_r = 0), & \delta_a \geq 0;\ \beta \geq 0 \\ -C_{y_s}(\alpha, |\beta|, \delta_a = -12, \delta_r = 0), & \delta_a \geq 0;\ \beta < 0 \\ C_{y_s}(\alpha, \beta, \delta_a = -12, \delta_r = 0), & \delta_a < 0;\ \beta \geq 0 \\ -C_{y_s}(\alpha, |\beta|, \delta_a = 12, \delta_r = 0), & \delta_a < 0;\ \beta < 0 \end{cases} \tag{D.10}$$

$$\Delta C_y(\delta_r) = |\delta_r| \,(C_y(\delta_r) - C^*_y)/25 \tag{D.11}$$

$$C_y(\delta_r) = \begin{cases} C_{y_s}(\alpha, \beta, \delta_a = 0, \delta_r = -25), & \delta_r < 0;\ \beta \geq 0 \\ -C_{y_s}(\alpha, |\beta|, \delta_a = 0, \delta_r = 25), & \delta_r < 0;\ \beta < 0 \\ C_{y_s}(\alpha, \beta, \delta_a = 0, \delta_r = 25), & \delta_r \geq 0;\ \beta \geq 0 \\ -C_{y_s}(\alpha, |\beta|, \delta_a = 0, \delta_r = -25), & \delta_r \geq 0;\ \beta < 0 \end{cases} \tag{D.12}$$

Similarly C_{ℓ_s} and C_{n_s} can be defined.

The static coefficients along body axes are obtained from:

$$C_y^* = C_{y_s} \tag{D.13}$$

$$C_\ell^* = C_{\ell_s} \cos\alpha - C_{n_s} \sin\alpha \tag{D.14}$$

$$C_n^* = C_{n_s} \cos\alpha + C_{\ell_s} \sin\alpha \tag{D.15}$$

The total lateral force and moment coefficients along body axes are are then given by:

$$C_y = C_y^* + C_{y_p} \frac{pb}{2V} + C_{y_r} \frac{rb}{2V} \tag{D.16}$$

$$C_\ell = C_\ell^* + C_{\ell_p} \frac{pb}{2V} + C_{\ell_r} \frac{rb}{2V} \tag{D.17}$$

$$C_n = C_n^* + C_{n_p} \frac{pb}{2V} + C_{n_r} \frac{rb}{2V} \tag{D.18}$$

The wind tunnel model has been compared against identified model and discussed in detail elsewhere. For the sake of conciseness it will not be discussed again here. The salient feature of the model was its high complexity thus providing a thorough check out of the identification technique.

Time histories of the sixteen maneuvers are given in the following pages in Figures D-1 through D-16.

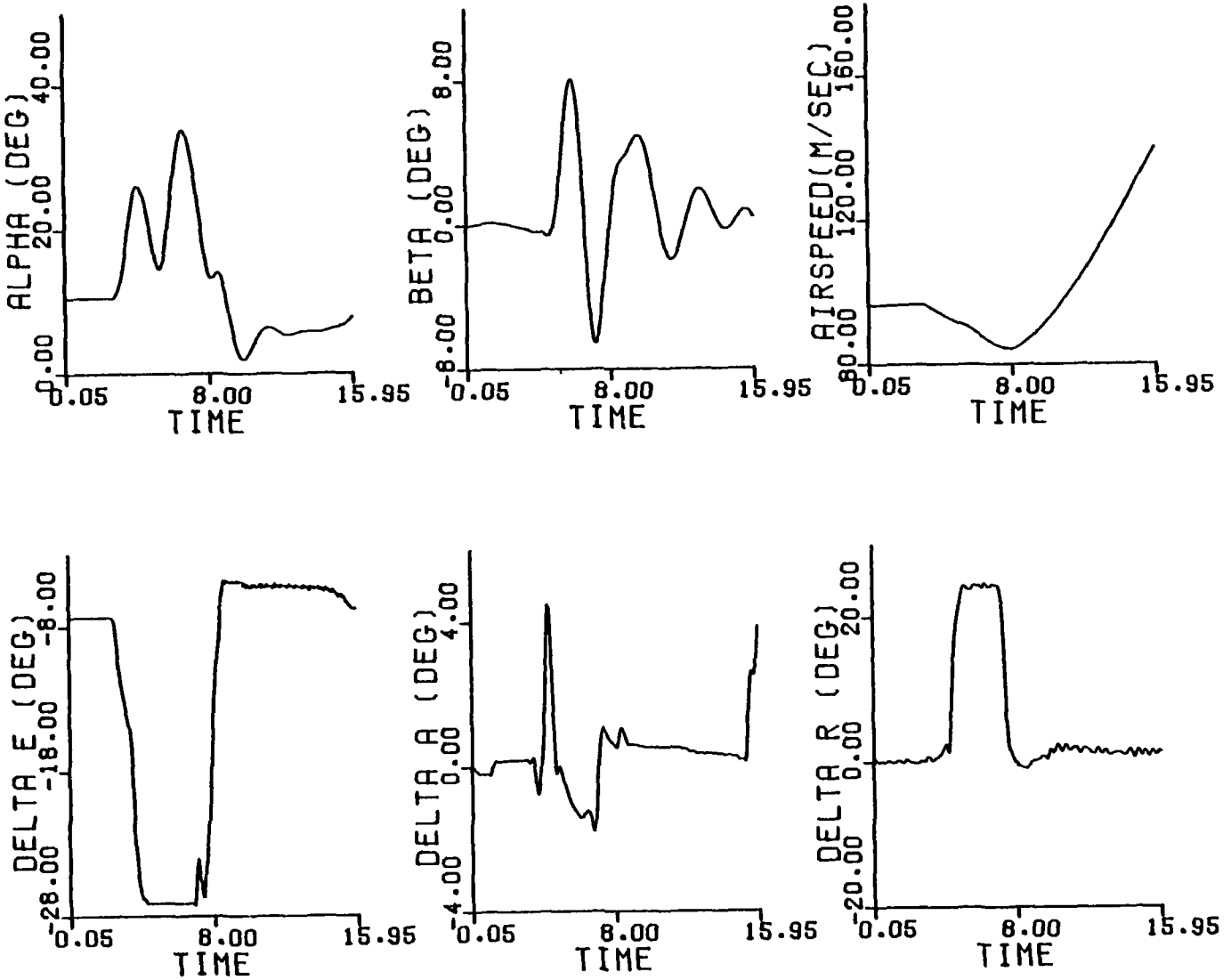

Figure D-1 Time Histories of Simulated Maneuvers (Maneuver 1)

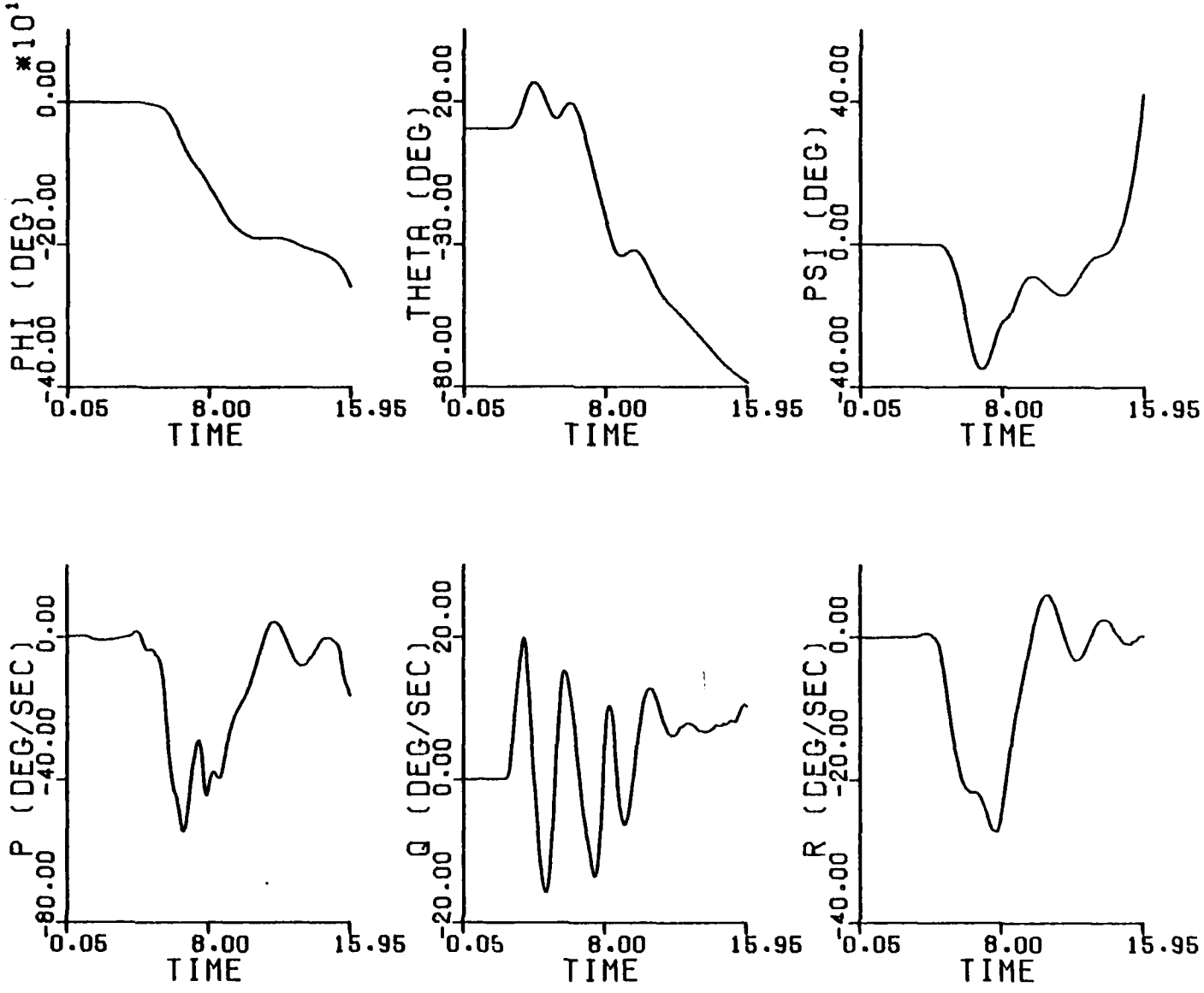

Figure D-1 (Concluded)

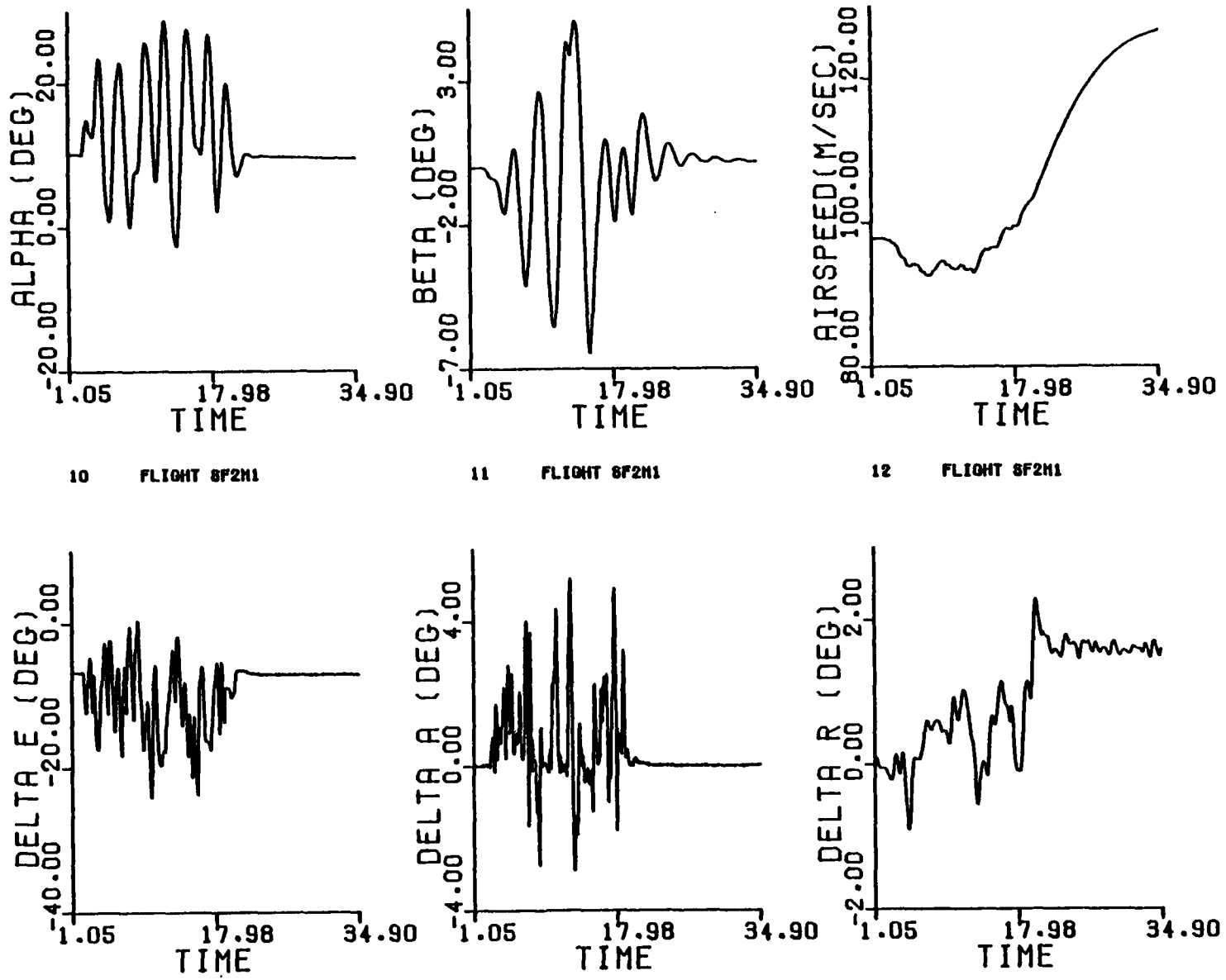

Figure D-2 Time Histories of Simulated Maneuvers (Maneuver 2)

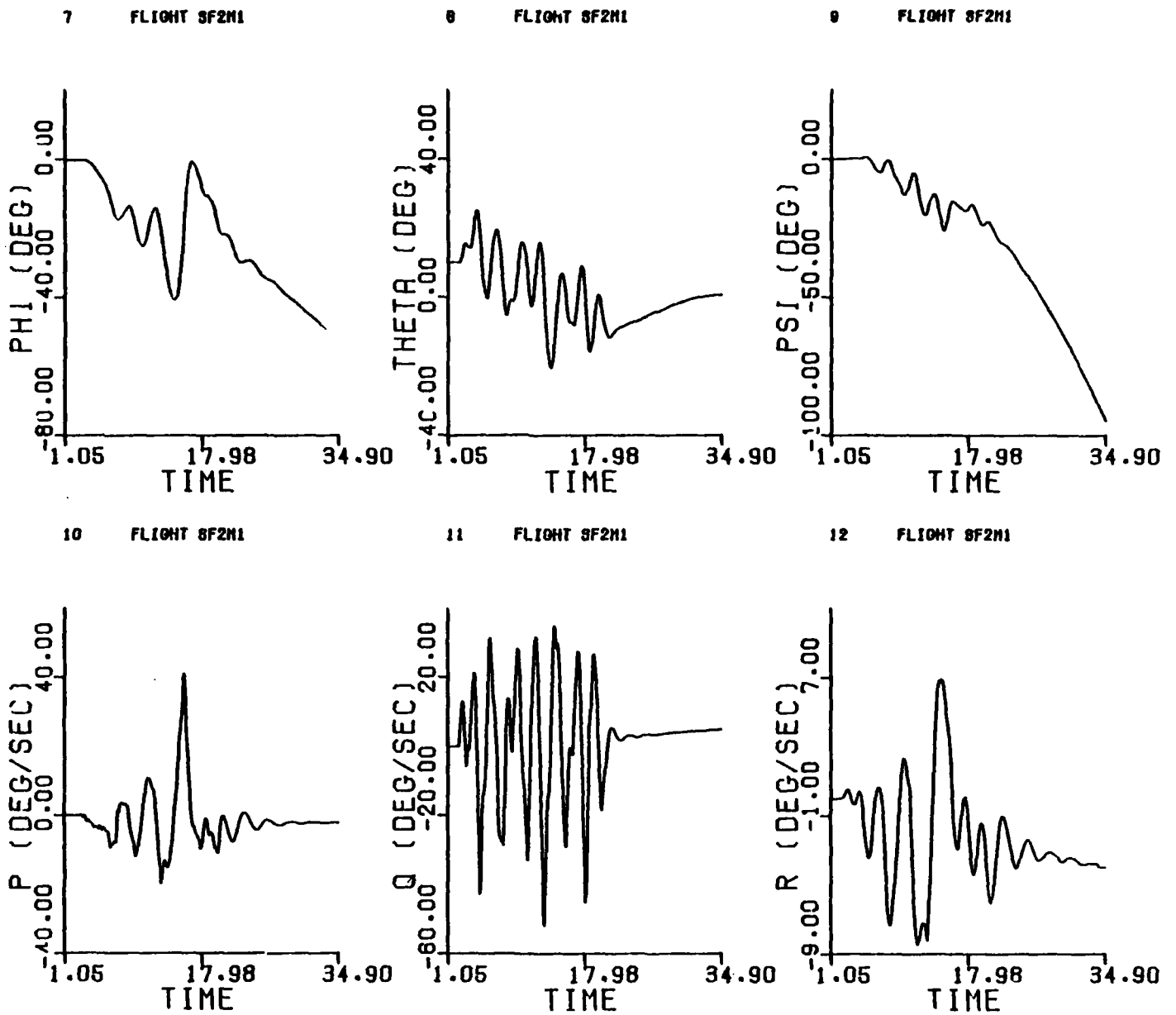

Figure D-2 (Concluded)

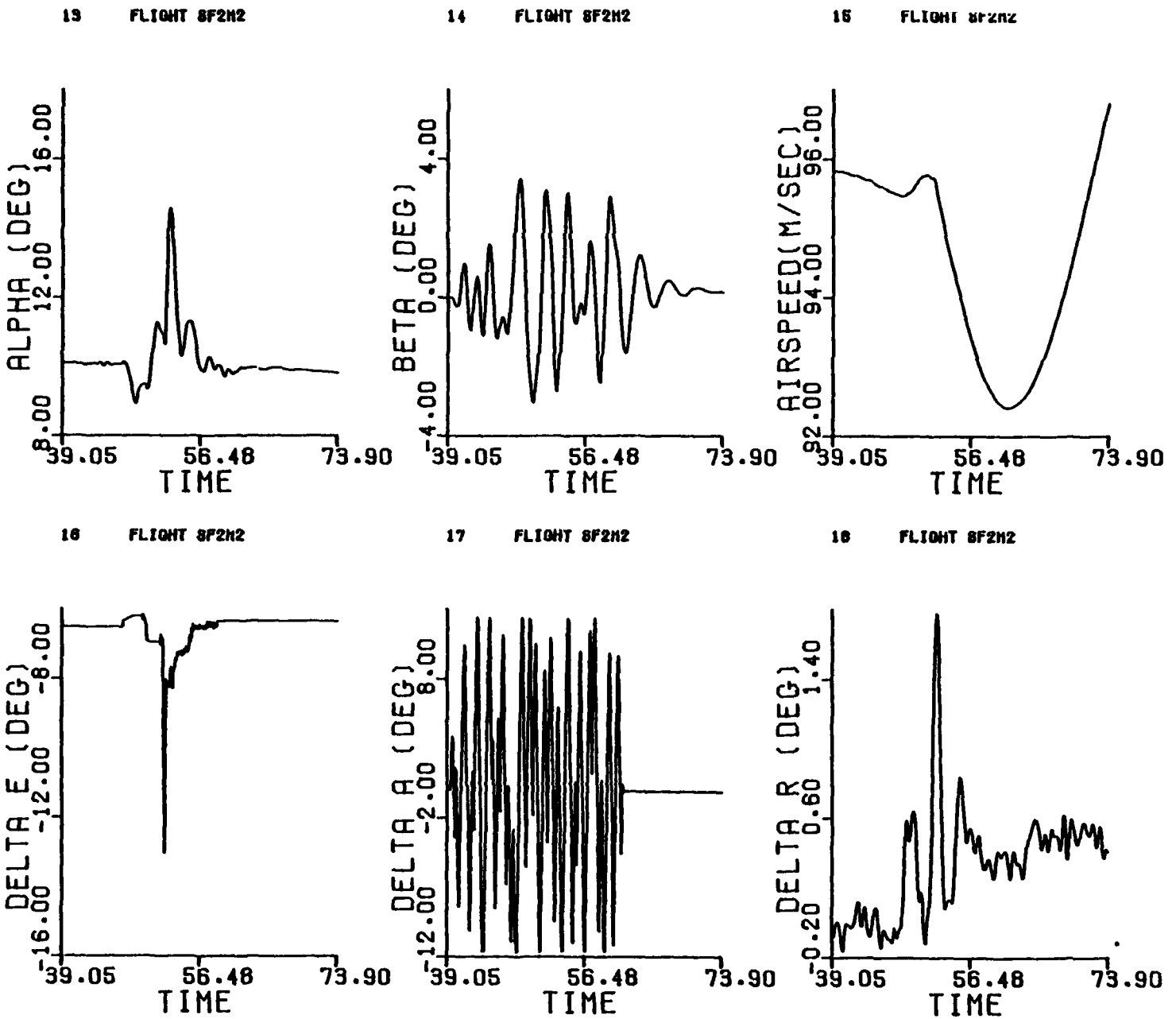

Figure D-3 Time Histories of Simulated Maneuvers (Maneuver 3)

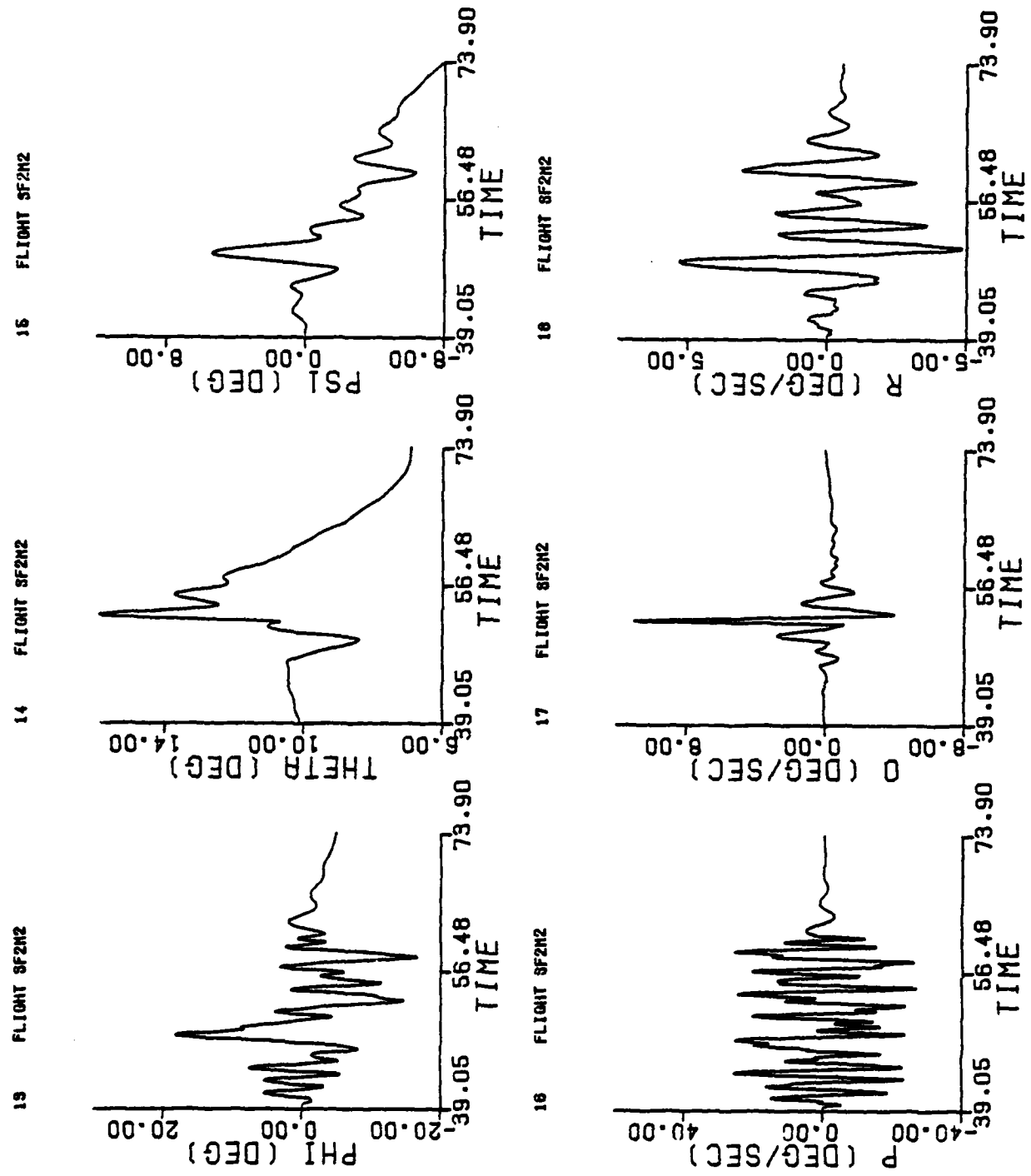

Figure D-3 (Concluded)

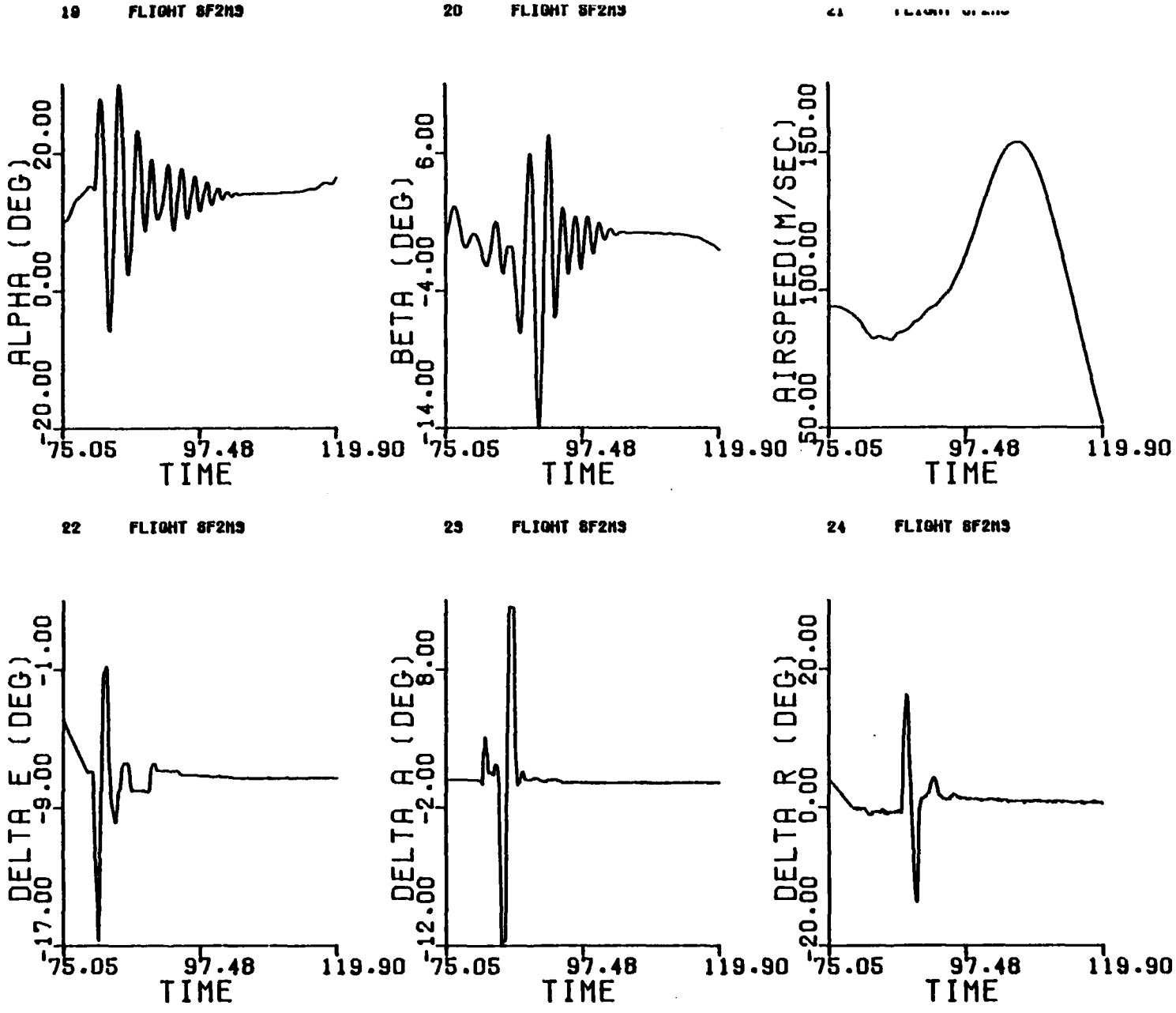

Figure D-4 Time Histories of Simulated Maneuvers (Maneuvers 4)

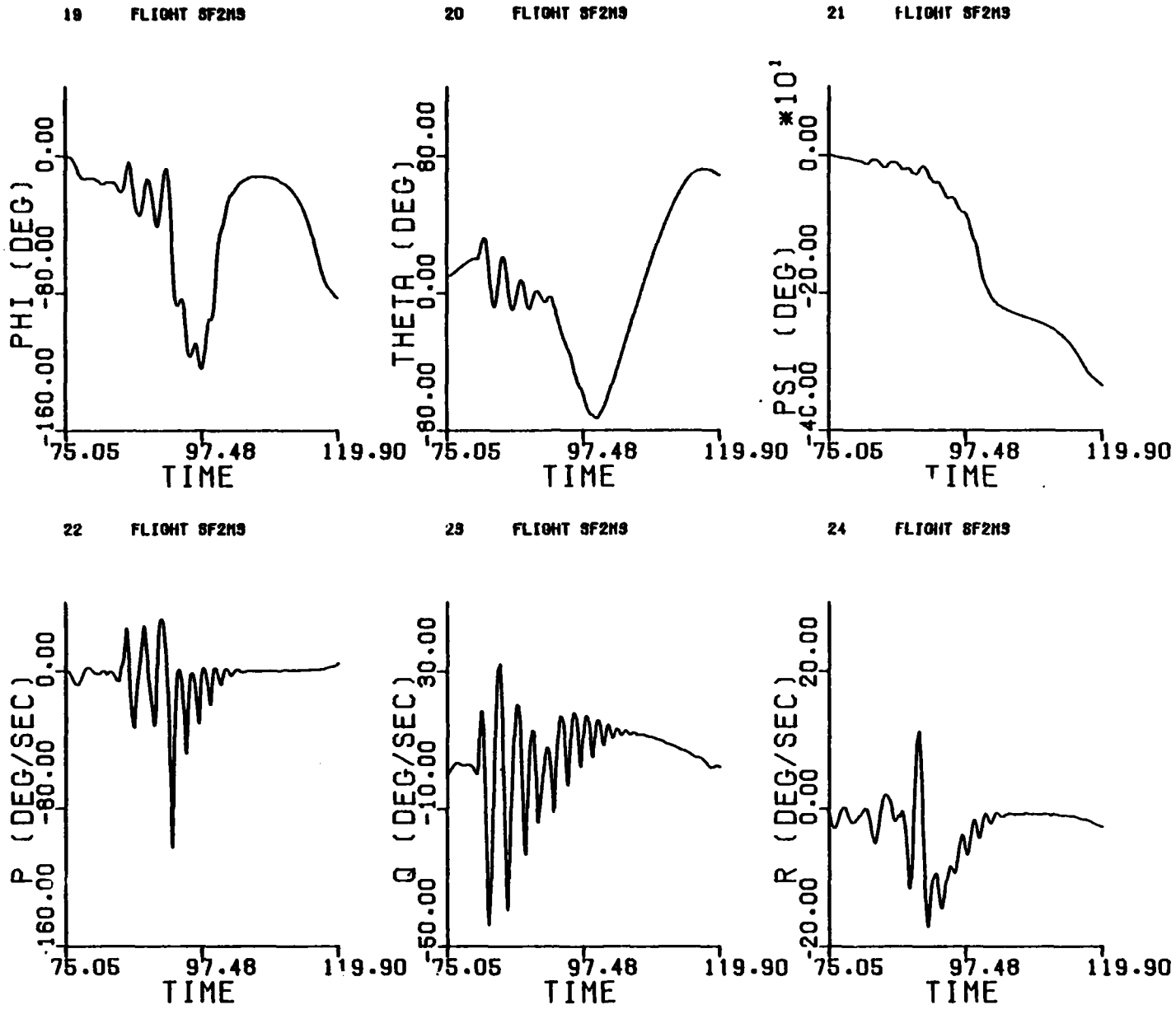

Figure D-4 (Concluded)

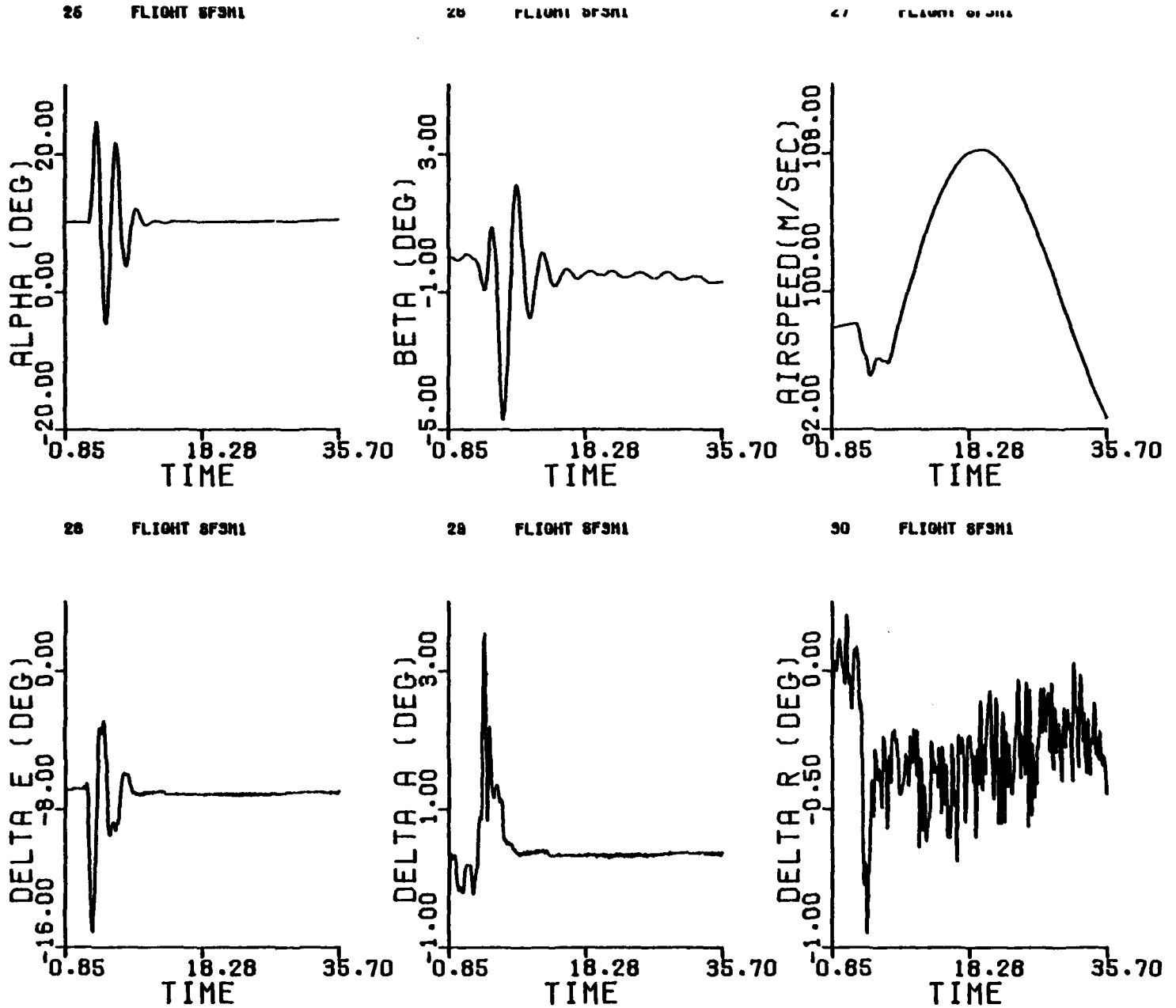

Figure D-5 Time Histories of Simulated Maneuvers (Maneuver 5)

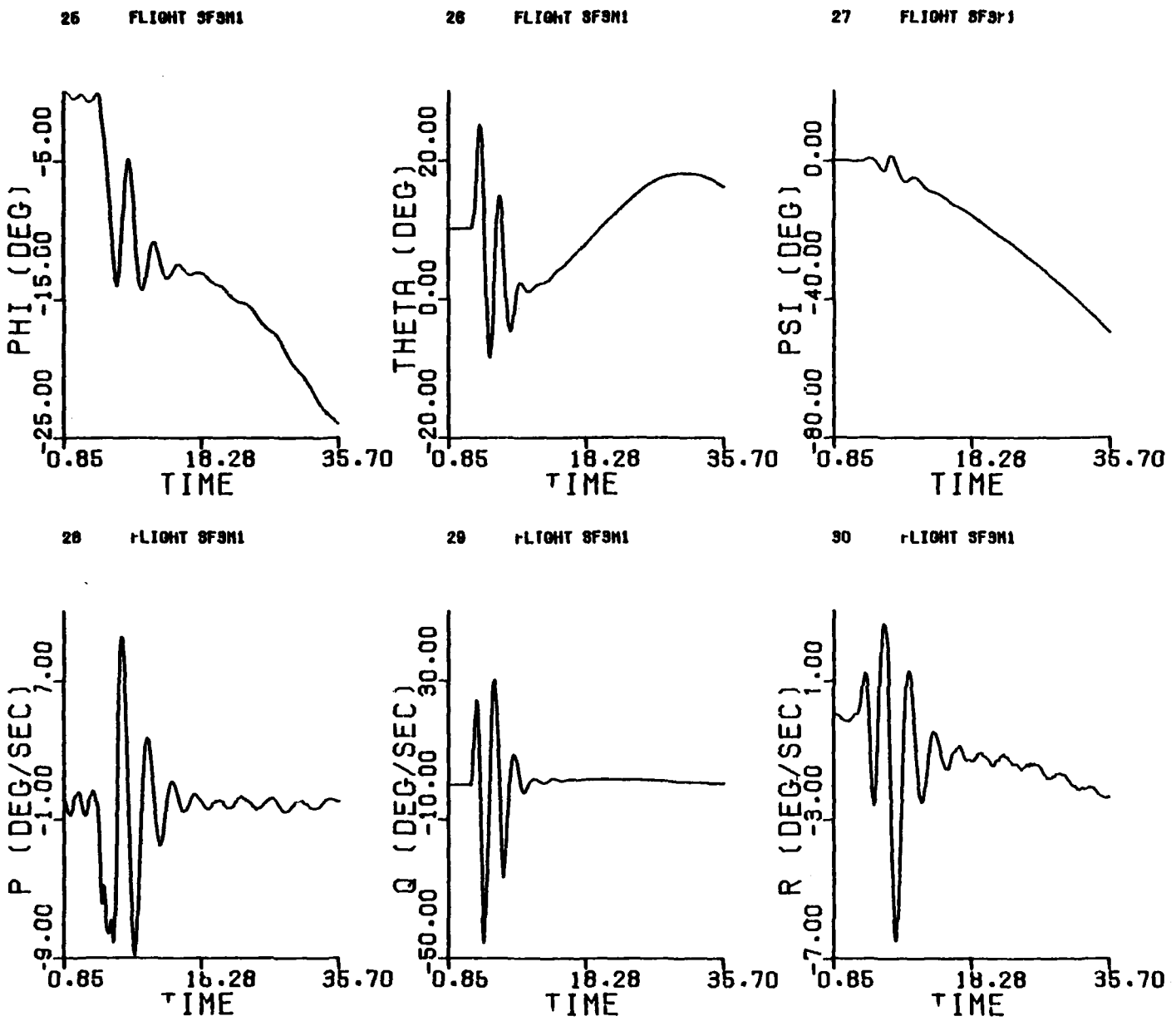

Figure D-5 (Concluded)

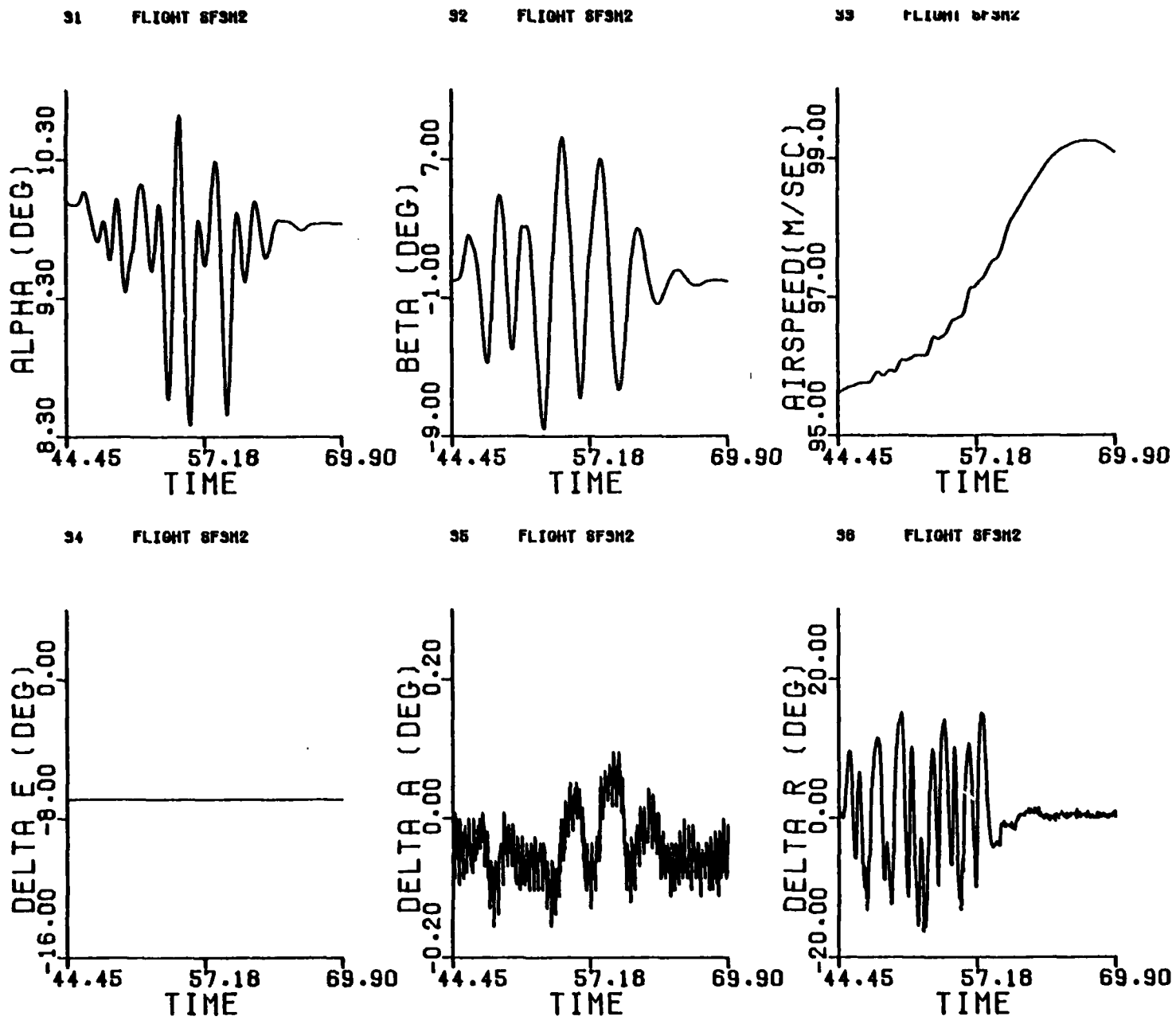

Figure D-6 Time Histories of Simulated Maneuvers (Maneuver 6)

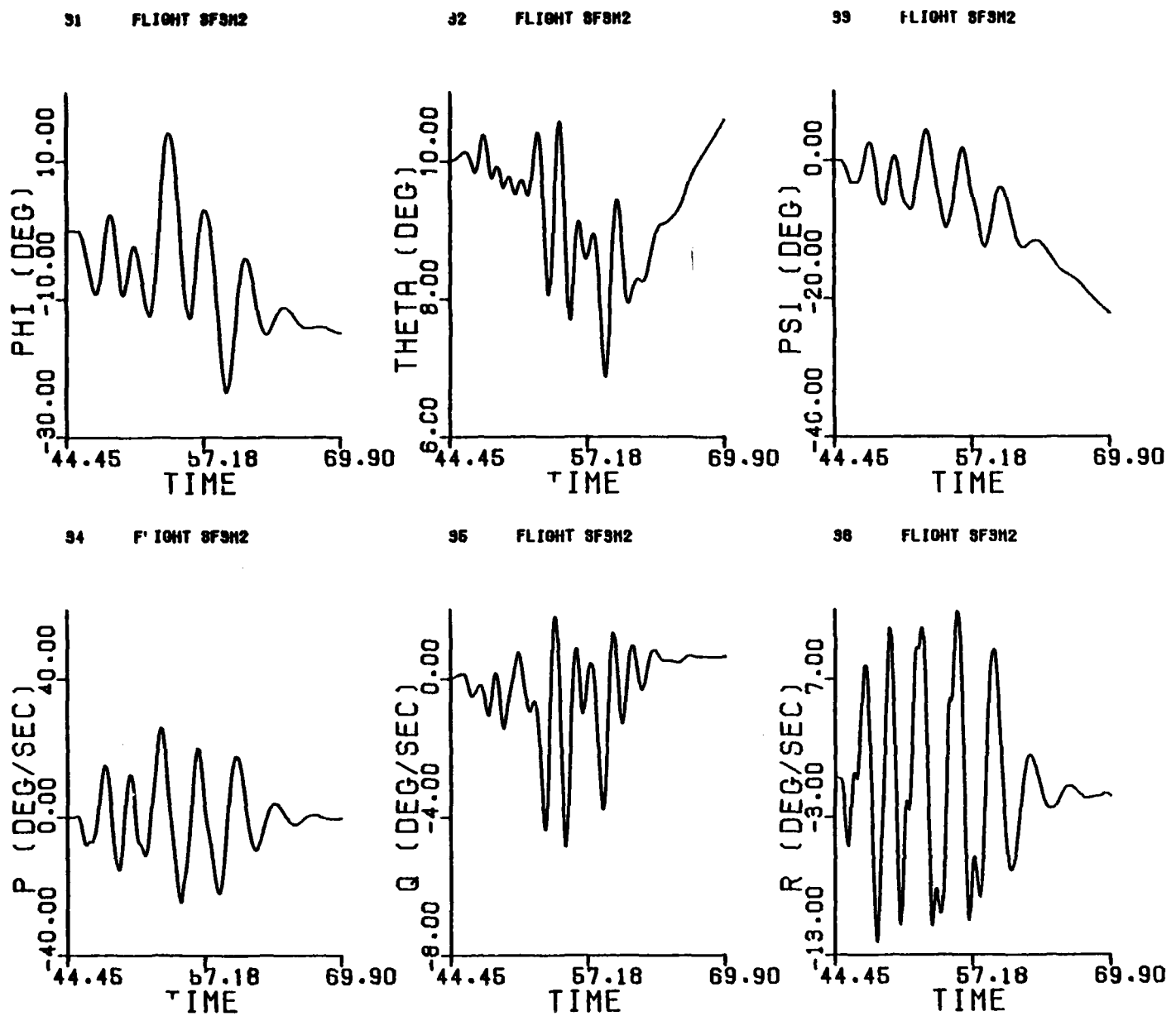

Figure D-6 (Concluded)

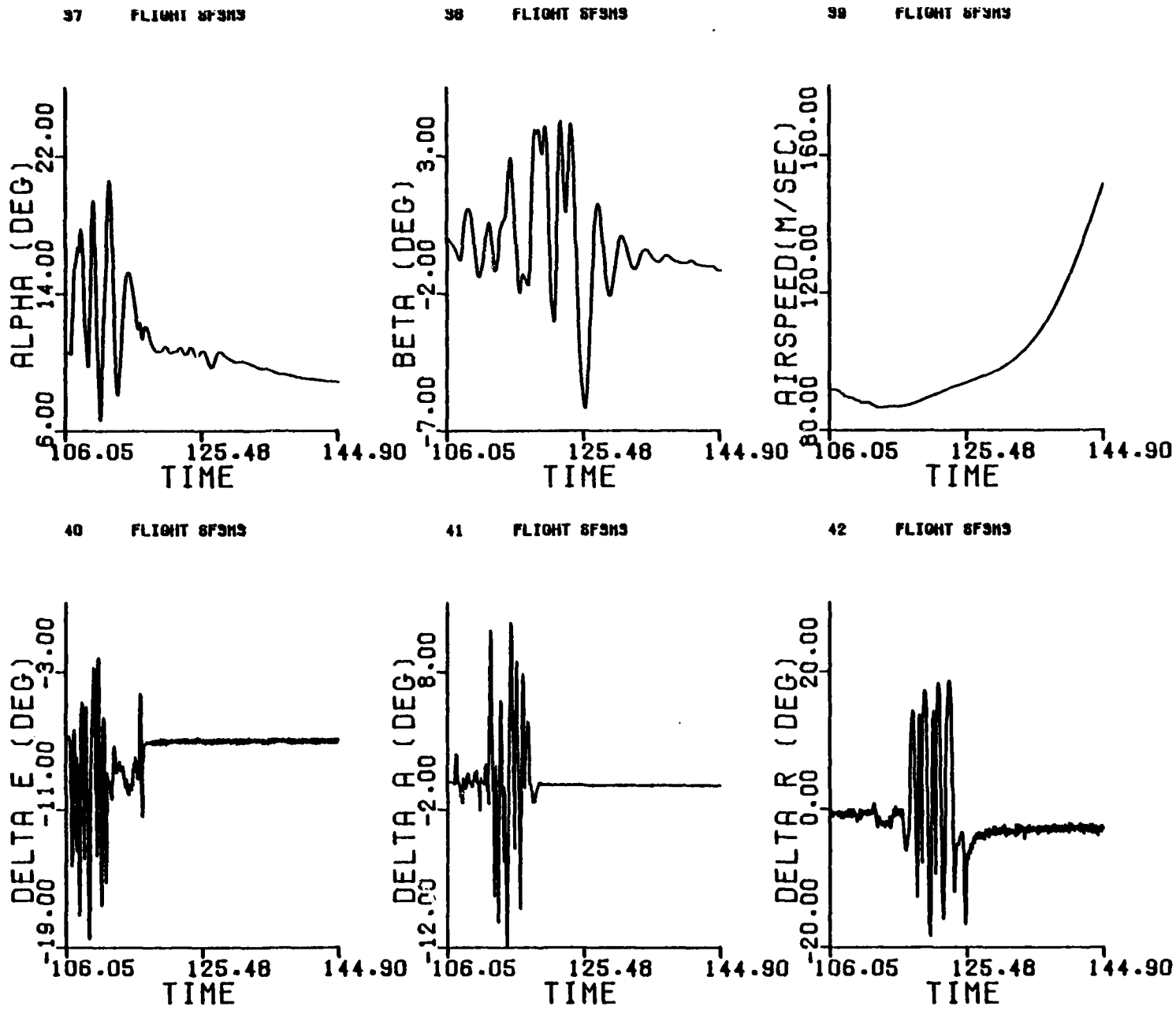

Figure D-7 Time Histories of Simulated Maneuvers (Maneuver 7)

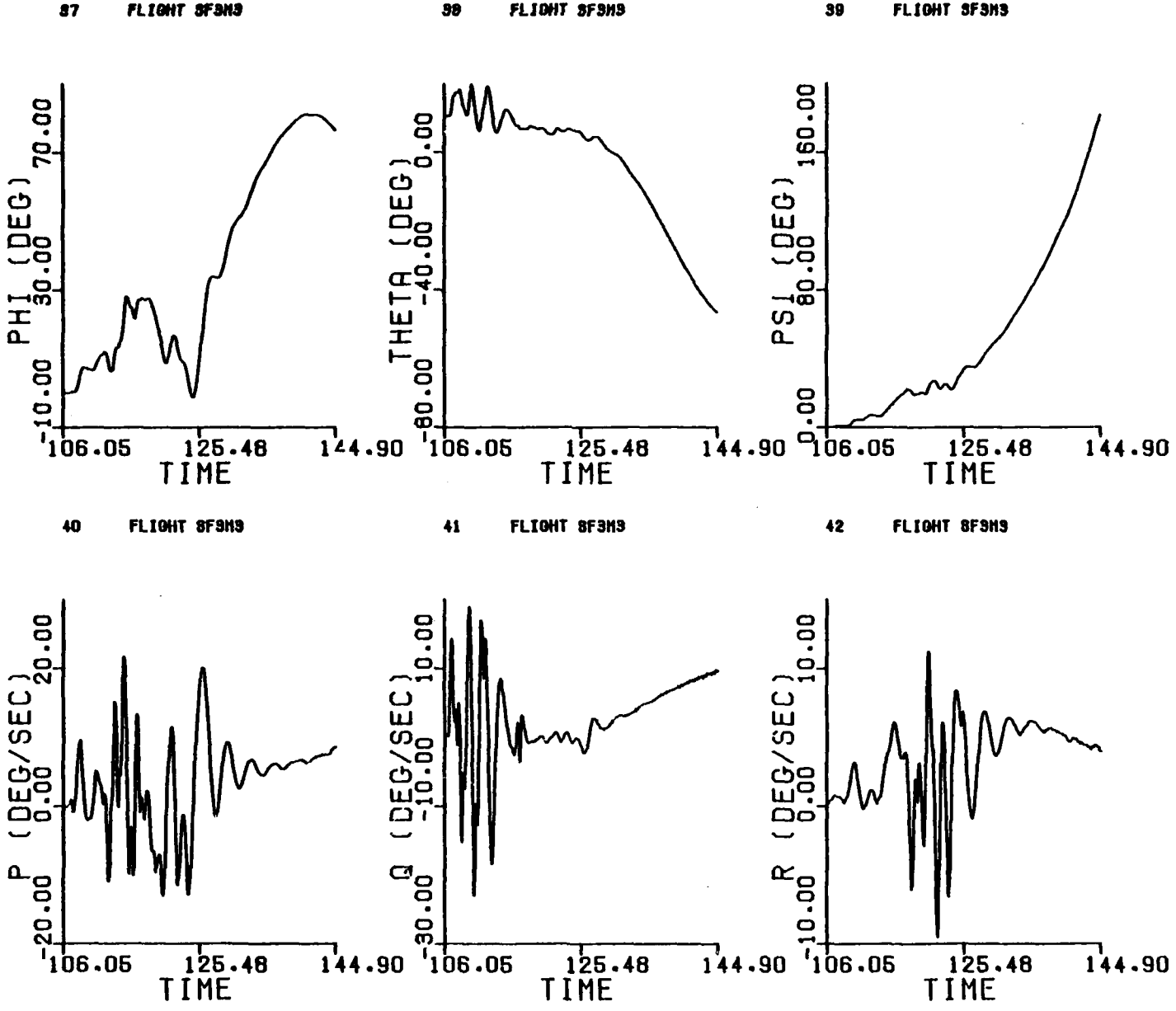

Figure D-7 (Concluded)

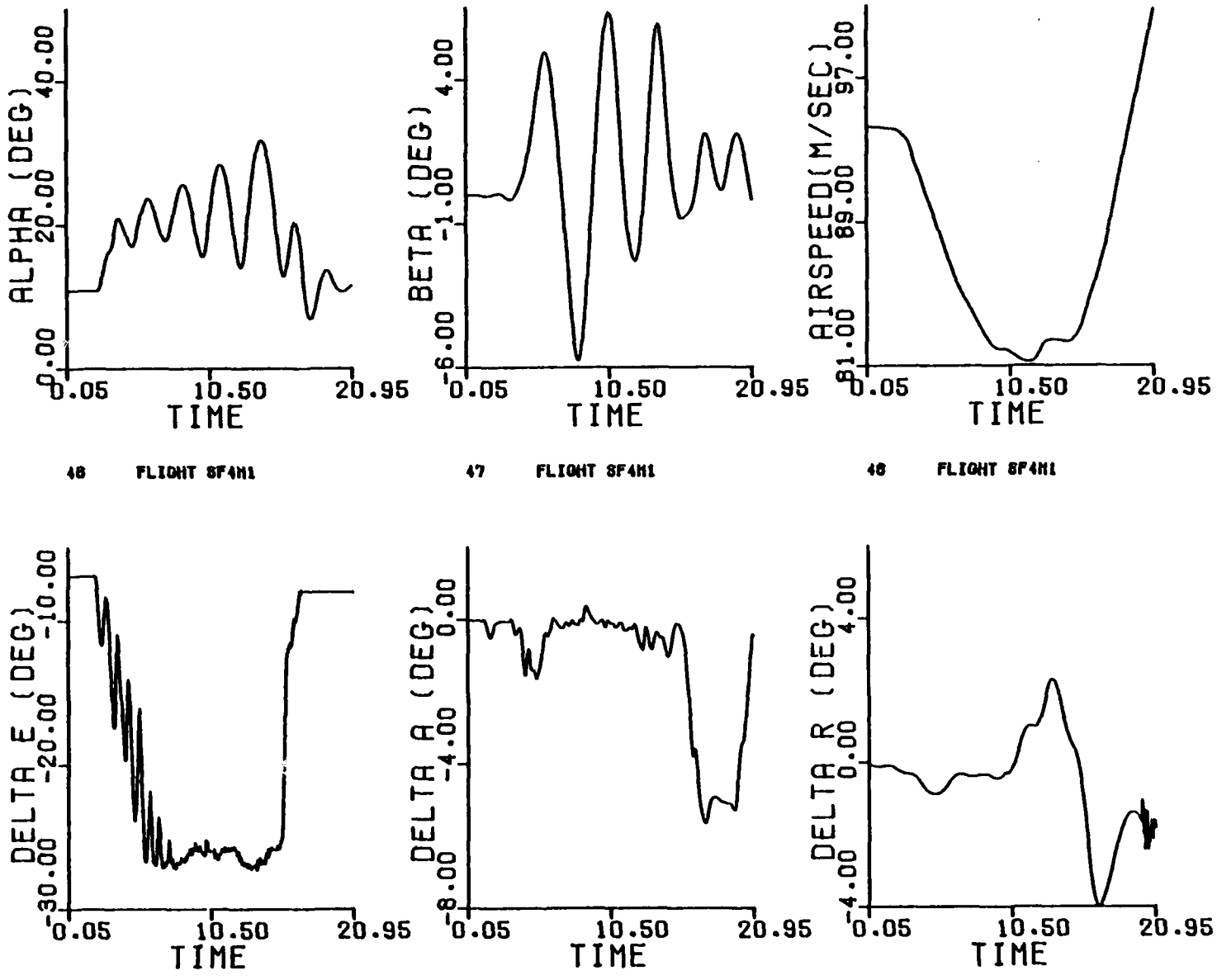

Figure D-8 Time Histories of Simulated Maneuvers (Maneuver 8)

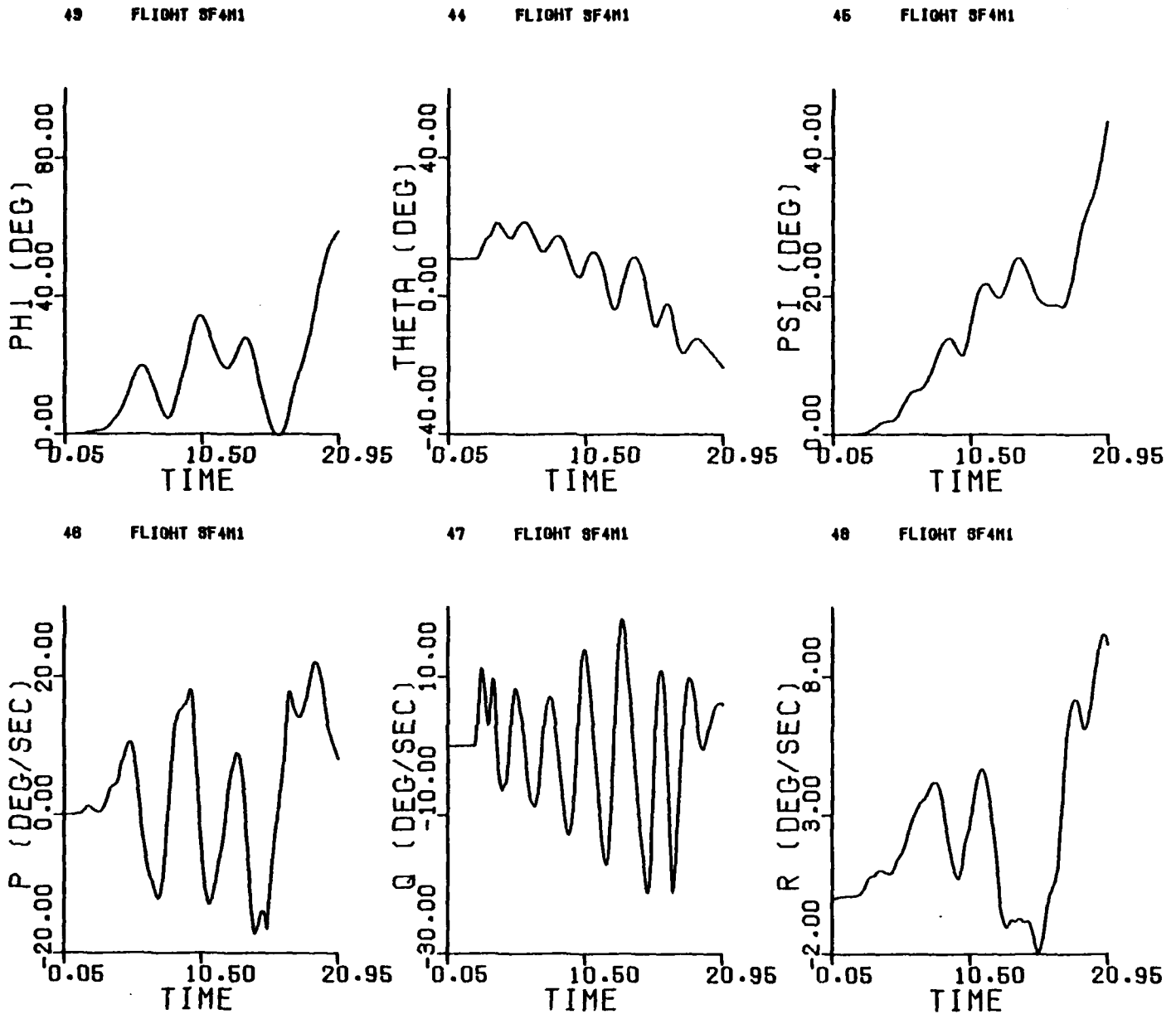

Figure D-8 (Concluded)

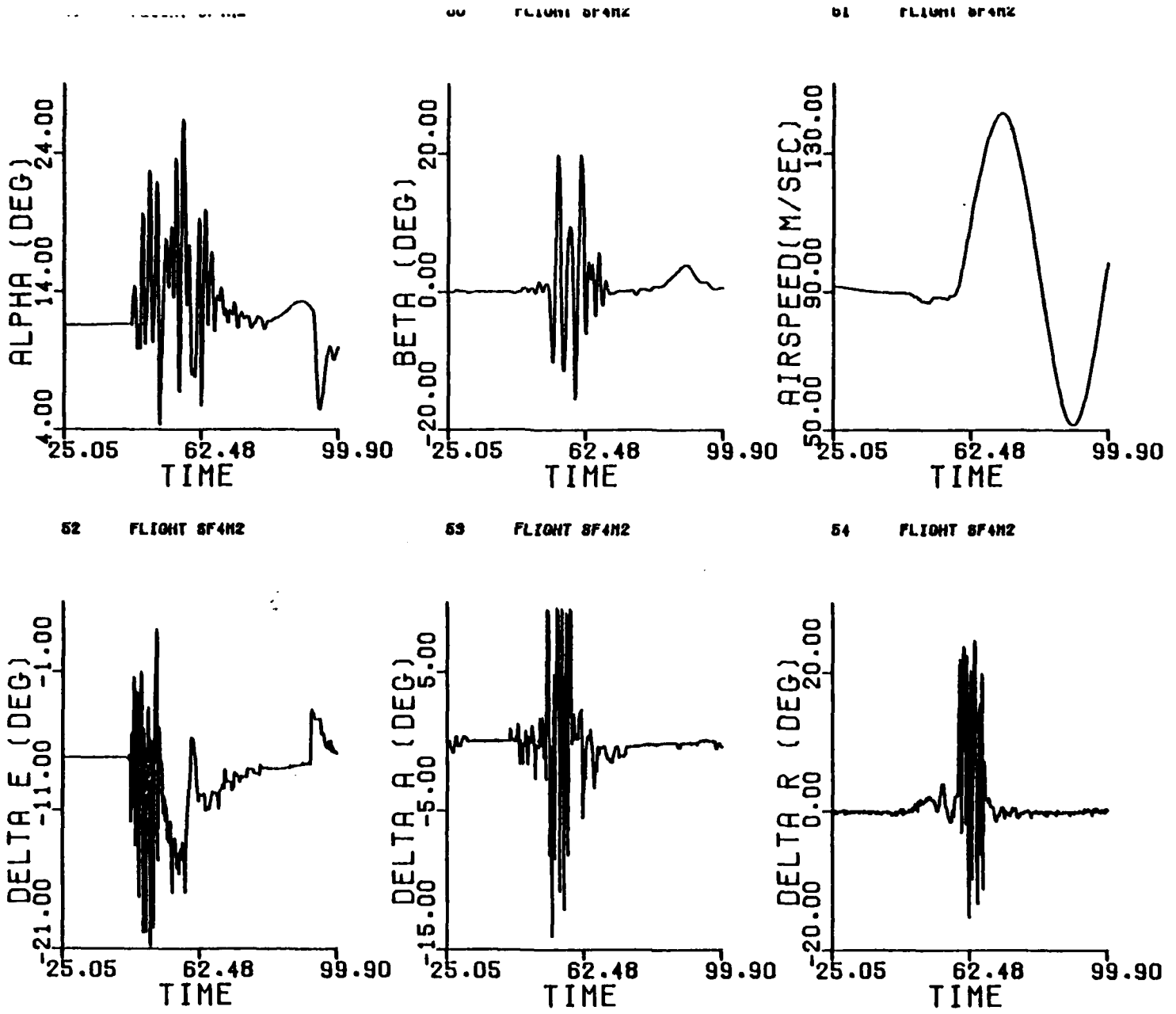

Figure D-9 Time Histories of Simulated Maneuvers (Maneuver 9)

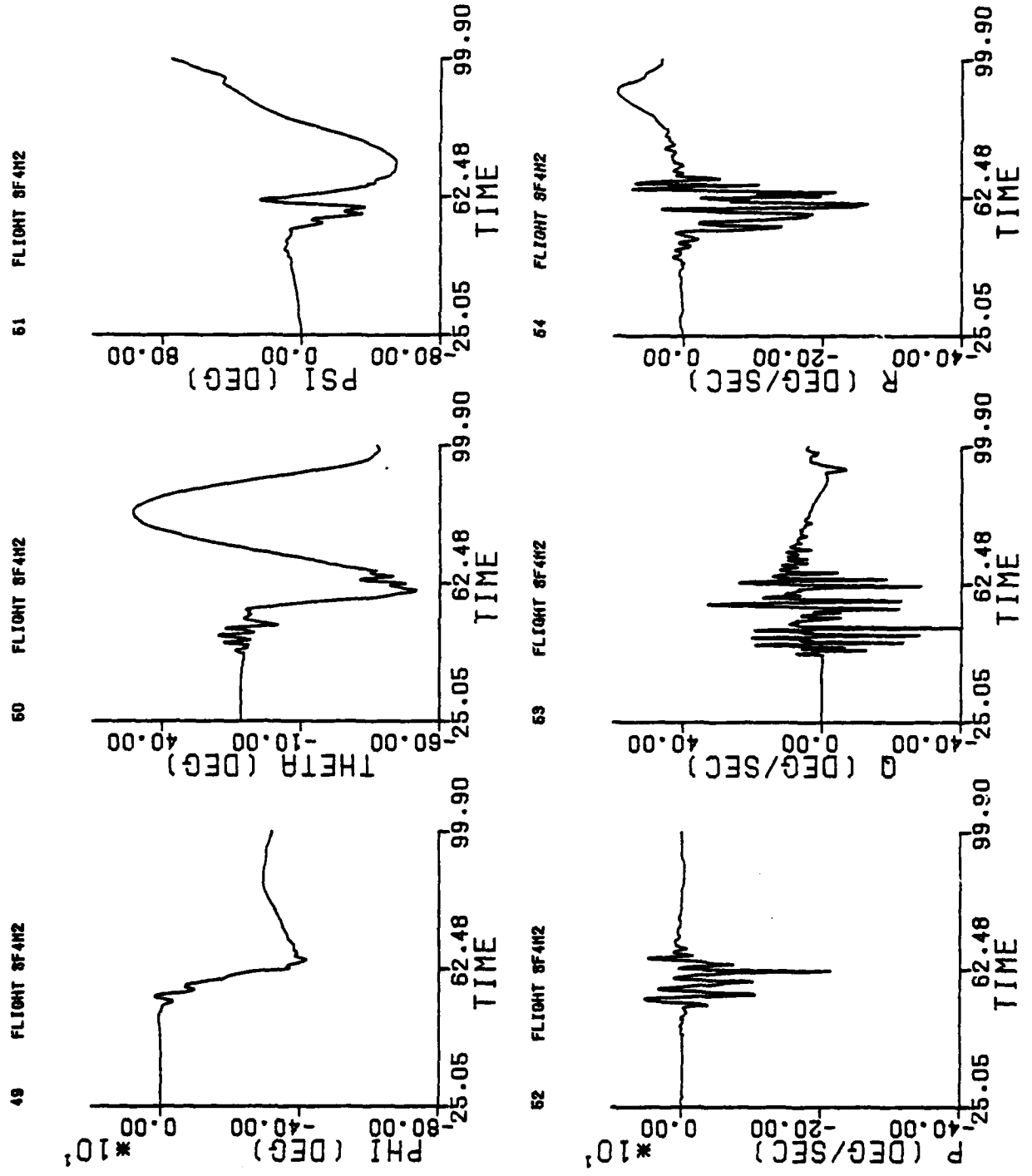

Figure D-9 (Concluded)

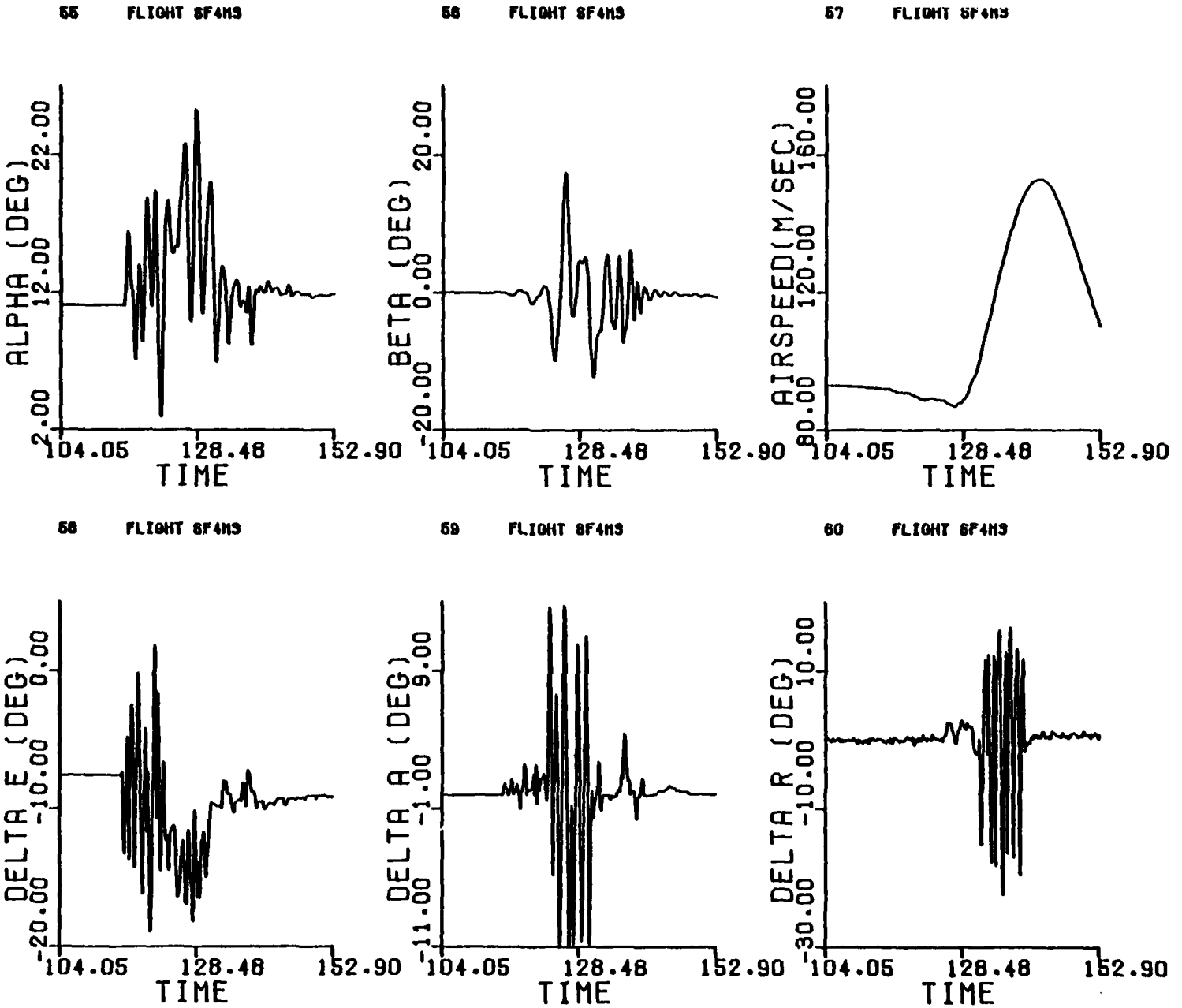

Figure D-10 Time Histories of Simulated Maneuvers (Maneuver 10)

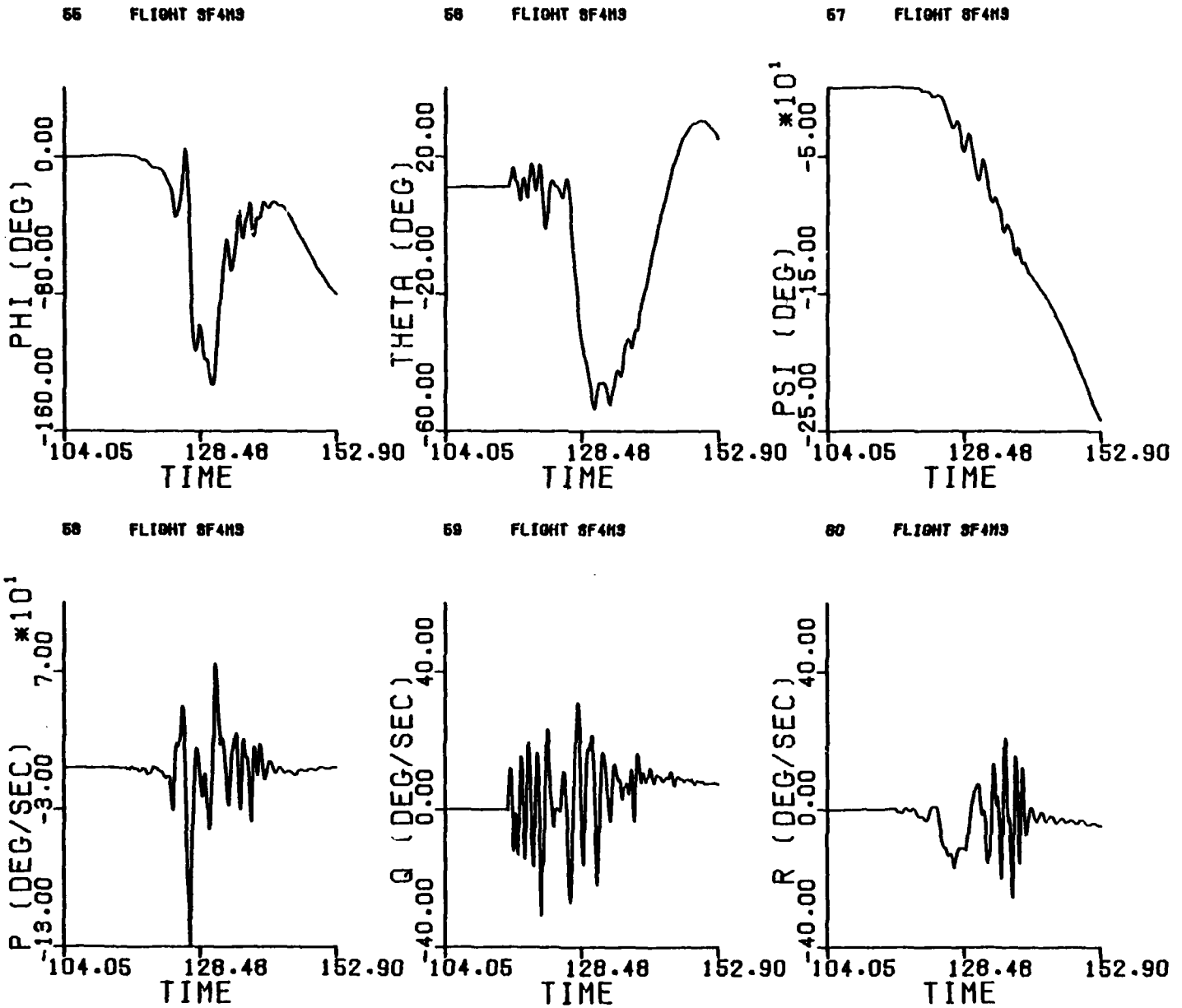

Figure D-10 (Concluded)

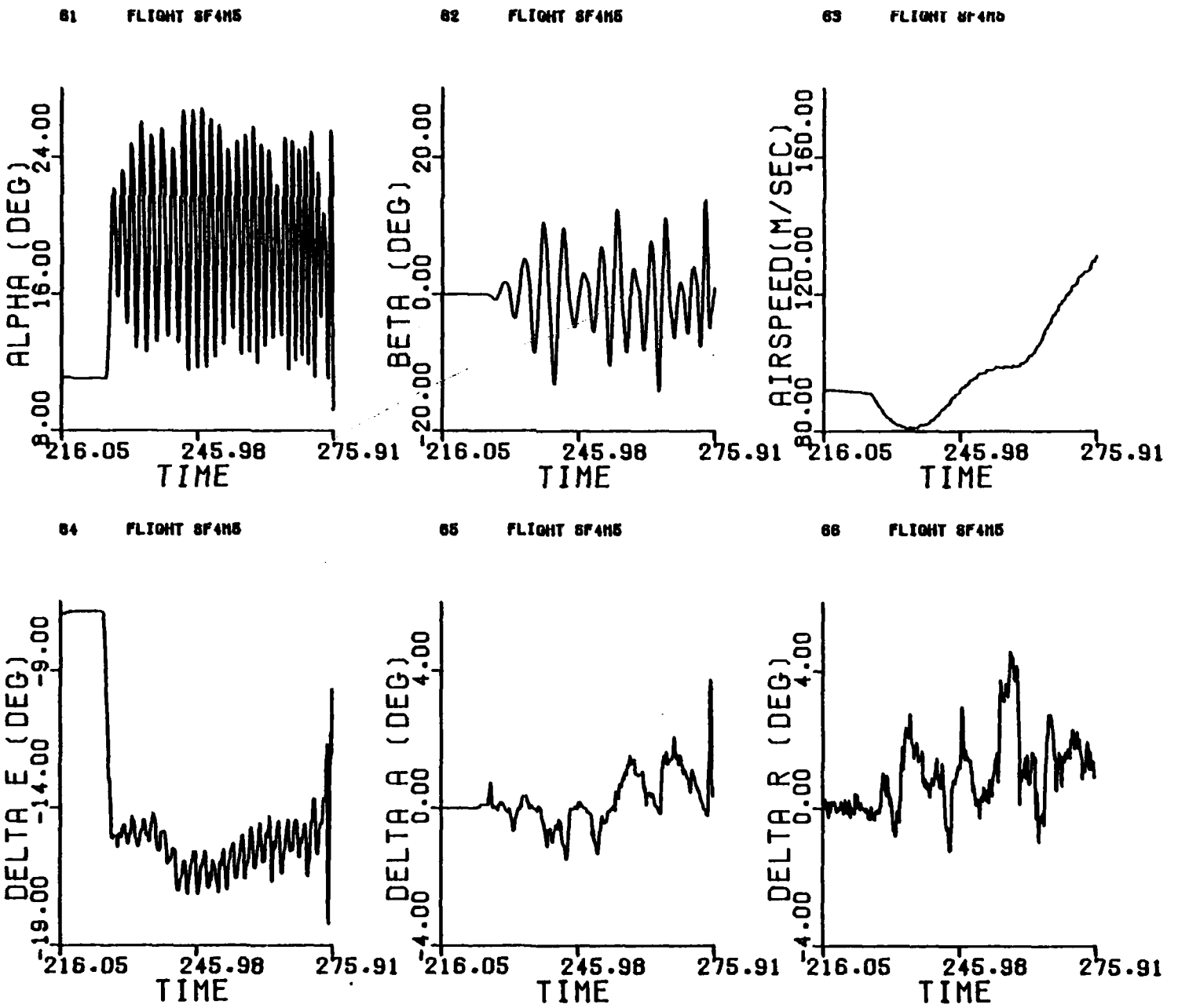

Figure D-11 Time Histories of Simulated Maneuvers (Maneuver 11)

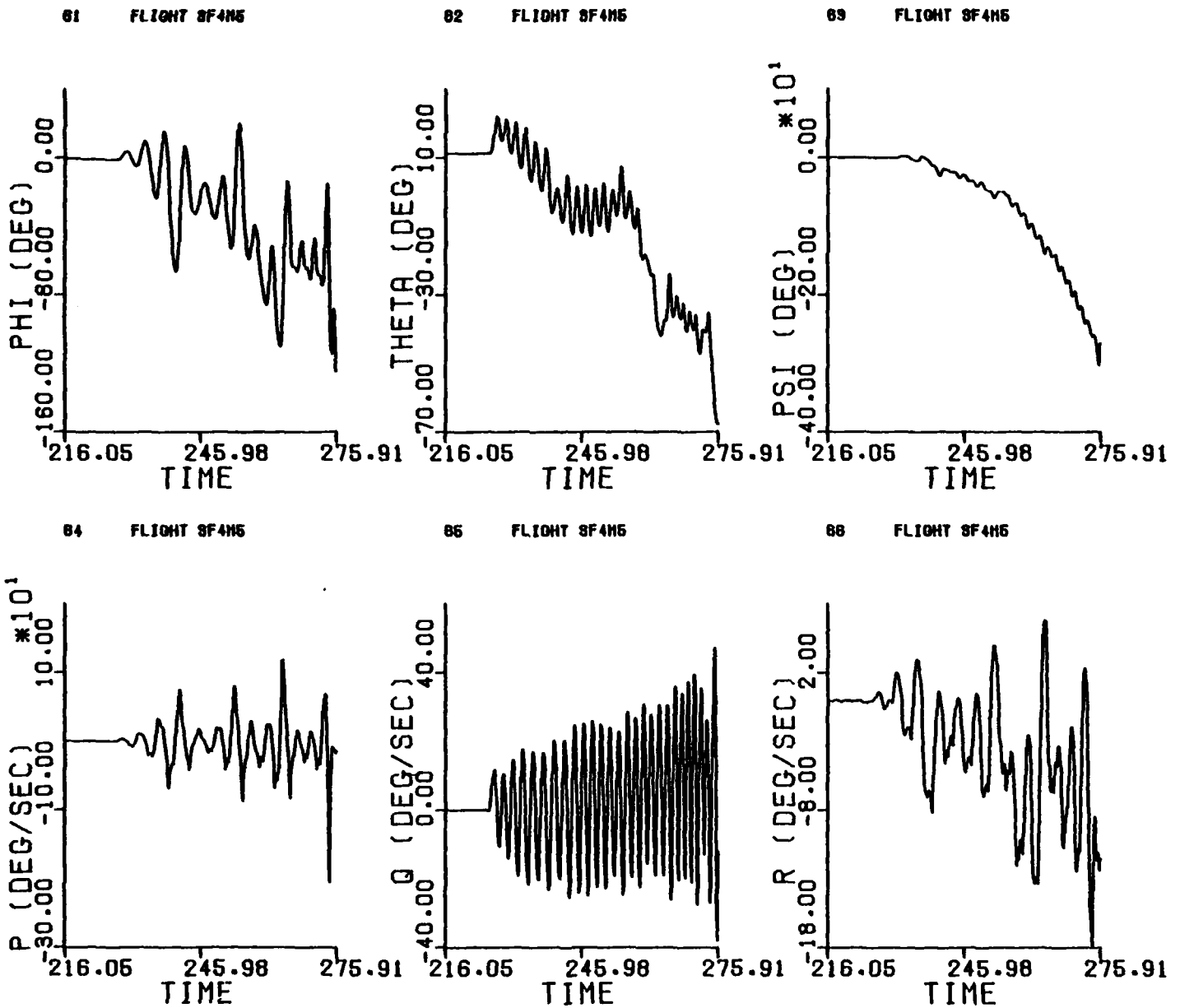

Figure D-11 (Concluded)

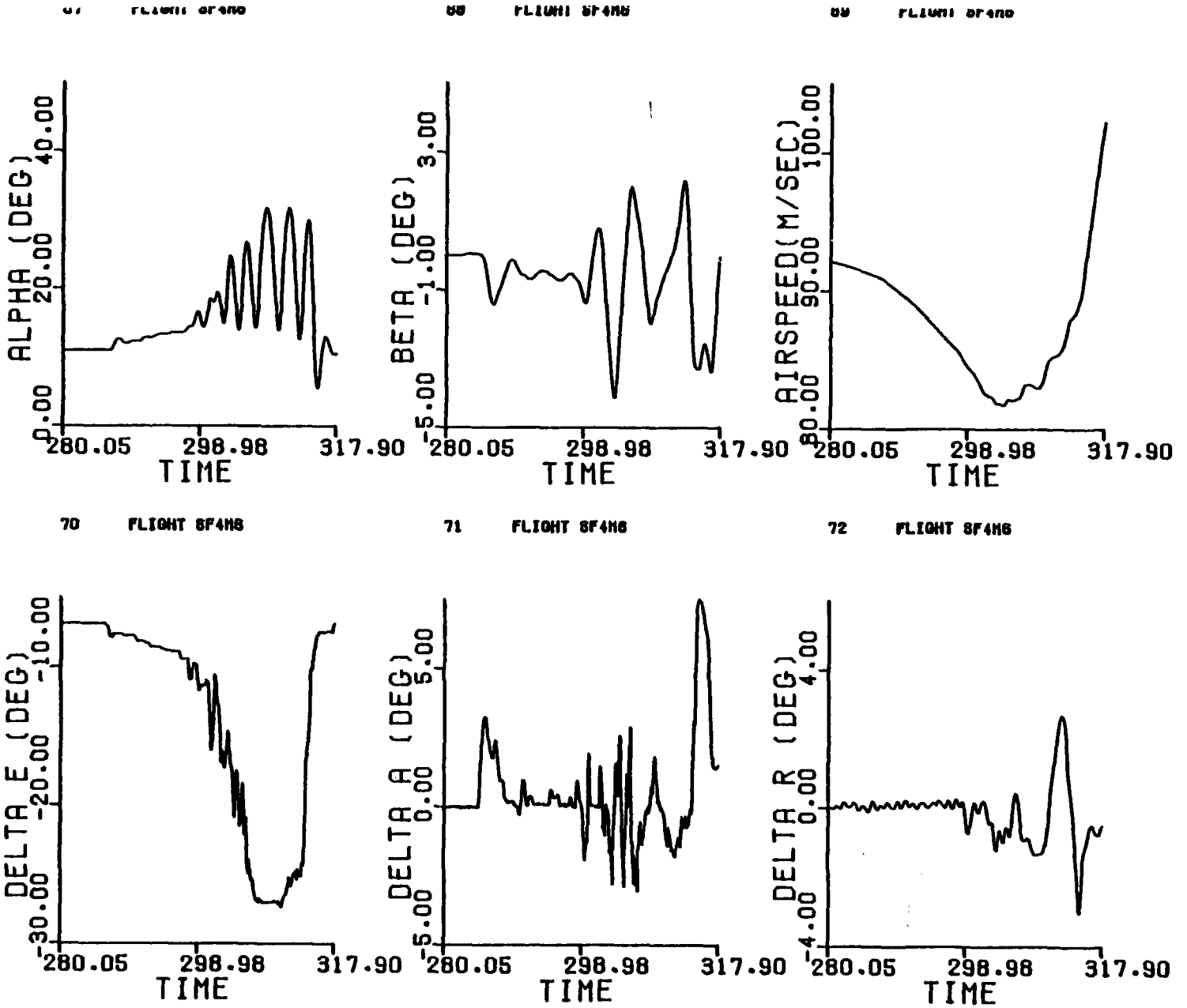

Figure D-12 Time Histories of Simulated Maneuvers (Maneuver 12)

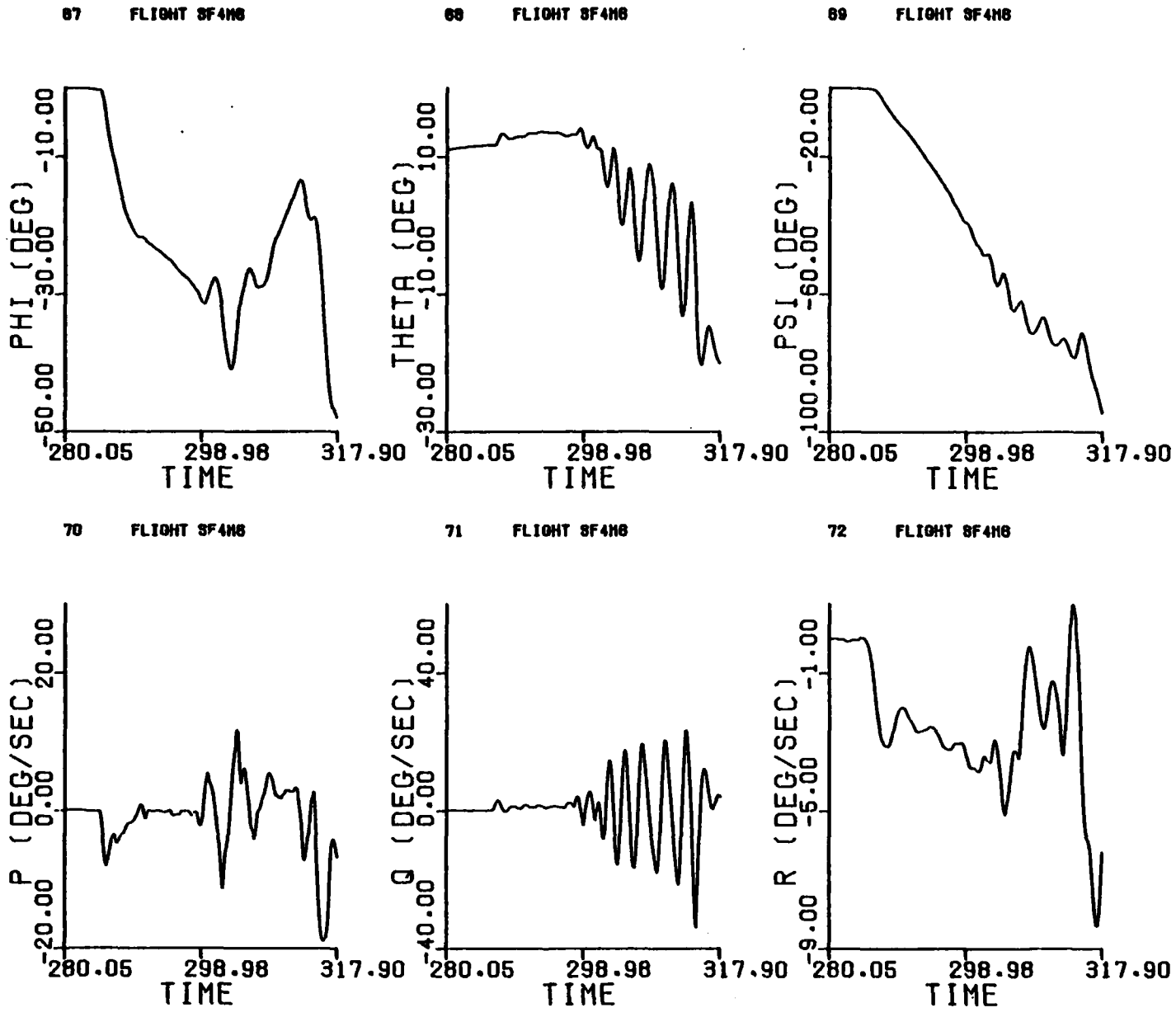

Figure D-12 (Concluded)

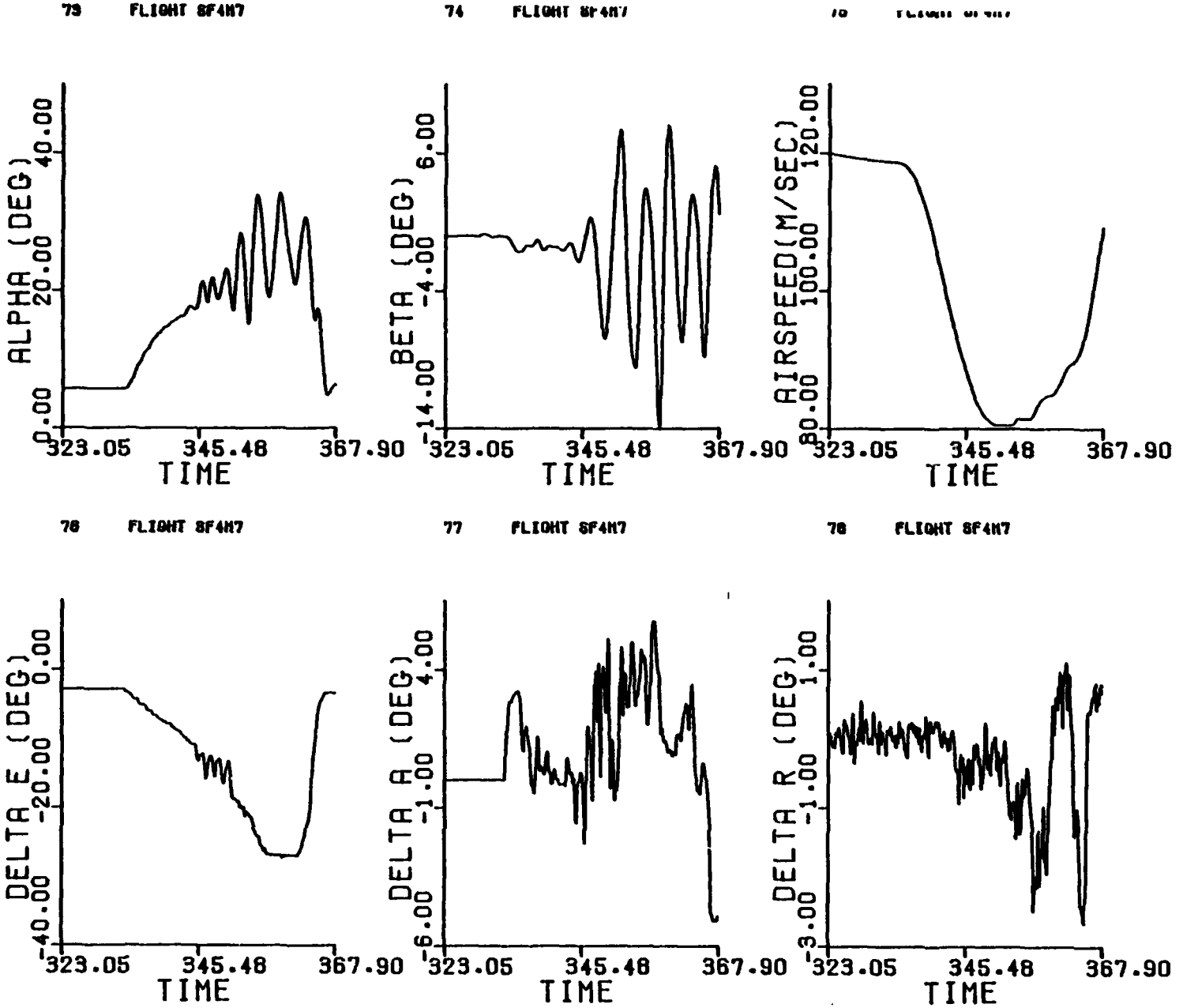

Figure D-13 Time Histories of Simulated Maneuvers (Maneuver 13)

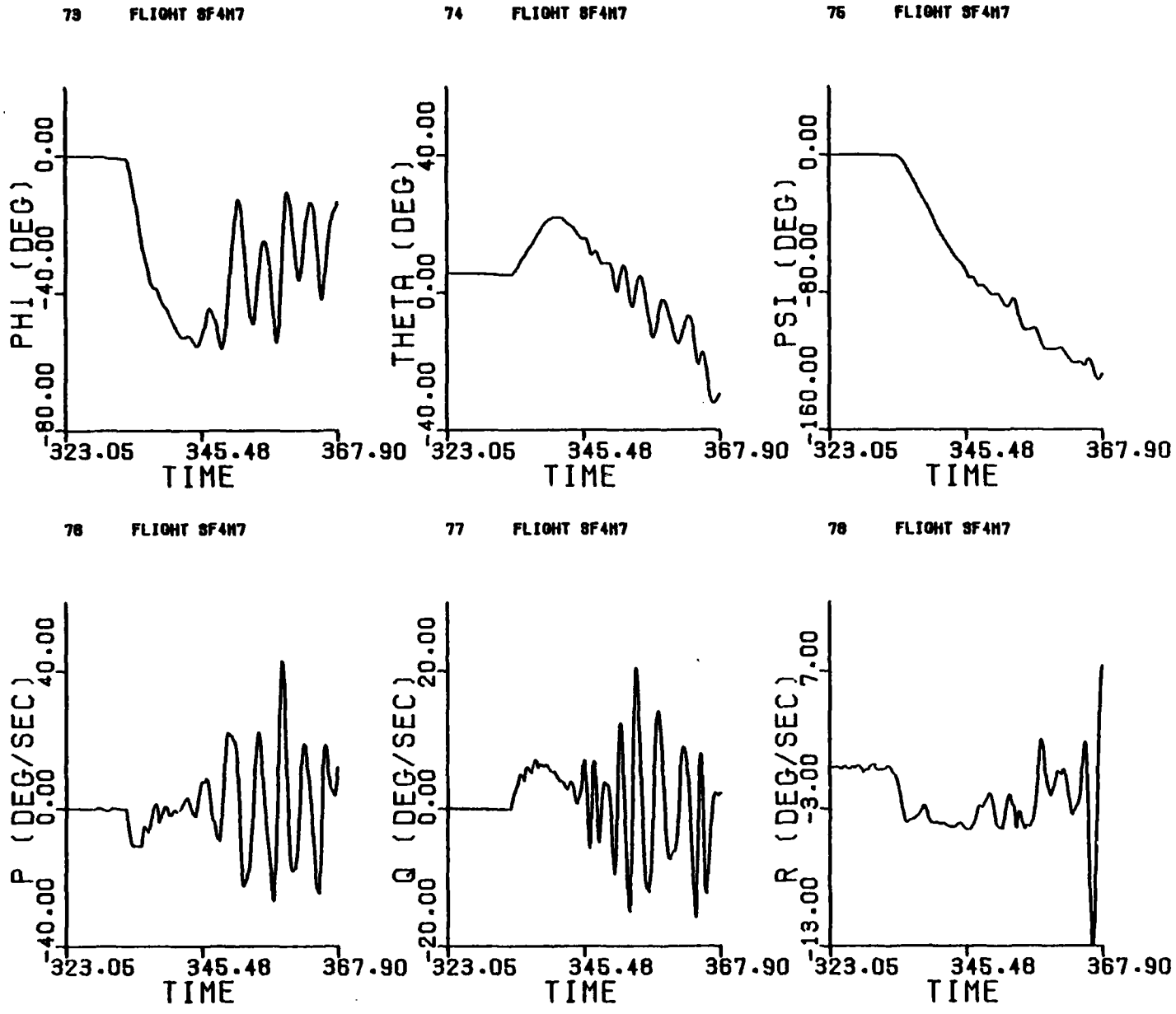

Figure D-13 (Concluded)

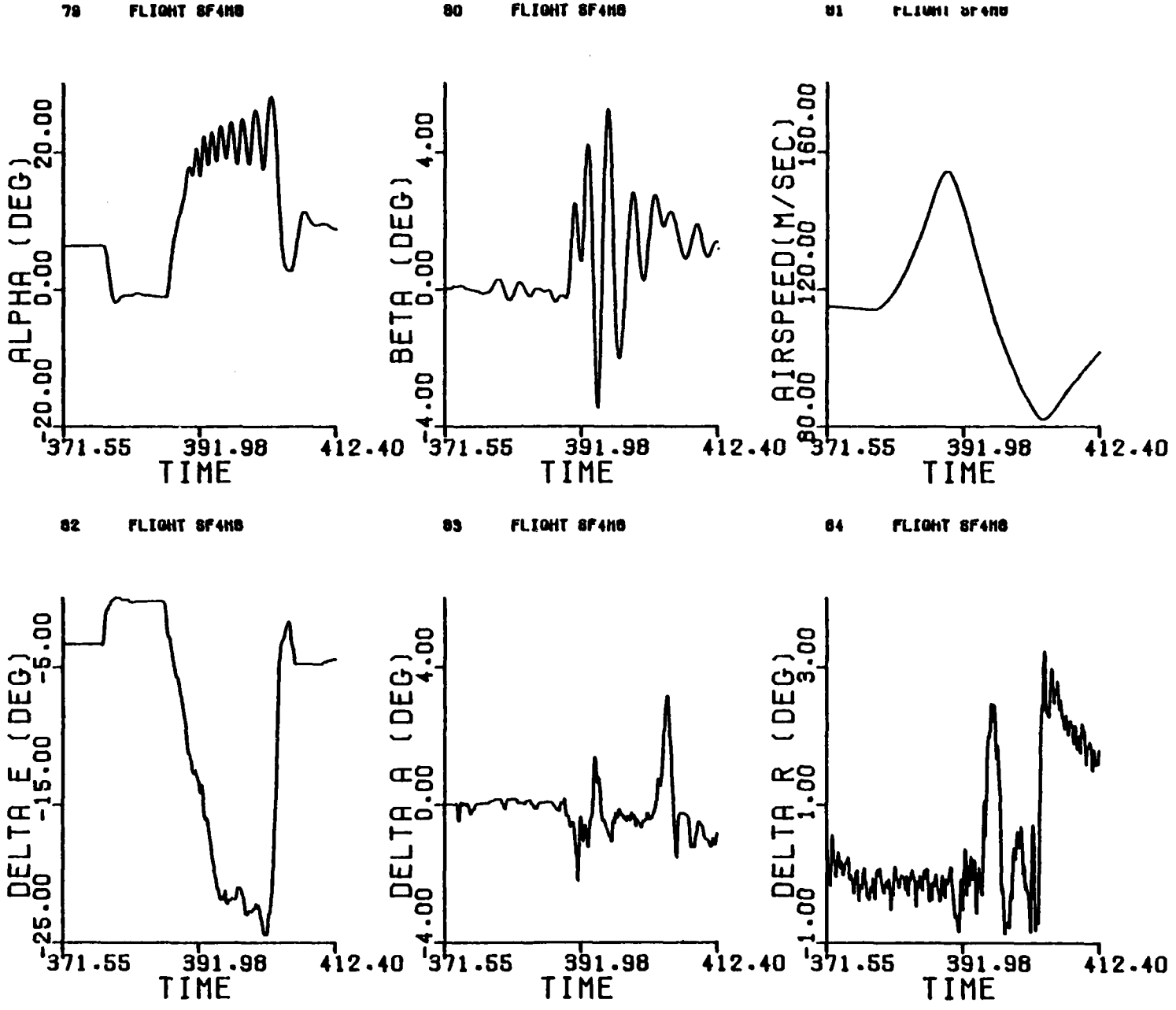

Figure D-14 Time Histories of Simulated Maneuvers (Maneuver 14)

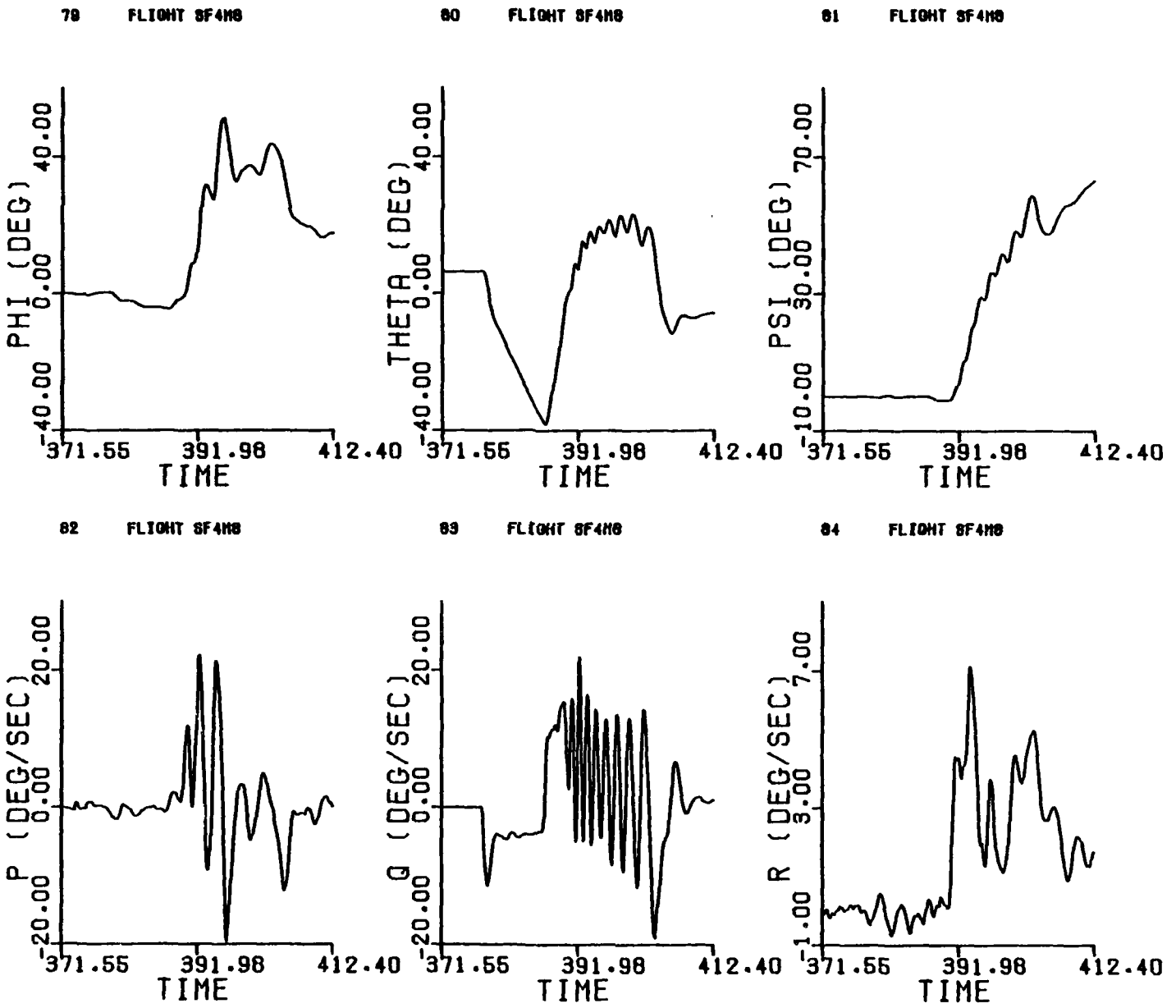

Figure D-14 (Concluded)

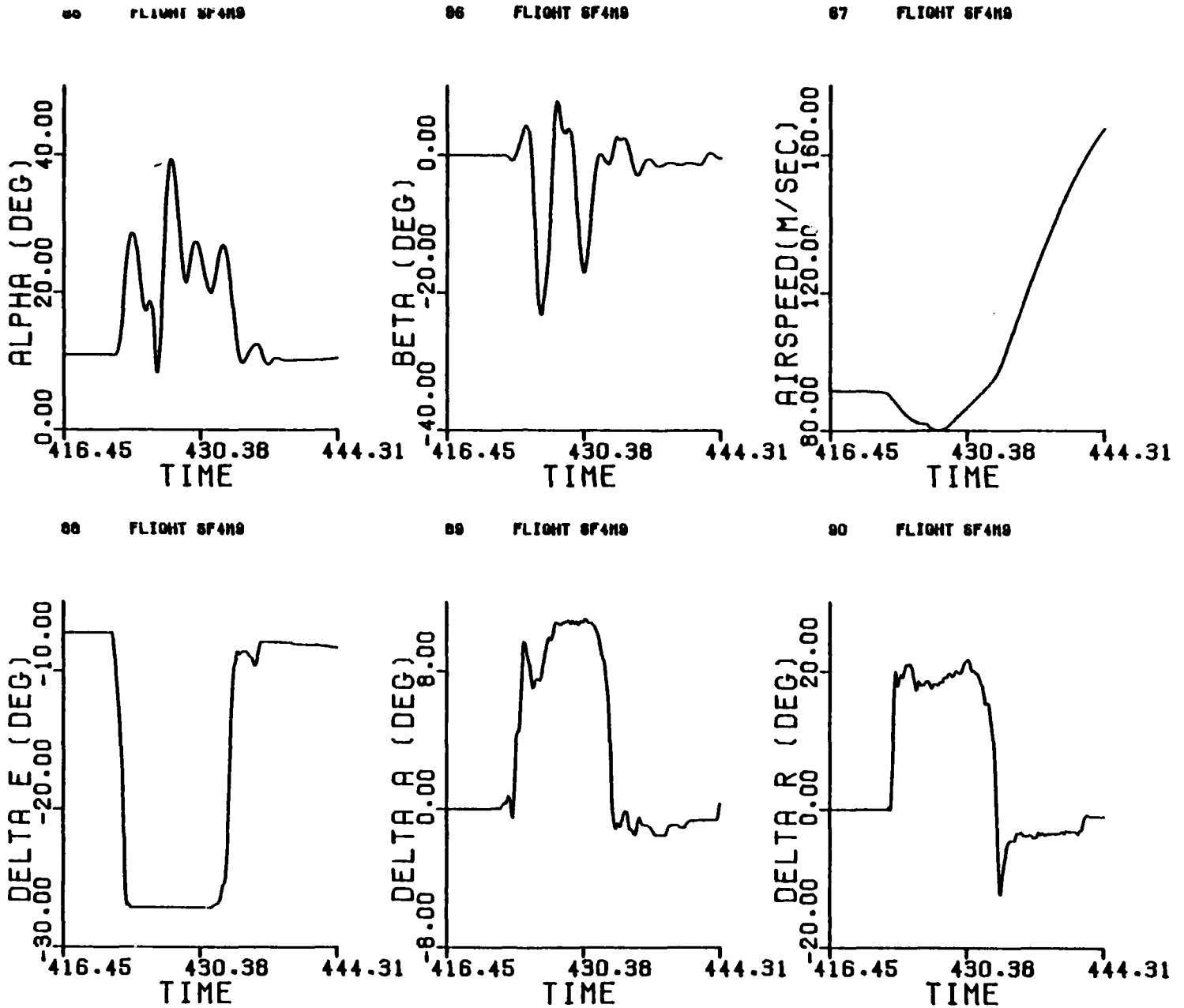

Figure D-15 Time Histories of Simulayed Maneuvers (Maneuver 15)

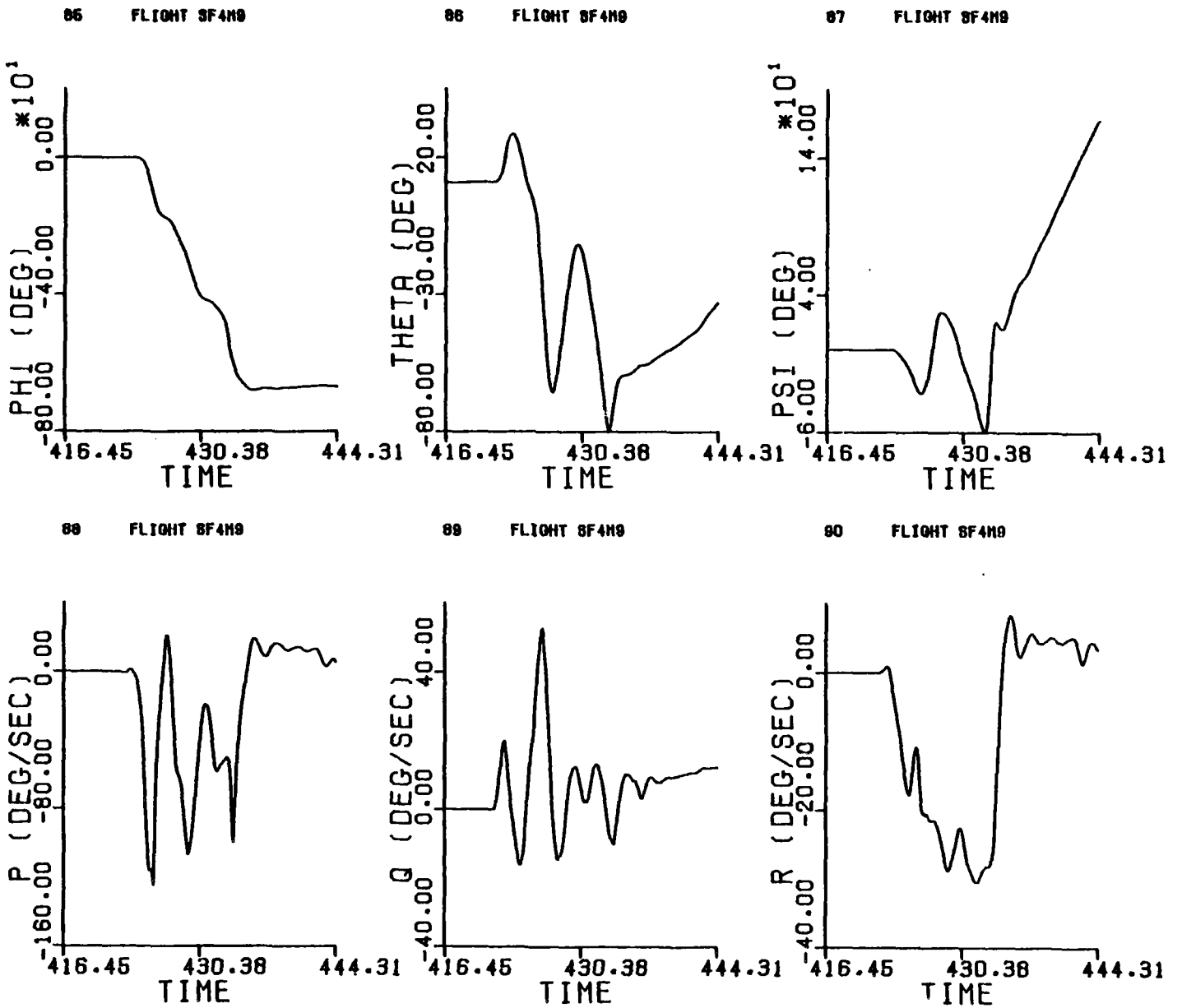

Figure D-15 (Concluded)

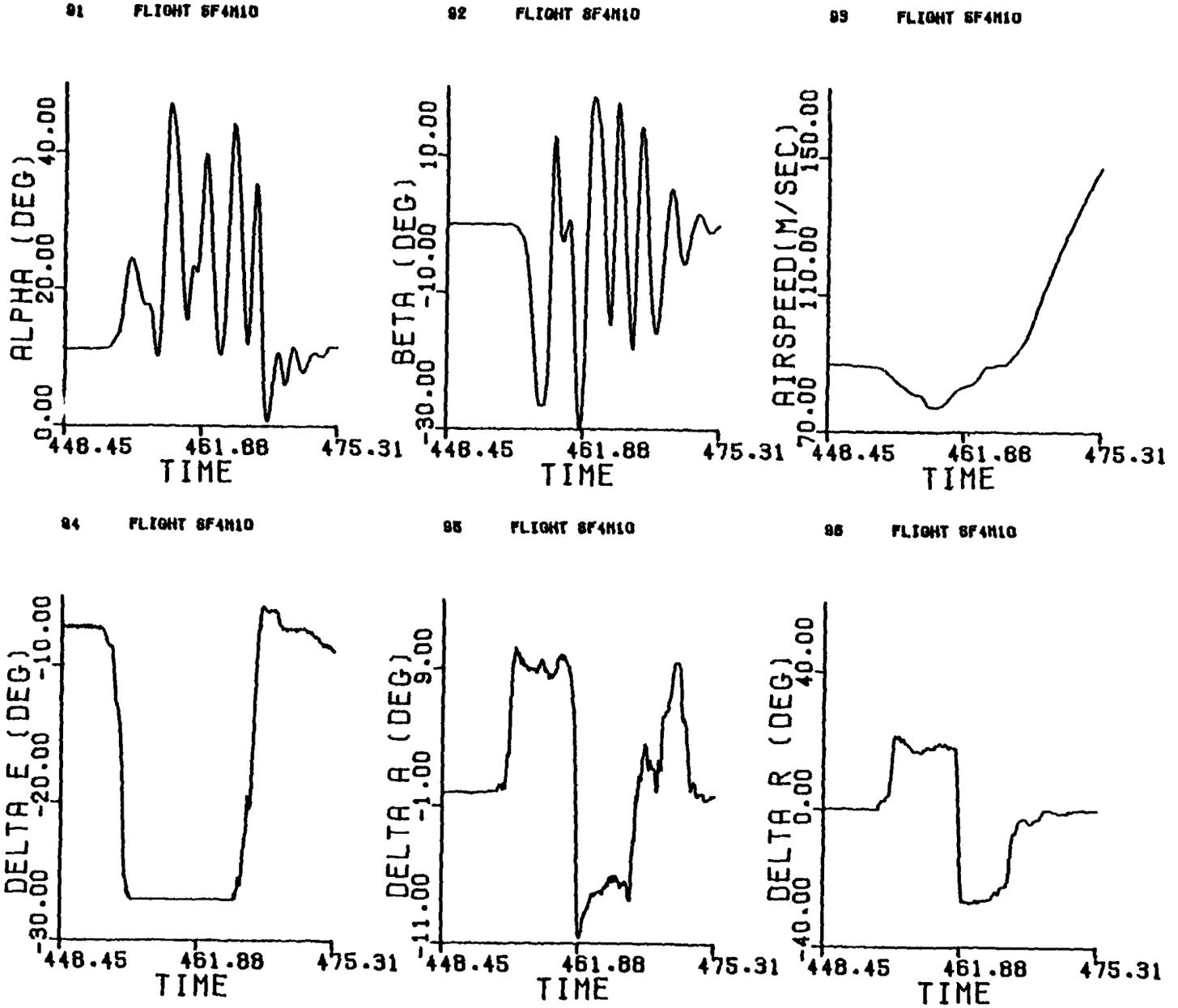

Figure D-16 Time Histories of Simulated Maneuvers (Maneuver 16)

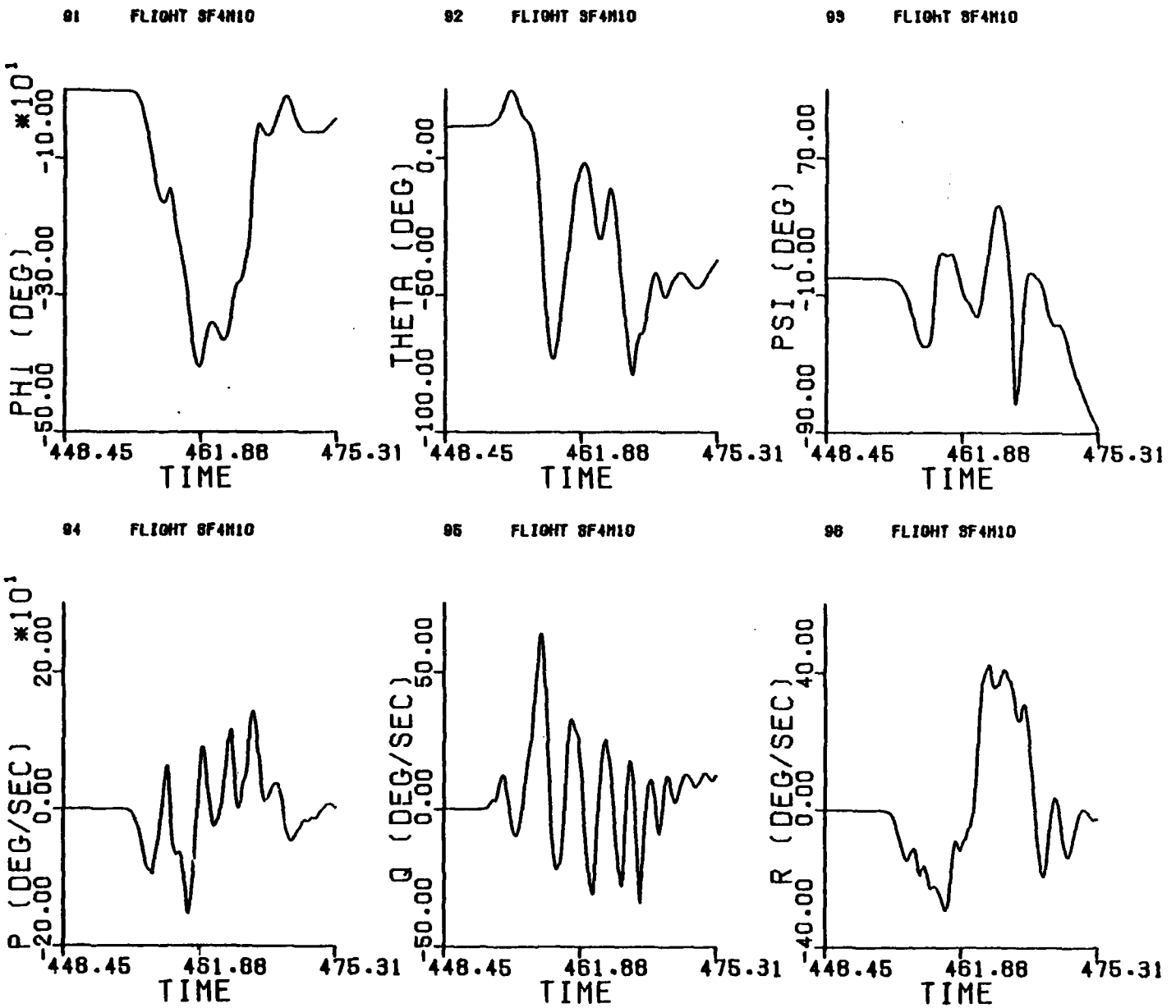

Figure D-16 (Concluded)

APPENDIX E

ESTIMATION RESULTS OF THE SYNTHETIC DATA: TABLES AND CURVES

Tables E-1 through E-3 contain the RMS values of the estimation errors. These RMS values are obtained by taking the difference between the noise-free measurements and the measurements obtained through substituting the estimated states into the measurements equations. The RMS values in these tables are for Maneuvers 1-3, 5-16. The results for Maneuver 4 are contained in Section 3.

The RMS residuals obtained by taking the difference between the true values of $B_1(t)$, $B_2(t)$, . . . , $B_6(t)$ and their estimates are given in Tables E-4 and E-5 for Maneuvers 1-3, 5-16.

The comparisons between the true values of $B_i(t)$, $i = 1, 2, \ldots, 6$, and their estimated values are given in Figures E-1 through E-6 for Maneuvers 1 and 3.

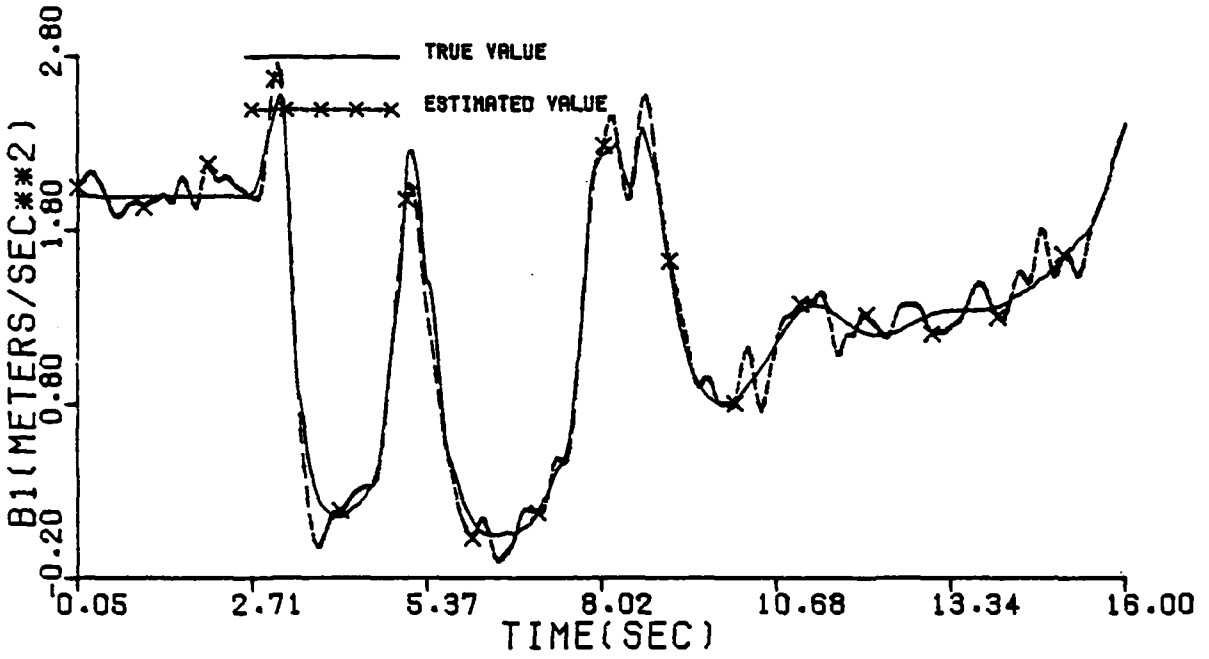

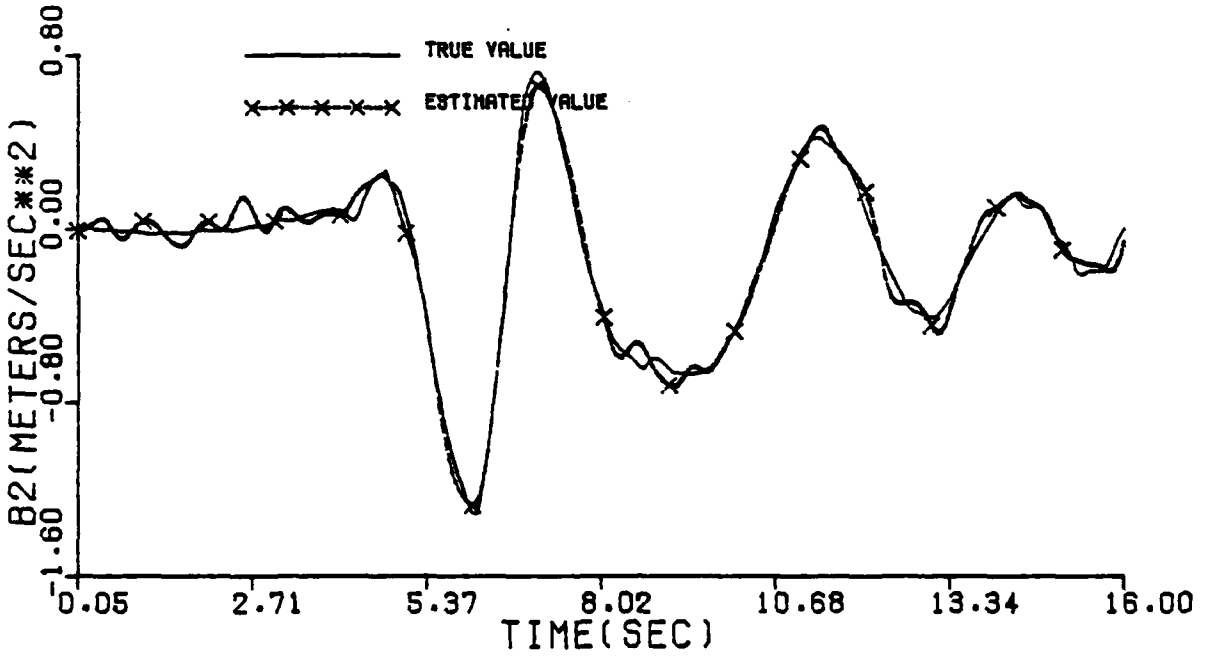

Figure E-1 Comparison Between the True and the Estimated Values of $B_1(t)$ and $B_2(t)$ for Maneuver 1

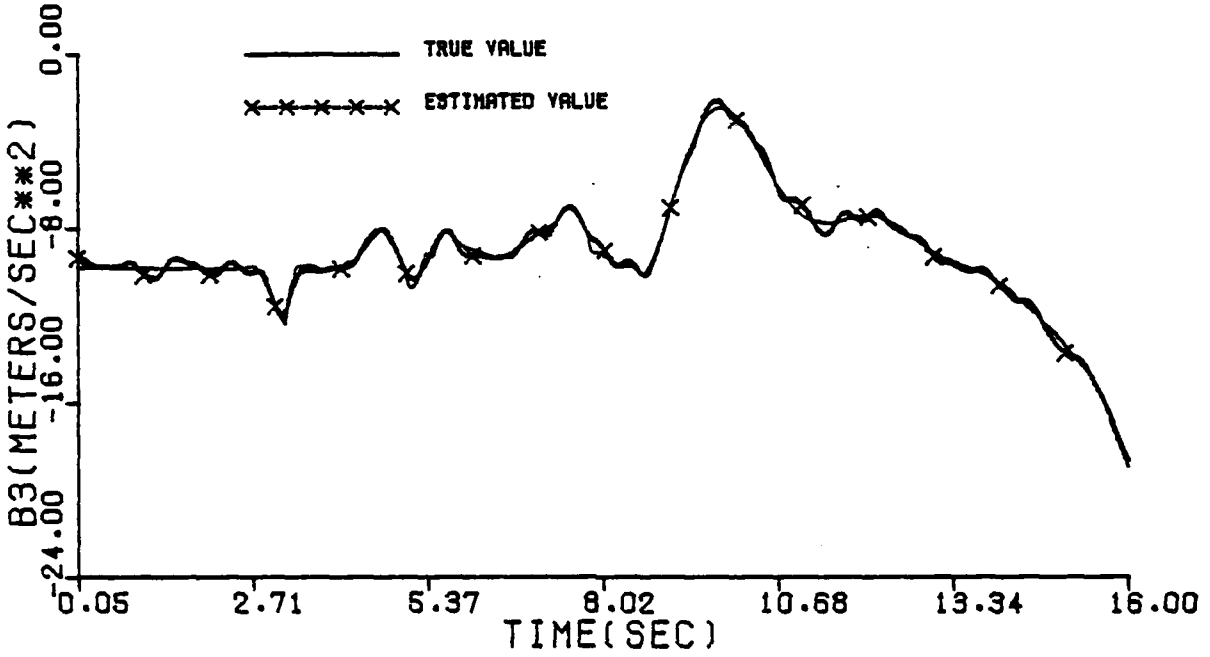

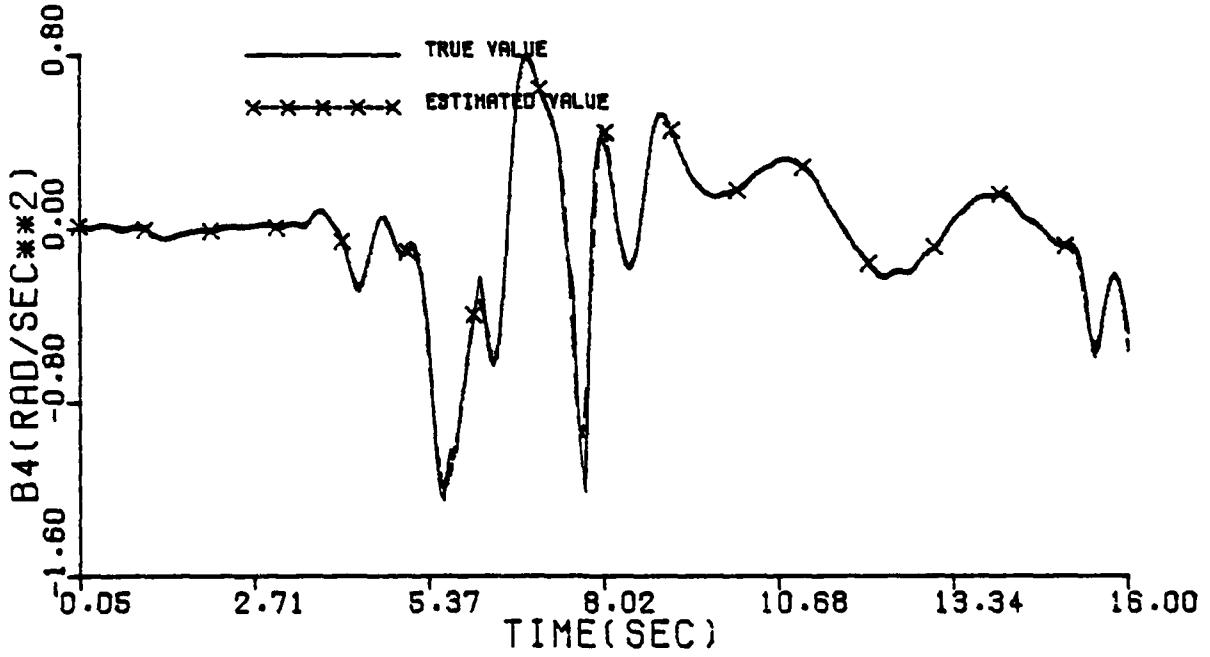

Figure E-2. Comparison Between the True and the Estimated Values of $B_3(t)$ and $B_4(t)$ for Maneuver 1

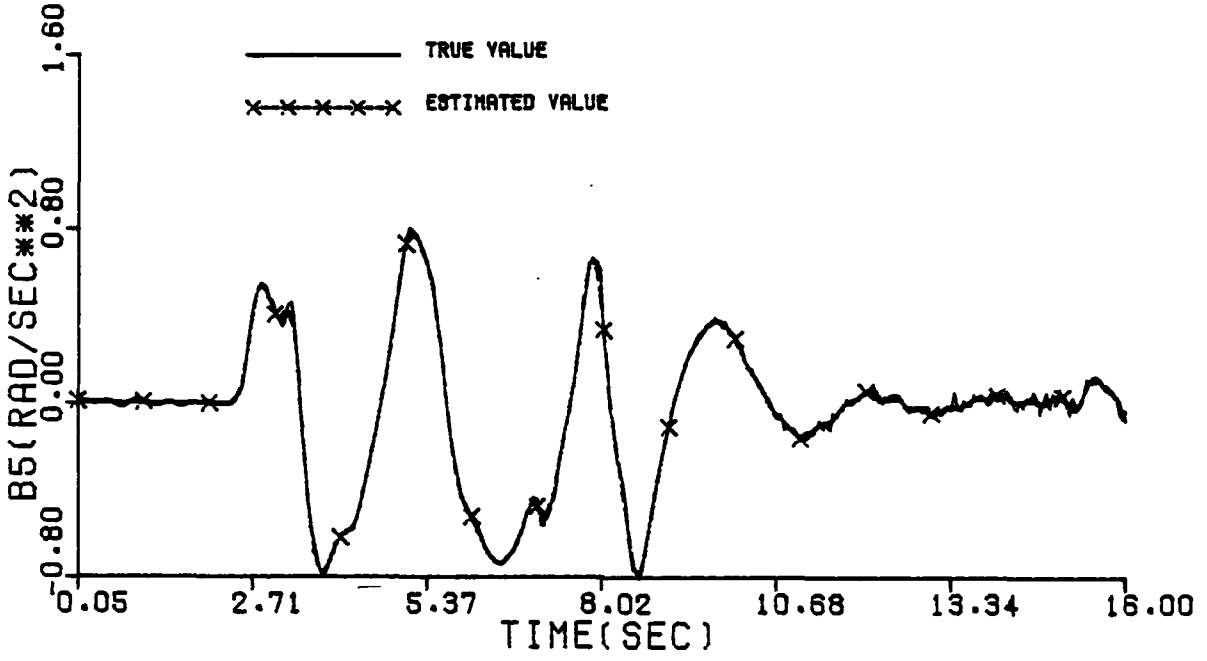

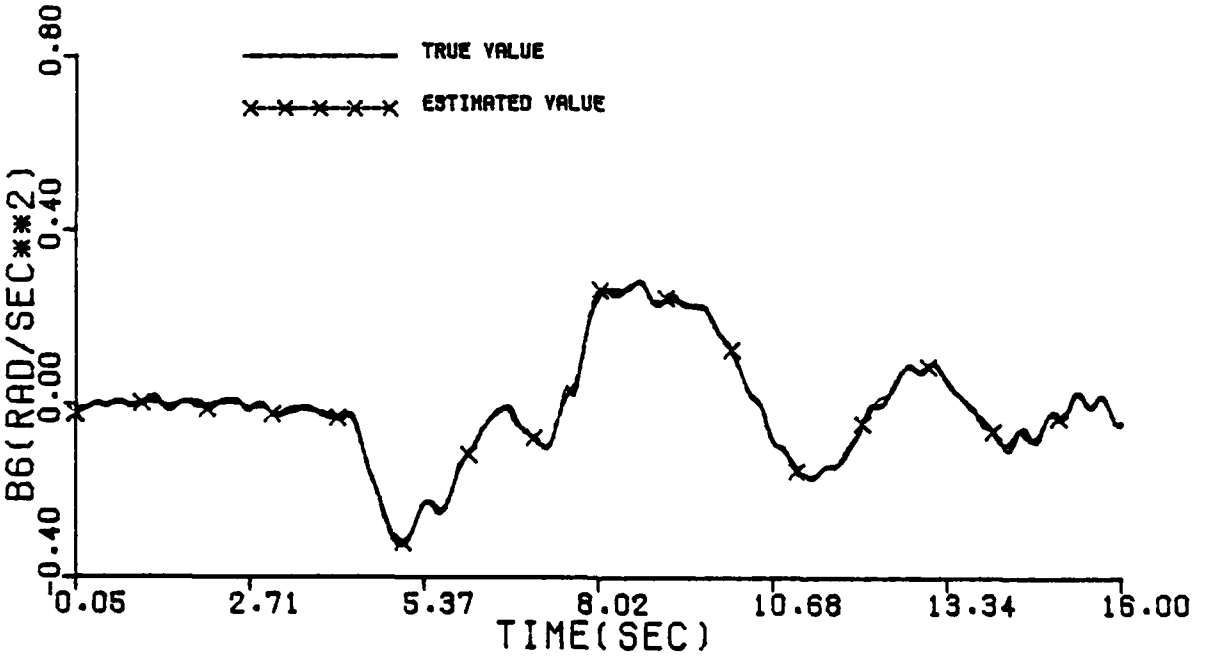

Figure E-3 Comparison Between the True and the Estimated Values of $B_5(t)$ and $B_6(t)$ for Maneuver 1

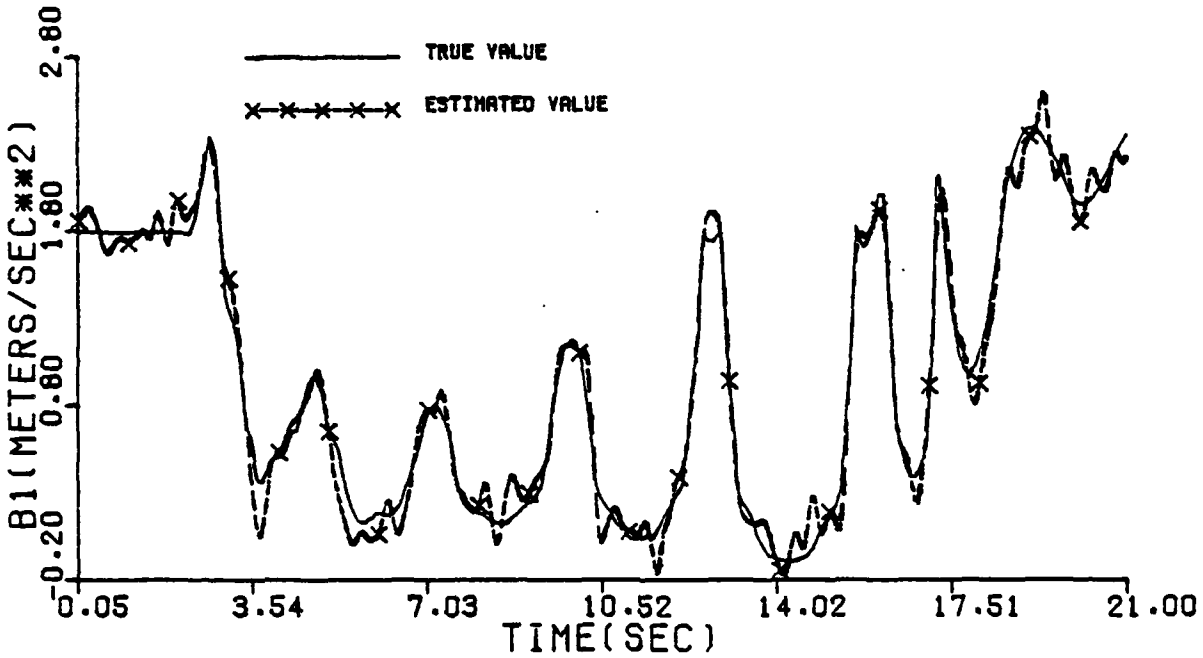

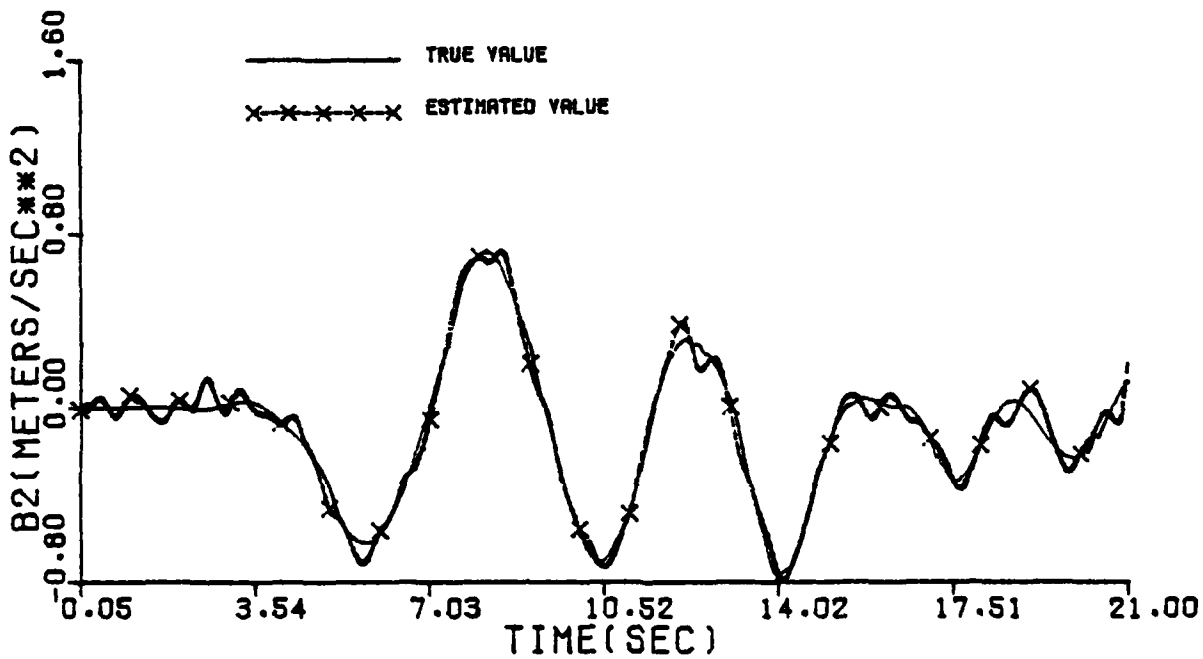

Figure E-4. Comparison Between the True and the Estimated Values of $B_1(t)$ and $B_2(t)$ for Maneuver 8.

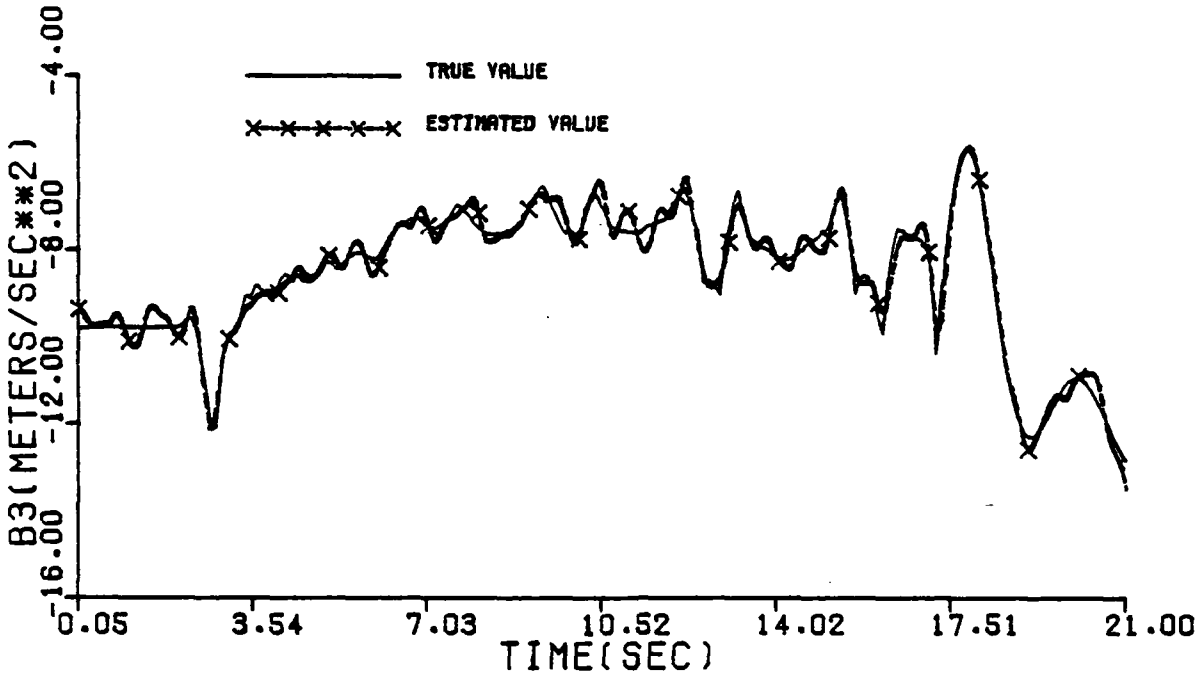

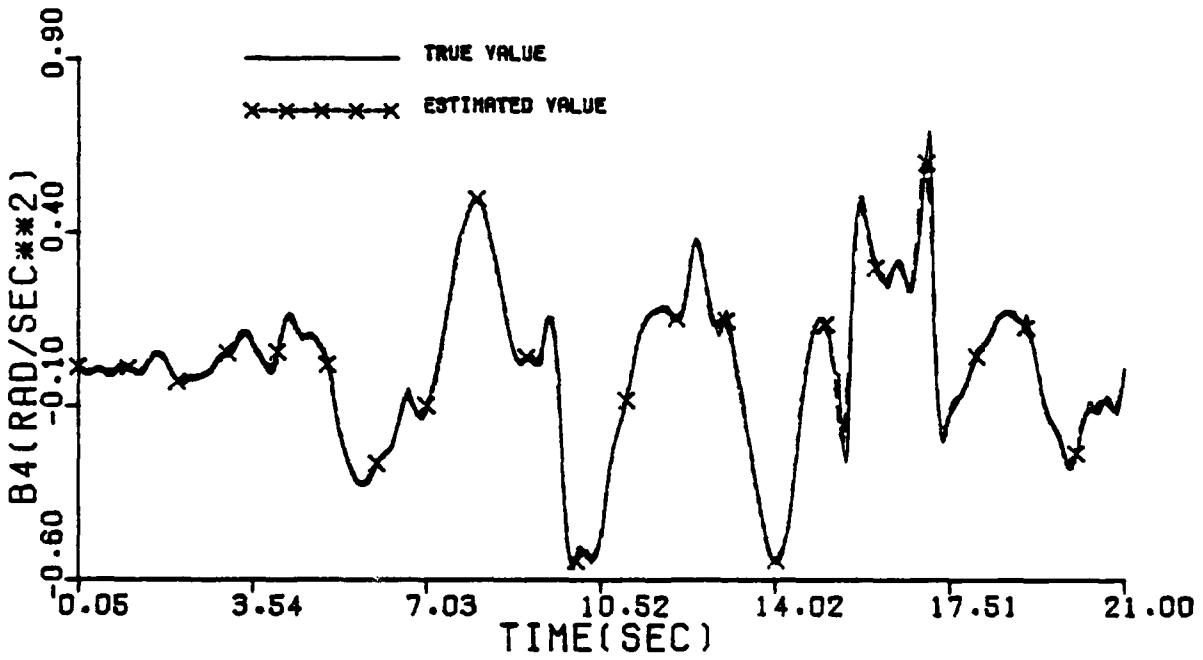

Figure E-5 Comparison Between the True and the Estimated Values of $B_3(t)$ and $B_4(t)$ for Maneuver 8

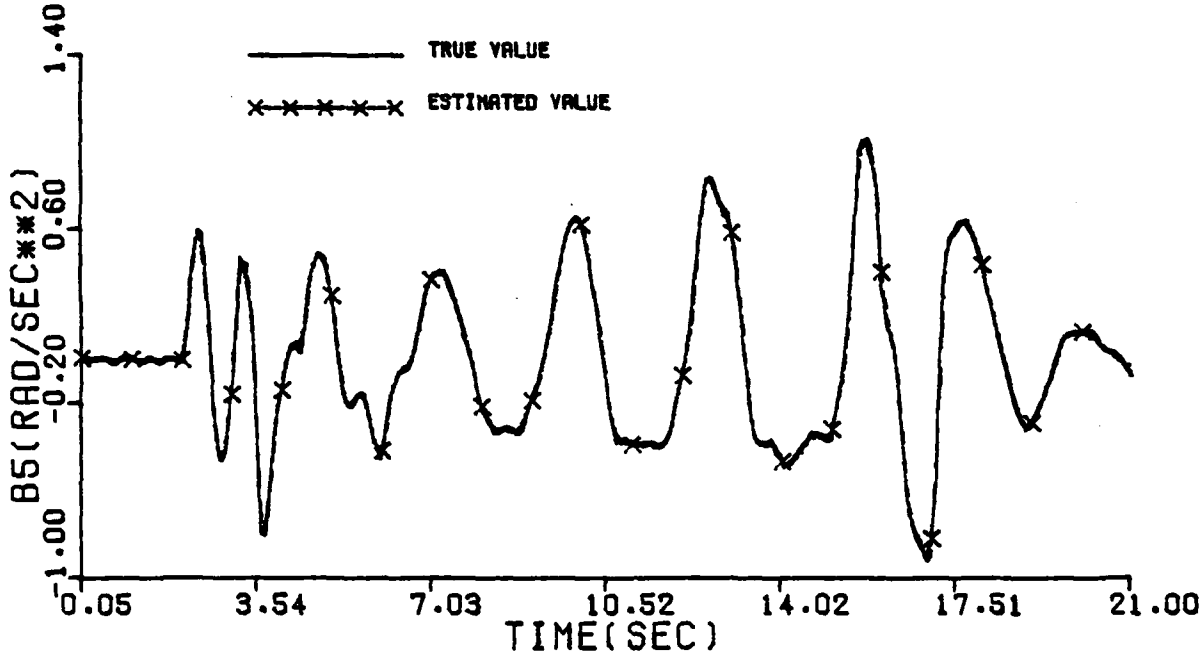

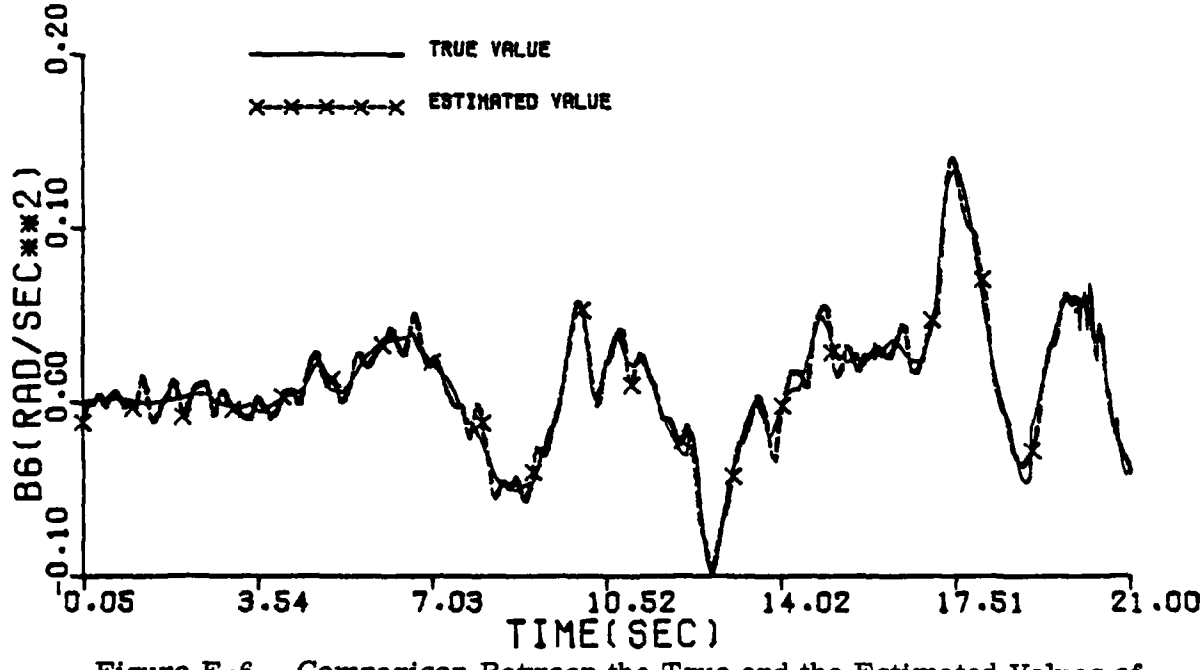

Figure E-6 Comparison Between the True and the Estimated Values of $B_5(t)$ and $B_6(t)$ for Maneuver 8.

Table E-1 Comparison Between Measurement Noise and Estimation Error Levels for Maneuvers 1-3, 5 and 6

Measured Quantity	Descriptive Name	Units	(1σ) Measurement Noise Level	RMS Value of Estimation Error				
				No. 1	No. 2	No. 3	No. 5	No. 6
Z_1	A X NOSE	m/sec^2	.24	.11	.14	.11	.12	.12
Z_2	A Z C G	m/sec^2	1.05	.22	.30	.21	.24	.21
Z_3	A Z NOSE	m/sec^2	1.05	.24	.33	.22	.28	.27
Z_4	A Z TAIL	m/sec^2	1.05	.23	.35	.23	.26	.27
Z_5	A Z R	m/sec^2	1.05	.29	.39	.31	.24	.27
Z_6	A Z L	m/sec^2	1.05	.30	.38	.32	.25	.30
Z_7	A Y E G	m/sec^2	.24	.05	.08	.08	.05	.06
Z_8	A Y NOSE	m/sec^2	.24	.06	.09	.09	.06	.07
Z_9	A Y TAIL	m/sec^2	.24	.06	.09	.09	.06	.08
Z_{10}	THETA	rad	.00087	.0003	.0003	.0003	.0003	.0003
Z_{11}	PHI	rad	.00087	.0003	.0003	.0003	.0002	.0003
Z_{12}	Roll Rate	rad/sec	.0017	.0021	.0012	.0013	.0008	.0008
Z_{13}	Pitch Rate	rad/sec	.0017	.0010	.0014	.0010	.0014	.0007
Z_{14}	Yaw Rate	rad/sec	.0017	.0007	.0008	.0008	.0007	.0008
Z_{15}	Altitude	m	10.	1.2	0.7	0.9	1.1	1.4
Z_{16}	Air Speed	m/sec	.43	.08	.07	.06	.06	.06
Z_{17}	ALPHA	rad	.0028	.0006	.0006	.0005	.0005	.0005
Z_{18}	BETA	rad	.0028	.0003	.0004	.0004	.0004	.0004

Table E-2 Comparison Between Measurement Noise and Estimation Error Levels for Maneuvers 7-11

Measured Quantity	Descriptive Name	Units	Measurement (1σ) Noise Level	RMS Value of Estimation Error				
				No. 7	No. 8	No. 9	No. 10	No. 11
Z_1	A X NOSE	m/sec^2	.24	.12	.11	.12	.11	.16
Z_2	A Z C G	m/sec^2	1.05	.21	.22	.23	.22	.35
Z_3	A Z NOSE	m/sec^2	1.05	.27	.25	.26	.24	.37
Z_4	A Z TAIL	m/sec^2	1.05	.27	.23	.25	.25	.38
Z_5	A Z R	m/sec^2	1.05	.27	.25	.35	.33	.44
Z_6	A Z L	m/sec^2	1.05	.30	.24	.34	.33	.43
Z_7	A Y C G	m/sec^2	.24	.06	.05	.08	.08	.08
Z_8	A Y NOSE	m/sec^2	.24	.07	.06	.09	.09	.09
Z_9	A Y TAIL	m/sec^2	.24	.08	.06	.09	.09	.09
Z_{10}	THETA	rad	.00087	.0003	.0003	.0003	.0003	.0003
Z_{11}	PHI	rad	.00087	.0003	.0003	.0003	.0003	.0004
Z_{12}	Roll Rate	rad/sec	.0017	.0020	.0013	.0013	.0013	.0013
Z_{13}	Pitch Rate	rad/sec	.0017	.0020	.0011	.0011	.0011	.0013
Z_{14}	Yaw Rate	rad/sec	.0017	.0008	.0007	.0008	.0008	.0008
Z_{15}	Altitude	m	10.	1.4	1.1	2.4	2.1	4.7
Z_{16}	Air Speed	m/sec	.43	.06	.07	.06	.06	.06
Z_{17}	ALPHA	rad	.0028	.0005	.0006	.0006	.0006	.0006
Z_{18}	BETA	rad	.0028	.0004	.0004	.0004	.0004	.0005

Table E-3 Comparison Between Measurement Noise and Estimation Error Levels for Maneuvers 12-16

Measured Quantity	Descriptive Name	Units	Measurement (1σ) Noise Level	RMS Value of Estimation Error				
				No. 12	No. 13	No. 14	No. 15	No. 16
Z_1	A X NOSE	m/sec^2	.24	.12	.11	.12	.11	.12
Z_2	A Z C G	m/sec^2	1.05	.21	.20	.21	.22	.24
Z_3	A Z NOSE	m/sec^2	1.05	.23	.21	.22	.24	.28
Z_4	A Z TAIL	m/sec^2	1.05	.21	.20	.21	.24	.26
Z_5	A Z R	m/sec^2	1.05	.22	.21	.22	.33	.39
Z_6	A Z L	m/sec^2	1.05	.23	.21	.22	.33	.37
Z_7	A Y C G	m/sec^2	.24	.05	.05	.05	.08	.09
Z_8	A Y NOSE	m/sec^2	.24	.06	.06	.06	.09	.10
Z_9	A Y TAIL	m/sec^2	.24	.06	.06	.06	.09	.10
Z_{10}	THETA	rad	.00087	.0003	.0003	.0003	.0003	.0003
Z_{11}	PHI	rad	.00087	.0003	.0003	.0002	.0003	.0003
Z_{12}	Roll Rate	rad/sec	.0017	.0010	.0010	.0009	.0013	.0015
Z_{13}	Pitch Rate	rad/sec	.0017	.0010	.0008	.0009	.0010	.0012
Z_{14}	Yaw Rate	rad/sec	.0017	.0007	.0007	.0007	.0008	.0009
Z_{15}	Altitude	m	10.	1.1	1.7	0.7	0.9	1.5
Z_{16}	Air Speed	m/sec	.43	.06	.06	.06	.07	.07
Z_{17}	ALPHA	rad	.0028	.0006	.0005	.0005	.0005	.0007
Z_{18}	BETA	rad	.0028	.0004	.0004	.0004	.0004	.0007

Table E-4 RMS of the Estimation Error of B_i (t), i = 1, 2, . . . , 6, for Maneuvers 1-3, 5-9

Estimated Quantity	Units	RMS Value of Estimation Error							
		1	2	3	5	6	7	8	9
B_1	m/sec^2	.11	.14	.11	.12	.11	.12	.11	.12
B_2	m/sec^2	.05	.07	.07	.05	.06	.06	.05	.07
B_3	m/sec^2	.22	.30	.21	.24	.20	.21	.22	.23
B_4	rad/sec^2	.04	.05	.05	.01	.01	.04	.02	.05
B_5	rad/sec^2	.02	.04	.02	.03	.01	.04	.02	.03
B_6	rad/sec^2	.01	.01	.01	.01	.01	.01	.01	.01

Table E-5 RMS of the Estimation Error of B_i (t), i = 1, 2, . . . , 6, for Maneuvers 10-16

Estimated Quantity	Units	RMS Value of Estimation Error						
		10	11	12	13	14	15	16
B_1	m/sec^2	.11	.16	.12	.11	.12	.11	.12
B_2	m/sec^2	.08	.08	.05	.05	.05	.07	.08
B_3	m/sec^2	.22	.35	.21	.20	.21	.22	.23
B_4	rad/sec^2	.05	.05	.02	.01	.01	.05	.06
B_5	rad/sec^2	.02	.04	.02	.01	.01	.02	.03
B_6	rad/sec^2	.01	.01	.01	.01	.01	.01	.01

APPENDIX F

MODELING RESULTS: TABLES

Table F-1 LONGITUDINAL MODEL EQUATIONS FOR ADDITIONAL REGIONS

1) $-4^{o} \leq \alpha < 0^{o}$, $0^{o} \leq |\beta| \leq 2^{o}$, $-10^{o} \leq \delta_e \leq 0^{o}$

$$C_x = -0.0184$$

$$C_z = 0.2371 - 4.856\,(\alpha + 4/57.3) - 0.8969\,\delta_e - 4.4385\,\frac{q\bar{c}}{2V}$$

$$C_m = 0.0302 - 0.9556\,(\alpha + 4/57.3) - 1.5100\,\delta_e - 13.1871\,\frac{q\bar{c}}{2V}$$

2) $8^{o} \leq \alpha \leq 12^{o}$, $10^{o} \leq \beta \leq 15^{o}$, $-10^{o} \leq \delta_e \leq -5^{o}$

$$C_x = 0.0562 + 0.9528\,(\alpha - 8/57.3)$$

$$C_z = -0.694 - 5.5204\,(\alpha - 8/57.3) - 1.9000\,(\delta_e + 5/57.3) - 24.5206\,\frac{q\bar{c}}{2V}$$

$$C_m = -0.0715 - 1.1750\,(\alpha - 8/57.3) - 1.8634\,(\delta_e + 5/57.3) - 14.6395\,\frac{q\bar{c}}{2V}$$

3) $20^{o} \leq \alpha \leq 25^{o}$, $10^{o} \leq |\beta| \leq 15^{o}$, $-17^{o} \leq \delta_e \leq -13^{o}$

$$C_x = -0.047528 - 0.3964\,(\alpha - 20/57.3) + 0.2553\,(|\beta| - 10/57.3) - 0.3815\,(\delta_e + 13/57.3)$$

$$C_z = -0.08654 - 0.5347\,(\alpha - 20/57.3) - 0.7022\,(|\beta| - 10/57.3) - 0.1086\,(\delta_e + 13/57.3) + (-2.2145 + 32.4\,\alpha - 20/57.3)\,\frac{q\bar{c}}{2V}$$

$$C_m = -0.1070 - 1.478\,(\alpha - 20/57.3) - 0.5959\,(|\beta| - 10/57.3) - 0.6877\,(\delta_e + 13/57.3) + (1.2442 - 31.26\,\overline{\alpha - 20/57.3})\,\frac{q\bar{c}}{2V}$$

Table F-2 Comparison of Estimated and Wind Tunnel Values of Average C_{y_β}

α (deg)	$0^\circ \leq \lvert\beta\rvert < 2^\circ$		$2^\circ \leq \lvert\beta\rvert < 5^\circ$		$5^\circ \leq \lvert\beta\rvert \leq 10^\circ$	
	Estimated	Wind Tunnel	Estimated	Wind Tunnel	Estimated	Wind Tunnel
0.	-0.9218	-0.7563	-0.8135	-0.7238	-0.6387	-0.8113
4.0000	-0.8082	-0.8336	-0.8014	-0.8002	-0.6387	-0.8583
6.0000	-0.8660	-0.7993	-0.8014	-0.8002	-0.6387	-0.8858
8.0000	-0.7026	-0.7649	-0.8237	-0.8537	-0.9093	-0.9133
10.0000	-0.7019	-0.6518	-0.9154	-0.8718	-0.9030	-0.9213
12.0000	-0.6947	-0.5386	-0.8991	-0.8900	-0.7556	-0.9293
13.0000	-0.6643	-0.6517	-0.8530	-0.8566	-0.7556	-0.7747
14.0000	-0.7649	-0.7648	-0.7197	-0.8232	-0.4445	-0.6201
15.0000	-0.8437	-0.6733	-0.8127	-0.6381	-0.5211	-0.4895
16.0000	-0.7002	-0.7104	-0.7990	-0.9107	-0.7517	-0.7720
17.0000	-0.7316	-0.7462	-0.8012	-0.8087	-0.8303	-0.7441
18.0000	-0.9010	-0.7820	-0.7759	-0.7068	-0.6950	-0.7162
19.0000	-0.9270	-0.8565	-0.7782	-0.7458	-0.7409	-0.6945
20.0000	-0.8468	-0.9309	-0.7842	-0.7849	-0.6745	-0.6727
22.5000	-0.9004	-0.9324	-0.6974	-0.7105	-0.8154	-0.7574
25.0000	-0.9783	-0.9339	-0.7037	-0.6361	-0.8050	-0.8422
27.5000	-1.1869	-0.9998	-0.7080	-0.7296	-0.9233	-0.8531
30.0000	-0.9601	-1.0656	-0.9425	-0.8231	-0.0156	-0.8640

Table F-3 Comparison of Estimated and Wind Tunnel Values of Average $C_{y_{\delta_r}}$

α (deg)	$0^\circ \leq \lvert\beta\rvert < 2^\circ$		$2^\circ \leq \lvert\beta\rvert < 5^\circ$		$5^\circ \leq \lvert\beta\rvert \leq 10^\circ$	
	Estimated	Wind Tunnel	Estimated	Wind Tunnel	Estimated	Wind Tunnel
0 - 4	0.2653	0.1076	0.	0.0923	0.0775	0.0913
4 - 6	0.	0.1046	0.	0.0916	0.0775	0.0991
6 - 8	0.1351	0.1042	0.	0.0921	0.0775	0.1033
8 - 10	0.0870	0.1038	0.0782	0.0927	0.1001	0.1074
10 - 12	0.1157	0.1036	0.0814	0.0930	0.0481	0.1003
12 - 13	0.1148	0.1033	0.0687	0.0933	0.	0.0933
13 - 14	0.1017	0.1002	0.0662	0.0875	0.	0.0740
14 - 15	0.0900	0.0970	0.0727	0.0817	0.	0.0547
15 - 16	0.0691	0.0891	0.	0.0759	0.0845	0.0608
16 - 17	0.0750	0.0767	0.0594	0.0728	0.0784	0.0737
17 - 18	0.0772	0.0718	0.0494	0.0694	0.0815	0.0678
18 - 19	0.0795	0.0668	0.0704	0.0661	0.	0.0619
19 - 20	0.1010	0.0608	0.0734	0.0621	0.0407	0.0611
20 - 22.5	0.0705	0.0548	0.0905	0.0582	0.	0.0602
22.5 - 25	0.	0.0496	0.0550	0.0537	0.0482	0.0545
25 - 27.5	0.0354	0.0444	0.0347	0.0493	0.	0.0488
27.5 - 30	0.0205	0.0462	0.	0.0489	0.	0.0459
30 - 35	0.	0.0480	0.	0.0485	0.0251	0.0430

Table F-4 Comparison of Estimated and Wind Tunnel Values of Average $C_{y_{\delta_r}}$

α (deg)	$0^\circ \leq \lvert\beta\rvert < 2^\circ$		$2^\circ \leq \lvert\beta\rvert < 5^\circ$		$5^\circ \leq \lvert\beta\rvert \leq 10^\circ$	
	Estimated	Wind Tunnel	Estimated	Wind Tunnel	Estimated	Wind Tunnel
0 - 4	0.	0.1252	0.	0.1440	0.1131	0.1563
4 - 6	0.	0.1292	0.1330	0.1485	0.1131	0.1595
6 - 8	0.1648	0.1318	0.1330	0.1509	0.1131	0.1593
8 - 10	0.1209	0.1344	0.1428	0.1533	0.1752	0.1591
10 - 12	0.1388	0.1310	0.1481	0.1471	0.1434	0.1574
12 - 13	0.1237	0.1276	0.1350	0.1409	0.1498	0.1558
13 - 14	0.1419	0.1211	0.1255	0.1342	0.1498	0.1601
14 - 15	0.1076	0.1146	0.1366	0.1274	0.1177	0.1645
15 - 16	0.0829	0.1077	0.1518	0.1165	0.	0.1388
16 - 17	0.	0.0935	0.1105	0.0946	0.	0.0966
17 - 18	0.	0.0822	0.0717	0.0800	0.1186	0.0827
18 - 19	0.0804	0.0710	0.0613	0.0654	0.0771	0.0687
19 - 20	0.0916	0.0625	0.0312	0.0576	0.	0.0592
20 - 22.5	0.0534	0.0541	0.	0.0498	0.0288	0.0496
22.5 - 25	0.	0.0544	0.0618	0.0540	0.	0.0534
25 - 27.5	0.0568	0.0546	0.	0.0583	0.	0.0572
27.5 - 30	0.0361	0.0597	0.0235	0.0632	0.0298	0.0613
30 - 35	0.	0.0649	0.	0.0682	0.0312	0.0655

Table F-5 Comparison of Estimated and Wind Tunnel Values of Average $C_{y_{\delta_a}}$

α (deg)	$0^\circ \leq \lvert\beta\rvert < 2^\circ$		$2^\circ \leq \lvert\beta\rvert < 5^\circ$		$5^\circ \leq \lvert\beta\rvert \leq 10^\circ$	
	Estimated	Wind Tunnel	Estimated	Wind Tunnel	Estimated	Wind Tunnel
0 - 4	0.	0.0462	0.	0.0541	0.	0.0538
4 - 6	0.	0.0356	0.	0.0505	0.	0.0630
6 - 8	0.	0.0182	0.	0.0263	0.	0.0447
8 - 10	0.	0.0008	0.	0.0020	0.0677	0.0264
10 - 12	0.	0.0066	0.	0.0272	0.	0.0672
12 - 13	0.	0.0123	0.0812	0.0524	0.1286	0.1080
13 - 14	0.	0.0234	0.1382	0.0593	0.1286	0.0998
14 - 15	0.0713	0.0345	0.0395	0.0662	0.0726	0.0916
15 - 16	0.0792	0.0259	0.	-0.0010	0.	0.0039
16 - 17	0.	0.0265	0.	0.0023	0.0674	0.0272
17 - 18	0.	0.0300	0.0974	0.0220	0.	0.0371
18 - 19	0.	0.0335	0.	0.0418	0.1663	0.0470
19 - 20	0.	0.0264	0.	0.0394	0.0737	0.0347
20 - 22.5	0.	0.0193	0.	0.0370	0.	0.0224
22.5 - 25	0.	0.0016	0.0700	0.0174	0.0630	0.0014
25 - 27.5	0.	-0.0160	0.	-0.0021	0.	-0.0197
27.5 - 30	0.	-0.0284	0.	-0.0232	-0.0524	-0.0331
30 - 35	0.	-0.0408	-0.1041	-0.0443	-0.0728	-0.0464

Table F-6 Comparison of Estimated and Wind Tunnel Values of Average $C_{y_{\delta_a}}$

α (deg)	$0^\circ \leq \lvert\beta\rvert < 2^\circ$		$2^\circ \leq \lvert\beta\rvert < 5^\circ$		$5^\circ \leq \lvert\beta\rvert \leq 10^\circ$	
	Estimated	Wind Tunnel	Estimated	Wind Tunnel	Estimated	Wind Tunnel
0 - 4	0.	0.0467	0.2787	0.0651	0.	0.0587
4 - 6	0.	0.0315	0.	0.0400	0.	0.0335
6 - 8	0.	0.0286	0.	0.0388	0.	0.0332
8 - 10	0.0410	0.0258	0.0452	0.0376	0.0397	0.0329
10 - 12	0.	0.0226	0.0652	0.0347	0.	0.0277
12 - 13	0.	0.0193	0.	0.0318	0.	0.0225
13 - 14	0.	0.0179	0.	0.0087	0.	0.0072
14 - 15	-0.0235	0.0164	0.	-0.0144	0.	-0.0081
15 - 16	0.	0.0370	0.	-0.0346	0.	-0.0186
16 - 17	0.0526	0.0257	0.	-0.0288	-0.0570	-0.0123
17 - 18	0.0757	0.0154	0.	-0.0200	0.	0.0005
18 - 19	0.	0.0052	0.	-0.0112	0.	0.0133
19 - 20	0.	0.0033	0.0887	0.0093	0.	0.0305
20 - 22.5	0.	0.0014	0.1017	0.0298	0.	0.0476
22.5 - 25	0.	-0.0022	0.	0.0422	0.	0.0581
25 - 27.5	-0.0514	-0.0057	0.	0.0545	0.	0.0686
27.5 - 30	-0.1705	-0.0104	0.	0.0407	0.	0.0626
30 - 35	-0.1705	-0.0150	-0.1506	0.0269	0.	0.0566

Table F-7

COMPARISON OF ESTIMATED AND WIND TUNNEL VALUES OF C_{y_r}

α(deg)	Wind Tunnel	Estimated		
		$0^o \leq \lvert\beta\rvert < 2^o$	$2^o \leq \lvert\beta\rvert < 5^o$	$5^o \leq \lvert\beta\rvert \leq 10^o$
0	0.55	0.5285	0	0
4	0.53	0.6522	0.4285	0
6	0.505	0	0.4285	0
8	0.48	0.5546	0.5334	0.5908
10	0.46	0.3892	0.4871	0
12	0.44	0.4541	0.4571	0
13	0.447	0.6364	0	0
14	0.455	0.3485	0.4575	0
15	0.450	0.3512	0	0.5441
16	0.445	0.5423	0	0.4885
17	0.39	0	0	0.5738
18	0.25	0.2311	0	0
19	0.275	0	0.3687	0
20	0.29	0.2012	0.2732	0
22	0.3	0	0.3287	0
25	0.315	0	0	0
27	0.358	0.2912	0	0
32.500	0.405	0	-0.4832	0

Table F-8 Comparison of Estimated and Wind Tunnel Values of Average $C_{\ell_{\delta_r}}$

α (deg)	$0^\circ \leq \lvert\beta\rvert < 2^\circ$		$2^\circ \leq \lvert\beta\rvert < 5^\circ$		$5^\circ \leq \lvert\beta\rvert \leq 10^\circ$	
	Estimated	Wind Tunnel	Estimated	Wind Tunnel	Estimated	Wind Tunnel
0 - 4	0.	0.0155	0.0161	0.0150	0.0128	0.0143
4 - 6	0.	0.0153	0.	0.0150	0.0128	0.0144
6 - 8	0.0174	0.0149	0.	0.0146	0.0128	0.0141
8 - 10	0.0139	0.0146	0.0137	0.0142	0.0139	0.0139
10 - 12	0.0142	0.0141	0.0137	0.0147	0.0126	0.0154
12 - 13	0.	0.0137	0.0152	0.0153	0.0250	0.0170
13 - 14	0.0083	0.0134	0.0159	0.0162	0.0250	0.0189
14 - 15	0.0127	0.0132	0.0179	0.0171	0.	0.0209
15 - 16	0.0130	0.0127	0.0143	0.0175	0.0158	0.0221
16 - 17	0.0099	0.0109	0.0158	0.0147	0.0270	0.0188
17 - 18	0.0097	0.0089	0.0154	0.0118	0.0168	0.0157
18 - 19	0.0064	0.0070	0.0093	0.0089	0.0143	0.0127
19 - 20	0.0066	0.0071	0.0085	0.0079	0.0073	0.0097
20 - 22.5	0.0054	0.0072	0.0103	0.0069	0.0079	0.0067
22.5 - 25	0.	0.0071	0.0070	0.0075	0.	0.0073
25 - 27.5	0.0101	0.0069	0.0058	0.0081	0.0071	0.0080
27.5 - 30	0.	0.0038	0.0270	0.0019	0.	-0.0012
30 - 35	0.	0.0006	-0.0167	-0.0044	0.	-0.0104

Table F-9 Comparison of Estimated and Wind Tunnel Values of Average $C_{\ell_{\delta_r}}$

α (deg)	$0^\circ \leq \lvert\beta\rvert < 2^\circ$		$2^\circ \leq \lvert\beta\rvert < 5^\circ$		$5^\circ \leq \lvert\beta\rvert \leq 10^\circ$	
	Estimated	Wind Tunnel	Estimated	Wind Tunnel	Estimated	Wind Tunnel
0 - 4	0.	0.0158	0.0148	0.0167	0.0143	0.0178
4 - 6	0.	0.0150	0.0134	0.0160	0.0143	0.0180
6 - 8	0.0134	0.0149	0.0134	0.0159	0.0143	0.0176
8 - 10	0.0138	0.0147	0.0154	0.0157	0.0158	0.0171
10 - 12	0.0143	0.0141	0.0147	0.0143	0.0161	0.0143
12 - 13	0.0142	0.0135	0.0128	0.0128	0.0068	0.0114
13 - 14	0.0136	0.0125	0.0110	0.0108	0.0068	0.0081
14 - 15	0.0176	0.0116	0.0063	0.0089	0.	0.0048
15 - 16	0.0152	0.0100	0.0064	0.0066	0.	0.0016
16 - 17	0.0173	0.0080	0.	0.0061	0.	0.0013
17 - 18	0.	0.0074	0.0094	0.0063	0.	0.0011
18 - 19	0.0069	0.0068	0.0074	0.0065	0.0113	0.0008
19 - 20	0.0084	0.0075	0.	0.0073	0.	0.0017
20 - 22.5	0.0082	0.0082	0.0064	0.0081	0.0035	0.0027
22.5 - 25	0.0052	0.0063	0.0121	0.0065	0.0055	0.0028
25 - 27.5	0.0057	0.0044	0.	0.0049	0.	0.0030
27.5 - 30	0.0034	0.0044	0.0107	0.0080	-0.0104	0.0106
30 - 35	0.	0.0043	0.	0.0112	0.0147	0.0182

Table F 10 Estimated Values of Average $C\ell_\alpha$

α (deg)	$0^\circ \leq \lvert\beta\rvert < 2^\circ$	$2^\circ \leq \lvert\beta\rvert < 5^\circ$	$5^\circ \leq \lvert\beta\rvert \leq 10^\circ$
0 - 4	0.	0.	0.
4 - 6	0.	0.	0.
6 - 8	0.	0.	0.
8 - 10	0.	0.	-0.0205
10 - 12	0.	0.	0.
12 - 13	0.	0.	0.
13 - 14	0.	0.	0.
14 - 15	0.	0.	0.
15 - 16	0.	0.	0.
16 - 17	0.	0.1315	0.
17 - 18	0.	0.0576	0.1125
18 - 19	0.	0.	0.
19 - 20	0.	0.0609	0.
20 - 22.5	0.	0.	0.0444
22 - 25	0.	0.0159	0.0270
25 - 27.5	0.	0.	0.
27 - 30	0.	0.0266	0.
30 - 35	-0.0446	-0.0825	-0.1541

Table F-11 ESTIMATED VALUE OF $C_{\ell_{p\alpha}}$

	Estimated		
α(deg)	$0^\circ \leq \lvert\beta\rvert < 2^\circ$	$2^\circ \leq \lvert\beta\rvert < 5^\circ$	$5^\circ \leq \lvert\beta\rvert \leq 10^\circ$
0	0	1.2672	0.1556
4	-2.6910	0	0.1556
6	0	0	0.1556
8	0	0	0
10	1.6017	1.8868	2.3044
11	6.7775	4.1287	3.6924
13	6.0588	5.8826	3.6924
14	10.5690	10.3835	8.6769
15	24.8933	23.8968	24.7578
16	14.1890	11.9654	14.5607
17	0	0	-2.4819
18	-6.6689	-6.2384	-7.0379
19	-9.3653	-12.6470	-8.9929
20	-0.9109	-1.3264	-0.5460
22	-3.9284	-4.3695	-5.0747
25	0	0	0
27	-2.1175	0	0
30	-0.4477	-0.6367	0

Table F-12 ESTIMATED VALUE OF $C_{\ell_{r\alpha}}$

	Estimated		
α (deg)	$0^\circ \leq \lvert\beta\rvert < 2^\circ$	$2^\circ \leq \lvert\beta\rvert < 5^\circ$	$5^\circ \leq \lvert\beta\rvert \leq 10^\circ$
0	0	0.6385	-0.4331
4	0	0	-0.4331
6	0	0	-0.4331
8	0	0	-0.4331
10	0	0	0
12	14.1570	0	7.2825
13	0	0	7.2825
14	7.7380	6.2149	0
15	0	0	0
16	0	0	0
17	0	-9.5115	0
18	0	-8.3432	0
19	-12.1400	0	-19.1830
20	-2.4842	0	0
22	0	0	0
25	0	0	0
27	0	0	0
30	0	0	2.9820

Table F-13 Comparison of Estimated and Wind Tunnel Values of Average $C_{n_{\delta_a}}$

α (deg)	$0^\circ \leq \lvert\beta\rvert < 2^\circ$		$2^\circ \leq \lvert\beta\rvert < 5^\circ$		$5^\circ \leq \lvert\beta\rvert \leq 10^\circ$	
	Estimated	Wind Tunnel	Estimated	Wind Tunnel	Estimated	Wind Tunnel
0 - 4	-0.0151	-0.0100	0.	-0.0097	0.	-0.0085
4 - 6	-0.0117	-0.0088	-0.0154	-0.0086	0.	-0.0087
6 - 8	-0.0047	-0.0087	-0.0154	-0.0080	0.	-0.0091
8 - 10	-0.0085	-0.0086	-0.0070	-0.0070	-0.0091	-0.0096
10 - 12	-0.0092	-0.0064	-0.0078	-0.0058	-0.0101	-0.0062
12 - 13	-0.0062	-0.0042	-0.0083	-0.0043	0.	-0.0029
13 - 14	0.	-0.0021	0.	-0.0026	0.	0.0021
14 - 15	0.0026	-0.0001	0.	-0.0008	0.0096	0.0071
15 - 16	0.	0.0010	0.	0.0021	0.0078	0.0117
16 - 17	0.	0.0033	0.	0.0063	0.0128	0.0152
17 - 18	0.	0.0035	0.0089	0.0053	0.0116	0.0126
18 - 19	0.	0.0037	0.	0.0044	0.0073	0.0099
19 - 20	0.	0.0012	0.	0.0002	0.0096	0.0040
20 - 22.5	0.0048	-0.0014	0.	-0.0040	0.0040	-0.0019
22.5 - 25	0.	-0.0029	-0.0080	-0.0046	0.	-0.0061
25 - 27.5	-0.0070	-0.0044	-0.0076	-0.0051	0.	-0.0104
27.5 - 30	-0.1090	-0.0013	-0.0065	-0.0020	0.0127	-0.0083
30 - 35	0.0067	0.0018	0.0065	0.0011	-0.0076	-0.0062

Table F-14 Comparison of Estimated and Wind Tunnel Values of Average Cn_{δ_a}

α (deg)	$0^\circ \leq \lvert\beta\rvert < 2^\circ$		$2^\circ \leq \lvert\beta\rvert < 5^\circ$		$5^\circ \leq \lvert\beta\rvert \leq 10^\circ$	
	Estimated	Wind Tunnel	Estimated	Wind Tunnel	Estimated	Wind Tunnel
0 - 4	-0.0123	-0.0142	-0.0192	-0.0174	-0.0166	-0.0128
4 - 6	-0.0162	-0.0137	-0.0159	-0.0168	-0.0166	-0.0116
6 - 8	-0.0115	-0.0139	-0.0159	-0.0164	-0.0166	-0.0116
8 - 10	-0.0124	-0.0141	-0.0172	-0.0160	-0.0141	-0.0117
10 - 12	-0.0117	-0.0118	-0.0170	-0.0119	-0.0172	-0.0078
12 - 13	-0.0102	-0.0096	-0.0111	-0.0079	-0.0083	-0.0040
13 - 14	-0.0076	-0.0077	0.	-0.0044	-0.0083	-0.0011
14 - 15	-0.0059	-0.0057	0.	-0.0010	-0.0020	0.0017
15 - 16	0.	-0.0055	0.	-0.0030	0.	-0.0035
16 - 17	0.	-0.0038	0.	-0.0038	-0.0079	-0.0076
17 - 18	-0.0053	-0.0006	-0.0067	0.0003	-0.0124	-0.0014
18 - 19	0.	0.0027	0.	0.0044	0.	0.0048
19 - 20	0.	0.0018	0.0076	0.0040	0.0128	0.0080
20 - 22.5	0.	0.0009	0.0075	0.0037	0.0163	0.0112
22.5 - 25	0.	-0.0024	0.	-0.0026	0.0090	0.0055
25 - 27.5	-0.0062	-0.0058	0.	-0.0090	0.	-0.0003
27.5 - 30	0.	-0.0027	-0.0111	-0.0083	0.	-0.0043
30 - 35	-0.0100	0.0004	-0.0222	-0.0077	0.	-0.0083

Table F-15 Estimated Values of Average C_{n_α}

α (deg)	$0^\circ \leq \lvert\beta\rvert < 2^\circ$	$2^\circ \leq \lvert\beta\rvert < 5^\circ$	$5^\circ \leq \lvert\beta\rvert \leq 10^\circ$
0 - 4	0.	0.	0.
4 - 6	0.	0.	0.
6 - 8	-0.0042	0.	0.
8 - 10	0.	0.	-0.0164
10 - 12	0.	0.	-0.0254
12 - 13	0.	0.0245	-0.0254
13 - 14	0.	0.	-0.0254
14 - 15	-0.0108	-0.0826	-0.2200
15 - 16	0.	-0.0878	-0.1585
16 - 17	0.	-0.0816	-0.1316
17 - 18	-0.0163	-0.0493	-0.0763
18 - 19	0.	0.	-0.0391
19 - 20	0.	0.	0.
20 - 22.5	0.	0.0073	0.0172
22 - 25	0.	0.0076	0.0171
25 - 27.5	0.	-0.0080	0.
27 - 30	0.	0.	0.
30 - 35	-0.0069	0.0045	0.

Table F-16 ESTIMATED VALUE OF $C_{n_{r\alpha}}$

	Estimated		
α (deg)	$0^\circ \leq \lvert\beta\rvert < 2^\circ$	$2^\circ \leq \lvert\beta\rvert < 5^\circ$	$5^\circ \leq \lvert\beta\rvert \leq 10^\circ$
0	0	0	0
4	0	0	0
6	0	0	0
8	0	0	0
10	0	0	0
12	0	0	0
13	0	0	0
14	2.9110	0	-5.4219
15	0	0	0
16	5.2109	0	0
17	0	0	0
18	-2.4083	-4.1690	-6.2156
20	0	0.7845	1.3860
22	0	0	0
25	0	-0.8470	0
27	0	-1.1626	3.4870
30	-1.3187	-1.8826	-2.1706

Table F-17 LATERAL PARAMETERS FOR ADDITIONAL REGIONS

Region 1: $-4^{\circ} \leq \alpha < 0^{\circ}$, $0^{\circ} \leq |\beta| \leq 2^{\circ}$

Region 2: $8^{\circ} \leq \alpha \leq 12^{\circ}$, $10^{\circ} \leq |\beta| \leq 15^{\circ}$

Region 3: $20^{\circ} \leq \alpha < 22.5^{\circ}$, $10^{\circ} \leq |\beta| \leq 15^{\circ}$

Region 4: $22.5^{\circ} \leq \alpha < 25^{\circ}$, $10^{\circ} \leq |\beta| \leq 15^{\circ}$

Region	C_{y_o}	C_{y_α}	C_{y_β}	$C_{y_{\delta_a^+}}$	$C_{y_{o_a^-}}$
1	0.0007	-	-0.5776	-	-
2	-0.1553	-	-0.8150	-	-
3	-0.1316	-	-0.8656	-	0.1115
4	-0.1344	-	-0.7710	-0.2638	-

Region	$C_{y_{\delta_r^+}}$	$C_{y_{\delta_r^-}}$	C_{y_p}	C_{y_r}	$C_{y_{p\alpha}}$	$C_{y_{r\alpha}}$
1	-	-	0.5839	0.6152	-	-
2	0.1617	0.1545	-	0.6481	-	-
3	0.0556	-	-	-	-	-
4	-	0.1268	-0.0870	0.6106	-	-

Table F-17 LATERAL PARAMETERS (Cont'd)

Region	C_{ℓ_o}	C_{ℓ_α}	C_{ℓ_β}	$C_{\ell_{\delta_a}^+}$	$C_{\ell_{\delta_a}^-}$
1	0.0	-	-0.1487	-0.1500	-0.1782
2	-0.0270	-	-0.0917	-0.1685	-0.1686
3	-0.0251	-	-0.1860	-0.0794	-
4	-0.0246	-	-0.1441	-	-0.1084

Region	$C_{\ell_{\delta_r}^+}$	$C_{\ell_{\delta_r}^-}$	C_{ℓ_p}	C_{ℓ_p}	$C_{\ell_{p\alpha}}$	$C_{\ell_{r\alpha}}$
1	-	-	-0.7178	0.1567	-	-
2	0.0230	0.0161	-0.7311	0.2084	-	-
3	-	-0.0636	-	-	-1.2000	-
4	-0.0308	-	-	-	-7.1036	3.3587

Table F-17 LATERAL PARAMETERS (Cont'd)

Region	C_{n_o}	C_{n_α}	C_{n_β}	$C_{n_{\delta_a}+}$	$C_{n_{\delta_a}-}$
1	0.0	-	0.1098	-	-
2	0.0160	-	0.0130	-0.0182	-0.0090
3	-0.0007	0.0281	-0.0105	-	0.0105
4	0.0	0.0351	0.0	-	-

Region	$C_{n_{\delta_r}+}$	$C_{n_{\delta_r}-}$	C_{n_p}	C_{n_r}	$C_{n_{p\alpha}}$	$C_{n_{r\alpha}}$
1	-0.0383	-0.0593	-	-0.2748	-	-
2	-0.0600	-0.0575	-0.0663	-0.2146	-	-
3	-0.0232	-0.0199	-0.0577	-	-	-
4	-0.0298	-0.0228	-0.0652	-0.0521	-	2.6847

APPENDIX G

This appendix contains the predicted responses and the comparisons with the wind tunnel responses for Maneuvers 1-3, 5-10, 12-16 and the first half of Maneuver 11. Note that four pages of plots are given for each maneuver. Each page contains two states. Altogether the responses for the states α, β, V, p, q, r, θ and ϕ are given. The solid line is the response of the wind tunnel model and dotted lines with crosses represent the response of the identified model. All the response plots are given in Figure G.1. Figs. G.2(a) through G.2(d) demonstrate the sensitivity of the aircraft model response to small deviations in the states.

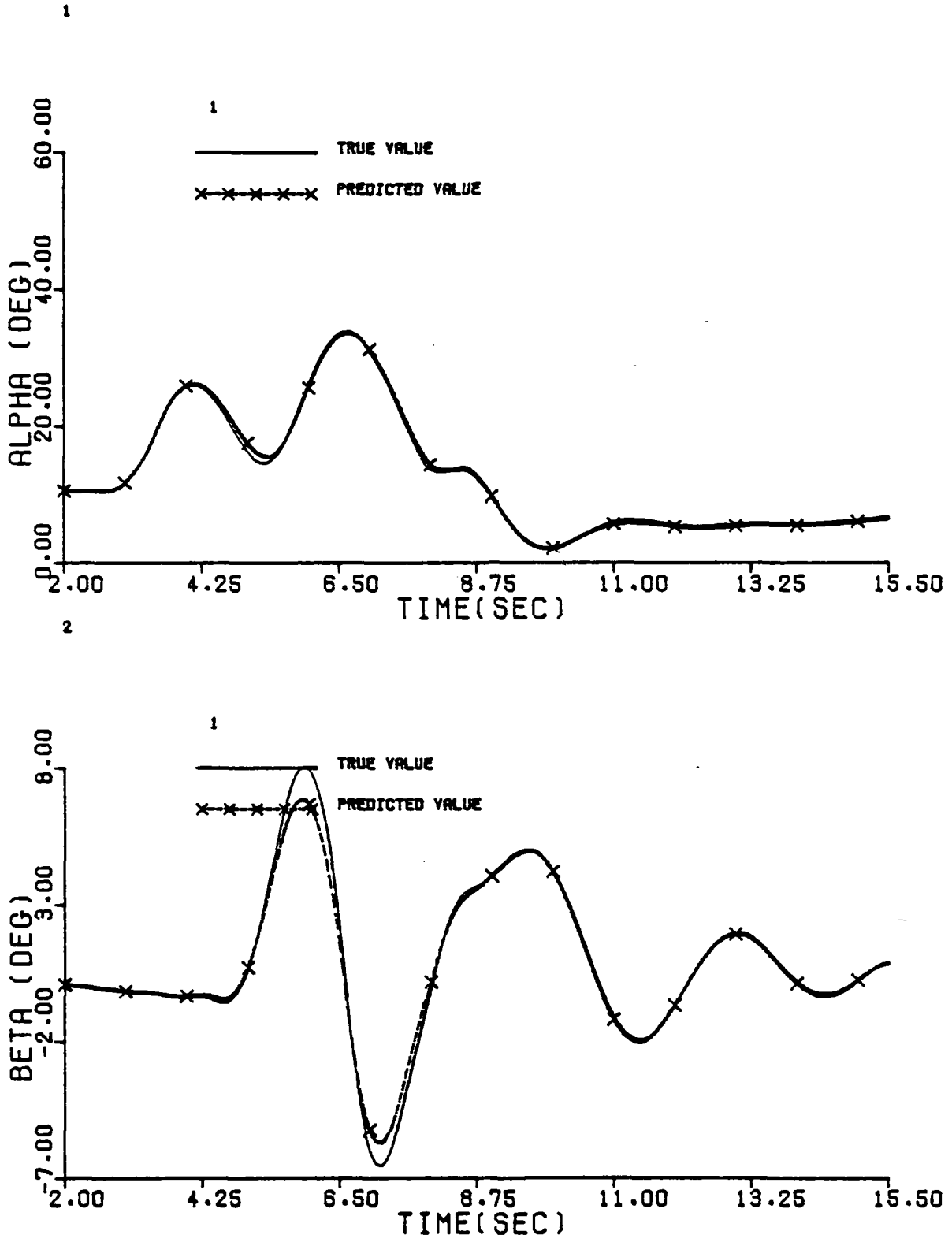

Figure G.1 Comparison of Predicted and True Time Histories for Processed Maneuvers (Maneuver 1)

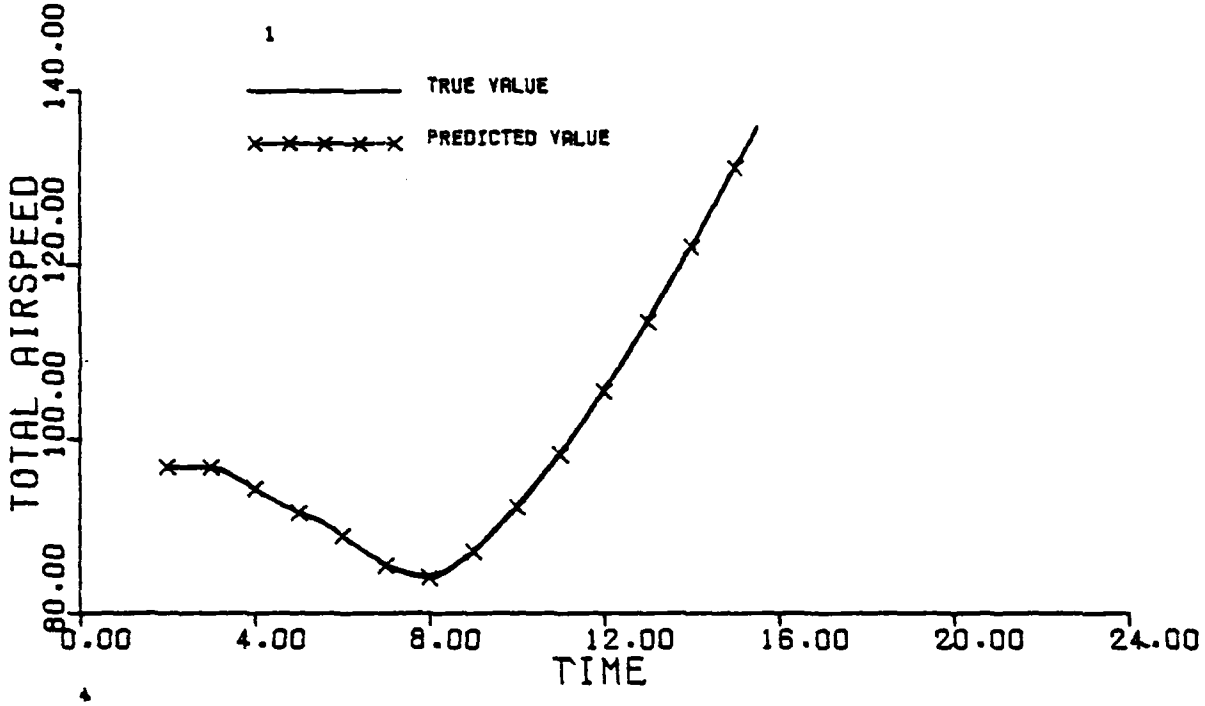

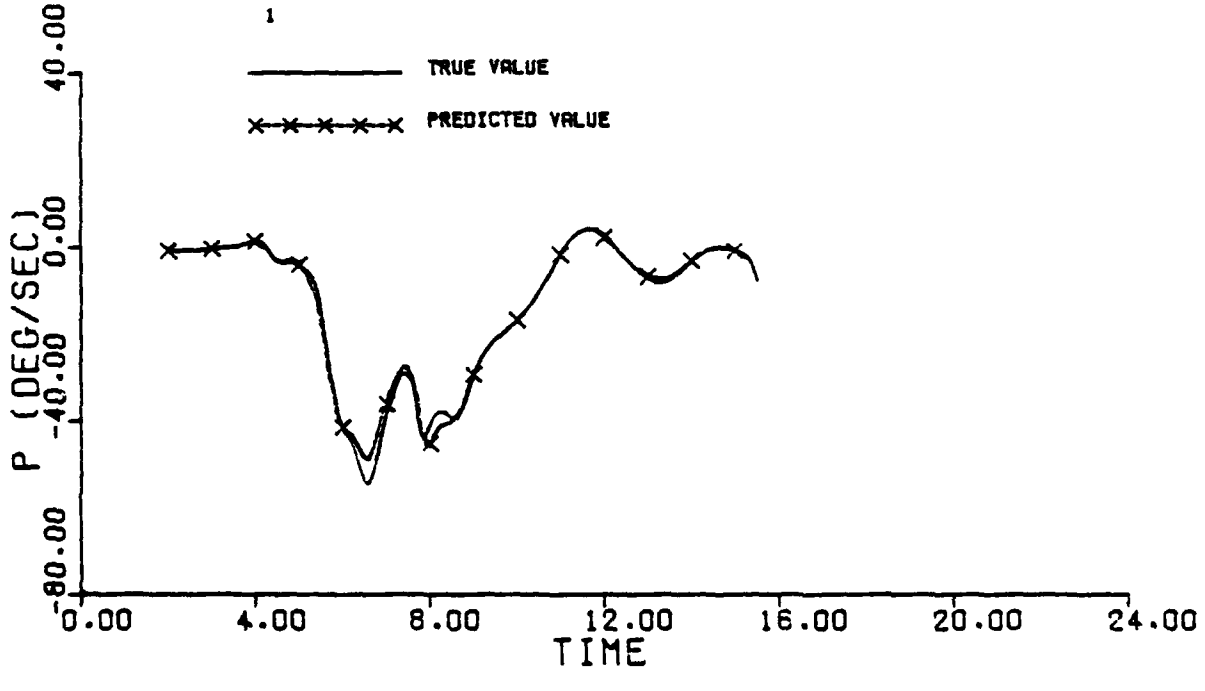

Figure G.1 Continued (Maneuver 1)

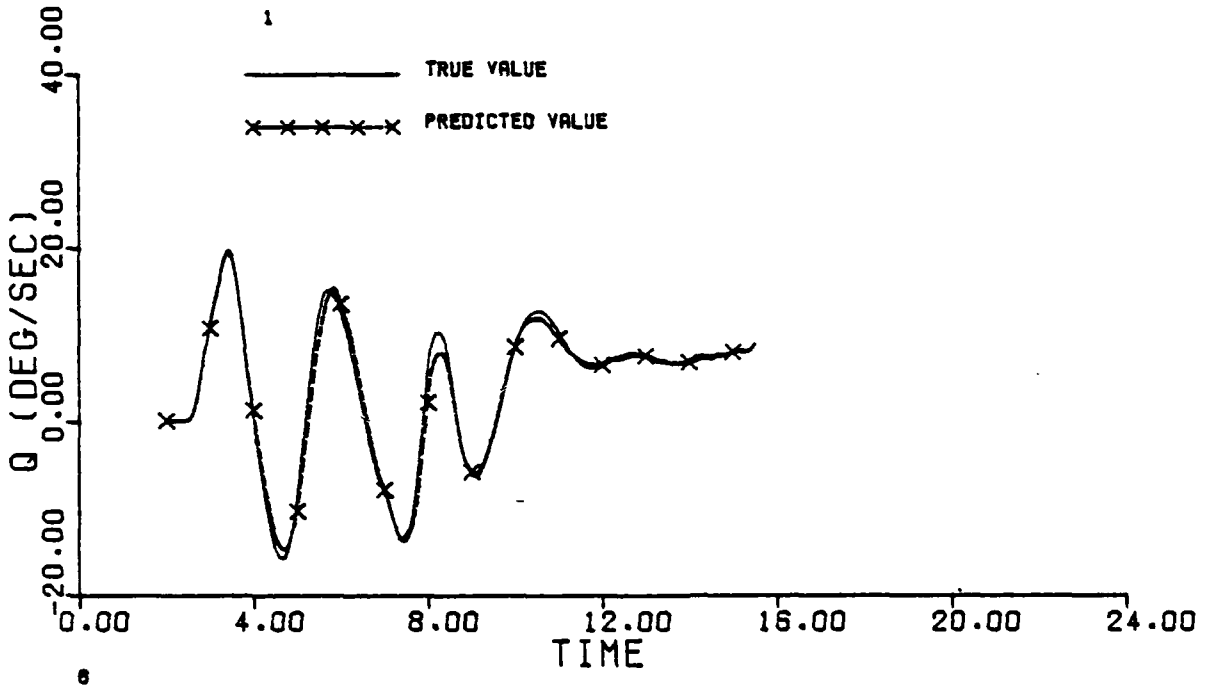

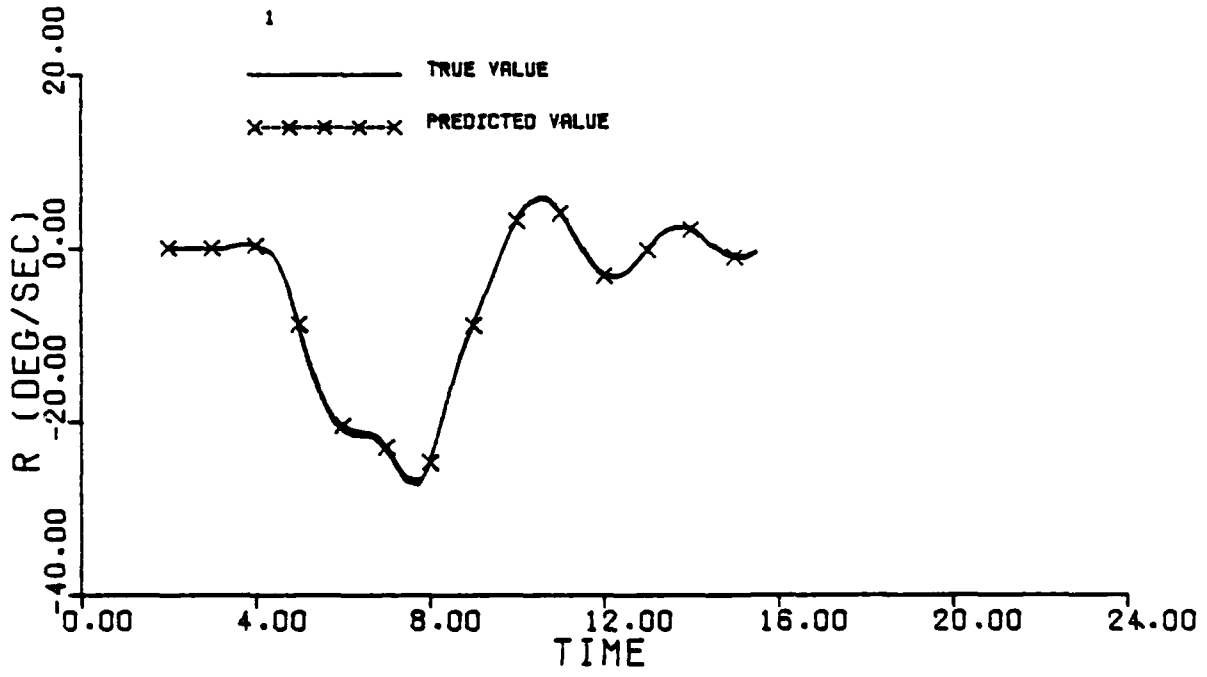

Figure G.1 Continued (Maneuver 1)

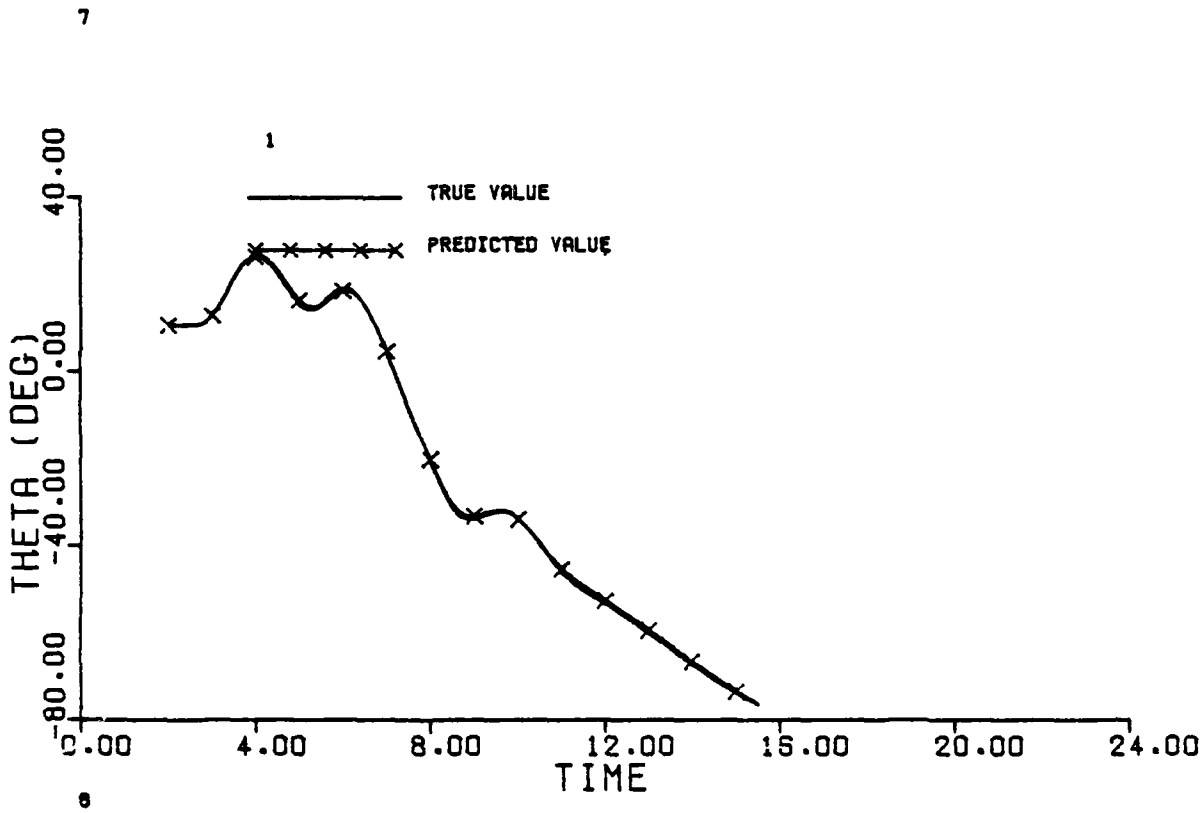

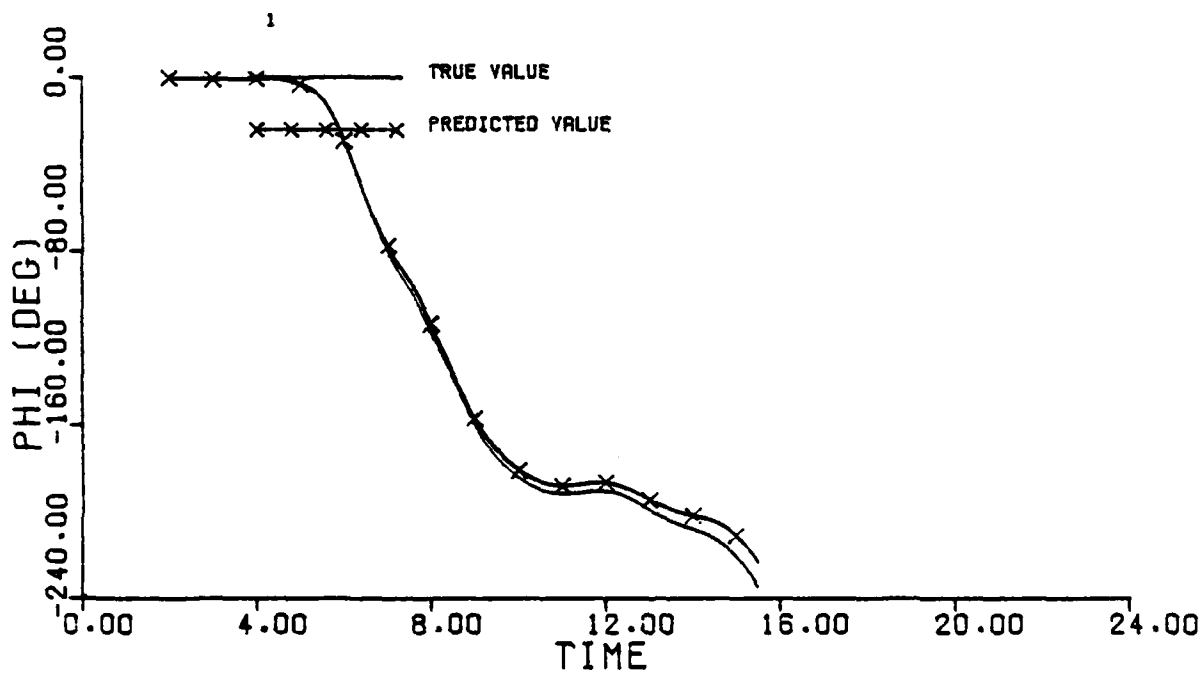

Figure G.1 Continued (Maneuver 1)

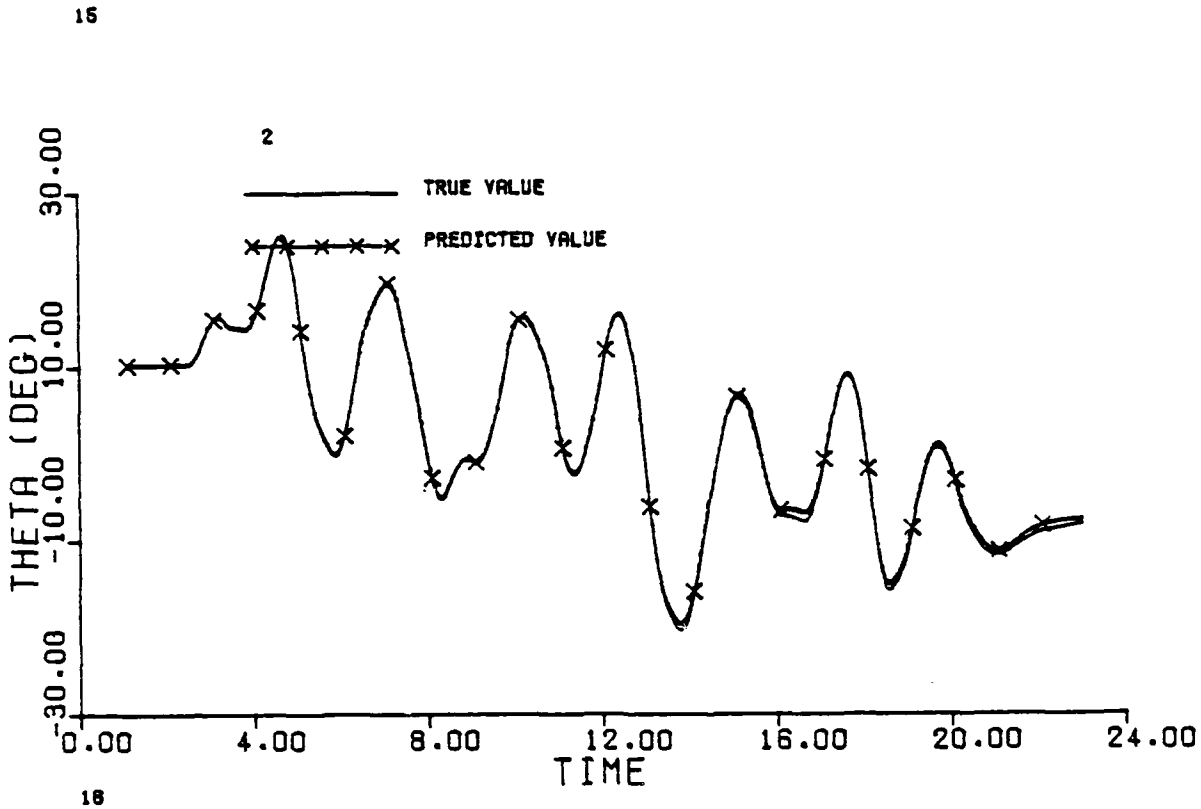

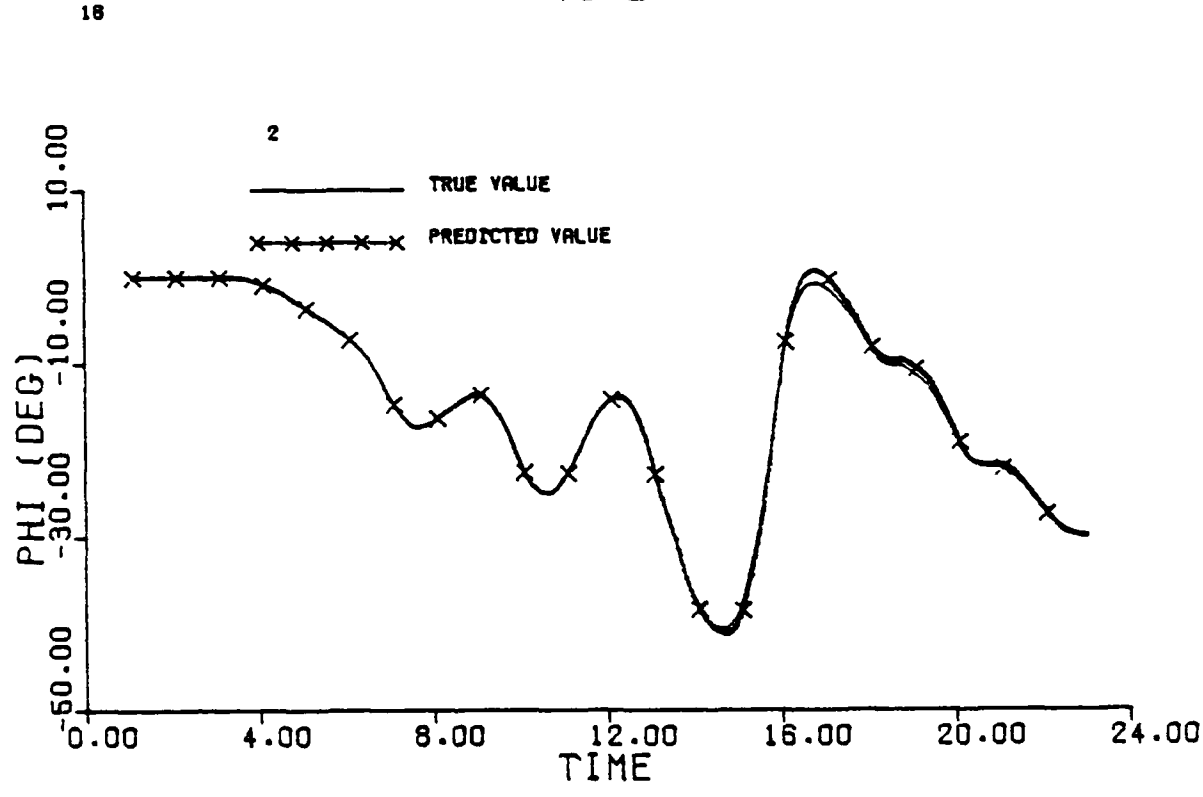

Figure G.1 Continued (Maneuver 2)

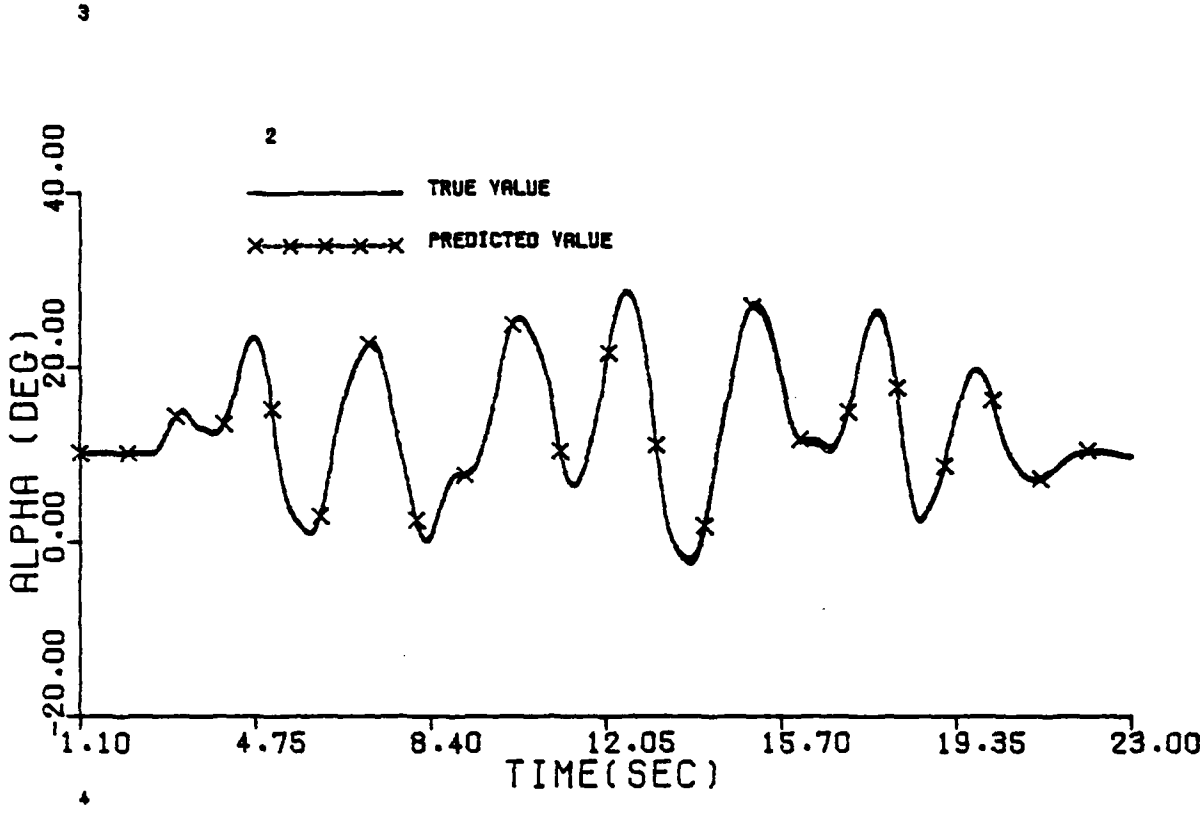

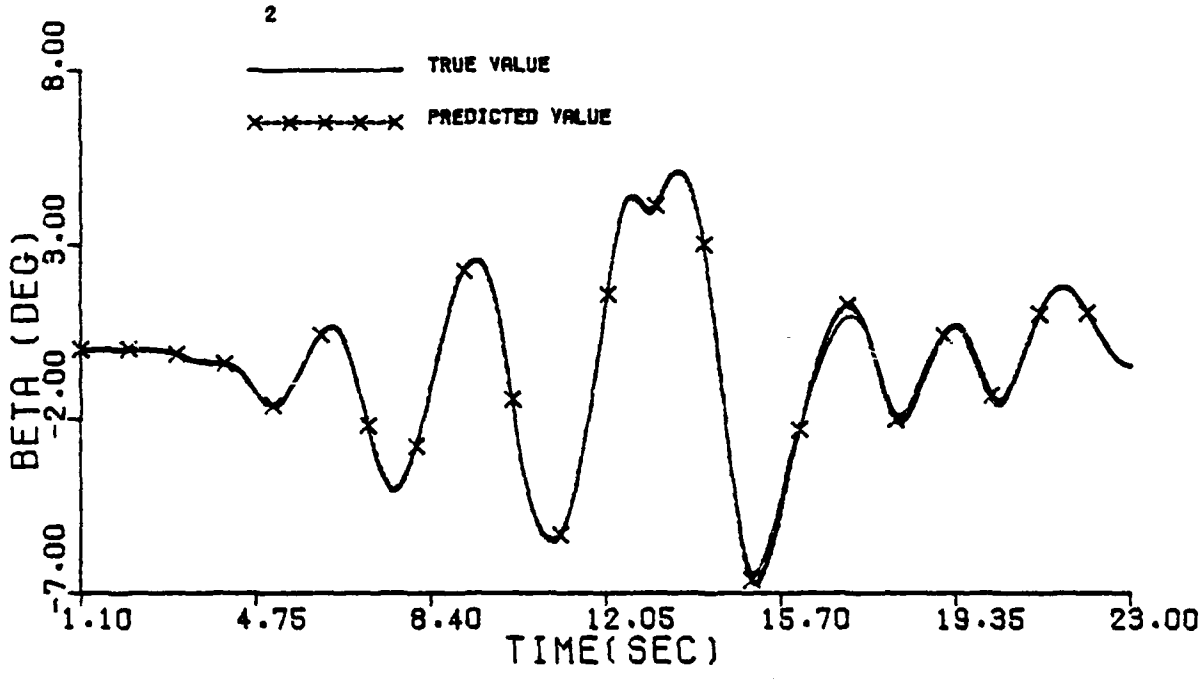

Figure G.1 (Maneuver 2)

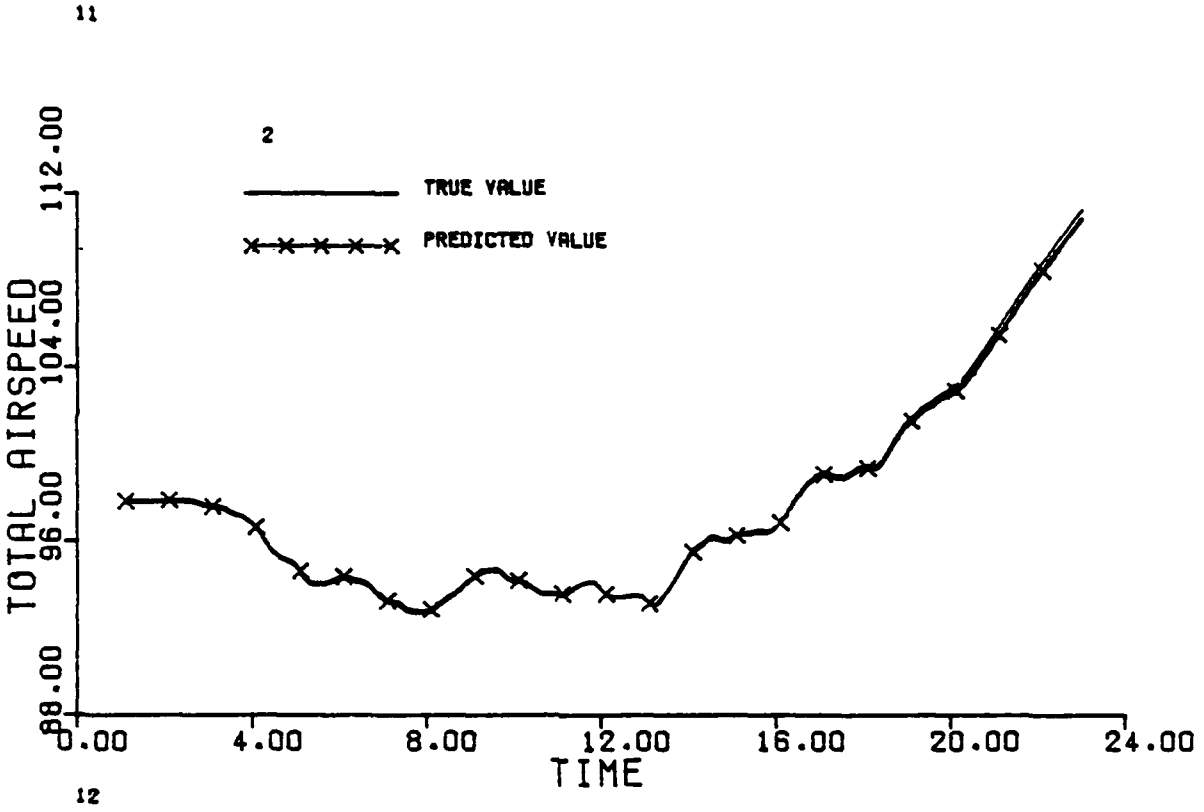

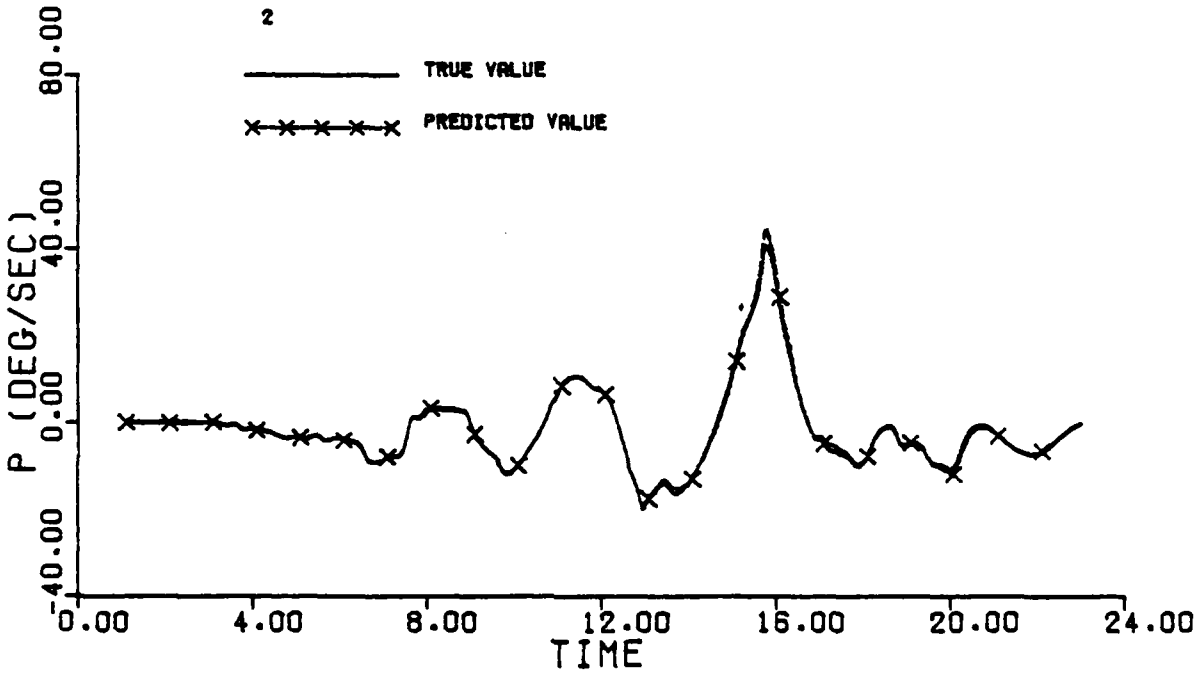

Figure G.1 Continued (Maneuver 2)

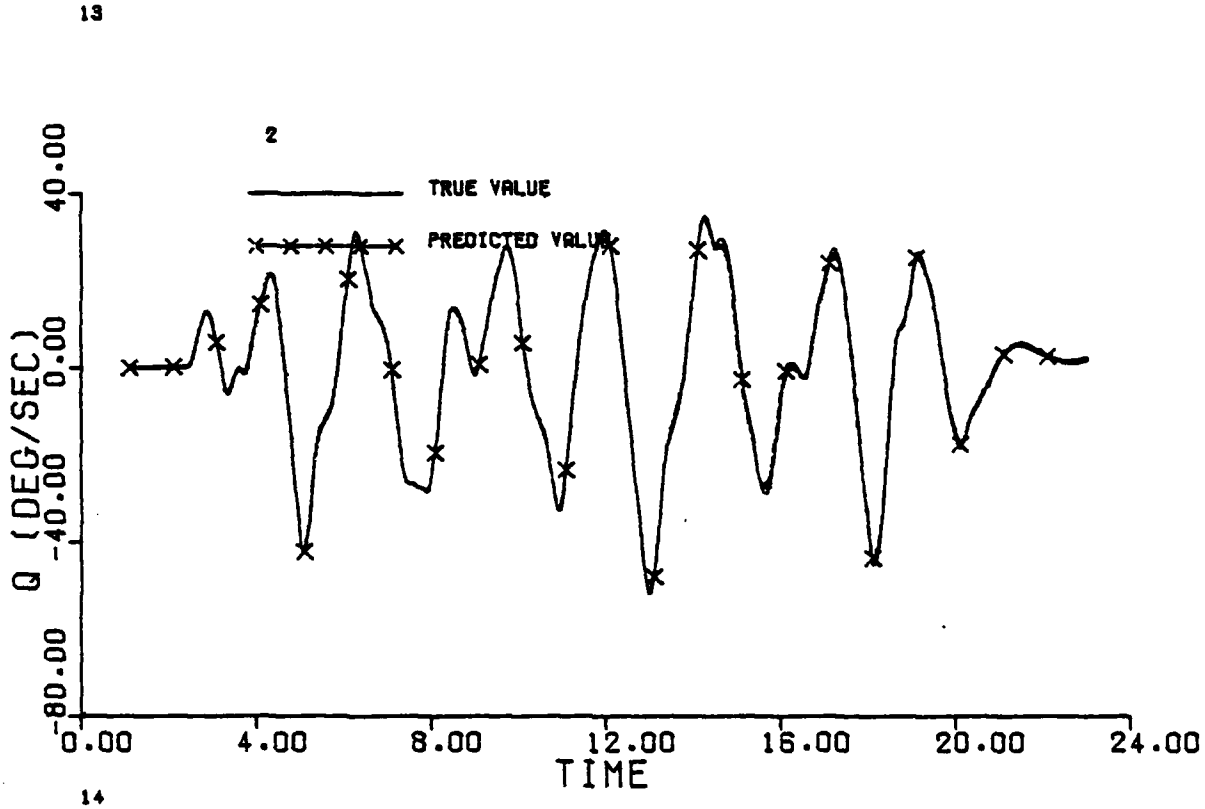

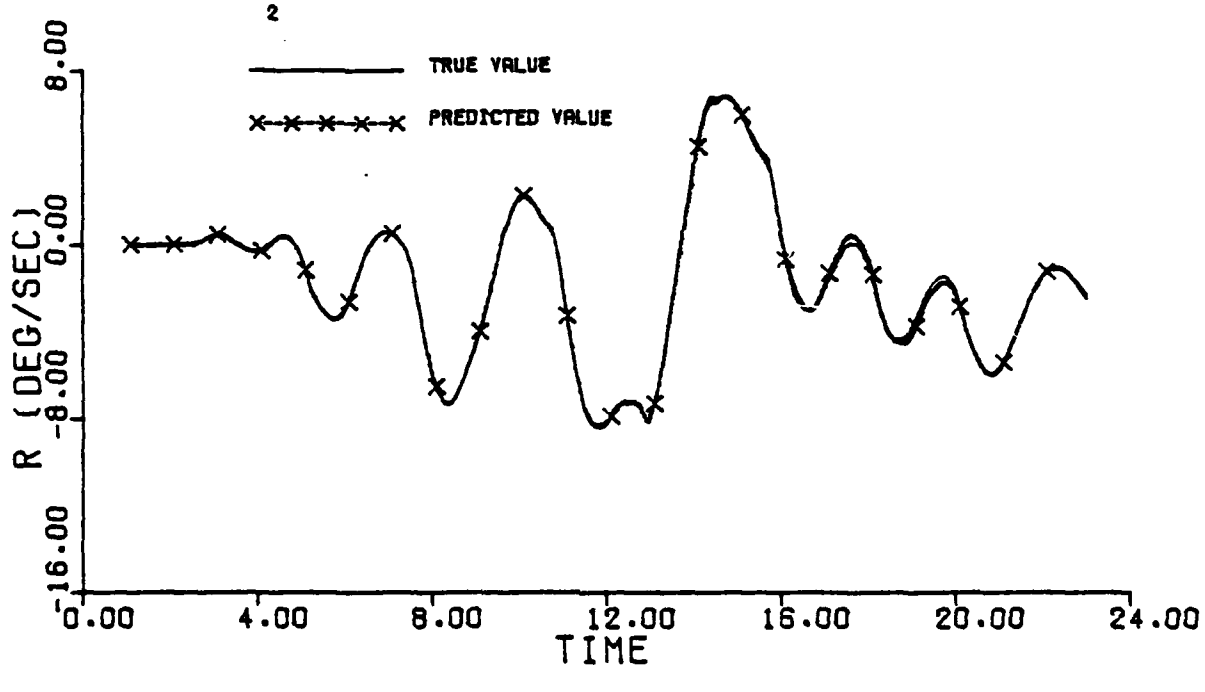

Figure G.1 Continued (Maneuver 2)

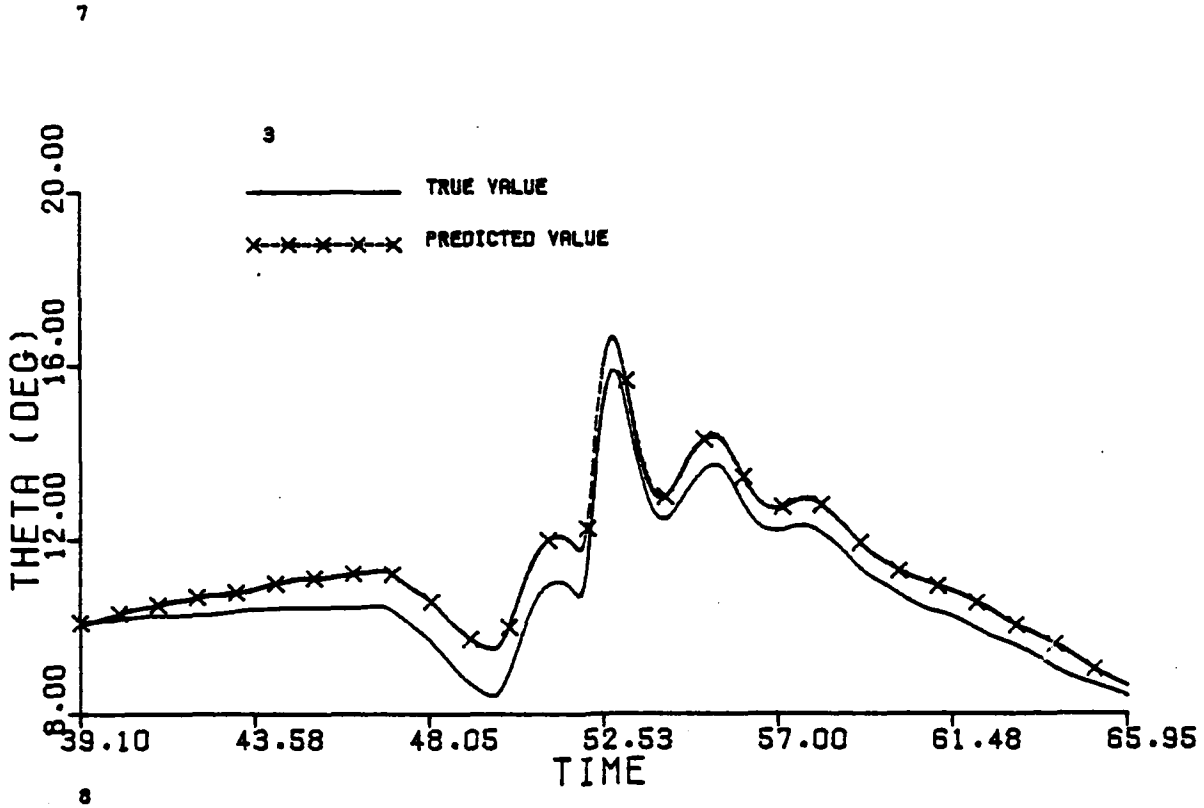

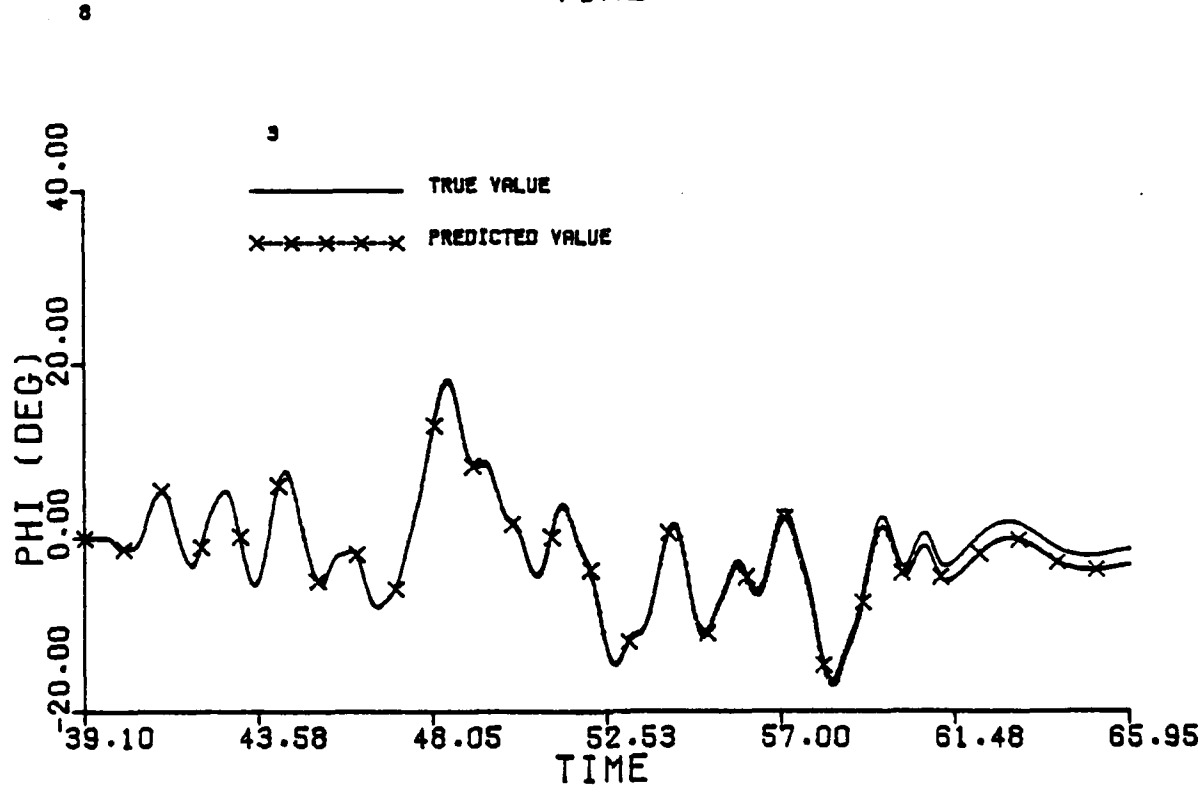

Figure G.1 Continued (Maneuver 3)

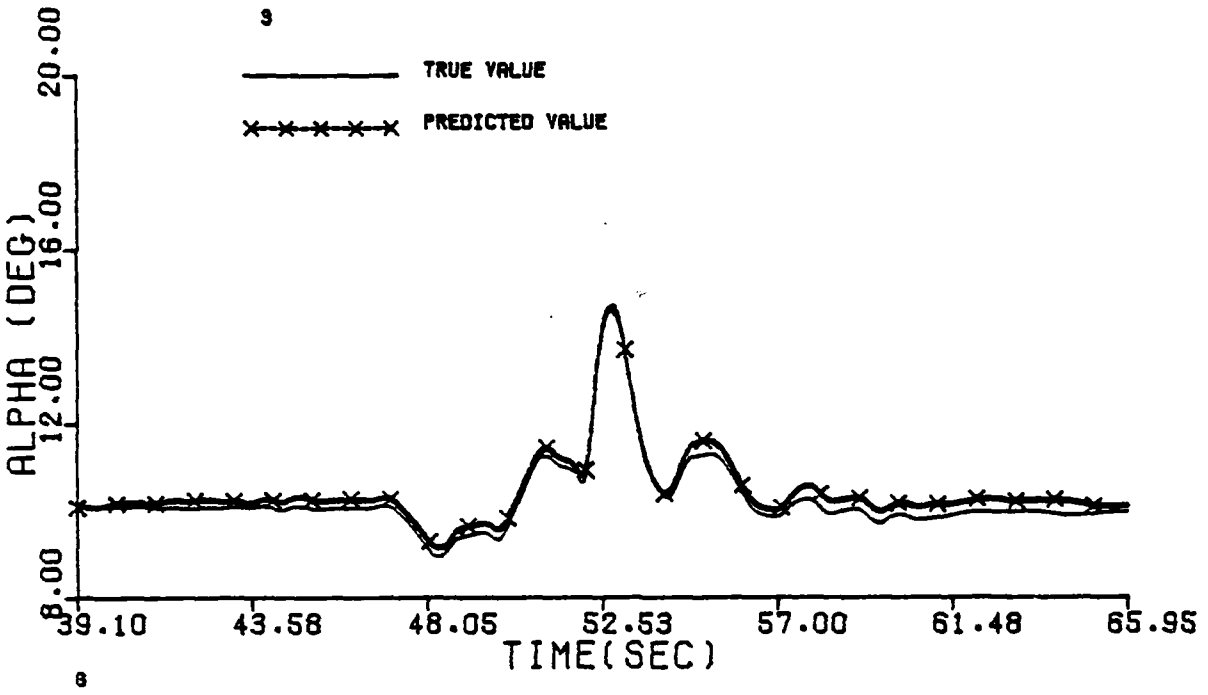

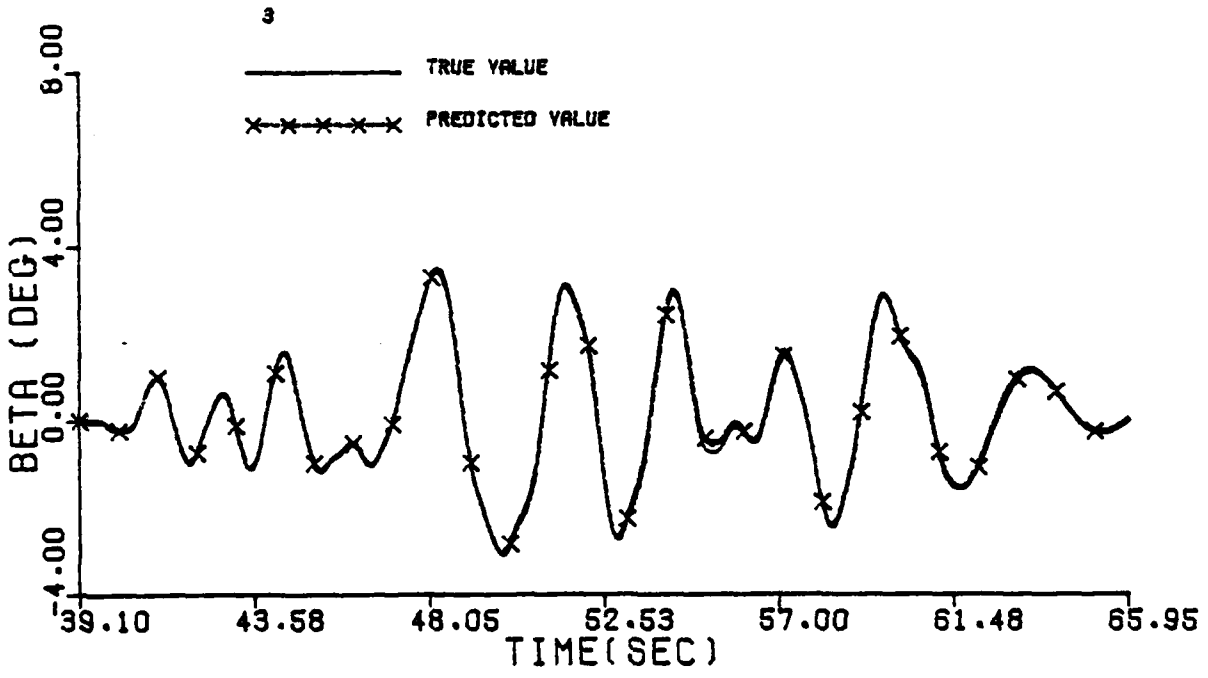

Figure G.1 Continued (Maneuver 3)

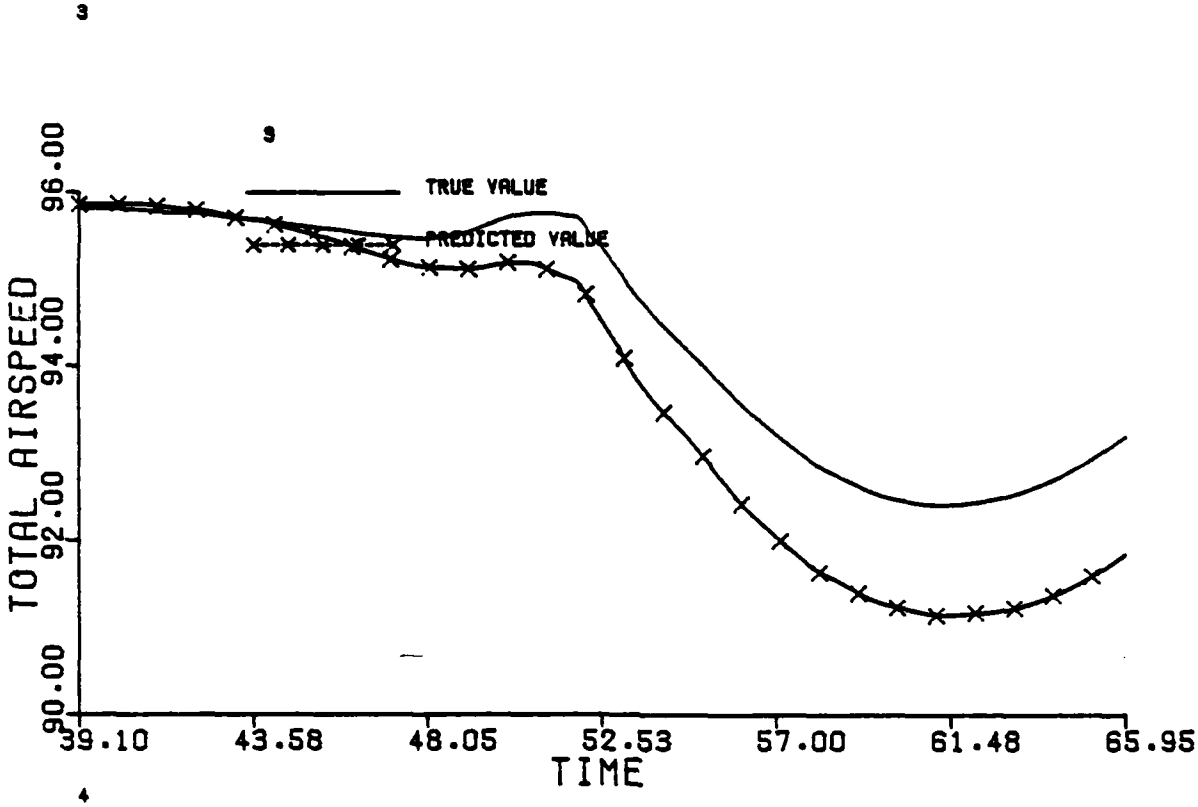

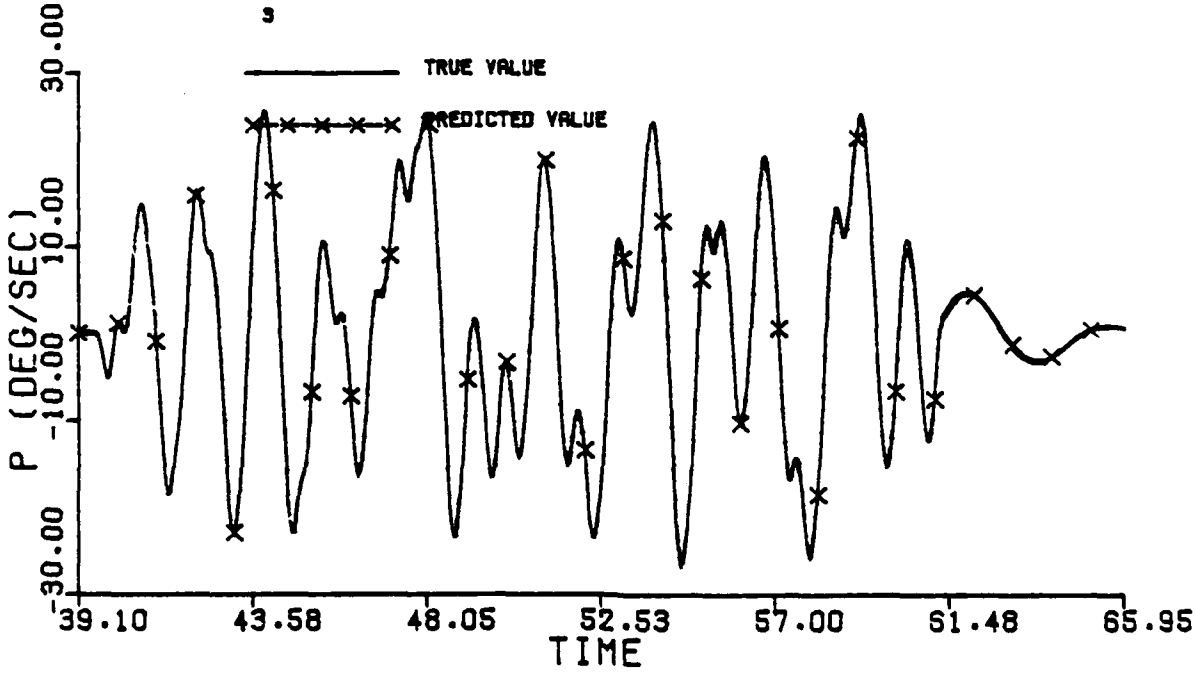

Figure G.1 Continued (Maneuver 3)

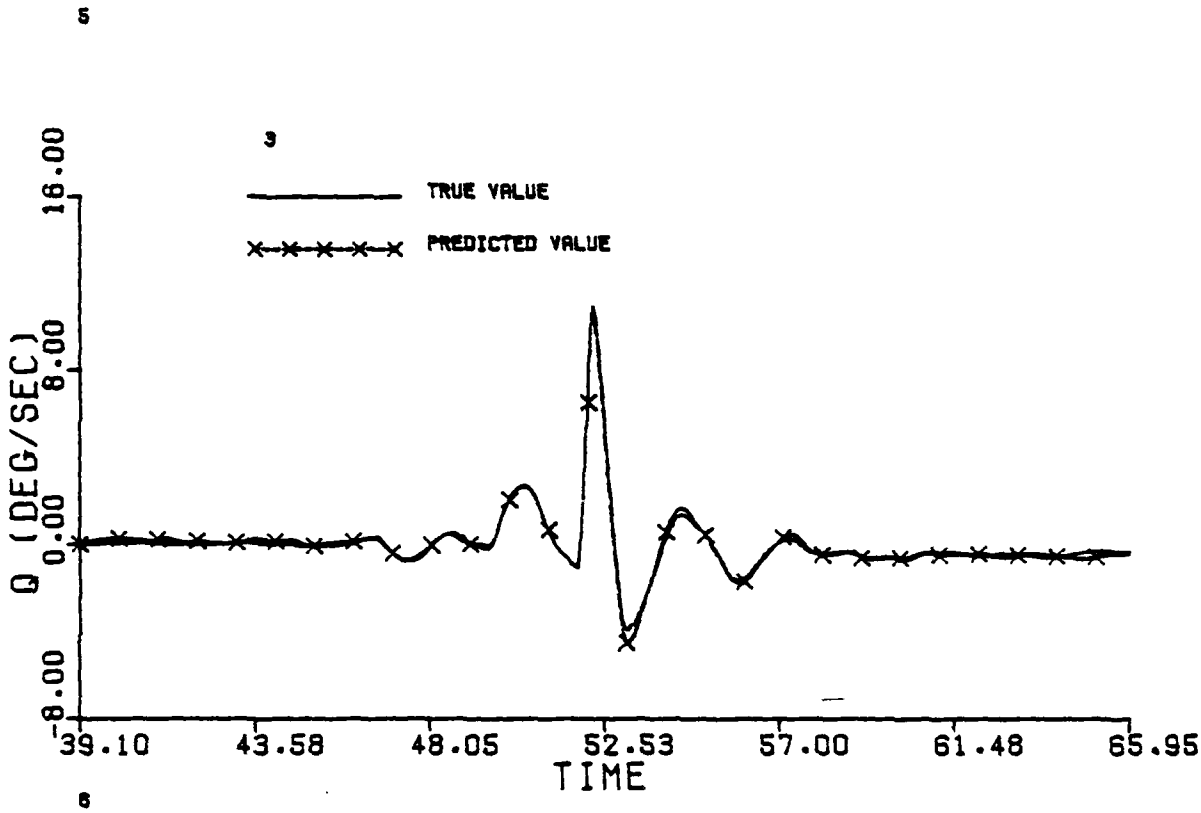

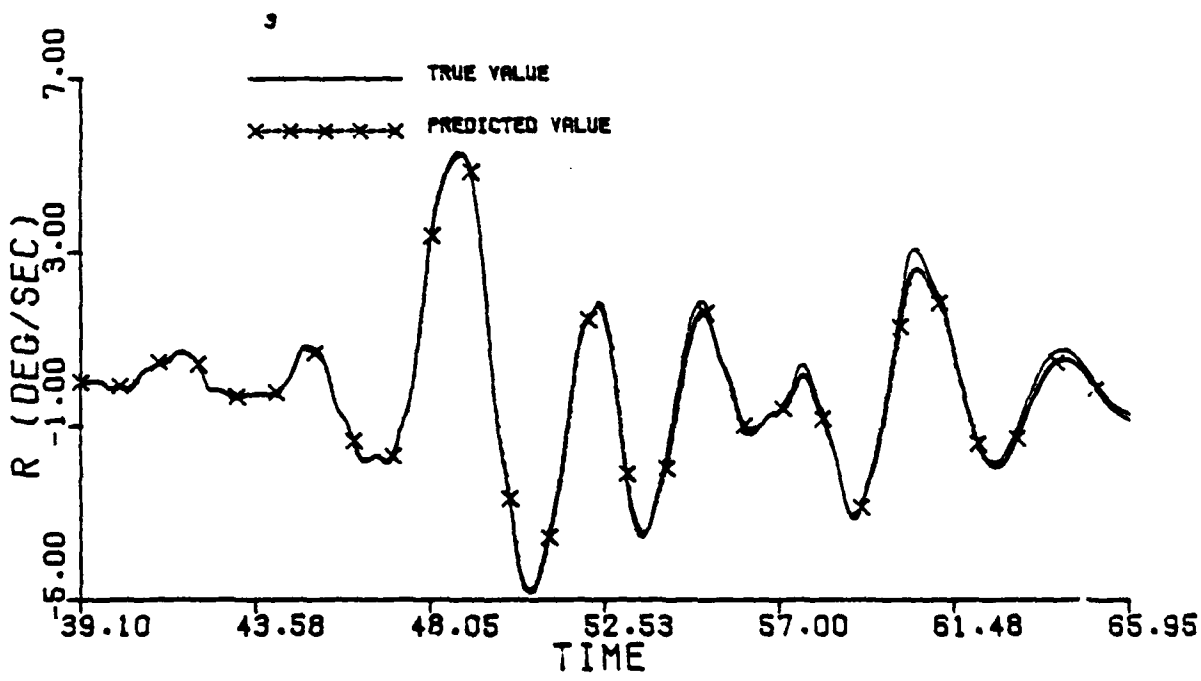

Figure G.1 Continued (Maneuver 3)

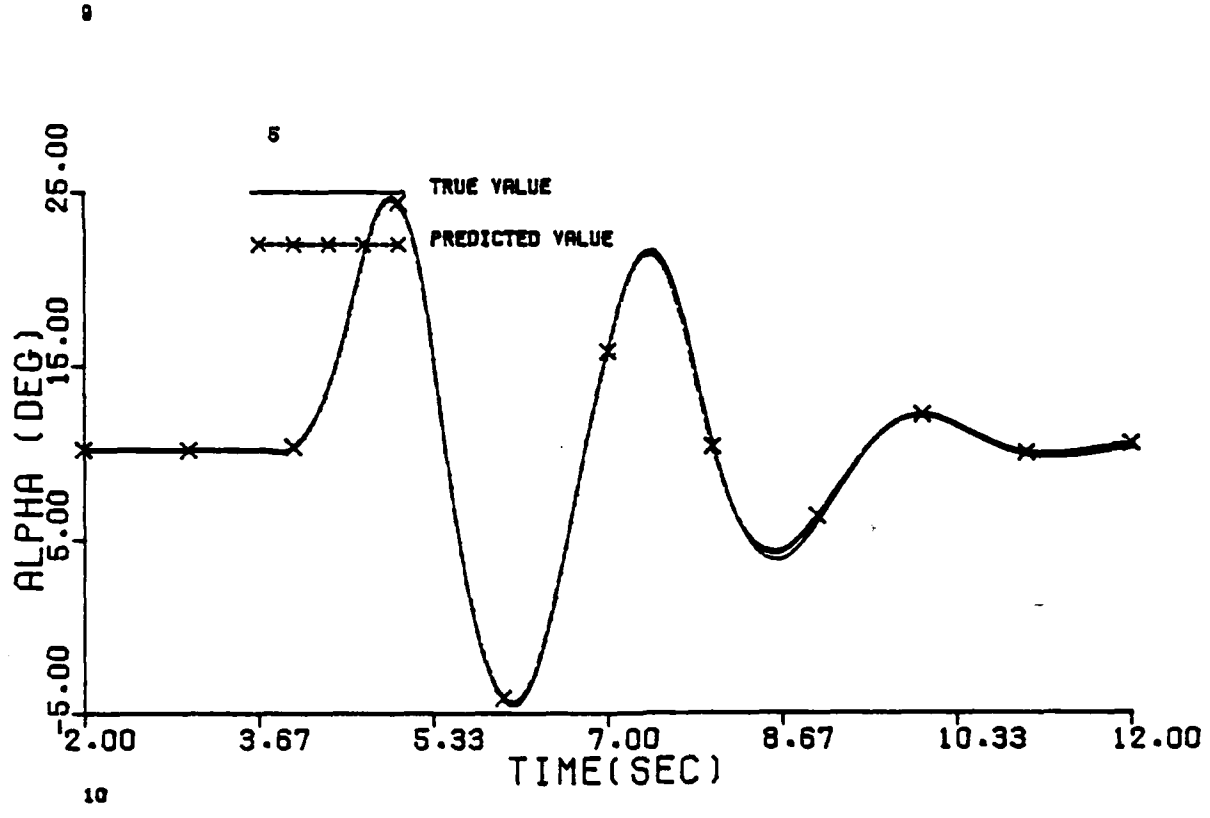

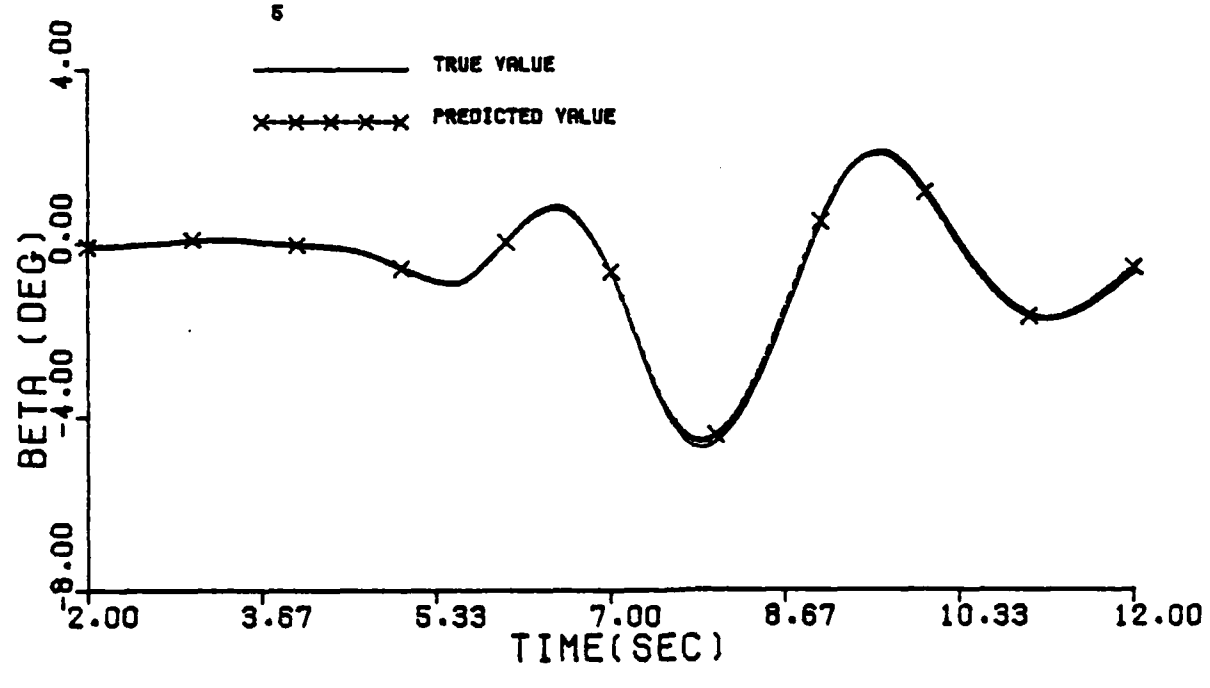

Figure G.1 Continued (Maneuver 5)

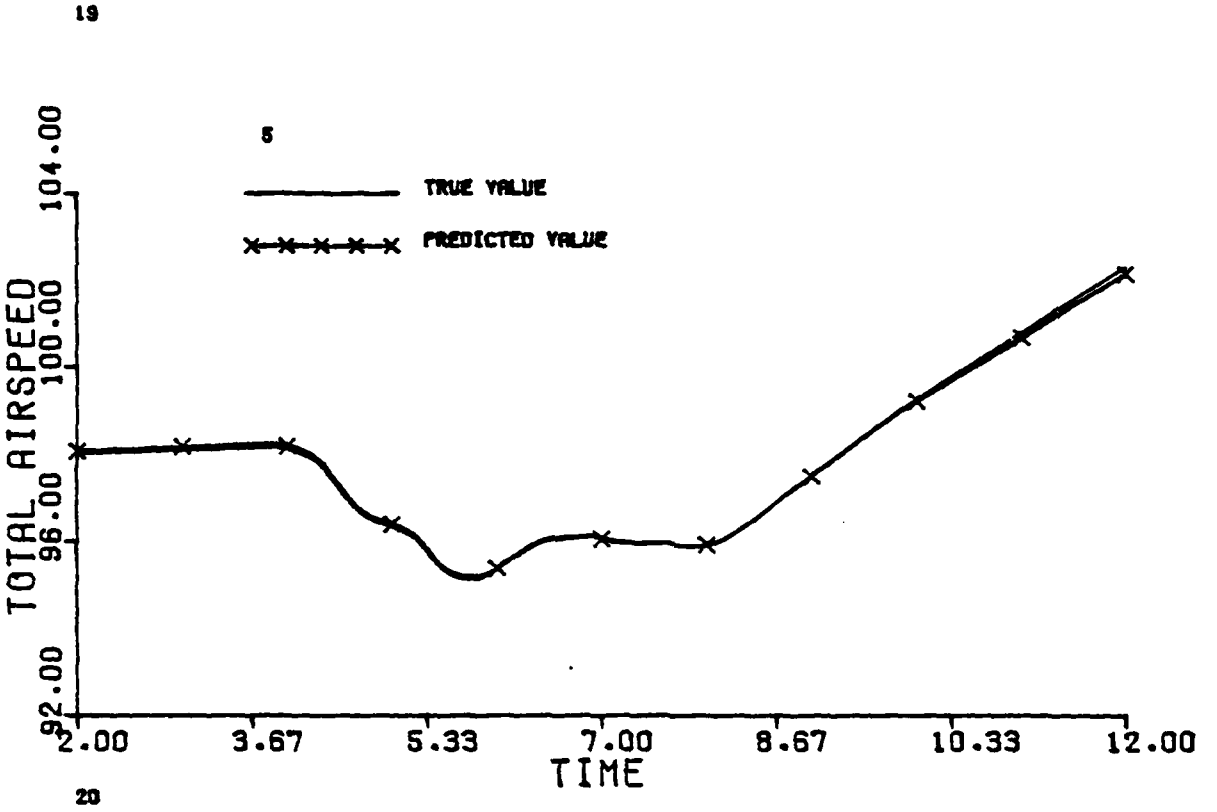

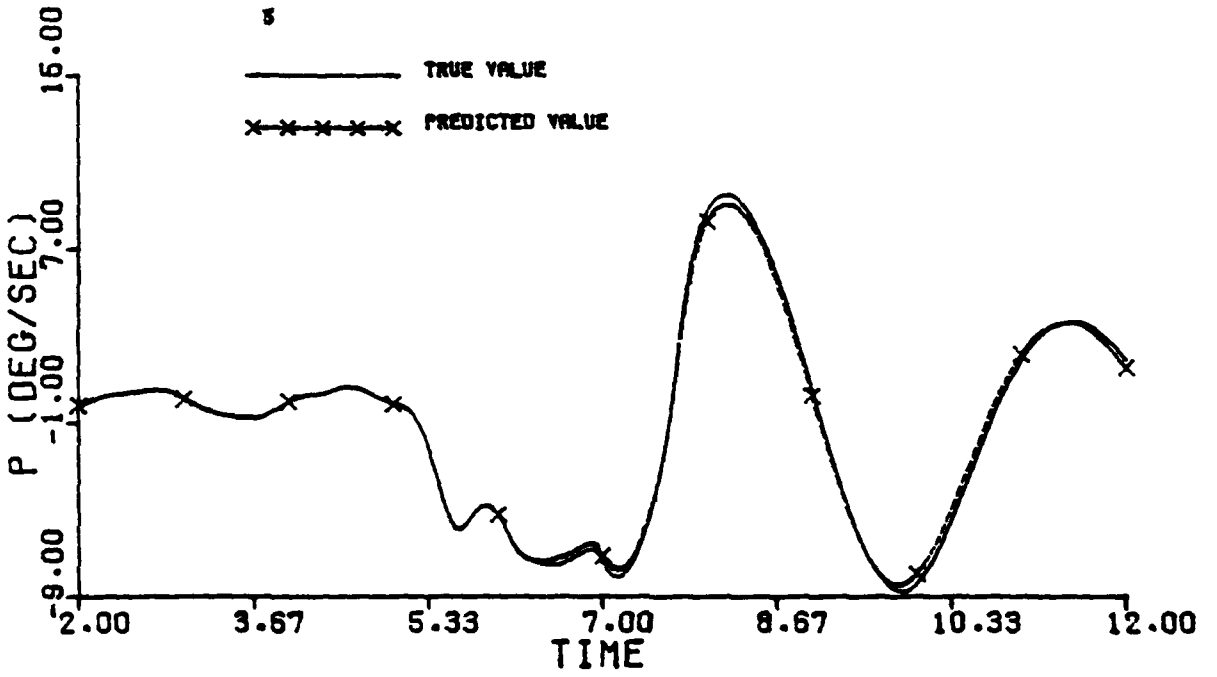

Figure G.1 Continued (Maneuver 5)

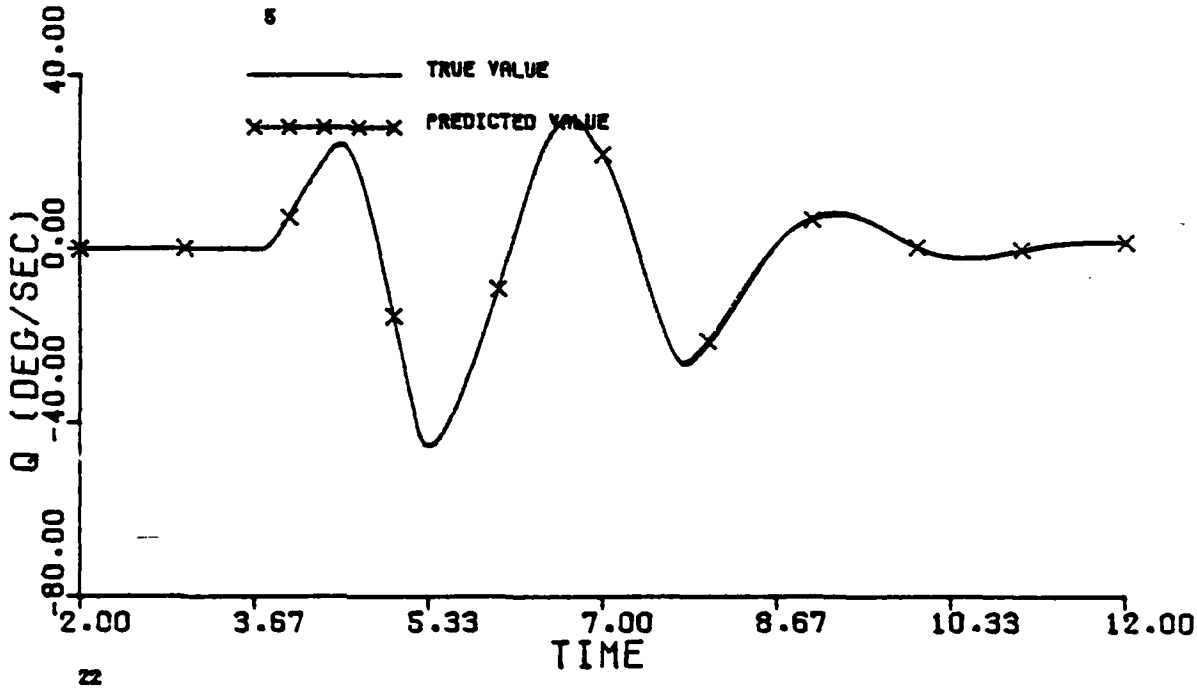

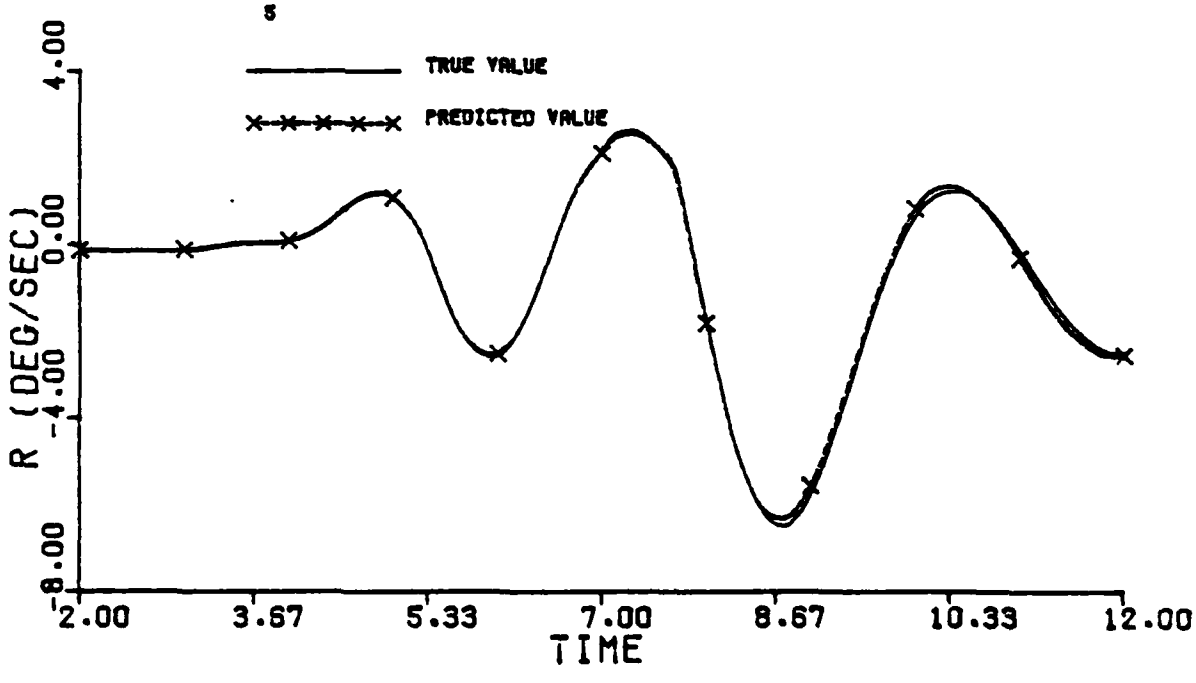

Figure G.1 Continued (Maneuver 5)

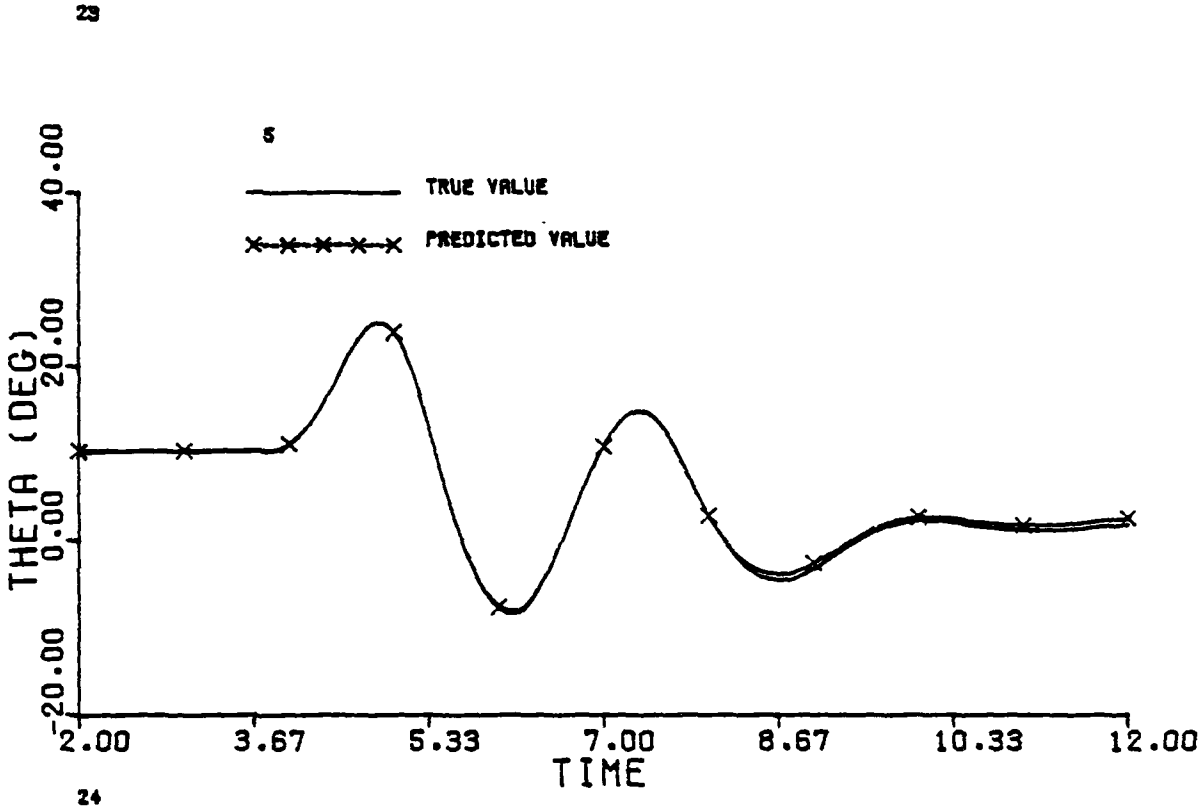

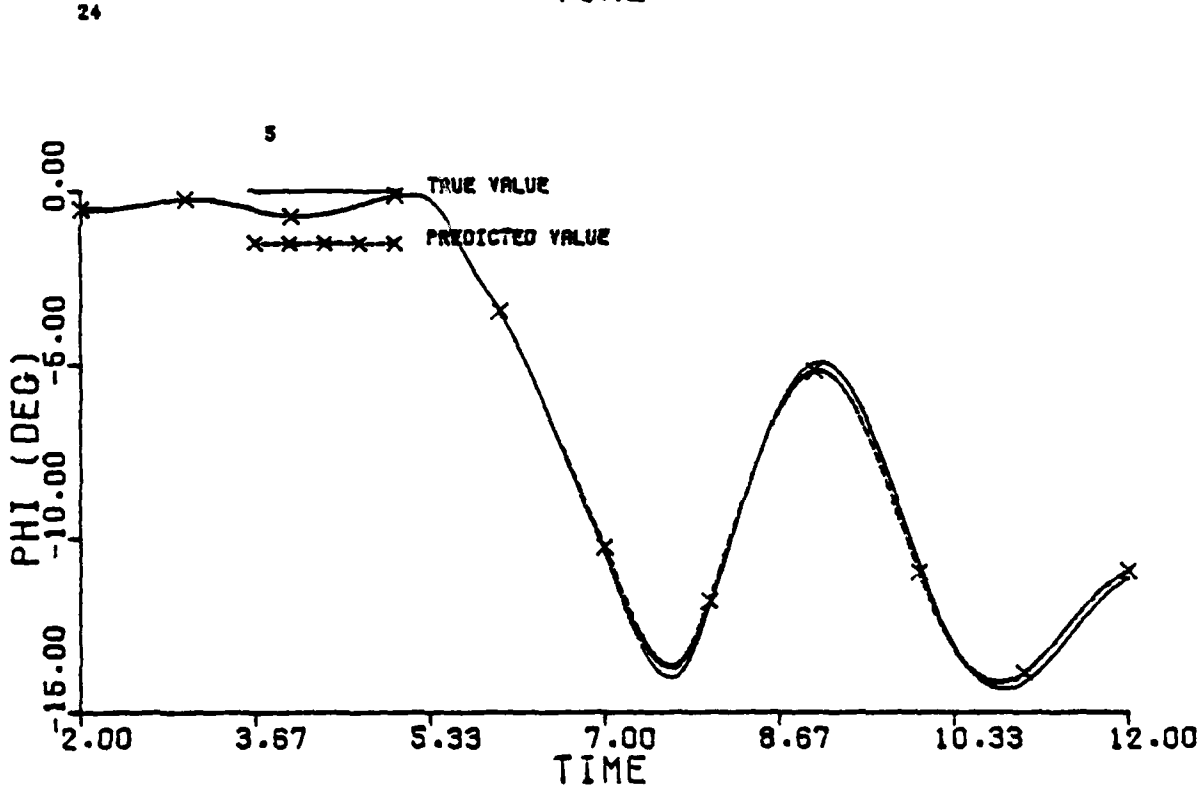

Figure G.1 Continued (Maneuver 5)

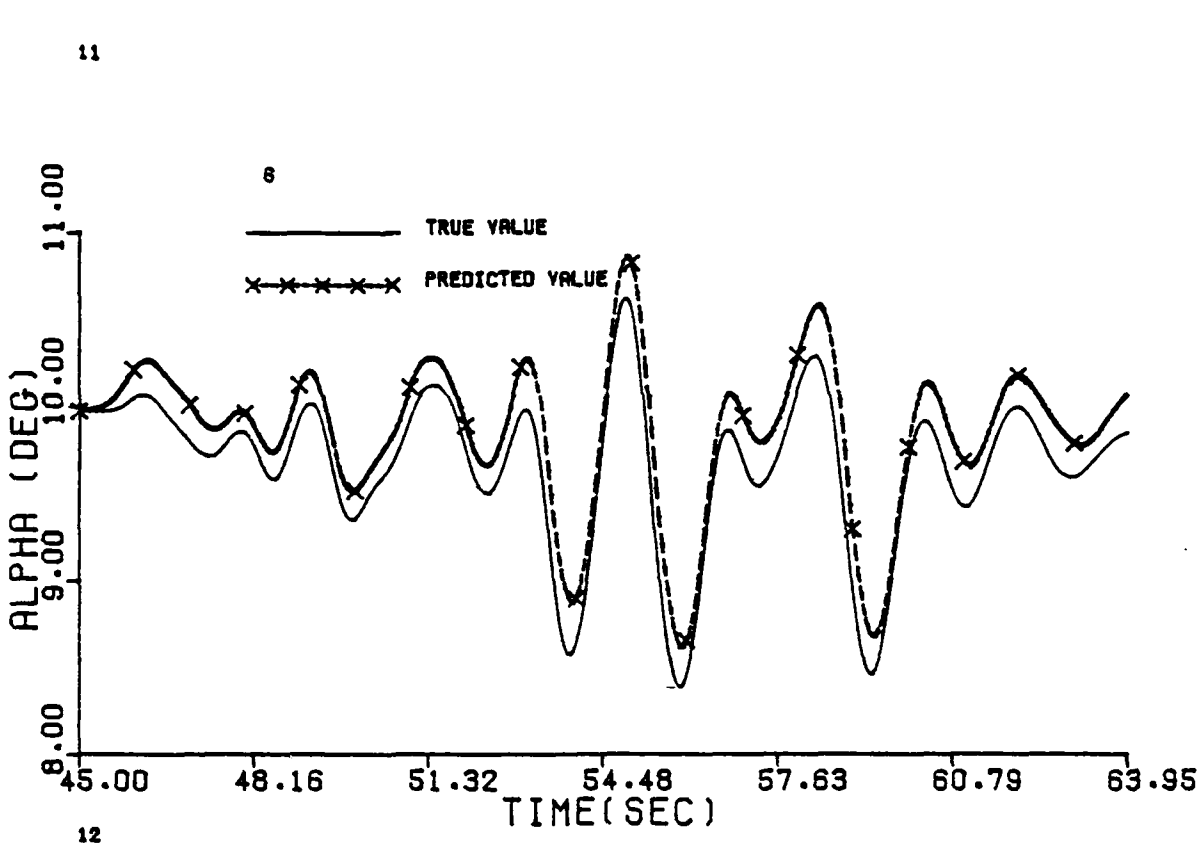

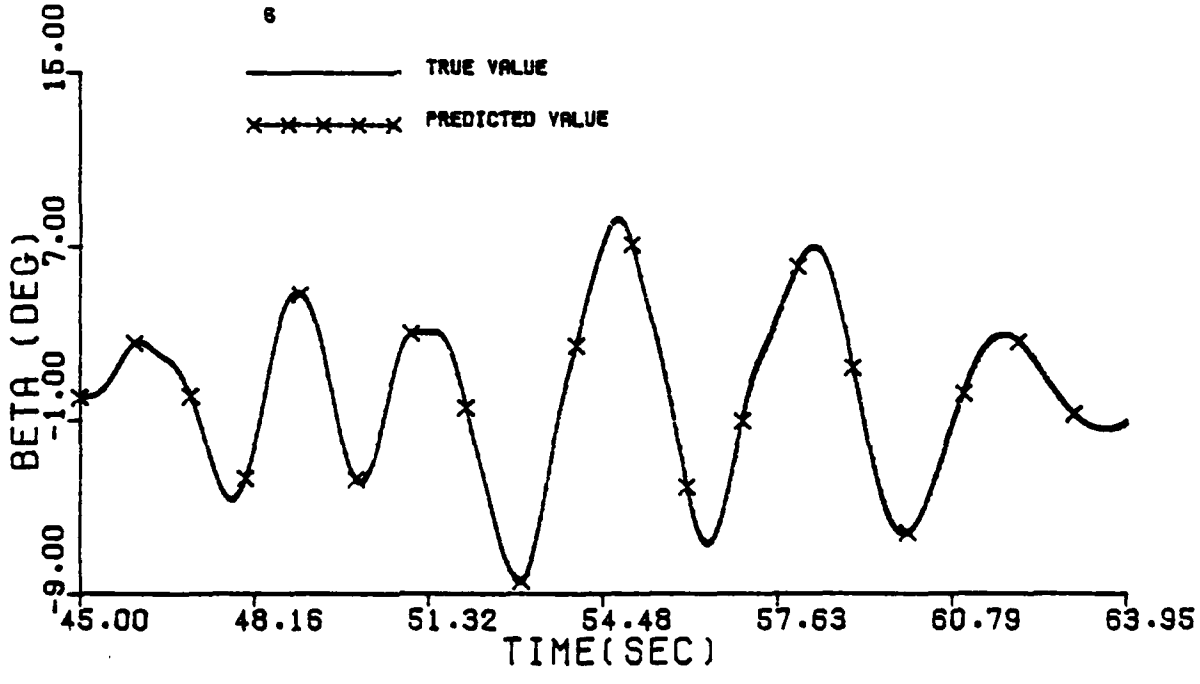

Figure G.1 Continued (Maneuver 6)

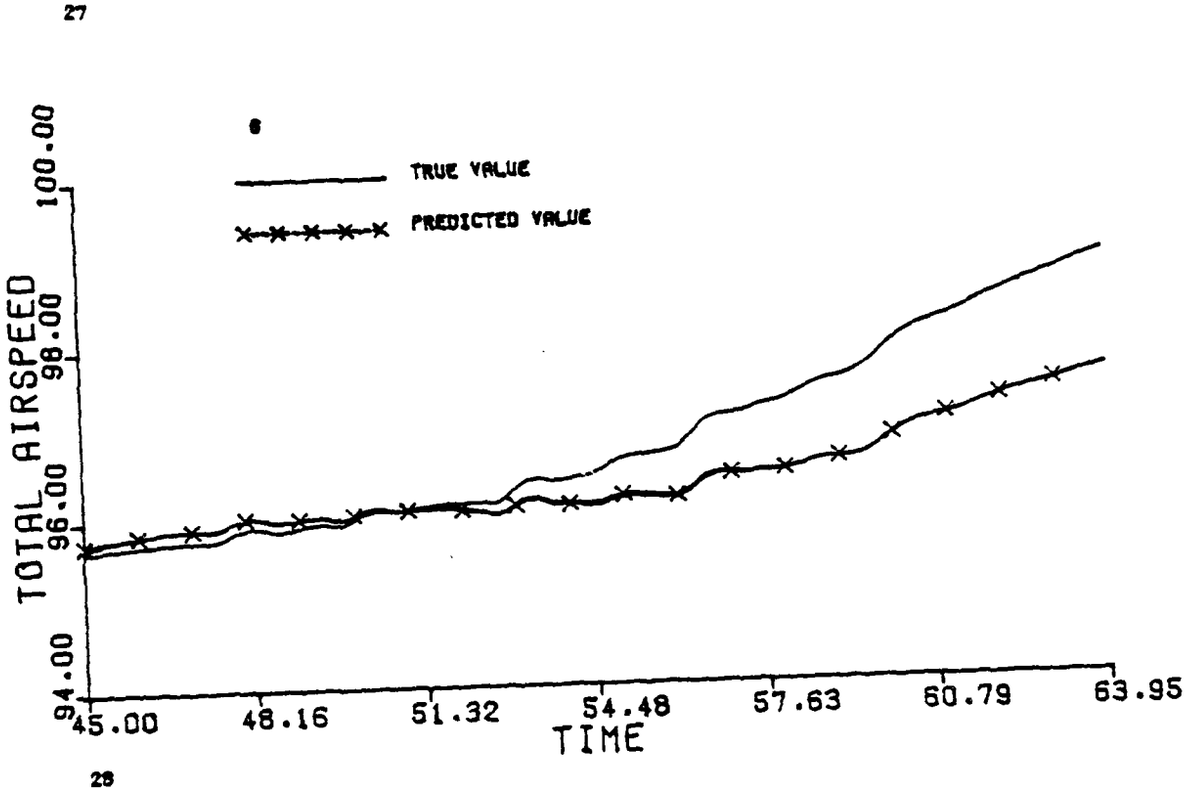

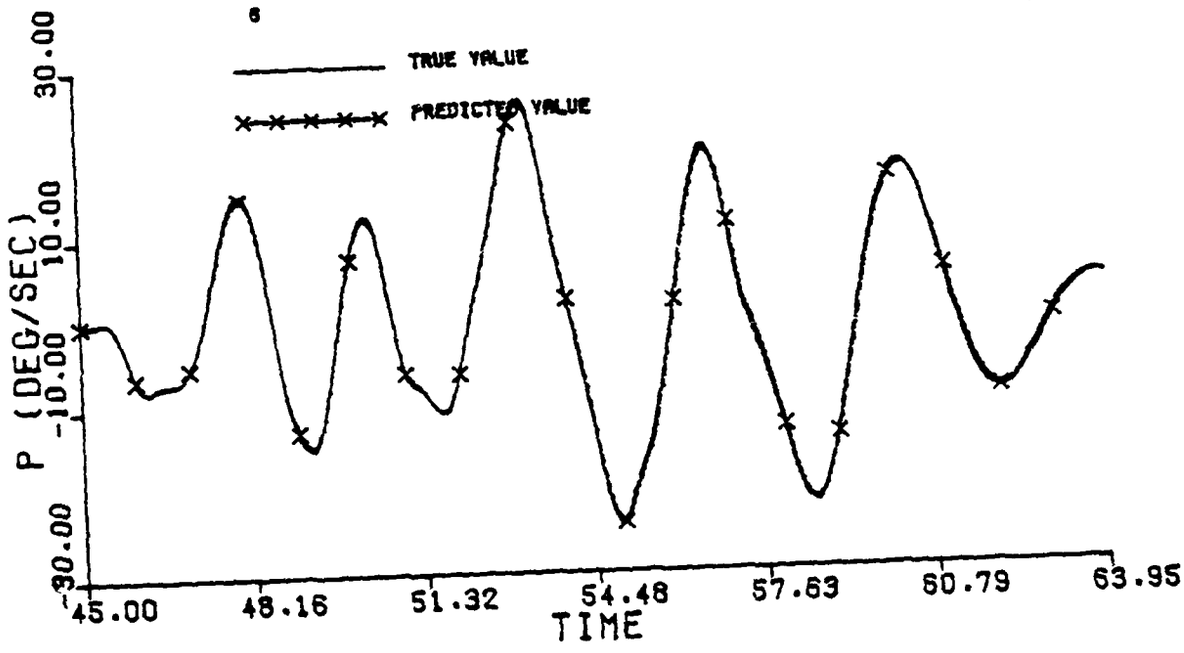

Figure G.1 Continued (Maneuver 6)

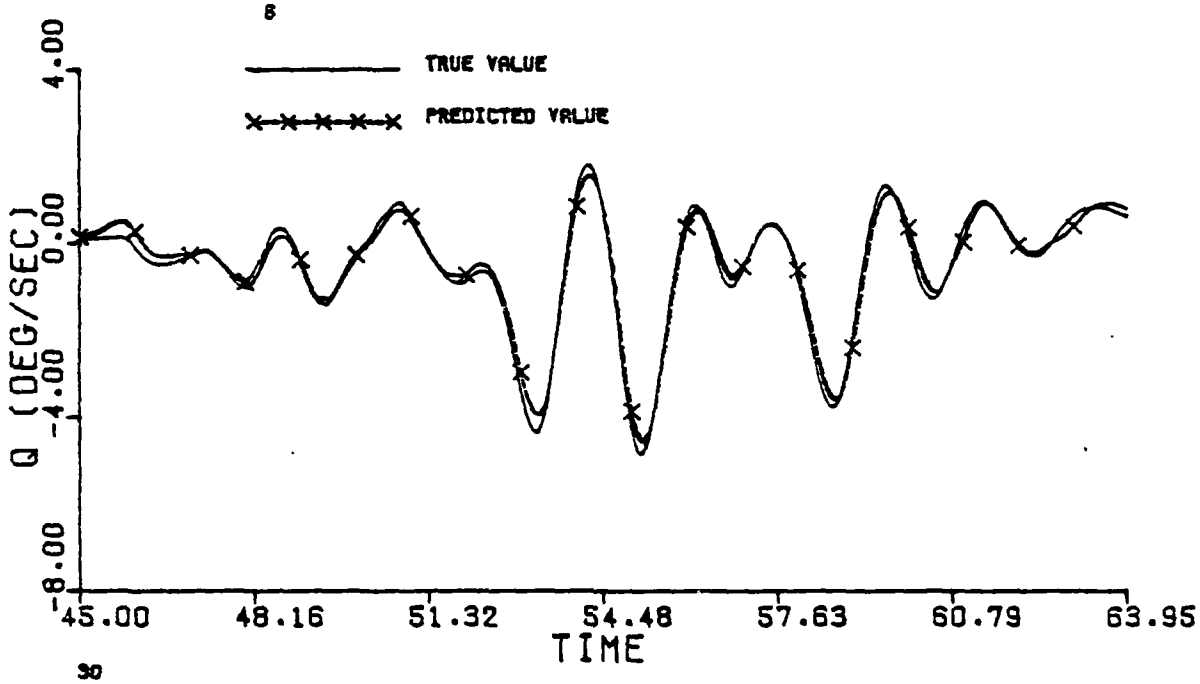

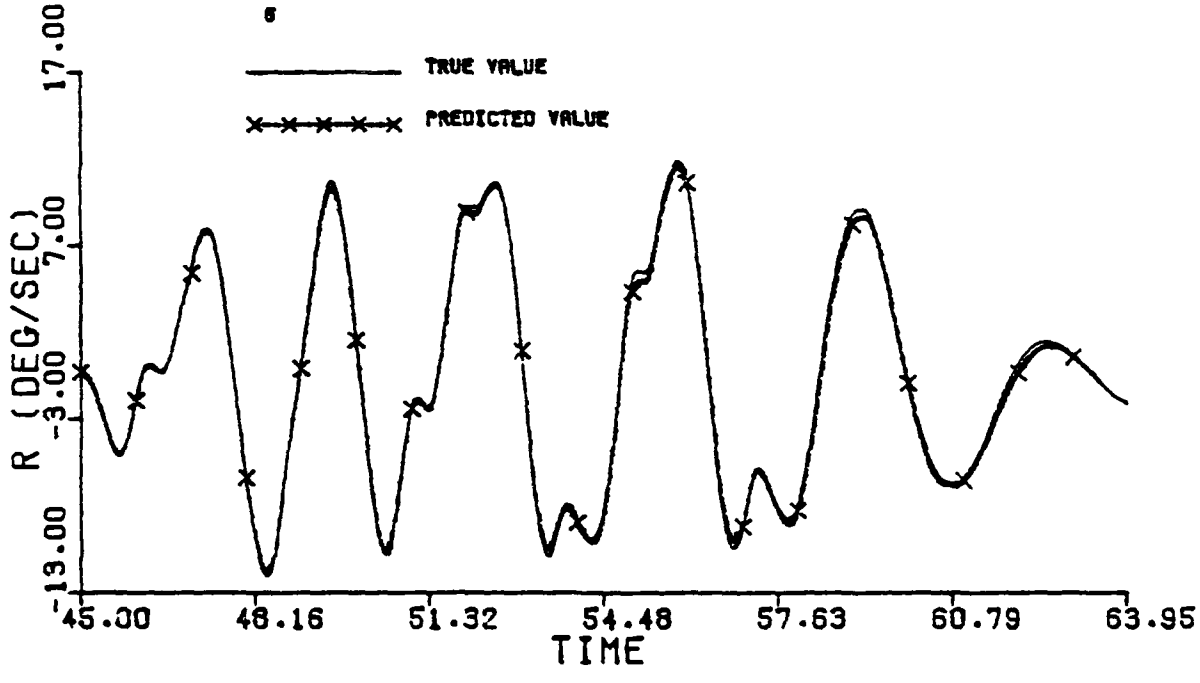

Figure G.1 Continued (Maneuver 6)

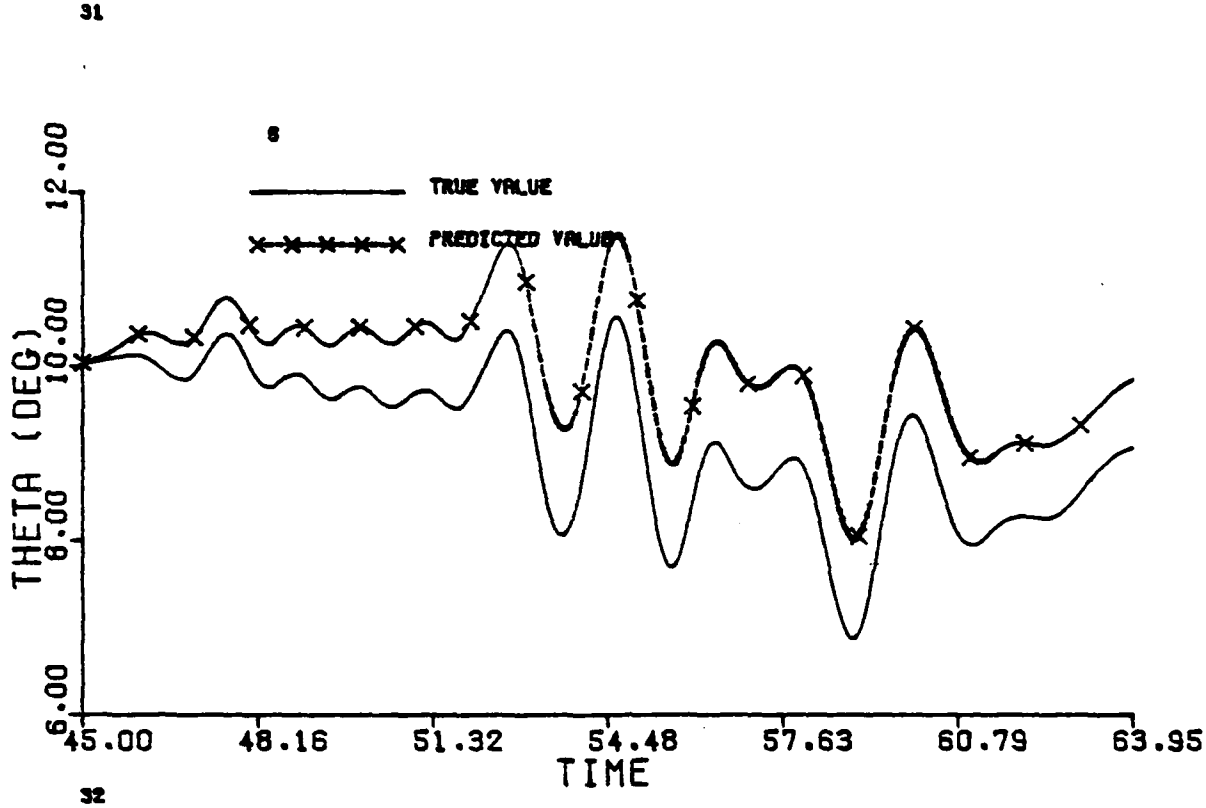

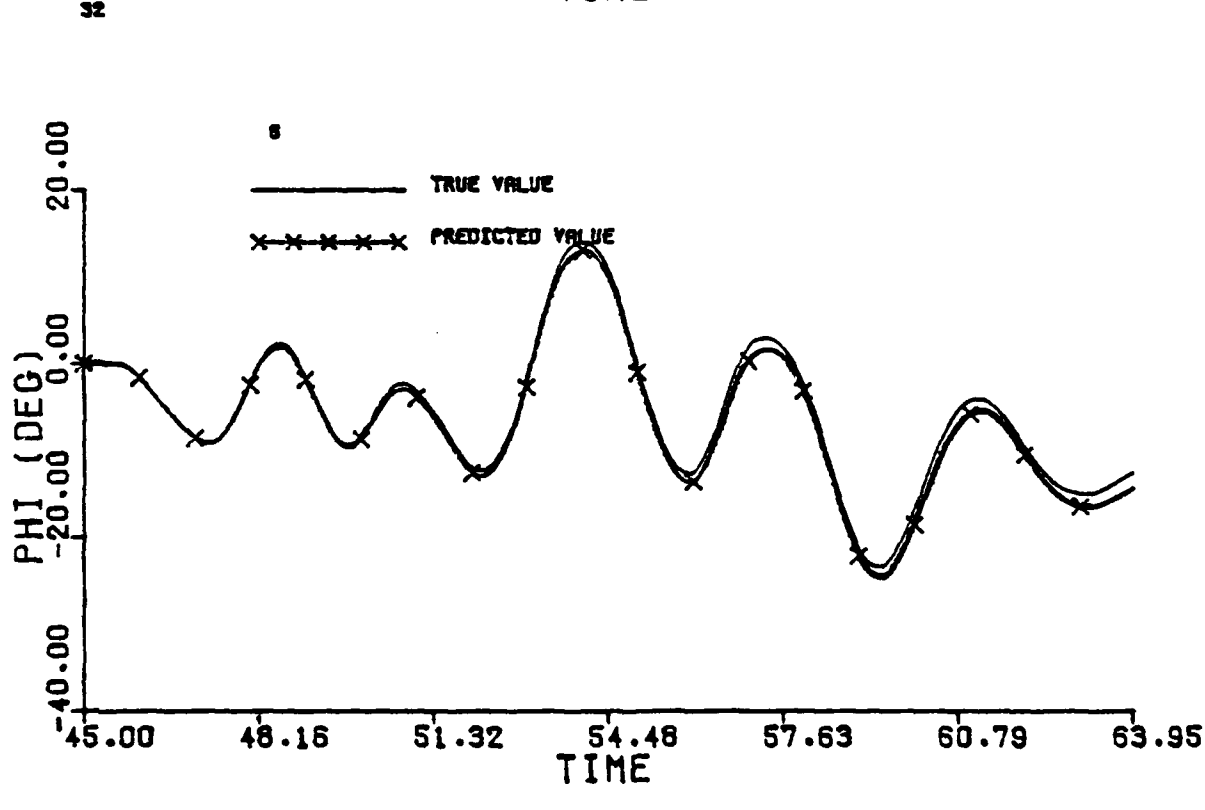

Figure G.1 Continued (Maneuver 6)

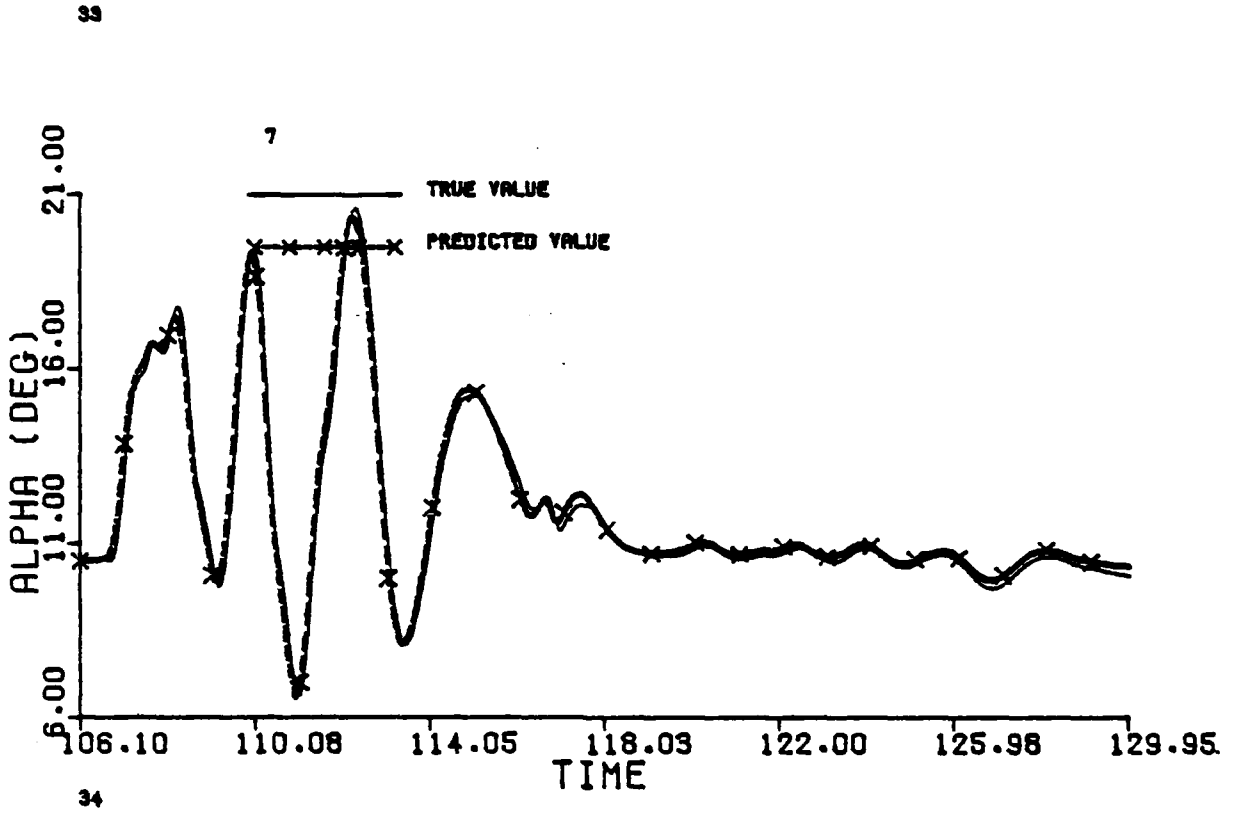

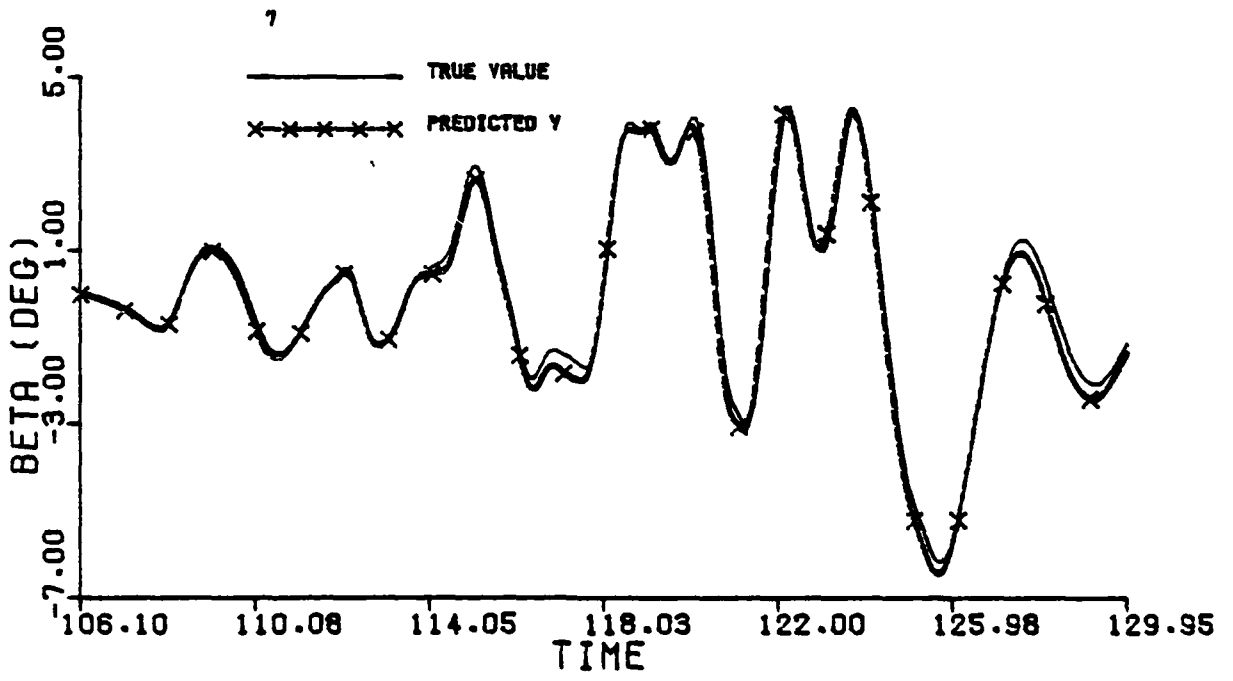

Figure G.1 Continued (Maneuver 7)

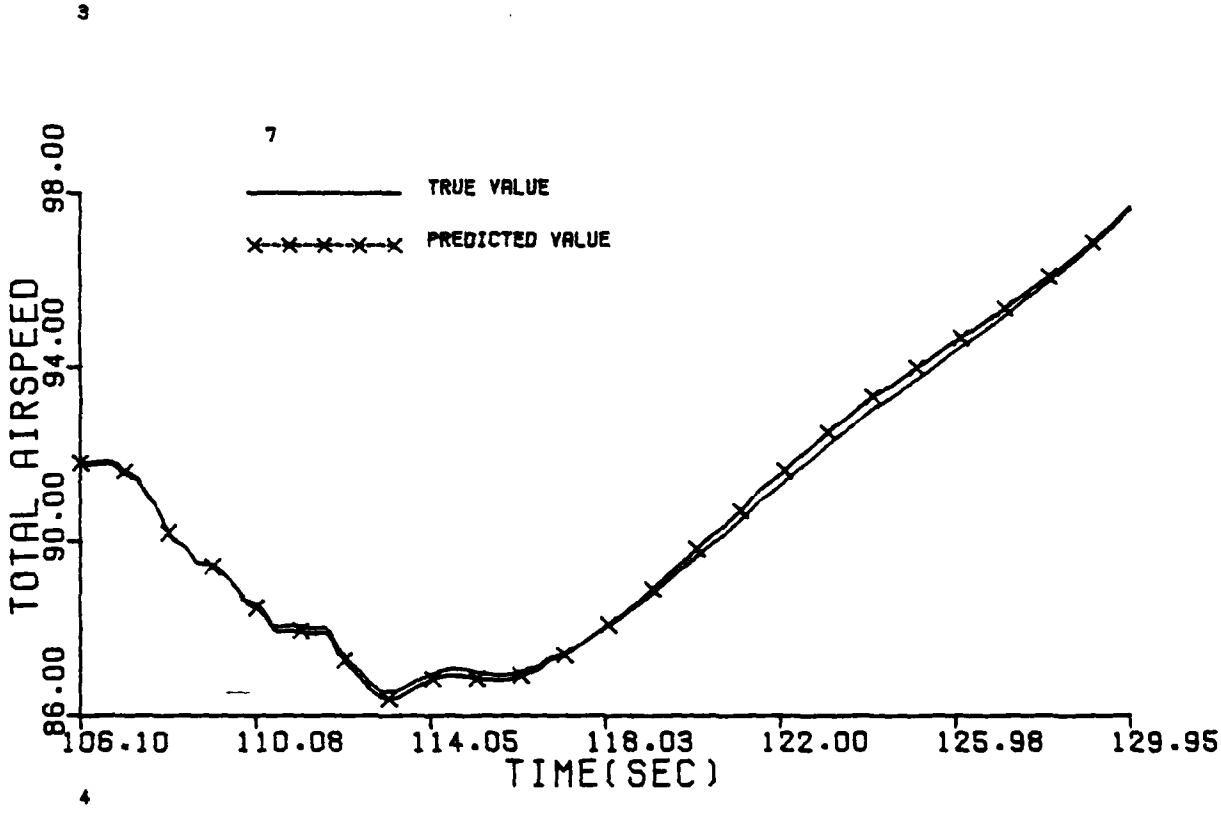

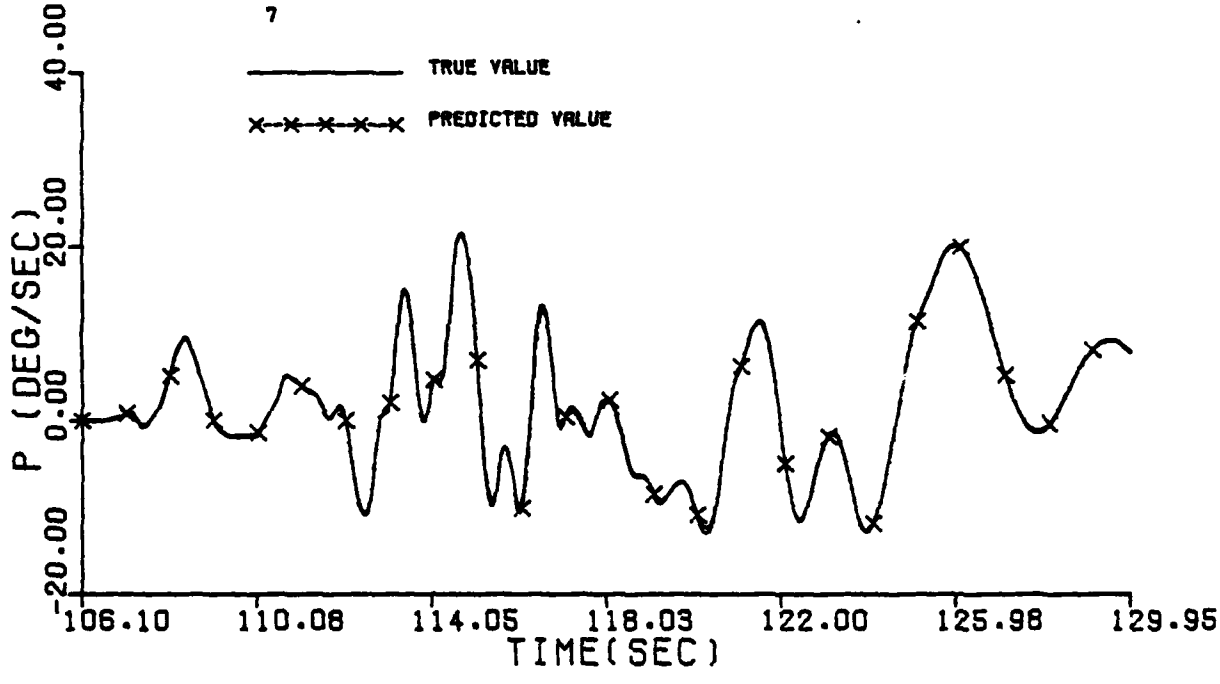

Figure G.1 Continued (Maneuver 7)

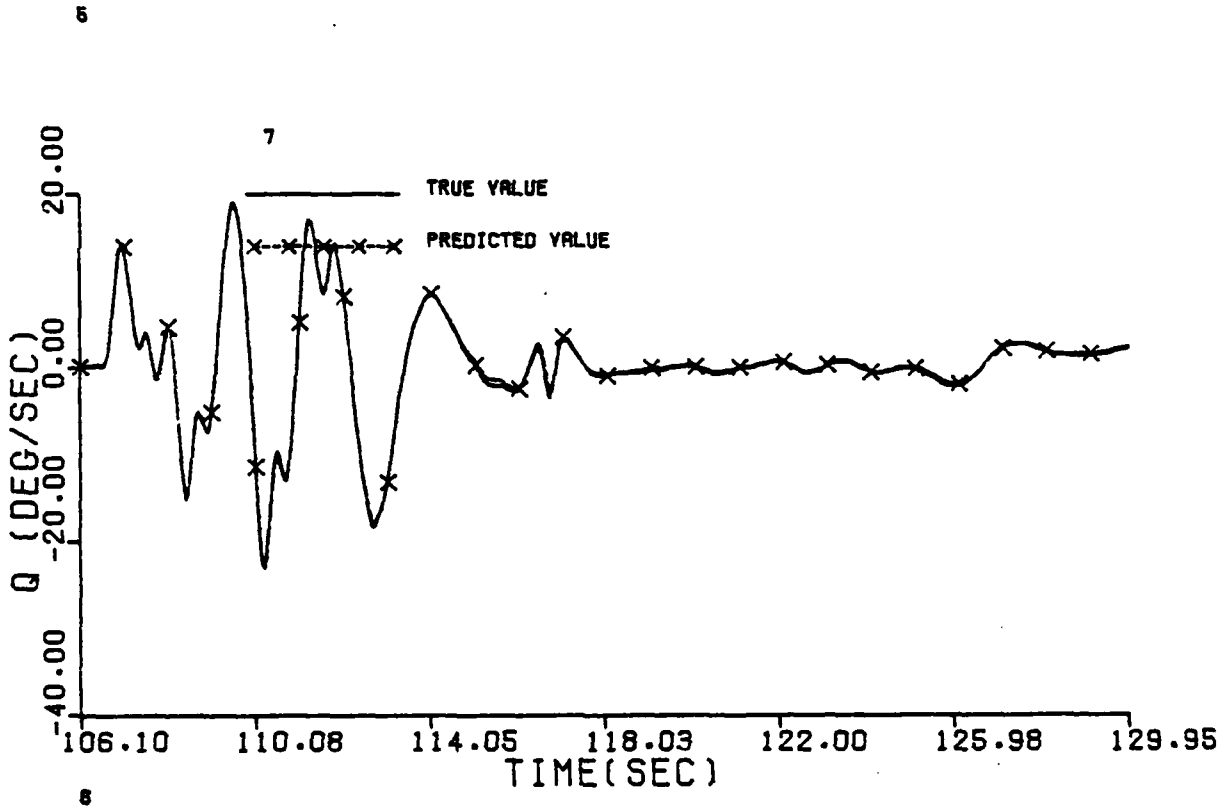

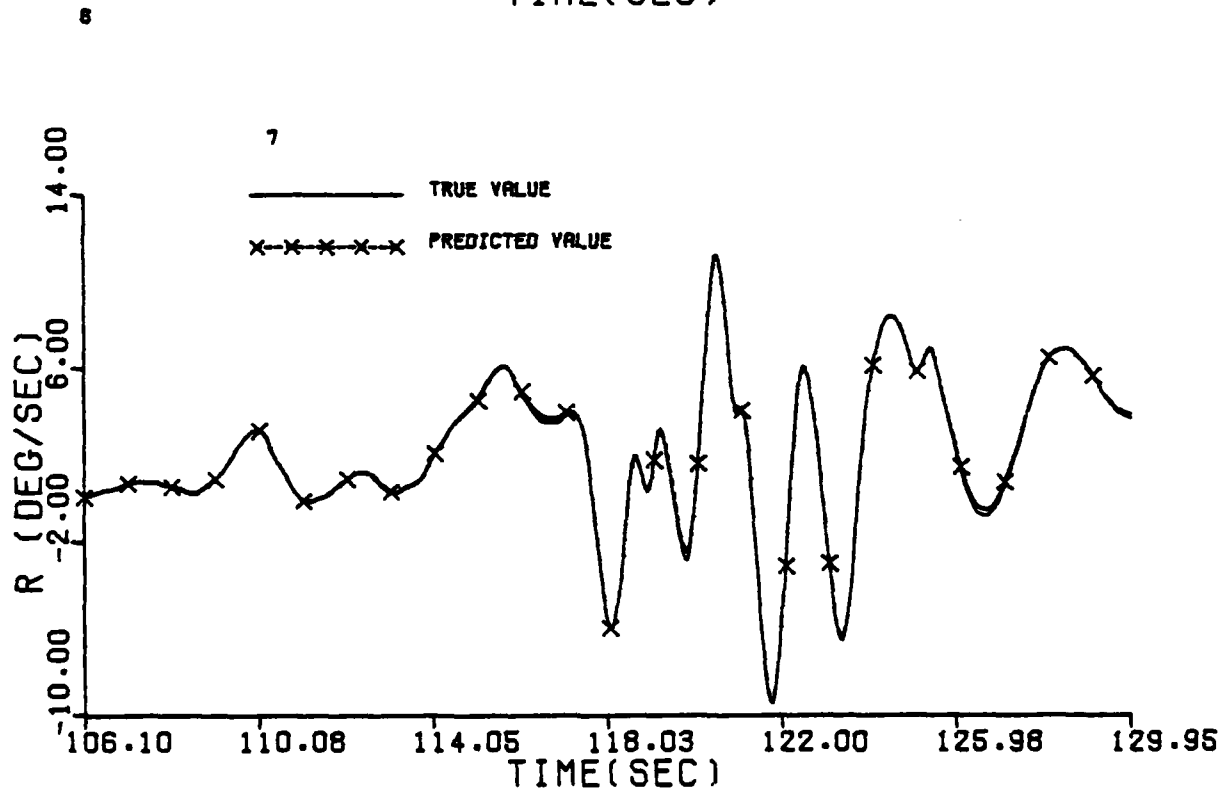

Figure G.1 Continued (Maneuver 7)

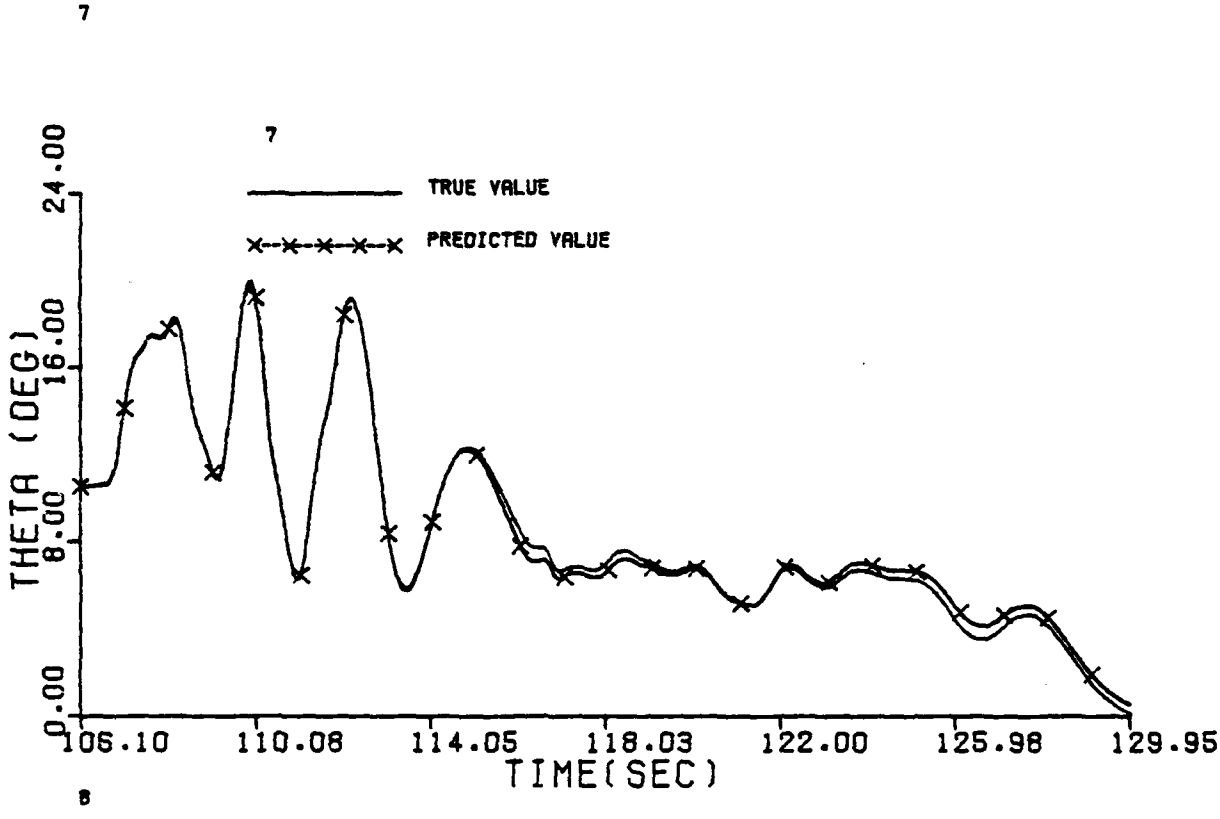

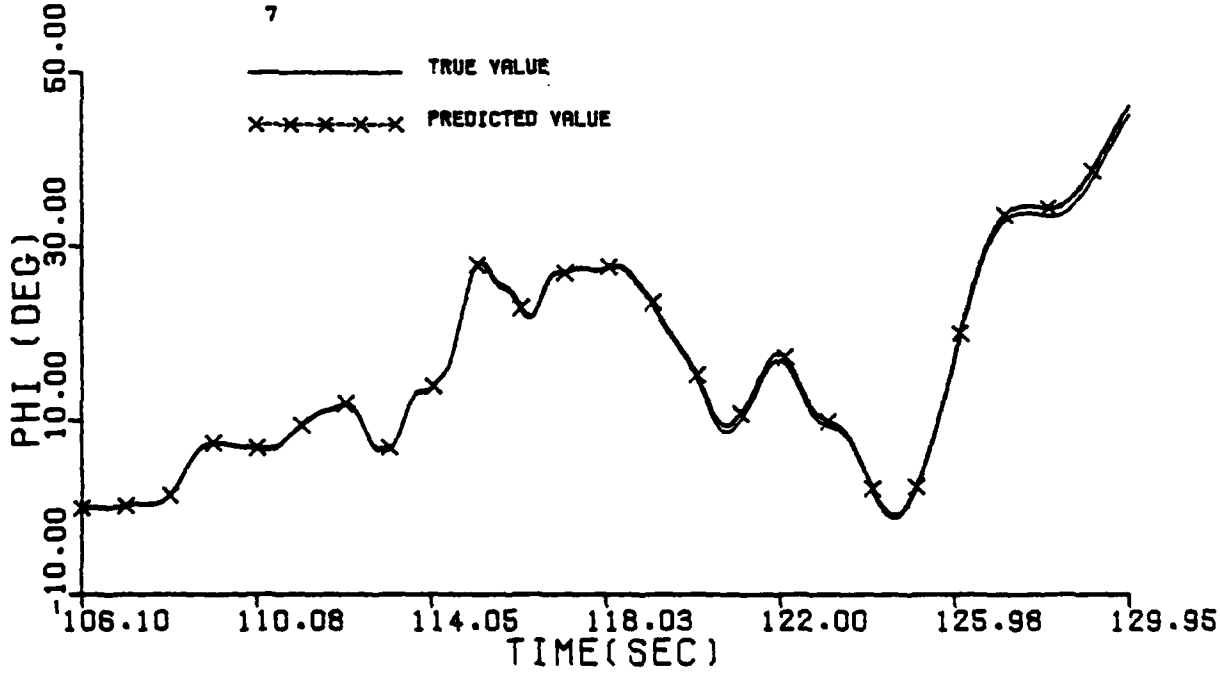

Figure G.1 Continued (Maneuver 7)

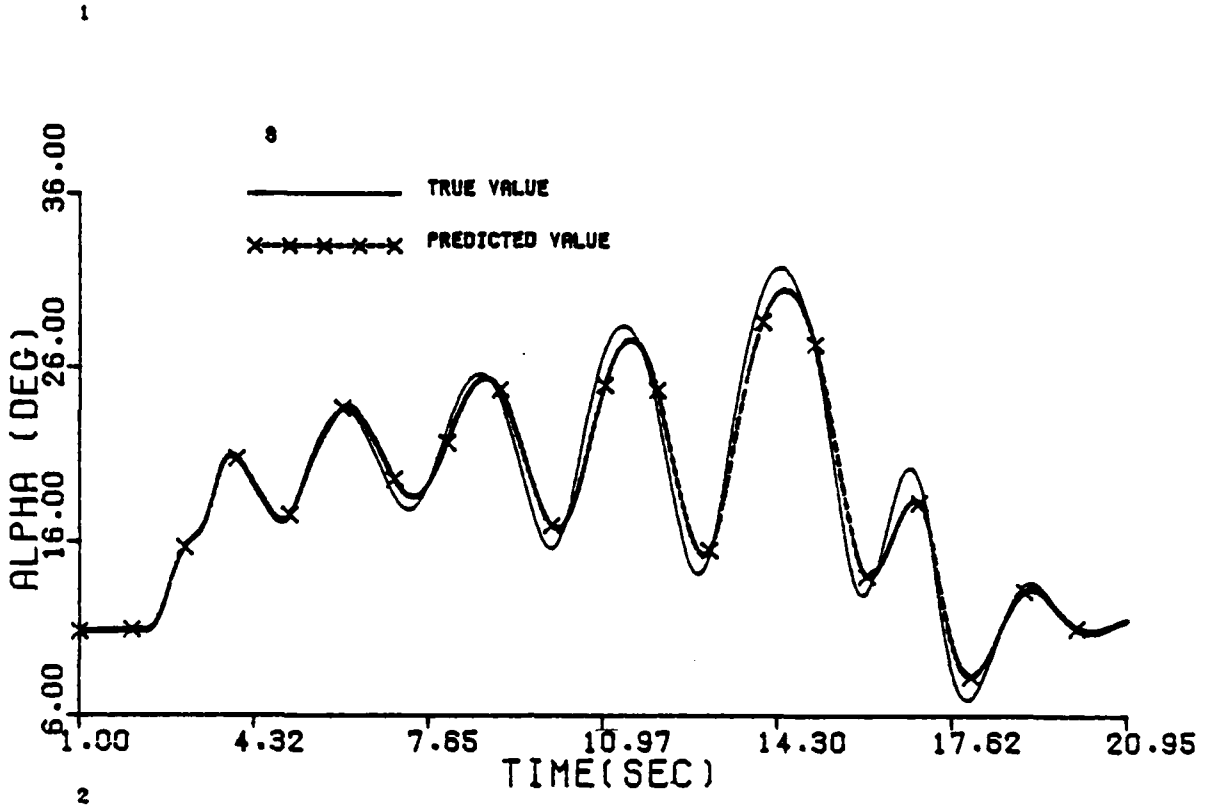

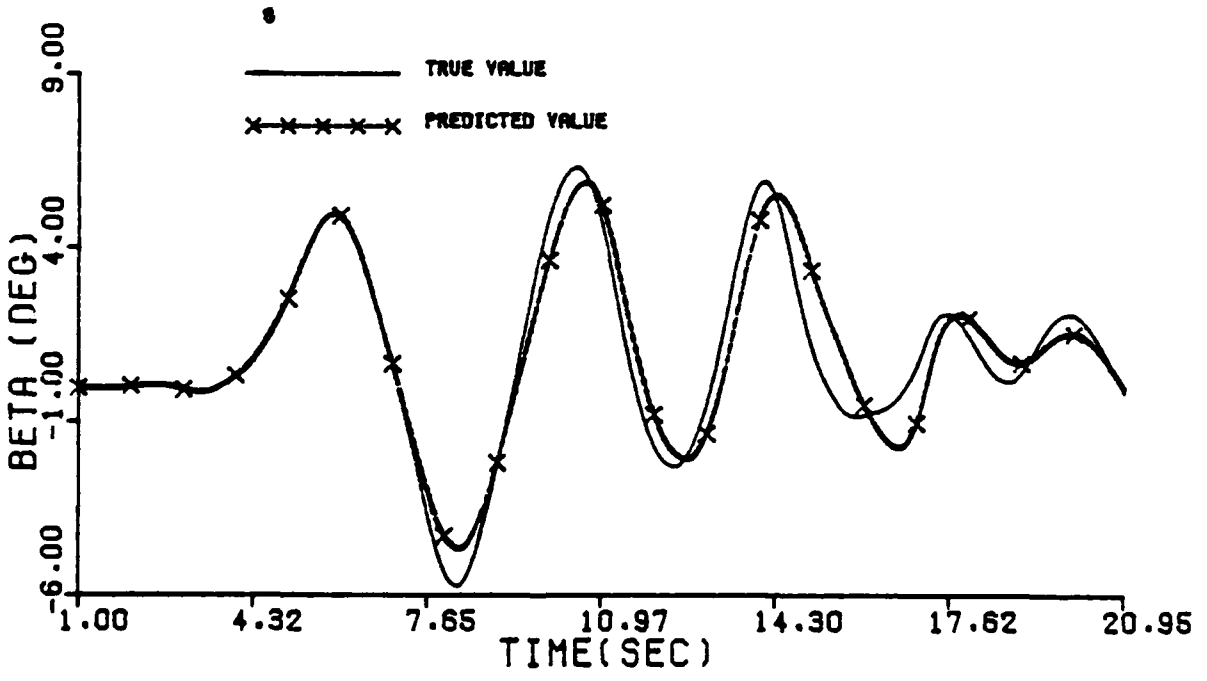

Figure G.1 Continued (Maneuver 8)

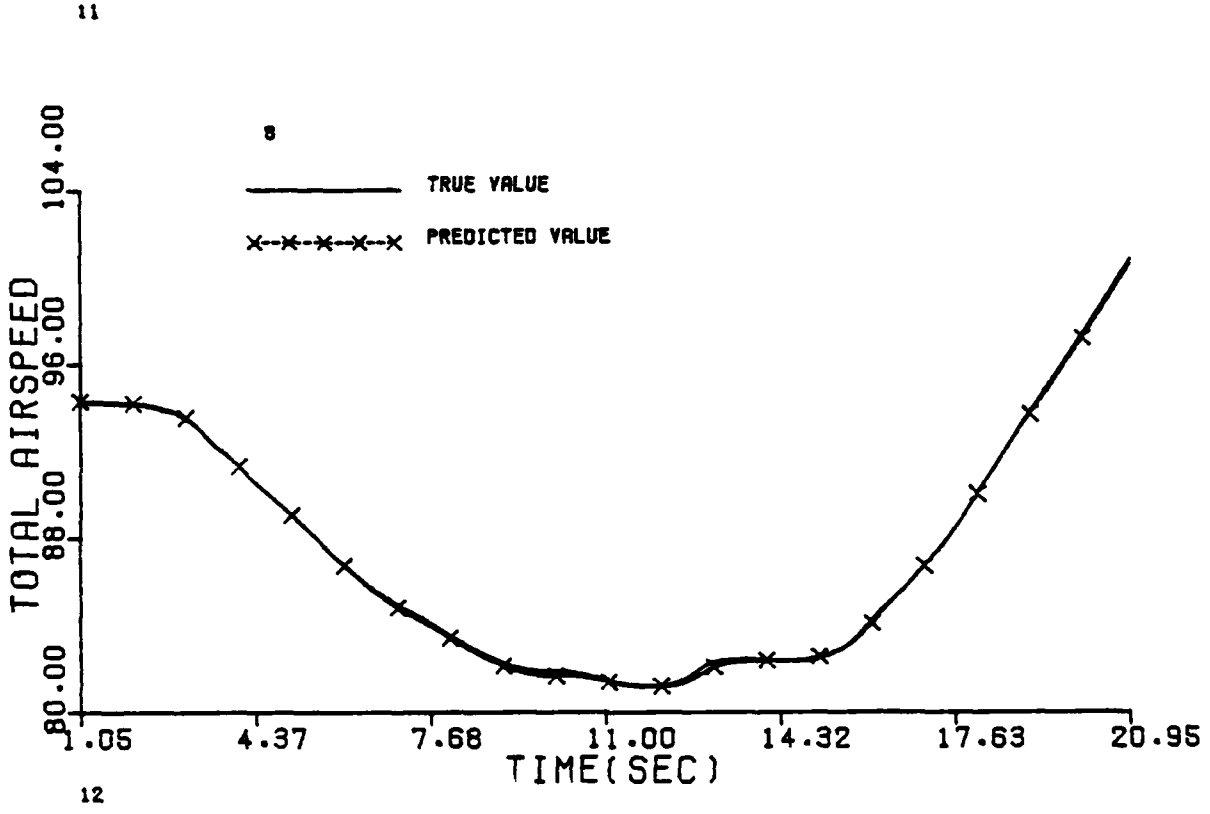

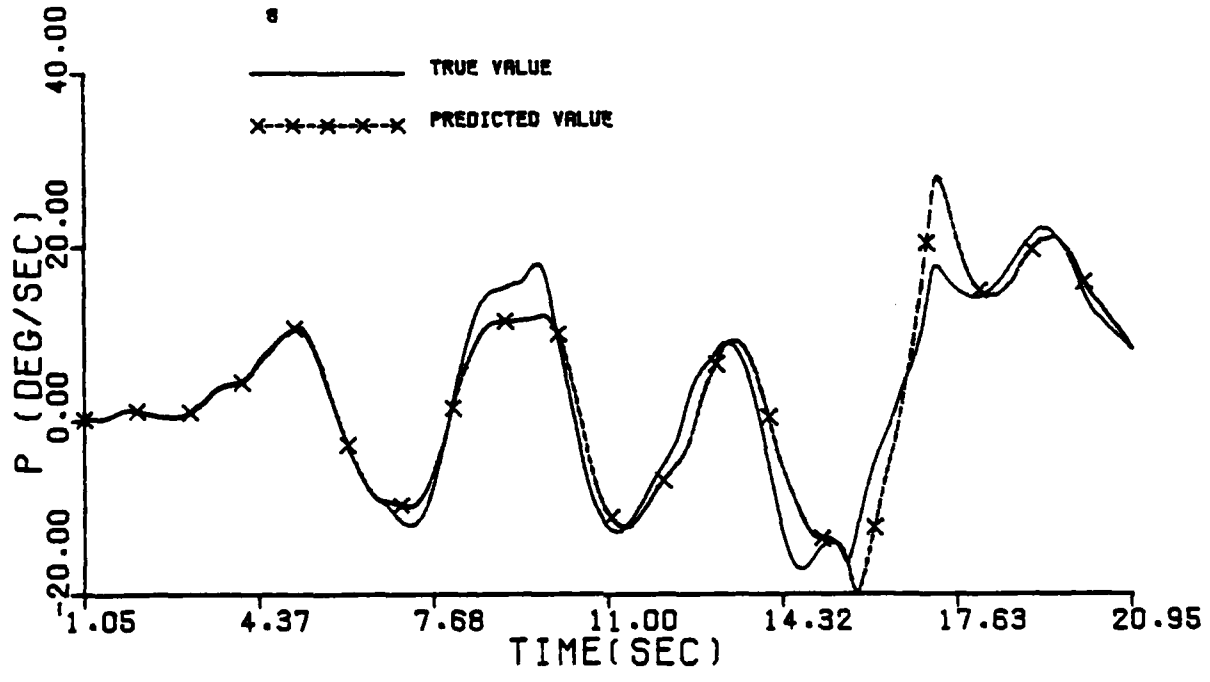

Figure G.1 Continued (Maneuver 8)

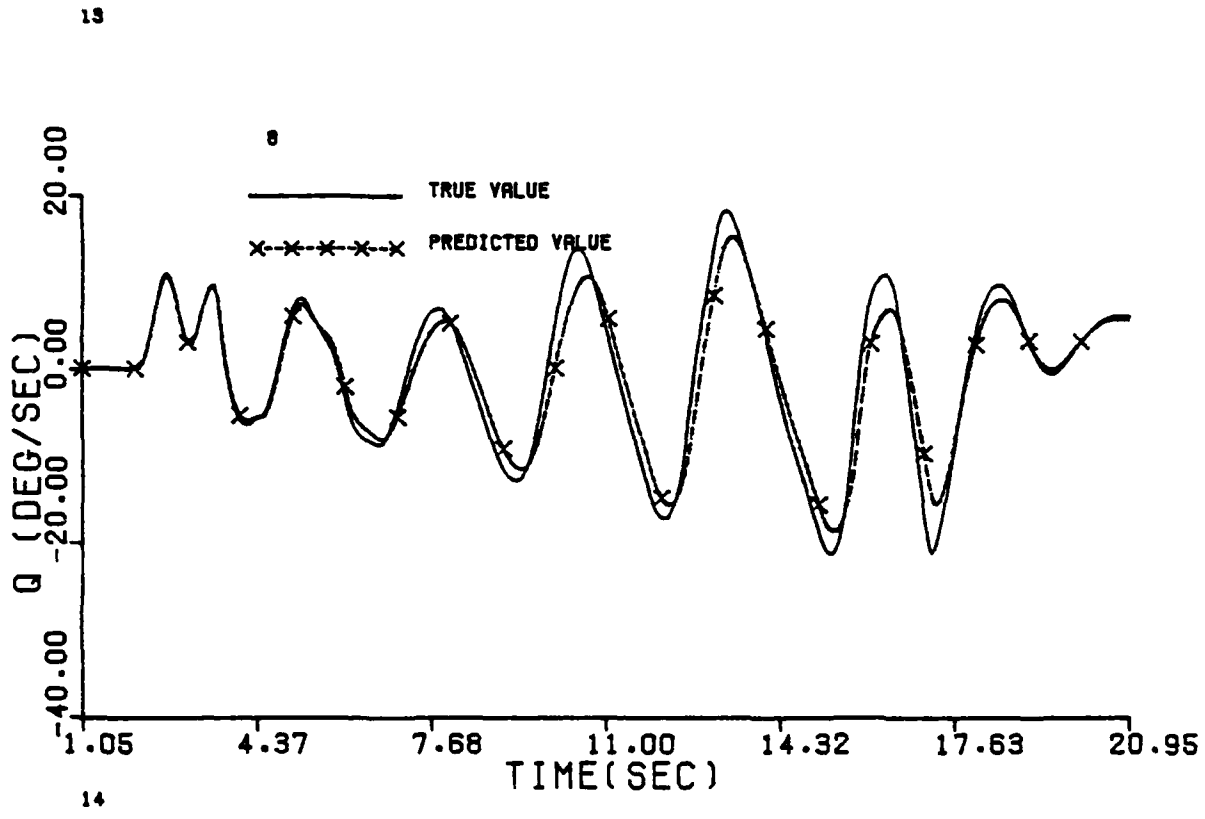

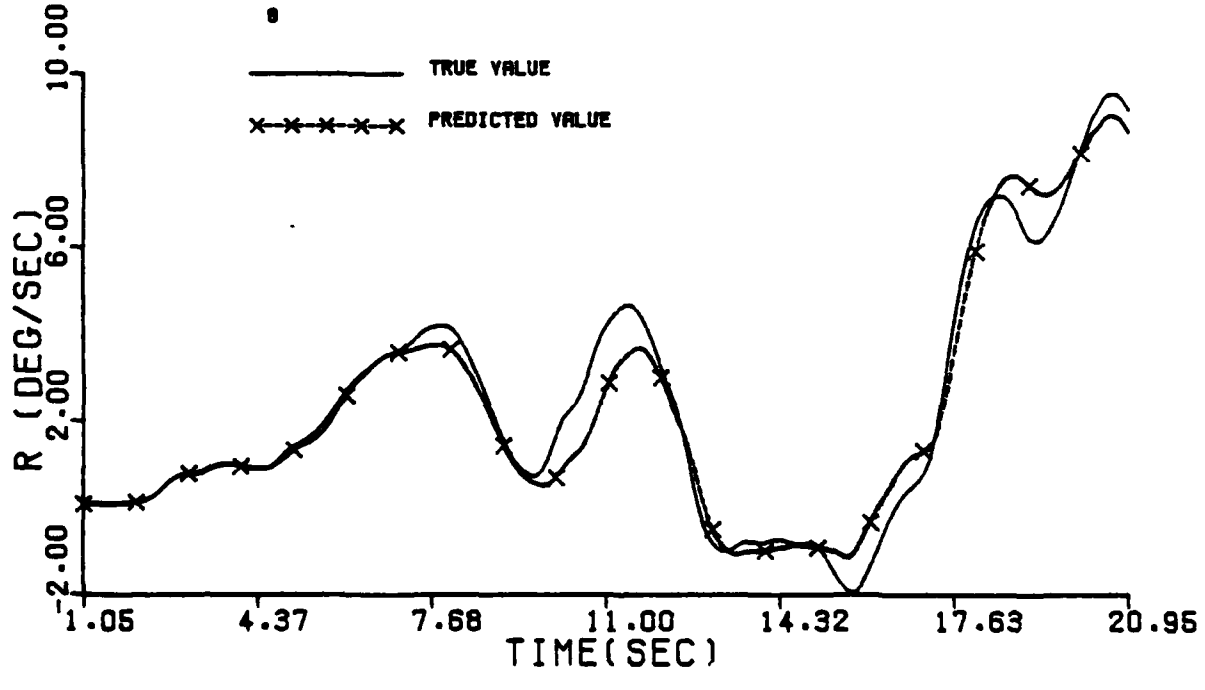

Figure G.1 Continued (Maneuver 8)

15

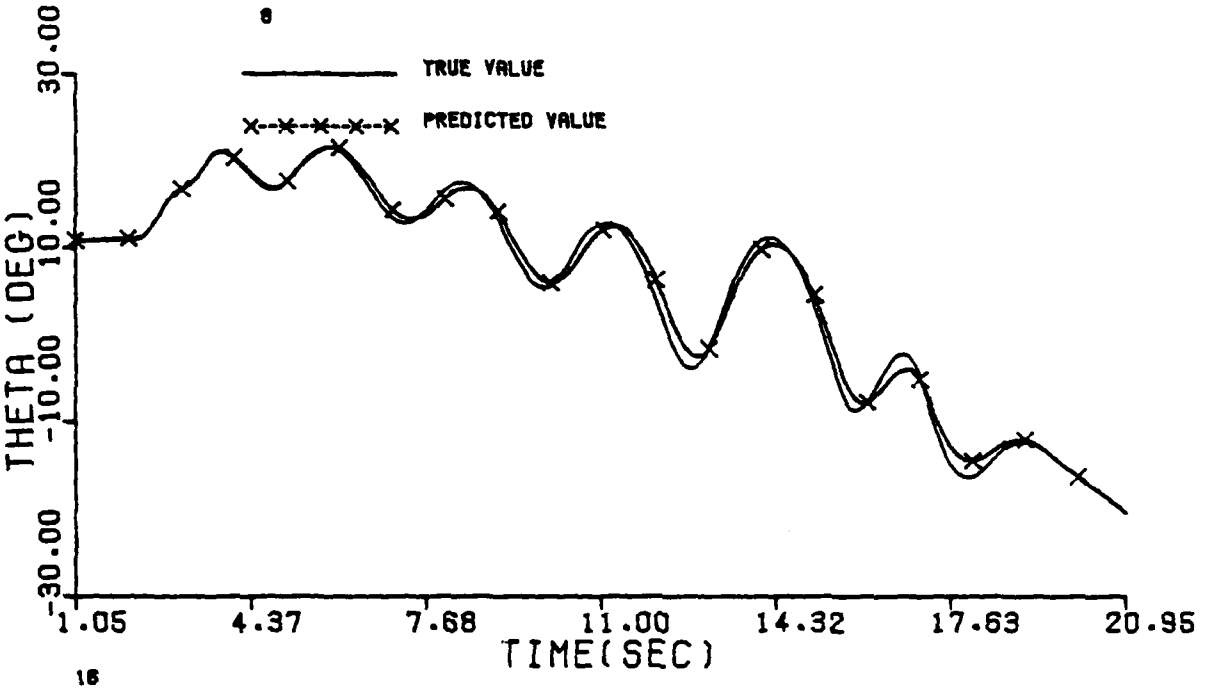

16

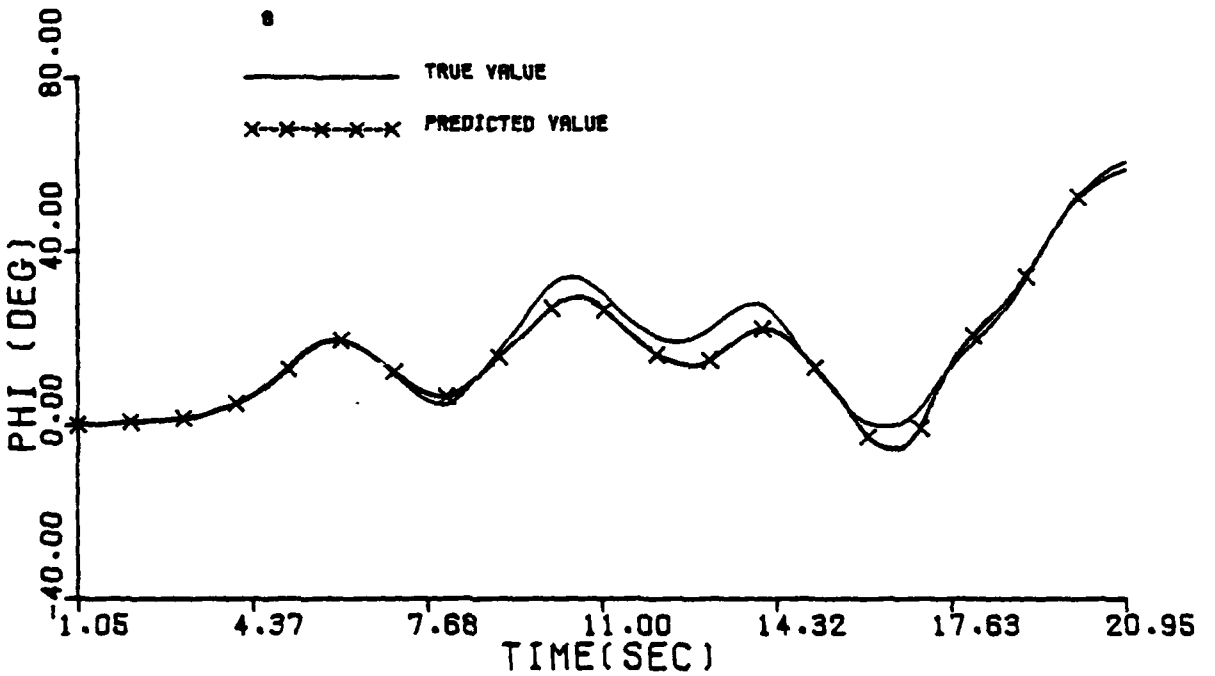

Figure G.1 Continued (Maneuver 8)

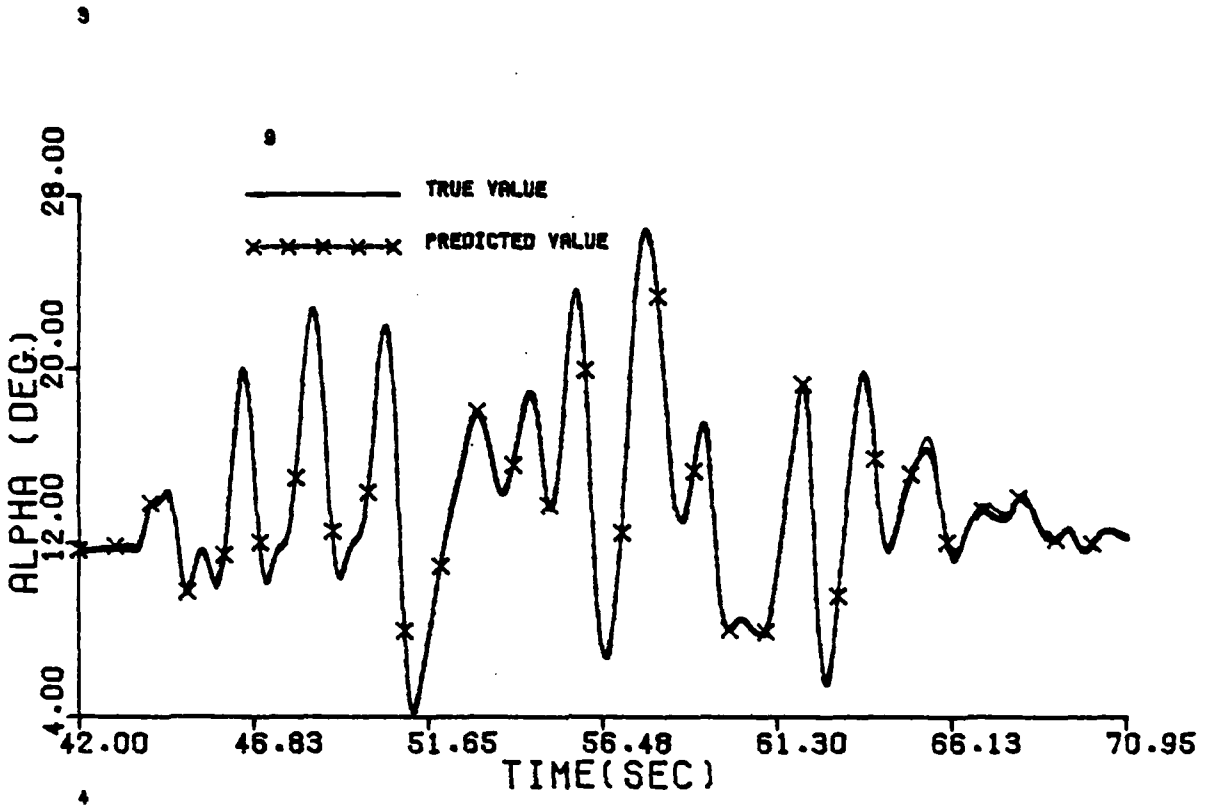

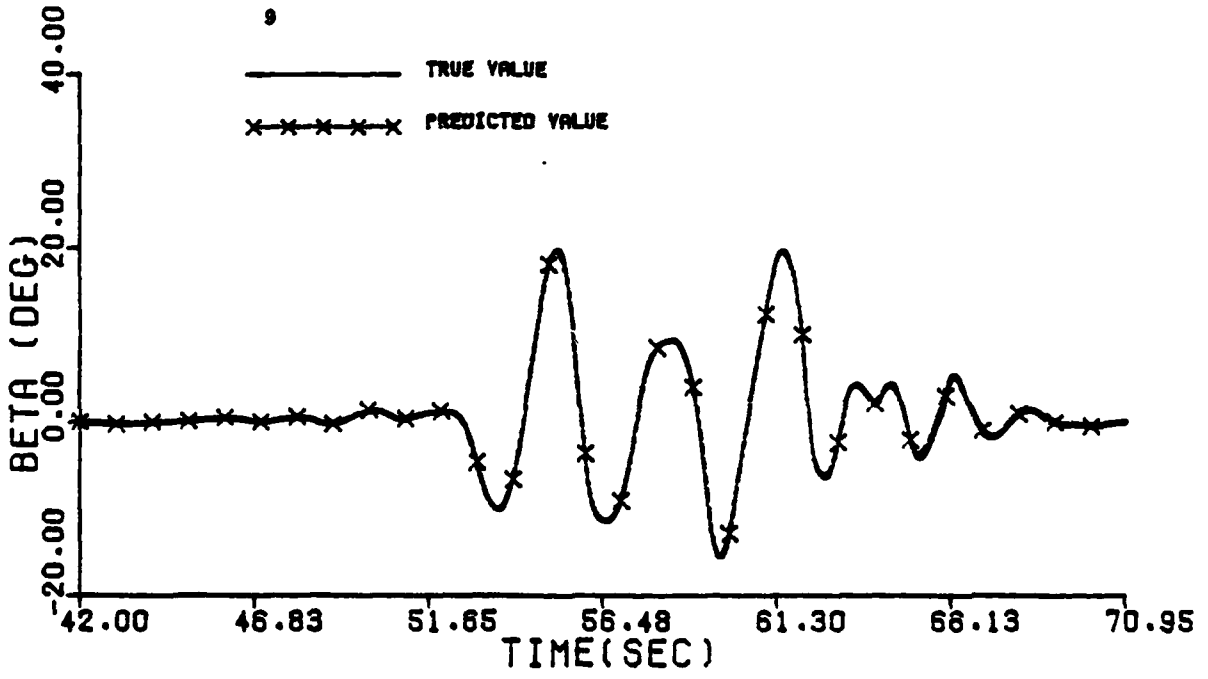

Figure G.1 Continued (Maneuver 9)

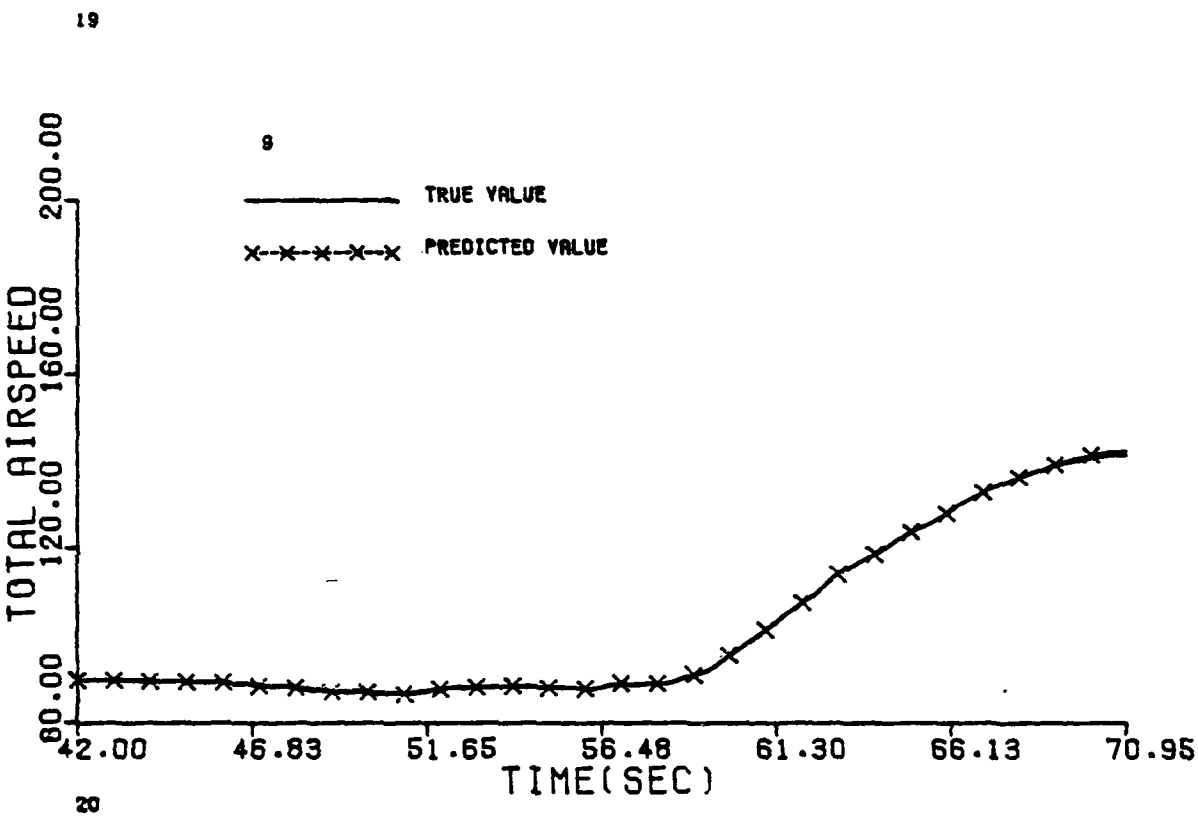

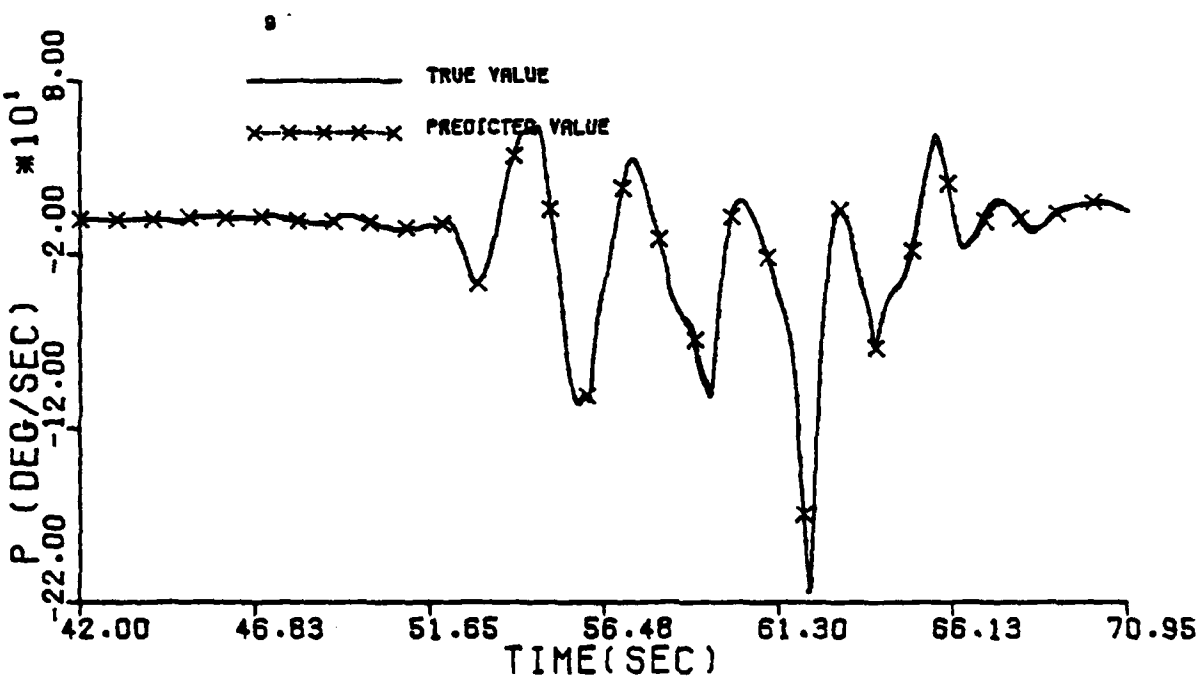

Figure G.1 Continued (Maneuver 9)

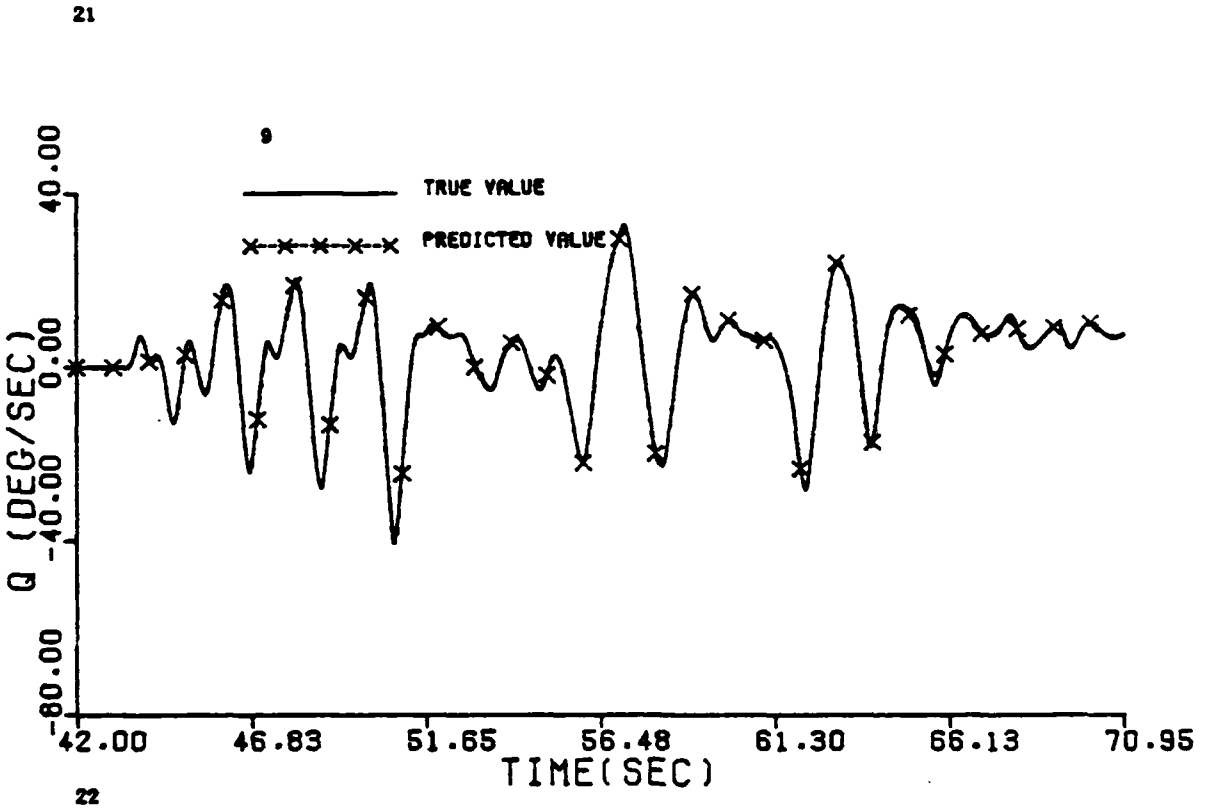

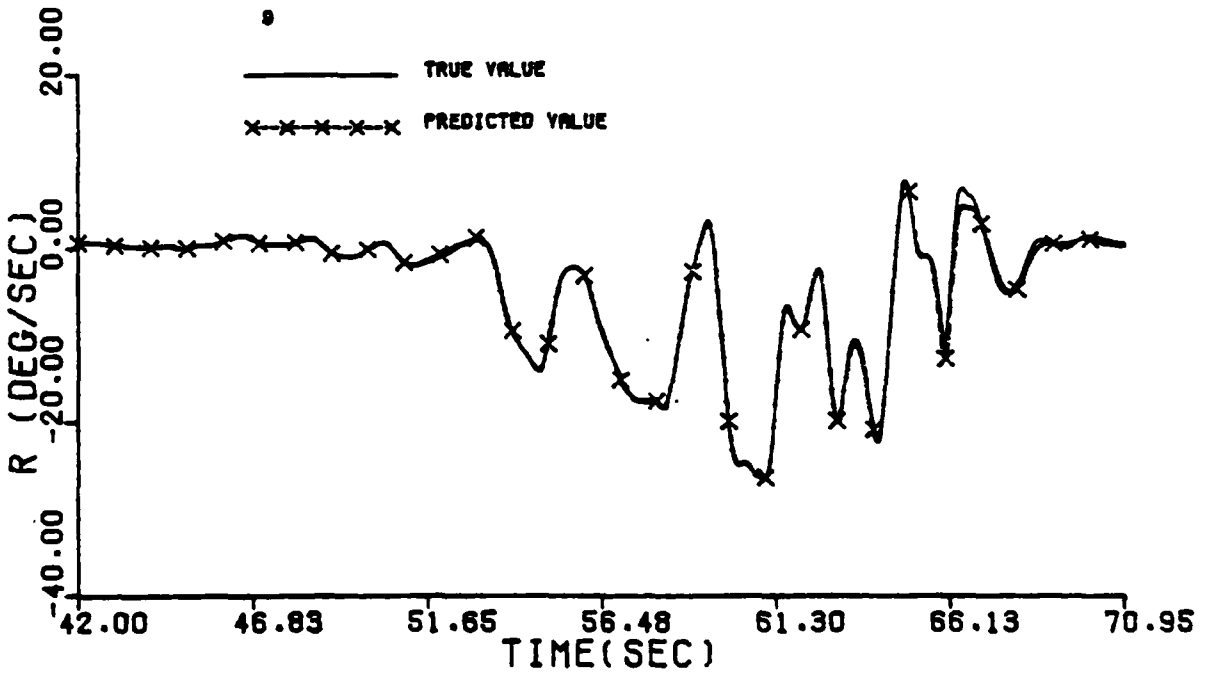

Figure G.1 Continued (Maneuver 9)

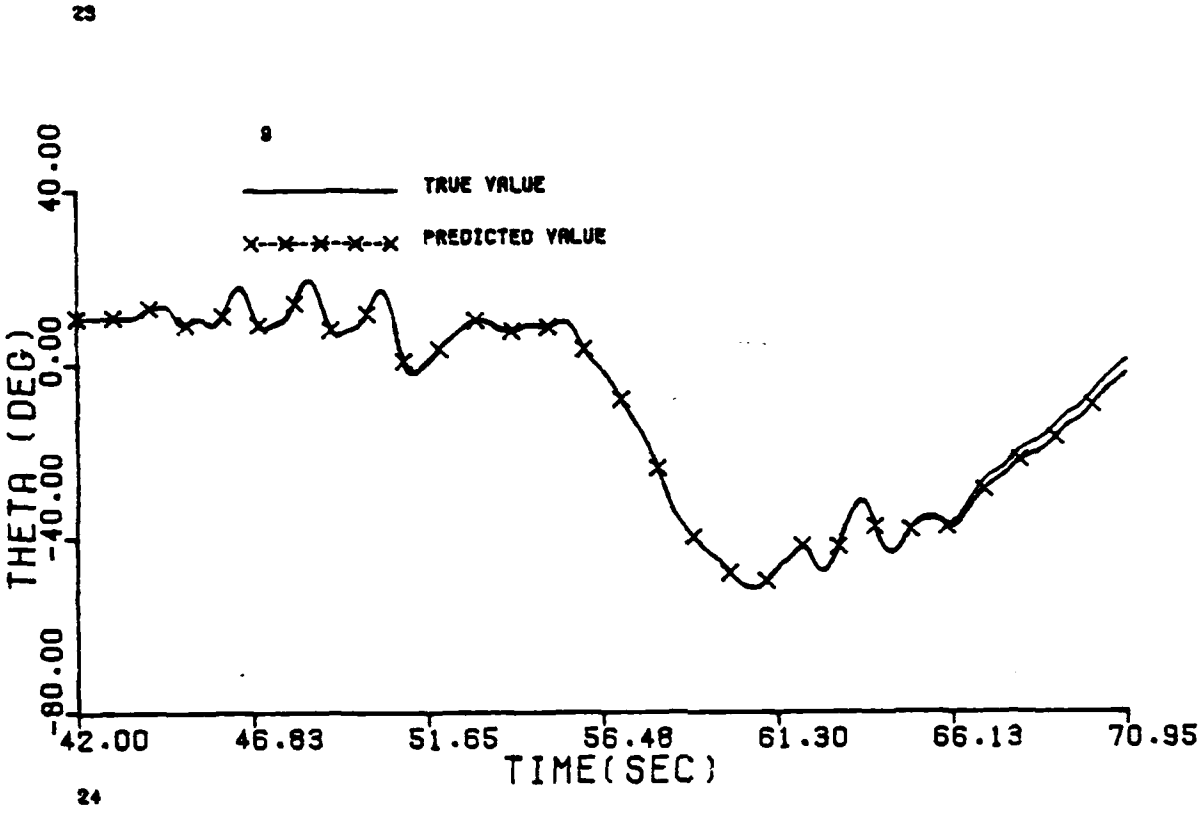

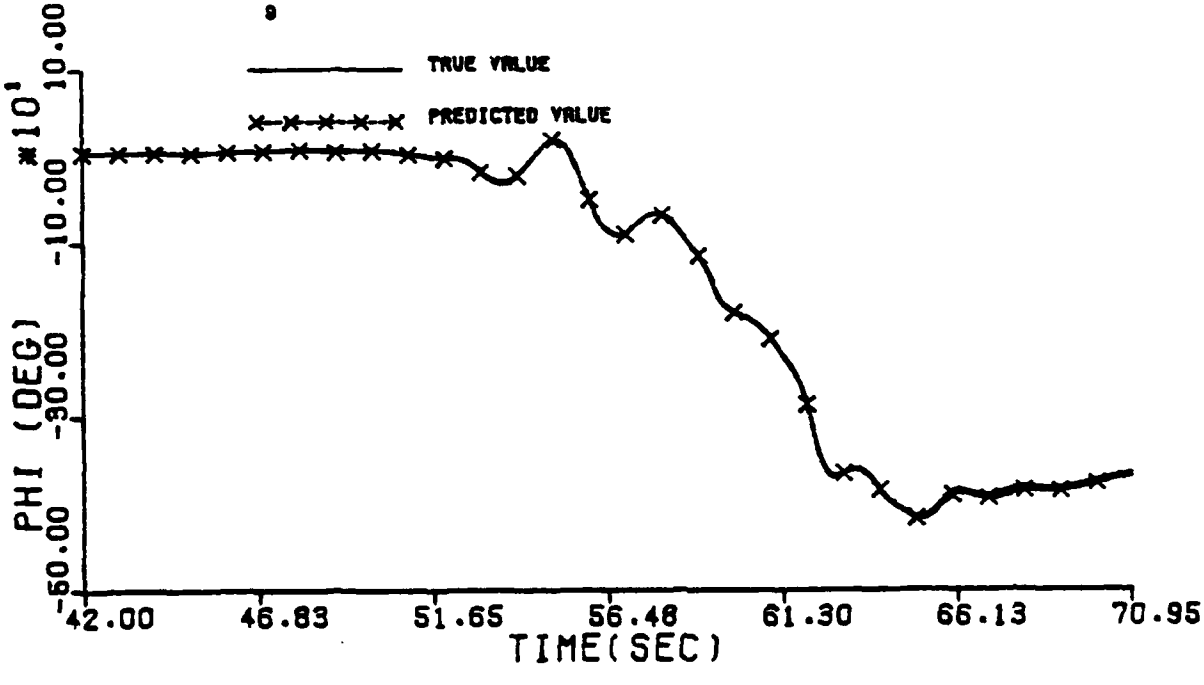

Figure G.1 Continued (Maneuver 9)

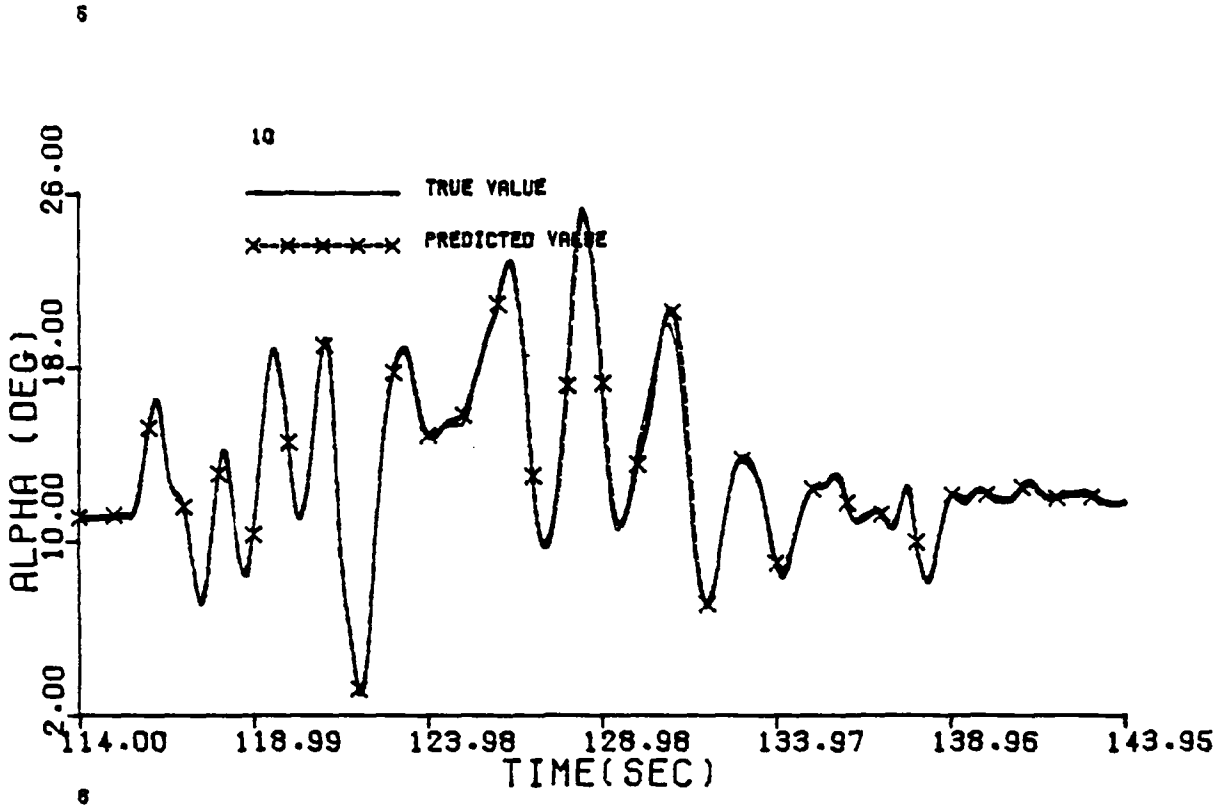

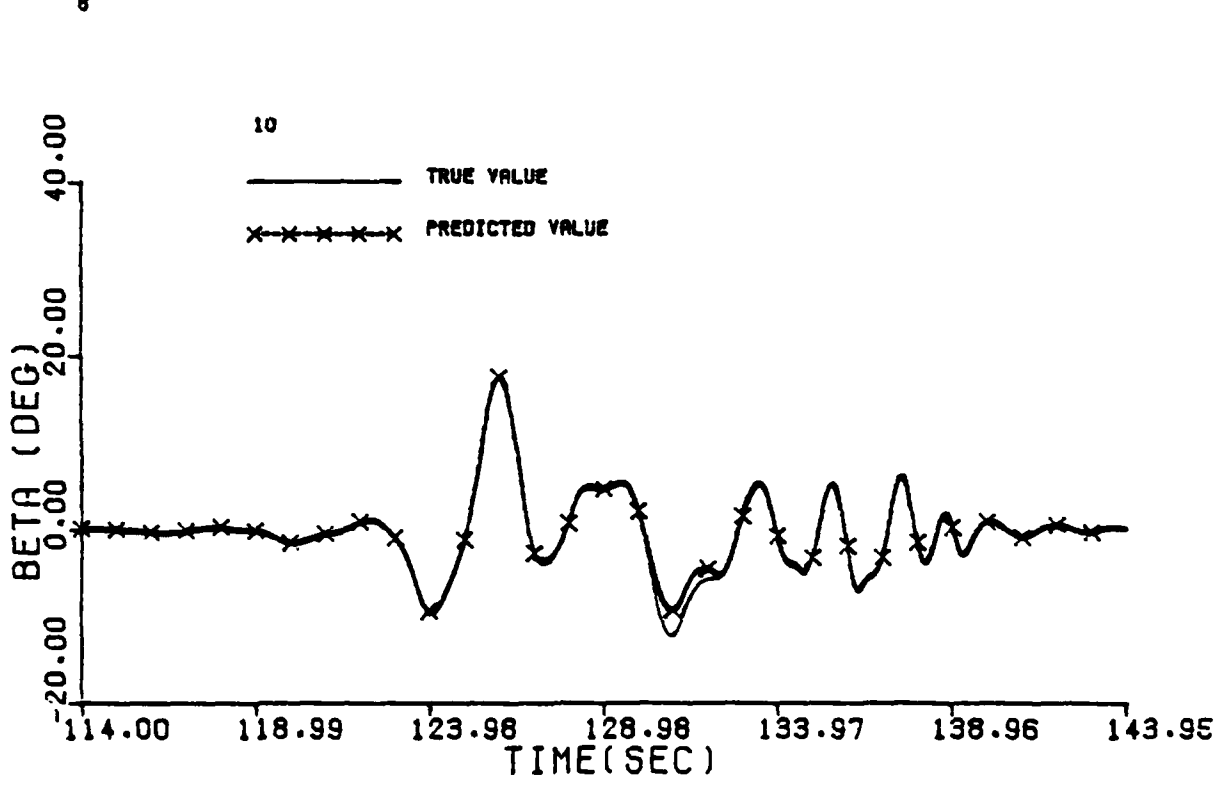

Figure G.1 Continued (Maneuver 10)

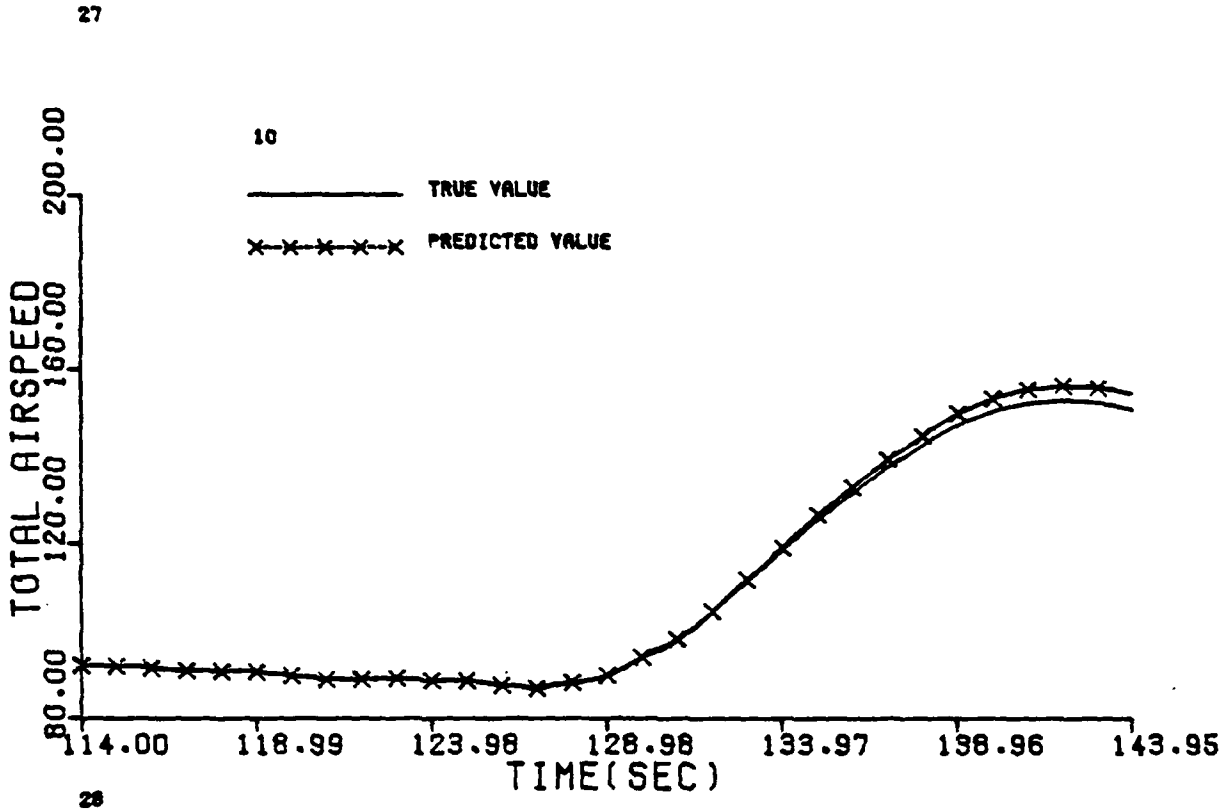

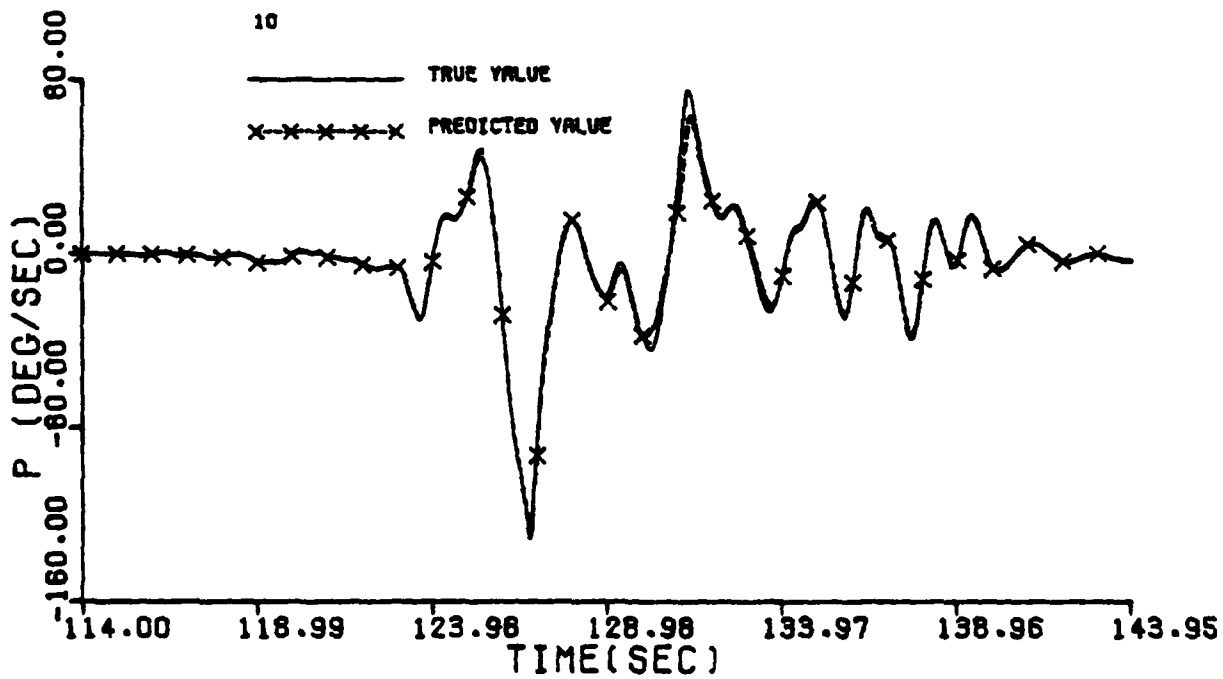

Figure G.1 Continued (Maneuver 10)

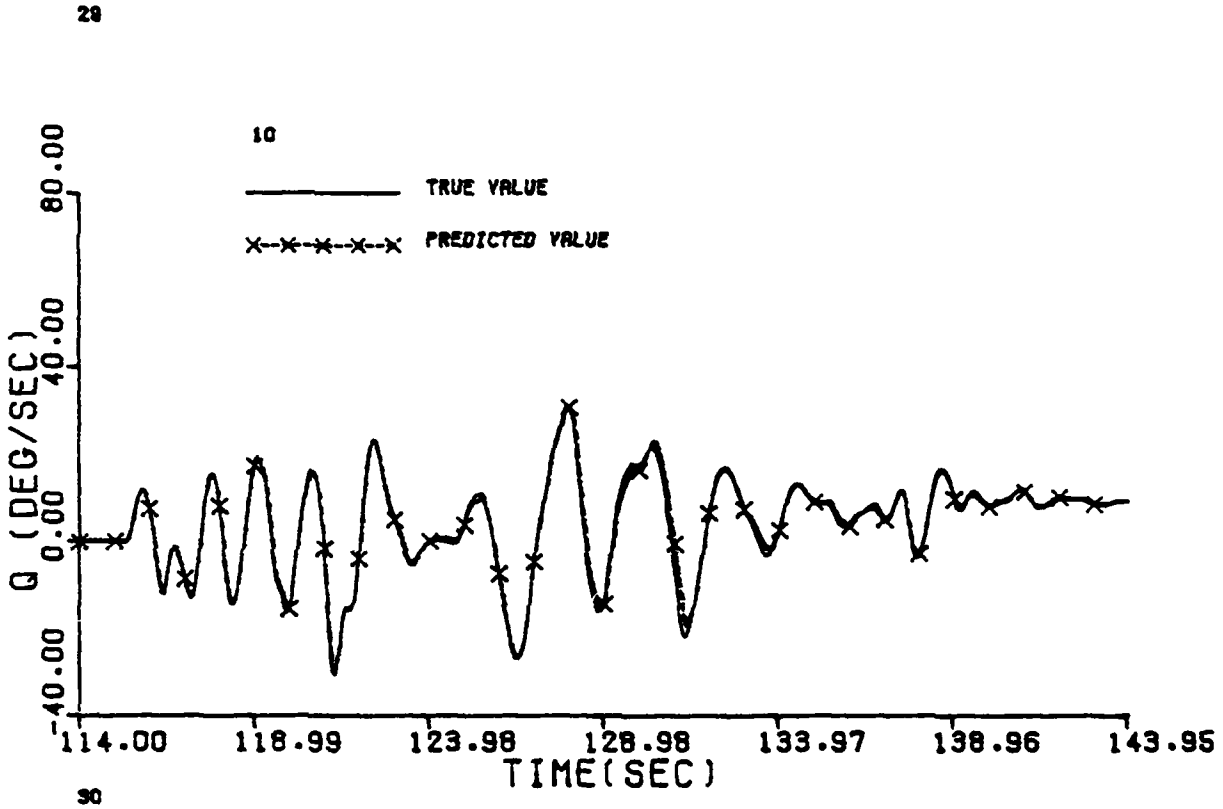

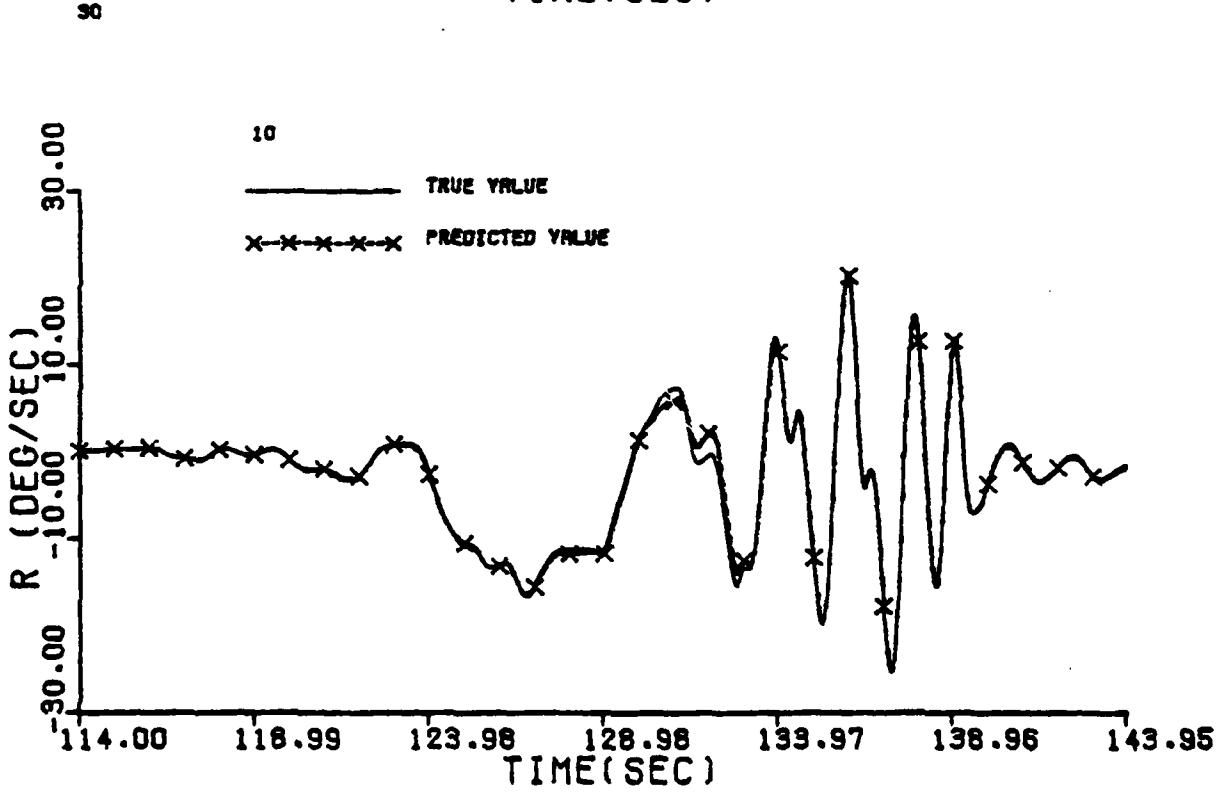

Figure G.1 Continued (Maneuver 10)

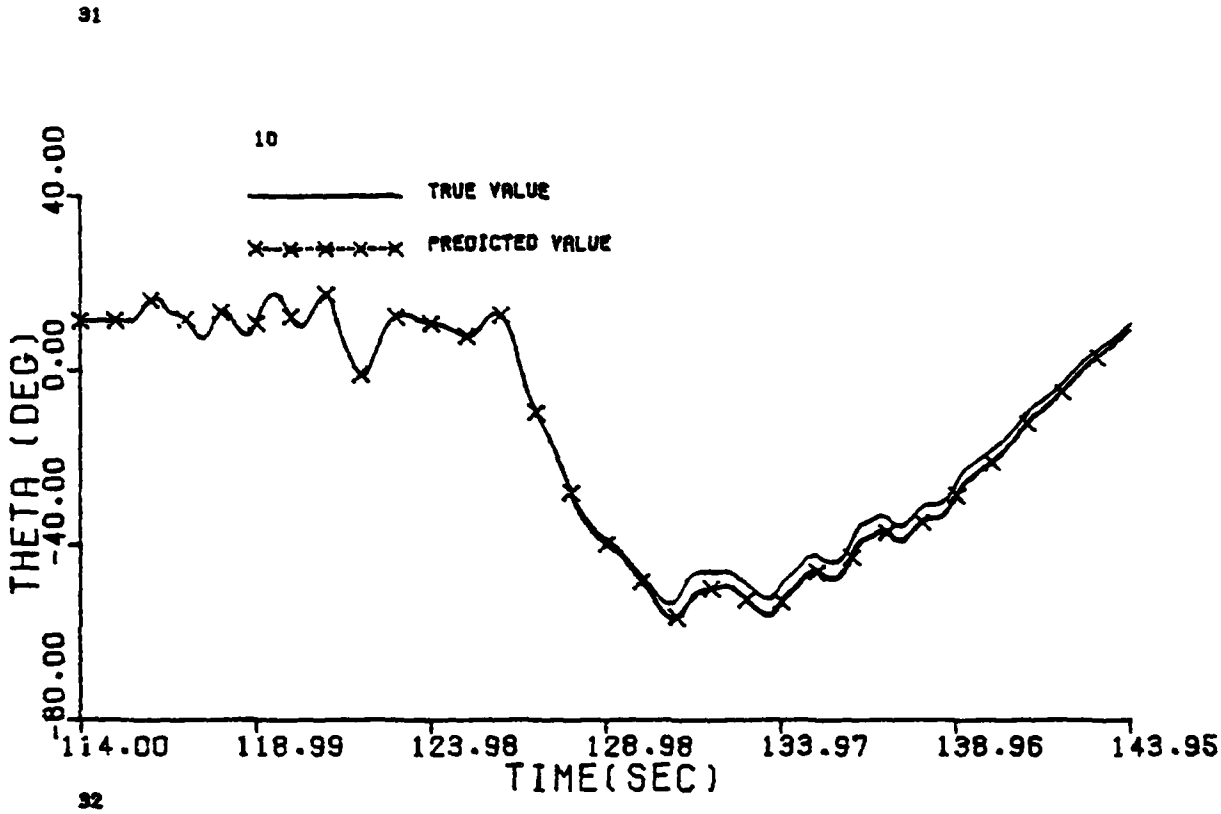

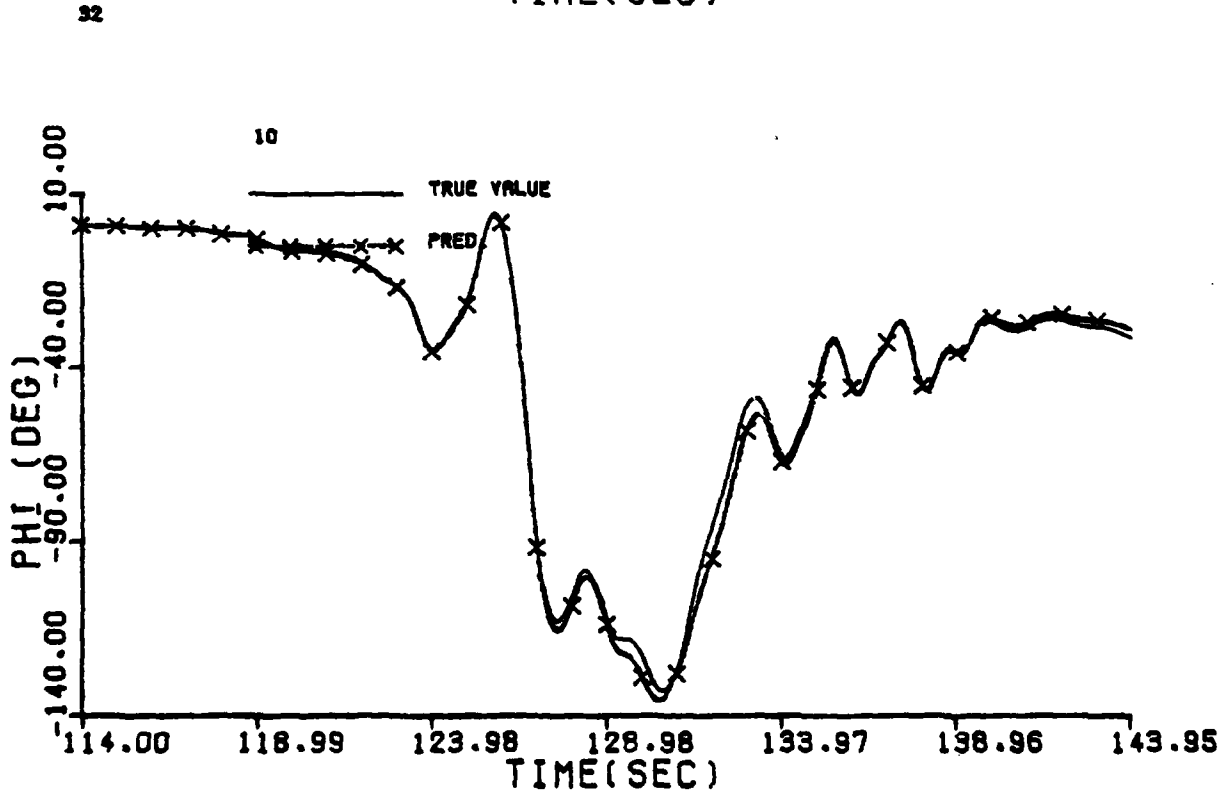

Figure G.1 Continued (Maneuver 10)

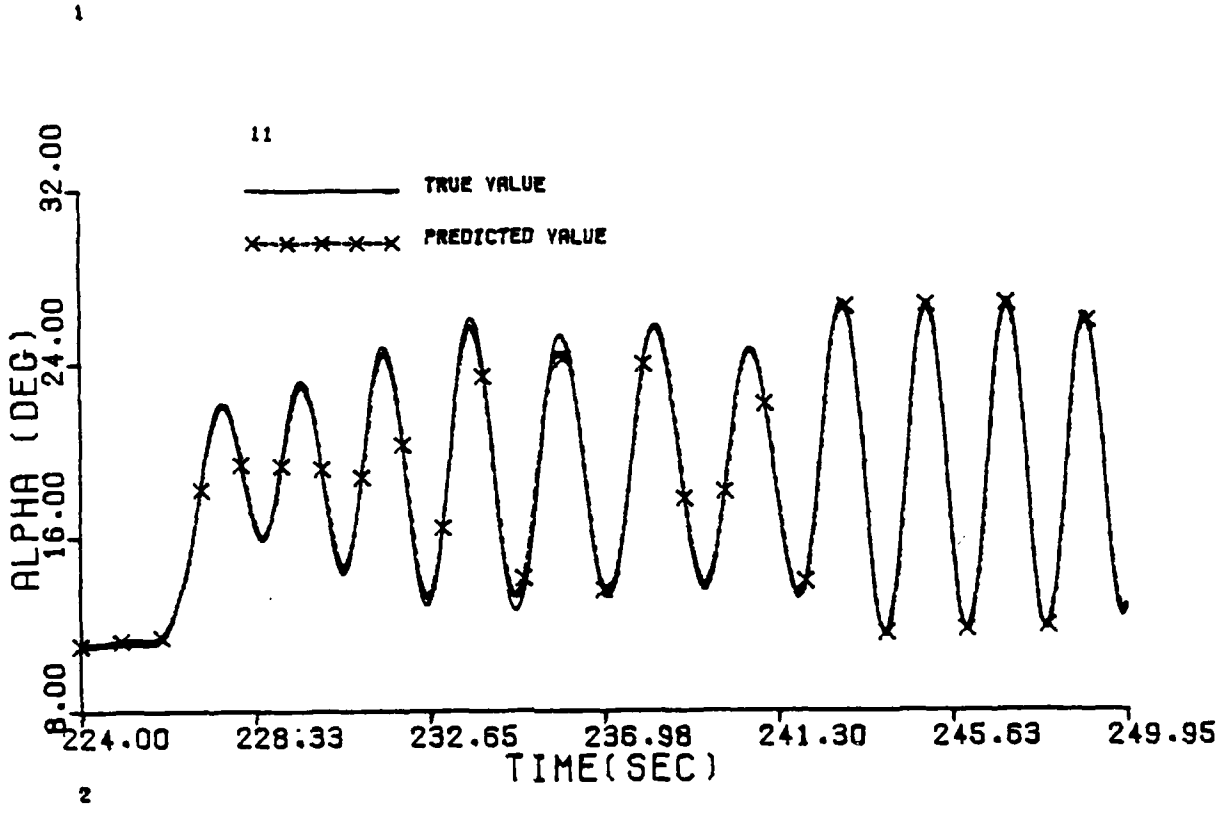

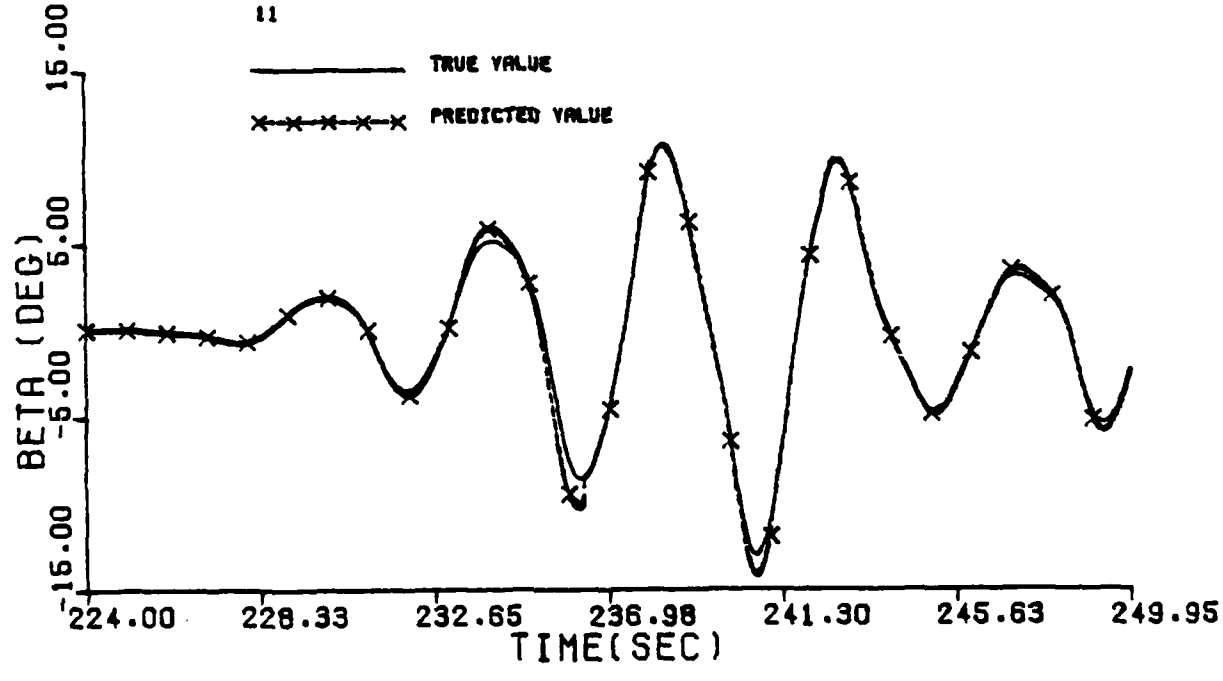

Figure G.1 Continued (Maneuver 11)

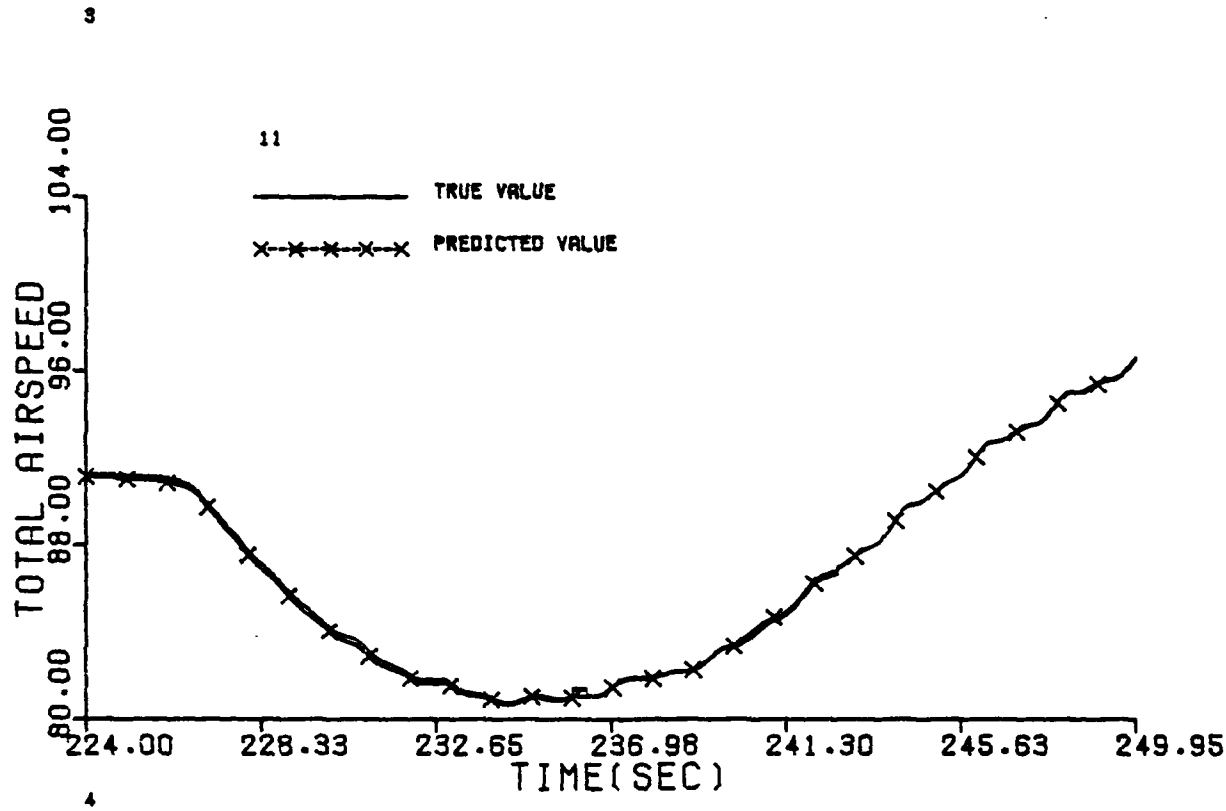

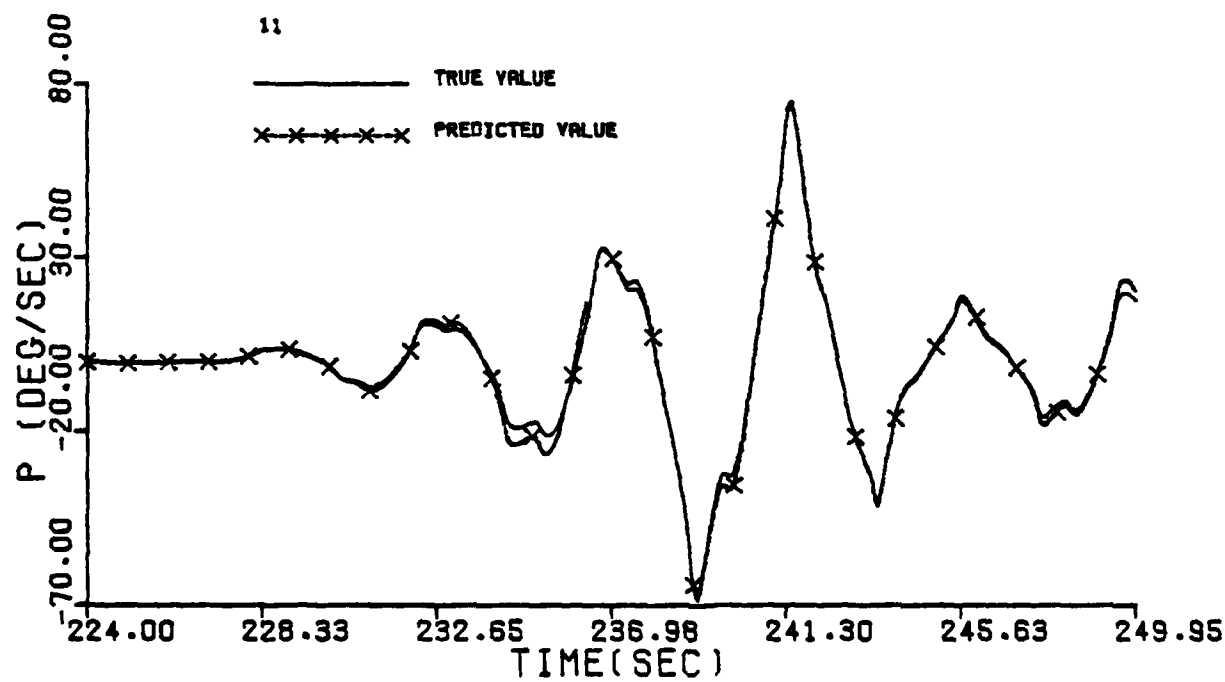

Figure G.1 Continued (Maneuver 11)

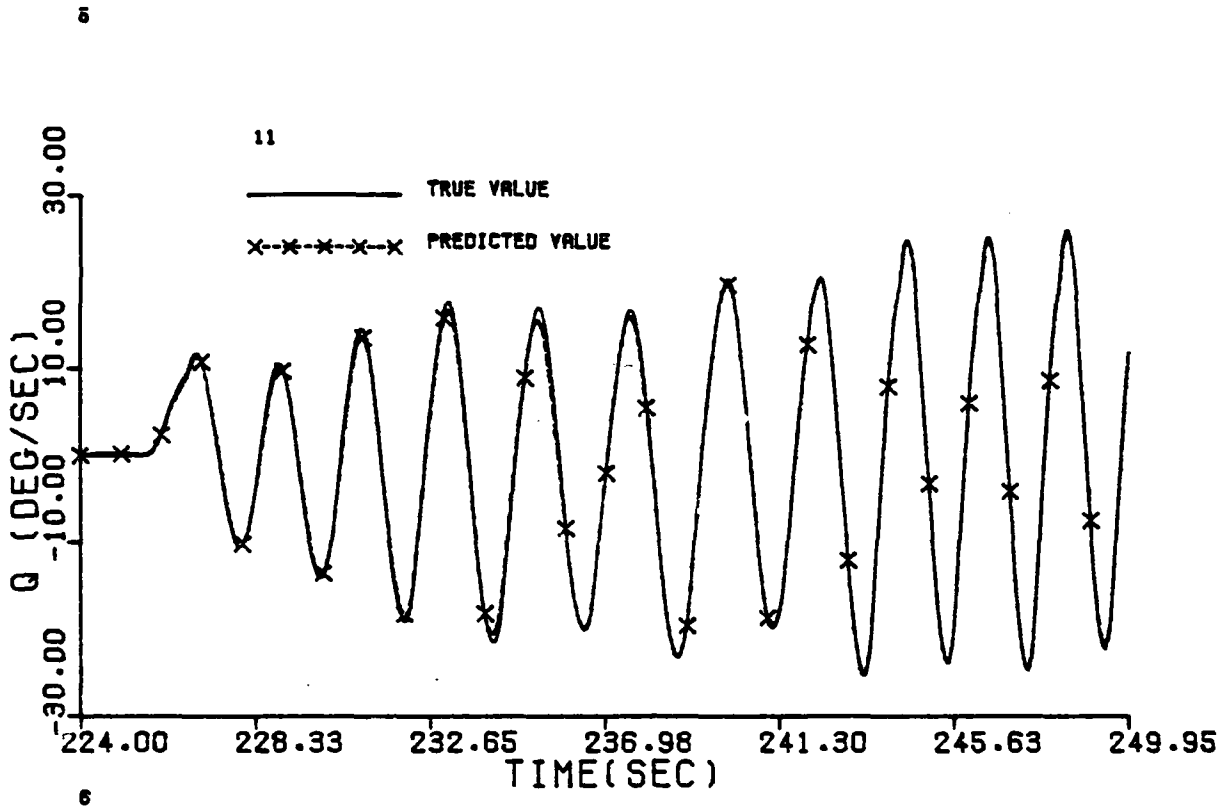

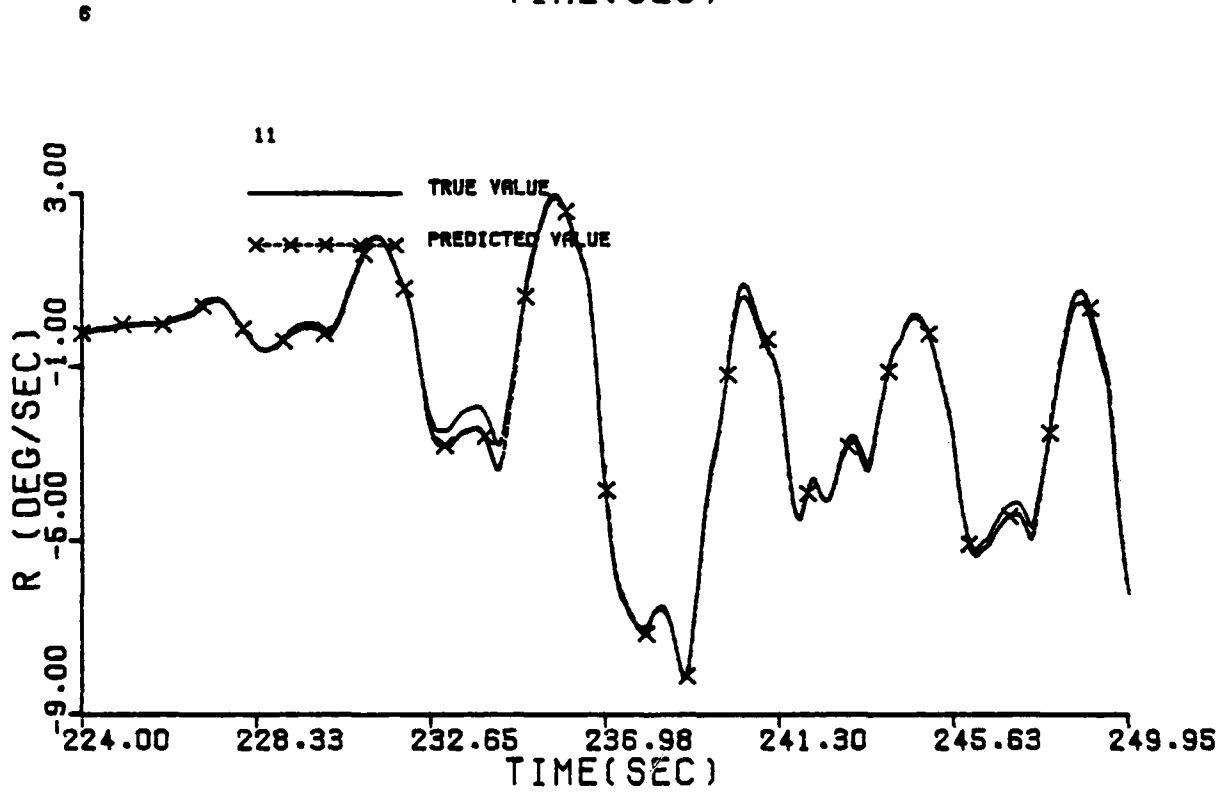

Figure G.1 Continued (Maneuver 11)

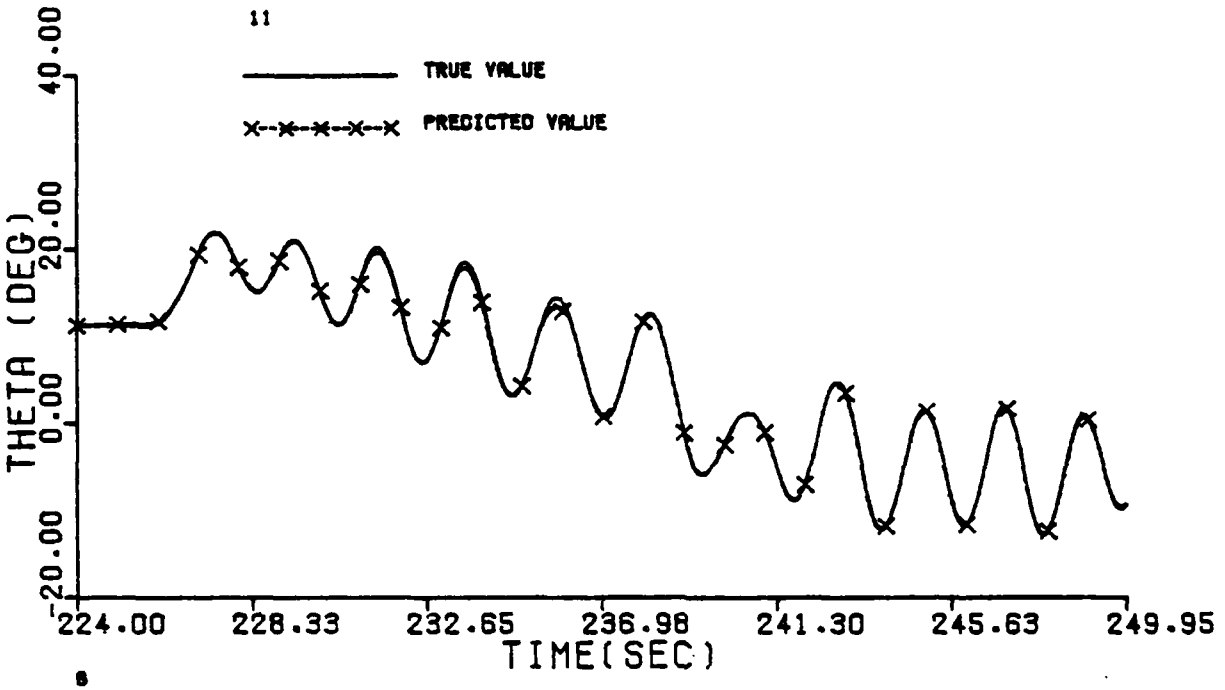

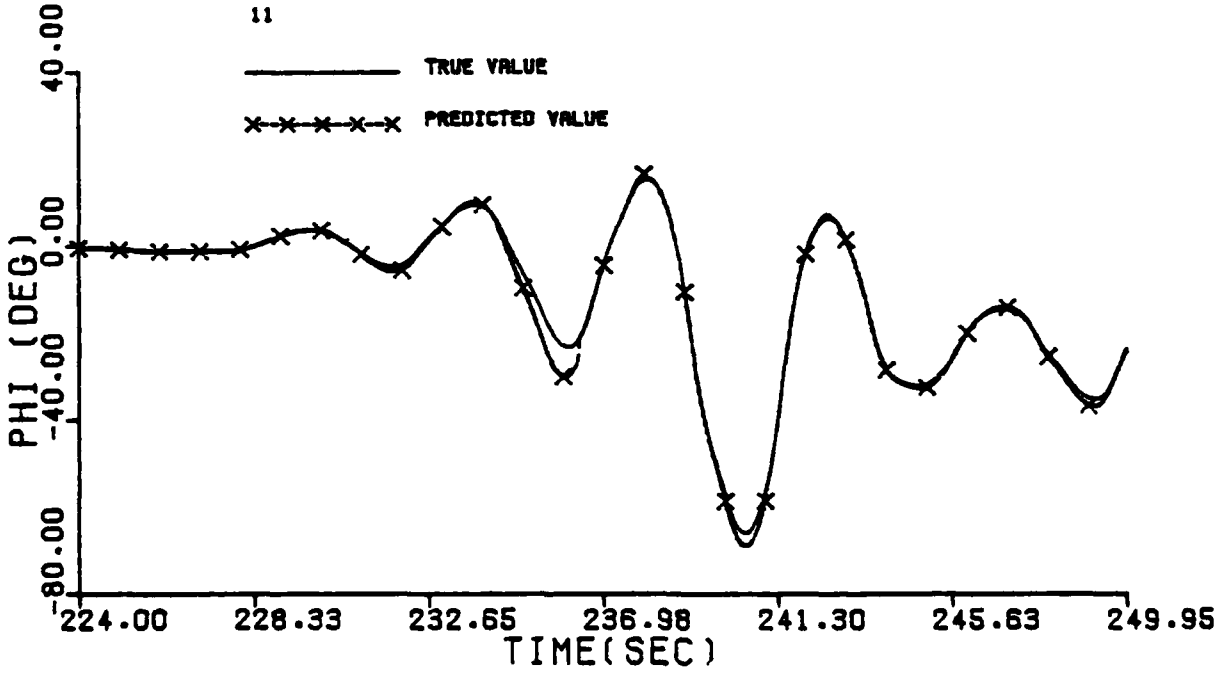

Figure G.1 Continued (Maneuver 11)

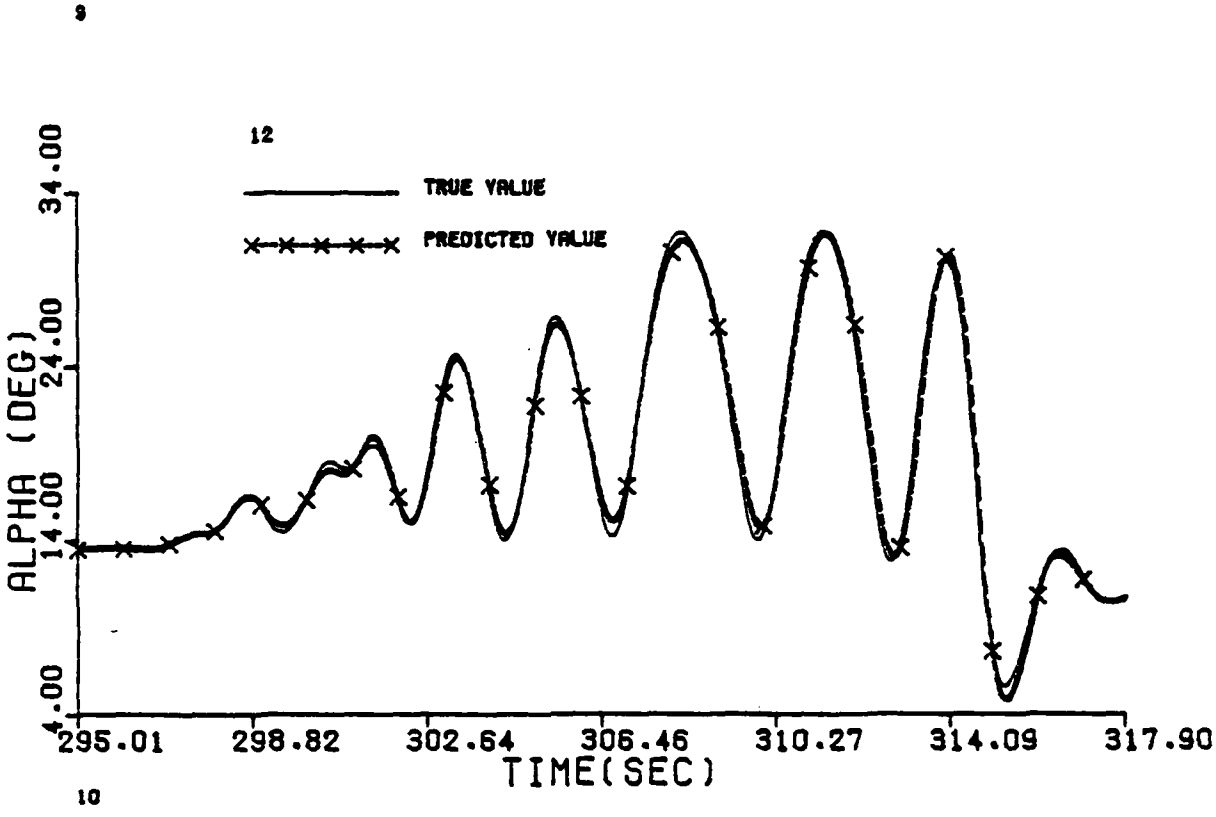

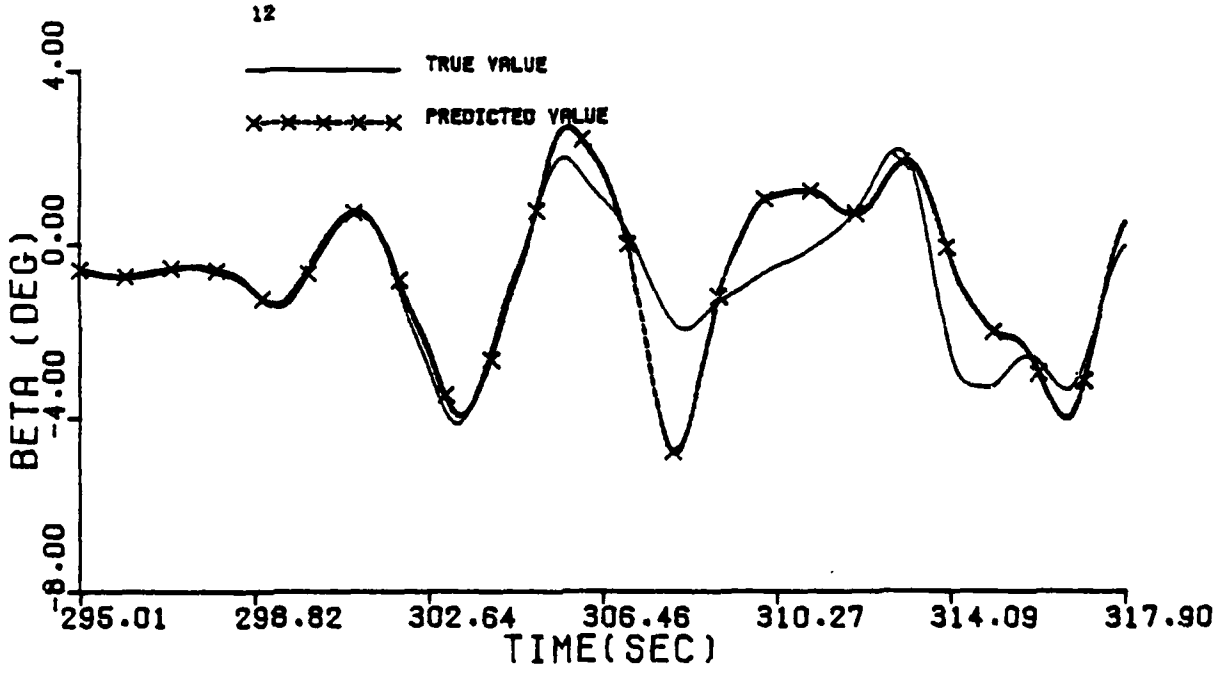

Figure G.1 Continued (Maneuver 12)

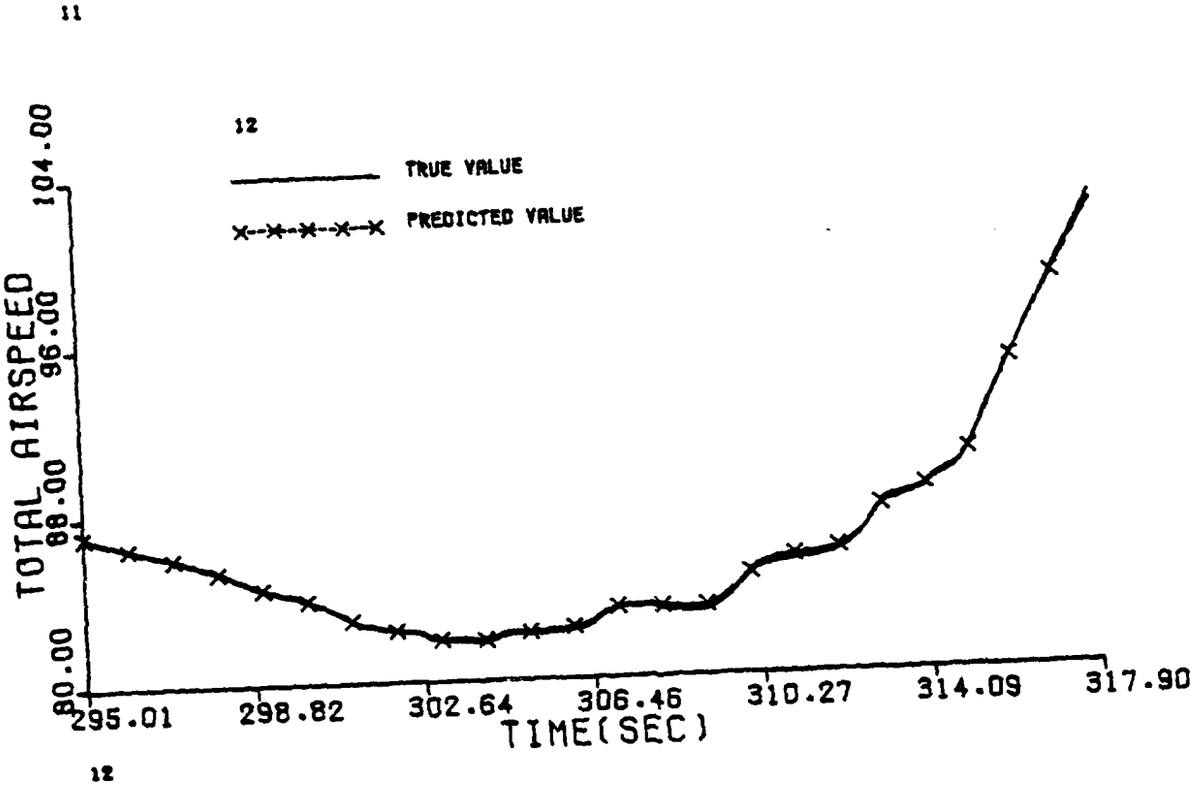

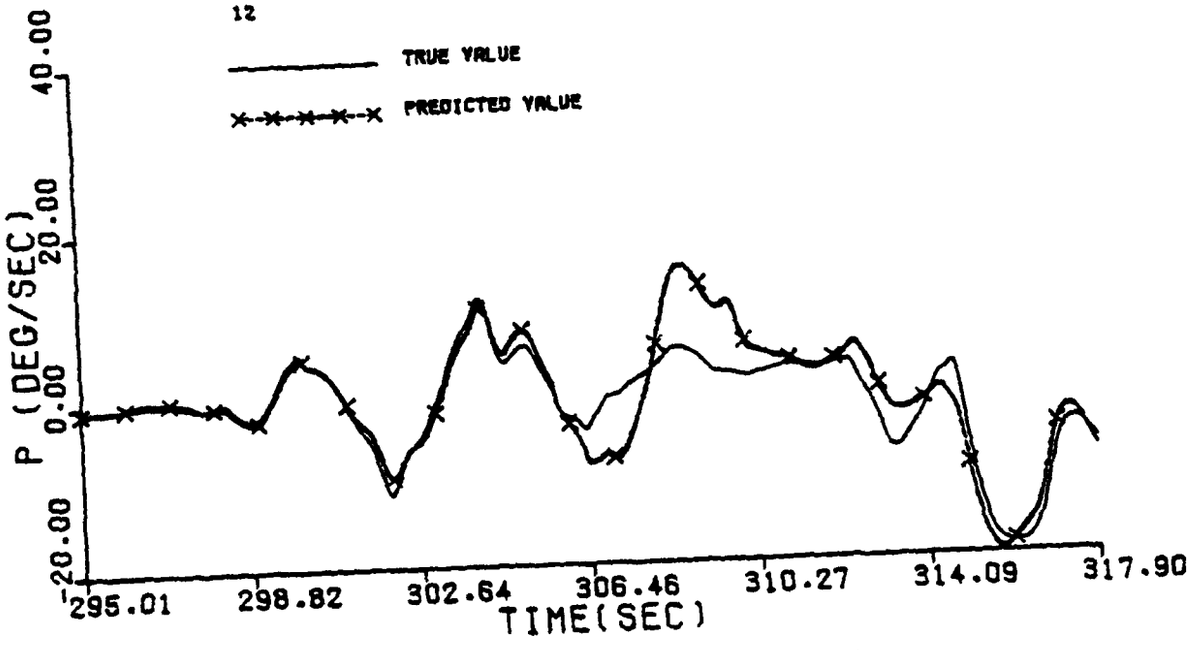

Figure G.1 Continued (Maneuver 12)

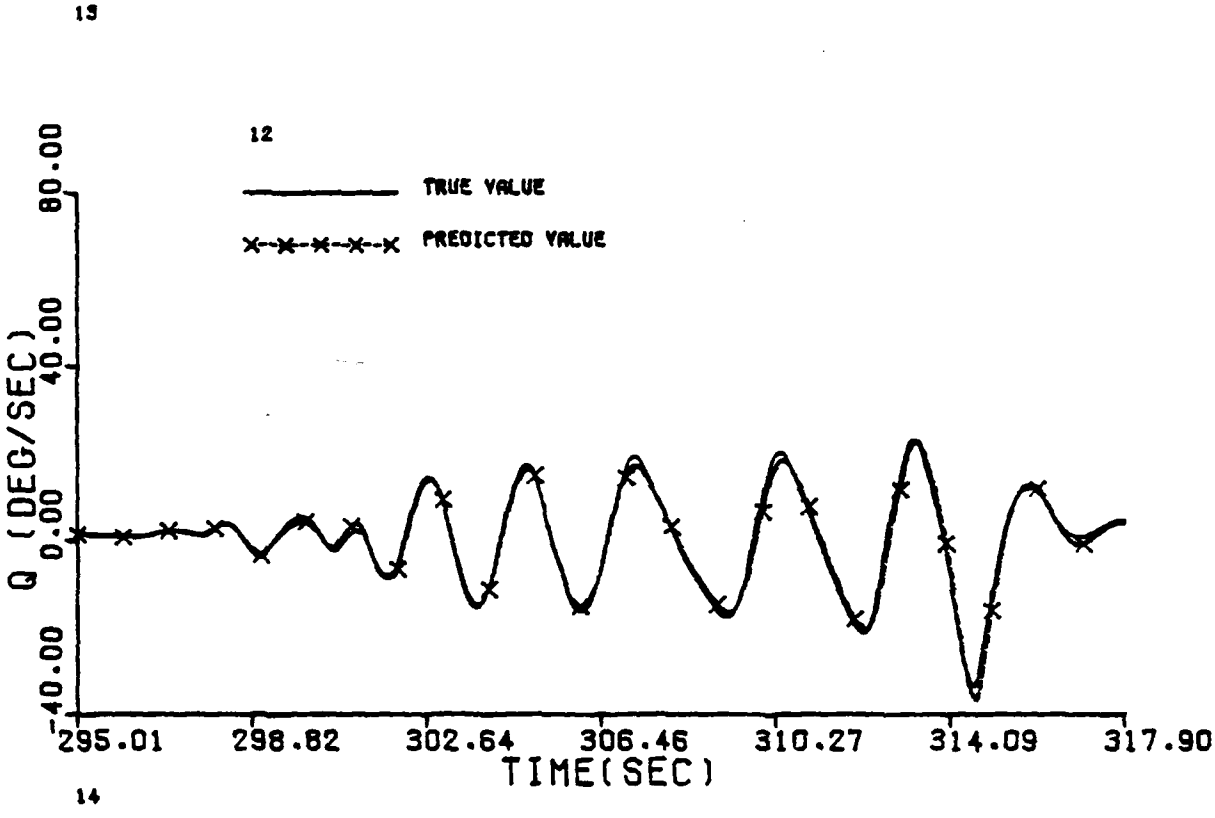

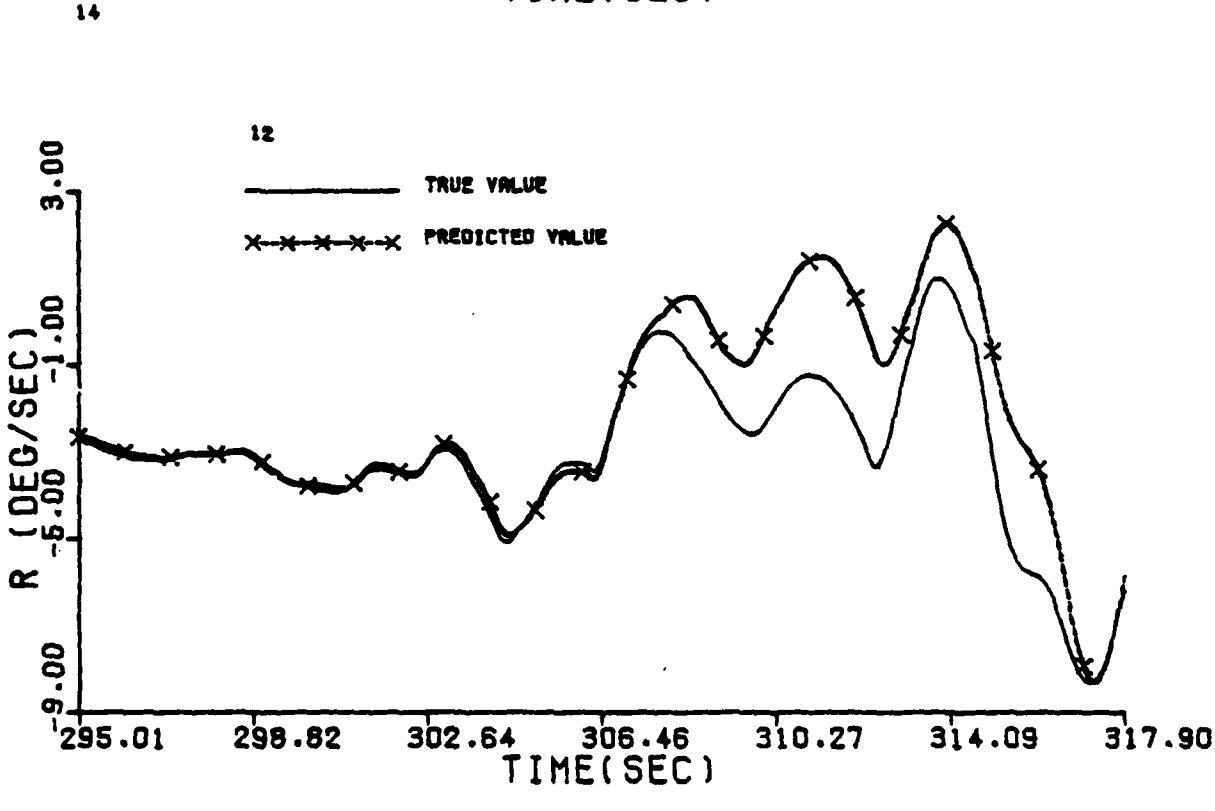

Figure G.1 Continued (Maneuver 12)

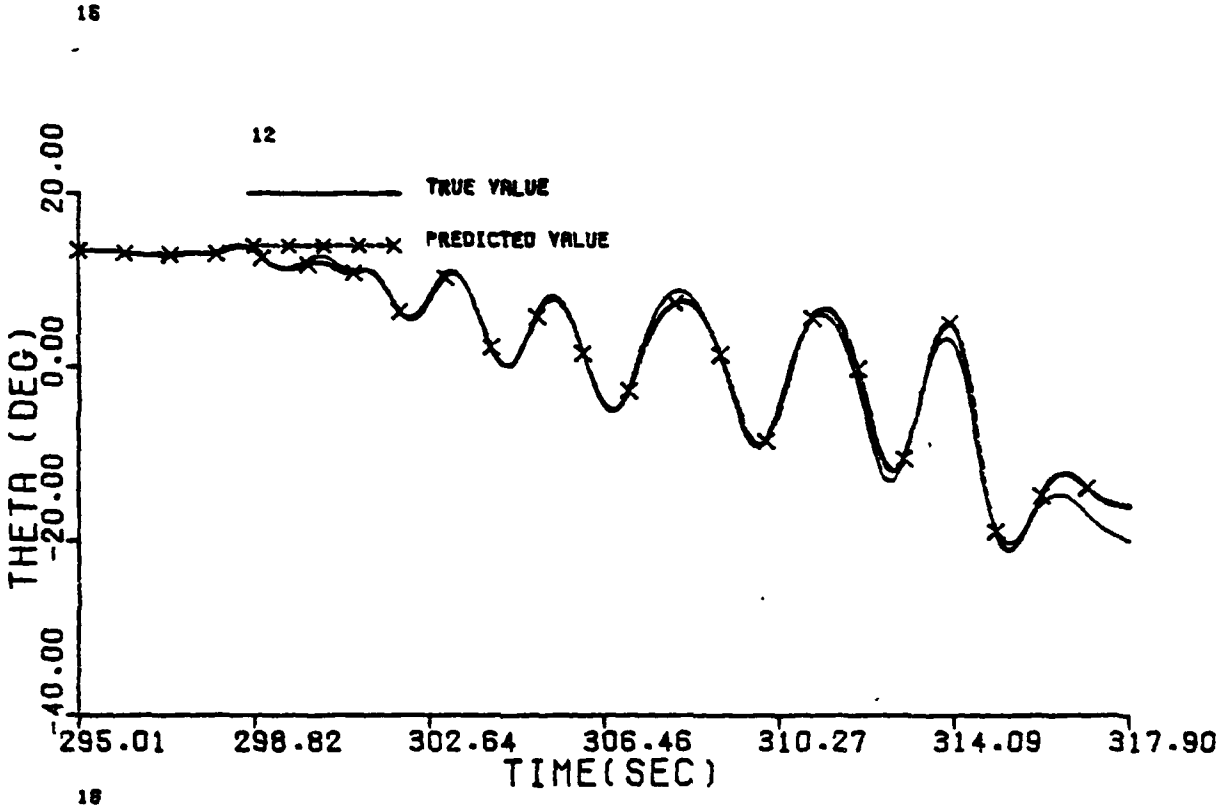

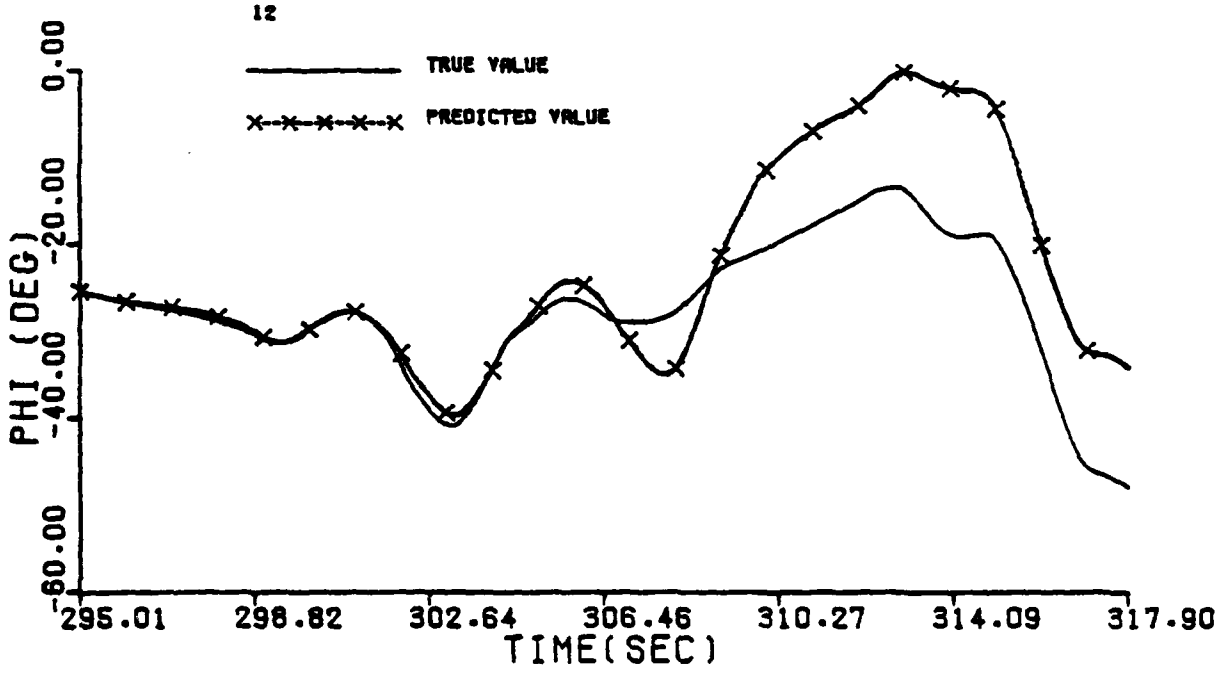

Figure G.1 Continued (Maneuver 12)

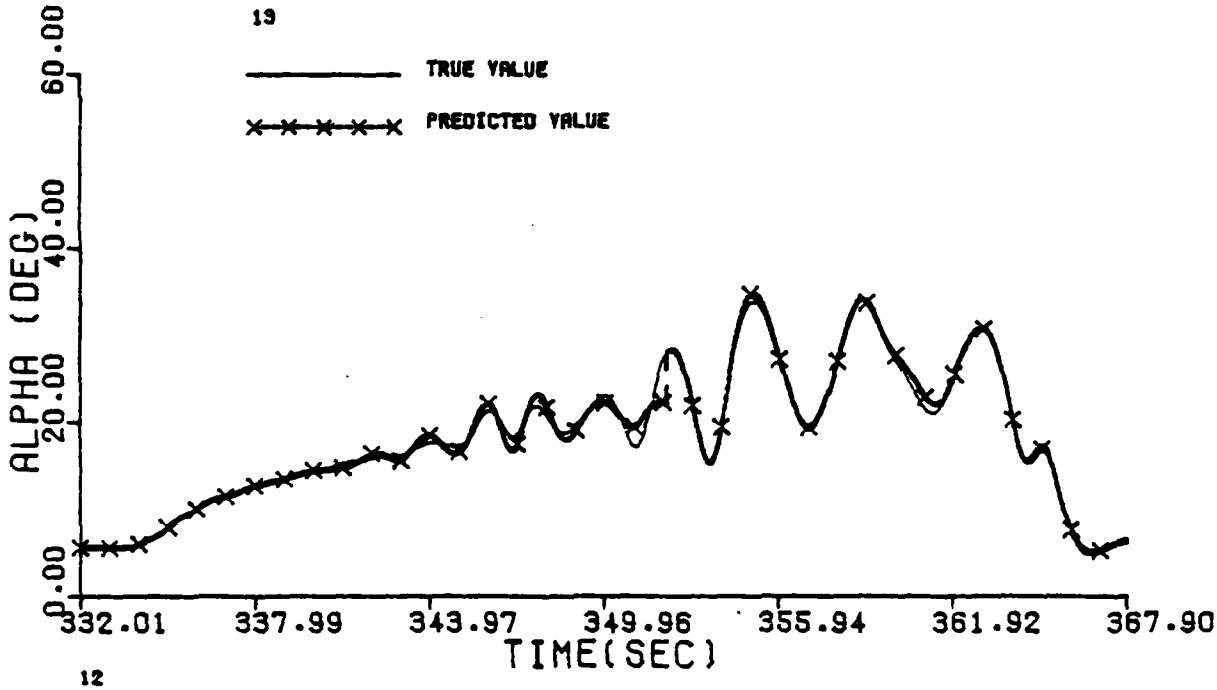

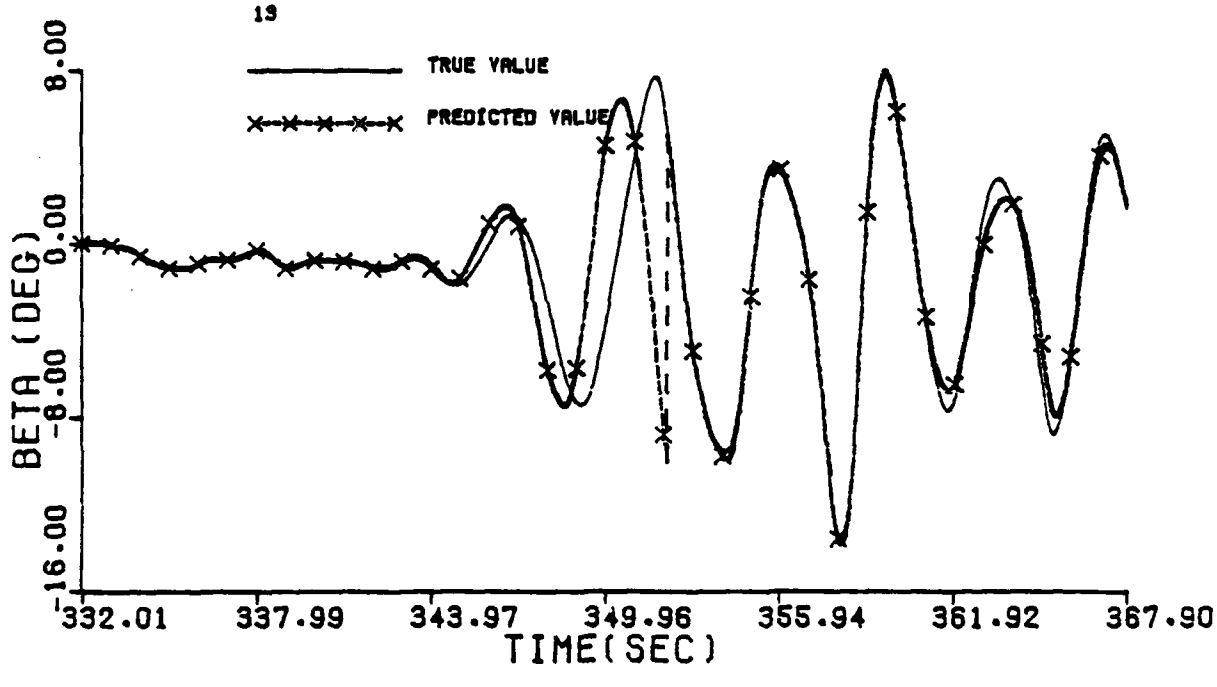

Figure G.1 Continued (Maneuver 13)

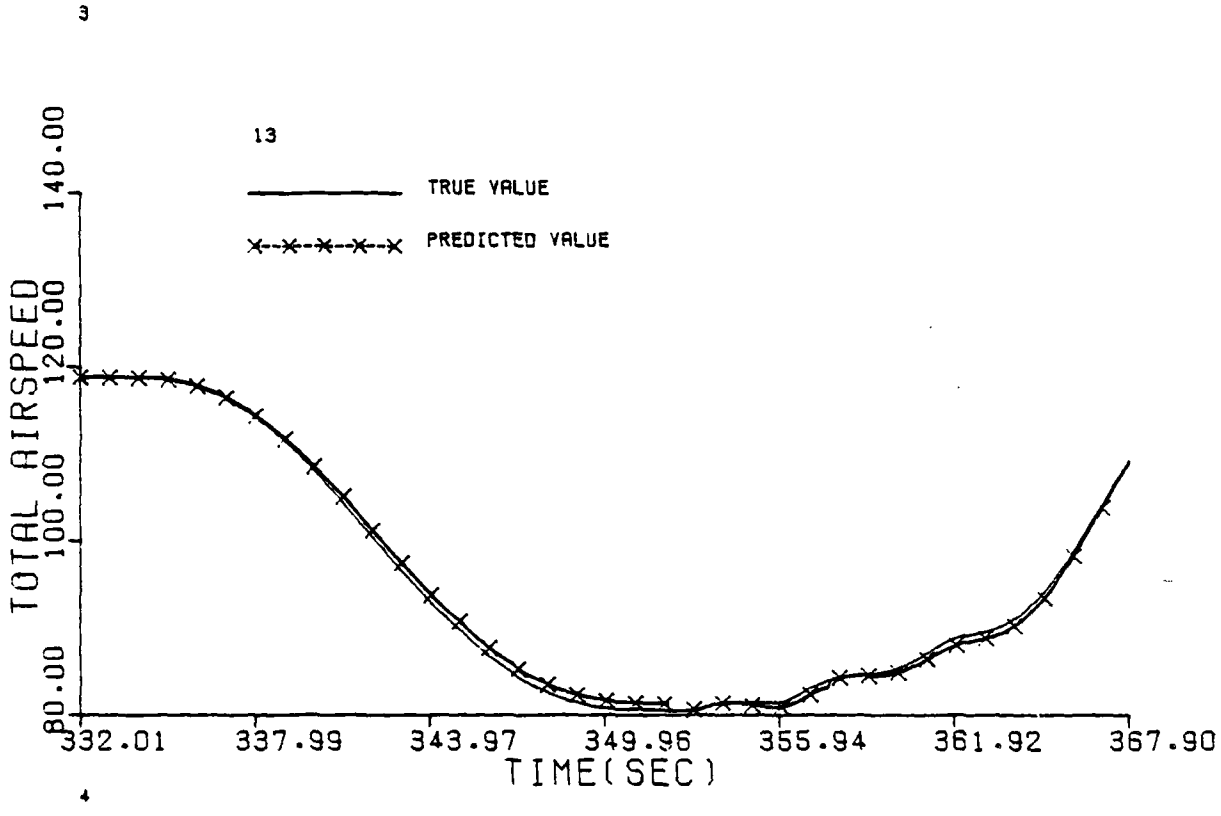

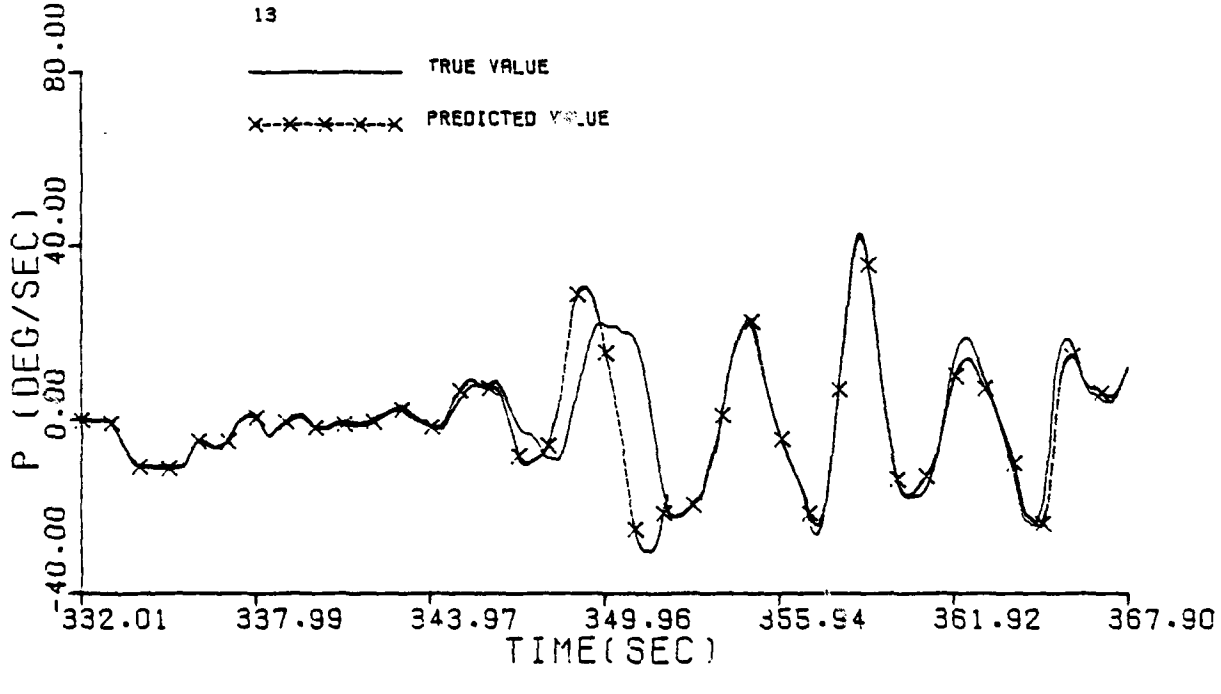

Figure G.1 Continued (Maneuver 13)

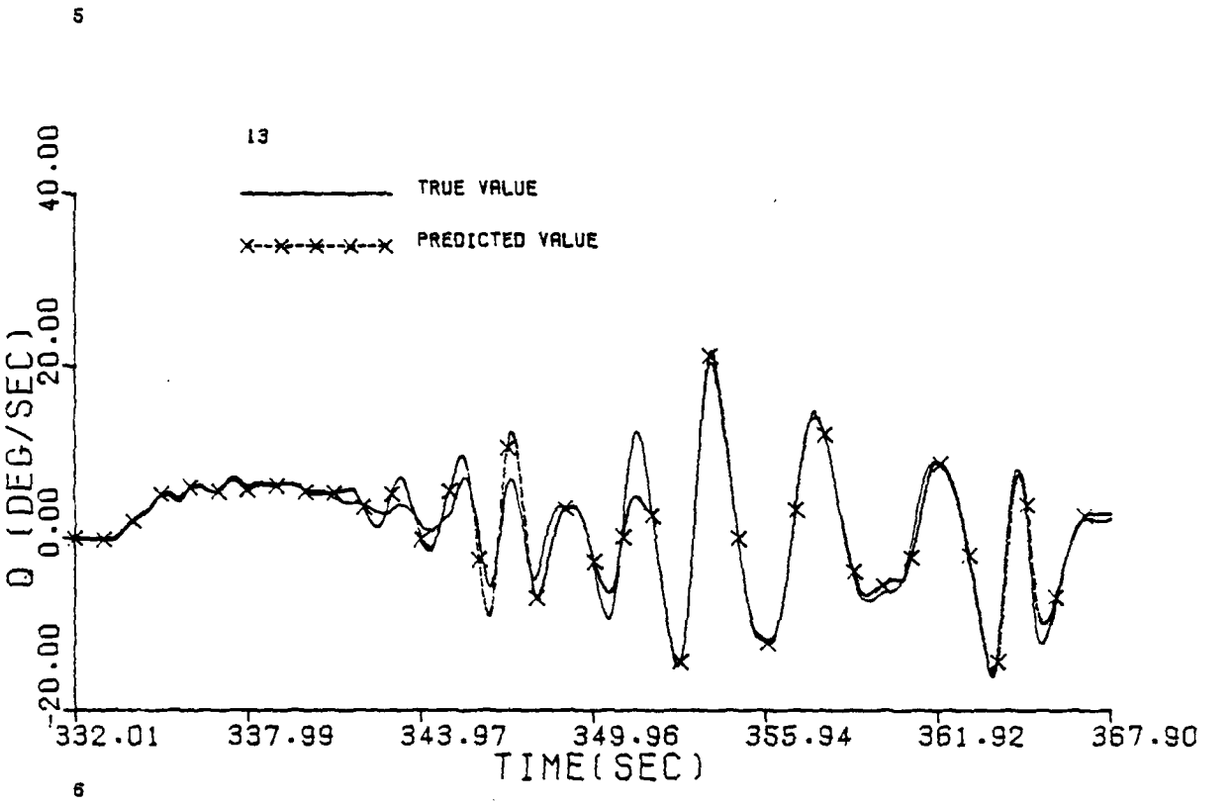

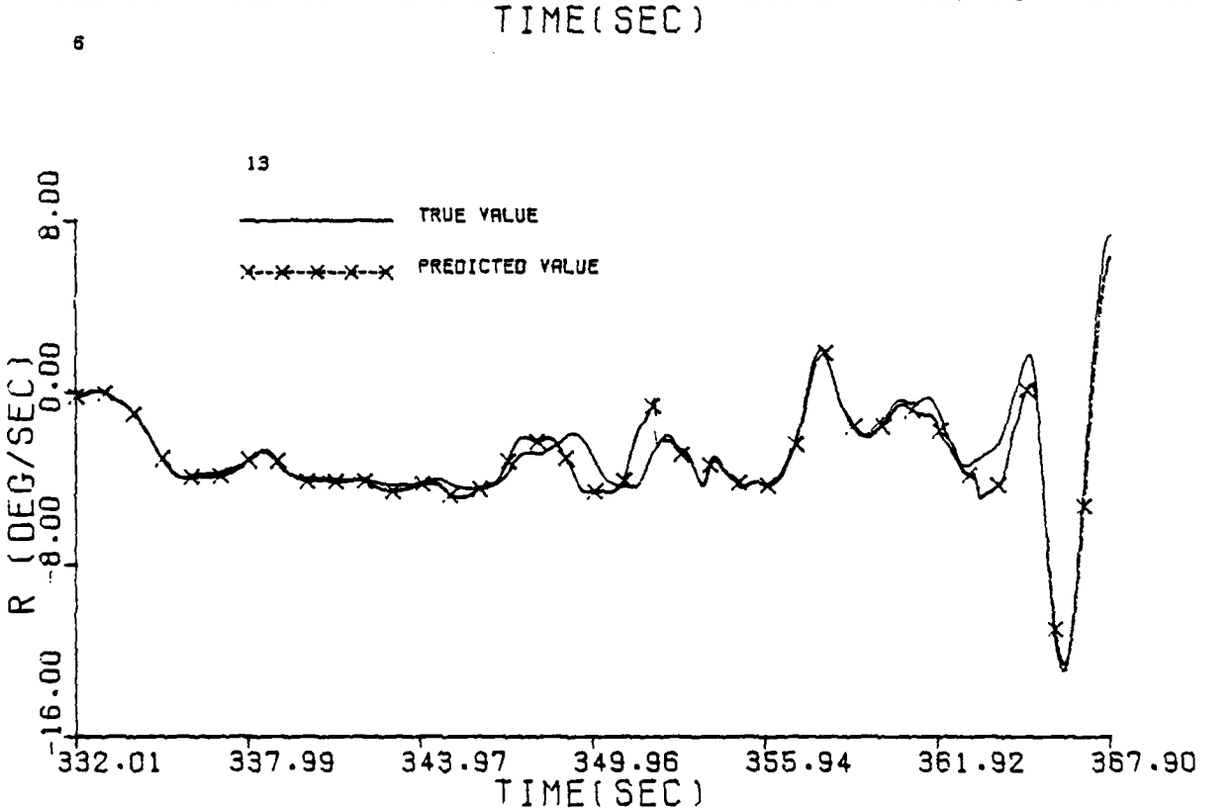

Figure G.1 Continued (Maneuver 13)

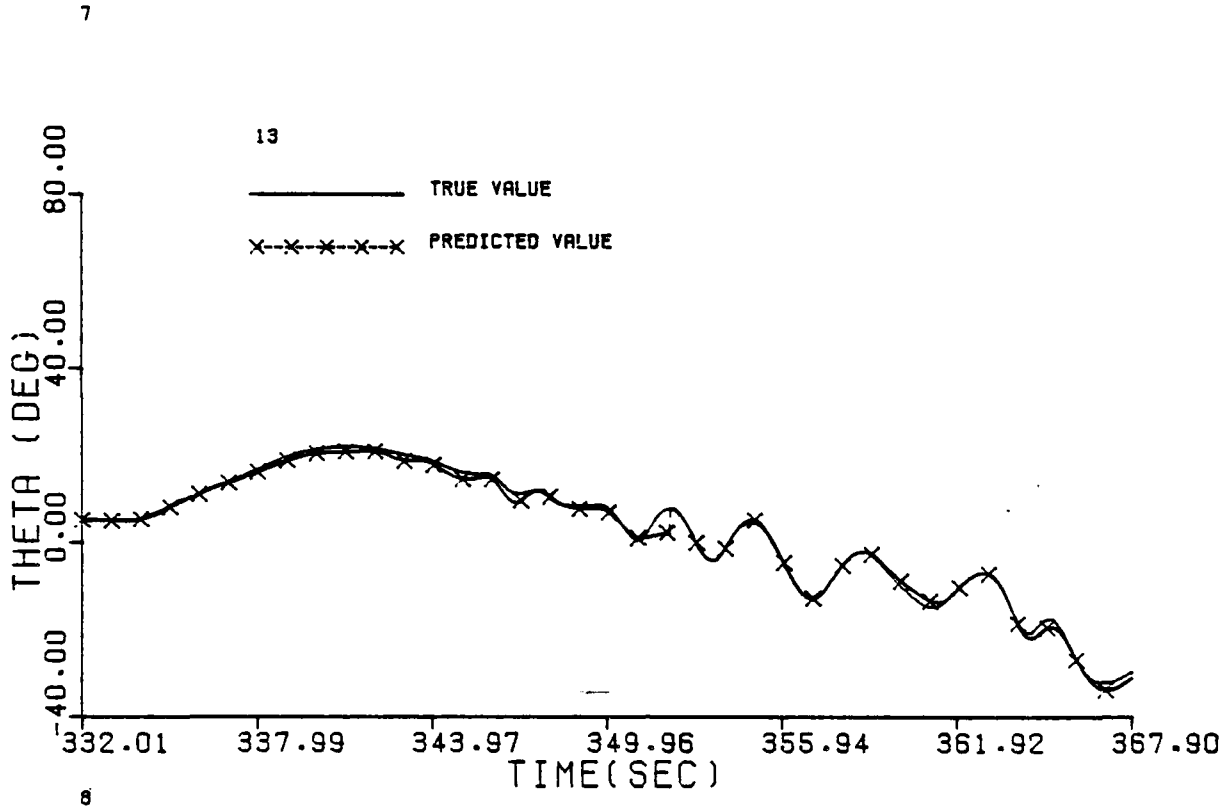

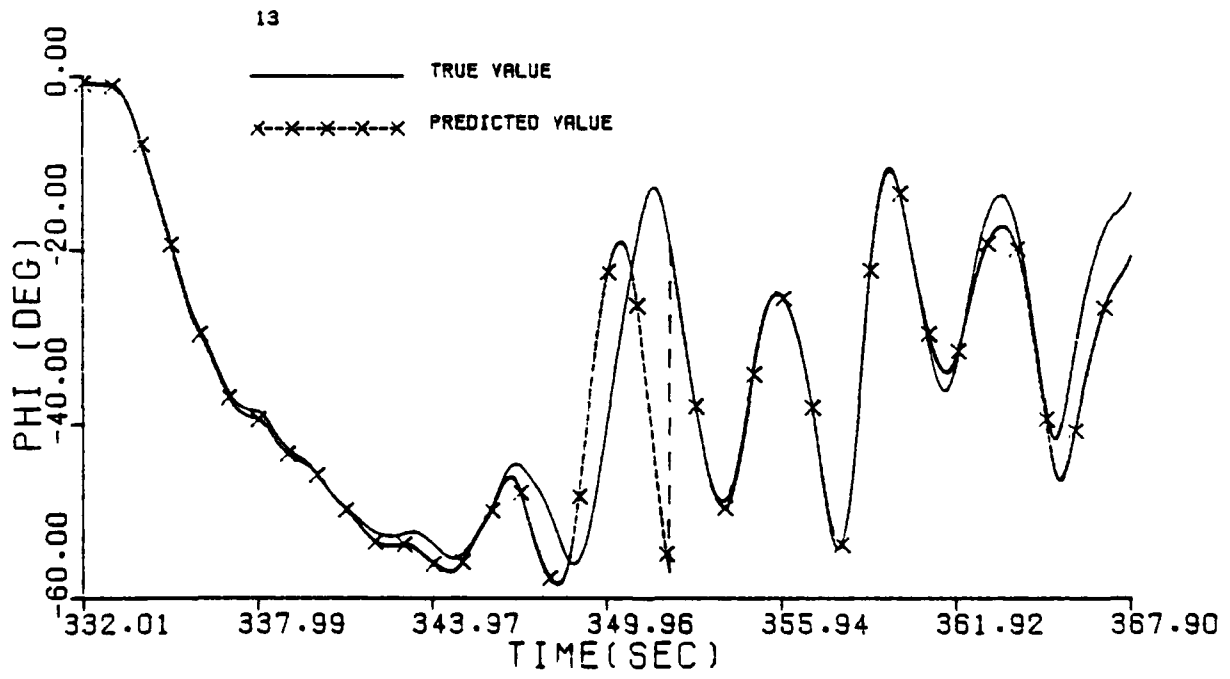

Figure G.1 Continued (Maneuver 13)

13

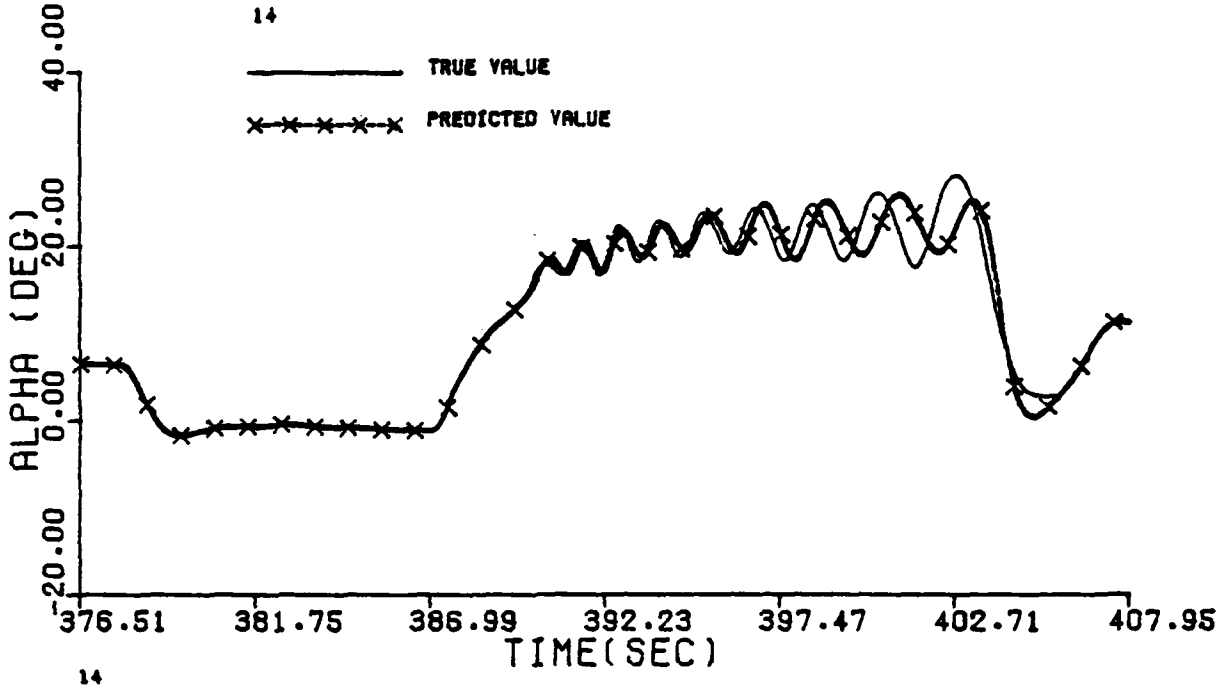

14

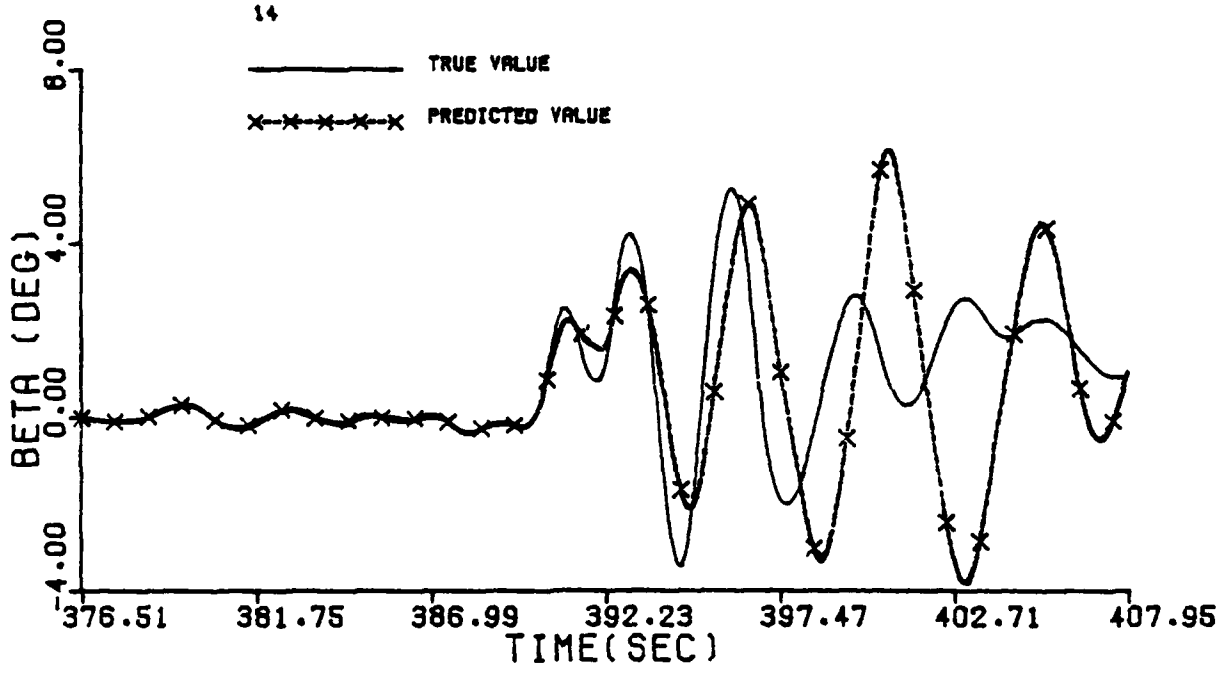

Figure G.1 Continued (Maneuver 14)

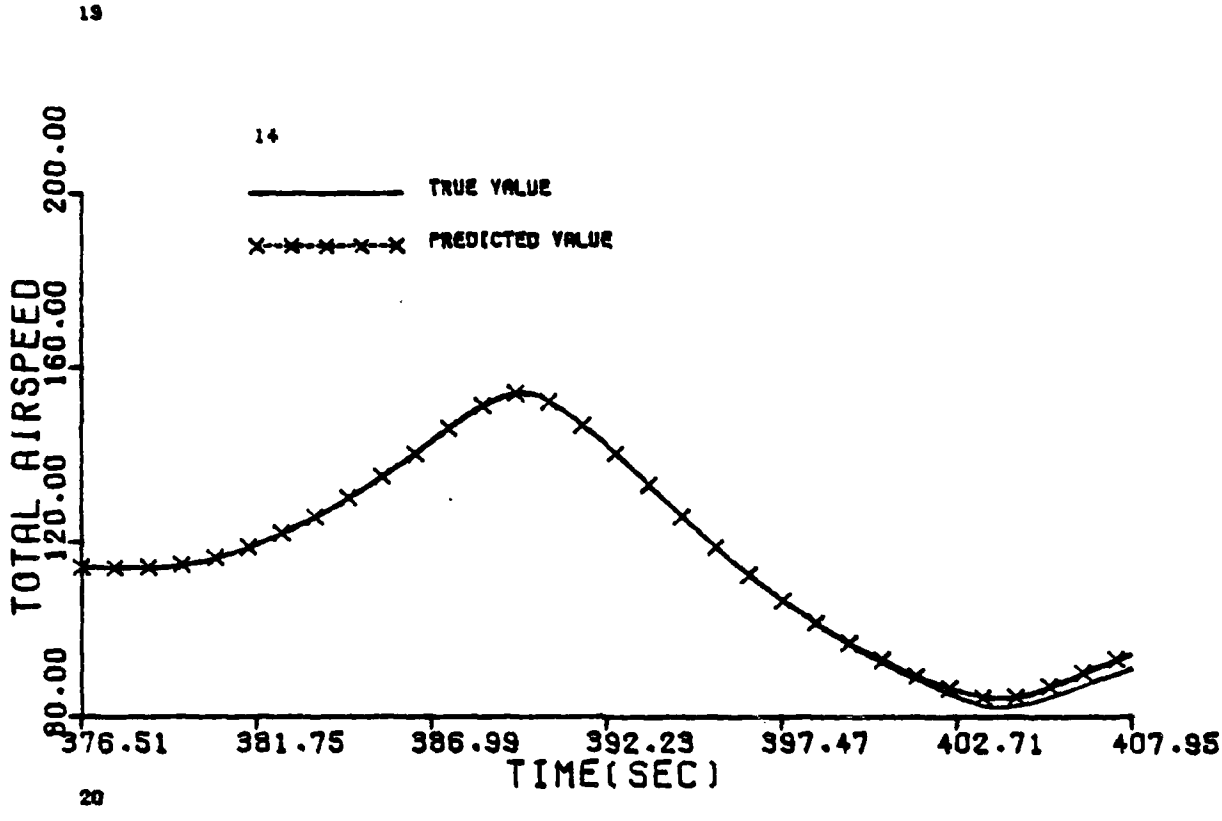

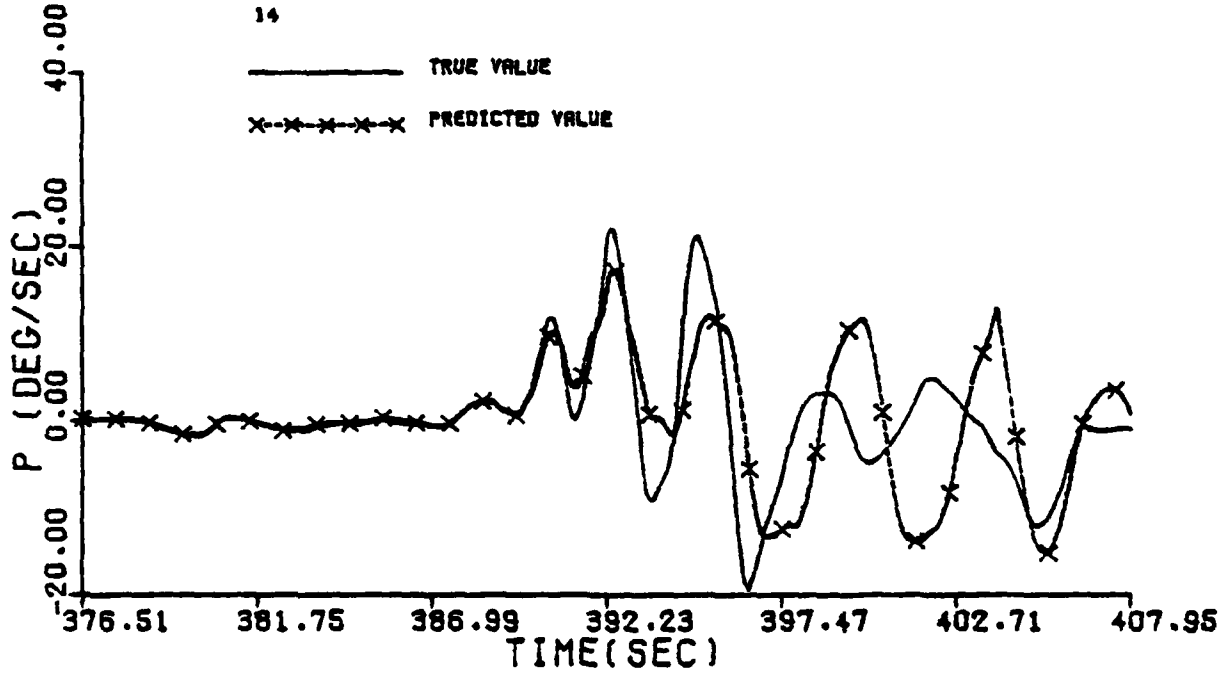

Figure G.1 Continued (Maneuver 14)

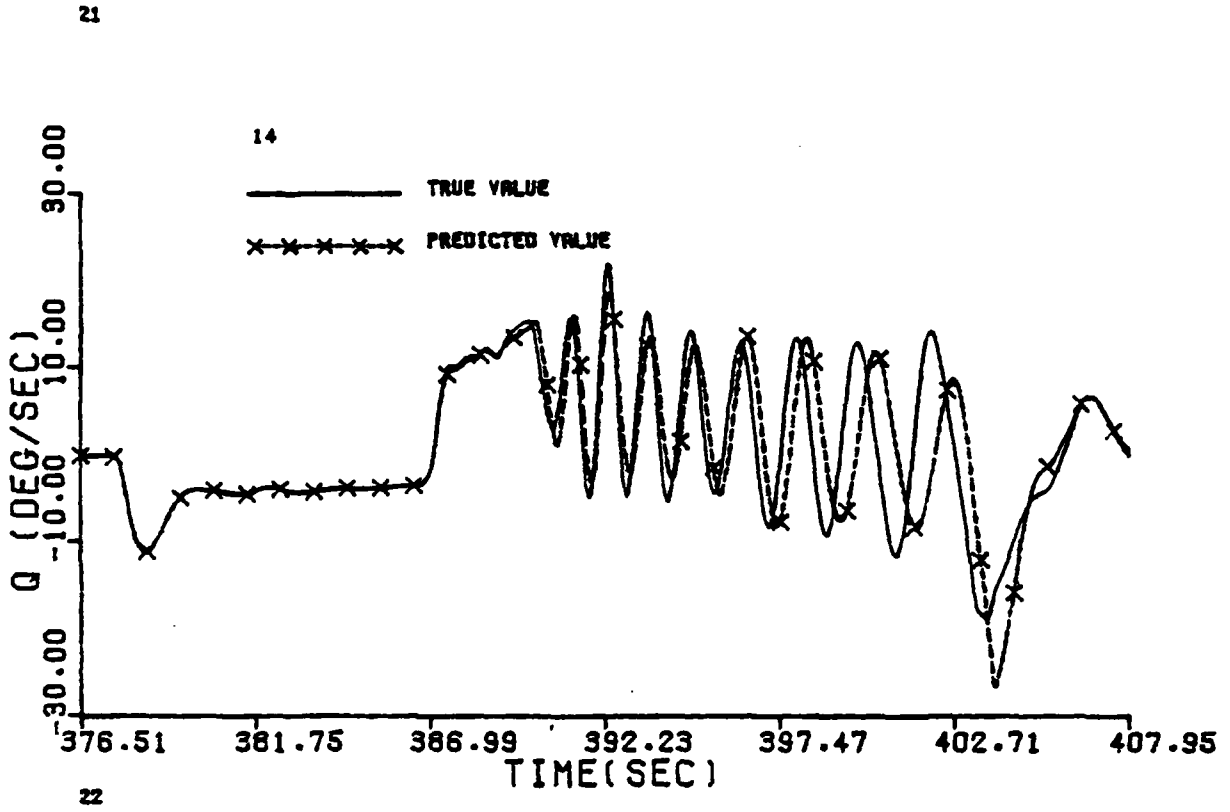

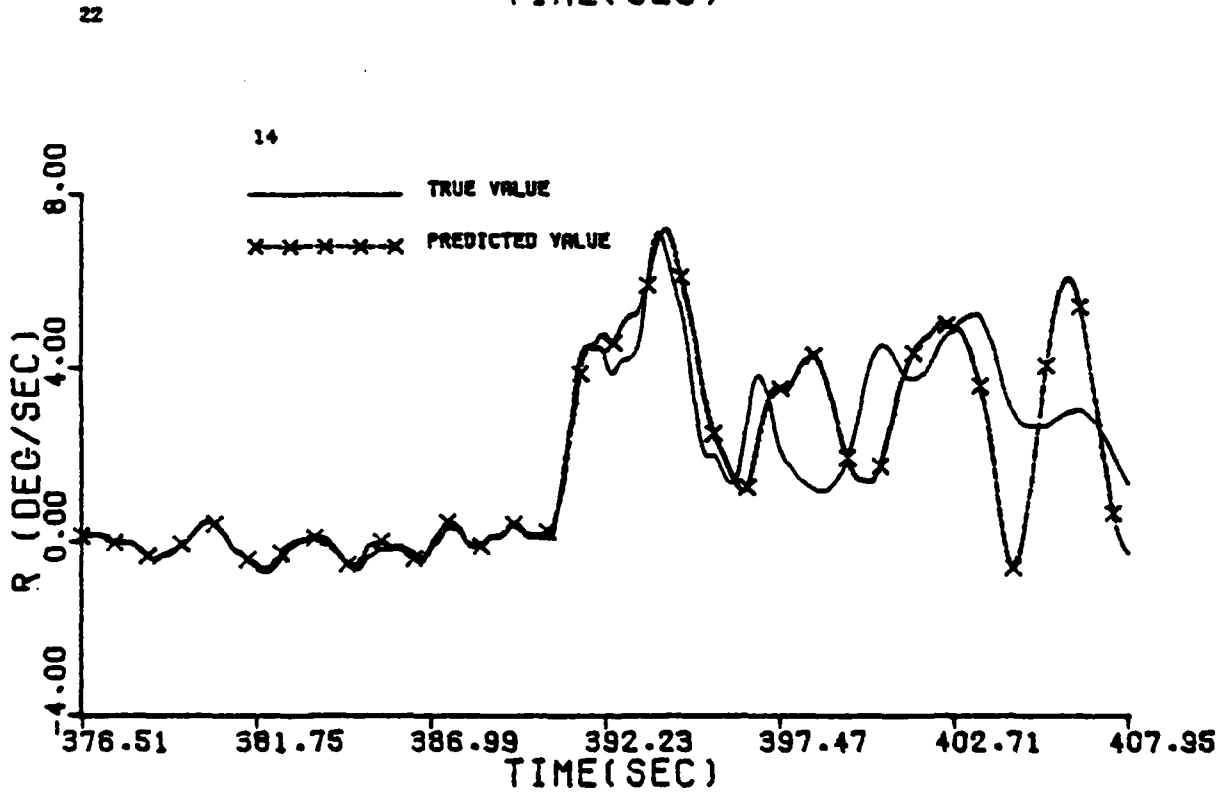

Figure G.1 Continued (Maneuver 14)

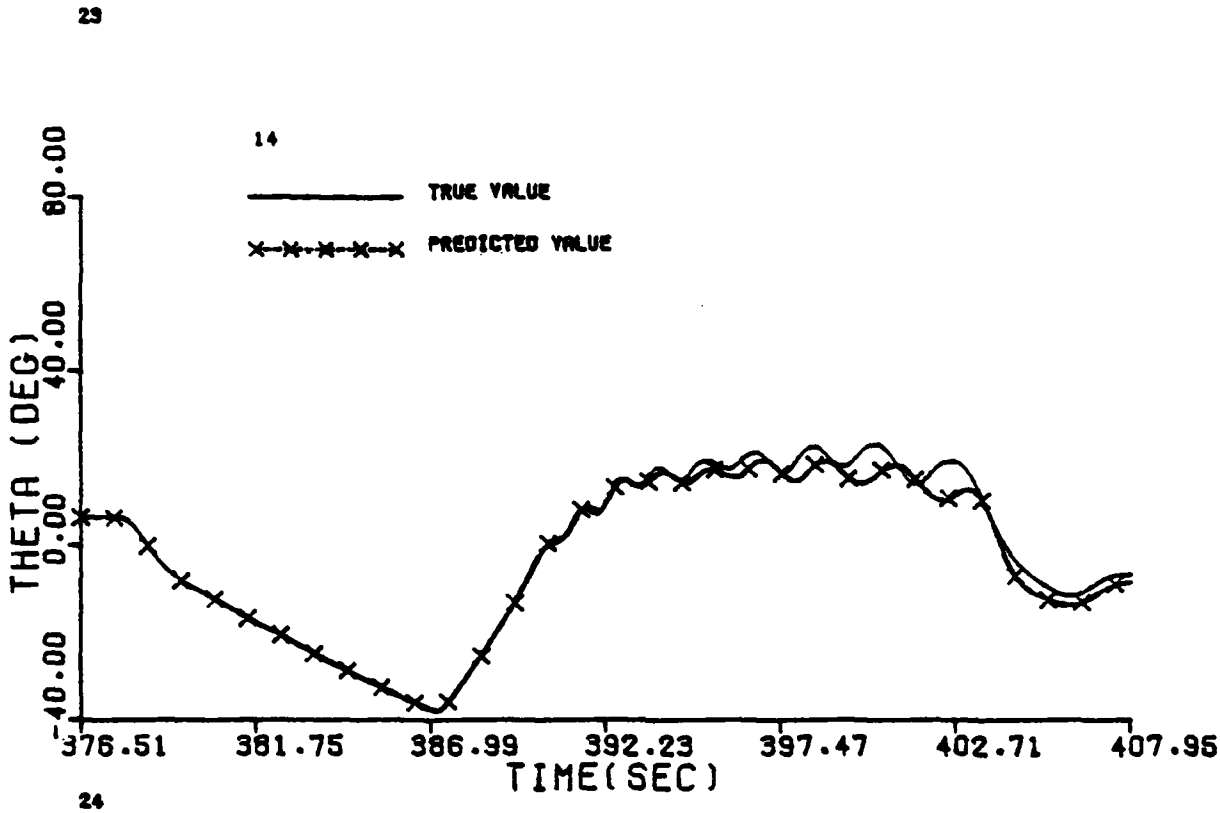

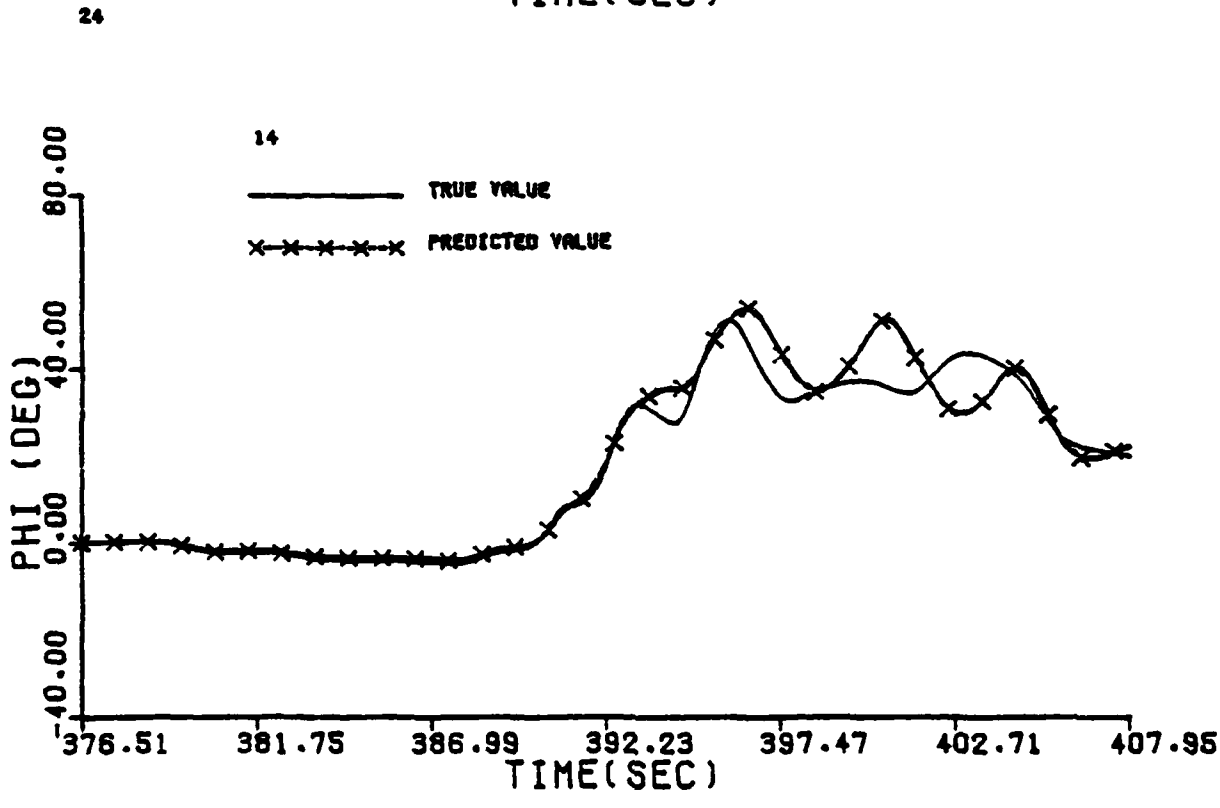

Figure G.1 Continued (Maneuver 14)

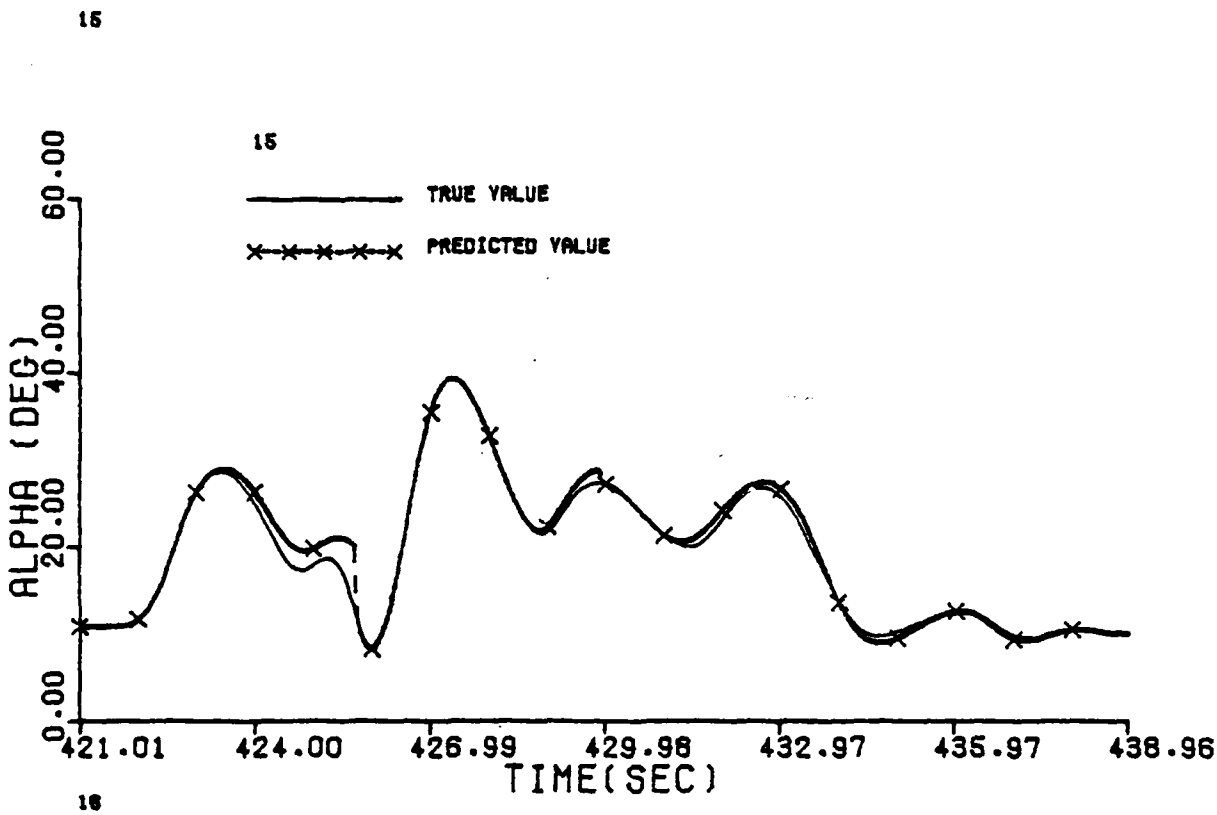

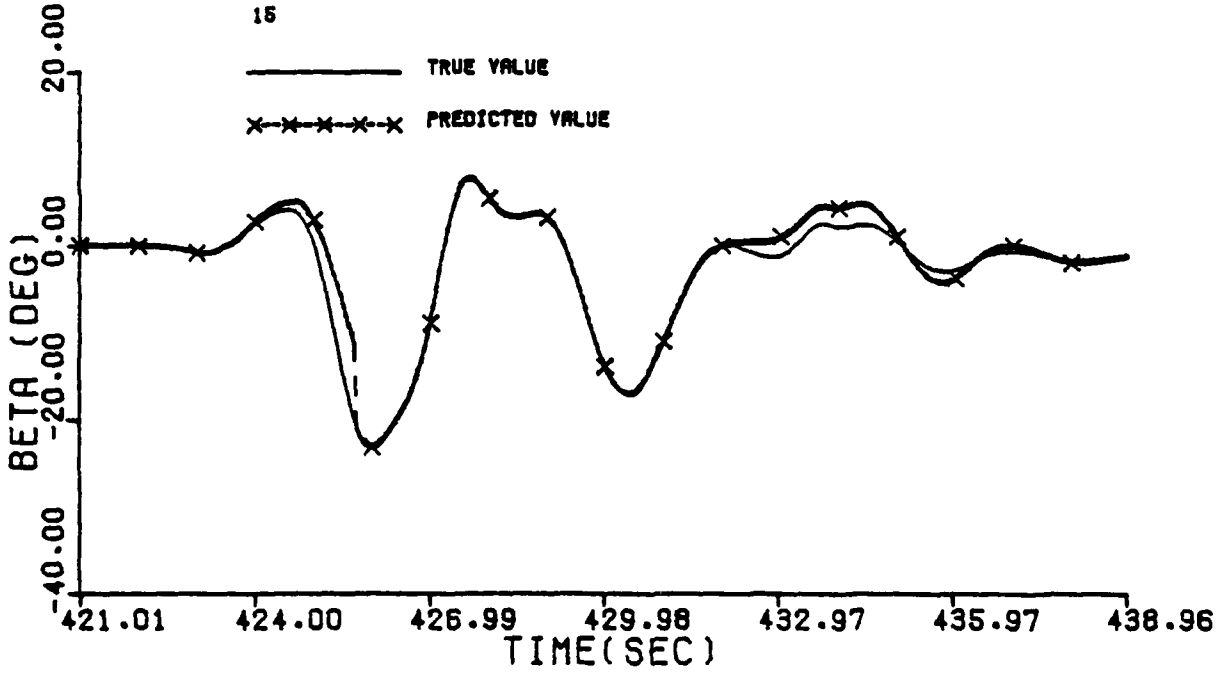

Figure G.1 Continued (Maneuver 15)

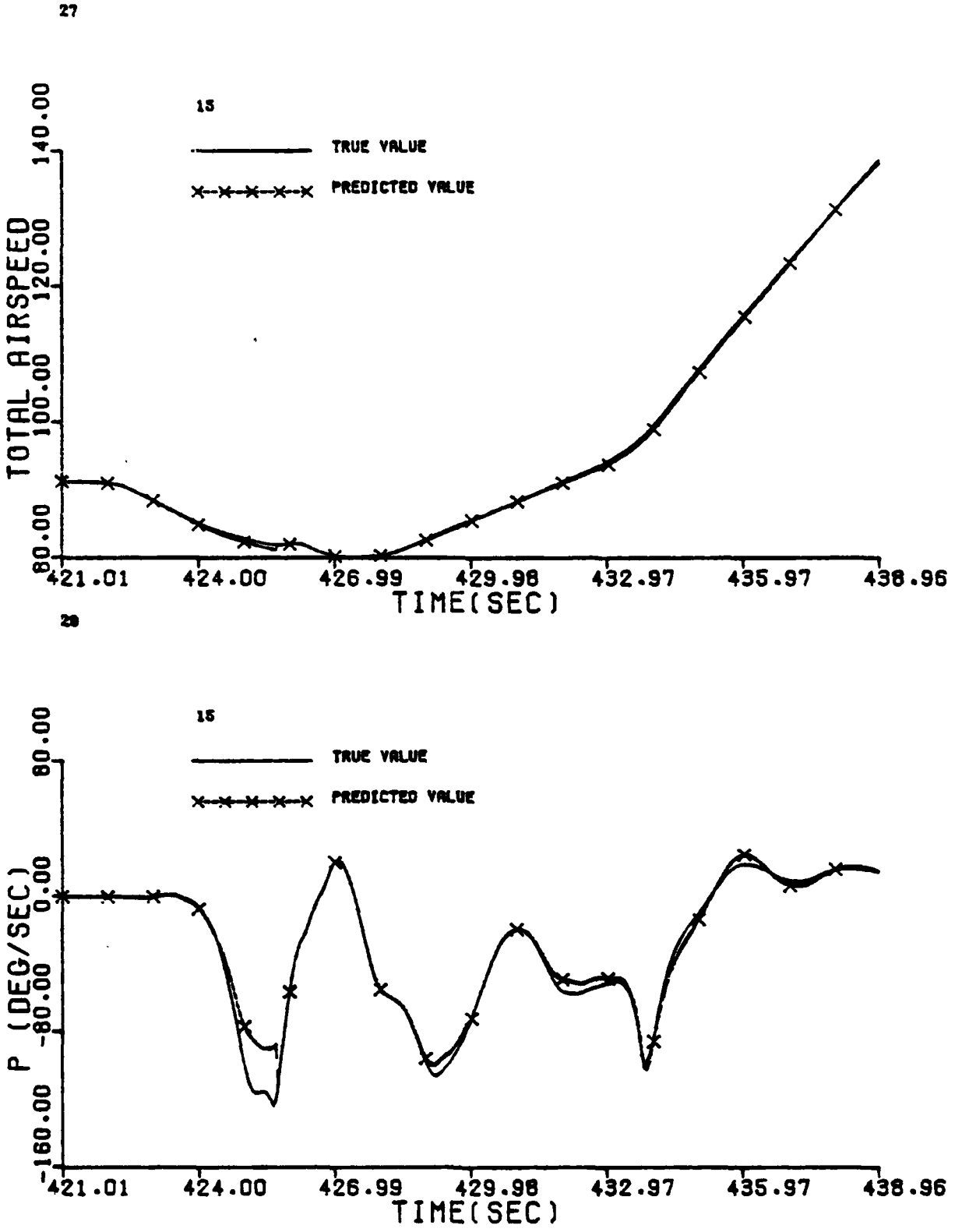

Figure G.1 Continued (Maneuver 15)

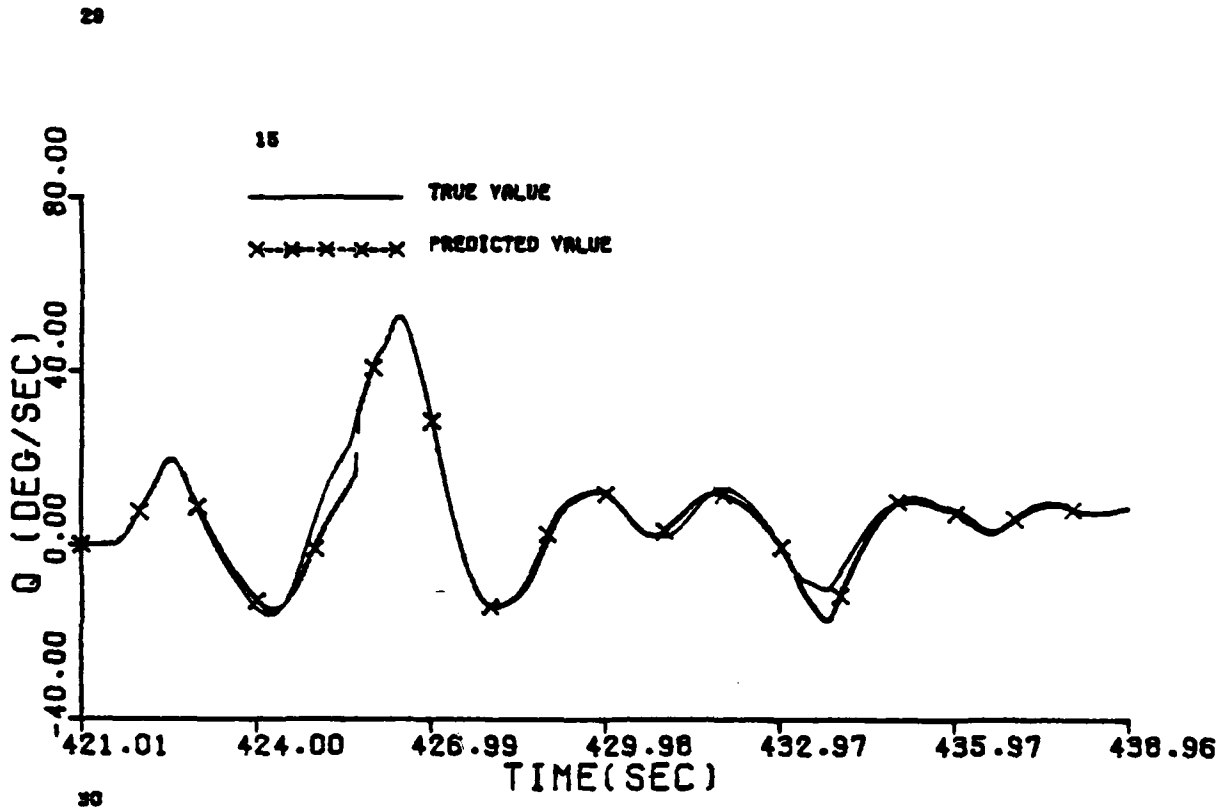

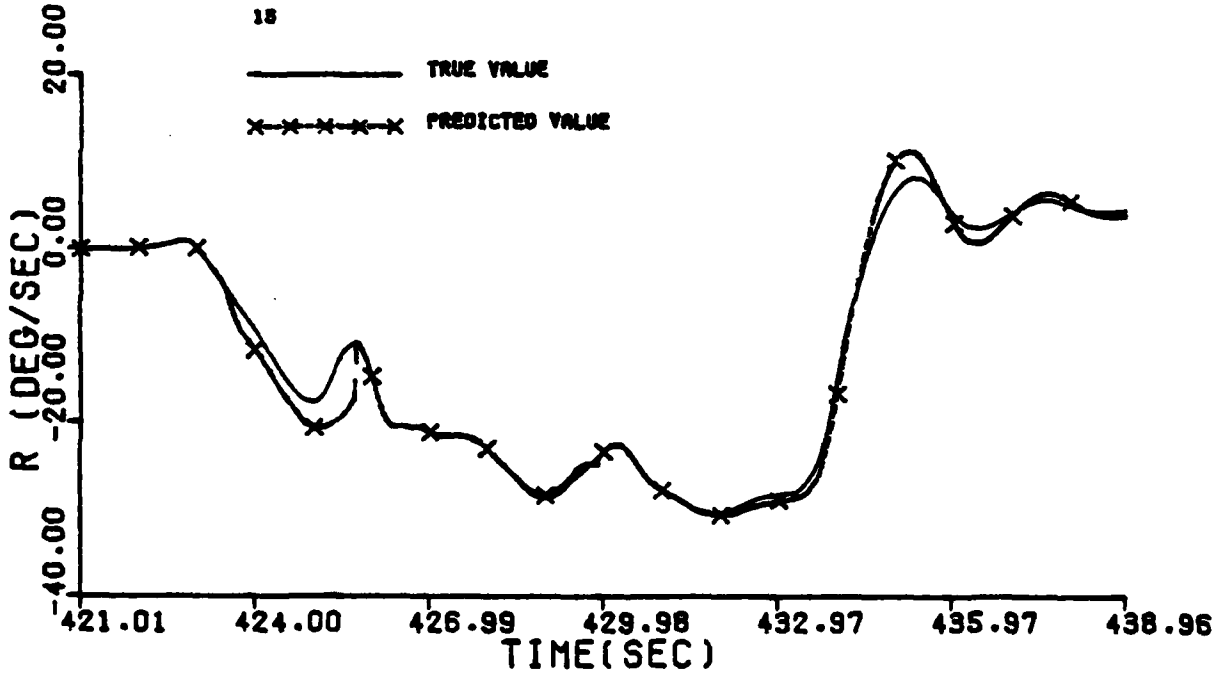

Figure G.1 Continued (Maneuver 15)

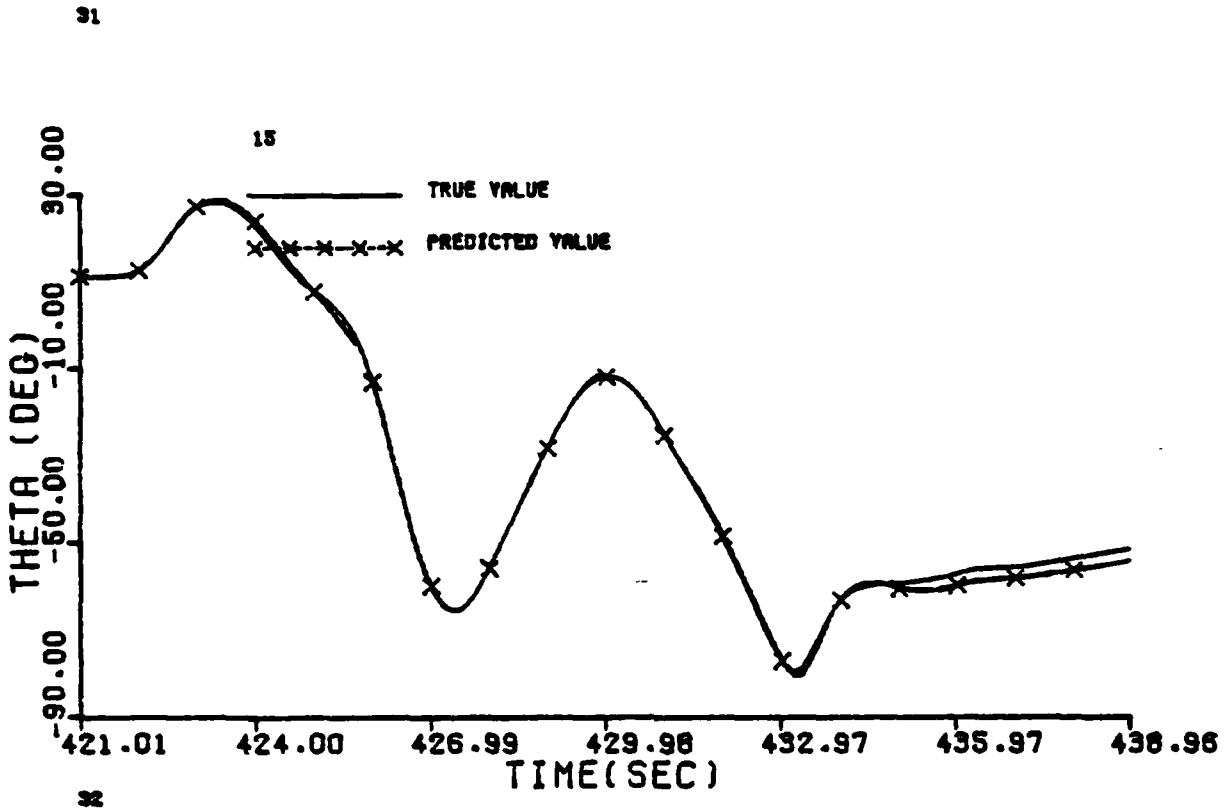

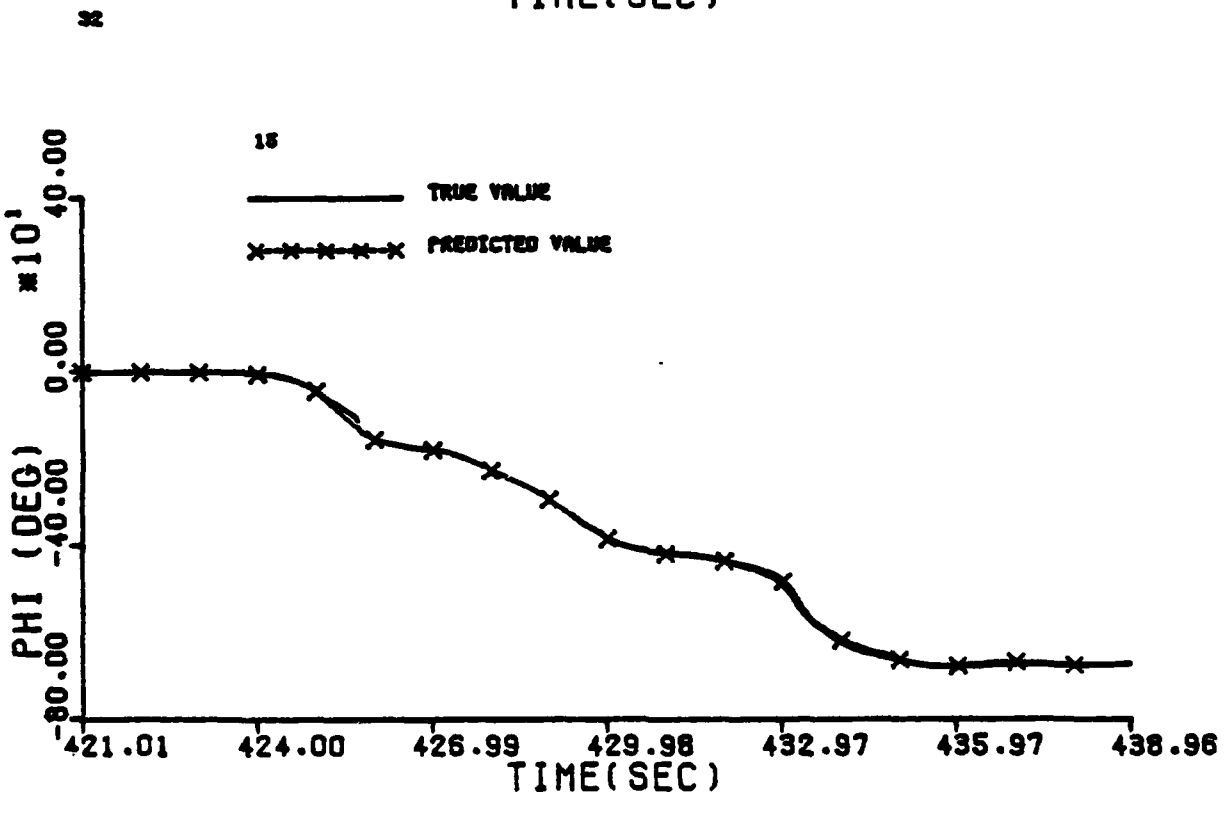

Figure G.1 Continued (Maneuver 15)

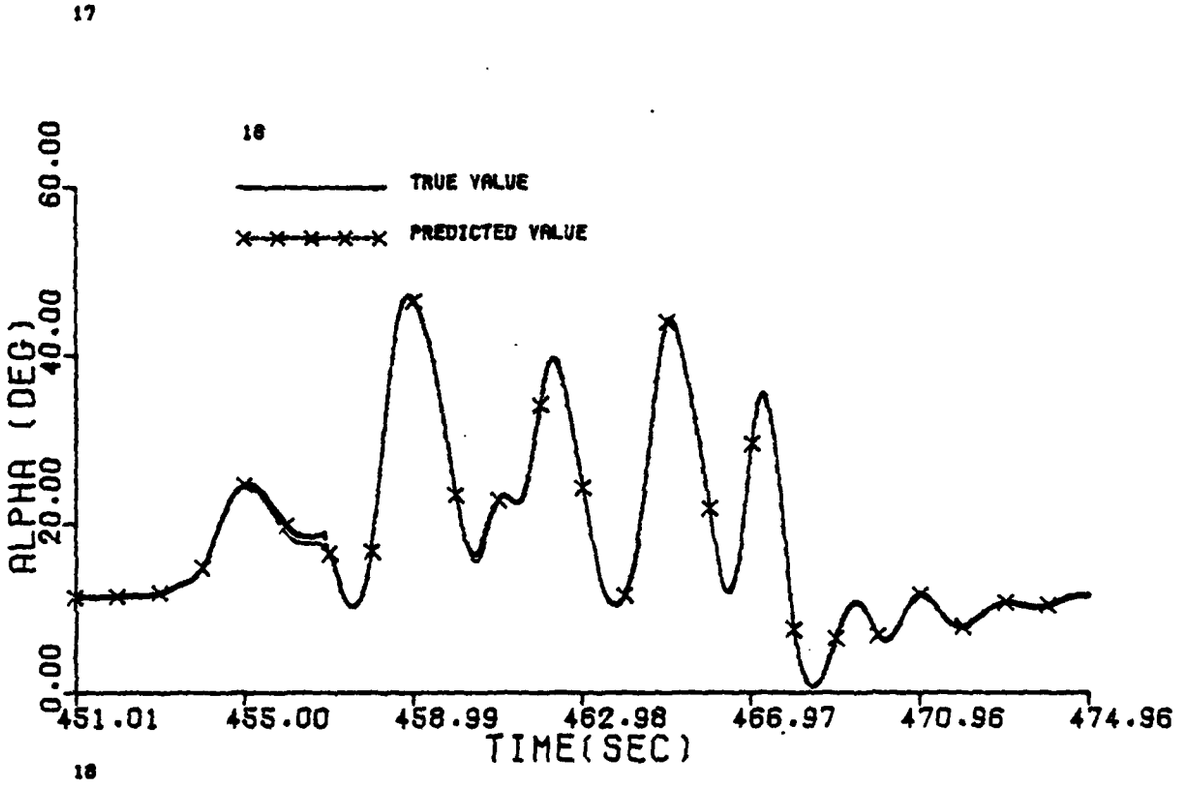

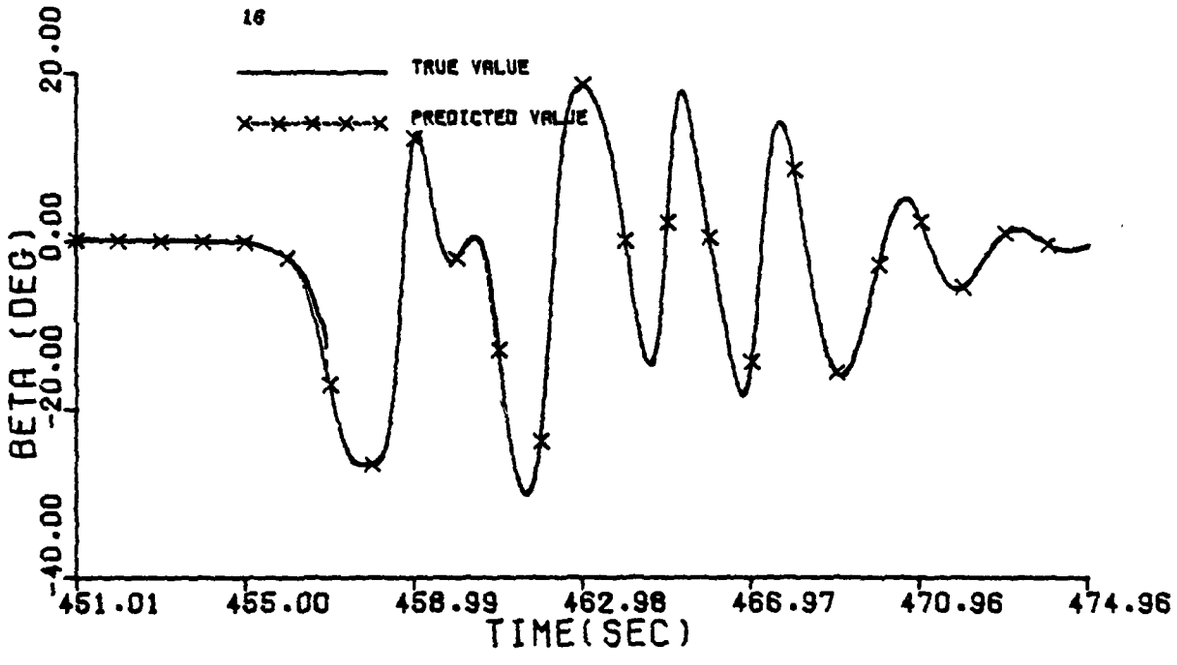

Figure G.1 Continued (Maneuver 16)

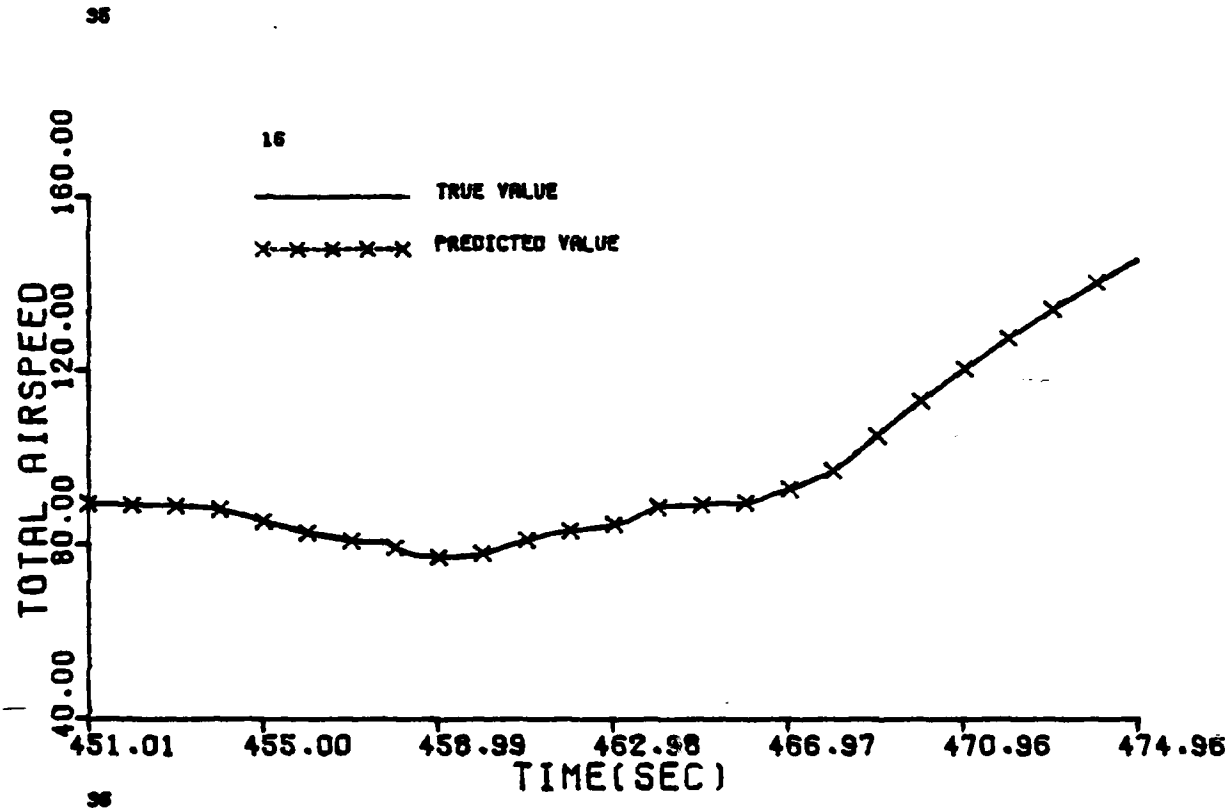

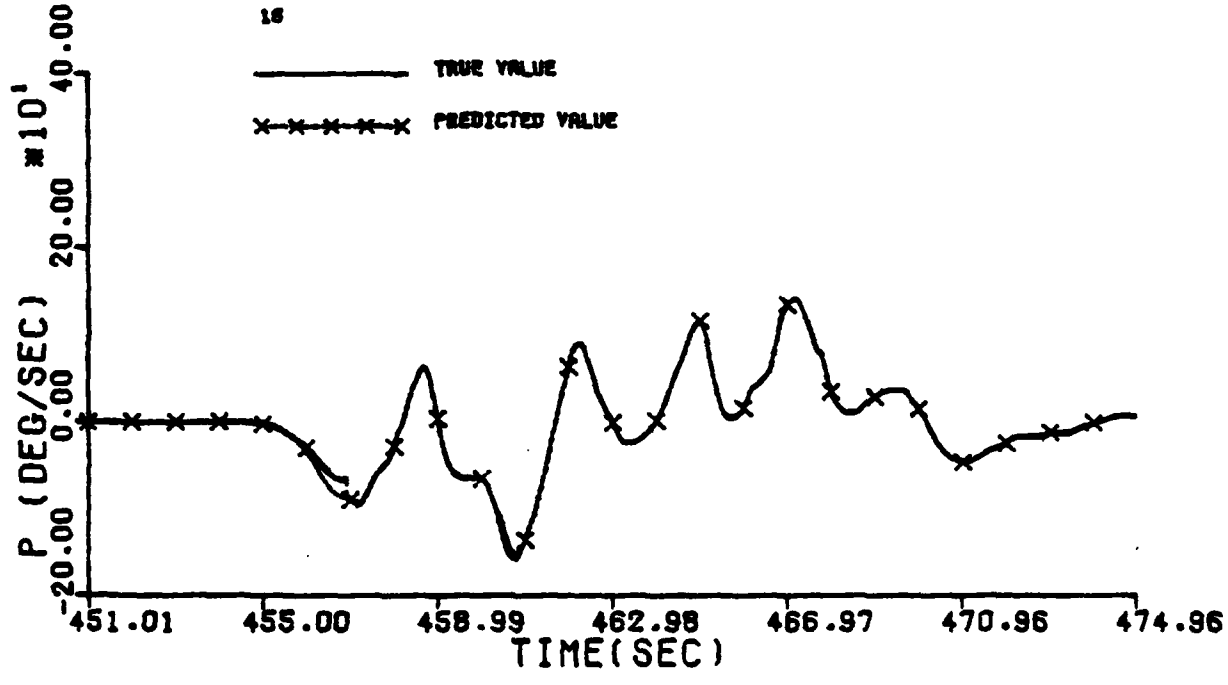

Figure G.1 Continued (Maneuver 16)

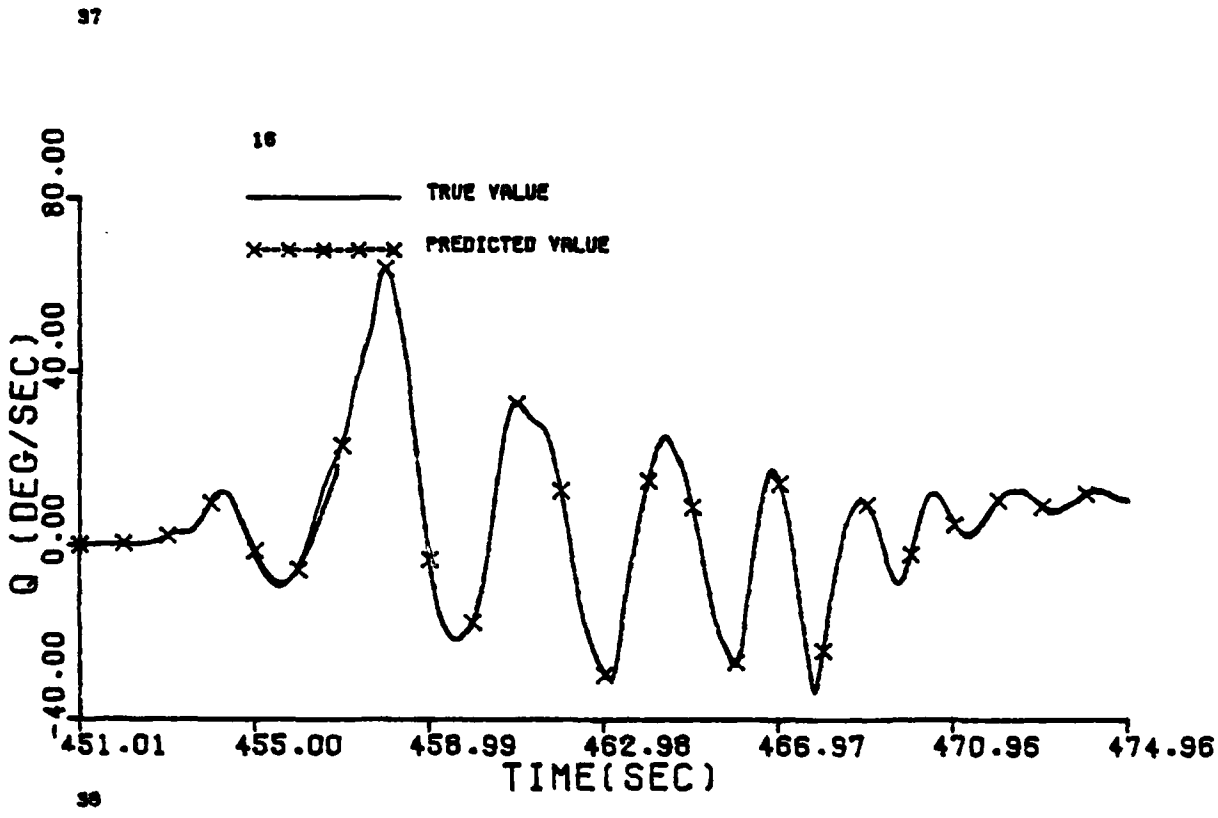

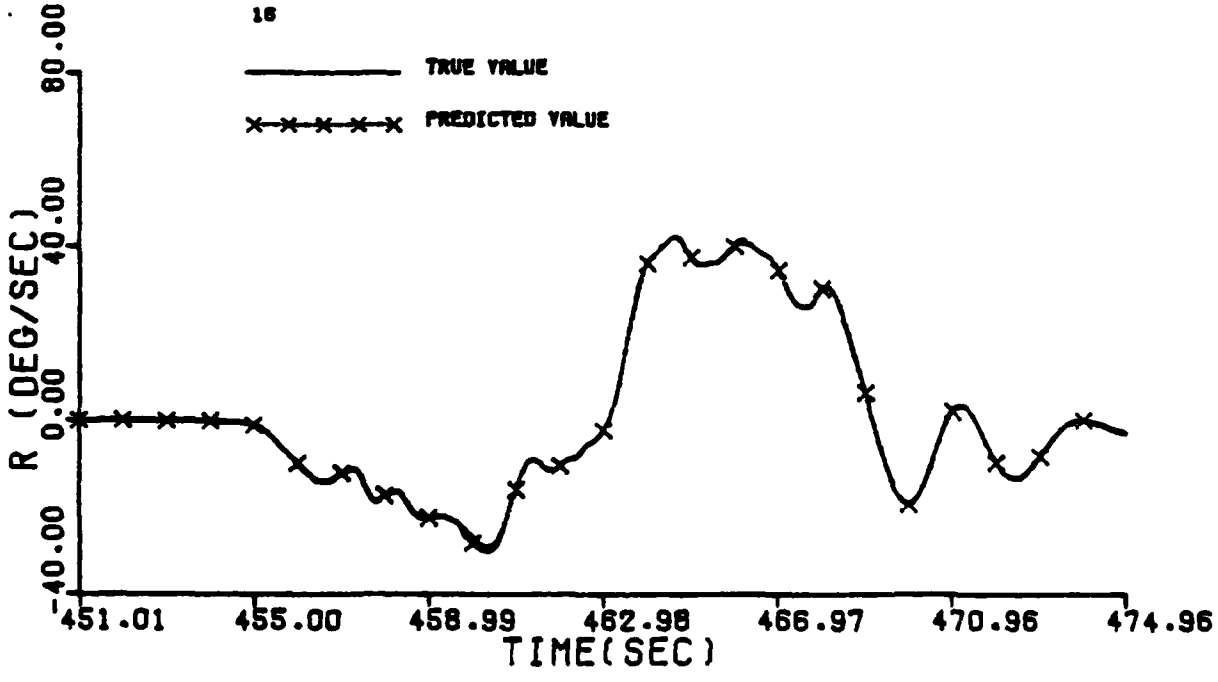

Figure G.1 Continued (Maneuver 16)

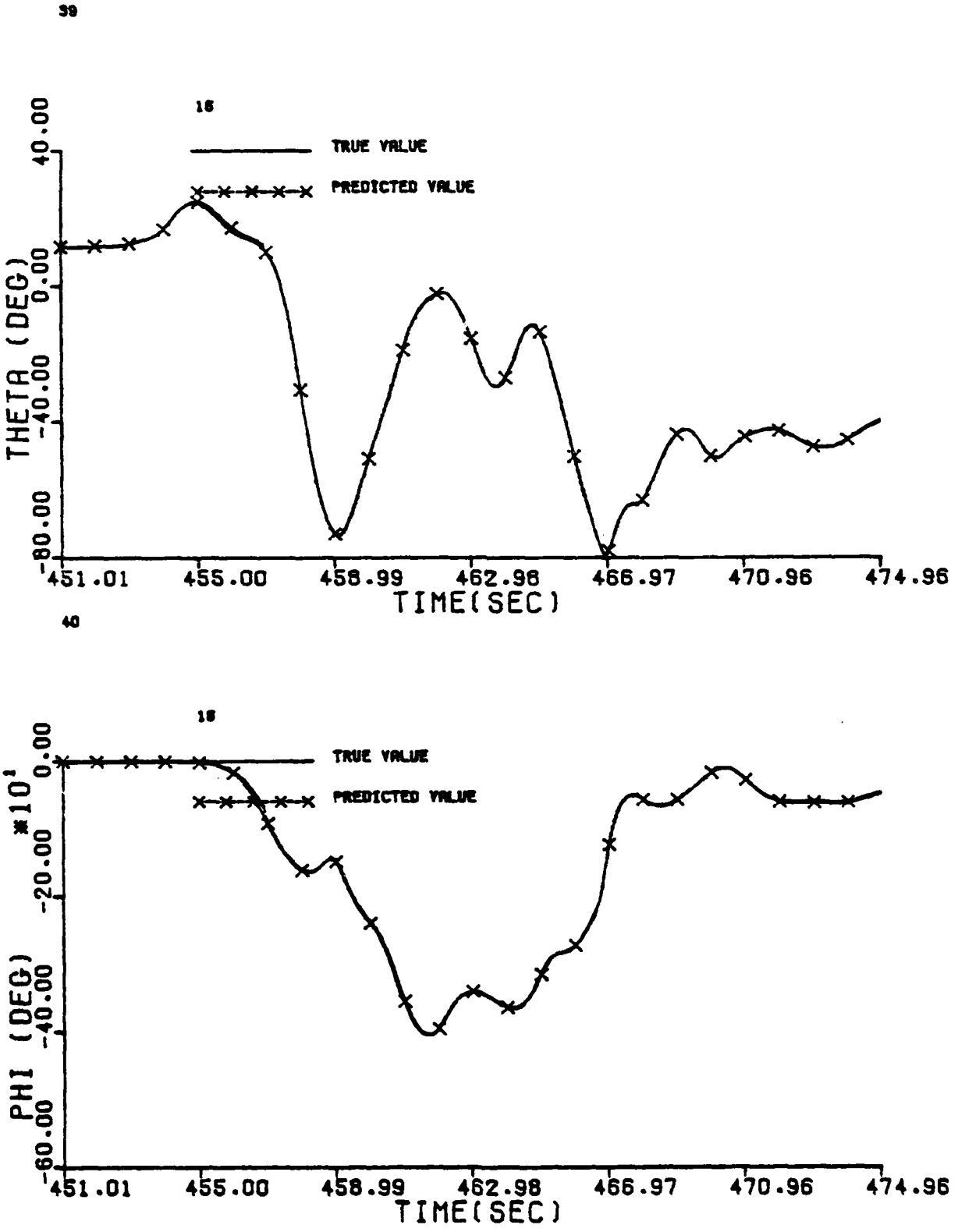

Figure G.1 Continued (Maneuver 16)

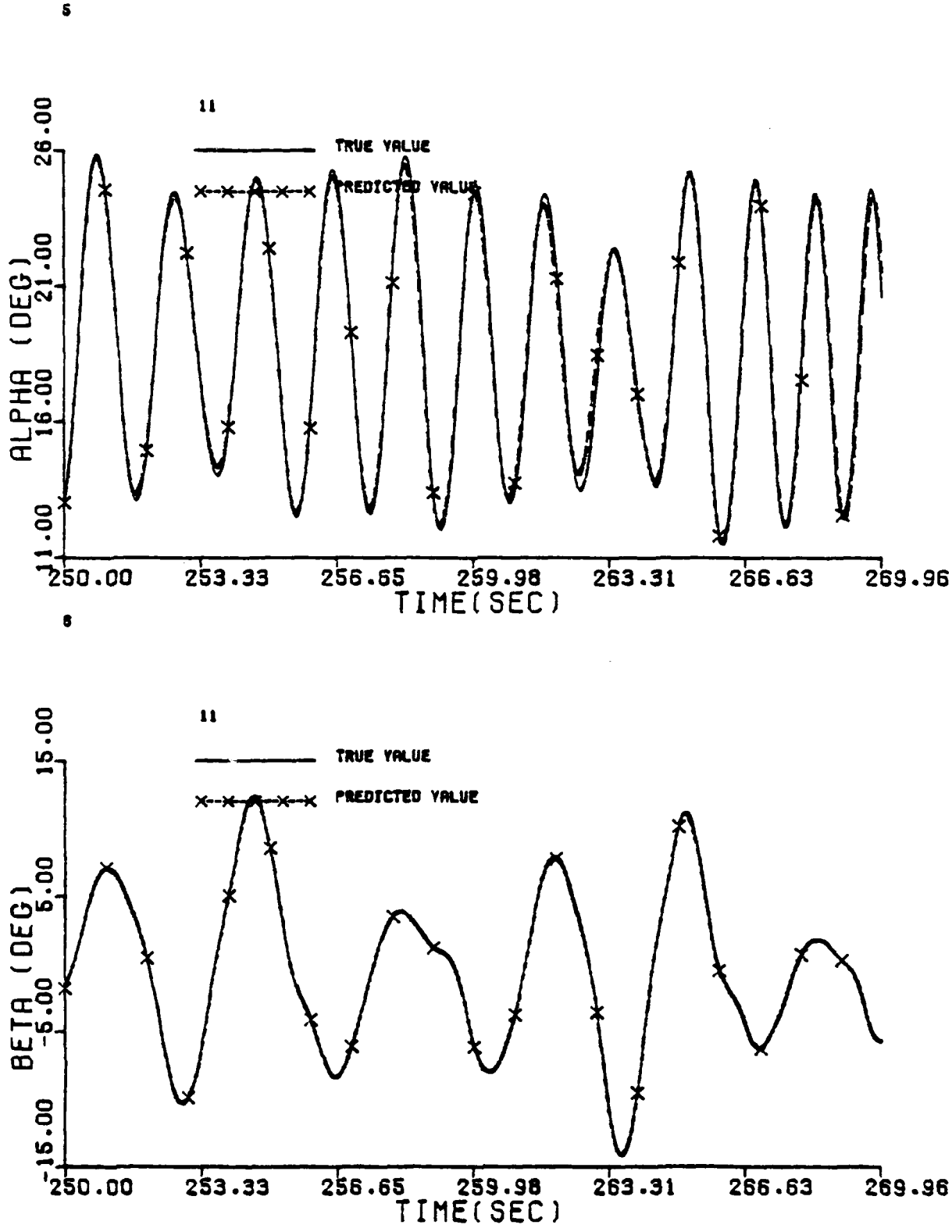

Figure G.2(a) Model Response Using Estimated Time Histories of Lateral States

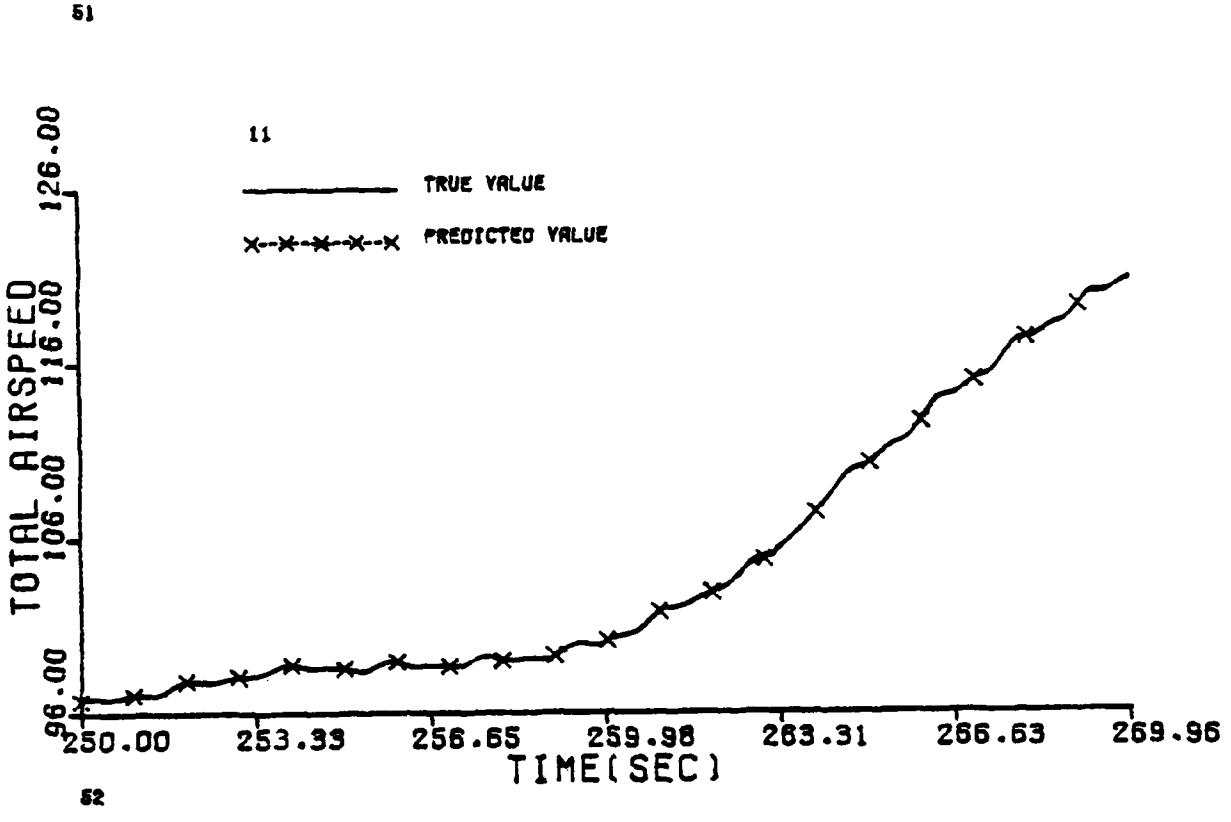

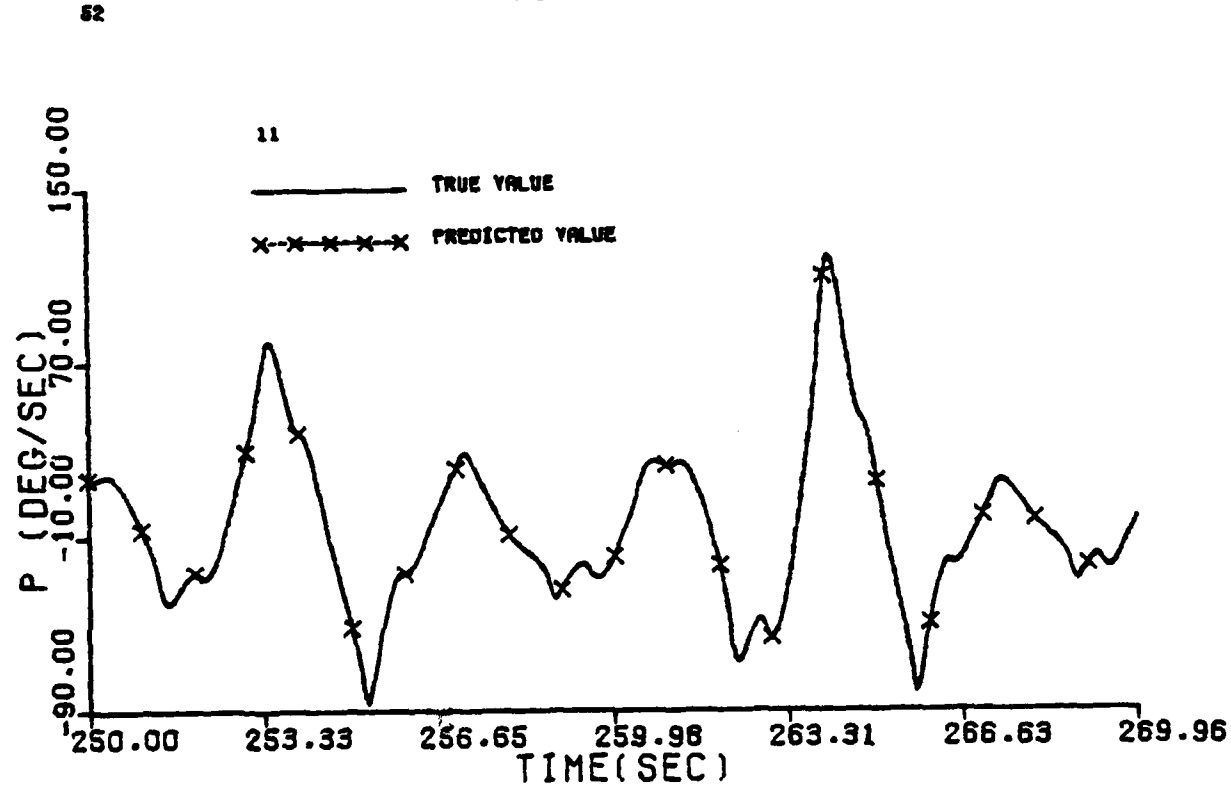

Figure G.2(a) Continued

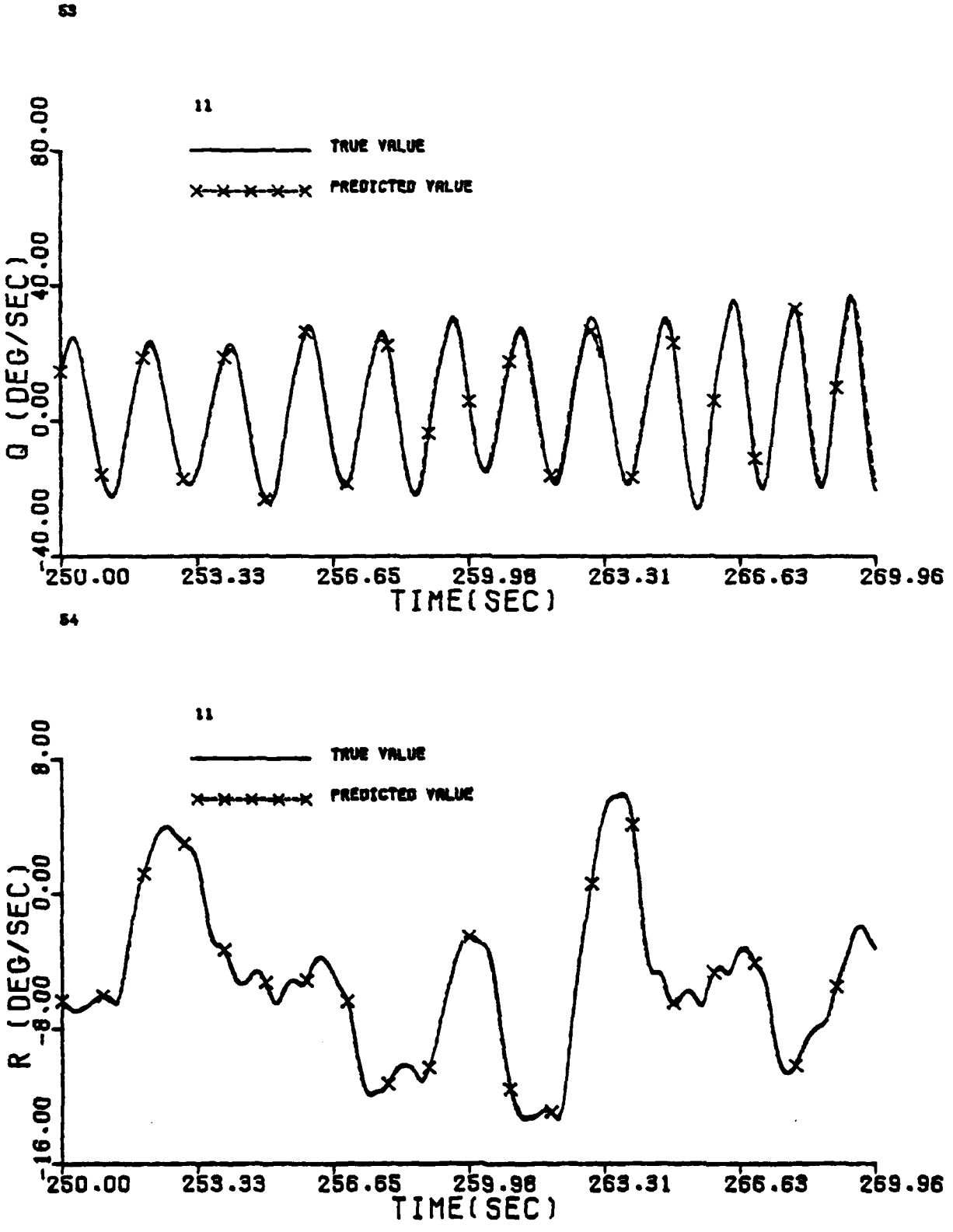

Figure G.2(a) Continued

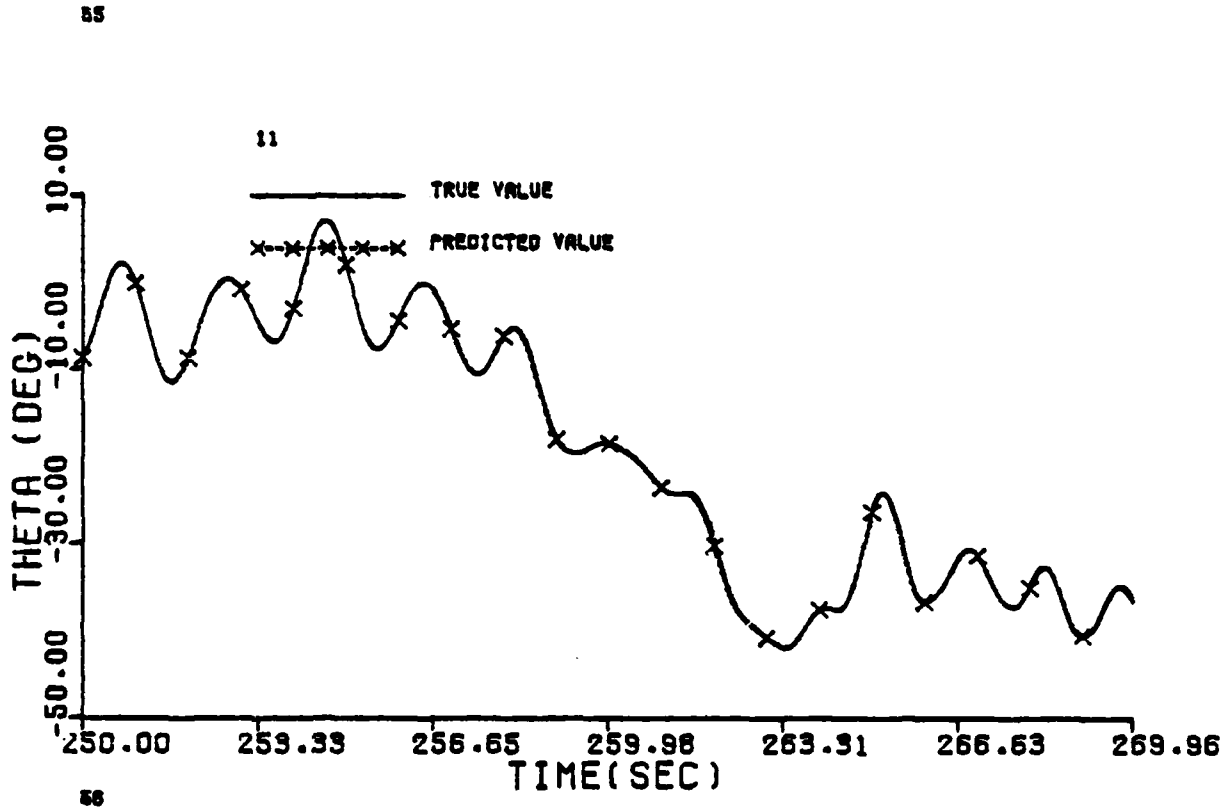

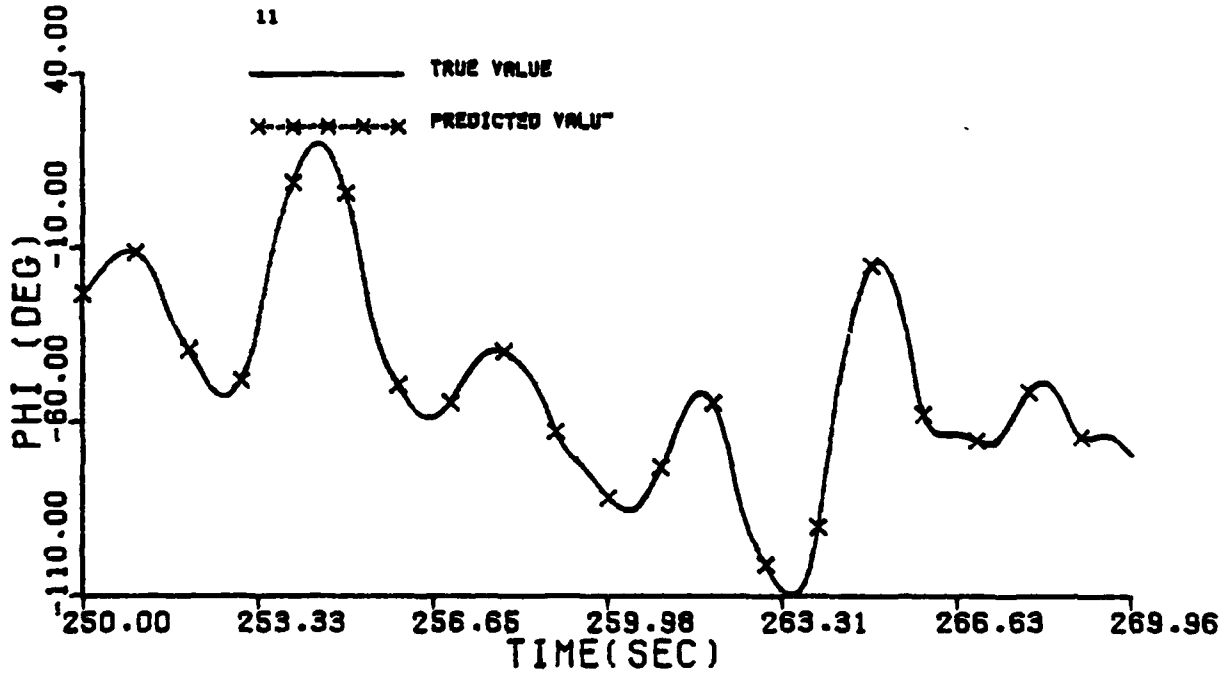

Figure G.2(a) Concluded

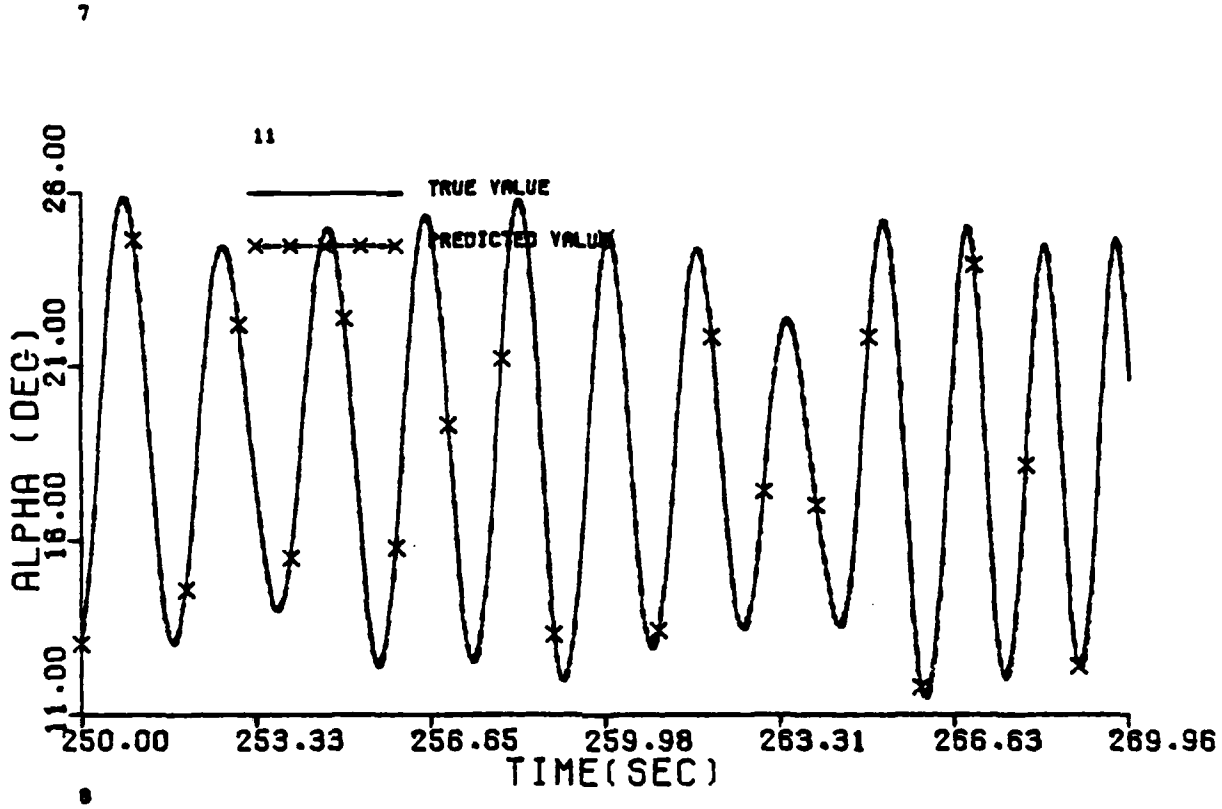

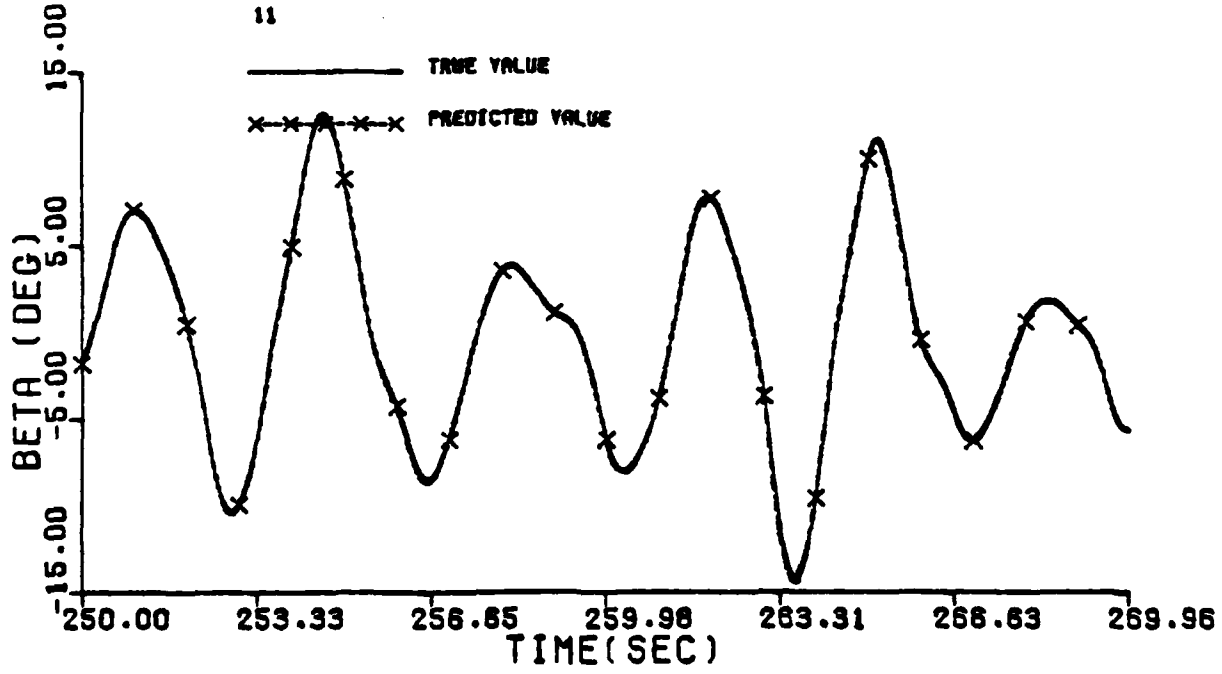

Figure G.2(b) Model response Using Estimated Time Histories of Longitudinal States

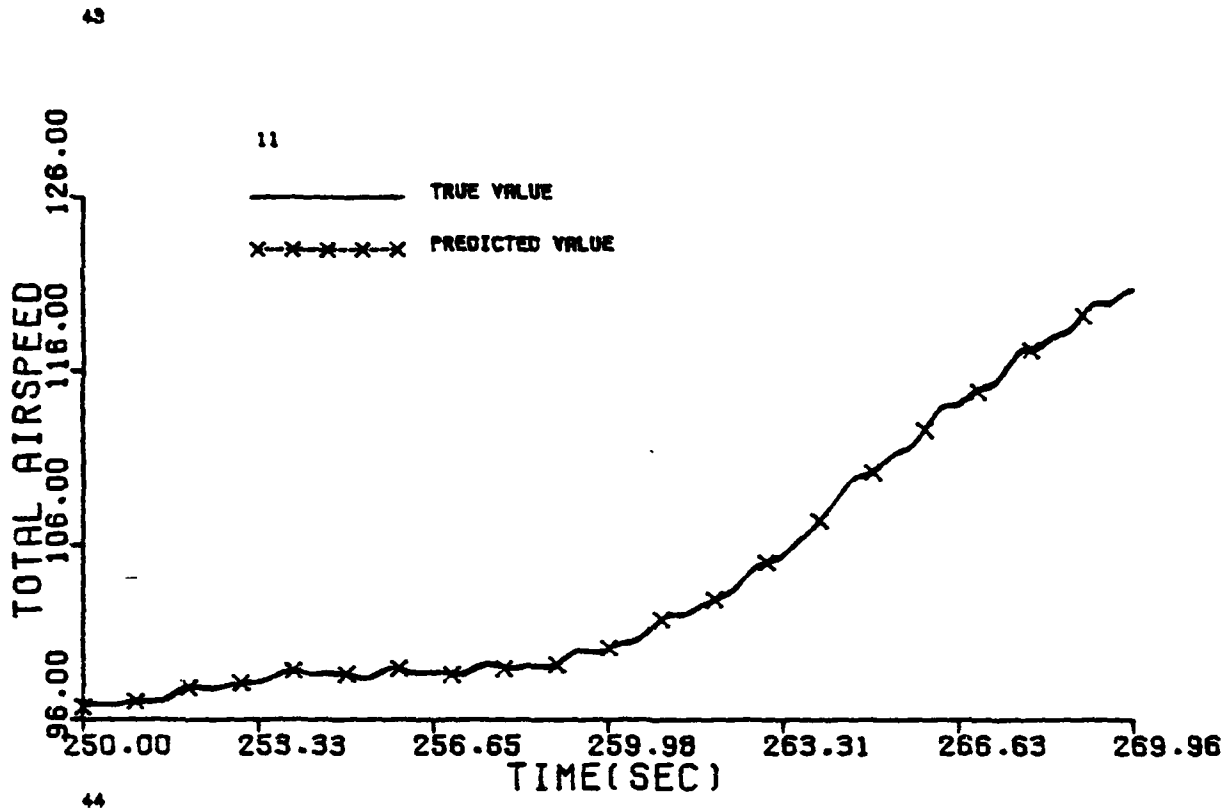

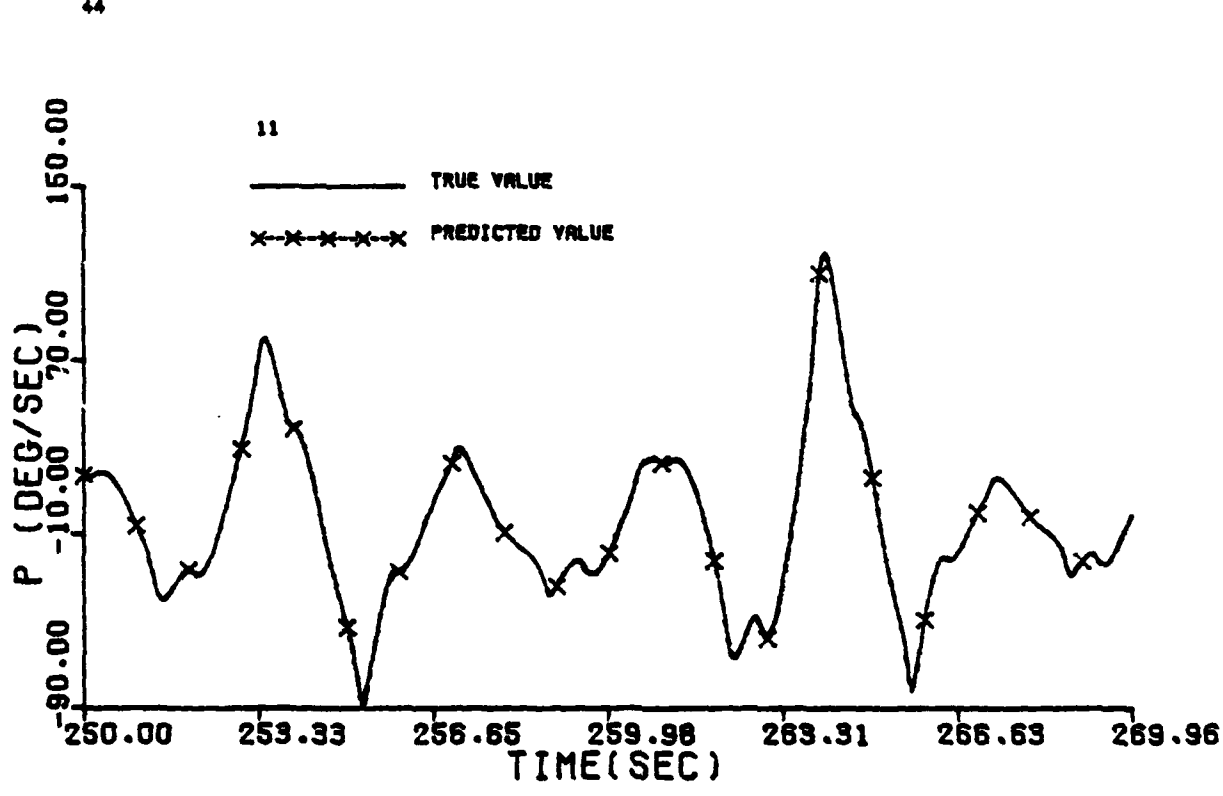

Figure G.2(b) Continued

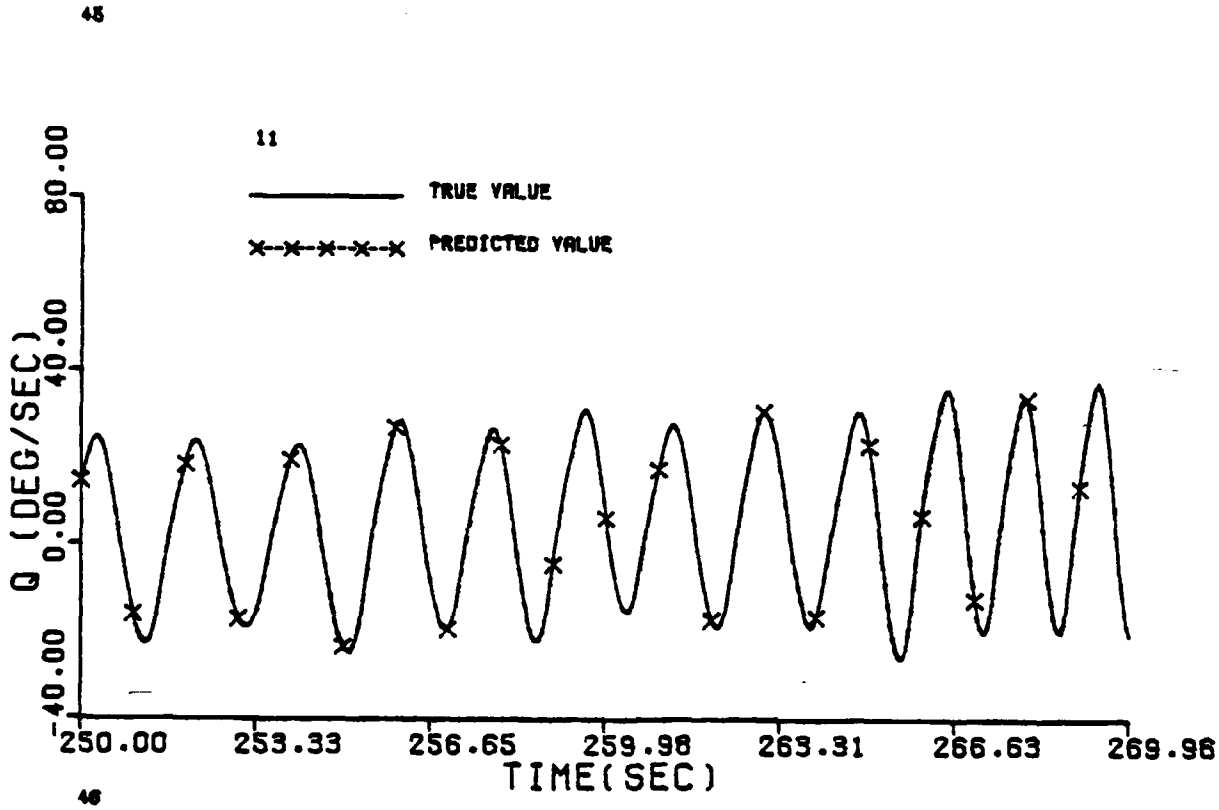

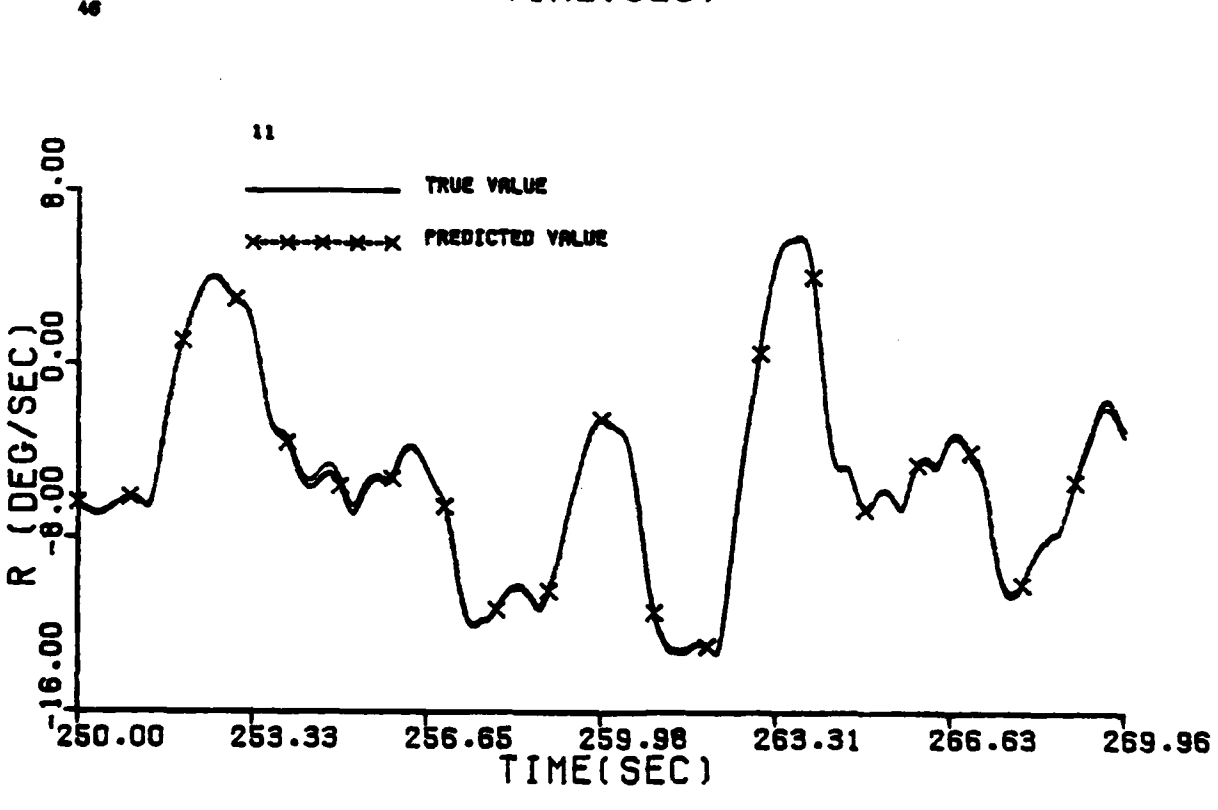

Figure G.2(b) Continued

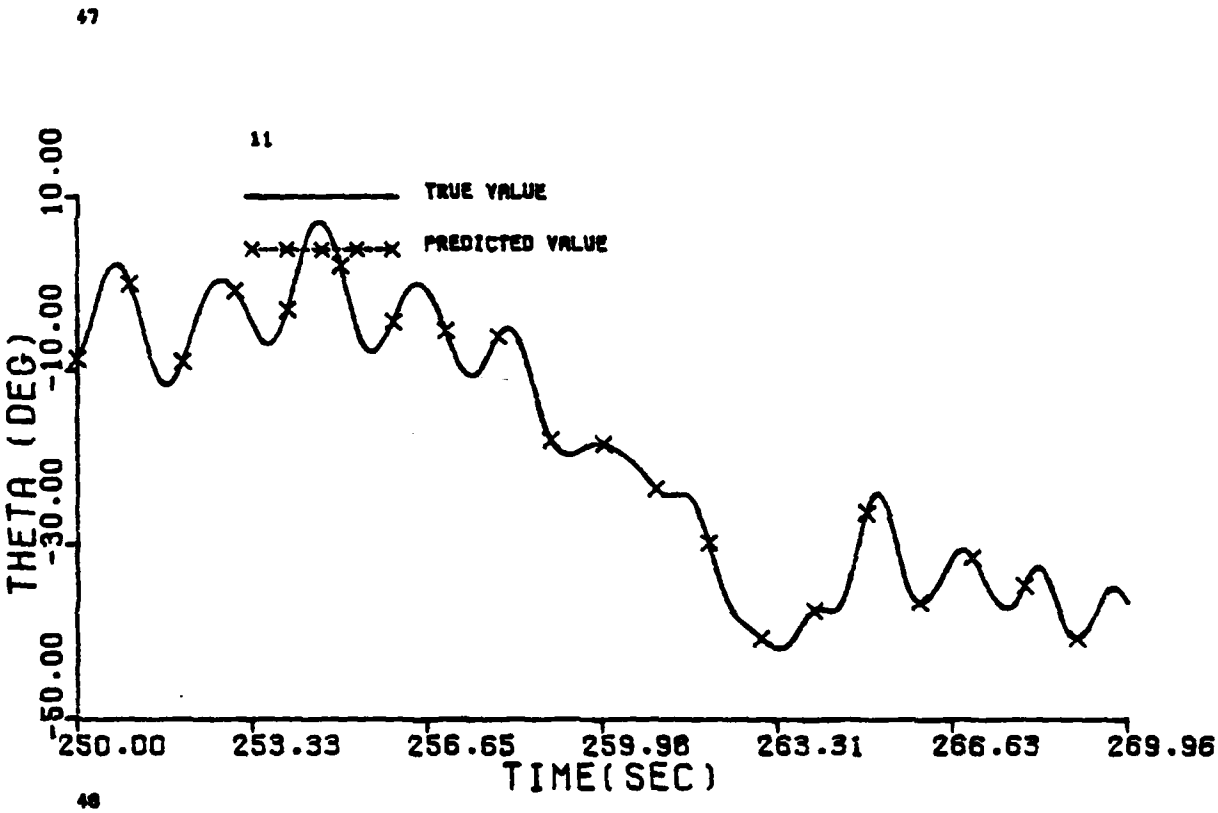

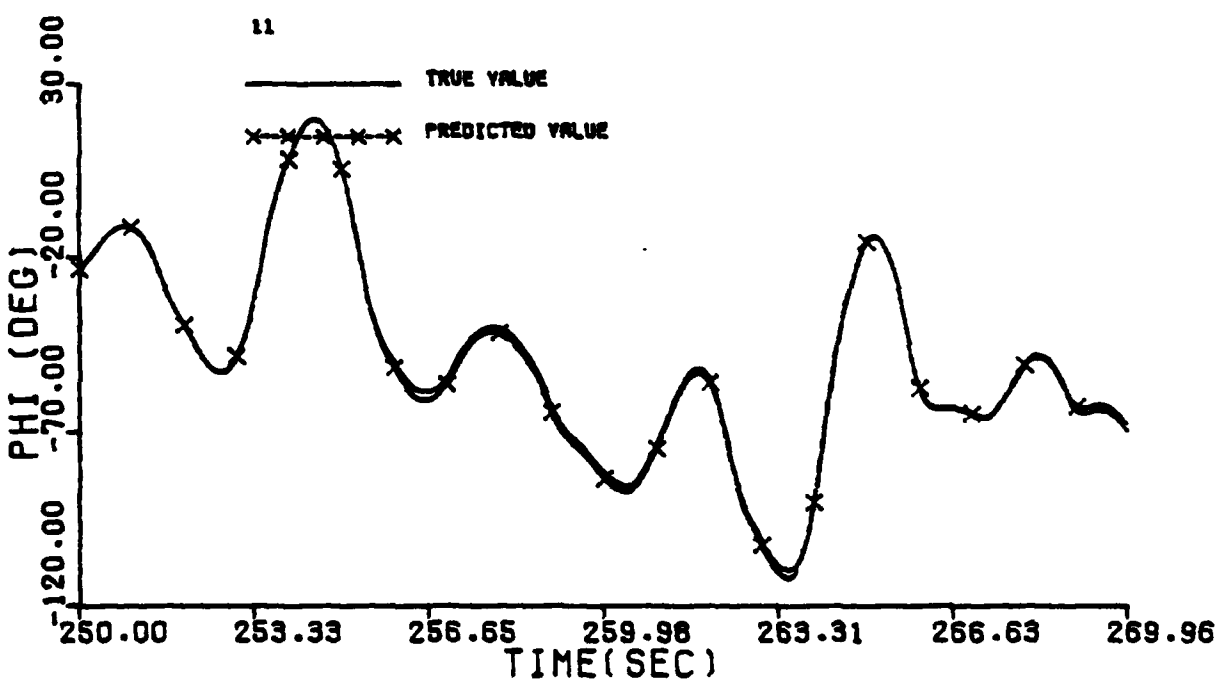

Figure G.2(b) Concluded

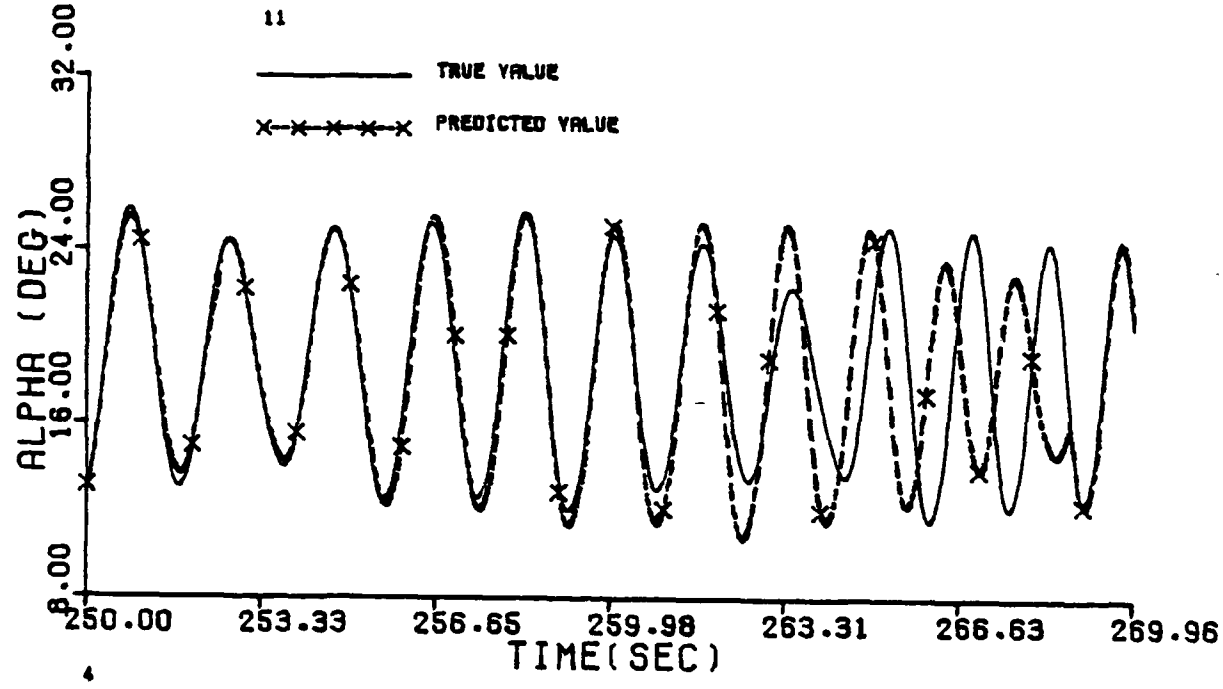

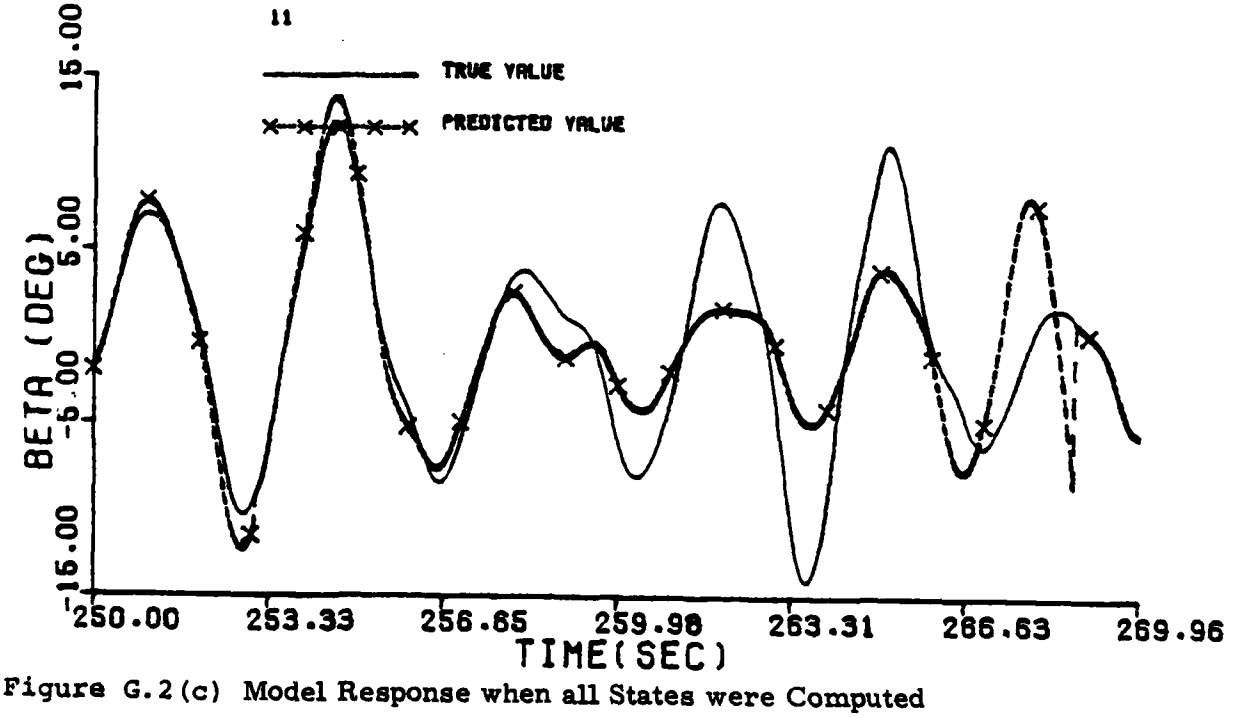

Figure G.2(c) Model Response when all States were Computed

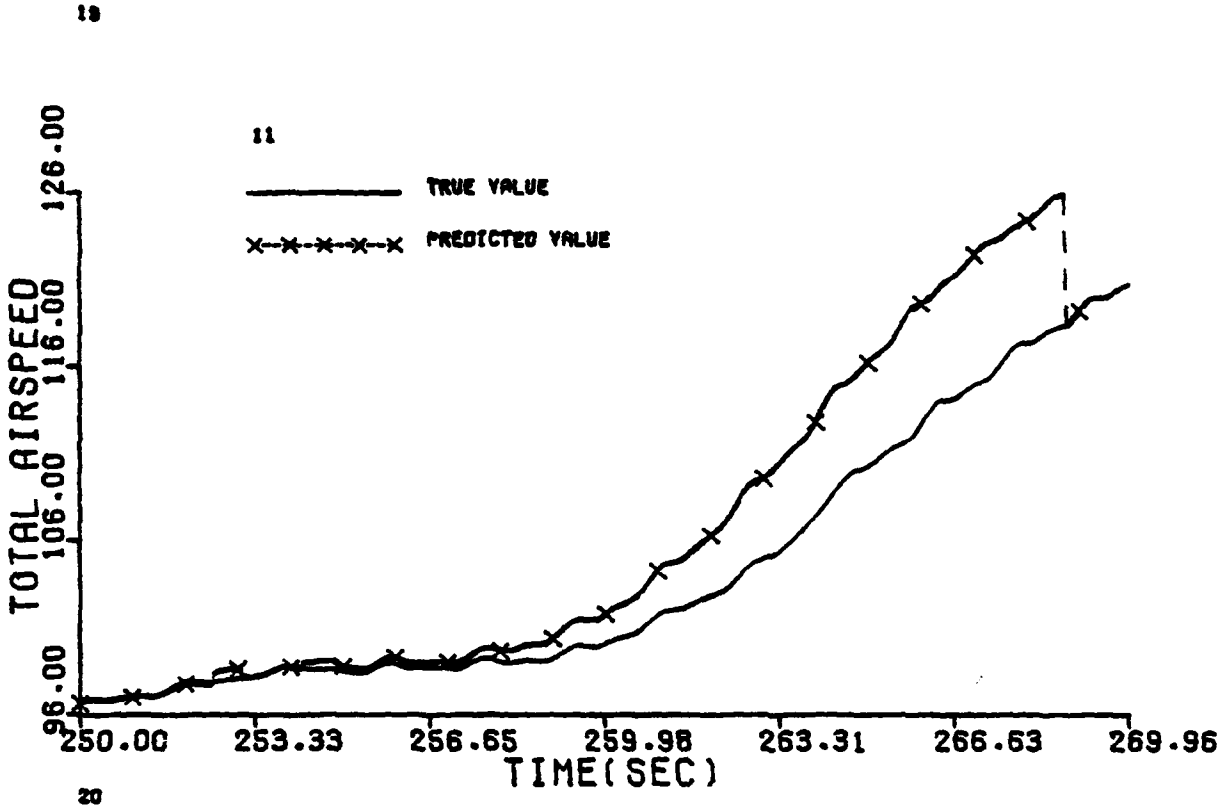

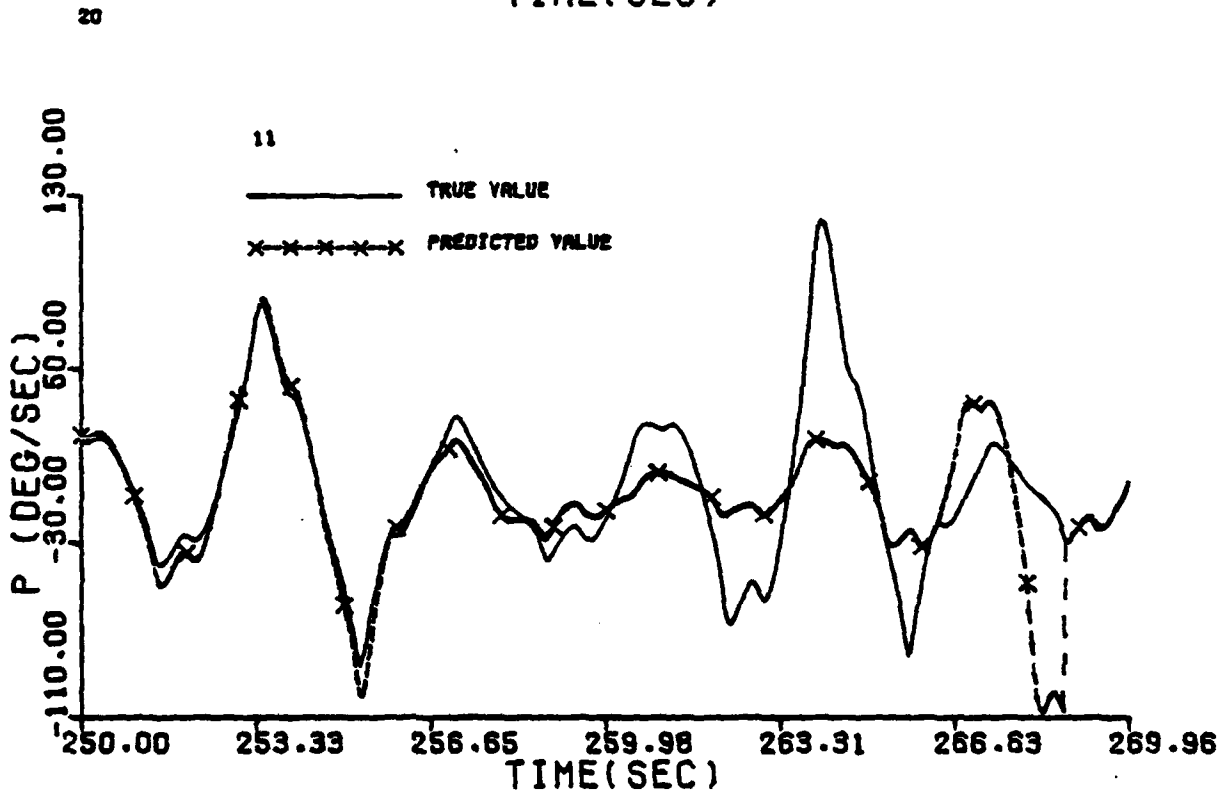

Figure G.2(c) Continued

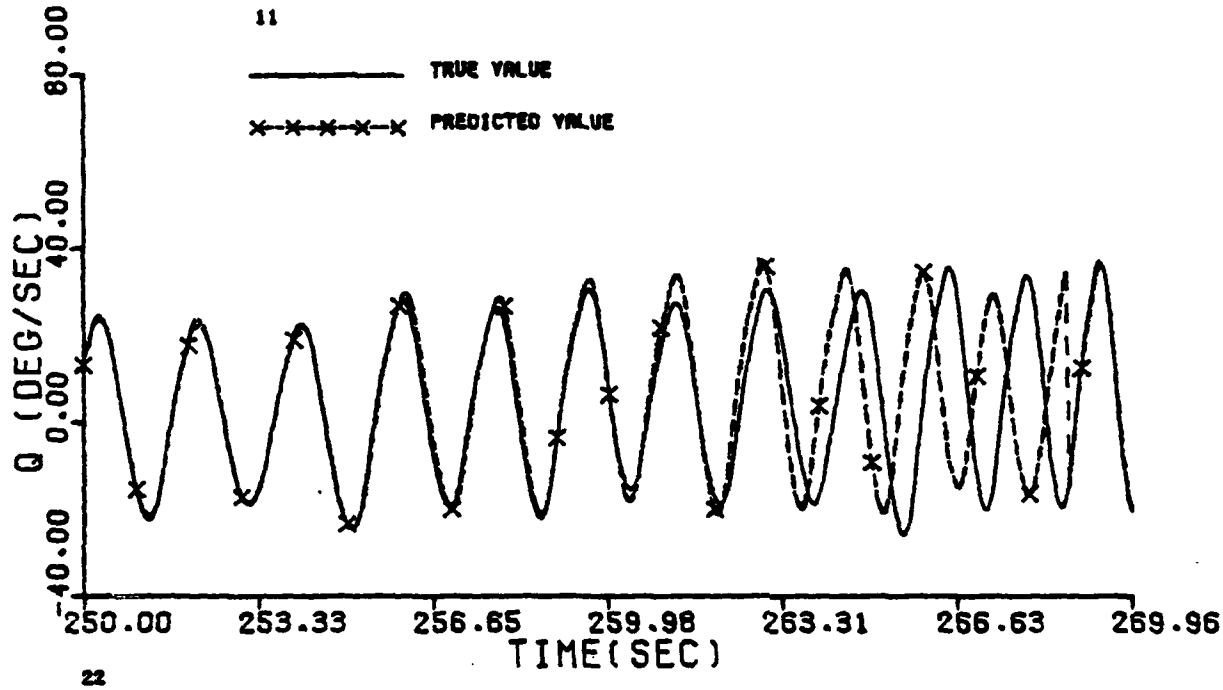

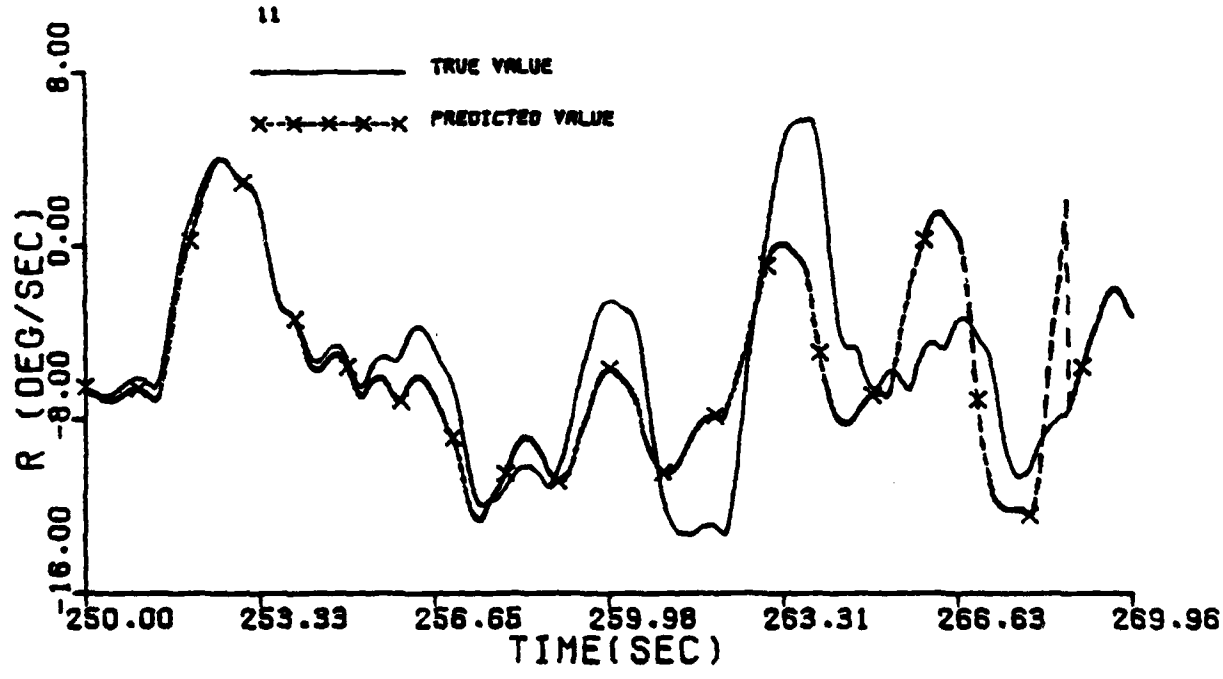

Figure G.2(c) Continued

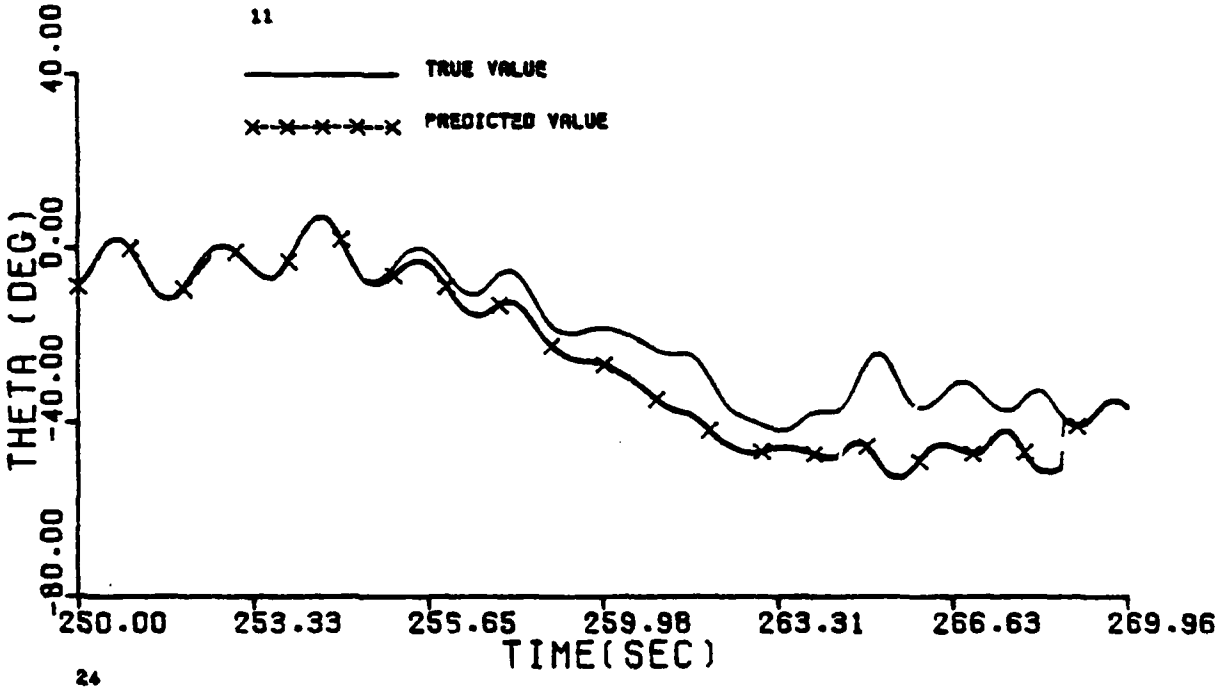

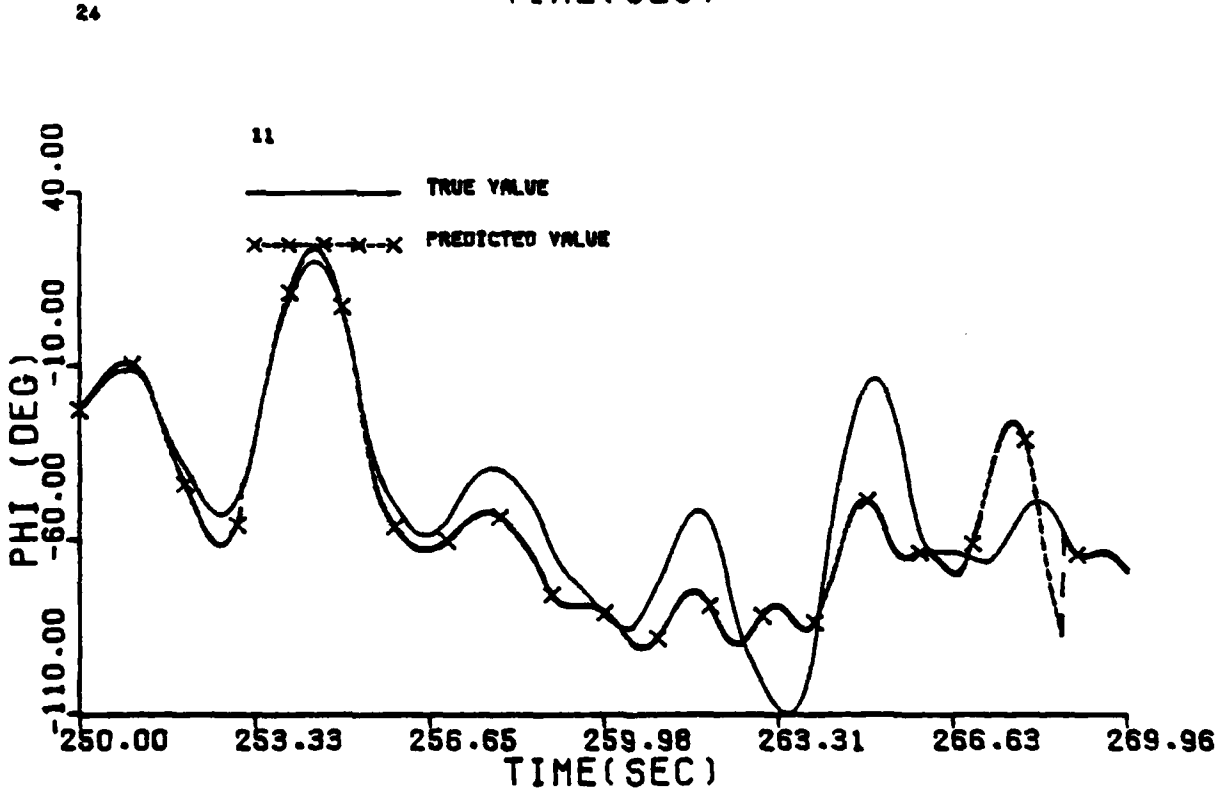

Figure G.2(c) Concluded

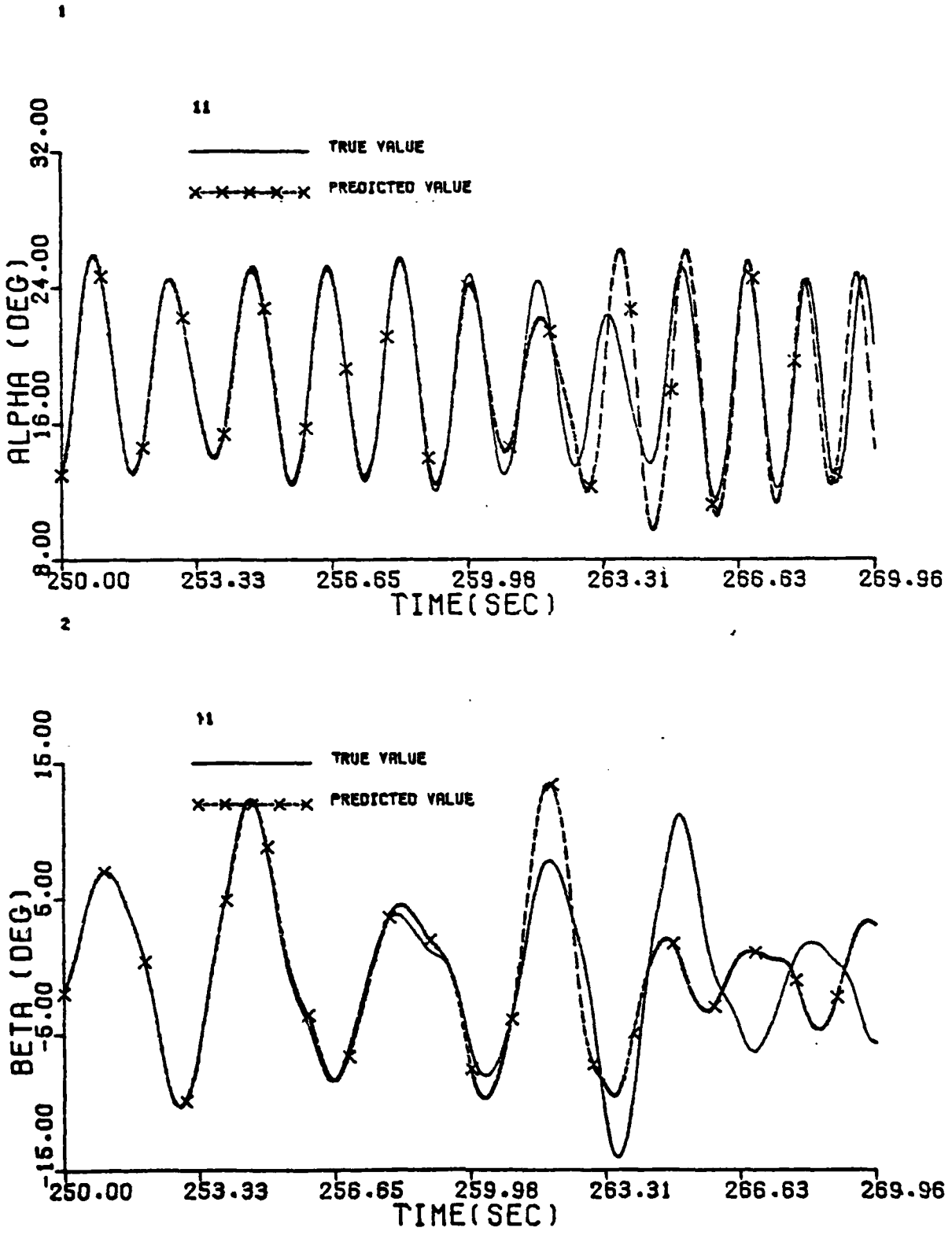

Figure G.2(d) Response of Wind Tunnel Model with Small Perturbations in α and β at 254 and 256 seconds

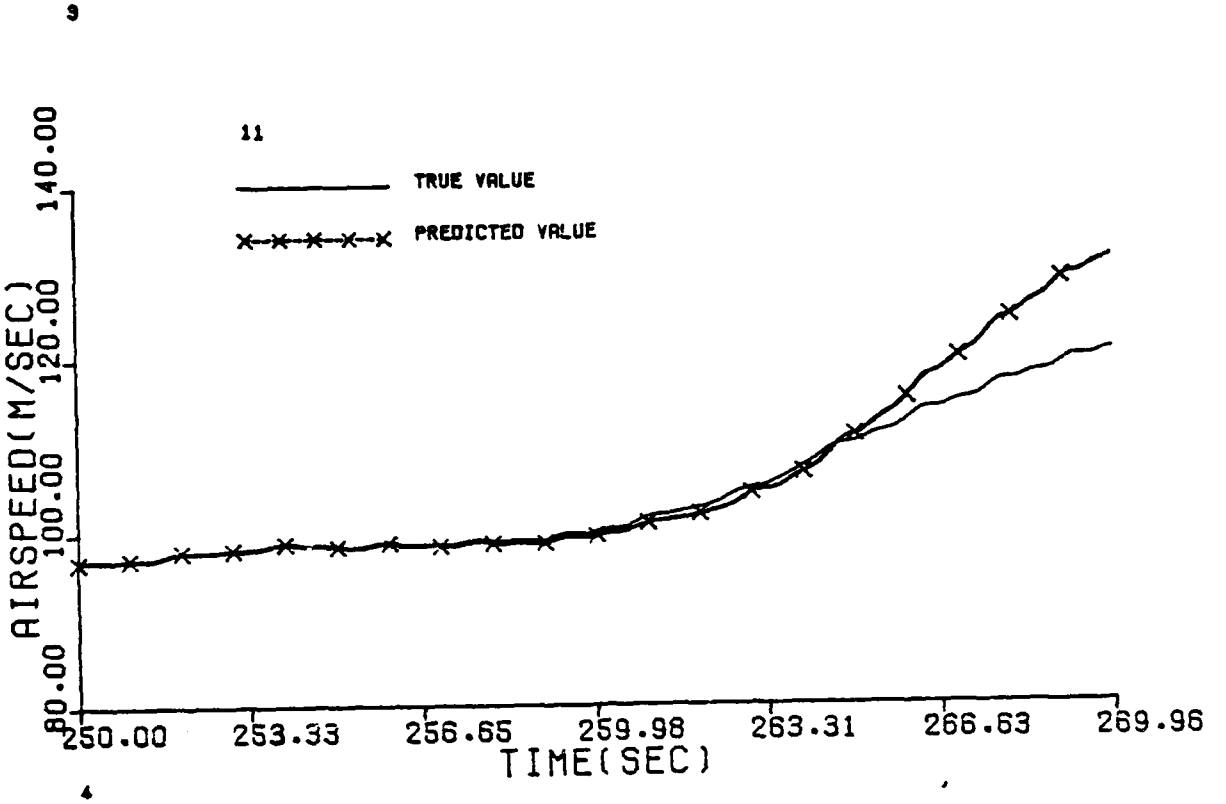

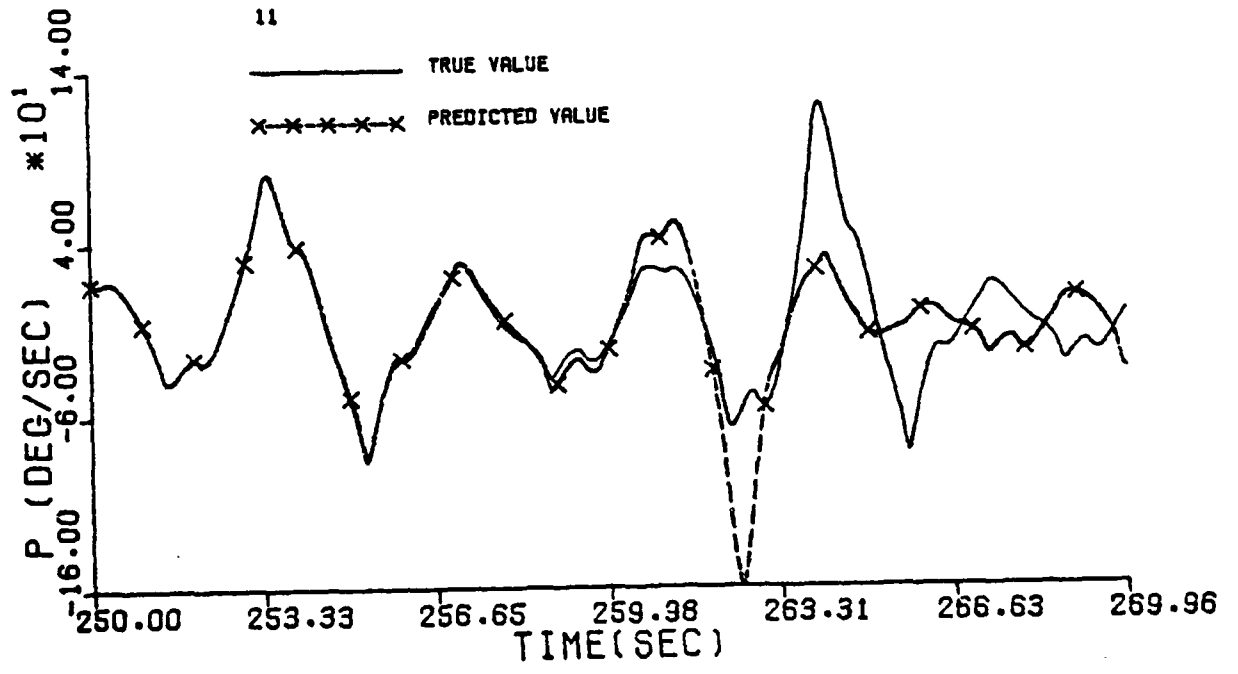

Figure G.2(d) Continued

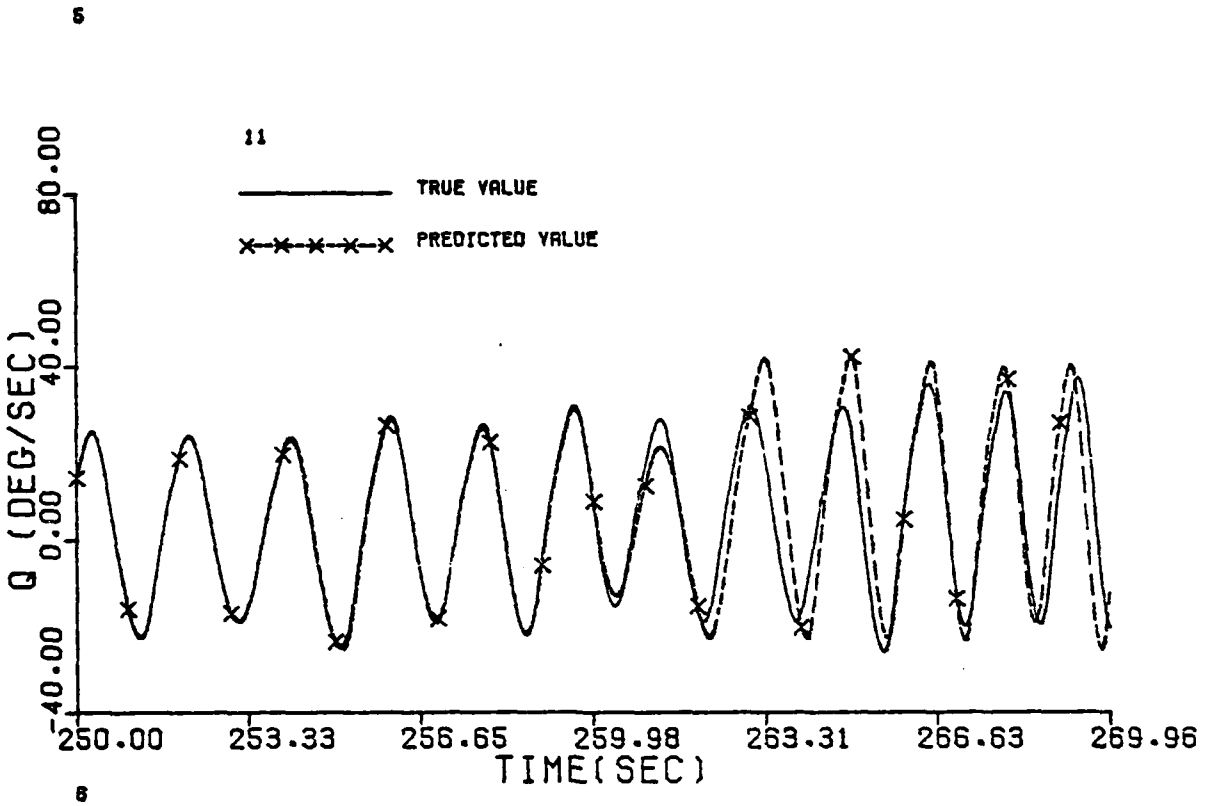

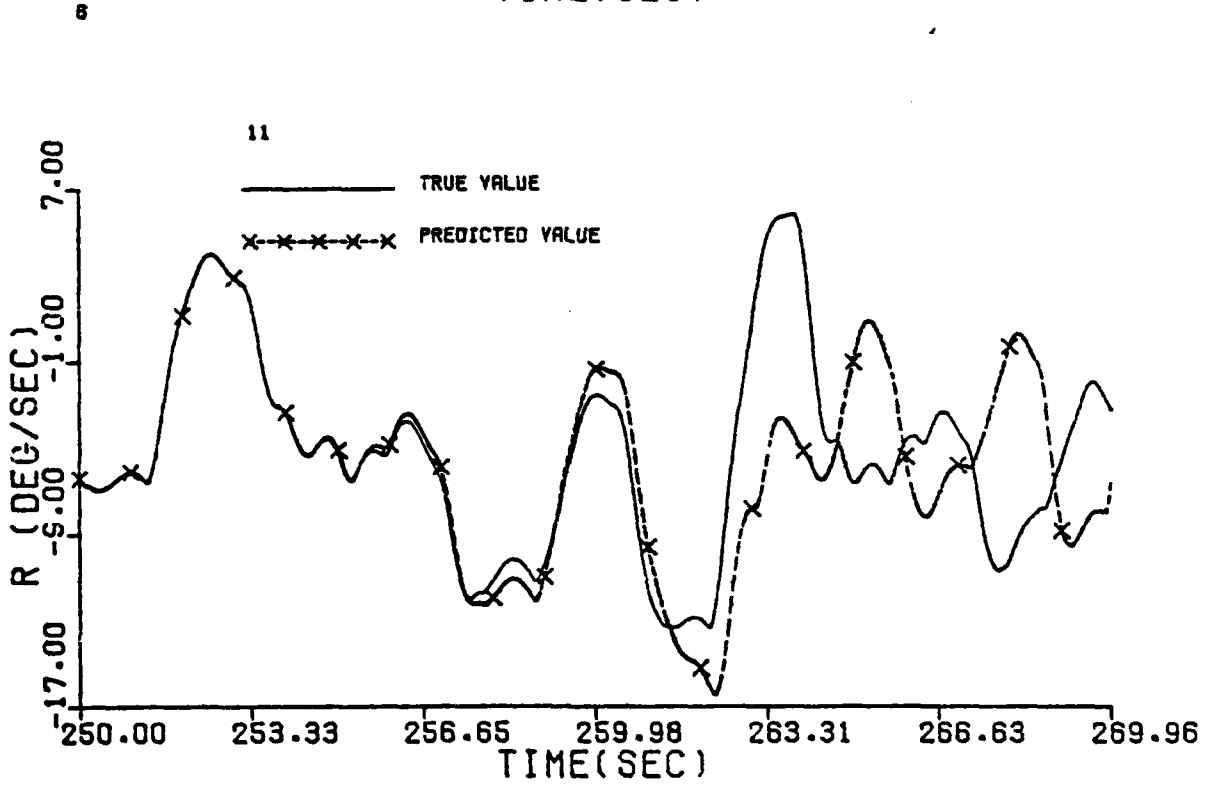

Figure G.2(d) Continued

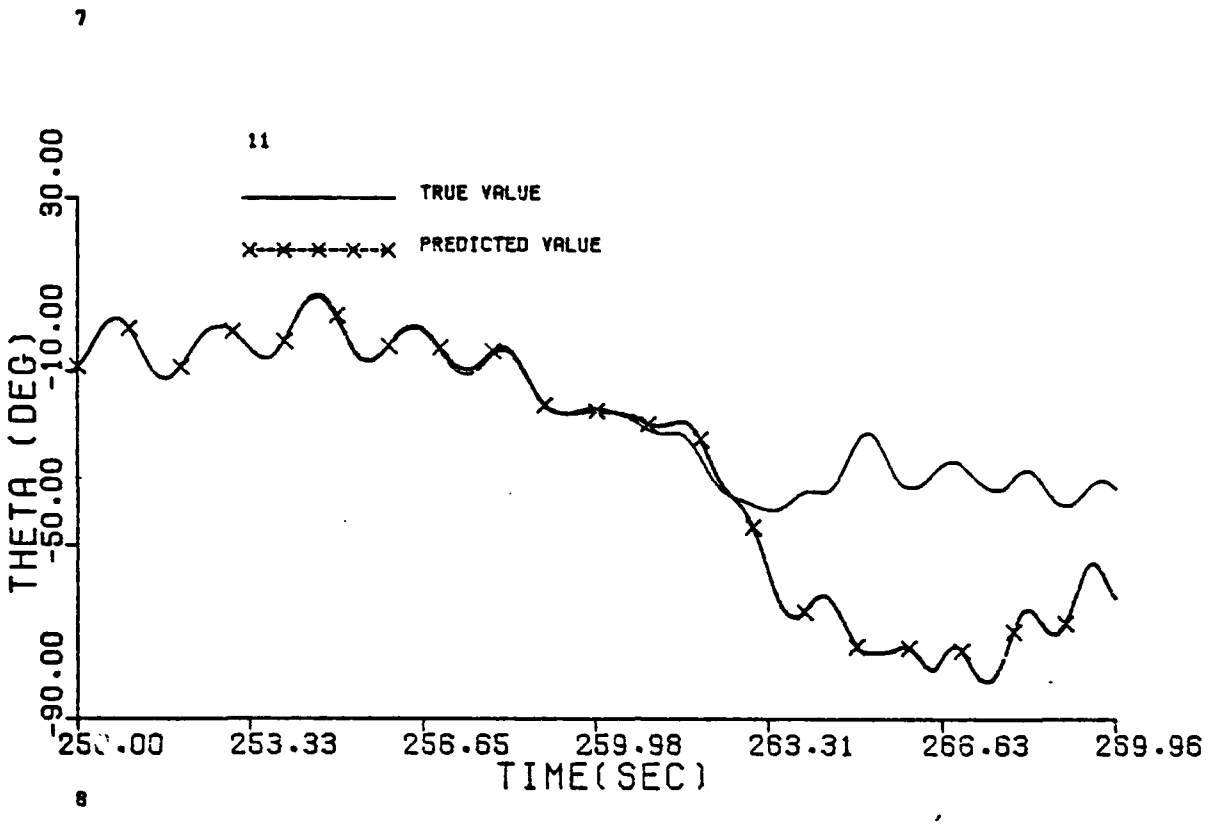

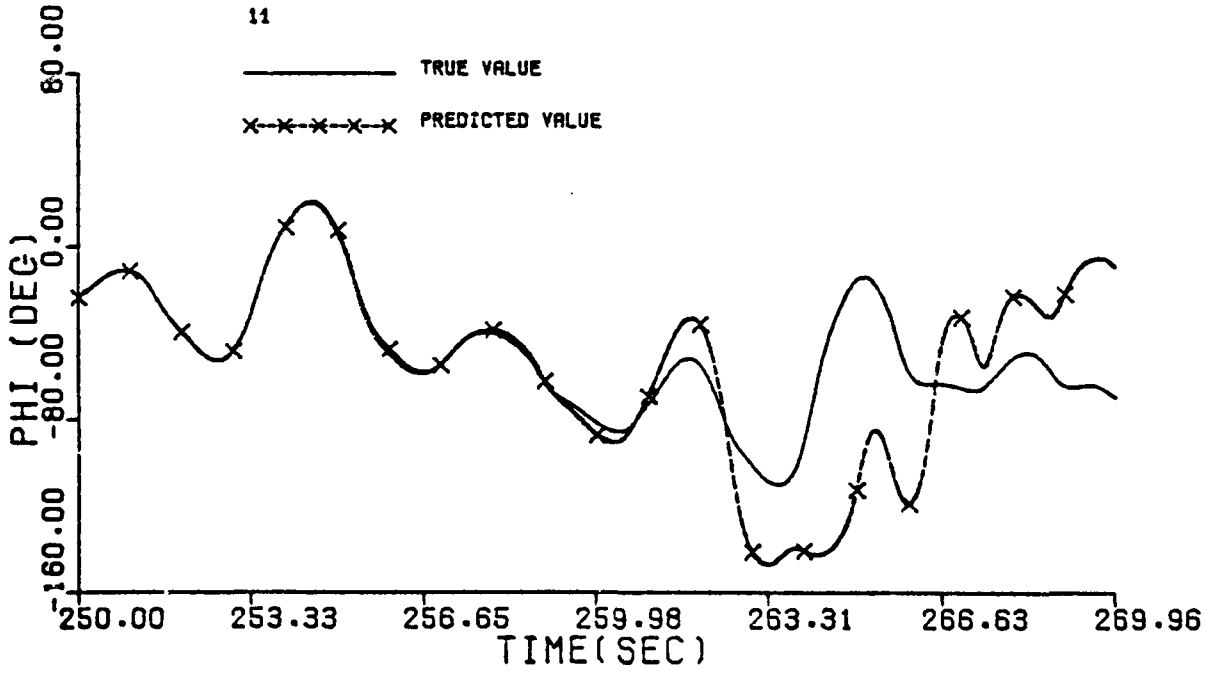

Figure G.2(d) Concluded